

AJNR

AMERICAN JOURNAL OF NEURORADIOLOGY

JULY 2015
VOLUME 36
NUMBER 7
WWW.AJNR.ORG

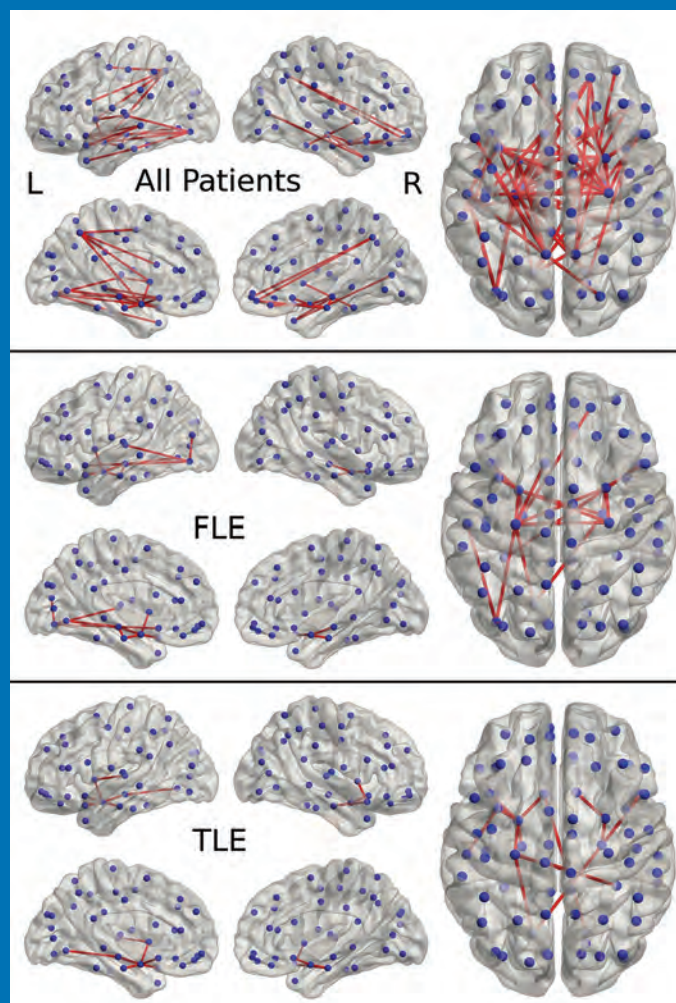
THE JOURNAL OF DIAGNOSTIC AND
INTERVENTIONAL NEURORADIOLOGY

Ultra-high-field MR neuroimaging

Prognosis of patients with glioblastoma
with dynamic MR

Spinal cord venous anastomoses by flat panel
catheter angiotomography

Official Journal ASNR • ASFNR • ASHNR • ASPNR • ASSR



Engineered

by MicroVention®



HYDROGEL ADVANCED COILS

The clinical benefits of **hydrogel** NOW engineered with the softness of bare platinum on the **V-Trak® Advanced Coil System**.

INDICATIONS FOR USE:

The HydroCoil® Embolic System (HES) is intended for the endovascular embolization of intracranial aneurysms and other neurovascular abnormalities such as arteriovenous malformations and arteriovenous fistulae. The HES is also intended for vascular occlusion of blood vessels within the neurovascular system to permanently obstruct blood flow to an aneurysm or other vascular malformation and for arterial and venous embolizations in the peripheral vasculature. The device should only be used by physicians who have undergone pre-clinical training in all aspects of HES procedures as prescribed by MicroVention.

MICROVENTION, V-Trak, HydroCoil, HydroFrame, HydroFill and HydroSoft are registered trademarks of MicroVention, Inc. Scientific and clinical data related to this document are on file at MicroVention, Inc. Refer to Instructions for Use, contraindications and warnings for additional information. Federal (USA) law restricts this device for sale by or on the order of a physician. © 2015 MicroVention, Inc. 6/15



Frame, Fill, Finish



HydroFrame[®]
HydroCoil[®] Embolic System



HydroFill[®]
HydroCoil[®] Embolic System



HydroSoft[®]
HydroCoil[®] Embolic System

- CLINICALLY STUDIED HYDROGEL
- EFFECTIVE^{1,2,3}
- ESTABLISHED SAFETY PROFILE⁴
- SOFTER DESIGN⁵

For more information or a product demonstration,
contact your local MicroVention representative:



MicroVention, Inc.

Worldwide Headquarters

1311 Valencia Avenue

Tustin, CA 92780 USA

MicroVention UK Limited

MicroVention Europe, S.A.R.L.

MicroVention Deutschland GmbH

microvention.com

PH +1.714.247.8000

PH +44 (0) 191 258 6777

PH +33 (1) 39 21 77 46

PH +49 211 210 798-0

References

1. Speirs, Burke, Lee, and Ala. The next generation HydroCoil: initial clinical experience with the HydroFill embolic coil. J NeuroIntervent Surg, 2013.
2. Brinjikiji et al. Abstract 112. Presented at: International Stroke Conference 2015, Nashville, Tennessee, February 11-13, 2015.
3. Lee, Seo, Less, Cho, Kang and Han. Mid-term outcome of intracranial aneurysms treated with HydroSoft coils compared to historical controls treated with bare platinum coils: a single-center experience. Acta Neurochir, 156:1687-1694, 2014.
4. Laymond et al. Patients prone to recurrence after endovascular treatment: periprocedural results of the PRET randomized trial on large and recurrent aneurysms, AJNR AM J Neuroradiol, 2014.
5. Data on file at MicroVention, Inc.



Penumbra System[®]

ACE[™]

64

Penumbra 

www.penumbrainc.com

AJNR

AMERICAN JOURNAL OF NEURORADIOLOGY

JULY 2015
VOLUME 36
NUMBER 7
WWW.AJNR.ORG

Publication Preview at www.ajnr.org features articles released in advance of print. Visit www.ajnrblog.org to comment on AJNR content and chat with colleagues and AJNR's News Digest at <http://ajnrndigest.org> to read the stories behind the latest research in neuroimaging.

PERSPECTIVES

1203 *J.S. Ross*

REVIEW ARTICLES

- 1204 **Ultra-High-Field MR Neuroimaging** *P. Balchandani and T.P. Naidich*
- 1216 **Mechanisms of Healing in Coiled Intracranial Aneurysms: A Review of the Literature** *W. Brinjikji, D.F. Kallmes, and R. Kadirvel*

SOCIAL MEDIA VIGNETTE

1223 **Social Media and Public Outreach: A Physician Primer** *A. Radmanesh, R. Duszak, and R.T. Fitzgerald*

PATIENT SAFETY

1225 **Imaging the Paranasal Region with a Third-Generation Dual-Source CT and the Effect of Tin Filtration on Image Quality and Radiation Dose** *M.M. Lell, M.S. May, M. Brand, A. Eller, T. Buder, E. Hofmann, M. Uder, and W. Wuest*

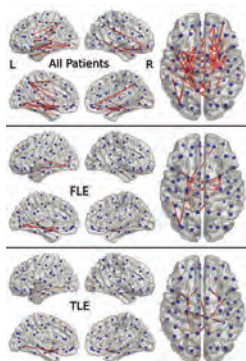
ADULT BRAIN

- 1231 **Arterial Spin-Labeling Parameters Influence Signal Variability and Estimated Regional Relative Cerebral Blood Flow in Normal Aging and Mild Cognitive Impairment: FAIR versus PICORE Techniques** *K.-O. Lövgren, M.-L. Montandon, M. Viallon, C. Rodriguez, S. Toma, X. Golay, P. Giannakopoulos, and S. Haller*
- 1237 **Use of Standardized Uptake Value Ratios Decreases Interreader Variability of [¹⁸F] Flortetapir PET Brain Scan Interpretation** *A.P. Nayate, J.G. Dubroff, J.E. Schmitt, I. Nasrallah, R. Kishore, D. Mankoff, and D.A. Pryma; for the Alzheimer's Disease Neuroimaging Initiative*

COMMENTARY

- 1245 **Establishing Amyloid PET Imaging Biomarkers: Ongoing Efforts** *S. Minoshima*
- 1247 **Prognostic Value of Dynamic Susceptibility Contrast-Enhanced and Diffusion-Weighted MR Imaging in Patients with Glioblastomas** *G. Çoban, S. Mohan, F. Kural, S. Wang, D.M. O'Rourke, and H. Poptani*
- 1253 **Chordoid Meningioma: Differentiating a Rare World Health Organization Grade II Tumor from Other Meningioma Histologic Subtypes Using MRI** *J.B. Pond, T.G. Morgan, K.J. Hatanpaa, Z.F. Yetkin, B.E. Mickey, and D.B. Mendelsohn*
- 1259 **Diffusion Tensor Imaging Mapping of Brain White Matter Pathology in Mitochondrial Optic Neuropathies** *D.N. Manners, G. Rizzo, C. La Morgia, C. Tonon, C. Testa, P. Barboni, E. Malucelli, M.L. Valentino, L. Caporali, D. Strobbe, V. Carelli, and R. Lodi*
- 1266 **Negative Susceptibility Vessel Sign and Underlying Intracranial Atherosclerotic Stenosis in Acute Middle Cerebral Artery Occlusion** *S.K. Kim, W. Yoon, T.W. Heo, M.S. Park, and H.K. Kang*

-  Indicates Editor's Choices selection
-  Indicates Fellows' Journal Club selection
-  Indicates open access to non-subscribers at www.ajnr.org
-  Indicates article with supplemental on-line table
-  Indicates article with supplemental on-line photo
-  Indicates article with supplemental on-line video
-  Indicates Evidence-Based Medicine Level 1
-  Indicates Evidence-Based Medicine Level 2



Disrupted global and regional structural networks in children with localization-related epilepsy.



Trevo[®] XP

PROVUE RETRIEVER

Take Control. Capture More.

The newly designed Trevo[®] XP ProVue Retriever takes proven Trevo Retriever performance to new levels for **easy delivery, easy placement, and easy visualization.**

When you're in control, it's amazing what you can capture.

stryker[®]
Neurovascular

-   **1272 Degree of Collaterals and Not Time Is the Determining Factor of Core Infarct Volume within 6 Hours of Stroke Onset** *E. Cheng-Ching, J.A. Frontera, S. Man, J. Aoki, Y. Tateishi, F.K. Hui, D. Wisco, P. Ruggieri, M.S. Hussain, and K. Uchino*
-  **1277 Whole-Brain Susceptibility-Weighted Thrombus Imaging in Stroke: Fragmented Thrombi Predict Worse Outcome** *P.P. Gratz, G. Schroth, J. Gralla, H.P. Mattle, U. Fischer, S. Jung, P. Mordasini, K. Hsieh, R.K. Verma, C. Weisstanner, and M. El-Koussy*
- 1283 Early MRI Characteristics after MRI-Guided Laser-Assisted Cingulotomy for Intractable Pain Control** *S.H. Sundararajan, P. Belani, S. Danish, and I. Keller*
- 1288 Intravenous Infusion of Nitroglycerine Leads to Increased Permeability on Dynamic Contrast-Enhanced MR Imaging in Pig Brains** *J. Carl, D.A. Tideman, S. Ravn, K. Lund, S.O. Magnisdottir, and B. Kjærgaard*

INTERVENTIONAL

-    **1293 Deconstructive and Reconstructive Techniques in Treatment of Vertebrobasilar Dissecting Aneurysms: A Systematic Review and Meta-Analysis** *Ö. Sönmez, W. Brinjikji, M.H. Murad, and G. Lanzino*
-  **1299 Endoluminal Reconstruction for Nonsaccular Aneurysms of the Proximal Posterior Cerebral Artery with the Pipeline Embolization Device** *D.W. Zumofen, M. Shapiro, T. Becske, E. Raz, M.B. Potts, H.A. Riina, and P.K. Nelson*
- 1303 Application of a Novel Brain Arteriovenous Malformation Endovascular Grading Scale for Transarterial Embolization** *D.L. Bell, T.M. Leslie-Mazwi, A.J. Yoo, J.D. Rabinov, W.E. Butler, J.E. Bell, and J.A. Hirsch*
- 1310 Narrowing the Expertise Gap for Predicting Intracranial Aneurysm Hemodynamics: Impact of Solver Numerics versus Mesh and Time-Step Resolution** *M.O. Khan, K. Valen-Sendstad, and D.A. Steinman*
- 1317 Endovascular Recanalization in Acute Ischemic Stroke Using the Solitaire FR Revascularization Device with Adjunctive C-Arm CT Imaging** *B.D. Mitchell, P. Chinnadurai, G. Chintalapani, H.A. Morsi, H. Shaltoni, and M.E. Mawad*

HEAD & NECK

-   **1321 Treatment of Benign Thyroid Nodules: Comparison of Surgery with Radiofrequency Ablation** *Y. Che, S. Jin, C. Shi, L. Wang, X. Zhang, Y. Li, and J.H. Baek*
- 1326 Intratympanic Contrast in the Evaluation of Menière Disease: Understanding the Limits** *J. Bykowski, J.P. Harris, M. Miller, J. Du, and M.F. Mafee*
- 1333 Visualization of the Peripheral Branches of the Mandibular Division of the Trigeminal Nerve on 3D Double-Echo Steady-State with Water Excitation Sequence** *H. Fujii, A. Fujita, A. Yang, H. Kanazawa, K. Buch, O. Sakai, and H. Sugimoto*
- 1338 Predicting the Prognosis of Oral Tongue Carcinoma Using a Simple Quantitative Measurement Based on Preoperative MR Imaging: Tumor Thickness versus Tumor Volume** *H. Hu, K.-L. Cheng, X.-Q. Xu, F.-Y. Wu, Y.-S. Tyan, C.-H. Tsai, and C.-Y. Shen*
-  **1343 Using Texture Analysis to Determine Human Papillomavirus Status of Oropharyngeal Squamous Cell Carcinomas on CT** *K. Buch, A. Fujita, B. Li, Y. Kawashima, M.M. Qureshi, and O. Sakai*
-  **1349 Direct Cranial Nerve Involvement by Gliomas: Case Series and Review of the Literature** *M.C. Mabray, C.M. Glastonbury, M.D. Mamlouk, G.E. Punch, D.A. Solomon, and S. Cha*
- 1355 Parry Romberg Syndrome: 7 Cases and Literature Review** *M. Wong, C.D. Phillips, M. Hagiwara, and D.R. Shatzkes*

PEDIATRICS

-     **1362 Disrupted Global and Regional Structural Networks and Subnetworks in Children with Localization-Related Epilepsy** *E. Widjaja, M. Zamyadi, C. Raybaud, O.C. Snead, S.M. Doesburg, and M.L. Smith*



American Society of Spine Radiology

2016 Annual Symposium • February 18-21, 2016

Hyatt Regency Coconut Point • Bonita Springs, FL

- Stillwater Spa with 18 treatment rooms, Watsu pool, and beauty salon
- Big Hickory Island Beach
- Spectacular waterfalls and pool features, as well as a spacious sundeck
- Family pool with 140-foot corkscrew water slide and hot tub, heated adult pool with hot tub, cold-plunge pool with waterfall
- 18-hole Raymond Floyd designed Raptor Bay golf course and club
- 24-hour Hyatt StayFit gym with cardio theater
- Bicycle and kayak rentals
- Dolphin watch eco-tours and sunset cruises
- Video arcade
- Har-Tru clay tennis courts
- Camp Hyatt®



A tropical paradise centrally located between Fort Myers and Naples, Florida in the upscale community of Bonita Springs. With stunning views of the Gulf Coast, Hyatt Regency Coconut Point Resort and Spa offers casual elegance and southern style hospitality, personalized service and attention to detail at every turn.



SAVE THE DATE

  **1369 Assessment of MRI-Based Automated Fetal Cerebral Cortical Folding Measures in Prediction of Gestational Age in the Third Trimester** J. Wu, S.P. Awate, D.J. Licht, C. Clouchoux, A.J. du Plessis, B.B. Avants, A. Vossough, J.C. Gee, and C. Limperopoulos

  **1375 Cranial Nerve Abnormalities in Oculo-Auriculo-Vertebral Spectrum** R. Manara, D. Brotto, S. Ghiselli, R. Mardari, I. Toldo, G. Schifano, E. Cantone, R. Bovo, and A. Martini

SPINE

 **1381 Transmedullary Venous Anastomoses: Anatomy and Angiographic Visualization Using Flat Panel Catheter Angiotomography** L. Gregg and P. Gailloud

1389 CELEBRATING 35 YEARS OF THE AJNR

BOOK REVIEWS R.M. Quencer, Section Editor

Please visit www.ajnrblog.org to read and comment on Book Reviews.



THE FOUNDATION OF THE ASNR 

**THE FOUNDATION OF THE ASNR SYMPOSIUM 2016:
EMERGENCY NEURORADIOLOGY
MAY 21-22**

**ASNR 54TH ANNUAL MEETING
MAY 23-26**



Howard A. Rowley, MD, ASNR 2016 Program Chair/President-Elect
Programming developed in cooperation with ...

American Society of Functional Neuroradiology (ASFNR)
Christopher G. Filippi, MD

American Society of Head and Neck Radiology (ASHNR)
Lindell R. Gentry, MD

American Society of Pediatric Neuroradiology (ASPNR)
Erin Simon Schwartz, MD

American Society of Spine Radiology (ASSR)
Gregory J. Lawler, MD

Society of NeuroInterventional Surgery (SNIS)
Charles J. Prestigiacomo, MD

American Society of Neuroradiology (ASNR) Health Policy Committee
Robert M. Barr, MD, FACR

Computer Science and Informatics (CSI) Committee
John L. Go, MD

Research Scientists Committee
Dikoma C. Shungu, PhD

ASNR 54TH ANNUAL MEETING
c/o American Society of Neuroradiology
800 Enterprise Drive, Suite 205
Oak Brook, Illinois 60523-4216
Phone: 630-574-0220
Fax: 630 574-0661
www.asnr.org/2016

**SCAN NOW
TO VISIT
OUR WEBSITE**



SAVE THE DATE... MAY 21-26, 2016
WASHINGTON MARRIOTT WARDMAN PARK • WASHINGTON DC

Official Journal:

American Society of Neuroradiology
 American Society of Functional Neuroradiology
 American Society of Head and Neck Radiology
 American Society of Pediatric Neuroradiology
 American Society of Spine Radiology

EDITOR-IN-CHIEF

Jeffrey S. Ross, MD

Staff Neuroradiologist, Barrow Neurological Institute, St. Joseph's Hospital, Phoenix, Arizona

SENIOR EDITORS

Harry J. Cloft, MD, PhD

Professor of Radiology and Neurosurgery, Department of Radiology, Mayo Clinic College of Medicine, Rochester, Minnesota

Thierry A.G.M. Huisman, MD

Professor of Radiology, Pediatrics, Neurology, and Neurosurgery, Chairman, Department of Imaging and Imaging Science, Johns Hopkins Bayview, Director, Pediatric Radiology and Pediatric Neuroradiology, Johns Hopkins Hospital, Baltimore, Maryland

C.D. Phillips, MD, FACR

Professor of Radiology, Weill Cornell Medical College, Director of Head and Neck Imaging, New York-Presbyterian Hospital, New York, New York

Pamela W. Schaefer, MD

Clinical Director of MRI and Associate Director of Neuroradiology, Massachusetts General Hospital, Boston, Massachusetts, Associate Professor, Radiology, Harvard Medical School, Cambridge, Massachusetts

Charles M. Strother, MD

Professor of Radiology, Emeritus, University of Wisconsin, Madison, Wisconsin

Jody Tanabe, MD

Professor of Radiology and Psychiatry, Chief of Neuroradiology, University of Colorado, Denver, Colorado

EDITORIAL BOARD

Ashley H. Aiken, *Atlanta, Georgia*
 A. James Barkovich, *San Francisco, California*
 Walter S. Bartynski, *Charleston, South Carolina*
 Barton F. Branstetter IV, *Pittsburgh, Pennsylvania*
 Jonathan L. Brisman, *Lake Success, New York*
 Julie Bykowski, *San Diego, California*
 Donald W. Chakeres, *Columbus, Ohio*
 Asim F. Choudhri, *Memphis, Tennessee*
 Alessandro Cianfoni, *Lugano, Switzerland*
 Colin Derdeyn, *St. Louis, Missouri*
 Rahul S. Desikan, *San Diego, California*
 Richard du Mesnil de Rochemont, *Frankfurt, Germany*
 Clifford J. Eskey, *Hanover, New Hampshire*
 Massimo Filippi, *Milan, Italy*
 David Fiorella, *Cleveland, Ohio*
 Allan J. Fox, *Toronto, Ontario, Canada*
 Christine M. Glastonbury, *San Francisco, California*
 John L. Go, *Los Angeles, California*
 Wan-Yuo Guo, *Taipei, Taiwan*
 Rakesh K. Gupta, *Lucknow, India*
 Lotfi Hacin-Bey, *Sacramento, California*
 David B. Hackney, *Boston, Massachusetts*
 Christopher P. Hess, *San Francisco, California*
 Andrei Holodny, *New York, New York*
 Benjamin Huang, *Chapel Hill, North Carolina*
 George J. Hunter, *Boston, Massachusetts*
 Mahesh V. Jayaraman, *Providence, Rhode Island*
 Valerie Jewells, *Chapel Hill, North Carolina*
 Timothy J. Kaufmann, *Rochester, Minnesota*
 Kenneth F. Layton, *Dallas, Texas*
 Ting-Yim Lee, *London, Ontario, Canada*
 Michael M. Lell, *Erlangen, Germany*
 Michael Lev, *Boston, Massachusetts*
 Karl-Olof Lovblad, *Geneva, Switzerland*
 Franklin A. Marden, *Chicago, Illinois*
 M. Gisele Matheus, *Charleston, South Carolina*
 Joseph C. McGowan, *Merion Station, Pennsylvania*
 Kevin R. Moore, *Salt Lake City, Utah*
 Christopher J. Moran, *St. Louis, Missouri*
 Takahisa Mori, *Kamakura City, Japan*
 Suresh Mukherji, *Ann Arbor, Michigan*
 Amanda Murphy, *Toronto, Ontario, Canada*
 Alexander J. Nemeth, *Chicago, Illinois*
 Laurent Pierot, *Reims, France*
 Jay J. Pillai, *Baltimore, Maryland*
 Whitney B. Pope, *Los Angeles, California*
 M. Judith Donovan Post, *Miami, Florida*
 Tina Young Poussaint, *Boston, Massachusetts*
 Joana Ramalho, *Lisbon, Portugal*

Otto Rapalino, *Boston, Massachusetts*
 Àlex Rovira-Cañellas, *Barcelona, Spain*
 Paul M. Ruggieri, *Cleveland, Ohio*
 Zoran Rumboldt, *Rijeka, Croatia*
 Amit M. Saindane, *Atlanta, Georgia*
 Erin Simon Schwartz, *Philadelphia, Pennsylvania*
 Aseem Sharma, *St. Louis, Missouri*
 J. Keith Smith, *Chapel Hill, North Carolina*
 Maria Vittoria Spampinato, *Charleston, South Carolina*
 Gordon K. Sze, *New Haven, Connecticut*
 Krishnamoorthy Thamburaj, *Hershey, Pennsylvania*
 Kent R. Thielen, *Rochester, Minnesota*
 Cheng Hong Toh, *Taipei, Taiwan*
 Thomas A. Tomsick, *Cincinnati, Ohio*
 Aquilla S. Turk, *Charleston, South Carolina*
 Willem Jan van Rooij, *Tilburg, Netherlands*
 Arastoo Vossough, *Philadelphia, Pennsylvania*
 Elysa Widjaja, *Toronto, Ontario, Canada*
 Max Wintermark, *Charlottesville, Virginia*
 Ronald L. Wolf, *Philadelphia, Pennsylvania*
 Kei Yamada, *Kyoto, Japan*

EDITORIAL FELLOW

Hillary R. Kelly, *Boston, Massachusetts*

SPECIAL CONSULTANTS TO THE EDITOR

AJNR Blog Editor

Neil Lall, *Denver, Colorado*

Case of the Month Editor

Nicholas Stence, *Aurora, Colorado*

Case of the Week Editors

Juan Pablo Cruz, *Santiago, Chile*

Sapna Rawal, *Toronto, Ontario, Canada*

Classic Case Editor

Sandy Cheng-Yu Chen, *Taipei, Taiwan*

Clinical Correlation Editor

Christine M. Glastonbury, *San Francisco, California*

Facebook Editor

Peter Yi Shen, *Sacramento, California*

Health Care and Socioeconomics Editor

Pina C. Sanelli, *New York, New York*

Physics Editor

Greg Zaharchuk, *Stanford, California*

Podcast Editor

Yvonne Lui, *New York, New York*

Twitter Editor

Ryan Fitzgerald, *Little Rock, Arkansas*

YOUNG PROFESSIONALS ADVISORY COMMITTEE

Asim K. Bag, *Birmingham, Alabama*

Anna E. Nidecker, *Sacramento, California*

Peter Yi Shen, *Sacramento, California*

Founding Editor

Juan M. Taveras

Editors Emeriti

Mauricio Castillo, Robert I. Grossman,

Michael S. Huckman, Robert M. Quencer

Managing Editor

Karen Halm

Electronic Publications Manager

Jason Gantenberg

Executive Director, ASNR

James B. Gantenberg

Director of Communications, ASNR

Angelo Artemakis

AJNR (Am J Neuroradiol ISSN 0195-6108) is a journal published monthly, owned and published by the American Society of Neuroradiology (ASNR), 800 Enterprise Drive, Suite 205, Oak Brook, IL 60523. Annual dues for the ASNR include \$170.00 for journal subscription. The journal is printed by Cadmus Journal Services, 5457 Twin Knolls Road, Suite 200, Columbia, MD 21045; Periodicals postage paid at Oak Brook, IL and additional mailing offices. Printed in the U.S.A. POSTMASTER: Please send address changes to American Journal of Neuroradiology, P.O. Box 3000, Denville, NJ 07834, U.S.A. Subscription rates: nonmember \$380 (\$450 foreign) print and online, \$305 online only; institutions \$440 (\$510 foreign) print and basic online, \$875 (\$940 foreign) print and extended online, \$365 online only (basic), extended online \$790; single copies are \$35 each (\$40 foreign). Indexed by PubMed/Medline, BIOSIS Previews, Current Contents (Clinical Medicine and Life Sciences), EMBASE, Google Scholar, HighWire Press, Q-Sensei, RefSeek, Science Citation Index, and SCI Expanded. Copyright © American Society of Neuroradiology.



49th Annual Meeting | American Society of

Head & Neck Radiology

Comprehensive Head and Neck Imaging

September 9 - 13, 2015

Naples Grande Beach Resort
Naples, Florida

27.5 AMA PRA Category 1 Credit(s)TM

Certain sessions of the meeting program
will be submitted for SAM qualification.

**Hands-on US and US-Guided Biopsy Seminar
Friday, September 11, 2015**

Separate Registration Required
Registration is Limited to 20 Attendees Per Session.

Not accredited for AMA PRA Category 1 Credit(s)TM

For More Information, visit www.ashnr.org



First described in 1751, NGC 2070, also called the Tarantula Nebula, is a large emission nebula in the Large Magellanic Cloud (LMC) in the southern constellation of Dorado. This image was remotely acquired from Australia using a 20" Planewave corrected Dall-Kirkham telescope, Planewave Ascension Mount, and FLI-09000 camera (3056 x 3056 with 12 micron pixels). It was shot with narrowband filters (H α , OIII, SII) using a series of 5-minute exposures with 3 hours total imaging time, and registered, stacked, and combined in PixInsight, with additional postprocessing in Photoshop. This image was formed using the Hubble palette, which assigns red to SII, green to H α , and blue to OIII.

Jeffrey S. Ross, Barrow Neurological Institute, Phoenix, Arizona

Ultra-High-Field MR Neuroimaging

P. Balchandani and T.P. Naidich



ABSTRACT

SUMMARY: At ultra-high magnetic fields, such as 7T, MR imaging can noninvasively visualize the brain in unprecedented detail and through enhanced contrast mechanisms. The increased SNR and enhanced contrast available at 7T enable higher resolution anatomic and vascular imaging. Greater spectral separation improves detection and characterization of metabolites in spectroscopic imaging. Enhanced blood oxygen level–dependent contrast affords higher resolution functional MR imaging. Ultra-high-field MR imaging also facilitates imaging of nonproton nuclei such as sodium and phosphorus. These improved imaging methods may be applied to detect subtle anatomic, functional, and metabolic abnormalities associated with a wide range of neurologic disorders, including epilepsy, brain tumors, multiple sclerosis, Alzheimer disease, and psychiatric conditions. At 7T, however, physical and hardware limitations cause conventional MR imaging pulse sequences to generate artifacts, requiring specialized pulse sequences and new hardware solutions to maximize the high-field gain in signal and contrast. Practical considerations for ultra-high-field MR imaging include cost, siting, and patient experience.

ABBREVIATIONS: B_0 = magnetic field; B_1 = radiofrequency field; BOLD = blood oxygen level–dependent; CT-PRESS = constant time point-resolved spectroscopic sequence; ITSS = intratumoral susceptibility signal; MRSI = MR spectroscopic imaging; RF = radiofrequency; SAR = specific absorption rate; WHO = World Health Organization

From the initial grainy images of the human brain obtained in the late 1970s,¹ MR imaging has progressed to provide exquisite images of brain anatomy and function and metabolic composition, making MR imaging integral to nearly all current neurologic evaluations.² Two major determinants of MR image quality, SNR and contrast, both increase with field strength (Table).^{3,4} Therefore, MR imaging scanners operating at field strengths of 7T (and up to 11.7T) have the potential to improve lesion detection, enhance lesion characterization, improve treatment planning, and help elucidate the mechanisms underlying disease. This review addresses the advantages and limitations of ultra-high-field MR imaging and MR spectroscopy and discusses some of the major clinical applications to the brain. Physical and technical challenges of high-field MR imaging and some current solutions to

these challenges are outlined, as are practical aspects of placing an ultra-high-field scanner in an imaging facility.

Improved Visualization of the Brain at 7T

Structural Imaging. Because SNR scales with field strength (Table),^{4,5} 7T MR imaging provides higher resolution images within reasonable scanning times, compared with lower field studies.^{6–13} At 7T, therefore, MR imaging displays finer anatomic detail, increases lesion conspicuity, and more accurately characterizes brain abnormalities. Figure 1, for example, illustrates 7T axial and coronal-oblique turbo spin-echo images of the hippocampus obtained from healthy volunteers at 450- μ m in-plane resolution and 2-mm section thickness.

Vascular and Functional Imaging. Increasing the field strength provides opportunities for novel MR imaging contrast mechanisms, including improved susceptibility, blood oxygen level–dependent (BOLD) and flow-dependent contrast. MR imaging sensitivity to susceptibility effects scales with field strength (Table), making it possible to more effectively depict venous microvasculature, microbleeds, and iron and calcium deposits through susceptibility-weighted imaging.¹⁴ Figure 2 illustrates a MIP of an SWI obtained at 7T.

The increased T2*dephasing due to deoxygenated blood should enhance BOLD contrast, permitting higher resolution functional MR imaging.¹⁵ Furthermore, the component of the

From the Translational and Molecular Imaging Institute (P.B.) and Department of Radiology (P.B., T.P.N.), Icahn School of Medicine at Mount Sinai, New York, New York.

This work was funded by the National Institutes of Health/National Institute of Neurological Disorders and Stroke grant R00 NS070821; Icahn School of Medicine Capital Campaign, Translational and Molecular Imaging Institute, and Department of Radiology, Icahn School of Medicine at Mount Sinai; and Siemens Healthcare.

Please address correspondence to Priti Balchandani, PhD, Translational and Molecular Imaging Institute, Icahn School of Medicine at Mount Sinai, 1470 Madison Ave, New York, NY 10029; e-mail: priti.balchandani@mssm.edu

Indicates open access to non-subscribers at www.ajnr.org

<http://dx.doi.org/10.3174/ajnr.A4180>

Relationship of imaging parameters and main magnetic field strength

Imaging Property	Relationship with Main Magnetic Field Strength	Observed Trend in Practice
SNR	$SNR \propto B_0$	SNR increases linearly with B_0 ; however, a linear increase may not be achievable in the presence of inhomogeneity and changing tissue relaxation ^{4,5}
Resolution	Resolution $\propto n^{0.33}$ When B_0 is increased by a factor of n	In practice, further increases in resolution may be achieved because of improvements in detector and gradient design and enhanced contrast-to-noise ratio for some types of imaging sequences acting in conjunction with increased field strength
T1 (in sec)	$T1 = 1/(0.35 + 0.64 \times B_0^{-0.7})$	This is a heuristic approximation (in SI units) for cortical gray matter ⁴ ; generally T1 values for different tissues lengthen and converge with field strength
T2* (in sec)	$T2^* = 1/(7 + 3.5 \times B_0)$	This is a heuristic approximation (in SI units) for cortical gray matter ^{4,97,98}
Apparent T2	Decrease with B_0	Theoretically, field strength has little effect on the spin-spin relaxation governing intrinsic T2 ⁹⁹ ; however, due to effects such as spins diffusing through susceptibility microgradients, apparent T2 shortens for some spin-echo sequences ^{98,100,101}
Sensitivity to susceptibility	$\Delta\phi \propto B_0 \times TE$	In practice, higher B_0 enables the use of shorter TEs to maintain the same phase effect; coupled with higher SNR, this results in improved resolution and speed
Spectral resolution in MRSI	$\Delta F \propto B_0$	Although the separation of spectral peaks increases with field strength, increased B_0 inhomogeneity within a voxel will cause broadening of peaks, counteracting this benefit; better shimming and smaller voxel volumes are required to prevent peak broadening
CSL error	CSL $\propto B_0 \times$ section thickness/ (RF bandwidth)	In MRSI, this results in substantial shifts in selected volumes for metabolites resonating at different frequencies; high bandwidth RF pulses, such as adiabatic pulses can mitigate CSL error

Note:— $\Delta\phi$ indicates the phase difference between 2 tissues; ΔF , frequency separation between metabolite peaks; CSL, chemical shift localization; SI, International System of Units.

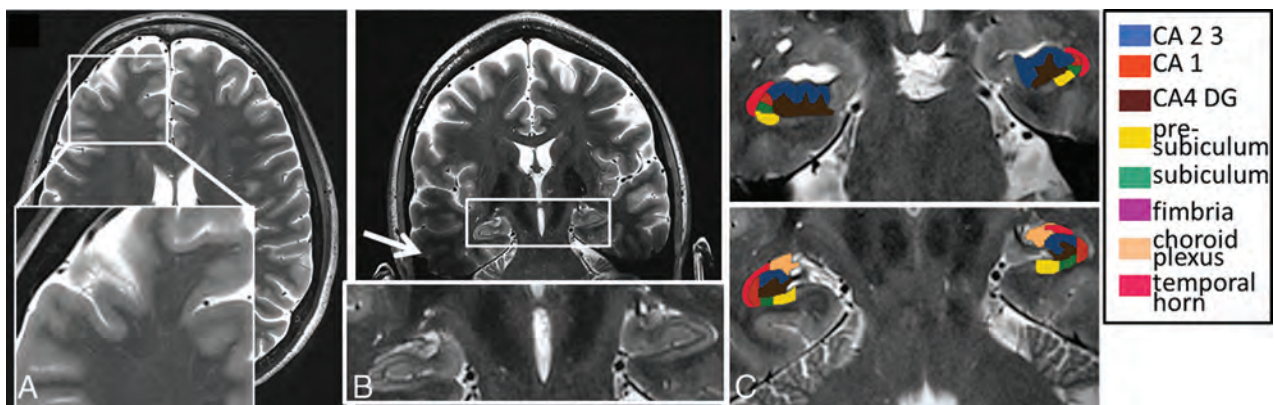


FIG 1. High-resolution axial (A) and coronal oblique (B) images of the brain obtained at 7T. The 450- μm in-plane resolution enables visualization of the hippocampus in fine detail. C, Effective hippocampal subfield segmentation may be performed on a 7T TSE image. Subfields were manually traced courtesy of Dr Jason Bini on high-resolution coronal TSE images on OsiriX Image Viewing Software (<http://www.osirix-viewer.com>) by using the segmentation work by Van Leemput et al¹⁰² as a guide. Scanner: whole-body 7T MR imaging (Magnetom; Siemens). RF coil: Nova 32-channel head coil (Nova Medical, Wilmington, Massachusetts). Scan parameters: number of sections = 25, section thickness = 2 mm, FOV = 23 cm, grid size = 512 \times 512, resolution = 0.44 \times 0.44 \times 2 mm³, scanning time = 6 minutes and 30 seconds.

BOLD signal that arises from smaller blood vessels also scales with field strength, so the BOLD signal has better spatial correlation to oxygen extraction and is more tightly coupled to the underlying neuronal activity.^{16,17}

The T1 values of tissue increase with field strength (Table). At 7T, the higher SNR and longer T1 values for tissue enhance suppression of static background signal in TOF angiography, increasing overall contrast and the detectability of smaller arteries.¹⁸ Figure 3 shows a TOF image obtained at 7T depicting the multiple arterial branches arising from the anterior and middle cerebral trunks.

MR Spectroscopic Imaging. The chemical shift differences among metabolite resonances are directly proportional to field strength

(Table). The combination of increased SNR and increased spectral separation of metabolite peaks results in higher resolution spectroscopic images and improved spectral quantification.⁵ Figure 4 shows a spectrum obtained at 7T with a constant time point-resolved spectroscopic (CT-PRESS) pulse sequence described by Mayer and Spielman.¹⁹ Greater numbers of metabolites become detectable as SNR and peak separation increase.

DTI. The increased SNR at 7T, coupled with improved receiver coils, has been shown to increase the certainty and accuracy of determining DTI-based parameters such as fractional anisotropy, compared with 3T and 1.5T.²⁰ Figure 5 illustrates streamlines generated from diffusion-weighted data obtained on a

7T whole-body MR imaging scanner (Magnetom; Siemens, Erlangen, Germany) by using an optimized Stejskal-Tanner sequence.²¹ A readout-segmented EPI method proposed by Heide-mann et al²² was used to overcome issues such as magnetic field (B_0) inhomogeneity. Unfortunately, for such an acquisition, total scanning time is impractically long (75 minutes), so new approaches, such as multiband excitations, are being explored to obtain these types of results within reasonable scanning times.^{23,24}

Multinuclear Imaging. Greater SNR provides a signal boost to nuclei other than protons, such as sodium-23 (^{23}Na) and phosphorus-31 (^{31}P), which provide a means of probing important cell processes, different metabolic pathways, and new relaxation mechanisms.²⁵⁻³⁴ Figure 6 illustrates a high-resolution ^{23}Na image obtained at 7T using a 3D attenuation-adapted projection reconstruction method described in Nagel et al.²⁶ The signal from sodium ^{23}Na is 30,000 times lower than the signal from protons, due to the smaller gyromagnetic ratio of sodium, lower concentration in biologic tissue, and rapid biexponential decay.³⁵ Nevertheless, the increased SNR available at 7T enables imaging at a resolution that depicts main anatomic features in the brain, even in the SNR-starved regime of the

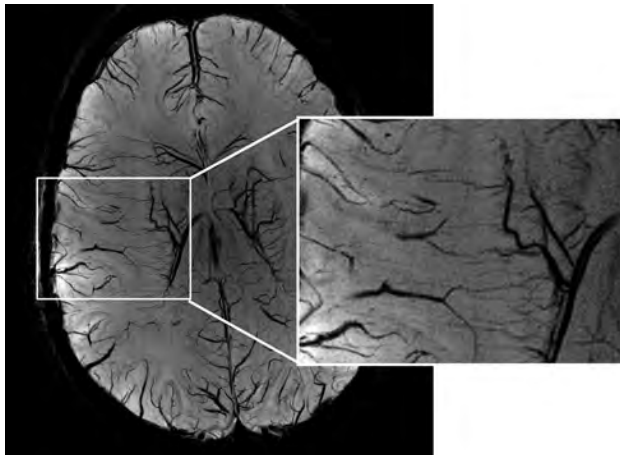


FIG 2. MIP of a 7T susceptibility-weighted image of the brain of a healthy volunteer revealing tiny venules in the cortex. Scanner: whole-body 7T MR imaging (Magnetom; Siemens). RF coil: Nova 32-channel head coil. Scan parameters: resolution = $0.2 \times 0.2 \times 1.5 \text{ mm}^3$, MIP thickness = 12 mm over the set of sections, scanning time = 6 minutes and 2 seconds.

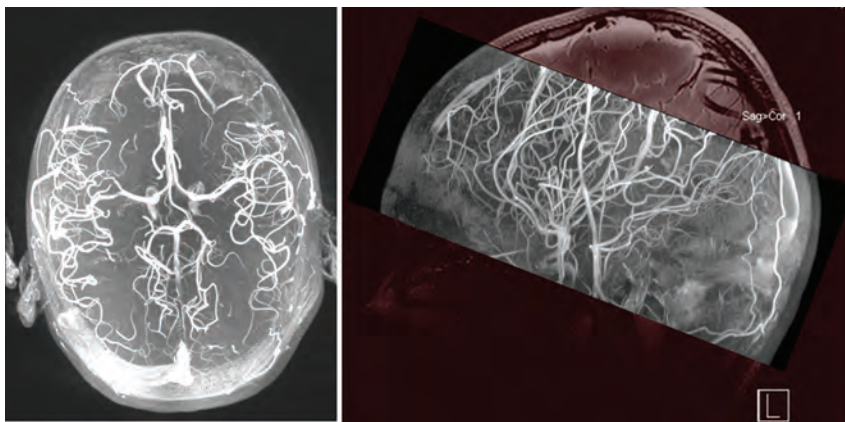


FIG 3. Time-of-flight angiography performed on a healthy volunteer at 7T. Axial and sagittal MIP of TOF images are shown. Scanner: whole-body 7T MR imaging (Magnetom; Siemens). RF coil: Nova 32-channel head coil. Scan parameters: resolution = $0.26 \times 0.26 \times 0.4 \text{ mm}^3$, scan time = 7 minutes and 56 seconds.

sodium nucleus. More recently, chlorine-35 (^{35}Cl), a nucleus that exhibits even lower MR imaging sensitivity than ^{23}Na , has been imaged within clinically feasible scanning times.²⁷ Early work indicates that ^{35}Cl imaging may reveal pathophysiologic changes associated with loss of chloride homeostasis.²⁷

Clinical Applications of 7T in Neuroradiology

High-resolution 7T imaging may now be used to improve the detection and characterization of abnormalities associated with a wide range of neurologic disorders, including epilepsy, brain tumors, multiple sclerosis, Alzheimer disease/dementia, and neuropsychiatric disorders.^{9,10,12,36-42}

Epilepsy. The improved resolution and novel contrast mechanisms available at 7T show structural and biochemical abnormalities in greater detail to delineate seizure foci, aid in surgical planning, and improve patient outcome. 7T detection of abnormalities not visible at 3T may obviate invasive evaluation through depth electrodes or provide the data needed to establish concordance with invasive evaluations. 7T MR imaging has already shown value for characterizing hippocampal sclerosis,^{38,42} cortical dysplasias,⁴³ and vascular malformations⁴⁴ associated with epilepsy. Figure 7A compares 3T and 7T FSE images in a patient with epilepsy with subtle left hippocampal abnormalities. Figure 7B shows the benefit of 7T imaging in a second patient with mesial temporal lobe epilepsy.

Brain Tumors. Ultra-high-field MR imaging may be applied in different ways to better visualize brain tumor pathology. Superior image quality and enhanced sensitivity to susceptibility have been leveraged at 8T to depict the neovasculature in a high-grade glioma.⁴⁰ ^1H -MR spectroscopic imaging (MRSI) at 7T has been shown to provide a benefit for measuring metabolic markers of tumor tissue, such as choline and *N*-acetylaspartate, with increased spectral and spatial resolution compared with 3T.⁴⁵

Sodium MR imaging greatly benefits from the increased SNR available at 7T. Sodium signal has been shown to increase in brain tumors.⁴⁶⁻⁴⁸ This signal increase is caused by the cellular energetic breakdown of Na^+ /potassium⁺-adenosine triphosphatase, by sustained cell depolarization initiating cell division and by increased extracellular space. Thus, the total sodium signal probes several aspects of tissue viability.²⁹ 7T ^{23}Na MR imaging using optimized pulse sequences has been performed in patients with brain tumors (14 World Health Organization [WHO] grades I-IV and 2 metastases).²⁵ Figure 8 shows total sodium (^{23}NaT) images (A-C) and relaxation-weighted (^{23}NaR) sodium images (D-F) of a glioblastoma (WHO grade IV) of the left mesial frontal lobe. The 2 pulse sequences used for these images are given in Nagel et al.²⁵

Total sodium images and relaxation-weighted sodium images provide complementary data. In particular, ^{23}NaT images provide a volume-weighted average of the intra- and extracellular sodium concentration, while the ^{23}NaR images provide

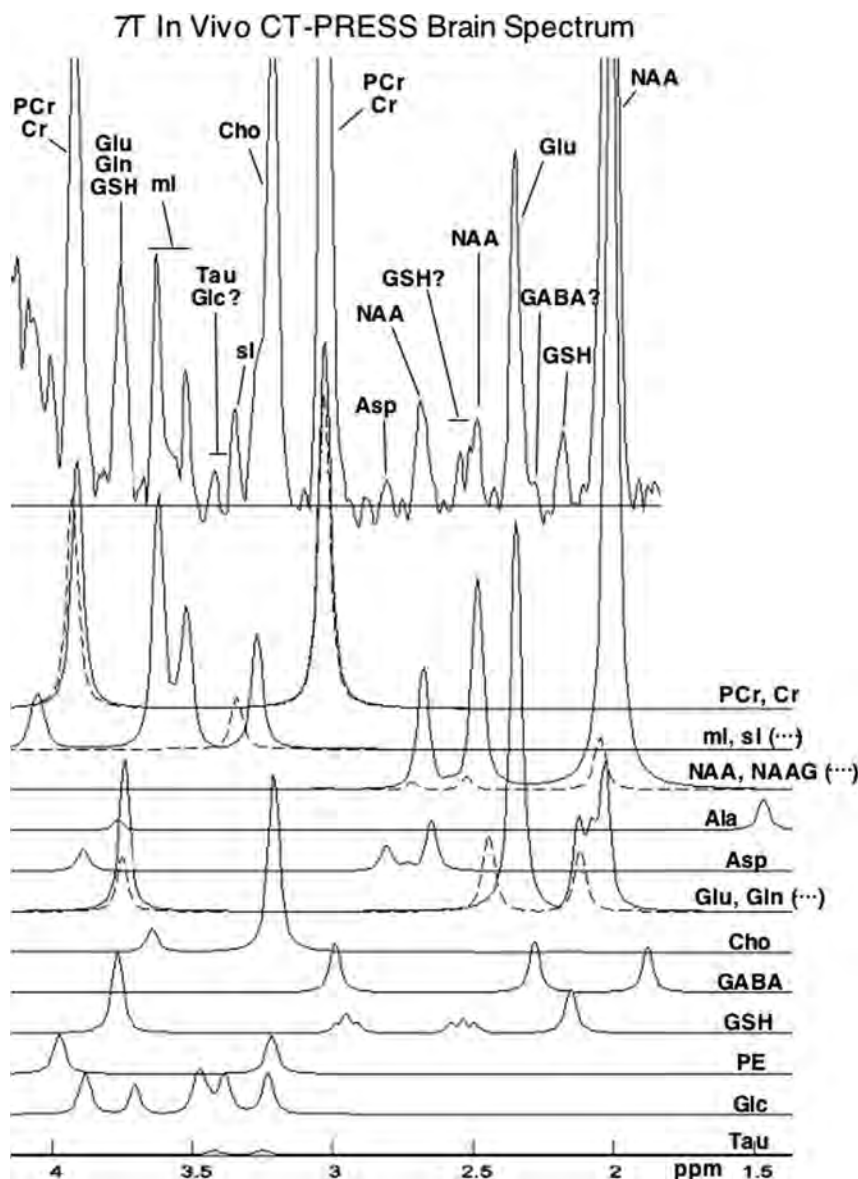


FIG 4. In vivo brain spectra acquired on a healthy volunteer by using a CT-PRESS sequence at 7T. Spectrum is courtesy of Drs Dirk Mayer and Daniel Spielman, Stanford University, Stanford, California. Plotted below the in vivo data are simulated spectra of individual metabolites, as generated by the CT-PRESS acquisitions.¹⁰³ Metabolites shown are: phosphocreatine (PCr), creatine (Cr), myo-inositol (ml), scyllo-inositol (sl), *N*-acetylaspartate (NAA), *N*-acetyl aspartylglutamate (NAAG), alanine (Ala), aspartate (Asp), glutamate (Glu), glutamine (Gln), Choline (Cho), gamma-aminobutyric acid (GABA), glutathione (GSH), phosphoethanolamine (PE), glucose (Glc), taurine (Tau). Scanner: 7T whole-body scanner (MR950; GE Healthcare, Milwaukee, Wisconsin). RF coil: Nova head coil. Scan parameters: resolution = $2 \times 2 \times 2 \text{ cm}^3$; voxel centrally located in the supertentorial brain, scanning time = 5 minutes.

signal from a compartment defined by ^{23}Na relaxation properties rather than intra- or extracellular histologic compartments. Nagel et al²⁵ found that total sodium was elevated in all tumor types. However, the relaxation-weighted sodium signal was elevated only in glioblastomas, not in WHO grades I–III tumors. ^{23}NaR , therefore, provides a noninvasive method for correct MR imaging distinction between WHO grade IV gliomas and WHO grades I–III tumors. In Figure 8, the total sodium signal is elevated in the entire tumor, while the relaxation-weighted signal increase is localized to the central tumor portion, consistent with the influx of ^{23}Na into cells in that region.

with venular dilation, and chronic lesions, with venular pruning and loss.⁵⁴ Any vascular pathology associated with MS lesions may be assessed in vivo through highly sensitive T2* and susceptibility-weighted imaging at 7T.^{55,56} SWI at ultra-high fields also allows very effective depiction of the tiny venules within plaques in the cortex as shown in the image obtained at 7T from a patient with MS in Fig 10.

Alzheimer Disease. One early pathologic change in Alzheimer disease is neuronal loss in specific subfields of the hippocampus.⁵⁷ High-resolution hippocampal imaging at 7T has been proposed

Another MR imaging parameter, intratumoral susceptibility signals (ITSSs), correlates with tumor malignancy and may contribute to a grading system for gliomas.^{49,50} Park et al⁵⁰ showed that the Spearman correlation coefficients between ITSS degree and glioma grade were 0.88 (95% CI, 0.79–0.94). Microvascular proliferation is a primary feature of glioblastoma, often resulting in microhemorrhages. These act as the source of ITSS within these lesions. Hemorrhage is an uncommon feature of B-cell primary CNS lymphoma, resulting in little-to-no ITSS within these lesions.⁵¹ Therefore, in addition to helping to grade gliomas, ITSS is useful for differentiating glioblastoma and primary CNS lymphoma.⁵¹ Because 7T MR imaging enhances sensitivity to susceptibility effects, 7T offers improved contrast and more detailed assessment of ITSS. Figure 9 shows TSE imaging and SWI acquired at 3T and 7T for a patient with a histopathologically confirmed left temporal glioblastoma. The MR imaging was performed before neurosurgery or any other treatment. ITSSs are more apparent and better resolved in the 7T SWI. The structural appearance of the tumor may be assessed in fine detail in Fig 9A.

Multiple Sclerosis. 7T MR imaging has particular utility for visualizing the pathologic features of MS. The addition of 7T anatomic scans to clinical 3T imaging protocols improves classification of lesions at the cortical boundary⁵² and improves the detection and display of gray matter lesions.¹⁰ Local field shift maps that are sensitive to susceptibility differences in tissue have been used to quantify the pathologic increase in iron concentration in the basal ganglia of patients with MS versus controls.⁵³ This method has also been used to detect iron-rich macrophages at the periphery of MS plaques.⁵³ Early active MS lesions may be associated

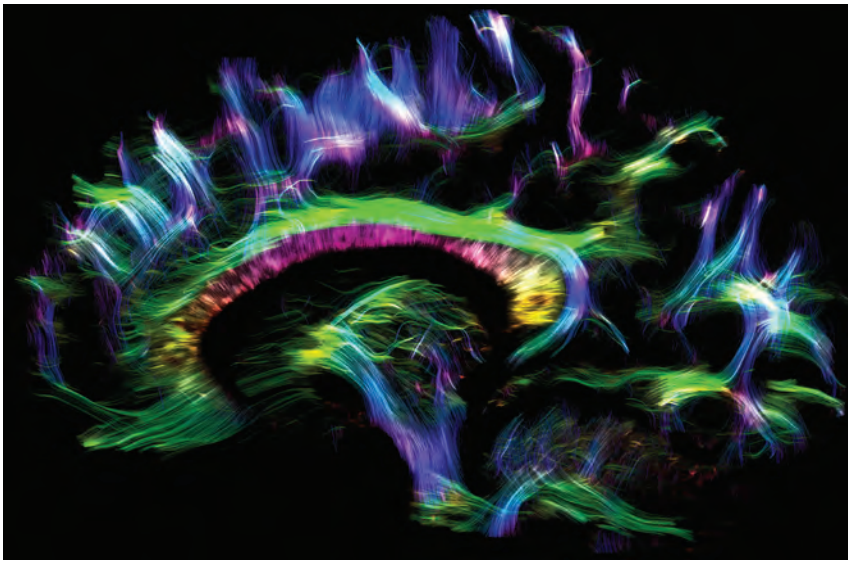


FIG 5. Tractography performed by using diffusion imaging at 7T with readout-segmented EPI and parallel imaging. Image courtesy of Dr Robin Heidemann, Max Planck Institute for Human Cognitive and Brain Sciences, Leipzig, Germany. Scanner: whole-body 7T MR imaging (Magnetom; Siemens). RF coil: Nova 24-channel head coil. Scan parameters: b-value of 1000 s/mm², resolution = 1 × 1 × 1 mm³, 30 diffusion directions, generalized autocalibrating partially parallel acquisition acceleration factor = 3, TE/TR = 60/11,000 ms, scanning time = 75 minutes.

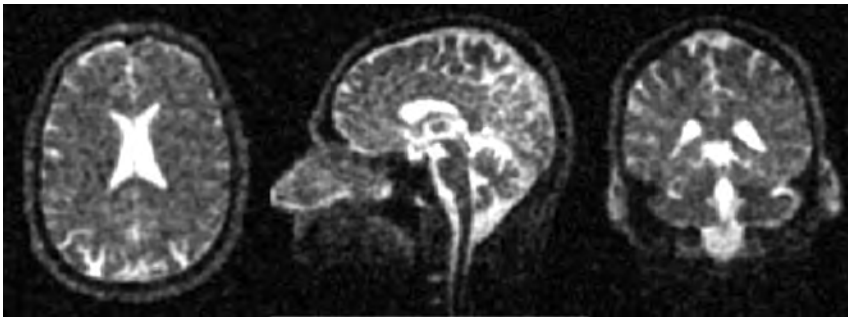


FIG 6. Sodium brain image of a healthy volunteer obtained at 7T using a 3D attenuation-adapted projection reconstruction. Images courtesy of Dr Armin Nagel, the German Cancer Research Center, Heidelberg, Germany. Scanner: whole-body 7T MR imaging (Magnetom; Siemens). RF coil: double-resonant (¹H = 297.2 MHz; ²³Na = 78.6 MHz) quadrature birdcage coil (Rapid Biomed, Rimpf, Germany). Scan parameters: resolution = 2 × 2 × 2 mm³, scanning time = 20 minutes.

as an effective tool for revealing these changes.⁹ 7T MR imaging has already shown differences in the cornu ammonis 1 hippocampal subfield of patients with mild Alzheimer disease compared with controls.³⁵ Figure 11 illustrates 7T images of the left hippocampus of age-matched healthy individuals (A) versus those with amnesic mild cognitive impairment (B) and probable Alzheimer disease (C). With increasing disease severity, the stratum radiatum/lacunosum-moleculare (thin apical dark band of tissue) becomes thinner, the dentate gyrus/CA3 region becomes greatly diminished in size, and the entire hippocampus shrinks in relation to the surrounding CSF.

Ultra-high-field MR imaging is also being used to investigate the possible increase in tissue iron associated with early-stage amyloid pathology. The cerebral cortex of patients with Alzheimer disease was studied by 7T T2*-weighted imaging to calculate the relative phase shift, a parameter that is sensitive to iron content. This study revealed increased phase shift within the cortex of patients with Alzheimer disease versus controls.⁵⁸ Therefore, relative phase shift, measured

through 7T T2*-weighted imaging, may serve as a potential early imaging marker for Alzheimer disease.

Psychiatric Illness. The etiology of mood and anxiety disorders such as major depressive disorder remains poorly understood.⁵⁹ Study results have been divergent, with no clear consensus on proper neuroimaging markers for these conditions.^{2,60} However, it is known that the medial prefrontal cortex and temporolimbic structures, including the hippocampus and amygdala, are critical nodes in major depression.^{57,61-63} Furthermore, high-spatial-resolution MR imaging at 4.7T and 7T successfully differentiates among hippocampal subfields and should, therefore, provide a more sensitive marker for psychiatric disease than does total hippocampal volume.^{12,13,64} Huang et al⁶⁵ have already conducted high-field (4.7T) hippocampal subfield analysis in a group of patients with major depressive disorder, showing volume reductions in the cornu ammonis 1-3 and dentate gyrus hippocampal subfields and the posterior hippocampal body and tail for unmedicated patients with major depressive disorder versus controls. Further comprehensive high-field studies combining high-resolution anatomic scans with DTI and ¹H-MRSI should help in detecting morphologic abnormalities, disruptions in connectivity,⁶⁶ and reduced glial and neuronal cell attenuation⁶⁷⁻⁶⁹ associated with psychiatric disorders.

Technical and Physical Limitations

The present use of ultra-high-field MR imaging is limited by technical and patient concerns. The technical issues include inhomogeneity of both the main magnetic field and the applied radiofrequency (RF) field (B₁), errors in chemical shift localization, and increased deposition of RF power within the patient. These cause image artifacts, limit section number/spatial coverage, and limit the use of MR spectroscopy.

B₀ Inhomogeneity. B₀ inhomogeneity directly scales with field strength (Table). In MR imaging, this results in distortion of both the geometry and the intensity of images. Single- or few-shot rapid acquisition schemes such as echo-planar imaging or spiral imaging are particularly susceptible to geometric distortions due to susceptibility effects. In MR spectroscopy, B₀ changes among voxels manifest as spectral shifts for the metabolite peaks. As a result, frequency-selective pulses that are designed to operate on particular spectral bands are less effective. Water and lipid suppression techniques become less effective. The varying B₀ field

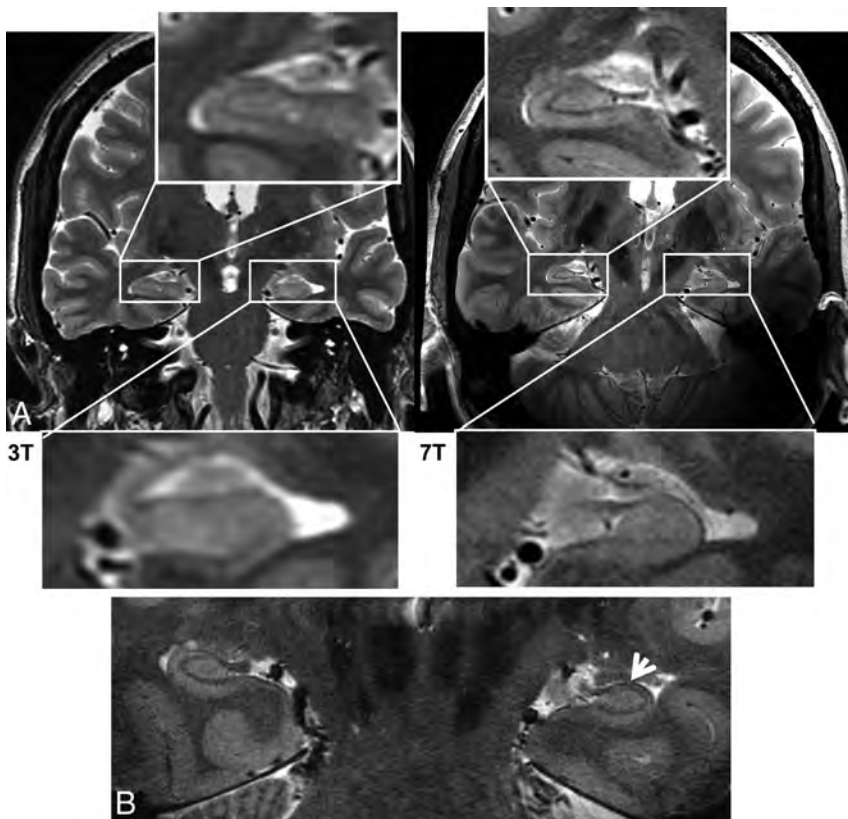


FIG 7. A, 3T and 7T coronal FSE images obtained for a patient with mesial temporal lobe epilepsy. Subtle left hippocampal abnormalities are visualized in greater detail in the 7T image. B, In a second patient with mesial temporal lobe epilepsy, loss of gray matter in the left hippocampus is detected at 7T (white arrow), after no abnormalities were reported at 3T. Images are courtesy of Drs Michael Zeineh, Manoj Saranathan, and Brian Rutt, Stanford University, Stanford, California. Scanners: whole-body 3T and 7T MR imaging (MR950; GE Healthcare). RF coils: standard 3T head coil (GE Healthcare) and Nova 7T head coil. Scan parameters: section thickness = 2 mm, resolution = $0.22 \times 0.22 \times 2 \text{ mm}^3$, scanning time = 10 minutes.

within a voxel broadens the metabolite peaks, reduces the SNR, and increases peak overlap. To combat this effect, robust referencing schemes, advanced B_0 shimming, and decreased voxel volumes are required.

B_1 Inhomogeneity. One of the most difficult problems to overcome at high magnetic fields is the severe B_1 inhomogeneity over the volume of interest. As the B_0 field increases to 7T, the RF operating wavelength becomes comparable with the diameter of the human head, resulting in a severe reduction of B_1 strength in the brain periphery compared with the isocenter.⁷⁰ This ultimately leads to signal drop-out and unexpected changes in contrast. Standard pulse sequences using conventional RF pulses for excitation and refocusing are very susceptible to changes in B_1 , resulting in spatially varying contrast and SNR in structural and spectroscopic images.

Lack of an RF Transmit Body Coil. A third major technical issue has been the lack of an RF transmit body coil, making it necessary to integrate a dedicated RF transmit coil into head RF coil designs. This integration increases the complexity of RF head coil design. A few robust transmit/receive head coils are now becoming available for use at 7T, potentially resolving this problem. Such coils are usually supplied by the manufacturer at the time of scanner purchase.

RF Power Deposition. RF power deposition, measured as the spe-

cific absorption rate (SAR), theoretically increases as the square of B_0 . Although other effects may partially compensate for this in practice, there is still a tighter limit on the number, duration, and amplitude of applied RF pulses in a given time period at 7T compared with 3T. For some commonly used MR imaging pulse sequences that use many closely spaced high-flip-angle RF pulses, such as fast spin-echo or turbo spin-echo (depending on the vendor), these pulses severely limit the number of sections that may be acquired. See Fig 12 for the simulated B_1 and SAR in the brain at 7T compared with 3T.

Changing Relaxation Behavior. Relaxation constants change as a function of field strength (Table). T1 values lengthen and converge for most tissues as the field strength increases. T2* values decrease with field strength, resulting in enhanced contrast due to iron deposits, calcifications, and deoxygenated blood but also increased signal loss at tissue interfaces on gradient recalled-echo images. The exact, heuristically derived relationships between T1 and T2* and B_0 are provided in the Table. At higher field strengths, apparent T2 values also shorten for spin-echo sequences due to diffusion effects through microgradients surrounding capillaries. The specific effect on T2 will depend on tissue type. The apparent T2 was experimentally found to shorten from 76 to 47 ms in frontal gray matter and

from 71 to 47 ms in white matter, when moving from 3T to 7T.⁷¹ Single-echo sequences such as diffusion-weighted EPI are particularly vulnerable to such T2 shortening. In addition, such single-echo or few-echo series have distortions due to B_0 and B_1 inhomogeneity. Sequence timing must be changed to account for these effects and achieve the desired contrast. In particular, longer TRs and shorter TEs are required to maximize signal and contrast.

Increased Chemical Shift Localization Error. MR spectroscopy is planned within a volume of interest specified at the scanner. However, the precise location of the volume achieved shifts with the RF pulse and with the resonant frequency of the metabolite. This spatial offset is called the chemical shift localization error. Because each metabolite to be studied has a different resonant frequency, each metabolite volume is spatially shifted with respect to the others. As a result, the volume in which all of the metabolites can be imaged together is smaller than the volume initially specified. The degree of the shift is proportional to the magnetic field strength (B_0), proportional to the section width, and inversely proportional to the bandwidth of the applied RF pulse. Cho and NAA, for example, are separated by 1.2 ppm. This translates into a frequency separation of 153 Hz at 3T, but 360 Hz at 7T. Because chemical shift localization error is linearly proportional to this

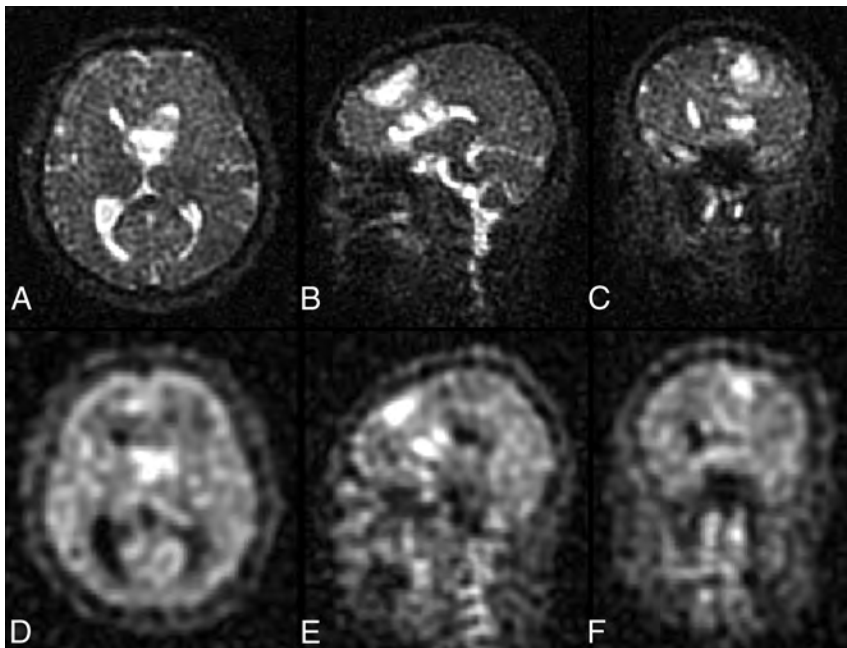


FIG 8. A–C, Images of total sodium content for a patient with a glioblastoma of the mesial frontal lobe. Total sodium signal is elevated in tumor tissue. D–F, Images of relaxation-weighted sodium signal of the same patient. This provides sodium levels from a different tissue compartment and is only elevated in the central portion of the tumor. Images are courtesy of Drs Armin Nagel and Armin Biller, German Cancer Research Center, Heidelberg, Germany. Scanner: whole-body 7T MR imaging (Magnetom; Siemens). RF coil: rapid double-resonant ($^1\text{H} = 297.2\text{ MHz}$; $^{23}\text{Na} = 78.6\text{ MHz}$) quadrature birdcage coil. Scan parameters: resolution = $2.5 \times 2.5 \times 2.5\text{ mm}^3$, scanning time = 13 minutes (A–C); resolution = $5.5 \times 5.5 \times 5.5\text{ mm}^3$, scanning time = 10 minutes (D–F).

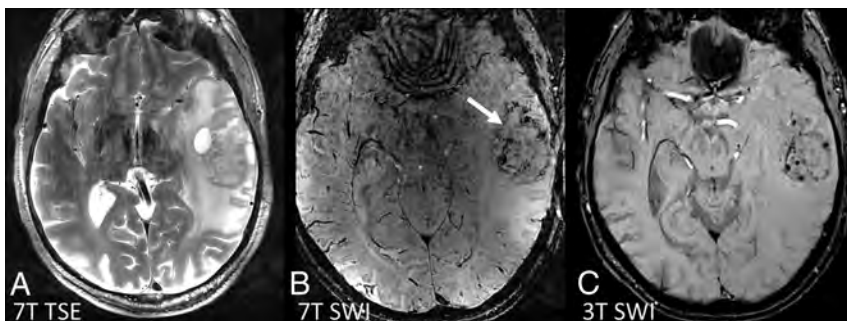


FIG 9. A, High-resolution TSE image of a left temporal glioblastoma. B, 7T SWI provides improved depiction of intratumoral vessels and hemorrhages (white arrow) compared with SWI at 3T (C). Images are provided by Dr Alexander Radbruch, Heidelberg University Hospital and German Cancer Research Center, Heidelberg, Germany. Scanner: whole-body 7T MR imaging (Magnetom; Siemens). RF coil: Nova 32-channel head coil. Scan parameters: resolution = $0.3 \times 0.3 \times 2\text{ mm}^3$, scanning time = 4 minutes and 13 seconds (A); resolution = $0.7 \times 0.7 \times 2.5\text{ mm}^3$, scanning time = 3 minutes and 18 seconds (B); resolution = $0.4 \times 0.4 \times 0.4\text{ mm}^3$, scanning time = 6 minutes and 17 seconds (C).

frequency shift, the usable volume in which MR spectroscopy can be performed is reduced at 7T.

Engineering Solutions

Solutions to some of the technical issues at 7T include customized RF pulse and pulse sequence designs to produce uniform transmission profiles while minimizing deposited RF energy (SAR). Development of specialized hardware such as multiple transmit coils for RF signal transmission is also necessary.

Customized RF Pulses and Pulse Sequences. Creative RF pulse and pulse sequence design may be used to overcome many of the physical limitations of existing hardware so that the full signal gain

and enhanced contrast afforded by 7T may be exploited. RF pulses are rapid changes in the amplitude and/or frequency of the applied RF field. They are designed to rotate the net magnetization into the transverse plane so that it is detected by an RF coil. A pulse sequence is a set of RF pulses followed by spatially varying magnetic field gradients to encode the received signal. Adiabatic pulses are a special class of RF pulses that, above a certain amplitude called the “adiabatic threshold,” uniformly rotate magnetization, independent of B_1 field variations. These adiabatic RF pulses may be used to provide uniform flip angles in the presence of a nonuniform B_1 field.^{72–74}

Methods have been proposed to systematically design adiabatic pulses to achieve the same behavior as conventional RF pulses.⁷⁵ 2D selectivity may also be achieved by sampling an adiabatic pulse waveform with small-tip-angle spatial subpulses and coupling the pulse with an oscillating gradient waveform.^{76,77} The sampled envelope provides selectivity in the first dimension, while the subpulses provide selectivity in the second dimension. When the dimension selected by the sampled envelope is set to frequency (instead of space), the pulse acts as an adiabatic spatial-spectral pulse and provides spatial and spectral selectivity. Such specialized RF pulses may be used in existing and new MR imaging pulse sequences to enable robust operation at higher fields. Although new design considerations arise with the use of these pulses, they may be integrated seamlessly into many MR imaging pulse sequences, including those used for anatomic spectroscopic and diffusion-weighted imaging. Essentially, they provide the same contrast or tissue parameters, while combatting field inhomogeneity and remaining within safe RF power limits.^{73,77–83}

Tailored RF Pulses to Compensate for B_1

Inhomogeneities. Another solution to B_1 inhomogeneity is to create pulses that are specifically designed to compensate for the nonuniformities in the B_1 field. The B_1 field map for every subject may be measured by using new fast and accurate B_1 -mapping methods.^{84,85} Then, 2D tailored RF pulses may be designed to cancel the B_1 variation and achieve a consistent flip angle throughout the FOV.^{86,87} These tailored 2D pulses require less RF power than adiabatic pulses but may have greater sensitivity to B_0 inhomogeneity.

Parallel Imaging and Lower Flip Angle Schedules. Parallel imaging may be used in conjunction with segmented readouts to accelerate

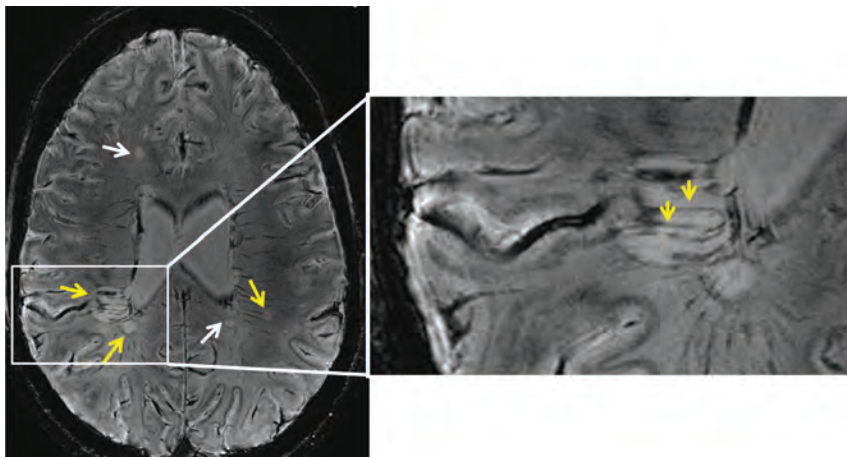


FIG 10. 7T SWI of a patient with MS. MS plaques (white and yellow arrows) and tiny veins within MS plaques (yellow arrows) become visible with the high resolution and enhanced contrast afforded by the 7T scanner. Images courtesy of Professor Siegfried Trattnig and Dr Günther Grabner, Medical University of Vienna, Vienna, Austria. Scanner: whole-body 7T MR imaging (Magnetom; Siemens). RF coil: Nova 32-channel head coil. Scan parameters: SWI sequence: resolution = $0.3 \times 0.3 \times 1.2 \text{ mm}^3$, scanning time = 10 minutes.

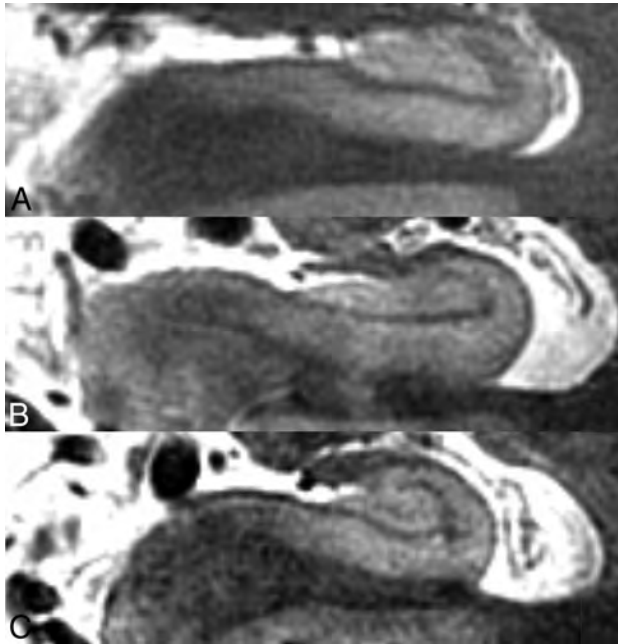


FIG 11. Left hippocampus imaged at 7T across aged-matched patient populations. Healthy control (A), amnesic mild cognitive impairment (B), and probable Alzheimer disease (C). Images courtesy of Drs Jeffrey Bernstein, Brian Rutt, and Geoffrey Kerchner, Stanford University, Stanford, California. Scanner: whole-body 7T MR imaging (MR950; GE Healthcare). RF coil: Nova 32-channel head coil. Scan parameters: FSE sequence: section orientation = coronal oblique intersecting perpendicular to longitudinal axis of hippocampus, TE/TR = 49/6000 ms, 16 sections, section thickness = 1.5 mm, resolution = $0.22 \times 0.22 \times 1.5 \text{ mm}^3$, scanning time = 13 minutes.

acquisition times to overcome some of the SAR limitations and B_0 field distortions.²² Lower flip angle schedules have been designed to achieve contrast similar to that achieved by trains of high flip angle RF pulses like TSE and FSE sequences. These may also help to reduce the amount of RF energy deposited.⁸⁸

Specialized Parallel Transmit Hardware. Another method to gain more control over the transmitted B_1 profile is to use specialized

hardware solutions such as parallel transmit arrays. By using multiple transmit coils, parallel transmit arrays divide the RF field into multiple, partially overlapping, spatial regions. These arrays may then be used to improve B_1 field homogeneity in 2 ways: One way is by B_1 shimming. This involves altering the amplitude and/or phase of the RF waveform transmitted on each channel to mitigate the B_1 nonuniformity. The second way is by applying a different RF pulse to each transmit channel to customize the transmitted B_1 field. This technique may be used to create a more nearly homogeneous B_1 field over the full region of interest or to customize the B_1 field in a specially defined region of interest.⁸⁹⁻⁹¹

Currently, the heterogeneous SAR profiles resulting from multiple RF transmission are not fully understood, limiting flip angles to very small values to remain within safety limits. Furthermore, such an approach requires acquisition of subject-specific field maps to generate the custom RF pulses and requires the scanner to be equipped with parallel transmit hardware. Thus it remains valuable to have single-channel solutions for uniform B_1 -insensitive, section-selective RF excitation.

Multinuclear Imaging. When imaging nuclei other than hydrogen, different physical considerations come into play. In fact, nuclei such as sodium, with lower gyromagnetic ratios, have more uniform B_1 profiles and behave in a manner similar to that of protons at 1.5T. However, their resonant frequency, relatively low SNR, and different relaxation behavior require the use of custom-tuned RF coils and specialized sequences that rapidly encode spatial frequency space to capture the signal.^{26,30,92,93}

Practical Considerations

Siting. The ease of siting a 7T magnet has greatly improved in recent years. Because they are now actively shielded, 7T MR systems have become more compact and easy to site. Active shielding eliminates the need to place approximately 400 tons of iron shielding into the walls of the magnet room. Heretofore, such “passive” shielding may have been as thick as 12 inches (30.48 cm) to reduce the stray magnetic field that would otherwise emanate in all directions from the magnet.

Cost. One factor in operating a 7T scanner has been helium boil-off. Newer magnets are “zero boil-off,” resulting in very little helium leak with time, reducing helium costs after initial magnet installation. A second factor has been economy of scale. Because manufacturers produce far fewer high-field magnets than 1.5T magnets, the unit cost of 7T MR imaging scanners remains high. Although prices vary according to vendor, 7T installations can cost approximately \$10 million in the United States. As a larger number of research institutions and clinics adopt ultra-high-field scanners, these scanners will

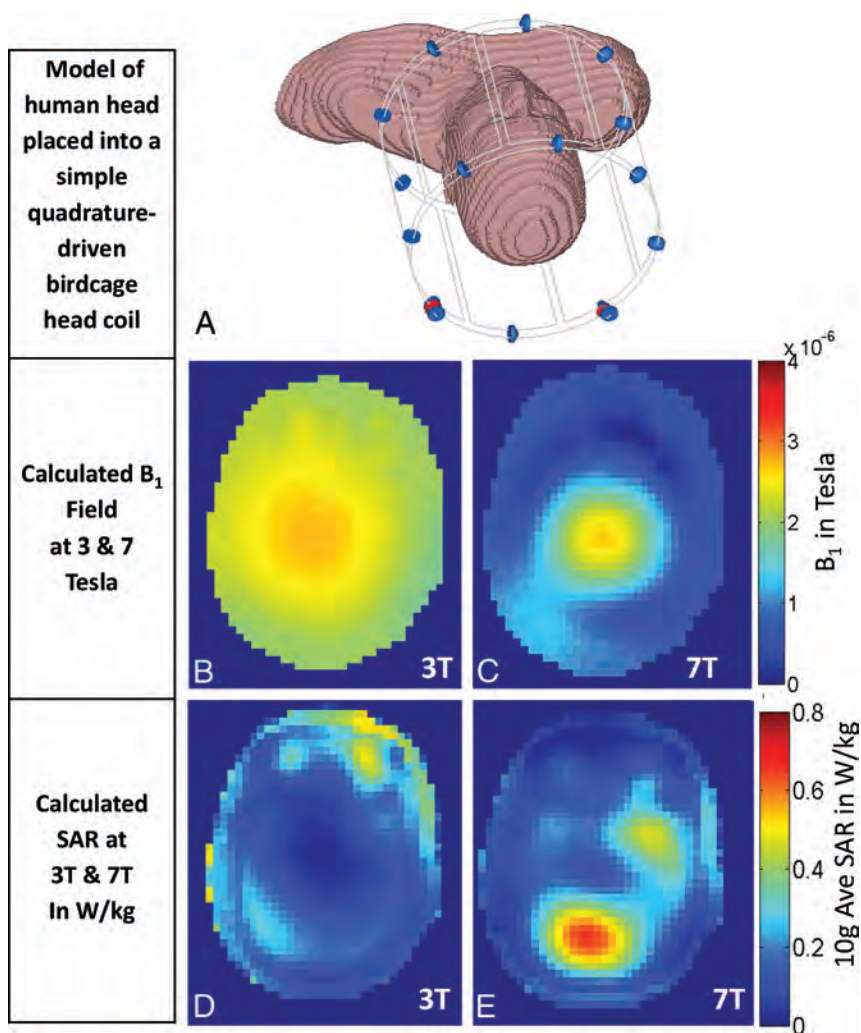


FIG 12. Differences between the transmitted B_1 fields and the specific absorption rates at 3T and 7T. A, Model of a human head placed in a simple quadrature-driven birdcage head coil. B and C, Simulated transmitted B_1 field (B_1^+) for 3T (B) and 7T (C). At 7T, wave-propagation effects cause more severe variation of the B_1 field than is seen at 3T. D and E, Simulated SAR in the head model for 3T and 7T (in Watts per kilogram). SAR simulations show increased RF power deposition and greater spatial heterogeneity at 7T than at 3T. At 7T, one must contend with 2 physical limitations, the greater inhomogeneity in the transmit B_1 field and the increased SAR deposition. These simulations were performed by Dr Bei Zhang at the Icahn School of Medicine, Mount Sinai, New York. A commercial finite-difference time domain software, CST Microwave Studio (Computer Simulation Technology, Darmstadt, Germany), was used to simulate electric and magnetic fields within the head for “Donna” in the Computer Simulation Technology virtual family. The B_1 map was obtained by using 1W for the input power. The resolution of Donna is $1.875 \times 1.875 \times 2 \text{ mm}^3$.

become mass produced, the manufacturing processes will become more streamlined, and the unit cost should decline.

The number of ultra-high-field scanner installations continues to grow as researchers harness the increased signal to push the boundaries of resolution and contrast. Currently, there are forty-three 7T installations worldwide, 19 of which are in the United States. Five magnets have been installed that are above 7T field strength and 7 more have been ordered.

FDA Approval. 7T whole-body human scanners are still pending 510K approval by the US FDA. However, the FDA has already designated MR imaging scanners functioning at 8T and below as nonsignificant risk for adults and children. For infants 1 month or younger, this limit is presently 4T. Human research at 7T at medical and academic institutions is governed by their respective in-

stitutional review boards. Some manufacturers have announced interest in obtaining the FDA 510K clearance for 7T human scanners. The role of researchers and clinicians in showing the clinical value of these scanners in humans will be pivotal to obtaining this approval.

Patient Experience

Risks at 7T are similar to those at 1.5T and 3T. However, there are some added considerations in terms of patient comfort and safety.

Transitory Physiologic Effects. With regard to patient comfort level, the 7T scanner is very similar to 3T, except for limited transitory physiologic effects. Among the most frequently reported are dizziness and vertigo. These are due to magnetohydrodynamic forces exerted on ionic fluids in the inner ear as a person moves through the fringe field. To minimize these effects, patients are instructed not to move their heads quickly while near or in the magnet. For the same reason, 7T scan tables are programmed to move very slowly to ensure slow motion of the patient through the fringe field. Metallic taste in the mouth has also been reported and is likely due to electrolysis of metallic chemicals in dental fillings while moving through the field.⁹⁴ All effects disappear when the person is out of the magnet.

Noise Levels, RF Energy Deposition, and Peripheral Nerve Stimulation. Noise levels, RF energy deposition, and peripheral nerve stimulation are presently minimized by adherence to the conservative safety guidelines set by regulatory bodies such as the FDA and institutional safety committees. Acoustic noise in the scanner is a result of Lorentz forces on gradient

windings producing bulk vibration. The Lorentz force is dependent on both the magnitude of the magnetic field and the orientation of the current-carrying gradient coil with respect to that field. For similar coil geometry and positioning, the Lorentz force should scale directly with the field strength. However, the exact scaling law between acoustic noise and field strength is difficult to determine because magnet bore and gradient coil geometry do play a significant role.⁹⁵ Noise dampening, noise insulation, and encapsulation and sequence protocol design are used to bring noise down to comfortable levels, as specified by the FDA. At present, the safe noise level is set at 99 dB(A) with the use of ear protection.⁹⁵ Systems have been tested to operate within these specified comfort levels.

RF energy deposition within the patient, quantified as the specific

absorption rate, is closely tracked by SAR monitors to ensure that the sequences used do not exceed the conservative safety limits specified by the FDA. Peripheral nerve stimulation, which is related to the speed of switching gradients, is also monitored and limited. It is not field strength-dependent.

Implantable Devices. Currently, only 2 contrast injectors and a radiofrequency identification device chip are approved for 7T scanners.⁹⁶ However, researchers are testing a wide range of implantable devices to permit 7T MR scanning in a wider range of patients.

Conclusions and Future Directions

Ultra-high-field MR imaging has great potential to display in vivo subtle abnormalities that are not detectable at lower field strengths. Increasing the field strength provides opportunities to visualize subtle anatomic abnormalities associated with disease; reveal spatially varying metabolite ratios between smaller structures; isolate functional signal that is more tightly coupled to underlying neuronal activity; image microvasculature and blood products in great detail; and tap into the signal from nuclei other than protons, revealing new information about cellular activity. By using novel RF pulse and pulse sequence designs, we can overcome the technical barriers confounding ultra-high-field MR imaging and fully exploit the SNR advantage and enhanced contrast to visualize the brain in unprecedented detail. The combination of high-resolution anatomic, spectroscopic, and functional MR imaging at 7T has the potential to be a powerful, noninvasive toolset for improved diagnosis and treatment of a wide range of neurologic diseases and disorders.

Continued technical development of new signal transmission and readout methods is needed to overcome the physical limitations of performing high-field imaging in vivo within reasonable times and appropriate safety limits. Additional clinical studies are needed to demonstrate the value of 7T for disease diagnosis, treatment, and management. It is expected that continued advances in high-field imaging will lead to a new understanding of neurologic disease and improved detection and treatment of such diseases. These will propel the field forward.

Disclosures: Priti Balchandani—**RELATED:** Grant: National Institutes of Health, Comments: NIH-NINDS R00 NS070821, includes support for travel to meetings for the study or other purposes; **Other:** Siemens*; **UNRELATED:** Grants/Grants Pending: National Institutes of Health,* Comments: NIH-NINDS R00 NS070821; **Patents (planned, pending or issued):** patents filed with Stanford University and Icahn School of Medicine at Mount Sinai, Comments: 1) Priti Balchandani, Daniel Spielman, and John Pauly, "Method to Design Adiabatic RF Pulses Using the Shinnar-Le Roux Algorithm," US patent 8,473,536; 2) Priti Balchandani, Daniel Spielman, and John Pauly, "Method for Magnetic Resonance Spectroscopic Imaging," US patent 7,966,053; 3) Priti Balchandani, John Pauly, and Daniel Spielman, "Slice-selective Tunable-flip Adiabatic Low peak-power Excitation Pulse," US patent 7,683,618; 4) Priti Balchandani, John Pauly, and Daniel Spielman, "Self-Refocused Spatial-Spectral Pulse Pair," US patent 7,821,263; 5) Priti Balchandani, Rebecca Feldman, and Haisam Islam, "Implementation of a Self-Refocused Adiabatic Spin Echo Pulse-Pair Modulated Using the Power Independent of the Number Of Slices (technique for simultaneous B1-insensitive multislice imaging)," US provisional patent submitted; **Royalties:** Some royalties received from patents listed above; **Travel/Accommodations/Meeting Expenses Unrelated to Activities Listed:** Siemens, Comments: visit to 7T sites; **OTHER RELATIONSHIPS:** I am employed by Icahn School of Medicine at Mount Sinai. Therefore, I am financially supported by the Icahn School of Medicine Capital Campaign, Translational and Molecular Imaging Institute, and Department of Radiology. Some of the images included in this article were obtained as part of my research at Mount Sinai. *Money paid to the institution.

ACKNOWLEDGMENTS

We would like to thank Dr Christina Triantafyllou for providing information on the prevalence and availability of high-field MR imaging scanners and Dr Bernd Stoeckel for his input on current technical capabilities and limitations of 7T scanners.

REFERENCES

1. Clow H, Young IR. **Britain's brains produce first NMR scans.** *New Scientist* 1978;80:588
2. Atlas SW. *Magnetic Resonance Imaging of the Brain and Spine.* Vol. 1. Philadelphia: Lippincott Williams & Wilkins; 2009
3. Kraff O, Fischer A, Nagel AM, et al. **MRI at 7 Tesla and above: demonstrated and potential capabilities.** *J Magn Reson Imaging* 2015;41:13–33
4. Duyn JH. **The future of ultra-high field MRI and fMRI for study of the human brain.** *Neuroimage* 2012;62:1241–48
5. Uğurbil K, Adriany G, Andersen P, et al. **Ultrahigh field magnetic resonance imaging and spectroscopy.** *Magn Reson Imaging* 2003; 21:1263–81
6. Fatterpekar GM, Naidich TP, Delman BN, et al. **Cytoarchitecture of the human cerebral cortex: MR microscopy of excised specimens at 9.4 Tesla.** *AJNR Am J Neuroradiol* 2002;23:1313–21
7. Naidich TP, Duvernoy HM, Delman BN, et al. *Vascularization of the Cerebellum and the Brain Stem.* Vienna: Springer-Verlag; 2009
8. Duvernoy H, Cattin F, Naidich TP, et al. *The Human Hippocampus: Functional Anatomy, Vascularization and Serial Sections with MRI.* 3rd ed. Berlin: Springer-Verlag; 2005
9. Kerchner GA. **Ultra-high field 7T MRI: a new tool for studying Alzheimer's disease.** *J Alzheimers Dis* 2011;26(suppl 3):91–95
10. Kollia K, Maderwald S, Putzki N, et al. **First clinical study on ultra-high-field MR imaging in patients with multiple sclerosis: comparison of 1.5T and 7T.** *AJNR Am J Neuroradiol* 2009;30:699–702
11. Thomas BP, Welch EB, Niederhauser BD, et al. **High-resolution 7T MRI of the human hippocampus in vivo.** *J Magn Reson Imaging* 2008;28:1266–72
12. Wisse LE, Gerritsen L, Zwanenburg JJ, et al. **Subfields of the hippocampal formation at 7 T MRI: in vivo volumetric assessment.** *Neuroimage* 2012;61:1043–49
13. Prudent V, Kumar A, Liu S, et al. **Human hippocampal subfields in young adults at 7.0 T: feasibility of imaging.** *Radiology* 2010;254:900–06
14. Haacke EM, Mittal S, Wu Z, et al. **Susceptibility-weighted imaging: technical aspects and clinical applications, part 1.** *AJNR Am J Neuroradiol* 2009;30:19–30
15. Sanchez-Panchuelo RM, Besle J, Beckett A, et al. **Within-digit functional parcellation of Brodmann areas of the human primary somatosensory cortex using functional magnetic resonance imaging at 7 Tesla.** *J Neurosci* 2012;32:15815–22
16. Duong TQ, Yacoub E, Adriany G, et al. **Microvascular BOLD contribution at 4 and 7 T in the human brain: gradient-echo and spin-echo fMRI with suppression of blood effects.** *Magn Reson Med* 2003;49:1019–27
17. Yacoub E, Duong TQ, Van De Moortele PF. **Spin-echo fMRI in humans using high spatial resolutions and high magnetic fields.** *Magn Reson Med* 2003;49:655–64
18. Bae KT, Park SH, Moon CH, et al. **Dual-echo arteriovenography imaging with 7T MRI.** *J Magn Reson Imaging* 2010;31:255–61
19. Mayer D, Spielman DM. **Detection of glutamate in the human brain at 3 T using optimized constant time point resolved spectroscopy.** *Magn Reson Med* 2005;54:439–42
20. Polders DL, Leemans A, Hendrikse J, et al. **Signal to noise ratio and uncertainty in diffusion tensor imaging at 1.5, 3.0, and 7.0 Tesla.** *J Magn Reson Imaging* 2011;33:1456–63
21. Morelli JN, Runge VM, Feiwel T, et al. **Evaluation of a modified Stejskal-Tanner diffusion encoding scheme, permitting a marked reduction in TE, in diffusion-weighted imaging of stroke patients at 3 T.** *Invest Radiol* 2010;45:29–35

22. Heidemann RM, Porter DA, Anwander A, et al. **Diffusion imaging in humans at 7T using readout-segmented EPI and GRAPPA.** *Magn Reson Med* 2010;64:9–14
23. Feinberg DA, Setsompop K. **Ultra-fast MRI of the human brain with simultaneous multi-slice imaging.** *J Magn Reson* 2013;229:90–100
24. Setsompop K, Cohen-Adad J, Gagoski BA, et al. **Improving diffusion MRI using simultaneous multi-slice echo planar imaging.** *Neuroimage* 2012;63:569–80
25. Nagel AM, Bock M, Hartmann C, et al. **The potential of relaxation-weighted sodium magnetic resonance imaging as demonstrated on brain tumors.** *Invest Radiol* 2011;46:539–47
26. Nagel AM, Laun FB, Weber MA, et al. **Sodium MRI using a density-adapted 3D radial acquisition technique.** *Magn Reson Med* 2009;62:1565–73
27. Nagel AM, Lehmann-Horn F, Weber MA, et al. **In vivo 35Cl MR imaging in humans: a feasibility study.** *Radiology* 2014;271:585–95
28. Thulborn KR, Davis D, Snyder J, et al. **Sodium MR imaging of acute and subacute stroke for assessment of tissue viability.** *Neuroimaging Clin N Am* 2005;15:639–53, xi–xii
29. Boada FE, LaVerde G, Jungreis C, et al. **Loss of cell ion homeostasis and cell viability in the brain: what sodium MRI can tell us.** *Curr Top Dev Biol* 2005;70:77–101
30. Qian Y, Zhao T, Wiggins GC, et al. **Sodium imaging of human brain at 7 T with 15-channel array coil.** *Magn Reson Med* 2012;68:1807–14
31. Qian Y, Zhao T, Zheng H, et al. **High-resolution sodium imaging of human brain at 7 T.** *Magn Reson Med* 2012;68:227–33
32. Qiao H, Zhang X, Zhu XH, et al. **In vivo 31P MRS of human brain at high/ultrahigh fields: a quantitative comparison of NMR detection sensitivity and spectral resolution between 4 T and 7 T.** *Magn Reson Imaging* 2006;24:1281–86
33. Moser E, Stahlberg F, Ladd ME, et al. **7-T MR: from research to clinical applications?** *NMR Biomed* 2012;25:695–716
34. Trattinig S, Zbyn S, Schmitt B, et al. **Advanced MR methods at ultrahigh field (7 Tesla) for clinical musculoskeletal applications.** *Eur Radiol* 2012;22:2338–46
35. Madelin G, Kline R, Walvick R, et al. **A method for estimating intracellular sodium concentration and extracellular volume fraction in brain in vivo using sodium magnetic resonance imaging.** *Sci Rep* 2014;4:4763
36. Kerchner GA, Hess CP, Hammond-Rosenbluth KE, et al. **Hippocampal CA1 apical neuropil atrophy in mild Alzheimer disease visualized with 7-T MRI.** *Neurology* 2010;75:1381–87
37. Henry TR, Chupin M, Lehericy S, et al. **Hippocampal sclerosis in temporal lobe epilepsy: findings at 7 T.** *Radiology* 2011;261:199–209
38. Zeineh MM, Parvizi J, Balchandani P, et al. **Ultra-high resolution 7.0T MRI of medial temporal lobe epilepsy.** In: *Proceedings of the Annual Meeting of the International Society for Magnetic Resonance in Medicine*, Honolulu, Hawaii. April 18–24, 2009
39. Grabner G, Nöbauer I, Elandt K, et al. **Longitudinal brain imaging of five malignant glioma patients treated with bevacizumab using susceptibility-weighted magnetic resonance imaging at 7 T.** *Magn Reson Imaging* 2012;30:139–47
40. Yuh WT, Christoforidis GA, Koch RM, et al. **Clinical magnetic resonance imaging of brain tumors at ultrahigh field: a state-of-the-art review.** *Top Magn Reson Imaging* 2006;17:53–61
41. Eapen M, Zald DH, Gatenby JC, et al. **Using high-resolution MR imaging at 7T to evaluate the anatomy of the midbrain dopaminergic system.** *AJNR Am J Neuroradiol* 2011;32:688–94
42. Breyer T, Wanke I, Maderwald S, et al. **Imaging of patients with hippocampal sclerosis at 7 Tesla: initial results.** *Acad Radiol* 2012;17:421–26
43. Madan N, Grant PE. **New directions in clinical imaging of cortical dysplasias.** *Epilepsia* 2009;50:9–18
44. Schlamann M, Maderwald S, Becker W, et al. **Cerebral cavernous hemangiomas at 7 Tesla: initial experience.** *Acad Radiol* 2010;17:3–6
45. Lupo JM, Li Y, Hess CP, et al. **Advances in ultra-high field MRI for the clinical management of patients with brain tumors.** *Curr Opin Neurol* 2011;24:605–15
46. Thulborn KR, Davis D, Adams H, et al. **Quantitative tissue sodium concentration mapping of the growth of focal cerebral tumors with sodium magnetic resonance imaging.** *Magn Reson Med* 1999;41:351–59
47. Thulborn KR, Lu A, Atkinson IC, et al. **Quantitative sodium MR imaging and sodium bioscales for the management of brain tumors.** *Neuroimaging Clin N Am* 2009;19:615–24
48. Ouwerkerk R, Bleich KB, Gillen JS, et al. **Tissue sodium concentration in human brain tumors as measured with 23Na MR imaging.** *Radiology* 2003;227:529–37
49. Deistung A, Schweser F, Wiestler B, et al. **Quantitative susceptibility mapping differentiates between blood depositions and calcifications in patients with glioblastoma.** *PLoS One* 2013;8:e57924
50. Park MJ, Kim HS, Jahng GH, et al. **Semiquantitative assessment of intratumoral susceptibility signals using non-contrast-enhanced high-field high-resolution susceptibility-weighted imaging in patients with gliomas: comparison with MR perfusion imaging.** *AJNR Am J Neuroradiol* 2009;30:1402–08
51. Radbruch A, Wiestler B, Kramp L, et al. **Differentiation of glioblastoma and primary CNS lymphomas using susceptibility weighted imaging.** *Eur J Radiol* 2013;82:552–56
52. Tallantyre EC, Morgan PS, Dixon JE, et al. **3 Tesla and 7 Tesla MRI of multiple sclerosis cortical lesions.** *J Magn Reson Imaging* 2010;32:971–77
53. Hammond KE, Metcalf M, Carvajal L, et al. **Quantitative in vivo magnetic resonance imaging of multiple sclerosis at 7 Tesla with sensitivity to iron.** *Ann Neurol* 2008;64:707–13
54. Ge Y, Law M, Herbert J, et al. **Prominent perivenular spaces in multiple sclerosis as a sign of perivascular inflammation in primary demyelination.** *AJNR Am J Neuroradiol* 2005;26:2316–19
55. Ge Y, Zohrabian VM, Grossman RI. **Seven-Tesla magnetic resonance imaging: new vision of microvascular abnormalities in multiple sclerosis.** *Arch Neurol* 2008;65:812–16
56. Quinn MP, Kremenutzky M, Menon RS. **Venocentric lesions: an MRI marker of MS?** *Front Neurol* 2013;4:98
57. Small SA, Schobel SA, Buxton RB, et al. **A pathophysiological framework of hippocampal dysfunction in ageing and disease.** *Nat Rev Neurosci* 2011;12:585–601
58. van Rooden S, Versluis MJ, Liem MK, et al. **Cortical phase changes in Alzheimer's disease at 7T MRI: a novel imaging marker.** *Alzheimers Dement* 2014;10:e19–26
59. Drevets WC. **Neuroimaging and neuropathological studies of depression: implications for the cognitive-emotional features of mood disorders.** *Curr Opin Neurobiol* 2001;11:240–49
60. Wang Z, Neylan TC, Mueller SG, et al. **Magnetic resonance imaging of hippocampal subfields in posttraumatic stress disorder.** *Arch Gen Psychiatry* 2010;67:296–303
61. Drevets WC. **Neuroimaging studies of mood disorders.** *Biol Psychiatry* 2000;48:813–29
62. Price JL, Drevets WC. **Neurocircuitry of mood disorders.** *Neuropsychopharmacology* 2010;35:192–216
63. McKinnon MC, Yucel K, Nazarov A, et al. **A meta-analysis examining clinical predictors of hippocampal volume in patients with major depressive disorder.** *J Psychiatry Neurosci* 2009;34:41–54
64. Malykhin NV, Lebel RM, Coupland NJ, et al. **In vivo quantification of hippocampal subfields using 4.7 T fast spin echo imaging.** *Neuroimage* 2010;49:1224–30
65. Huang Y, Coupland NJ, Lebel RM, et al. **Structural changes in hippocampal subfields in major depressive disorder: a high-field magnetic resonance imaging study.** *Biol Psychiatry* 2013;74:62–68
66. Liao Y, Huang X, Wu Q, et al. **Is depression a disconnection syndrome? Meta-analysis of diffusion tensor imaging studies in patients with MDD.** *J Psychiatry Neurosci* 2013;38:49–56
67. Miguel-Hidalgo JJ, Baucom C, Dille G, et al. **Glial fibrillary acidic protein immunoreactivity in the prefrontal cortex distinguishes**

- younger from older adults in major depressive disorder. *Biol Psychiatry* 2000;48:861–73
68. Cotter D, Mackay D, Chana G, et al. **Reduced neuronal size and glial cell density in area 9 of the dorsolateral prefrontal cortex in subjects with major depressive disorder.** *Cereb Cortex* 2002;12:386–94
 69. Si X, Miguel-Hidalgo JJ, O'Dwyer G, et al. **Age-dependent reductions in the level of glial fibrillary acidic protein in the prefrontal cortex in major depression.** *Neuropsychopharmacology* 2004;29:2088–96
 70. Vaughan JT, Garwood M, Collins CM, et al. **7T vs. 4T: RF power, homogeneity, and signal-to-noise comparison in head images.** *Magn Reson Med* 2001;46:24–30
 71. Cox EF, Gowland PA. **Simultaneous quantification of T2 and T'2 using a combined gradient echo-spin echo sequence at ultrahigh field.** *Magn Reson Med* 2010;64:1440–45
 72. Tannús A, Garwood M. **Adiabatic pulses.** *NMR Biomed* 1997;10:423–34
 73. Garwood M, Delabarre L. **The return of the frequency sweep: designing adiabatic pulses for contemporary NMR.** *J Magn Reson* 2001;153:155–77
 74. Balchandani P, Glover G, Pauly J, et al. **Improved slice-selective adiabatic excitation.** *Magn Reson Med* 2014;71:75–82
 75. Balchandani P, Pauly J, Spielman D. **Designing adiabatic radio frequency pulses using the Shinnar-Le Roux algorithm.** *Magn Reson Med* 2010;64:843–51
 76. Conolly S, Pauly J, Nishimura D, et al. **Two-dimensional selective adiabatic pulses.** *Magn Reson Med* 1992;24:302–13
 77. Balchandani P, Pauly J, Spielman D. **Interleaved narrow-band PRESS sequence with adiabatic spatial-spectral refocusing pulses for 1H MRSI at 7T.** *Magn Reson Med* 2008;59:973–79
 78. Balchandani P, Spielman D. **Fat suppression for 1H MRSI at 7T using spectrally selective adiabatic inversion recovery.** *Magn Reson Med* 2008;59:980–88
 79. Balchandani P, Qiu D. **Semi-adiabatic Shinnar-Le Roux pulses and their application to diffusion tensor imaging of humans at 7T.** *Magn Reson Imaging* 2014;32:804–12
 80. Scheenen TW, Heerschap A, Klomp DW. **Towards 1H-MRSI of the human brain at 7T with slice-selective adiabatic refocusing pulses.** *MAGMA* 2008;21:95–101
 81. van Kalleveen IM, Koning W, Boer VO, et al. **Adiabatic turbo spin echo in human applications at 7 T.** *Magn Reson Med* 2012;68:580–87
 82. Moore J, Jankiewicz M, Zeng H, et al. **Composite RF pulses for B1+-insensitive volume excitation at 7 Tesla.** *J Magn Reson* 2010;205:50–62
 83. Boer VO, Siero JC, Hoogduin H, et al. **High-field MRS of the human brain at short TE and TR.** *NMR Biomed* 2011;24:1081–88
 84. Sacolick LJ, Wiesinger F, Hancu I, et al. **B1 mapping by Bloch-Siegert shift.** *Magn Reson Med* 2010;63:1315–22
 85. Khalighi MM, Rutt BK, Kerr AB. **Adiabatic RF pulse design for Bloch-Siegert B1+ mapping.** *Magn Reson Med* 2013;70:829–35
 86. Saekho S, Yip CY, Noll DC, et al. **Fast-kz three-dimensional tailored radiofrequency pulse for reduced B1 inhomogeneity.** *Magn Reson Med* 2006;55:719–24
 87. Cloos MA, Boulant N, Luong M, et al. **kT-points: short three-dimensional tailored RF pulses for flip-angle homogenization over an extended volume.** *Magn Reson Med* 2012;67:72–80
 88. Saranathan M, Tourdias T, Kerr AB, et al. **Optimization of magnetization-prepared 3-dimensional fluid attenuated inversion recovery imaging for lesion detection at 7 T.** *Invest Radiol* 2014;49:290–98
 89. Zhu Y. **Parallel excitation with an array of transmit coils.** *Magn Reson Med* 2004;51:775–84
 90. Grissom W, Yip CY, Zhang Z, et al. **Spatial domain method for the design of RF pulses in multicoil parallel excitation.** *Magn Reson Med* 2006;56:620–69
 91. Katscher U, Börnert P, Leussler C, et al. **Transmit SENSE.** *Magn Reson Med* 2003;49:144–50
 92. Wang L, Wu Y, Chang G, et al. **Rapid isotropic 3D-sodium MRI of the knee joint in vivo at 7T.** *J Magn Reson Imaging* 2009;30:606–14
 93. Staroswiecki E, Bangerter NK, Gurney PT, et al. **In vivo sodium imaging of human patellar cartilage with a 3D cones sequence at 3 T and 7 T.** *J Magn Reson Imaging* 2010;32:446–51
 94. Chakeres DW, Kangarlu A, Boudoulas H, et al. **Effect of static magnetic field exposure of up to 8 Tesla on sequential human vital sign measurements.** *J Magn Reson Imaging* 2003;18:346–52
 95. Robitaille P-M. **Ultra high field magnetic resonance imaging: a historical perspective.** In: Robitaille P-M, Berliner LJ, eds. *Ultra High Field Magnetic Resonance Imaging.* New York: Springer; 2006; 26:1–17
 96. Shellock FG. MRISAFETY.com. www.mrisafety.com. Accessed September 20, 2014
 97. Peters AM, Brookes MJ, Hoogenraad FG, et al. **T2* measurements in human brain at 1.5, 3 and 7 T.** *Magn Reson Imaging* 2007;25:748–53
 98. Uludağ K, Müller-Bierl B, Uğurbil K. **An integrative model for neuronal activity-induced signal changes for gradient and spin echo functional imaging.** *Neuroimage* 2009;48:150–65
 99. Solomon I. **Relaxation processes in a system of two spins.** *Phys Rev* 1955;99:559
 100. Bartha R, Michaeli S, Merkle H, et al. **In vivo 1H2O T2+ measurement in the human occipital lobe at 4T and 7T by Carr-Purcell MRI: detection of microscopic susceptibility contrast.** *Magn Reson Med* 2002;47:742–50
 101. Michaeli S, Garwood M, Zhu XH, et al. **Proton T2 relaxation study of water, N-acetylaspartate, and creatine in human brain using Hahn and Carr-Purcell spin echoes at 4T and 7T.** *Magn Reson Med* 2002;47:629–33
 102. Van Leemput K, Bakker A, Benner T, et al. **Automated segmentation of hippocampal subfields from ultra-high resolution in vivo MRI.** *Hippocampus* 2009;19:549–57
 103. Gu M, Zahr NM, Spielman DM, et al. **Quantification of glutamate and glutamine using constant-time point-resolved spectroscopy at 3 T.** *NMR Biomed* 2013;26:164–72

Mechanisms of Healing in Coiled Intracranial Aneurysms: A Review of the Literature

W. Brinjikji, D.F. Kallmes, and R. Kadirvel



ABSTRACT

SUMMARY: Recanalization of intracranial aneurysms following endovascular coiling remains a frustratingly common occurrence. An understanding of the molecular and histopathologic mechanisms of aneurysm healing following coil embolization is essential to improving aneurysm occlusion rates. Histopathologic studies in coiled human and experimental aneurysms suggest that during the first month postcoiling, thrombus formation and active inflammation occur within the aneurysm dome. Several months following embolization, the aneurysm is excluded from the parent vessel by formation of a neointimal layer, which is often thin and discontinuous, across the aneurysm neck. Numerous coil modifications and systemic therapies have been tested in animals and humans in an attempt to improve the aneurysm-healing process; these modifications have met with variable levels of success. In this review, we summarize the histopathologic and molecular biology of aneurysm healing and discuss how these findings have been applied in an attempt to improve angiographic outcomes in patients with intracranial aneurysms.

ABBREVIATION: MMP = matrix metalloproteinase

Coil embolization is increasingly used for treatment of intracranial aneurysms.¹ While coil embolization has been shown to be safe and effective in the occlusion of the aneurysmal sac, recanalization of the treated aneurysm, resulting in retreatment, occurs in approximately 10%–20% of cases.^{2,3} Because of the high recanalization rates following endovascular coiling, much research has been performed to further understand the biologic mechanisms of aneurysm healing following coil embolization. Such research is often difficult to perform and apply because aneurysms developed in preclinical animal models often do not emulate the conditions of the human aneurysm. Human aneurysm samples are often limited, and histologic and genetic studies are difficult to perform.⁴

Developing an understanding of biologic processes that are conducive to aneurysm healing following coil embolization is essential to improving patient outcomes. Endovascular coiling focuses on the structure and geometry of aneurysms rather than their biologic foundation. Greater understanding of biologic mechanisms of aneurysm healing allows investigators to develop new strategies or make modifications to current devices to accelerate healing and decrease recanalization rates. In this review ar-

ticle, we summarize the current state of the literature regarding the biology of aneurysm healing postcoiling and discuss future directions in aneurysm biology research.

Mechanism of Recurrence

The major limitations of endovascular treatment are, with time, incomplete occlusion and recurrence or recanalization.^{2,3} There is a strong relationship among aneurysm volume, packing attenuation, and recurrence.^{5–8} The rate of complete obliteration with coils is low in large and giant aneurysms treated with coils; the simple fact that aneurysm volume is cubic in relation to the aneurysm diameter yet coil volume is only linear with deposited coil length guarantees progressively lower packing attenuation with increasing aneurysm size. In general, even in tightly packed, small aneurysms, 75% of the aneurysm sac is filled with thrombus following coil embolization.^{5–8}

Aneurysms often recur early after treatment. Raymond and Darsaut⁹ reported that nearly 50% of subsequent recurrences were present by 6 months after coiling in humans. Various mechanisms underlying late aneurysm recanalization have been proposed, including the following: 1) growth of the aneurysm itself,^{10,11} 2) poor thrombus organization as a result of the biologically inert platinum coil construction,¹² 3) instability of fresh, unorganized thrombus and degradation by fibrolysis, 4) continued transmission of blood pulsation affecting the association of the coil-thrombus complex,¹³ 5) lack of neointima formation across the neck of aneurysm,¹⁴ and 6) formation of

From the Department of Radiology, Mayo Clinic, Rochester, Minnesota.

Please address correspondence to Waleed Brinjikji, MD, 200 1st St SW, Rochester, MN 55905; e-mail: brinjikji.waleed@mayo.edu

Indicates open access to non-subscribers at www.ajnr.org

Indicates article with supplemental on-line table.

<http://dx.doi.org/10.3174/ajnr.A4175>

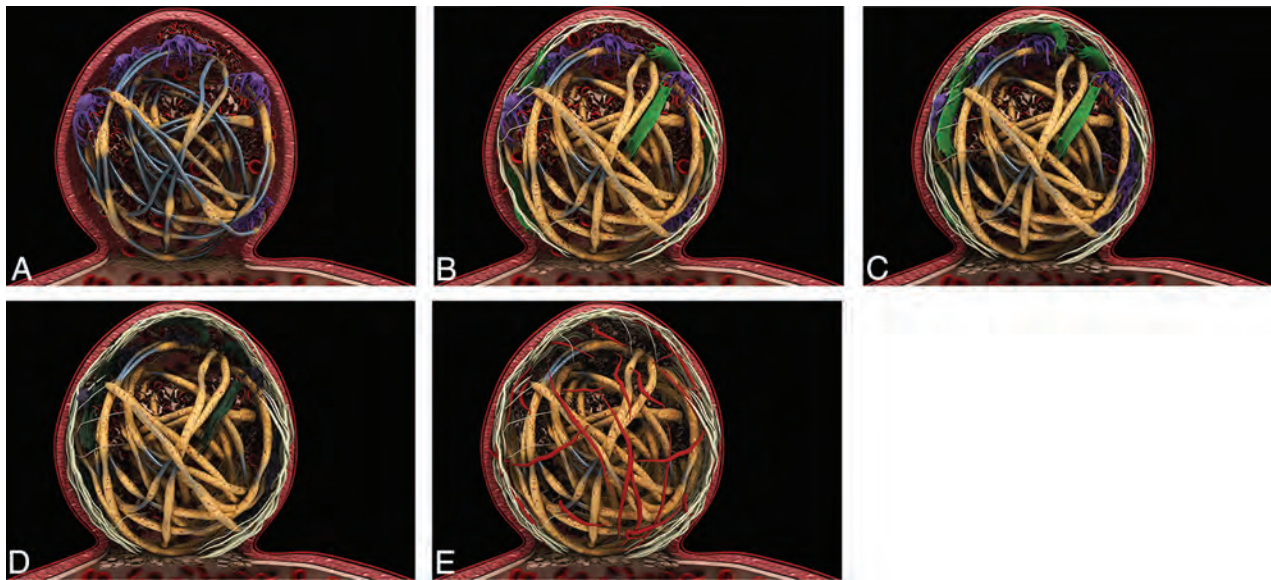


FIG 1. A, Zero-to-7 days: thin fibrin layer covers the coils (tan). Macrophage invasion is seen in the coil periphery (purple). Unorganized thrombus surrounds the coils (red). A thin-but-incomplete fibrin layer is seen at the aneurysm neck. B, One-to-2 weeks: increased fibrin coating of the coils (tan). Macrophages in the coil periphery (purple) and myofibroblast invasion (green) are seen. Note the thin fibrin layer at aneurysm neck. Endothelialization at the neck periphery and along the coil is seen. C, Two weeks to 1 month: increased myofibroblast invasion (green). Thrombus is more organized (red), and macrophages in the aneurysm periphery (purple) are seen. Note increased endothelialization of the aneurysm neck. D, One-to-3 months: decreased cellularity occurs within the aneurysm. Myofibroblasts (dark green) and macrophages (dark purple) die through apoptosis. Note increased endothelialization of the aneurysm neck. E, Three months plus: the aneurysm dome is acellular. Vascularized connective tissue is seen in the aneurysm dome (red fibers). Note increased fibrin coverage of coils (tan) and endothelialization of the aneurysm neck. There is a progressive increase in the amount of collagen within the aneurysm through 3 months.

neovessels inside the aneurysms lumen, exposing the aneurysm cavity to blood flow.

Histopathologic Mechanism of Aneurysm Healing following Bare Platinum Coil Embolization

Histologic Findings of Human Cases. A number of case reports and small case series have demonstrated the histopathologic findings of coiled human aneurysms.^{4,15-23} A summary of histopathology studies in humans is provided in the On-line Table. Histopathologic studies have demonstrated that blood clot composed of red blood cells and fibrin is generally present within the first week of aneurysm coiling.^{15,17,22-24} By the end of the first week following coil embolization, fibroblasts and macrophages begin to invade the clot and foreign body giant cells begin to proliferate about the coils. No endothelialization of the neck occurs within the first week; however, fibrin formation along the coil surface of the aneurysm neck has been reported in some cases (Fig 1A).²³ One-to-two weeks following coil embolization, coils within the dome begin to be covered with fibrin. Inflammatory cell, macrophage, and fibroblast invasion occurs in most patients. At the site of the aneurysm neck, a thin fibrin membrane forms (Fig 1B).^{15,17,19,23} Some studies have reported that a thin layer of endothelial cells begins to form along the coils of the aneurysm neck during this time.¹⁷ Two weeks to 1 month following coil embolization, coils in the aneurysm dome are generally covered by a thin layer of fibrin. Fibroblast invasion of the clot in the dome is most vigorous at this phase. In addition, there is continued invasion of the aneurysm dome by inflammatory cells, macrophages, and fibrocytes. Some collagen deposition occurs during this time as well. At the aneurysm neck, there is increased neo-

intima formation with deposition of a thin layer of fibrin along the coil surface of the neck (Fig 1C).^{15,17,18,21,23} Endothelialization at the edges of the neck has been reported.¹⁸

One-to-three months following embolization, coils remain covered by fibrin. Macrophages have been reported present within the aneurysm sac; however, inflammatory cells are largely absent. Some capillaries are seen in the aneurysm dome as well.^{15,23} At the aneurysm neck, a thin membrane is present, which has been shown to consist of endothelial cells and fibroblasts (Fig 1D). Three-to-twelve months following embolization, there is increased vascularized connective tissue within the aneurysm dome and about the coils. Continued foreign body reaction with multinucleated giant cells is seen about the aneurysm coils.^{17,23,25} One case report demonstrated that the neck is completely covered by a layer of long slender cells resembling endothelium during this time (Fig 1E).¹⁷ After 1 year, the coil is generally incorporated into the aneurysm wall. The aneurysm dome is generally filled with a vascular fibrous connective tissue. There is continued foreign body response with multinucleated giant cells surrounding the coil. Inflammatory cells and macrophages are generally a minor component because there is little inflammatory cellular reaction. The aneurysm neck is generally completely covered with a thin layer of fibrous tissue and endothelial cells. In general, endothelial cells are seen encroaching along the coils at the aneurysm neck.^{4,15,16,20,23-26}

Histologic Findings in Animal Models following Bare Platinum Coil Embolization

Thrombus Formation, Myofibroblast Invasion, and Extracellular Matrix Deposition. The formation of thrombus is essential to

providing a provisional matrix to allow recruitment of cells involved in the aneurysm-healing process.^{4,27,28} Complete thrombus organization within the aneurysm cavity is associated with improved healing and neointima formation and is best appreciated in aneurysms with increased packing attenuation and small volumes.²⁹ Within the first 2 weeks of coil embolization, stasis induced by the coils results in the formation of unorganized thrombus in the aneurysm dome (Fig 2A, -B).^{27,28} The core of the thrombus is typically acellular; however, myofibroblasts can be seen in the periphery of the thrombus. The origin of these myofibroblasts remains unclear because some suggest that myofibroblasts arise from differentiation of macrophages present within the thrombus, while others suggest that they arise from the aneurysm wall.^{27,28} During 4 weeks, there is progressive infiltration of the aneurysm dome by myofibroblasts. Myofibroblast infiltration of the aneurysm dome is important because these cells promote collagen synthesis and deposition and express contractile protein processes essential to most wound healing. However, in the case of the rabbit model of intracranial aneurysms, sparse collagen deposition is seen in the aneurysm dome following myofibroblast infiltration and contraction of the aneurysm sac has yet to be appreciated in experimental models.²⁷ At approximately 4 weeks following coil embolization, these myofibroblasts undergo apoptosis and are no longer present in the aneurysm dome.²⁷ After 10 weeks, the aneurysm dome is primarily composed of vascularized, loose hypocellular tissue (Fig 2G, -H).

Apoptosis. At approximately 4 weeks following coil embolization, myofibroblasts begin to undergo apoptosis.²⁷ Histologic studies of rabbit aneurysms have demonstrated that there is increased expression of activated cleaved caspases at 4 weeks following coil embolization.²⁷ Apoptosis of myofibroblasts in the aneurysm dome has been shown to be mediated by both intrinsic (B-cell lymphoma 2/mitochondrial-mediated) and extrinsic (tumor necrosis factor- α /receptor-mediated) pathways of apoptosis.³⁰

In a study of 20 rabbit aneurysms undergoing coil embolization, Kadirvel et al³¹ found that the apoptotic cells in the aneurysm sac were predominantly myofibroblasts. Apoptosis of cells in the aneurysm dome is thought to occur due to lack of physiologic stimulation from pulsatile flow secondary to the stasis induced by the aneurysm coils. This explanation is further supported by the fact that markers of apoptosis are strongly expressed in the aneurysm dome, but not at the aneurysm neck. Furthermore, studies suggest that low wall shear stress diminishes the ability of the aneurysm wall to function and maintain a healthy endothelium and upregulates expression of matrix metalloproteinases, molecules thought to play a role in aneurysm formation and recanalization.³² A study performed by Qi et al³² found that low shear stress promotes both vascular smooth muscle cell migration and apoptosis in the rat aorta.

Neointima Formation and Endothelialization. The biology of the aneurysm neck differs from that of the aneurysm dome. Recruitment of endothelial cells to the site of the aneurysm neck is thought to be essential to ensuring adequate healing of the treated aneurysm. Rabbit models generally demonstrate only a single, partial layer of endothelial cells at the aneurysm neck (Fig 2C-F).^{4,15,17,19,21,23,24} Swine models of aneurysm healing demon-

strate robust neointima formation with a thick layer of vascular smooth muscle cells and robust deposition of endothelial cells.^{4,33} Endothelial cells are primarily seen growing along the coils at the aneurysm neck; this feature has led some investigators to believe that the endothelial cells arise from the adjacent vessel wall.^{18,25} However, recent studies suggest that endothelial cells found at the aneurysm neck may originate from bone marrow-derived endothelial progenitor cells rather than migration of adjacent endothelial cells.^{34,35} Studies in humans suggest that circulating endothelial progenitor cells are mobilized after endovascular therapy; these findings suggest that vessel injury promotes mobilization of the endothelial progenitor cells to the aneurysm neck.³⁶ Promotion of endothelial growth along the aneurysm neck is a potential therapeutic target to improve aneurysm healing.

Similarity and Differences in the Wound-Healing Process. Early studies suggested that the mechanism of aneurysm healing following coil embolization would be similar to the well-studied and well-understood wound-healing process. The wound-healing process is classically thought to comprise 4 phases: hemostasis, inflammation, proliferation, and remodeling.³⁷ The inflammatory phase depends on recruitment of inflammatory cells such as neutrophils and macrophages, which deposit new extracellular matrix.³⁸ Following resolution of the inflammatory phase, fibroblasts and myofibroblasts begin to enter the wound site during the proliferation phase.³⁹ This process also relies on neovascularization of the wound to supply fibroblasts and epithelial cells and promote cell migration.⁴⁰ Following migration of fibroblasts, the fibroblasts begin to proliferate and lay down collagen matrix (primarily type III collagen) in the wound site. Later in the proliferative phase, angiogenesis ceases and fibroblasts begin to differentiate into myofibroblasts. Myofibroblasts bind to the surrounding collagen matrix and then contract the wound through contraction of actin.³⁹ This process leads to the maturation phase during which the previously deposited type III collagen is replaced by type I collagen and the wound organizes to restore normal tissue strength and apoptosis of cells that are no longer needed, such as endothelial cells and myofibroblasts, occurs.^{41,42}

The process of wound healing differs from that of aneurysm healing following coil embolization. Perhaps the most important difference is that the extensive collagen matrix seen following healing of a wound is not seen following coil embolization. Histologic and gene-expression studies have demonstrated that collagen is not highly expressed in treated aneurysms, both well-healed and poorly healed. The role of myofibroblasts, however, is likely similar in both healing wounds and coiled aneurysms. Myofibroblasts are thought to promote retraction of the aneurysm wall just as they promote wound retraction. Thus, early apoptosis of myofibroblasts, when the aneurysm is still not fully healed, is of so much interest. Prevention of myofibroblastic apoptosis early in the aneurysm-healing process could allow the aneurysm-healing process to more closely emulate the wound-healing process, resulting in improved occlusion rates.

Molecular Biology of Aneurysm Healing and Recanalization. Prior studies have demonstrated that aneurysm recanalization often occurs early, within 6 months of aneurysm coiling.^{2,3} It is clear that much of the biologic activity associated with aneurysm healing

occurs early, within 4 weeks of coil embolization, and is fairly complex. A number of studies have examined the histologic and biochemical features of recanalization as well as well-healed and poorly healed aneurysms. Proteomic analysis has demonstrated that densely packed aneurysms are associated with up-regulation of cell-to-cell signaling and cell-adhesion molecules within 2 weeks of coil embolization.⁴³ Significant differences in differential gene expression exist in well-healed and poorly healed aneurysms. Kadirvel et al⁴⁴ demonstrated that densely packed and well-healed aneurysms have higher expression of adhesion molecules, proteases, and cytokines compared with loosely packed aneurysms. This study found that loosely packed aneurysms did have high gene expression of types I and III collagen; however, histologic analysis found little collagen deposition in these aneurysms.⁴⁴

Osteopontin, a cell-adhesion molecule, has markedly increased expression in densely packed and well-healed aneurysms.^{44,45} This is important because osteopontin plays a key role in chemotaxis and wound healing and helps promote cell adhesion to the extracellular matrix and cell migration.⁴⁶ Furthermore, this molecule inhibits apoptosis and enhances cell proliferations. Case reports that have demonstrated the presence of bony metaplasia in the postcoiling aneurysm sac further highlight the potential role that osteopontin may play in aneurysm healing. Dai et al⁴⁷ reported 2 cases of bone formation, 1 in the aneurysmal sac and 1 in the aneurysm neck. Plenk et al⁴⁸ found cartilage neof ormation in 6 of 144 experimental aneurysms (4.2%) and bone formation in 9 of 144 experimental aneurysms (6.3%). The source of bone formation is still unknown. Potential sources include mesenchymal stem cells arising from the arterial wall, metaplasia of arterial wall smooth muscle cells into chondrocytes, and osteoblasts. These hypotheses are supported by the fact that osteopontin has been shown to promote differentiation of vascular smooth muscle and mesenchymal stem cells to an osteogenic phenotype.^{49,50} Given the potential role of osteopontin in aneurysmal healing, osteopontin has emerged as a potential therapeutic target.

The role of matrix metalloproteinases in aneurysm healing is currently controversial. Bouzaghane et al⁵¹ found that matrix metalloproteinase-9 (MMP-9) may play a key role in aneurysm recanalization in both murine and canine models. MMP-9 messenger RNA and protein were seen in higher concentrations in recanalized aneurysms compared with well-healed aneurysms. However, in a rabbit model, Kadirvel et al⁴⁴ found that MMP-9 was more highly expressed in well-healed aneurysms than in poorly healed ones. It is likely that MMP-9 expression has properties that are both conducive and inhibitory to aneurysm healing. On the one hand, MMP-9 may cause recanalization by promoting artery injury and aneurysm growth. However, on the other hand, MMP-9 is essential to many important facets of aneurysm healing. MMP-9 regulates migration of smooth muscle cells from the tunica media to the intima; this regulation helps promote neointima formation along the aneurysm neck, an essential component in aneurysm healing.^{44,52} Many studies by using rabbit, canine, and swine models have found that well-healed aneurysms demonstrate endothelial cell proliferation along the aneurysm neck, and MMP-9 may be essential to this process.

Characteristics of well-healed aneurysms

Characteristics
Anatomic/angiographic
Increased packing attenuation
Smaller aneurysm volume
High aspect ratio
Histologic
Complete thrombus formation
Myofibroblast infiltration
Collagen deposition in aneurysm dome
Complete endothelialized neointimal layer
Molecular
Osteopontin expression
Cell-signaling and cell-adhesion molecule expression
C-reactive protein
Fibronectin expression
Expression of inhibitors of apoptosis

Application of Biologic Findings

Many investigators have applied the findings from biologic studies to devising means of enhancing the aneurysm-healing process. A summary of the histopathologic and molecular biologic characteristics of well-healed and poorly healed aneurysms is found in the Table. These findings provide the framework for the device modifications and systemic therapies described below.

Modified Coils. Studies highlighting the importance of early thrombus formation in the aneurysm sac led to the development and testing of thrombogenic-/antithrombolytic-coated coils in the experimental rabbit model. However, early studies revealed that both conventional coils and antithrombolytic coils had similar histopathologic and angiographic findings, including a thin membrane of neointima covering the aneurysm neck and intraneurysmal scar formation.⁵³ Studies highlighting the importance of myofibroblasts in aneurysm healing led to the development of fibroblast-coated coils. Early studies in rabbits found that fibroblast allografts were viable and proliferated in the vascular space in rabbits and remained within the aneurysmal sac.⁵⁴ In a study of rabbits treated with fibroblast-coated coils, Dai et al^{55,56} found that fibroblast-coated coils accelerated early histologic healing and even promoted endothelialization of the aneurysm neck. However, these coils have yet to be tested in humans.

Due to the importance of attenuated packing of the aneurysmal sac in improving long-term occlusion rates, a number of second-generation coils have been developed. The HydroCoil (MicroVention, Tustin, California) was developed with an expandable polymer that allows improved aneurysm filling.⁵⁷ Matrix coils (Stryker, Kalamazoo, Michigan) carry a biodegradable polymer designed to amplify tissue response to the coil and improve aneurysm healing. In a study by using a swine model, Murayama et al⁵⁸ found that the Matrix coil accelerated aneurysm fibrosis and neointima formation without resultant parent artery stenosis. HydroCoil embolization has been shown to improve aneurysm filling and decrease aneurysm recanalization rates in experimental aneurysms, but without the aggressive cellular response seen with Matrix coils.⁵⁷ In a comparative study of Matrix and hydrogel coils in the rabbit model, Ding et al⁵⁹ found that HydroCoils resulted in improved long-term occlusion rates compared with Matrix and platinum coils, while Matrix coils had increased inflammation and coil compaction. In a histologic study of 2 human patients treated with Matrix coils, Szikora et

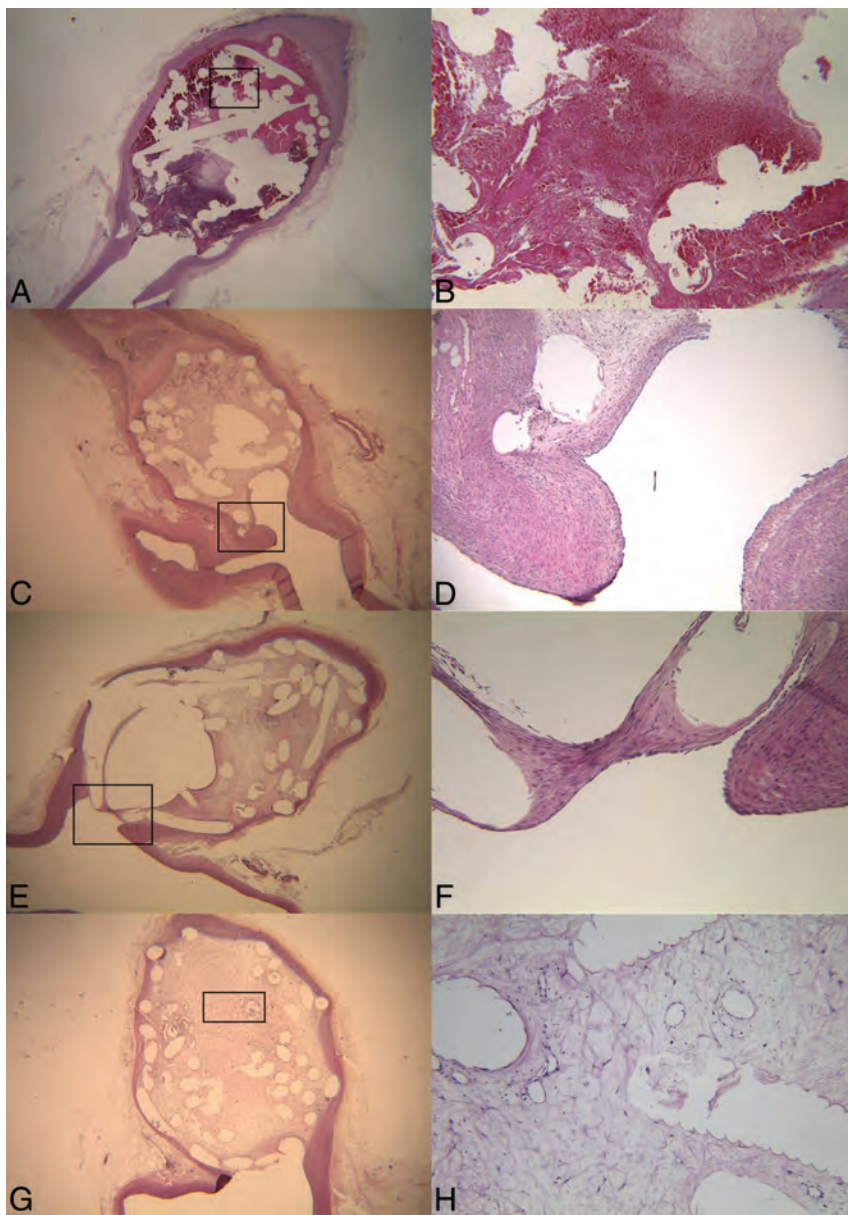


FIG 2. A and B, Histopathologic hematoxylin-eosin stains (original magnification $\times 15$ and $\times 60$, respectively) of a rabbit aneurysm dome 1 week postcoiling demonstrate unorganized thrombus filling the aneurysm dome around the coil loops. No endothelialization has occurred at the aneurysm neck. Histopathologic hematoxylin-eosin stains (original magnification $\times 10$ and $\times 150$, respectively) for a rabbit aneurysm dome 6 weeks postcoiling demonstrate loose connective tissue in the aneurysm dome surrounding the coil loops (C) and an incomplete layer of endothelium-lined neointima over the aneurysm neck (D). The neointima and endothelial cells at the neck interface are both continuous with that of the parent artery. E and F, Histopathologic hematoxylin-eosin stains (original magnification $\times 10$ and $\times 15$, respectively) 12 months postcoiling demonstrate loose connective tissue in the aneurysm dome surrounding coil loops (E) and a layer of neointima of variable thickness covering the aneurysm neck (F). The neointima and endothelial cells at the neck interface are both continuous with those of the parent artery. G and H, Histopathologic hematoxylin-eosin stains (original magnification, $\times 20$ and $\times 125$, respectively) of the aneurysm dome 12 months postcoiling demonstrate loose connective tissue in the aneurysm dome.

al²³ found no difference in the histologic appearance of Matrix-treated aneurysms compared with aneurysms treated with bare platinum coils at 1 week. However, at 6 months following coil embolization, the patient treated with Matrix coils had increased neovascularization, smooth muscle cell infiltration, and collagen deposition compared with the patient treated with bare platinum coils. Both HydroCoils and Matrix coils are on the market for use in humans.

Current studies suggest that modified coils are at least equivalent to platinum coils in humans.^{60,61}

Systemic Therapies. A number of systemic therapies have been tested to improve aneurysm healing. Because vitamin C is known to stimulate collagen synthesis and cross-linking, it was identified as a potential therapeutic agent for patients with coiling. However, a recent study by using the rabbit aneurysm model found that vitamin C did not result in improvement of aneurysm occlusion.⁶² Zhang et al⁶³ studied the therapeutic benefit of bone marrow–derived endothelial progenitor cell transfusion following aneurysm embolization in a rat model. In this study, bone marrow–derived endothelial progenitor cells were labeled and transfused following aneurysm embolization. Zhang et al demonstrated that the labeled cells accumulated at the aneurysm neck, accelerating repair and remodeling of the neck.

Other Therapies. A number of other therapies have been proposed to enhance aneurysm healing following coil embolization. Raymond et al⁶⁴ tested the efficacy of radiofrequency endothelial embolization following coil embolization in an arterial occlusion dog model and found that coiling with concomitant radiofrequency ablation was more effective in reducing recanalization rates than coiling alone. Cryoablation has also been tested but has not been shown to be as effective as radiofrequency ablation, at least in current animal models.⁶⁵ In situ low-dose radiation has also been tested and has been shown to inhibit recanalization following coil embolization. In a study comparing ³²P-coated coils with non-³²P-coated coils, Raymond et al found that the use of ³²P-coated coils resulted in improved aneurysm occlusion and more complete neointimal coverage of the aneurysm neck.^{66,67}

Future Directions

As mentioned previously, our understanding of the mechanisms of healing of coiled intracranial aneurysms has led to some practical improvements in coil technology aimed at decreasing the rates of aneurysm recurrence. Our review of the literature suggests that most of the healing process following coiling occurs within the first month postembolization. Future investigations should focus on means to induce and accelerate a healing response similar to that of wound healing with collagen deposition, resulting in in-

creased occlusion of the aneurysm dome. Coil-modification technologies and systemic administration of medications known to accelerate wound healing are potential means of accomplishing this aim. In addition, therapies and coil modifications aimed at increasing endothelialization of the aneurysm neck to completely exclude the aneurysm from the parent vessel are essential because both rabbit and human models demonstrate that endothelialization along the aneurysm neck is limited. Further research is also needed in improving animal models for embolization of intracranial aneurysms. There is currently no model of aneurysm rupture, growth, or mass effect that would be amenable to coil embolization. There are limited human postmortem examination specimens of postcoiled ruptured intracranial aneurysms.

CONCLUSIONS

The healing of the postcoiled intracranial aneurysm is a dynamic process. Much of the active healing process occurs within the first 4 weeks of coil embolization. Histopathologic studies have demonstrated that myofibroblasts play an important role in healing of the aneurysm dome, while endothelialization with endothelial progenitor cells is essential for healing the aneurysm neck. Gene and protein studies have demonstrated that factors such as MMPs and osteopontin may play an integral role in the aneurysm-healing process. Findings from histopathologic and molecular studies have been applied to develop treatment methods aimed at improving the aneurysm-healing process.

Disclosures: Waleed Brinjikji—UNRELATED: Grants/Grants Pending: Brain Aneurysm Foundation.* David F. Kallmes—RELATED: Grant: ev3*; UNRELATED: Board Membership: GE Healthcare (Cost Effectiveness Board); Consultancy: ev3.* Comments: pre-clinical and clinical research; Grants/Grants Pending: ev3.* MicroVention.* Sequent Medical.* Surmodics.* Codman*; Royalties: University of Virginia Patent Foundation (Spine Fusion). Ram Kadirvel—RELATED: Grant: National Institutes of Health (NS076491). * Money paid to the institution.

REFERENCES

- Brinjikji W, Lanzino G, Rabinstein AA, et al. **Age-related trends in the treatment and outcomes of ruptured cerebral aneurysms: a study of the Nationwide Inpatient Sample 2001–2009.** *AJNR Am J Neuroradiol* 2013;34:1022–27
- Crobeddu E, Lanzino G, Kallmes DF, et al. **Review of 2 decades of aneurysm-recurrence literature. Part 1. Reducing recurrence after endovascular coiling.** *AJNR Am J Neuroradiol* 2013;34:266–70
- Crobeddu E, Lanzino G, Kallmes DF, et al. **Review of 2 decades of aneurysm-recurrence literature. Part 2. Managing recurrence after endovascular coiling.** *AJNR Am J Neuroradiol* 2013;34:481–85
- Dai D, Ding YH, Danielson MA, et al. **Histopathologic and immunohistochemical comparison of human, rabbit, and swine aneurysms embolized with platinum coils.** *AJNR Am J Neuroradiol* 2005;26:2560–68
- Knap D, Gruszczynska K, Partyka R, et al. **Results of endovascular treatment of aneurysms depending on their size, volume and coil packing density.** *Neurol Neurochir Pol* 2013;47:467–75
- Leng B, Zheng Y, Ren J, et al. **Endovascular treatment of intracranial aneurysms with detachable coils: correlation between aneurysm volume, packing, and angiographic recurrence.** *J Neurointerv Surg* 2014;6:595–99
- Slob MJ, Sluzewski M, van Rooij WJ. **The relation between packing and reopening in coiled intracranial aneurysms: a prospective study.** *Neuroradiology* 2005;47:942–45
- Sluzewski M, van Rooij WJ, Slob MJ, et al. **Relation between aneurysm volume, packing, and compaction in 145 cerebral aneurysms treated with coils.** *Radiology* 2004;231:653–58
- Raymond J, Darsaut TE. **An approach to recurrent aneurysms following endovascular coiling.** *J Neurointerv Surg* 2011;3:314–18
- Abdihalim M, Watanabe M, Chaudhry SA, et al. **Are coil compaction and aneurysmal growth two distinct etiologies leading to recurrence following endovascular treatment of intracranial aneurysm?** *J Neuroimaging* 2014;24:171–75
- Hasan DM, Nadareyshvili AI, Hoppe AL, et al. **Cerebral aneurysm sac growth as the etiology of recurrence after successful coil embolization.** *Stroke* 2012;43:866–68
- Yuki I, Lee D, Murayama Y, et al. **Thrombus organization and healing in an experimental aneurysm model. Part II. The effect of various types of bioactive bioabsorbable polymeric coils.** *J Neurosurg* 2007;107:109–20
- Boecher-Schwarz HG, Ringel K, Kopacz L, et al. **Ex vivo study of the physical effect of coils on pressure and flow dynamics in experimental aneurysms.** *AJNR Am J Neuroradiol* 2000;21:1532–36
- Ozawa T, Tamatani S, Koike T, et al. **Histological evaluation of endothelial reactions after endovascular coil embolization for intracranial aneurysm: clinical and experimental studies and review of the literature.** *Interv Neuroradiol* 2003;9:69–82
- Bavinszki G, Talazoglu V, Killer M, et al. **Gross and microscopic histopathological findings in aneurysms of the human brain treated with Guglielmi detachable coils.** *J Neurosurg* 1999;91:284–93
- Castro E, Fortea F, Villoria F, et al. **Long-term histopathologic findings in two cerebral aneurysms embolized with Guglielmi detachable coils.** *AJNR Am J Neuroradiol* 1999;20:549–52
- Groden C, Hagel C, Delling G, et al. **Histological findings in ruptured aneurysms treated with GDCs: six examples at varying times after treatment.** *AJNR Am J Neuroradiol* 2003;24:579–84
- Horowitz MB, Purdy PD, Burns D, et al. **Scanning electron microscopic findings in a basilar tip aneurysm embolized with Guglielmi detachable coils.** *AJNR Am J Neuroradiol* 1997;18:688–90
- Ishihara S, Mawad ME, Ogata K, et al. **Histopathologic findings in human cerebral aneurysms embolized with platinum coils: report of two cases and review of the literature.** *AJNR Am J Neuroradiol* 2002;23:970–74
- Molyneux AJ, Ellison DW, Morris J, et al. **Histological findings in giant aneurysms treated with Guglielmi detachable coils: report of two cases with autopsy correlation.** *J Neurosurg* 1995;83:129–32
- Shimizu S, Kurata A, Takano M, et al. **Tissue response of a small saccular aneurysm after incomplete occlusion with a Guglielmi detachable coil.** *AJNR Am J Neuroradiol* 1999;20:546–48
- Stiver SI, Porter PJ, Willinsky RA, et al. **Acute human histopathology of an intracranial aneurysm treated using Guglielmi detachable coils: case report and review of the literature.** *Neurosurgery* 1998;43:1203–08
- Szikora I, Seifert P, Hanzely Z, et al. **Histopathologic evaluation of aneurysms treated with Guglielmi detachable coils or Matrix detachable microcoils.** *AJNR Am J Neuroradiol* 2006;27:283–88
- Nakahara T, Sakamoto S, Hamasaki O, et al. **Post-mortem pathological examination of two patients after intraaneurysmal embolization using Guglielmi detachable coils.** *Interv Neuroradiol* 2003;9(suppl 1):57–62
- Suda Y, Kikuchi K, Shioya H, et al. **Long-term histopathology of intracranial aneurysms after endovascular treatment with coil: report of two cases with ultrastructural evaluations by scanning electron microscopy.** *Interv Neuroradiol* 1999;5(suppl 1):225–31
- Mizoi K, Yoshimoto T, Takahashi A, et al. **A pitfall in the surgery of a recurrent aneurysm after coil embolization and its histological observation: technical case report.** *Neurosurgery* 1996;39:165–68; discussion 168–69
- Dai D, Ding YH, Kadirvel R, et al. **A longitudinal immunohistochemical study of the healing of experimental aneurysms after embolization with platinum coils.** *AJNR Am J Neuroradiol* 2006;27:736–41
- Kallmes DF, Helm GA, Hudson SB, et al. **Histologic evaluation of platinum coil embolization in an aneurysm model in rabbits.** *Radiology* 1999;213:217–22

29. Ding YH, Dai D, Kadirvel R, et al. **Relationship between aneurysm volume and histologic healing after coil embolization in elastase-induced aneurysms: a retrospective study.** *AJNR Am J Neuroradiol* 2008;29:98–101
30. Kadirvel R, Ding YH, Dai D, et al. **Molecular indices of apoptosis activation in elastase-induced aneurysms after embolization with platinum coils.** *Stroke* 2007;38:2787–94
31. Kadirvel R, Ding YH, Dai D, et al. **Intrinsic pathway-mediated apoptosis in elastase-induced aneurysms in rabbits.** *AJNR Am J Neuroradiol* 2010;31:165–69
32. Qi YX, Qu MJ, Long DK, et al. **Rho-GDP dissociation inhibitor alpha downregulated by low shear stress promotes vascular smooth muscle cell migration and apoptosis: a proteomic analysis.** *Cardiovasc Res* 2008;80:114–22
33. Mitome-Mishima Y, Yamamoto M, Yatomi K, et al. **Endothelial cell proliferation in swine experimental aneurysm after coil embolization.** *PLoS One* 2014;9:e89047
34. Fang X, Zhao R, Wang K, et al. **Bone marrow-derived endothelial progenitor cells are involved in aneurysm repair in rabbits.** *J Clin Neurosci* 2012;19:1283–86
35. Li ZF, Fang XG, Yang PF, et al. **Endothelial progenitor cells contribute to neointima formation in rabbit elastase-induced aneurysm after flow diverter treatment.** *CNS Neurosci Ther* 2013;19:352–57
36. Wei HJ, Wang D, Chen JL, et al. **Mobilization of circulating endothelial progenitor cells after endovascular therapy for ruptured cerebral aneurysms.** *Neurosci Lett* 2011;498:114–18
37. Yamaguchi Y, Yoshikawa K. **Cutaneous wound healing: an update.** *J Dermatol* 2001;28:521–34
38. Martin P, Leibovich SJ. **Inflammatory cells during wound repair: the good, the bad and the ugly.** *Trends Cell Biol* 2005;15:599–607
39. Hinz B. **Masters and servants of the force: the role of matrix adhesions in myofibroblast force perception and transmission.** *Eur J Cell Biol* 2006;85:175–81
40. Wong VW, Crawford JD. **Vasculogenic cytokines in wound healing.** *Biomed Res Int* 2013;2013:190486
41. Greenhalgh DG. **The role of apoptosis in wound healing.** *Int J Biochem Cell Biol* 1998;30:1019–30
42. Stadelmann WK, Digenis AG, Tobin GR. **Physiology and healing dynamics of chronic cutaneous wounds.** *Am J Surg* 1998;176:26S–38S
43. Kadirvel R, Ding YH, Dai D, et al. **Proteomic analysis of aneurysm healing mechanism after coil embolization: comparison of dense packing with loose packing.** *AJNR Am J Neuroradiol* 2012;33:1177–81
44. Kadirvel R, Ding YH, Dai D, et al. **Differential gene expression in well-healed and poorly healed experimental aneurysms after coil treatment.** *Radiology* 2010;257:418–26
45. Kadirvel R, Ding YH, Dai D, et al. **Differential expression of genes in elastase-induced saccular aneurysms with high and low aspect ratios.** *Neurosurgery* 2010;66:578–84; discussion 584
46. Giachelli CM, Liaw L, Murry CE, et al. **Osteopontin expression in cardiovascular diseases.** *Ann N Y Acad Sci* 1995;760:109–26
47. Dai D, Ding YH, Kadirvel R, et al. **Bone formation in elastase-induced rabbit aneurysms embolized with platinum coils: report of 2 cases.** *AJNR Am J Neuroradiol* 2007;28:1176–78
48. Plenk H Jr, Shum JC, Cruise GM, et al. **Cartilage and bone neof ormation in rabbit carotid bifurcation aneurysms after endovascular coil embolization.** *Eur Cell Mater* 2008;16:69–79
49. Chen Q, Shou P, Zhang L, et al. **An osteopontin-integrin interaction plays a critical role in directing adipogenesis and osteogenesis by mesenchymal stem cells.** *Stem Cells* 2014;32:327–37
50. Montezano AC, Zimmerman D, Yusuf H, et al. **Vascular smooth muscle cell differentiation to an osteogenic phenotype involves TRPM7 modulation by magnesium.** *Hypertension* 2010;56:453–62
51. Bouzeghrane F, Darsaut T, Salazkin I, et al. **Matrix metalloproteinase-9 may play a role in recanalization and recurrence after therapeutic embolization of aneurysms or arteries.** *J Vasc Interv Radiol* 2007;18:1271–79
52. Johnson JL, Dwivedi A, Somerville M, et al. **Matrix metalloproteinase (MMP)-3 activates MMP-9 mediated vascular smooth muscle cell migration and neointima formation in mice.** *Arterioscler Thromb Vasc Biol* 2011;31:e35–44
53. Bavinzski G, Richling B, Binder BR, et al. **Histopathological findings in experimental aneurysms embolized with conventional and thrombogenic/antithrombolytic Guglielmi coils.** *Minim Invasive Neurosurg* 1999;42:167–74
54. Marx WE, Cloft HJ, Helm GA, et al. **Endovascular treatment of experimental aneurysms by use of biologically modified embolic devices: coil-mediated intraaneurysmal delivery of fibroblast tissue allografts.** *AJNR Am J Neuroradiol* 2001;22:323–33
55. Dai D, Ding YH, Danielson MA, et al. **Endovascular treatment of experimental aneurysms with use of fibroblast transfected with replication-deficient adenovirus containing bone morphogenetic protein-13 gene.** *AJNR Am J Neuroradiol* 2008;29:739–44
56. Dai D, Ding YH, Danielson MA, et al. **Endovascular treatment of experimental aneurysms by use of fibroblast-coated platinum coils: an angiographic and histopathologic study.** *Stroke* 2007;38:170–76
57. Kallmes DF, Fujiwara NH. **New expandable hydrogel-platinum coil hybrid device for aneurysm embolization.** *AJNR Am J Neuroradiol* 2002;23:1580–88
58. Murayama Y, Tateshima S, Gonzalez NR, et al. **Matrix and bioabsorbable polymeric coils accelerate healing of intracranial aneurysms: long-term experimental study.** *Stroke* 2003;34:2031–37
59. Ding YH, Dai D, Lewis DA, et al. **Angiographic and histologic analysis of experimental aneurysms embolized with platinum coils, Matrix, and HydroCoil.** *AJNR Am J Neuroradiol* 2005;26:1757–63
60. McDougall CG, Johnston SC, Gholkar A, et al. **Bioactive versus bare platinum coils in the treatment of intracranial aneurysms: the MAPS (Matrix and Platinum Science) trial.** *AJNR Am J Neuroradiol* 2014;35:935–42
61. White PM, Lewis SC, Gholkar A, et al. **Hydrogel-coated coils versus bare platinum coils for the endovascular treatment of intracranial aneurysms (HELPS): a randomised controlled trial.** *Lancet* 2011;377:1655–62
62. Dai D, Yong-Hong D, Rezek I, et al. **Healing of saccular aneurysms following platinum coil embolization: lack of improved efficacy with vitamin C supplementation.** *J Neurointerv Surg* 2013;5:591–96
63. Zhang S, An Q, Li Q, et al. **Therapeutic benefit of bone marrow-derived endothelial progenitor cell transplantation after experimental aneurysm embolization with coil in rats.** *PLoS One* 2014;9:e90069
64. Raymond J, Savard P, Salazkin I, et al. **Radiofrequency endothelial ablation prevents recanalization after endovascular coil occlusion: in vitro and in vivo assessment.** *J Vasc Interv Radiol* 2010;21:101–07
65. Raymond J, Metcalfe A, Salazkin I, et al. **Endoluminal cryotherapy to prevent recanalization after endovascular occlusion with platinum coils.** *J Vasc Interv Radiol* 2006;17:1499–504
66. Raymond J, Leblanc P, Desfaits AC, et al. **In situ beta radiation to prevent recanalization after coil embolization of cerebral aneurysms.** *Stroke* 2002;33:421–27
67. Raymond J, Mounayer C, Salazkin I, et al. **Safety and effectiveness of radioactive coil embolization of aneurysms: effects of radiation on recanalization, clot organization, neointima formation, and surrounding nerves in experimental models.** *Stroke* 2006;37:2147–52

Social Media and Public Outreach: A Physician Primer

A. Radmanesh, R. Duszak, and R.T. Fitzgerald

The emergence of social media with easy and anywhere smartphone access has facilitated our society's information-craving behaviors to the point that many rely on the Web and social media to make health-related decisions. Recognizing this reality, many health care professionals and organizations have in recent years become increasingly visible on social media.

According to a database of health care organizations actively using social media, over 1500 US hospitals now have a social media presence. In California alone, 105 hospitals sponsor 444 social media accounts that include 53 YouTube accounts, 89 Facebook accounts, 69 Twitter accounts, 39 LinkedIn accounts, 78 Four-square accounts, and 11 blogs.¹

Many social media pages and on-line review sites used by patients are unfortunately vulnerable to bias and often inaccurate. Given the role of social media in forming the public's "image" of health care facilities and providers, a credible presence by those parties is more important than ever, particularly as crowd-sourced metrics potentially take root as a measure of quality.²

Patients should always be the primary focus of our work. To help shape ongoing reform efforts, the American College of Radiology recently launched the Imaging 3.0 initiative.³ One of its many goals is to improve patient awareness of the integral role of radiologists in their overall health care, and to enhance their understanding of and comfort with the tests and procedures they are undergoing. Social media can be a major facilitator of that culture shift.

The responsible use of social media provides golden opportunities for marketing physician services, as well as for contributing to public health by providing high quality on-line content that is both accurate and understandable to laypeople. Radiologists, for example, can leverage social media to help correct widespread and

frequently publicized fear-generating myths regarding the risks of ionizing radiation from diagnostic imaging.

Public perception of who we are and what we do is the engine of professional advocacy campaigns and important to the future of radiology as a specialty. Social media engagement with patients, their employers, policymakers, and lawmakers can be a strong vehicle to help accurately form that perception. A current example pertains to Medicare reimbursement for lung cancer screening. The June 2014 *Journal of the American College of Radiology* (#JACR) *tweet-chat* engaged both physicians and patients, and was focused on lung cancer screening—a hot topic with many public policy considerations—with an emphasis on patient experience. A tweet-chat is a live Twitter event that is usually moderated and focused around a general topic. To filter all the chatter on Twitter into a single conversation, a hashtag (#) is used. A set time is also established so that the moderator, guest, or host is available to engage in the conversation.⁴

Despite its enormous potentials, the boundless reach of social media creates legal and ethical challenges for physicians. The "4-sphere" concept provides a simple guiding framework for professional users of social media to avoid undesired ethical and legal consequences.⁵ It dictates that any social media activity should be in compliance with the media site's terms of service, professional standards, organizational policies, and individual best practices (Fig 1). To those ends, resources are available. Physicians are advised to familiarize themselves with policies developed by their health care organizations to address concerns of reputation, privacy, and productivity. The American Medical Association has published its own "Professionalism in the Use of Social Media" guidelines document.^{6,7}

Social media and on-line platforms are here to stay. Some platforms may fade away, but new ones will emerge. Based on current trends, media skills could eventually become a professional technical competency and a component of future medical education curricula.

Social media are new to many currently practicing physicians and that may generate anxiety. The avoidance of social media, however, does not protect us as professionals from our public. On the contrary, it constrains our on-line identity and cedes its control to nameless and often uninformed sources. We believe it is far better to be in control—to the degree we can—of what our pa-

From the Department of Radiology and Biomedical Imaging (A.R.), University of California, San Francisco, San Francisco, California; Department of Radiology (R.D.), Emory University School of Medicine, Atlanta, Georgia; Harvey L. Neiman Health Policy Institute (R.D.), Reston, Virginia; and Department of Radiology (R.T.F.), University of Arkansas, Little Rock, Arkansas.

Please address correspondence to Alireza Radmanesh, MD, Department of Radiology and Biomedical Imaging, University of California, San Francisco, 505 Parnassus Ave, L-352, San Francisco, CA 94143; e-mail: alireza.radmanesh@ucsf.edu; @AliRadmanMD

<http://dx.doi.org/10.3174/ajnr.A4100>

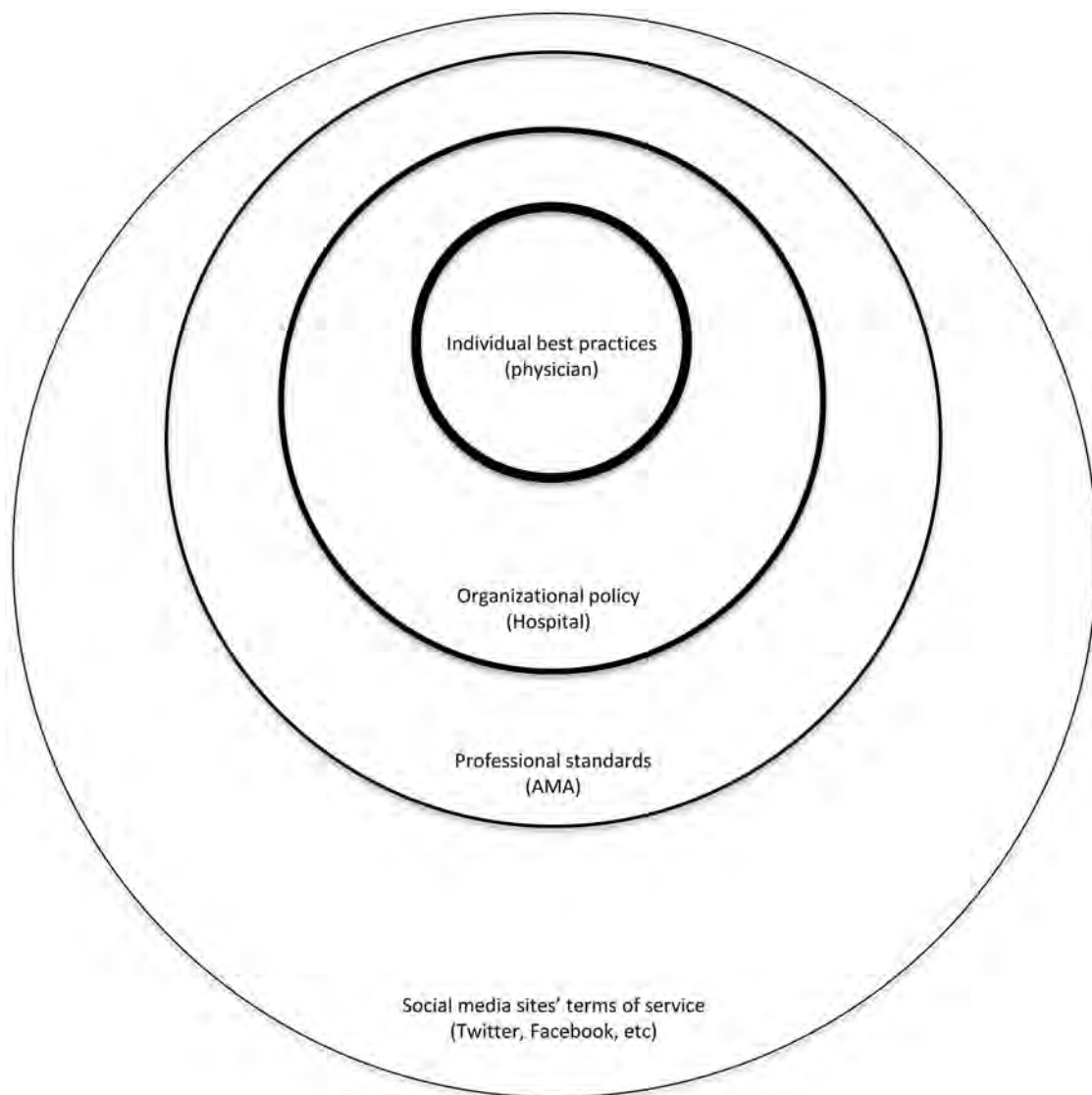


FIG 1. “Four-sphere” concept as a guiding framework for professional use of social media. Adapted from Gagnon et al.⁵

tients, colleagues, and others find about us using search engines and other on-line tools. At the end of the day, as our on-line and real identities increasingly converge, they together define who we are in the eyes of others.

REFERENCES

1. Mayo Clinic Center for Social Media. Health care social media list. <http://network.socialmedia.mayoclinic.org/hcsm-grid/>. Accessed July 5, 2014
2. Timian A, Rupcic S, Kachnowski S, et al. **Do patients “like” good care? Measuring hospital quality via Facebook.** *Am J Med Qual* 2013;28:374–82
3. Ellenbogen PH. **Imaging 3.0: what is it?** *J Am Coll Radiol* 2013;10:229
4. Cooper S. **The ultimate guide to hosting a tweet chat.** *Forbes*. September 30, 2013. <http://www.forbes.com/sites/stevecooper/2013/09/30/the-ultimate-guide-to-hosting-a-tweet-chat/>. Accessed July 2, 2014
5. Gagnon K, Sabus C. **Professionalism in a digital age: opportunities and considerations for using social media in health care.** *Phys Ther* 2015;95:406–14
6. American Medical Association. **Opinion 9.124—professionalism in the use of social media.** June 2011. <http://www.ama-assn.org/ama/pub/physician-resources/medical-ethics/code-medical-ethics/opinion9124.page?> Accessed July 8, 2014
7. Shore R, Halsey J, Shah K, et al. **Report of the AMA council on ethical and judicial affairs: professionalism in the use of social media.** *J Clin Ethics* 2011;22:165–72

Imaging the Paranasal Region with a Third-Generation Dual-Source CT and the Effect of Tin Filtration on Image Quality and Radiation Dose

M.M. Lell, M.S. May, M. Brand, A. Eller, T. Buder, E. Hofmann, M. Uder, and W. Wuest

ABSTRACT

BACKGROUND AND PURPOSE: CT is the imaging technique of choice in the evaluation of midface trauma or inflammatory disease. We performed a systematic evaluation of scan protocols to optimize image quality and radiation exposure on third-generation dual-source CT.

MATERIALS AND METHODS: CT protocols with different tube voltage (70–150 kV), current (25–300 reference mAs), prefiltration, pitch value, and rotation time were systematically evaluated. All images were reconstructed with iterative reconstruction (Advanced Modeled Iterative Reconstruction, level 2). To individually compare results with otherwise identical factors, we obtained all scans on a frozen human head. Conebeam CT was performed for image quality and dose comparison with multidetector row CT. Delineation of important anatomic structures and incidental pathologic conditions in the cadaver head was evaluated.

RESULTS: One hundred kilovolts with tin prefiltration demonstrated the best compromise between dose and image quality. The most dose-effective combination for trauma imaging was Sn100 kV/250 mAs (volume CT dose index, 2.02 mGy), and for preoperative sinus surgery planning, Sn100 kV/150 mAs (volume CT dose index, 1.22 mGy). “Sn” indicates an additional prefiltration of the x-ray beam with a tin filter to constrict the energy spectrum. Exclusion of sinonasal disease was possible with even a lower dose by using Sn100 kV/25 mAs (volume CT dose index, 0.2 mGy).

CONCLUSIONS: High image quality at very low dose levels can be achieved by using a Sn100-kV protocol with iterative reconstruction. The effective dose is comparable with that of conventional radiography, and the high image quality at even lower radiation exposure favors multidetector row CT over conebeam CT.

ABBREVIATIONS: CBCT = conebeam CT; CTDI_{vol} = volume CT dose index; HPM = high-pitch mode; MDCT = multidetector row CT; Sn = an additional prefiltration of the x-ray beam with a tin filter to constrict the energy spectrum

Projection radiography was used in the past for the evaluation of midface trauma and inflammatory sinonasal disease, but due to insufficient delineation of the complex anatomy, cross-sectional imaging has largely replaced radiography.^{1–4} Multidetector row CT (MDCT) has become the criterion standard due to its exquisite delineation of small bony details, 3D properties, short examination time, and relatively low cost. MDCT is, however, responsible for the most radiation exposure in medical imaging. MR imaging can also exquisitely depict sinonasal mucosal disease, thereby avoiding radiation exposure, but delineation of fine bony

structures is not optimal. Conebeam CT (CBCT), primarily introduced for dental applications, has evolved as an alternative to MDCT because its large flat panel detectors can image the maxillofacial region or even the complete head and provide excellent detail of bony anatomy, though only very limited soft-tissue information. CBCT provides high spatial resolution and low radiation exposure, though at the cost of longer image-acquisition times and, therefore, a higher risk of motion artifacts. In recent years, radiation dose-optimized MDCT protocols have been proposed, reducing the tube current from 170 effective mAs at 120 kV down to 33 effective mAs.⁵ Iterative reconstruction and special scanning techniques like high-pitch mode (HPM) and low-kilovolt scanning have further decreased radiation exposure.^{4,6,7} Radiation exposure is considered a relevant issue because sinonasal disease may require repetitive imaging in a relatively young, otherwise healthy patient population with radiosensitive organs within the field of direct exposure (ie, eye lenses) or scattered x-rays (ie, thyroid gland).

Image quality and radiation exposure should be individually

Received August 15, 2014; accepted after revision December 14.

From the Departments of Radiology (M.M.L., M.S.M., M.B., A.E., M.U., W.W.) and Orthodontics and Orofacial Orthopedics (E.H.); Department I (T.B.), Institute of Anatomy; and Imaging Science Institute (M.M.L., M.U.), University Erlangen, Erlangen, Germany.

Please address correspondence to Michael M. Lell, MD, Department of Radiology, University of Erlangen, Maximiliansplatz 1, 91054 Erlangen, Germany; e-mail: michael.lell@uk-erlangen.de

<http://dx.doi.org/10.3174/ajnr.A4270>

adapted to the specific clinical situations: While a high noise level may be acceptable in ruling out mucosal inflammation, less noise may be desired in the preoperative setting, where anatomic variants need to be ruled out and thin bony structures like the lamina papyracea and cribrosa must be assessed, especially if image-based navigation or robotic surgery is performed.⁸ Even higher image quality and therefore less noise are required for the assessment of trauma.

The aim of our study was to assess the image quality and radiation exposure of different MDCT protocols and to identify protocols with an optimal compromise between radiation exposure and image quality for specific indications.

MATERIALS AND METHODS

MDCT Image Acquisition and Reconstruction

The scans were performed on a cadaver head (see below) on a third-generation dual-source CT system (Somatom Definition Force; Siemens, Erlangen, Germany) in single-source helical mode with a detector collimation of 192×0.6 mm. Examinations were conducted with 5 different settings of the tube current (25, 50, 100, 150, 200 mAs) and 7 different tube-voltage settings (70, 80, 90, 100, Sn100, 120, Sn150 kV). “Sn” indicates an additional prefiltration of the x-ray beam with a tin filter to constrict the energy spectrum. Additional scans with 250 and 300 mAs were performed with Sn100 kV. Pitch values of 0.75 and 1.2 and gantry rotation times of 0.5 and 1.0 seconds were used, resulting in 148 different scan protocols.

All images were reconstructed with 0.6-mm section thickness, 0.4-mm section interval, FOV = 210 mm, sharp (bone) kernel (Hr64; Br64 in case of Sn100 kV), and iterative reconstruction (Advanced Modeled Iterative Reconstruction, level 2).

Conebeam CT

A clinical flat panel conebeam CT system (ProMax 3D; Planmeca, Helsinki, Finland) with a maximum FOV = 230×260 mm was used for comparison of image quality and radiation exposure. We used 2 clinical protocols: a high-resolution sinus protocol with a section thickness of 0.2 mm, 11 mA at 96 kV, and an FOV_{xy} of 130 mm, FOV_z of 160 mm, exposure time of 12.3 seconds; and a low-dose head protocol with a section thickness of 0.4 mm, 11 mA at 96 kV, an FOV_{xy} of 230 mm, FOV_z of 160 mm, exposure time 9.4 seconds.

Data Transfer and Image-Quality Assessment

The volume datasets were stored in DICOM format in our PACS system. A 3D postprocessing platform (syngo.via; Siemens) was used to display all datasets in MPR mode (1.5-mm thick sections, window-level setting of 3300/300 HU on two 21.2-inch (53.85 cm) high-resolution monitors (Radiforce RX 320; EIZO, Ishikawa, Japan) after removing all scan protocol-related information. The readers were allowed to adjust the window-level settings at their discretion. The datasets were analyzed by 2 readers with >10 years' experience in head and neck radiology.

Scan Object

A fresh frozen cadaver head of a white male adult was used for imaging. Ten anatomic regions (lamina papyracea, lamina cri-

brosa, nasal septum, ethmoid air cells, sinus walls, orbital floor, lacrimal duct, temporomandibular joint, tympanic cavity, mastoid cells); and 5 incidental “pathologic” conditions (calcified ICA plaque, temporomandibular joint osteoarthritis, intracranial air collections, paranasal and mastoid fluid collections) were evaluated with a 5-point Likert scale: 5 indicating excellent, 4, good; 3, moderate; 2, sufficient; 1, insufficient image quality. The overall rating for each protocol was defined by the worst rating of these 15 structures or findings. For trauma assessment, high image quality (score ≥ 4) was required. Image quality of ≥ 3 was considered sufficient for the preoperative evaluation for sinusitis surgery, and image quality of ≥ 2 , to detect or rule out sinusitis was considered acceptable. We did not perform noise measurements because noise values do not adequately reflect the diagnostic value in high-contrast objects.

To investigate the effects of different pitch values on image quality, we performed 1-to-1 comparisons of datasets after removing all identifying information, and data were displayed side by side in random order. The same procedure was performed for the different gantry-rotation times.

Estimation of Radiation Exposure

The estimation of the effective radiation dose (E) of the CT examination was based on the volume CT dose index (CTDI_{vol}) and the dose-length product derived from the patient protocol with use of the specific conversion coefficient: $E = (\text{mGy} \times \text{cm}) \times 0.0019$ ($\text{mSv} \times \text{mGy}^{-1} \times \text{cm}^{-1}$).⁹ In contrast to all other scans, the CTDI_{vol} in the patient protocol of the Sn100-kV scan is referenced to a 32-cm phantom. An additional conversion factor of 2.5 was applied to compensate for the different reference phantoms. All CTDI_{vol} values following are referring to the 16-cm phantom.

Statistical Analysis

Values are given as mean \pm SD. The image quality was measured by using an ordinal performance scale with 5 levels. Interrater agreement was assessed by using the Cohen weighted κ test. Fleiss equally arbitrary guidelines characterize a κ of >0.75 as excellent, 0.40–0.75 as fair to good, and <0.40 as poor. Significance levels of .05 were assumed. Statistical analysis was performed by using the software package SPSS Statistics, Version 19 (IBM, Armonk, New York).

RESULTS

The image quality differed significantly with dose. The readers did not detect significant differences in image quality between corresponding datasets acquired with a pitch value of 0.75 versus 1.2 or with a gantry-rotation time of 0.5 second versus 1 second.

Image quality for Sn100 kV/300 mAs and 250 mAs was rated perfect (score of 5) by both readers, and the corresponding CTDI_{vol} was 2.45 and 2.05 mGy. Image quality and the corresponding CTDI_{vol} of the other tube current and tube voltage combinations are given in Tables 1 and 2.

Interrater agreement was good ($\kappa = 0.71$). The most dose-effective combinations for trauma imaging (requiring a rating of ≥ 4) were Sn100 kV/250 mAs (CTDI_{vol} = 2.05 mGy), Sn150 kV/50 mAs (CTDI_{vol} = 2.61 mGy), and 90 kV/50 mAs (CTDI_{vol} = 3.23 mGy).

Table 1: Scan protocols and image quality^a

	200 mAs	150 mAs	100 mAs	50 mAs	25 mAs
70 kV	4	3	3	2	2
80 kV	5	4	3	2	2
90 kV	5	5	5	4	3
100 kV	5	5	5	4	3
100 kV + Sn	3	3	2	2	2
120 kV	5	5	5	4	3
150 kV + Sn	5	5	5	4	3

^a 5 indicates excellent image quality; 4, good image quality; 3, moderate quality; 2, sufficient for special indications; 1, insufficient.

Table 2: Scan protocols and CTDI_{vol}^a

	200 mAs	150 mAs	100 mAs	50 mAs	25 mAs
70 kV	5.71	4.27	2.84	1.41	0.71
80 kV	8.97	6.72	4.47	2.22	1.11
90 kV	13.05	9.78	6.50	3.23	1.62
100 kV	17.69	13.25	8.81	4.38	2.25
100 kV + Sn	1.62	1.22	0.82	0.4	0.2
120 kV	28.41	21.28	14.16	7.03	3.61
150 kV + Sn	10.56	7.91	5.26	2.61	1.34

^a All CTDI_{vol} values are converted to a 16-cm phantom.

The most dose-effective combinations for preoperative sinus surgery planning (requiring a rating of ≥ 3) were Sn100 kV/150 mAs (CTDI_{vol} = 1.22 mGy), Sn150 kV/25 mAs (CTDI_{vol} = 1.34 mGy), 90 kV/25 mAs (CTDI_{vol} = 1.62 mGy), and 100 kV/25 mAs (CTDI_{vol} = 2.25 mGy).

Both Sn100-kV and Sn150-kV protocols were associated with very low radiation exposure. The Sn100-kV protocols were associated with the lowest dose values, and high image quality sufficient for all indications was provided with tube currents of 300 mAs (CTDI_{vol} = 2.45 mGy) and 250 mAs (CTDI_{vol} = 2.05 mGy). These scan protocols provide better image quality at a comparable dose level than a 100-kV protocol without tin filtration and 25 mAs (Fig 1). Image quality of Sn100 kV and 150 mAs was sufficient for sinus surgery evaluation; the respective CTDI_{vol} was 1.22 mGy, a dose level that could not be matched with other kilovolt settings (Fig 2).

CBCT image ratings were 4 (good) for an FOV of 130 mm and 3 (moderate) for an FOV of 230 mm. The dose-area product was 2859 mGy \times cm² and 2115 mGy \times cm², respectively (Fig 3).

DISCUSSION

CT scanning of the sinuses is frequently performed; it has been estimated that approximately 4 million scans are obtained annually in the United States.¹⁰ Many of the patients are young, and examinations are often repeated. It is, therefore, mandatory to strictly follow the as low as reasonably achievable concept because the highly radiosensitive ocular lenses¹¹ are within the scan range. Whether and to what extent there is a carcinogenic effect of very low radiation exposure is of current debate.¹² Abundant data suggest that high image quality at low radiation exposure can be achieved with modern CT technology. Scanning at low-kilovolt settings results in a higher signal of iodine; thus, higher noise can be tolerated while maintaining the signal-to-noise ratio, contrast-to-noise ratio, and overall image quality.^{13,14} The dose-reduction potential is highest in CT angiography because of the high vascular attenuation.¹⁵⁻¹⁸ In nonenhanced CT, there is less potential of dose reduction by using low-kilovolt protocols, though the CT numbers of bone increase with decreasing kilovolt settings and the higher image noise in low kilovolts is a limiting factor. We demonstrated that the Sn100-kV protocol provided superior image quality compared with 70- to 90-kV protocols at equivalent dose levels. This has also been reported in a phantom study of chest CT, where Sn100 kV was rated superior to 70 kV for nodule detection.¹⁹ Tin filtration restricts the bandwidth of the x-ray energy spectrum that reaches the patient.

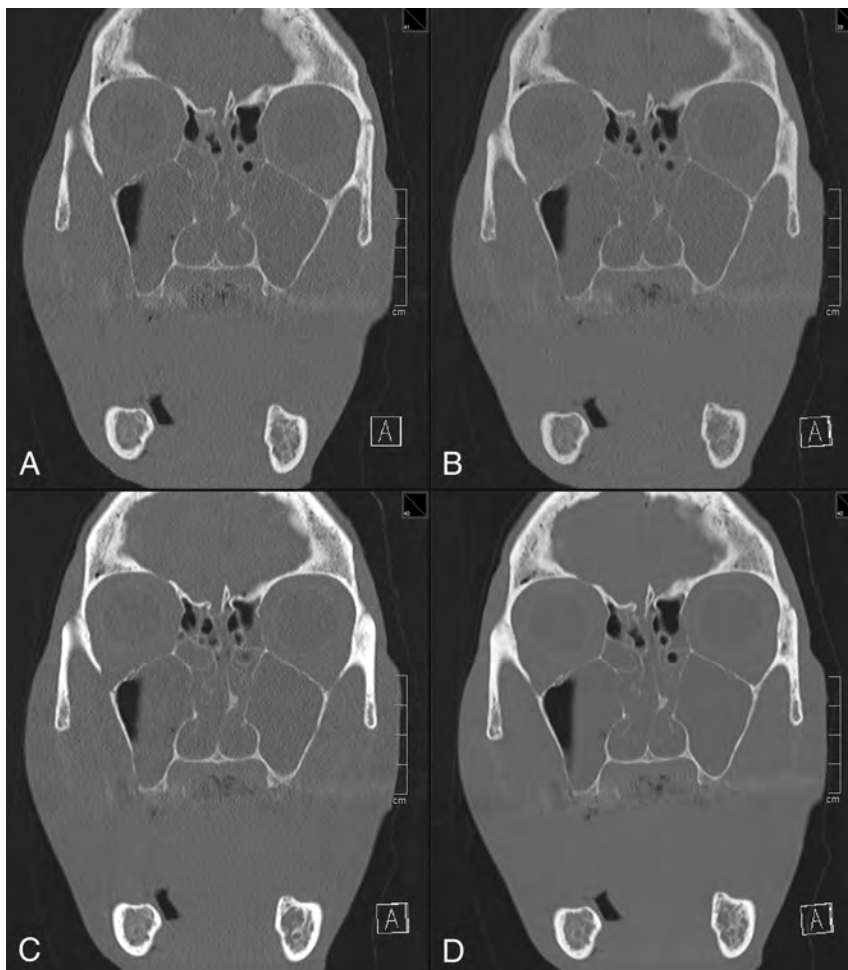


FIG 1. Dose-effective scan protocols achieving good image quality and high-dose reference protocol. The following image quality is considered sufficient for trauma imaging at the lowest dose. A, Sn100 kV/250 mAs. B, Sn150 kV/50 mAs. C, 90 kV/50 mAs. The following is a high-dose protocol. D, 120 kV/200 mAs is given as a reference. Coronal multiplanar reformation; section thickness, 1.5 mm; window width–level, 3300/300 HU.

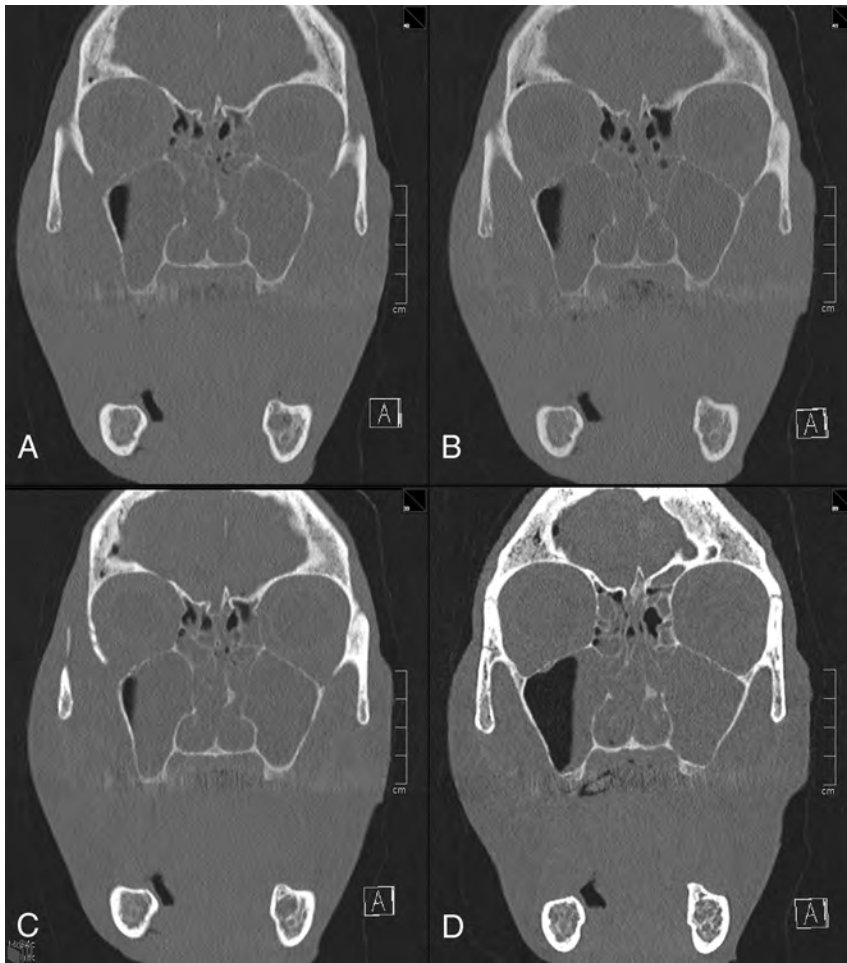


FIG 2. Dose-effective scan protocols achieving moderate image quality. The following image quality is considered sufficient for preoperative evaluation in noncomplicated sinusitis at the lowest dose. A, Sn100 kV/150 mAs. B, Sn150 kV/25 mAs. C, 90 kV/25 mAs. The following is a low-kilovolt protocol. D, 70 kV/100 mAs has higher attenuation values of bone but is associated with a higher dose. Coronal multiplanar reformation; section thickness, 1.5 mm; window width–level, 3300/300 HU.

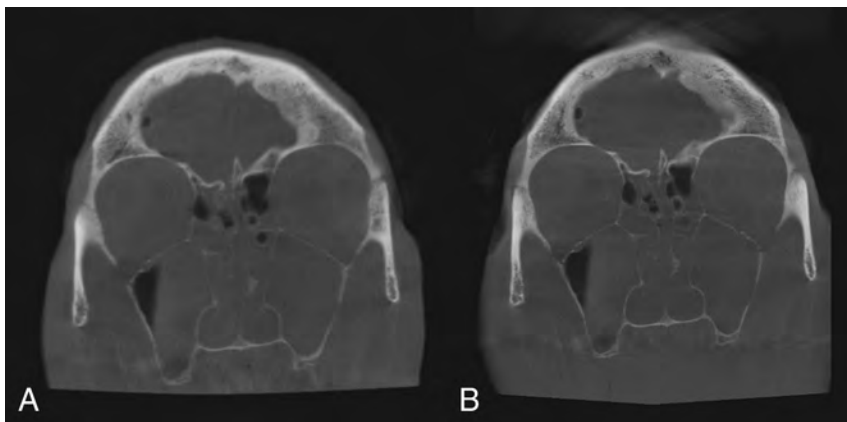


FIG 3. Conebeam CT with an FOV of 230 mm (A, moderate image quality) and FOV of 130 mm (B, good image quality). Note improvement of the delineation of bony structures with a smaller FOV and longer exposition time (B).

The effective dose (0.034 mSv for a typical scan range of 10 cm) is in the range of conventional projection x-ray techniques (digital panoramic radiograph, 0.022 mSv) and below that of conebeam CT (0.07–0.13 mSv).²⁰

exposure of tissue not relevant for diagnosis. Image quality and also radiation exposure differ significantly among CBCT systems.²⁵ While noise is relatively homogeneously distributed over the scan range in MDCT and can be balanced with tube current modula-

Schulz et al⁷ proposed using an HPM ($P = 3.0$) to minimize radiation exposure. They reported an average dose at the eye lens of 0.64 mGy and at the thyroid gland of 0.085 mGy. The same group published data of a patient cohort comparing conventional mode and HPM and stated that the effective dose may be reduced by half by using HPM, with a mean effective dose of 0.11 mSv.²¹ Aksoy et al²² compared conventional mode and HPM on a second-generation dual-source CT scanner and considered HPM with a tube current of 18 mAs at 80 kV sufficient to rule out sinus disease. The estimated effective dose was reported to be 0.02 mSv. Yang and Chen²³ and Bulla et al²⁴ criticized the reported dose values because the $CTDI_{vol}$ and dose-length product of HPM—a scan mode originally designed for cardiac and chest imaging—in the patient protocols of Siemens scanners are referenced to a 32-cm phantom and not to a 16-cm phantom, which is, by convention, used for head scans. To compensate for the difference, an additional conversion factor (>2 , dependent on scanner and prefiltration) is necessary. In addition, dose distribution along the z-axis is less homogeneous by using HPM, and over-ranging is higher compared with conventional pitch modes.¹⁶ This difference makes HPM less attractive for sinus imaging.

Aksoy et al²² stated that scans with 18 mAs at 80 kV are sufficient to rule out sinusitis, but they did not recommend that protocol in the preoperative setting. This finding is in line with our findings in which 80 kV and 25 mAs were rated sufficient for special indications only (rule out sinusitis). We identified the most dose-effective protocol with sufficient image quality for preoperative planning to be Sn100 kV and 150 mAs, resulting in an effective dose of 0.03 mSv for a typical 10-cm scan range.

While CBCT is increasingly popular, MDCT systems provide much higher flexibility in data acquisition and image reconstruction. The scan range can be individually adapted, while only fixed FOVs are given in CBCT, leading to expo-

tion and automatic exposure control algorithms, in CBCT, noise and reconstruction artifacts are unevenly distributed and increase from the central position toward the edges of the FOV. Iterative reconstruction algorithms can decrease overall image noise, but the appearance of the CT image may be altered by these algorithms. We used only a moderate setting of the iterative reconstruction algorithm in MDCT to avoid artifacts at delicate bone structures like the cribriform plate or the lamina papyracea.

In a recent study, MDCT and CBCT were performed on the same day for intraindividual comparison.²⁶ Instead of using dose-equivalent scan protocols, however, only “manufacturer recommended” protocols were applied; this application makes the comparison unbalanced in terms of dose and image quality. In another recent study, a comparison of MDCT and “simulated” CBCT was performed to evaluate the percentage of missed soft-tissue lesions, which was as low as 3.3%.²⁷ The authors used high-dose MDCT examinations ($CTDI_{vol} = 39.8\text{--}85.1$ mGy) as the reference and concluded that if one assumes appropriate selection of patients, CBCT can offer substantial radiation-dose reduction. These 2 reports are only the most recent ones of many suggesting that CBCT is more dose-efficient than MDCT. Two important conclusions can be drawn from these studies: First, in many imaging centers, low-dose MDCT protocols are still neglected, and second, appropriate patient selection is mandatory. We, therefore, propose different dose-optimized imaging protocols for specific indications in adults. Imaging of intracranial complications or tumor requires injection of contrast material, low noise levels, and therefore the use of standard dose protocols or MR imaging. For imaging the sinuses or midface trauma, the 3 most important tissue classes are bone, soft tissue, and air, which can be readily differentiated with low-dose protocols and do not necessitate contrast material injection. Still, image noise may not exceed a certain degree because otherwise, fissures, fracture lines, or a small dehiscence may not be detected. We found that Sn100 kV/250 mAs ($CTDI_{vol} = 2.02$ mGy) was the most dose-effective combination for trauma imaging. A little more noise could be tolerated in the presurgical evaluation of noncomplicated sinonasal inflammatory disease, but clear delineation of the cribriform plate, the lamina papyracea, the orbital walls, and neurovascular canals must be maintained. We identified Sn100 kV/150 mAs ($CTDI_{vol} = 1.22$ mGy) as the protocol providing sufficient information at the lowest dose. To rule out mucosal swelling or fluid retention, protocols with even lower exposure ($CTDI_{vol} = 0.2$ mGy) could be used, still providing non-superimposed 3D data.

Some limitations of our study need to be addressed. The evaluation of only 1 cadaveric head may be considered a limitation. However, for comparison of image quality, we consider the phantom having normal-sized sinus walls and extensive fluid collections within the sinuses more important than testing multiple phantoms. Additionally, we did not specify the organ dose of the thyroid and the eye lenses, yet with an effective dose of 0.03 mSv for the paranasal region, eye lenses and thyroid exposure is an order of magnitude smaller than that with standard sinus protocols.

CONCLUSIONS

Our study demonstrates that imaging the paranasal sinuses for preoperative planning with a third-generation dual-source CT is

feasible at very low radiation exposure (0.03 mSv) when using Sn100 kV and iterative reconstruction. We optimized scan protocols for specific indications at the lowest possible dose and found that the radiation exposure is comparable with that of conventional radiography. Future studies in a large patient population are needed to confirm the clinical value of such protocols.

Disclosures: Michael M. Lell—UNRELATED: Grants/Grants Pending: Bayer*; Payment for Lectures (including service on Speakers Bureaus): Bayer, Bracco, Siemens. Matthias S. May—UNRELATED: Payment for Lectures (including service on Speakers Bureaus): Siemens. Michael Uder—UNRELATED: Payment for Lectures (including service on Speakers Bureaus): Bracco, Medtronic, Siemens, GE Healthcare. *Money paid to the institution.

REFERENCES

1. Kaur J, Chopra R. **Three dimensional CT reconstruction for the evaluation and surgical planning of mid face fractures: a 100 case study.** *J Maxillofac Oral Surg* 2010;9:323–28
2. Hopper RA, Salemy S, Sze RW. **Diagnosis of midface fractures with CT: what the surgeon needs to know.** *Radiographics* 2006;26:783–93
3. Duvoisin B, Landry M, Chapuis L, et al. **Low-dose CT and inflammatory disease of the paranasal sinuses.** *Neuroradiology* 1991;33:403–06
4. Tack D, Widelec J, De Maertelaer V, et al. **Comparison between low-dose and standard-dose multidetector CT in patients with suspected chronic sinusitis.** *AJR Am J Roentgenol* 2003;181:939–44
5. Brem MH, Zamani AA, Riva R, et al. **Multidetector CT of the paranasal sinus: potential for radiation dose reduction.** *Radiology* 2007;243:847–52
6. Schulz B, Beeres M, Bodelle B, et al. **Performance of iterative image reconstruction in CT of the paranasal sinuses: a phantom study.** *AJNR Am J Neuroradiol* 2013;34:1072–76
7. Schulz B, Potente S, Zangos S, et al. **Ultra-low dose dual-source high-pitch computed tomography of the paranasal sinus: diagnostic sensitivity and radiation dose.** *Acta Radiol* 2012;53:435–40
8. Bumm K, Wurm J, Rachinger J, et al. **An automated robotic approach with redundant navigation for minimal invasive extended transphenoidal skull base surgery.** *Minim Invasive Neurosurg* 2005;48:159–64
9. Deak PD, Smal Y, Kalender WA. **Multisection CT protocols: sex- and age-specific conversion factors used to determine effective dose from dose-length product.** *Radiology* 2010;257:158–66
10. Stern SH, Spelic DC, Kaczmarek RV. **NEXT 2000: protocol for survey of computed tomography (CT).** December 18, 2000. http://www.crcpd.org/PDF/NEXT2000_CTPro1.pdf. Accessed August 10, 2014
11. Stewart FA, Akleyev AV, Hauer-Jensen M, et al, on behalf of ICRP. **ICRP publication 118: ICRP statement on tissue reactions and early and late effects of radiation in normal tissues and organs: threshold doses for tissue reactions in a radiation protection context.** *Ann ICRP* 2012;41:1–322
12. Candela-Juan C, Montoro A, Ruiz-Martinez E, et al. **Current knowledge on tumour induction by computed tomography should be carefully used.** *Eur Radiol* 2014;24:649–56
13. Eller A, May MS, Scharf M, et al. **Attenuation-based automatic kilovolt selection in abdominal computed tomography: effects on radiation exposure and image quality.** *Invest Radiol* 2012;47:559–65
14. Eller A, Wuest W, Scharf M, et al. **Attenuation-based automatic kilovolt (kV)-selection in computed tomography of the chest: effects on radiation exposure and image quality.** *Eur J Radiol* 2013;82:2386–91
15. Eller A, Wuest W, Kramer M, et al. **Carotid CTA: radiation exposure and image quality with the use of attenuation-based, automated kilovolt selection.** *AJNR Am J Neuroradiol* 2014;35:237–41
16. Lell MM, May M, Deak P, et al. **High-pitch spiral computed tomography: effect on image quality and radiation dose in pediatric chest computed tomography.** *Invest Radiol* 2011;46:116–23
17. Winklehner A, Goetti R, Baumüller S, et al. **Automated attenuation-based tube potential selection for thoracoabdominal computed to-**

- mography angiography: improved dose effectiveness. *Invest Radiol* 2011;46:767–73
18. Yu L, Fletcher JG, Grant KL, et al. **Automatic selection of tube potential for radiation dose reduction in vascular and contrast-enhanced abdominal pelvic CT.** *AJR Am J Roentgenol* 2013;201:W297–306
 19. Gordic S, Morsbach F, Schmidt B, et al. **Ultralow-dose chest computed tomography for pulmonary nodule detection: first performance evaluation of single energy scanning with spectral shaping.** *Invest Radiol* 2014;49:465–73
 20. Grünheid T, Kolbeck Schieck JR, Pliska BT, et al. **Dosimetry of a cone-beam computed tomography machine compared with a digital x-ray machine in orthodontic imaging.** *Am J Orthod Dentofacial Orthop* 2012;141:436–43
 21. Schell B, Bauer RW, Lehnert T, et al. **Low-dose computed tomography of the paranasal sinus and facial skull using a high-pitch dual-source system: first clinical results.** *Eur Radiol* 2011;21:107–12
 22. Aksoy EA, Ozden SU, Karaarslan E, et al. **Reliability of high-pitch ultra-low-dose paranasal sinus computed tomography for evaluating paranasal sinus anatomy and sinus disease.** *J Craniofac Surg* 2014;25:1801–04
 23. Yang WJ, Chen KM. **Letter to the editor re: low-dose computed tomography of the paranasal sinus and facial skull using a high-pitch dual-source system—first clinical results.** *Eur Radiol* 2011;21:1449–50; author reply 1451
 24. Bulla S, Blanke P, Langer M, et al. **Letter to the editor re: low-dose computed tomography of the paranasal sinus and facial skull using a high-pitch dual-source system—first clinical results.** *Eur Radiol* 2011;21:1447–48; author reply 1451
 25. Hofmann E, Schmid M, Sedlmair M, et al. **Comparative study of image quality and radiation dose of cone beam and low-dose multislice computed tomography: an in-vitro investigation.** *Clin Oral Investig* 2014;18:301–11
 26. Leiva-Salinas C, Flors L, Gras P, et al. **Dental flat panel CT in the evaluation of patients with inflammatory sinonasal disease: diagnostic efficacy and radiation dose savings.** *AJNR Am J Neuroradiol* 2014;35:2052–57
 27. Fakhran S, Alhilali L, Sreedher G, et al. **Comparison of simulated cone beam computed tomography to conventional helical computed tomography for imaging of rhinosinusitis.** *Laryngoscope* 2014;124:2002–06

Arterial Spin-Labeling Parameters Influence Signal Variability and Estimated Regional Relative Cerebral Blood Flow in Normal Aging and Mild Cognitive Impairment: FAIR versus PICORE Techniques

K.-O. Lövblad, M.-L. Montandon, M. Viallon, C. Rodriguez, S. Toma, X. Golay, P. Giannakopoulos, and S. Haller



ABSTRACT

BACKGROUND AND PURPOSE: Arterial spin-labeling is a noninvasive method to map cerebral blood flow, which might be useful for early diagnosis of neurodegenerative diseases. We directly compared 2 arterial spin-labeling techniques in healthy elderly controls and individuals with mild cognitive impairment.

MATERIALS AND METHODS: This prospective study was approved by the local ethics committee and included 198 consecutive healthy controls (mean age, 73.65 ± 4.02 years) and 43 subjects with mild cognitive impairment (mean age, 73.38 ± 5.85 years). Two pulsed arterial spin-labeling sequences were performed at 3T: proximal inversion with a control for off-resonance effects (PICORE) and flow-sensitive alternating inversion recovery technique (FAIR). Relative cerebral blood flow maps were calculated by using commercial software and standard parameters. Data analysis included spatial normalization of gray matter–corrected relative CBF maps, whole-brain average, and voxelwise comparison of both arterial spin-labeling sequences.

RESULTS: Overall, FAIR yielded higher relative CBF values compared with PICORE (controls, 32.7 ± 7.1 versus 30.0 ± 13.1 mL/min/100 g, $P = .05$; mild cognitive impairment, 29.8 ± 5.4 versus 26.2 ± 8.6 mL/min/100 g, $P < .05$; all, 32.2 ± 6.8 versus 29.3 ± 12.3 mL/min/100 g, $P < .05$). FAIR had lower variability (controls, 36.2% versus 68.8%, $P < .00001$; mild cognitive impairment, 18.9% versus 22.9%, $P < .0001$; all, 34.4% versus 64.9% $P < .00001$). The detailed voxelwise analysis revealed a higher signal for FAIR, notably in both convexities, while PICORE had higher signal predominantly in deep cerebral regions.

CONCLUSIONS: Overall, FAIR had higher estimated relative CBF and lower interindividual variability than PICORE. In more detail, there were regional differences between both arterial spin-labeling sequences. In summary, these results highlight the need to calibrate arterial spin-labeling sequences.

ABBREVIATIONS: ASL = arterial spin-labeling; FAIR = flow-sensitive alternating inversion recovery technique; MCI = mild cognitive impairment; PICORE = proximal inversion with a control for off-resonance effects; rCBF = relative cerebral blood flow

Arterial spin-labeling (ASL) is a noninvasive perfusion technique that uses the labeled spins in arterial water as an endogenous tracer. In principle, 2 images are acquired, 1 control image with no blood labeling and 1 tag image in which arterial blood is labeled. The technique was developed 2 decades ago¹ and is feasible on 1.5T scanners but became increasingly used with the introduction of clinical 3T scanners. Recent investigations high-

light the utility of ASL in the domain of neurodegeneration, notably mild cognitive impairment (MCI) and Alzheimer disease,²⁻⁵ for review.⁶ More recently, ASL was even able to predict very early cognitive decline in healthy elderly controls (ie, the earliest stage of neurodegeneration).⁷ These investigations demonstrated consistent reduction in relative cerebral blood flow (rCBF), notably in the posterior cingulate cortex, which overlaps the patterns of hypometabolism on [¹⁸F]FDG-PET in clinically overt and incipient cases of Alzheimer disease.⁸⁻¹¹ The correspondence between ASL and PET findings is consistent with the known perfusion-metabolism coupling in the brain.^{12,13}

Received November 17, 2014; accepted after revision December 5.

From the Divisions of Diagnostic and Interventional Neuroradiology (K.-O.L., M.-L.M., M.V., S.H.) and Psychiatry (C.R., S.T., P.G.), Geneva University Hospitals, Geneva, Switzerland; CREATIS (M.V.), UMR CNRS 5220–Institut National de la Santé et de la Recherche Médicale U1044, INSA de Lyon, Université de Lyon, Centre Hospitalier Universitaire de Saint Etienne, Saint Etienne, France; and Institute of Neurology (X.G.), University College London, London, United Kingdom.

This work was supported by Swiss National Foundation grant SNF 3200B0-116193 and SPUM 33CM30-124111. Collaboration with X.G. was supported by COST Action BM1103 on “ASL in Dementia” and by the National Institute for Health Research University College London Hospitals Biomedical Research Centre.

Please address correspondence to Sven Haller, MD, Service Neuro-Diagnostique et Neuro-Interventionnel DISIM, University Hospitals of Geneva, Rue Gabrielle Perret-Gentil 4, 1211 Geneva 14, Switzerland; e-mail: sven.haller@hcuge.ch

Indicates open access to non-subscribers at www.ajnr.org

Evidence-Based Medicine Level 2.

<http://dx.doi.org/10.3174/ajnr.A4291>

Summary of the essential imaging parameters for PICORE and FAIR ASL sequences

	PICORE Q2TIPS	FAIR-QUIPSS II
Matrix	64 × 64	64 × 64
No. of sections	20	24
Pixel size (mm ²)	3.44 × 3.44	3.44 × 3.44
Section thickness (mm)	6	4
Gap (mm)	1	0
FOV	220	220
Parallel imaging (GRAPPA)	2	2
Phase, partial Fourier	7/8	6/8
Section order	Ascending	Ascending
Section orientation	ACPC aligned	ACPC aligned
Fat saturation	Yes	Yes
Coil-combination algo	Sum of squares	Sum of squares
Bandwidth	2604 Hz/Px	2368 Hz/Px
Echo-spacing	0.47	0.49
Saturation slab	Parallel feet, gap = 25.6 mm, thickness = 110 mm	Parallel feet/head gap = 10 mm, thickness = 100 mm
TE (ms)	21	12
TR (ms)	5000	4000
T1 1 (ms)	700	600
T1 2 (ms)	1800	1600
Saturation stop time (ms)	1600	
Flow limit (cm/s)	5	100
No. of images	71	105
Total acquisition time	6 Minutes 12 seconds	7 Minutes 6 seconds
Mo reference image	No	Yes

Note:—ACPC indicates anterior/posterior commissure; algo, algorithm; Q2TIPS, quantitative imaging of perfusion with a single subtraction with thin-section T1, periodic saturation; QUIPSS II, quantitative imaging of perfusion using a single subtraction II; Mo, steady-state magnetization; GRAPPA, generalized autocalibrating partially parallel acquisitions.

In the context of neurocognitive decline, disease-related alterations in brain perfusion are a priori small, in particular in early stages of the disease. This feature implies that the optimal ASL sequence for the early detection of neurodegenerative processes should have a strong signal and, in particular, a low variability. Unfortunately, ASL has low intrinsic signal and contrast. Consequently, several techniques have been proposed to improve spin-labeling, thereby resulting in a higher signal, including the flow-sensitive alternating inversion recovery technique (FAIR)¹⁴ and the proximal inversion with a control for off-resonance effects (PICORE).¹⁵

In this prospective investigation, we directly compared 2 pulsed ASL sequences (PICORE versus FAIR) in 241 consecutive elderly controls and MCI participants. Both ASL sequences are in agreement with the recent recommendations on ASL imaging.¹⁶ We assessed whole-brain average and local signal strength and interindividual variability.

MATERIALS AND METHODS

Participants

The local ethics committee approved this prospective study, and all participants gave informed written consent before inclusion. A total of 241 consecutive subjects who had both PICORE and FAIR ASL sequences were included in this study from an ongoing cohort study with extensive neuropsychological evaluation and multiparametric MR imaging as described in detail before.⁷ The final sample consisted of 198 healthy controls (mean age, 73.65 ± 4.02 years; 116 women; Mini-Mental State Examination score,¹⁷ 28.36 ± 1.41) and 43 subjects with MCI (mean age, 73.38 ± 5.85 years; 15 women; Mini-Mental State Examination score, 26.93 ± 2.36).

MR Imaging

Imaging data were acquired on a clinical routine whole-body 3T MR imaging scanner (Magnetom Trio; Siemens, Erlangen, Germany). Two pulsed arterial spin-labeling approaches were performed for comparison: PICORE¹⁵ quantitative imaging of perfusion with a single subtraction with thin-section T1 periodic saturation (Q2TIPS) labeling scheme¹⁸ and FAIR¹⁴ combined with quantitative imaging of perfusion using a single subtraction II (QUIPSS II).¹⁹

The essential parameters for both ASL sequences are illustrated in the Table.

A structural 3D T1 sequence was obtained for spatial normalization (256 × 256 matrix; 176 sections, 1 × 1 × 1 mm³; TE, 2.3 ms; TR, 2300 ms). Additional sequences (T2-weighted, diffusion tensor imaging, fluid-attenuated inversion recovery) were acquired and analyzed to rule out concomitant diseases such as ischemic stroke and subdural hematomas and susceptibility artifacts from prior hemorrhage or space-occupying lesions. White matter lesions were analyzed according to the Fazekas score.²⁰ Mild-to-moderate white matter lesions (Fazekas 1–2) are very common in this age group and were not exclusion criteria. In contrast, participants with severe white matter lesion load (Fazekas 3) were excluded.

Statistical Analysis

The relative CBF values were calculated inline on the MR imaging scanner according to Luh et al¹⁸ and Wang et al¹⁹ and under the assumption of constant standard values for hematocrit, T1, λ, and inversion efficiency.

These rCBF maps were further processed with the fMRI of the Brain Software Library (FSL, Version 5.0.2.1; <http://www.fmrib.ox.ac.uk/fsl>) by using the following data-processing steps: masking of nonbrain voxels by using the Brain Extraction Tool (<http://fsl.fmrib.ox.ac.uk/fsl/fslwiki/BET>, part of FSL), linear registration of the ASL raw data to the same subject's 3D T1 data by using the FMRIB Linear Image Registration Tool (FLIRT; <http://www.fmrib.ox.ac.uk/>), nonlinear spatial registration of the high-resolution 3D T1 image to Montreal Neurological Institute standard space (the FMRIB Nonlinear Registration Tool, [FNIRT, <http://fsl.fmrib.ox.ac.uk/fsl/fslwiki/FNIRT>]), and application of this nonlinear transformation matrix to the ASL rCBF maps to spatially normalize the rCBF maps into Montreal Neurological Institute standard space. ASL rCBF is higher in gray matter than in white matter. To compensate for partial volume effects of the rCBF maps, we calculated gray matter-corrected rCBF maps as reported previously.^{4,5} In principle, the individual 3D T1 images were preprocessed by using FSL voxel-based morphometry to create individual gray matter maps, which were then used to mask the individual ASL rCBF maps to obtain individual gray matter-corrected rCBF maps.

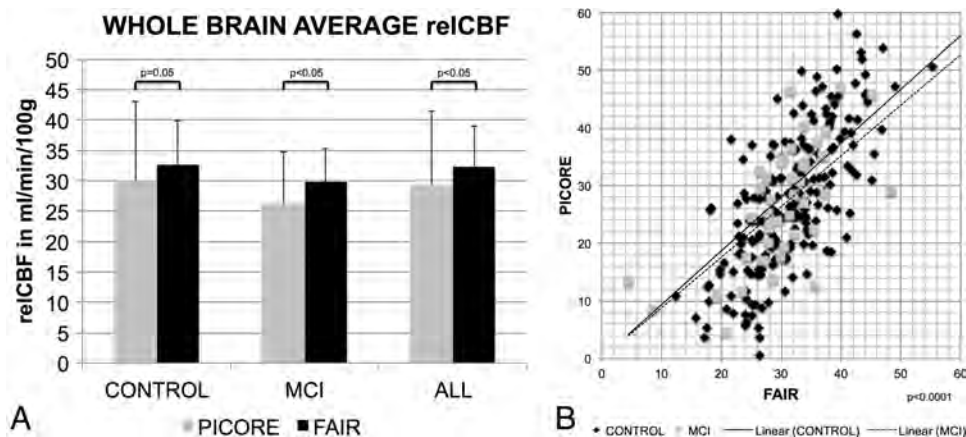


FIG 1. A, The whole-brain average rCBF (reICBF) values in milliliters/minute/100 g for the 2 ASL sequences, PICORE and FAIR, only for elderly control participants (CONTROL), only for MCI, and for ALL participants. FAIR provided significantly higher signal than PICORE ($P < .05$). The error bars indicate SD. B, The correlation of the whole-brain average rCBF between PICORE and FAIR was significant at $P < .0001$. The lines represent the linear fit for CONTROL and MCI with an intercept of zero.

First, we compared the whole-brain average rCBF values between the 2 ASL techniques by using paired t tests. Additionally, we calculated the Pearson correlation coefficient for the rCBF of both sequences.

Second, we calculated the whole-brain average relative SD as (Individual rCBF – Group Average rCBF)/Group Average rCBF. These relative SD values were compared between the 2 ASL techniques by using paired t tests.

Third, we applied a voxelwise permutation-based testing (Randomize, part of FSL; <http://fsl.fmrib.ox.ac.uk/fsl/fslwiki/randomise>), with threshold-free cluster-enhancement correction for multiple comparisons,²¹ considering fully corrected $P < .05$ as significant.

All analyses were performed 3 times: only for the 198 control participants, only for the 43 subjects with MCI, and for all 241 participants.

RESULTS

Whole-Brain Average rCBF

On average across the entire brain (ie, including gray and white matter), FAIR provided higher rCBF values compared with PICORE: controls, 32.7 ± 7.1 versus 30.0 ± 13.1 mL/min/100 g, $P = .05$; MCI, 29.8 ± 5.4 versus 26.2 ± 8.6 mL/min/100 g, $P < .05$; all, 32.2 ± 6.8 versus 29.3 ± 12.3 mL/min/100 g, $P < .05$ (Fig 1). The Pearson correlation for FAIR and PICORE was significant at $P < .0001$ for controls, MCI, and all. The slope of the correlation for all cases was 0.93 ± 0.03 (95% confidence interval, 0.86–0.99).

Interindividual Variability in rCBF

The interindividual variability in rCBF was estimated as relative to the deviation of the individual whole-brain average rCBF with respect to the corresponding group mean. FAIR had lower variability than PICORE: controls, 36.2% versus 68.8%, $P < .00001$; MCI, 18.9% versus 22.9%, $P < .0001$; all, 34.4% versus 64.9% $P < .00001$ (Fig 2).

Voxelwise Comparison between FAIR and PICORE

The average voxelwise rCBF values for FAIR, PICORE, and the difference between both sequences are illustrated in Fig 3.

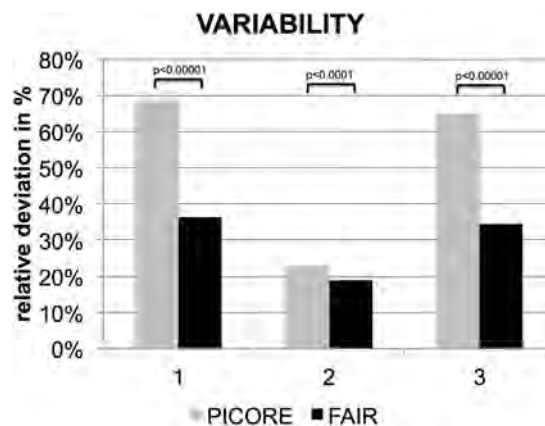


FIG 2. Significantly lower variability of the whole-brain average estimated rCBF for FAIR versus PICORE.

The direct voxelwise comparison between FAIR and PICORE revealed higher rCBF for FAIR in most brain areas, mainly the convexities, which partly corresponded to the anterior circulation. In contrast, PICORE provided higher signal compared with FAIR in the bilateral thalamus and occipital and infratentorial regions, largely but not completely respecting the posterior circulation. Exceptions for these vascular territories are the higher signal for PICORE in the bilateral head of caudate nucleus (lenticulostriate arteries, anterior circulation) and the posterior insula (middle cerebral artery, anterior circulation), while FAIR provided higher signal in the occipital pole (posterior cerebral artery territory) and posterior division of the cingulate gyrus (posterior cerebral artery, posterior circulation) (Fig 4).

DISCUSSION

Arterial spin-labeling is a promising neuroimaging technique for examining cognitive decline due to the close link between brain perfusion and brain metabolism.^{12,13} Accordingly, the patterns of hypoperfusion in ASL²⁻⁵ closely resemble hypometabolism in FDG-PET⁸⁻¹¹ in MCI and Alzheimer disease.⁶ Because disease-related alterations in brain perfusion in neurodegenerative diseases are a pri-

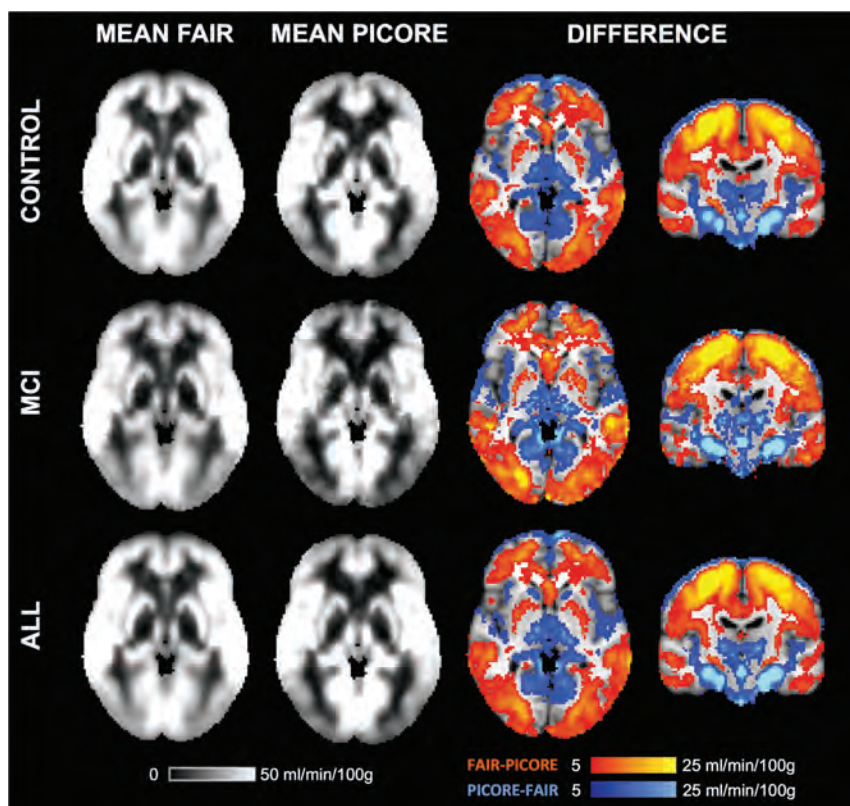


FIG 3. The average rCBF for FAIR, PICORE, and the difference between both ASL sequences.

ori small, notably at early stages of the disease, the implemented ASL sequence should have high signal and high reproducibility.

The direct comparison of 2 ASL sequences, which were both implemented with parameters in the range of recent guidelines,¹⁶ demonstrates that on average across the entire brain, FAIR had significantly lower variability compared with PICORE pulsed ASL, most probably due to the larger number of repetitions. Independent from any ASL pulse sequence, a focus on the large number of repetitions, if feasible, seems to lead to less variable results, even with a lower nominal volume.

Two additional observations merit discussion. First, the rCBF estimated by FAIR was significantly higher compared with PICORE. The rCBF calculation was performed with standard parameters by using commercially available software directly inline on the MR imaging scanner. Note that despite the highly significant correlation between the values obtained with these ASL sequences, there is still a systematic offset difference between them. Correspondingly, previous investigations comparing ASL and $H_2[^{15}O]$ -PET (water PET) as a reference standard^{22,23} as well as combined ASL and PET imaging^{24,25} also showed good correlations between ASL and water PET. The correlation coefficients are, however, unequal to 1. Likewise, another study compared 2D-versus-3D pseudocontinuous ASL and $H_2[^{15}O]$ -PET in 6 healthy controls, 6 subjects with MCI, and 1 patient with Alzheimer disease and again found a systematic offset between 2D-versus-3D ASL and between ASL-versus-water PET.²⁶ Moreover, the placement of the imaging slab significantly changed the rCBF estimation in ASL and the correlation with water PET,²⁷ indicating the need for rigorous standardization of this parameter. In

our study, the imaging slab was positioned by using the same orientation, and the labeling slab was always parallel to the imaging slab.

Respecting strict standardized procedures, we found that the reproducibility of the same ASL sequence both within and between sessions was fairly good.²⁸ Note that both ASL sequences in the current investigation are in agreement with recent recommendations¹⁶ and were performed within the same session. In the clinical applications of ASL, the sequence-related offset is likely even higher, considering additionally confounding factors such as different MR imaging vendors, machines, and head coils. In summary, these observations highlight the need to calibrate individual ASL sequences, for example, by using flow phantoms to detect subtle perfusion alterations related to neurodegeneration.

Second, when we assessed the regional differences between both ASL sequences in detail, FAIR had higher rCBF in both cerebral convexities, notably in the anterior circulation. In contrast, PICORE had higher values in deep, occipital, and infratentorial regions, largely respecting the posterior circulation. There were, however, certain exceptions to this rule. PICORE provided higher signal in the bilateral head of caudate nucleus and posterior insula, both part of the anterior circulation, while FAIR provided higher signal in the occipital pole and the posterior division of the cingulate gyrus, both part of the posterior circulation. Along the same lines, a previous investigation assessed the effect of imaging slab positioning and arterial transit time of ASL compared with $H_2[^{15}O]$ -PET.²⁷ The spatial distribution of the direct comparison between ASL and water PET partly overlaps the patterns of the current investigation, indicating that systematic ASL sequence-related differences in arterial transit time might contribute to the observed spatial differences between FAIR and PICORE. The exact origin of these regional differences between both ASL sequences, irrespective of the vascular territory, remains unclear. However, one of the differences between both ASL sequences was the use of a reference image for FAIR yet not for PICORE, which might lead to subtle differences between both sequences based on the level of T1-weighting between them.

Regarding the selective difference of perfusion in the posterior circulation, superselective or territorial ASL allows labeling of only selected vessels of the neck and demonstrated that, for example, the vascular supply of deep cerebral structures largely varies depending on the presence of the anatomic variant of a fetal configuration of the posterior cerebral artery.^{29,30} However, if anatomic variants are present within an individual, these equally affect both ASL sequences in our investigation. Consequently, such anatomic variants may explain regional ASL variations between individuals yet not between ASL sequences within the same indi-

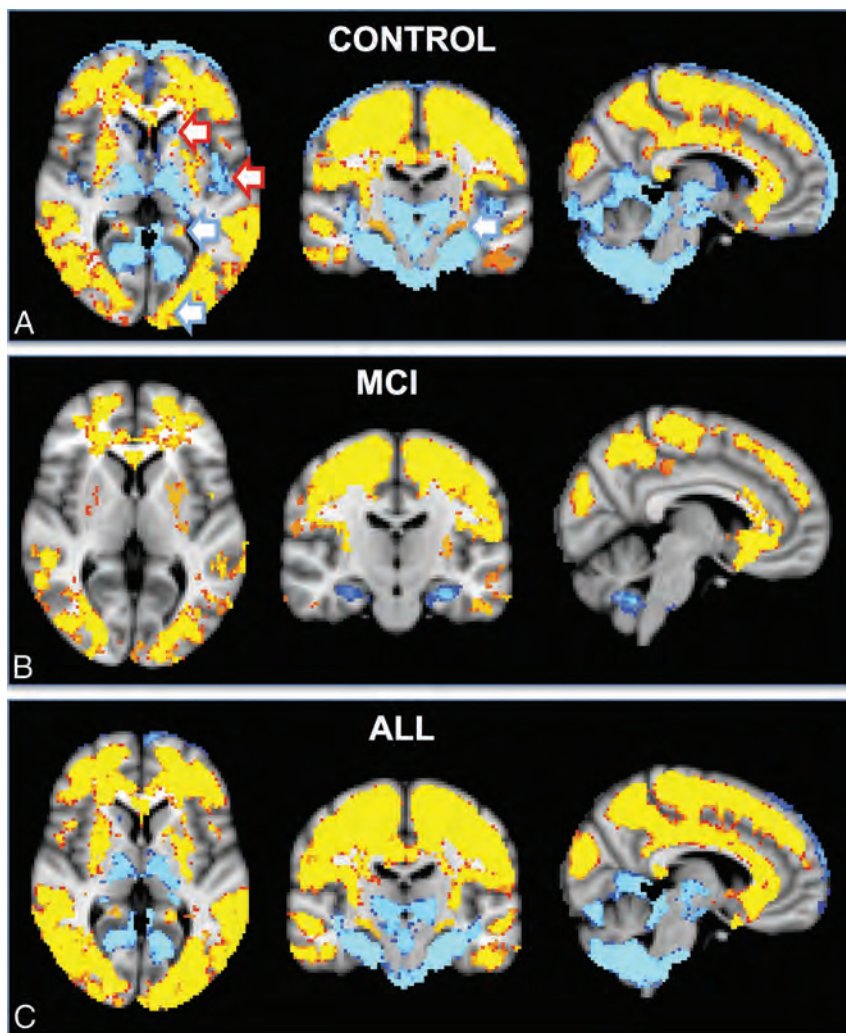


FIG 4. The spatial distribution of the differences between FAIR and PICORE ASL. Higher signal for FAIR (red-yellow) was present notably in both convexities, which largely but not completely respected the anterior circulation, for example posterior division of the cingulate gyrus (posterior cerebral artery, posterior circulation). In contrast, PICORE had higher signal in the bilateral thalami and occipital and infratentorial regions, largely but not completely respecting the posterior circulation and additionally in the bilateral head of caudate nucleus (lenticulostriate arteries, anterior circulation) and posterior insula (middle cerebral artery, anterior circulation).

vidual. A potential subtle difference in ASL imaging could also be related to the direction of the applied QUIPSS II/Q2TIPS saturation pulses. In the current investigation, these pulses were always parallel to the acquisition (and labeling) slabs, excluding a potential bias between both ASL sequences.

Most interesting, although PICORE had globally lower signal than FAIR, this was not the case in the bilateral mesial temporal regions. Mesial temporal atrophy is a well-known hallmark of Alzheimer disease,³¹ yet previous ASL studies did not reliably identify local hypoperfusion in this area.²⁻⁵ The observation that PICORE provides higher signal in this region indicates that this ASL sequence might be tuned to be particularly sensitive in regions prone to neurodegeneration.

Limitations

Both ASL sequences had different parameters, including spatial resolution (similar pixel size but different section thickness and partial Fourier factor) because they were individually optimized according

to the recommended standards and options available on our MR imaging scanner. Note that both ASL sequences used parameters that were, at the date of the study start, in agreement with the most recent guidelines.¹⁶ As mentioned above, in clinical settings, these variations are likely much more important when using different MR imaging scanners, head coils, and so forth, highlighting the need to calibrate each ASL sequence.

CONCLUSIONS

Overall, a large number of repetitions in our FAIR sequence had lower interindividual variability than the smaller number of repetitions in our PICORE sequence. The current implementation of FAIR is therefore recommended over the current implementation of PICORE for imaging in neurodegeneration. In more detail, the regional differences and global offset between both ASL sequences highlight the need to calibrate ASL sequences. Moreover, these results indicate that dedicated ASL sequences might be developed to assess specific target regions of the brain.

ACKNOWLEDGMENTS

We thank all volunteers and patients for participating in our study. We also thank Andreas J. Bartsch and Joseph Pfeuffer for their constructive help during the manuscript preparation.

Disclosures: Cristelle Rodriguez, Simona Toma—RELATED: Grant: Spezialprogramm Universitäre Medizin (SPUM) 33CM30_124111/1,* FNS 320030_129690/1,* Comments: the conversion of mild cognitive impairment to Alzheimer's disease; and early prediction of cognitive decline in very old individuals: combining disease-related, structural and functional markers. Xavier Golay—RELATED: Grant: European Cooperation in Science and Technology (COST) Agency,* Comments: Grant "BM1103: ASL in Dementia" is a cooperation grant throughout European Union countries, of which I am the Principal Investigator. Panteleimon Giannakopoulos—RELATED: Grant: SPUM 33CM30_124111/1,* FNS 320030_129690/1,* Comments: the conversion of mild cognitive impairment to Alzheimer's disease; and Early prediction of cognitive decline in very old individuals: combining disease-related, structural and functional markers; UNRELATED: Expert Testimony: witness reports for forensic psychiatry; Grants/Grants Pending: Swiss National Foundation for Research,* Comments: fees received by the University Hospitals of Geneva for clinical research (local private foundations which support pilot projects with small amounts of money); Payment for Lectures (including service on Speakers Bureau); University of Lausanne,* Fondation Leenaards, Lausanne,* pensions for old age psychiatry,* Comments: honoraria for conferences (usually less than US \$1000). Sven Haller—RELATED: Grant: Swiss National Science Foundation,* Comments: grant supporting the basic project; UNRELATED: Grants/Grants Pending: Swiss National Science Foundation*; Payment for Lectures (including service on Speakers Bureau); Various other sources.* *Money paid to the institution.

REFERENCES

1. Roberts DA, Detre JA, Bolinger L, et al. Quantitative magnetic resonance imaging of human brain perfusion at 1.5 T using steady-state inversion of arterial water. *Proc Natl Acad Sci U S A* 1994;91:33-37
2. Yoshiura T, Hiwatashi A, Noguchi T, et al. Arterial spin labeling at

- 3-T MR imaging for detection of individuals with Alzheimer's disease. *Eur Radiol* 2009;19:819–25
3. Yoshiura T, Hiwatashi A, Yamashita K, et al. Simultaneous measurement of arterial transit time, arterial blood volume, and cerebral blood flow using arterial spin-labeling in patients with Alzheimer disease. *AJNR Am J Neuroradiol* 2009;30:1388–93
 4. Dai W, Lopez OL, Carmichael OT, et al. Mild cognitive impairment and Alzheimer disease: patterns of altered cerebral blood flow at MR imaging. *Radiology* 2009;250:856–66
 5. Binnewijzend MA, Kuijter JP, Benedictus MR, et al. Cerebral blood flow measured with 3D pseudocontinuous arterial spin-labeling MR imaging in Alzheimer disease and mild cognitive impairment: a marker for disease severity. *Radiology* 2013;267:221–30
 6. Wolk DA, Detre JA. Arterial spin labeling MRI: an emerging biomarker for Alzheimer's disease and other neurodegenerative conditions. *Curr Opin Neurol* 2012;25:421–48
 7. Xekardaki A, Rodriguez C, Montandon ML, et al. Arterial spin labeling may contribute to the prediction of cognitive deterioration in healthy elderly individuals. *Radiology* 2015;274:490–99
 8. Bozoki AC, Korolev IO, Davis NC, et al. Disruption of limbic white matter pathways in mild cognitive impairment and Alzheimer's disease: a DTI/FDG-PET study. *Hum Brain Mapp* 2012;33:1792–802
 9. Pagani M, Dessi B, Morbelli S, et al. MCI patients declining and not-declining at mid-term follow-up: FDG-PET findings. *Curr Alzheimer Res* 2010;7:287–94
 10. Herholz K, Salmon E, Perani D, et al. Discrimination between Alzheimer dementia and controls by automated analysis of multi-center FDG PET. *Neuroimage* 2002;17:302–16
 11. Du AT, Jahng GH, Hayasaka S, et al. Hypoperfusion in frontotemporal dementia and Alzheimer disease by arterial spin labeling MRI. *Neurology* 2006;67:1215–20
 12. Buxton RB, Frank LR. A model for the coupling between cerebral blood flow and oxygen metabolism during neural stimulation. *J Cereb Blood Flow Metab* 1997;17:64–72
 13. Aubert A, Costalat R. A model of the coupling between brain electrical activity, metabolism, and hemodynamics: application to the interpretation of functional neuroimaging. *Neuroimage* 2002;17:1162–81
 14. Kim SG. Quantification of relative cerebral blood flow change by flow-sensitive alternating inversion recovery (FAIR) technique: application to functional mapping. *Magn Reson Med* 1995;34:293–301
 15. Wong EC, Buxton RB, Frank LR. Implementation of quantitative perfusion imaging techniques for functional brain mapping using pulsed arterial spin labeling. *NMR Biomed* 1997;10:237–49
 16. Alsop DC, Detre JA, Golay X, et al. Recommended implementation of arterial spin-labeled perfusion MRI for clinical applications: a consensus of the ISMRM perfusion study group and the European consortium for ASL in dementia. *Magn Reson Med* 2014 Apr 8. [Epub ahead of print]
 17. Folstein MF, Folstein SE, McHugh PR. "Mini-mental state": a practical method for grading the cognitive state of patients for the clinician. *J Psychiatr Res* 1975;12:189–98
 18. Luh WM, Wong EC, Bandettini PA, et al. QUIPSS II with thin-slice T1 periodic saturation: a method for improving accuracy of quantitative perfusion imaging using pulsed arterial spin labeling. *Magn Reson Med* 1999;41:1246–54
 19. Wang J, Licht DJ, Jahng GH, et al. Pediatric perfusion imaging using pulsed arterial spin labeling. *J Magn Reson Imaging* 2003;18:404–13
 20. Fazekas F, Chawluk JB, Alavi A, et al. MR signal abnormalities at 1.5 T in Alzheimer's dementia and normal aging. *AJR Am J Roentgenol* 1987;149:351–56
 21. Smith SM, Nichols TE. Threshold-free cluster enhancement: addressing problems of smoothing, threshold dependence and localisation in cluster inference. *Neuroimage* 2009;44:83–98
 22. Heijtel DF, Mutsaerts HJ, Bakker E, et al. Accuracy and precision of pseudo-continuous arterial spin labeling perfusion during baseline and hypercapnia: a head-to-head comparison with (1)(5)O H(2)O positron emission tomography. *Neuroimage* 2014;92:182–92
 23. Bokkers RP, Bremmer JP, van Berckel BN, et al. Arterial spin labeling perfusion MRI at multiple delay times: a correlative study with H(2)(15)O positron emission tomography in patients with symptomatic carotid artery occlusion. *J Cereb Blood Flow Metab* 2010;30:222–29
 24. Zhang K, Herzog H, Mauler J, et al. Comparison of cerebral blood flow acquired by simultaneous [15O]water positron emission tomography and arterial spin labeling magnetic resonance imaging. *J Cereb Blood Flow Metab* 2014;34:1373–80
 25. Stegger L, Martirosian P, Schwenzer N, et al. Simultaneous PET/MR imaging of the brain: feasibility of cerebral blood flow measurements with FAIR-TrueFISP arterial spin labeling MRI. *Acta Radiol* 2012;53:1066–72
 26. Kilroy E, Apostolova L, Liu C, et al. Reliability of two-dimensional and three-dimensional pseudo-continuous arterial spin labeling perfusion MRI in elderly populations: comparison with 15O-water positron emission tomography. *J Magn Reson Imaging* 2014;39:931–39
 27. Qiu M, Paul Maguire R, Arora J, et al. Arterial transit time effects in pulsed arterial spin labeling CBF mapping: insight from a PET and MR study in normal human subjects. *Magn Reson Med* 2010;63:374–84
 28. Wang Y, Saykin AJ, Pfeuffer J, et al. Regional reproducibility of pulsed arterial spin labeling perfusion imaging at 3T. *Neuroimage* 2011;54:1188–95
 29. Hendrikse J, Petersen ET, Chng SM, et al. Distribution of cerebral blood flow in the nucleus caudatus, nucleus lentiformis, and thalamus: a study of territorial arterial spin-labeling MR imaging. *Radiology* 2010;254:867–75
 30. Hartkamp NS, Petersen ET, De Vis JB, et al. Mapping of cerebral perfusion territories using territorial arterial spin labeling: techniques and clinical application. *NMR Biomed* 2013;26:901–12
 31. Fox NC, Warrington EK, Freeborough PA, et al. Presymptomatic hippocampal atrophy in Alzheimer's disease: a longitudinal MRI study. *Brain* 1996;119:2001–07

Use of Standardized Uptake Value Ratios Decreases Interreader Variability of [¹⁸F] Florbetapir PET Brain Scan Interpretation

A.P. Nayate, J.G. Dubroff, J.E. Schmitt, I. Nasrallah, R. Kishore, D. Mankoff, and D.A. Pryma;
for the Alzheimer's Disease Neuroimaging Initiative



ABSTRACT

BACKGROUND AND PURPOSE: Fluorine-18 florbetapir is a recently developed β -amyloid plaque positron-emission tomography imaging agent with high sensitivity, specificity, and accuracy in the detection of moderate-to-frequent cerebral cortical β -amyloid plaque. However, the FDA has expressed concerns about the consistency of interpretation of [¹⁸F] florbetapir PET brain scans. We hypothesized that incorporating automated cerebral-to-whole-cerebellar standardized uptake value ratios into [¹⁸F] florbetapir PET brain scan interpretation would reduce this interreader variability.

MATERIALS AND METHODS: This randomized, blinded-reader study used previously acquired [¹⁸F] florbetapir scans from 30 anonymized patients who were enrolled in the Alzheimer's Disease Neuroimaging Initiative 2. In 4 separate, blinded-reading sessions, 5 readers classified 30 cases as positive or negative for significant β -amyloid deposition either qualitatively alone or qualitatively with additional adjunct software that determined standardized uptake value ratios. A κ coefficient was used to calculate interreader agreement with and without the use of standardized uptake value ratios.

RESULTS: There was complete interreader agreement on 20/30 cases of [¹⁸F] florbetapir PET brain scans by using qualitative interpretation and on 27/30 scans interpreted with the adjunct use of standardized uptake value ratios. The κ coefficient for the studies read with standardized uptake value ratios (0.92) was significantly higher compared with the qualitatively read studies (0.69, $P = .006$).

CONCLUSIONS: Use of standardized uptake value ratios improves interreader agreement in the interpretation of [¹⁸F] florbetapir images.

ABBREVIATIONS: AD = Alzheimer disease; ADNI = Alzheimer's Disease Neuroimaging Initiative; EAD = early AD; EMCI = early mild cognitive impairment; LMCI = late mild cognitive impairment; SUVr = standardized uptake value ratios

Estimated to affect approximately 5.4 million Americans and 30 million people worldwide, Alzheimer disease (AD) is the most common type of dementia.^{1,2} Cortical β -amyloid deposition is 1 pathologic hallmark² and is hypothesized to be pathogenic for

AD.^{2,3} The ability to noninvasively detect cortical β -amyloid deposition could considerably improve clinical diagnosis because >33% of patients with early signs of AD will be inaccurately identified.⁴ Fluorine-18 florbetapir, a recently developed β -amyloid plaque positron-emission tomography imaging agent, rapidly en-

Received May 16, 2014; accepted after revision January 12, 2015.

From the Division of Nuclear Medicine and Clinical Molecular Imaging, Department of Radiology, University of Pennsylvania, Philadelphia, Pennsylvania.

Data used in the preparation of this article were obtained from the Alzheimer's Disease Neuroimaging Initiative database (<http://adni.loni.usc.edu>). As such, the investigators within the ADNI contributed to the design and implementation of the ADNI and/or provided data but did not participate in analysis or writing of this report. A complete listing of ADNI investigators can be found at http://www.adni.loni.usc.edu/wp-content/uploads/how_to_apply/ADNI_Acknowledgement_List.pdf.

This study was supported in part by a grant from Siemens (Hoffman Estates, Illinois). Data collection and sharing for this project were funded by the Alzheimer's Disease Neuroimaging Initiative (National Institutes of Health Grant U01 AG024904). ADNI is funded by the National Institute on Aging, the National Institute of Biomedical Imaging and Bioengineering, and through generous contributions from the following: Alzheimer's Association; Alzheimer's Drug Discovery Foundation; BioClinica; Biogen Idec; Bristol-Myers Squibb; Eisai; Elan Pharmaceuticals; Eli Lilly and Company; F. Hoffmann-La Roche and its affiliated company Genentech; GE Healthcare; Innogenetics, N.V.; IXICO; Janssen Alzheimer Immunotherapy Research & Development; Johnson & Johnson Pharmaceutical Research &

Development; Medpace; Merck; Meso Scale Diagnostics; NeuroRx Research; Novartis Pharmaceuticals Corporation; Pfizer; Piramal Imaging; Servier; Synarc; and Takeda Pharmaceutical Company. The Canadian Institutes of Health Research is providing funds to support ADNI clinical sites in Canada. Private sector contributions are facilitated by the Foundation for the National Institutes of Health (www.fnih.org). The grantee organization is the Northern California Institute for Research and Education, and the study is coordinated by the Alzheimer's Disease Cooperative Study at the University of California, San Diego. ADNI data are disseminated by the Laboratory for Neuro Imaging at the University of California, Los Angeles. This research was also supported by National Institutes of Health grants P30 AG010129 and K01 AG030514.

Research findings previously presented at: Annual Meeting the Radiological Society of North America, December 1–6, 2013; Chicago, Illinois.

Please address correspondence to D.A. Pryma, MD, 3400 Spruce St, 110 Donner Building, Philadelphia, PA; e-mail: daniel.pryma@uphs.upenn.edu

 Indicates open access to non-subscribers at www.ajnr.org

 Indicates article with supplemental on-line table.

<http://dx.doi.org/10.3174/ajnr.A4281>

ters the brain and specifically binds to cortical fibrillar β -amyloid.^{5,6} Pathologic findings demonstrate the high sensitivity (87%), specificity (95%), and accuracy (90%) of [¹⁸F] florbetapir in the detection of moderate-to-frequent cortical β -amyloid plaque by using the Consortium to Establish a Registry for Alzheimer's Disease criteria.⁷

Sufficient concern about the consistency of [¹⁸F] florbetapir PET brain scan interpretation led the FDA to withhold approval until an interpretation training program was implemented to reduce interreader variability.⁸⁻¹⁰ Imaging and pathologic studies have previously demonstrated that cerebral cortical regions, including the frontal lobe, parietal lobe, temporal lobe, precuneus, and anterior and posterior cingulate gyrus, are regions in which β -amyloid deposition is commonly found in patients with AD.^{5,11} These findings motivated quantitative analysis of [¹⁸F] florbetapir PET brain images, comparing differential binding between these cortical regions to the whole cerebellum, a site not prone to amyloid deposition, expressed as cerebral-to-whole-cerebellar standardized uptake value ratios (SUVr).^{5,12} Subsequent pathologic analysis demonstrated high sensitivity (97%), specificity (100%), and accuracy (98%) between [¹⁸F] florbetapir PET SUVr and postmortem immunohistochemical measurements of β -amyloid.^{5,7,12} These studies showed that a mean [¹⁸F] florbetapir SUVr value of >1.17 was strongly associated with an intermediate-to-high likelihood of a neuropathologic diagnosis of AD.^{5,12} However, SUVr are onerous to calculate manually, and manual placement of ROIs is prone to variability. Computer assistance could provide an easier method to incorporate SUVr into the interpretation process,^{13,14} and semiautomated software has been developed to facilitate SUVr calculations. The current standardized methodology for amyloid PET brain interpretation does not use SUVr,¹⁴ which might be useful to improve reader agreement. We hypothesized that adding SUVr to qualitative image interpretation of [¹⁸F] florbetapir PET brain scans would reduce interreader variability.

MATERIALS AND METHODS

Participants

This randomized, blinded-reader study used previous [¹⁸F] florbetapir scans from 60 anonymized patients (37 men and 23 women) who were enrolled in the Alzheimer's Disease Neuroimaging Initiative (ADNI) 2 and had already provided written informed consent. Fluorine-18 florbetapir PET brain scans were obtained at multiple sites; however, all sites followed the same ADNI 2 protocol.¹⁵ Studies were randomly selected from the ADNI 2 population data base and anonymized. Patient age ranged from 55 to 94 years; each patient had an established clinical diagnosis of normal, early mild cognitive impairment (EMCI), late mild cognitive impairment (LMCI), or early AD (EAD). We chose these groups (normal, EMCI, LMCI, and EAD) because their [¹⁸F] florbetapir PET studies were expected to be the most challenging to interpret and, therefore, could better test the potential benefit of using SUVr. In consultation with a biostatistician before the study, we determined that with 5 readers, approximately 30 cases would provide enough statistical power to test whether the addition of SUVr would provide a substantial improvement in reader consistency for our study. Due to the large ADNI data base

and the need to only include these groups, an uninvolved third party was used to select cases accordingly. The investigators played no role in choosing the cases, to maintain the blinded nature of the study. This study was approved by the local institutional review board.

Image Analysis and Reader Study

Five nuclear medicine board-certified or eligible physicians with no prior clinical experience in interpreting [¹⁸F] florbetapir PET brain scans (though some had experience with the studies in a research setting) and with varying years of clinical experience in nuclear medicine (3 readers had ≤ 3 years of experience, 1 reader had 8 years of experience, and 1 reader had 18 years of experience) underwent on-line [¹⁸F] florbetapir PET clinical training (<http://www.amyvidtraining.com>; Avid Radiopharmaceuticals, Philadelphia, Pennsylvania) before initiation of the study. The training included information about [¹⁸F] florbetapir, β -amyloid, and Alzheimer disease followed by demonstrations and self-assessment cases on study interpretation.

Fluorine-18 florbetapir PET brain scans of 60 participants were given 2 unique and random identifiers; each case was evaluated twice, once qualitatively and once with the inclusion of SUVr information. Each case was classified as either positive or negative for cortical β -amyloid deposition. All 60 cases were assigned to 4 reading sessions separated by at least 72 hours to avoid reader memory. All assignments were random except that no case was repeated during an individual session. For each case, the order of qualitative and SUVr-aided reads was also random.

We divided the 60 cases into 2 groups with the initial 30 cases to be used as a lead-in to give all readers a more similar experience in evaluating amyloid PET studies and using the SUVr software. The remaining 30 test cases were used for the test set. Readers never received feedback about their interpretations. Readers qualitatively interpreted the scans by using MIMfusion (MIM Software Inc, Cleveland Ohio) by determining the presence or absence of cortical β -amyloid deposition according to the clinical interpretation methodology. Axial, sagittal, and coronal images were presented, and the reader could manipulate image contrast to accentuate the gray-white interface as recommended by the training program.

SUVr cases were reviewed qualitatively on MIMfusion, and additionally SUVr were calculated automatically by using Scenium (Siemens, Erlangen, Germany). The SUVr software automatically registers [¹⁸F] florbetapir scans to the Montreal Neurological Institute atlas space and calculates the SUVr values without requiring any input from the user.¹⁶ However, the reader could review and manipulate the ROIs to fit the cerebral cortical gray matter and whole cerebellum, to assure proper anatomic registration. Readers recorded average cortical SUVr of these regions for each case along with the positive/negative interpretation. Because the SUVr values for all 5 readers were very similar, the manipulation of ROIs was at most minimal in all cases. Cortex-to-whole-cerebellum SUVr values were automatically calculated and presented by the software for 6 anatomically relevant cortical ROIs: frontal lobe, lateral parietal lobe, lateral temporal lobe, precuneus, and anterior and posterior cingulate gyrus, as well as the mean SUVr of these regions.¹² Prior studies demonstrated that with the aid of the average SUVr from these anatomic regions, sensitivity

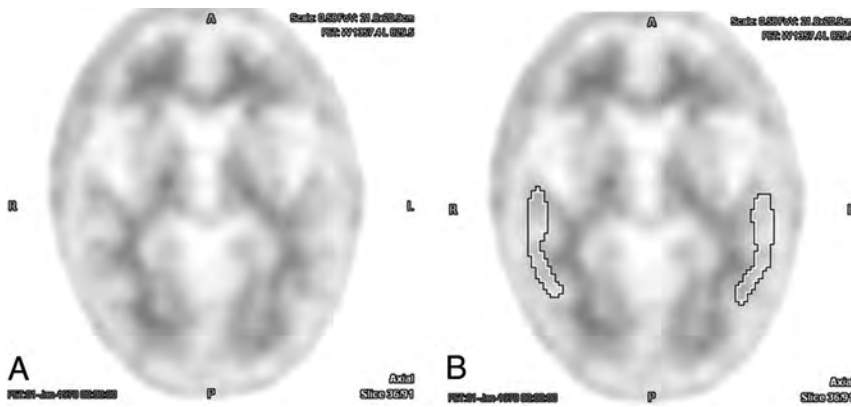


FIG 1. Example of an [¹⁸F] florbetapir PET brain scan with negative findings without (A) and with (B) ROIs centered over the bilateral temporal lobe cortex. There was perfect interreader agreement both with and without the aid of semiquantitative indices (average interreader SUVr = 0.97 ± 0.02).

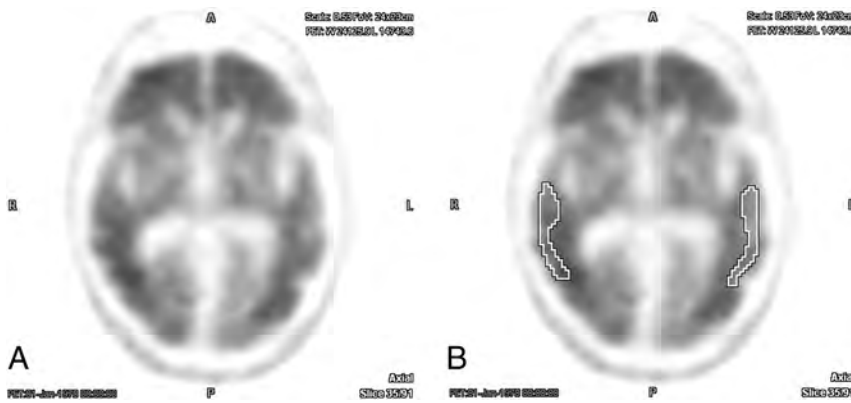


FIG 2. Example of an [¹⁸F] florbetapir PET brain scan with positive findings without (A) and with (B) ROIs centered over the bilateral temporal lobe cortex. There was perfect interreader agreement both with and without the aid of semiquantitative indices (average interreader SUVr = 1.78 ± 0.02).

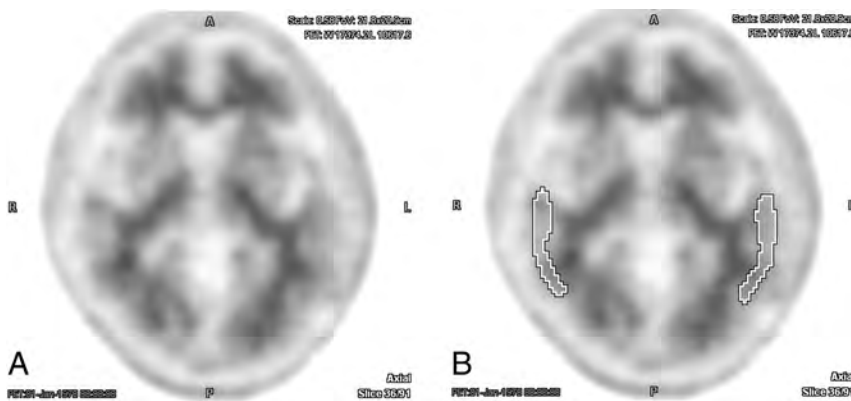


FIG 3. Example of a [¹⁸F] florbetapir PET brain scan without complete interreader agreement, displayed without (A) and with (B) an ROI over the temporal lobes. In this case, there was rater discordance both for qualitative interpretation and with the aid of semiquantitative indices (average interreader SUVr = 1.27 ± 0.05).

and specificity of reads increased by using both clinical diagnosis¹⁷ and pathology⁷ as comparisons. Although we chose to use the Scenium software to calculate SUVr, commercial programs from other vendors are available for calculating SUVr.^{5,12}

A recent study¹⁸ showed a high correlation between SUVr calculated by Scenium and other methods.^{5,7,19} Prior research suggested that a threshold for amyloid positivity was at SUVr ≥ 1.17.^{5,12} All readers were informed of this threshold. However, the SUVr value was available to the reader as an adjunct to assist in the primary qualitative interpretation. Therefore, the final interpretation relied on the reader's overall judgment, incorporating both the qualitative image data and SUVr. Sample cases are shown in Figs 1–3.

Statistical Analyses

The data were analyzed by using the R Statistical Computing Environment (<http://www.r-project.org/>).²⁰ To assess interrater reliability, we calculated the Fleiss multirater κ statistics for the 2 conditions separately (qualitative versus qualitative + SUVr) by using the “irr” package.²¹ Confidence intervals for each κ were calculated separately via bootstrap by using 1000 replicates. Statistical comparison was accomplished by the method for comparing correlated κ statistics described by Vanbelle and Albert.²² Briefly, for 2 correlated κ values, a difference score can be calculated such that

$$1) \quad \hat{\kappa}_D = \hat{\kappa}_{suvr} - \hat{\kappa}_{qualitative}$$

The distribution of this statistic can be estimated via bootstrap by calculating the difference score for q subsamples with replacement. A new estimator is then calculated that under the null hypothesis ($\hat{\kappa}_{qualitative} = \hat{\kappa}_{suvr}$) follows a t distribution with $q-1$ df :

$$2) \quad t_{\kappa_D} = \frac{\overline{\hat{\kappa}_D}}{SD(\hat{\kappa}_D)}$$

For the current study, a bootstrap analysis by using 1000 replicates was used for hypothesis testing. An α of .05 was set as the threshold for statistical significance.

For the interpretation of κ values, we used the magnitude guidelines published by Landis and Koch²³: Values of $\kappa < 0$ indicate no agreement; $\kappa = 0-0.20$, slight; $\kappa = 0.21-0.40$, fair; $\kappa = 0.41-0.60$, moderate; $\kappa = 0.61-0.80$,

excellent; and $\kappa = 0.81-1$, near-perfect agreement. Average interreader measurements of SUVr for the 4 different clinical diagnostic groups (normal, EMCI, LMCI, and EAD) were compared by using 1-way ANOVA with post hoc Tukey-

Kramer tests. We did not measure intrareader data per recommendations of the annual Clinical Trials Methodology Workshop of the Radiological Society of North America (https://www.rsna.org/Clinical_Trials_Methodology_Workshop.aspx).

RESULTS

One of the input images could not be successfully registered to the template for quantification due to nonstandard patient positioning. Most important, no disease process (eg, normal pressure hydrocephalus) or anatomic variant precluded this case being aligned to the template, and no similar issue arose with the other 59 cases. In this case, the readers could do only qualitative interpretation for both the qualitative and qualitative + SUVr reads. There was complete interreader agreement on 20 of 30 cases of [¹⁸F] PET brain scans by using qualitative-only interpretation and 27 of 30 scans interpreted with the adjunct use of the SUVr (On-line Table). Quantitative measures of interrater reliability confirmed excellent agreement between raters when using qualitative analysis alone ($\kappa = 0.69$; 95% CI, 0.50–0.82). The addition of SUVr data resulted in near-perfect agreement ($\kappa = 0.92$; 95% CI, 0.79–0.97). Interrater agreement was significantly increased with the addition of SUVr data ($t = 2.51, P = .006$) after adjusting for the correlated nature of the data.

Group differences in global SUVr were statistically significant ($P < .005$) with group means and SDs as follows: normal (1.05 ± 0.21), EMCI (1.27 ± 0.25), LMCI (1.32 ± 0.25), and EAD (1.65 ± 0.20). Post hoc Tukey-Kramer tests demonstrated significant mean differences between all pair-wise group combinations ($P < .0002$), with the exception of EMCI versus LMCI (not significant).

In the original 30 practice cases used as a lead-in, there was complete interreader agreement on 17 of 30 cases of [¹⁸F] florbetapir PET scans by using qualitative-only interpretation ($\kappa = 0.56$; 95% CI, 0.29–0.7) and 16 of 30 scans interpreted with the adjunct use of the SUVr ($\kappa = 0.55$; 95% CI, 0.36–0.73). These κ values were significantly different ($P < .05$) than the κ values achieved in our dataset of 30 cases. If all the data from the 60 cases were included for all 5 readers, then there was complete interreader agreement on 37/60 cases ($\kappa = 0.62$) only qualitatively evaluated and complete interreader agreement on 43/60 cases ($\kappa = 0.74$) when evaluated with the aid of SUVr. The κ values of all 60 cases evaluated with the aid of SUVr were higher than those of the same cases when only qualitatively evaluated; this approached but did not achieve statistical significance ($t = 1.34, P = .09$).

DISCUSSION

AD is the most common dementia to affect the elderly and traditionally has been diagnosed clinically.^{1,2} However, 10%–20% of patients clinically diagnosed with AD lack pathologic findings at postmortem examination.²⁴ Improved diagnosis could aid in medical and personal decision-making. Furthermore, on the basis of the suspected role of β -amyloid in the pathophysiology of AD, it has emerged as a potential drug target. In evaluating and potentially using such therapies, reliably establishing the presence of β -amyloid deposition would be of paramount importance. Recently, the Society of Nuclear Medicine and Molecular Imaging and the Alzheimer's Association proposed PET amyloid imaging

appropriate-use guidelines for patients who meet specific criteria.²⁵ For the test to be of greatest clinical utility, interreader variability needs to be minimized. We hypothesized that incorporating a method of quantification to standard image interpretation of [¹⁸F] florbetapir PET brain scans by the addition of SUVr would reduce interreader variability.

Our results show a significantly higher ($P = .006$) interreader agreement when [¹⁸F] florbetapir PET scans were evaluated with adjunctive SUVr data ($\kappa = 0.92$) compared with qualitative-only assessment of the same studies ($\kappa = 0.69$). This κ value of 0.69 is similar to the κ value in another study with 5 readers visually assessing 59 cases ($\kappa = 0.76$) and in a study with 2 readers visually assessing 46 cases ($\kappa = 0.71$).¹⁷ The values of our study are also similar to those seen with other β -amyloid imaging agents such as ¹¹C Pittsburgh compound-B.²⁶ The impact of the data of SUVr on κ values reported here is also higher than those seen in interobserver variability studies in lesion detection in other organ systems, for example, in the detection of pulmonary nodules with ($\kappa = 0.67$)²⁷ and without the use of computer-assisted detection software ($\kappa = 0.64$)²⁸ and the detection of breast lesions by using automatic breast scanners ($\kappa = 0.8$).²⁹

When [¹⁸F] florbetapir PET brain studies were read qualitatively, there was interreader disagreement in 9/30 (30%) cases; however, there was complete agreement between readers for 8 of these cases when independently evaluated with semiquantitative indices. With the adjunct use of the SUVr, there was interreader disagreement on 3/30 (10%) cases. One case was discrepant (interreader disagreement) on both qualitative and SUVr reads (the case in which the software failed to register the study to the atlas). In one of the remaining 2 discrepant cases, there was interreader disagreement on both the qualitative assessment and the assessment with the aid of SUVr; and on the other case, 1 reader interpreted the study differently than the others only on assessment with the aid of SUVr. The interreader average SUVr on these cases were 1.27 (range, 1.24–1.35) and 1.15 (range, 1.13–1.21) and were the closest to the threshold value of 1.17^{5,7,12} of the test cases (Fig 4). Therefore, we hypothesized that interreader disagreement on these 2 cases was probably a result of visually borderline scans because both of these subjects had diagnoses of early mild cognitive impairment, which often has intermediate values of SUVr.^{5,7,12}

Although we did not directly assess the extent of ROI manipulation by the readers, the manipulation by all readers was, at most, minimal as shown by the small SD between interreader average SUVr ($\leq 5\%$, On-line Table). These findings are concordant with a prior study that demonstrated minimal variance in the interrater reliability of manual and automated ROI delineation for Pittsburgh compound-B PET.³⁰ There was no certain relationship between the years of post-board certification and discrepancies, compared with most interpretations of individual cases (Table).

Our results also show a significant difference ($P < .0002$) in the values of SUVr between normal controls and patients with early mild and late mild cognitive impairment or EAD, with progressively higher SUVr values seen in patients with early mild and late mild cognitive impairment or EAD compared with normal patients, concordant with findings of prior studies.^{4,14,19} Com-

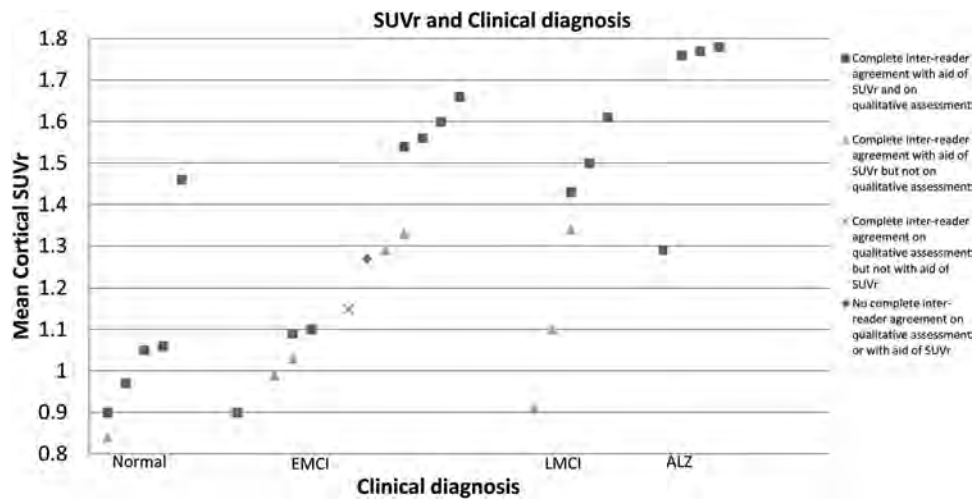


FIG 4. SUVr values for 29/30 test cases. No SUVr could be determined for one of the cases because input images could not be successfully registered to the template for quantification due to nonstandard patient positioning.

Comparison of years of experience in diagnostic imaging and discrepant reads (versus majority consensus) in 30 test cases

Years of Experience (after Radiology or Nuclear Medicine Residency)	Discrepant Reads on Qualitative Assessment	Discrepant Reads with Aid of SUVr
2	3	0
3	6 ^a	2 ^a
3	1	1
8	3	0
18	1	0

^a In 1 case, only qualitative interpretation for both the qualitative and qualitative + SUVr reads could be provided because input images could not be successfully registered to the template for quantification due to nonstandard patient positioning.

parison of SUVr between the EMCI and LMCI groups did not demonstrate a significant difference.

Our findings demonstrate that cases that had complete inter-reader agreement as positive for significant β -amyloid deposition with the aid of semiquantitative analysis but not complete agreement when qualitatively assessed had an interreader mean SUVr value of 1.32 ± 0.0 ($n = 3$). Cases that had complete agreement for positive scan findings by both methods had an interreader mean SUVr of 1.58 ± 0.15 ($n = 12$). These findings suggest that cases with values of SUVr closer to the cutoff value of 1.17 are often visually challenging and can therefore contribute to discrepant reads with qualitative assessment. However, a similar divergence in the mean SUVr was not seen in cases with discrepant interpretations by qualitative evaluation that were uniformly interpreted as negative with the aid of SUVr (interreader mean SUVr = 0.97 ± 0.1 ; $n = 5$) compared with cases that had complete interreader agreement for negative scan findings by both methods (interreader mean SUVr = 1.01 ± 0.09 ; $n = 7$). This finding is congruent with findings from prior studies^{5,12} and may be explained by the decreased [¹⁸F] florbetapir uptake seen in patients without significant β -amyloid cerebral cortical deposition and therefore creating a narrower range for SUVr values (Fig 4).

We designed our experiment to include 30 practice cases because all 5 readers had no prior clinical experience in interpreting [¹⁸F] florbetapir PET brain scans (which had just been approved

at the time of this study) and had varying amounts of research experience and varying years of experience in nuclear medicine. Therefore, we thought that the practice cases would help readers gain similar familiarity with the software and method. In the original 30 practice cases used as a lead-in, there was moderate inter-reader agreement between qualitative-only interpretation ($\kappa = 0.56$) and with the adjunct use of the SUVr ($\kappa = 0.55$). These κ values were significantly different ($P < .05$) than the κ values achieved in our dataset of 30 cases. This discrepancy is likely the result of inexperience and varying early proficiency in using the software. Improved agreement between readers was seen in our test set of the 30 cases for qualitative-only interpretation, emphasizing the importance of practice on physician performance. Improved agreement between readers on the test set compared with the training set when using SUVr signifies the need for familiarization with image analysis software and is congruent with findings seen in using other computer-aided diagnostic software such as in the detection of lesions on mammograms.³¹ Finally, the κ values of all 60 cases evaluated with the aid of SUVr were higher than those of the same cases when only qualitatively evaluated, showing a trend toward statistical significance ($P = .09$).

We could not determine the accuracy of interpretations in this study because no criterion standard pathologic data were available for the cohort. Clinical diagnosis is not the criterion standard for diagnosing Alzheimer disease³² and can be an unreliable diagnostic tool with 10%–20% of patients diagnosed with Alzheimer disease lacking pathology on postmortem histopathologic analysis²⁴; clinical diagnosis has intermediate sensitivity (84%) and low specificity (52.5%) in diagnosing Alzheimer disease.³³ Our findings show that 52% of mild cognitive impairment (EMCI + LMCI) cases were interpreted with complete interreader agreement as β -amyloid-positive with the aid of SUVr, while 37% of these mild cognitive impairment cases were interpreted with complete interreader agreement as β -amyloid-positive with qualitative-only assessment. Fourteen percent of cognitively normal cases were interpreted with complete interreader agreement as β -amyloid-positive, both with only qualitative assessment and with the aid of SUVr (On-line Table). These findings are congru-

ent with prior imaging studies¹³ and are within range of cortical β -amyloid deposition seen in postmortem case studies in cognitively normal, mildly cognitively impaired, and patients with Alzheimer disease.³³⁻³⁵ Our findings also demonstrate that the relationship between cognitive decline and the amount of cortical β -amyloid deposition is variable because we see studies with positive findings in all of our experimental groups (normal, EMCI, LMCI, and AD) and they are compatible with prior pathologic studies.³⁶ The degree of cortical β -amyloid deposition could have prognostic importance because recent studies have demonstrated that cognitively normal, mild cognitively impaired, and subjects with Alzheimer disease who have PET scans positive for amyloid demonstrate greater cognitive and global deterioration during an 18-month³⁷ and 3-year³⁸ follow-up than subjects with scans with negative findings.

We did not use the cutoff value of SUVr of 1.17 solely as a method to quantitatively interpret the scans. The study that determined this value had a small sample size of 19 patients, and studies in larger community-based samples with a broader distribution of SUVr would be needed to more definitively establish standard thresholds. Furthermore, the applicability of this value obtained from whole-brain cortical uptake to use in regional values is unknown.¹² In our study, the readers were aware of this empiric threshold and could choose to use it when evaluating the calculated regional and averaged regional SUVr value from [¹⁸F] florbetapir PET images.

We did not measure the intraobserver variability because we wanted to emulate the reading sessions as a standard clinical practice in which studies are assigned a single interpretation by an individual physician reader. In this regard, our methodology was similar to that in other studies examining interreader performance in diagnostic imaging with and without an intervention such as computer-aided diagnostic software. Parallel methodology has been used in lung disease,³⁹⁻⁴³ breast imaging,^{29,44-46} and Alzheimer disease,^{26,47} without determining intraobserver variability.

The most important limitation of our study is the absence of the criterion standard of pathologic analysis to establish the presence or absence of cerebral cortical β -amyloid deposition in our cohort of subjects to determine the accuracy of physician interpretations of the [¹⁸F] florbetapir PET studies. As such, we could not determine whether the use of SUVr improved diagnostic accuracy; our primary aim was to assess interreader variability. Prior studies have demonstrated a high correlation between PET SUVr and immunohistochemical measurements of β -amyloid,^{5,7,12} suggesting that improving agreement will likely improve diagnostic accuracy. However, while high interreader agreement is desirable in diagnostic testing, it will be important to directly evaluate the effect on diagnostic accuracy in future studies, especially in patients with mild cognitive impairment because prior studies have primarily focused on determining the accuracy of amyloid PET in cognitively normal individuals or patients with probable Alzheimer disease.^{5,7} Second, although it was meant as an adjunct tool, we did not determine or prescribe the degree to which readers used the SUVr values in determining their interpretations of scans. Third, due to differences in reader ROI manipulation, there was minimal variance in average SUVr values on the test cases; therefore, this minimal variance is a potential weakness of a semi-

automated method. Fourth, 1 case from our 30 test cases did not successfully register to the template for quantification due to non-standard patient positioning. Therefore, registration errors and other technical failures of the software are an additional potential weakness of such a semiautomated method.

CONCLUSIONS

Our results support the use of SUVr to improve interreader agreement in the interpretation of [¹⁸F] florbetapir images. Furthermore, using computer software to obtain values of SUVr can be an appealing and efficient option for nuclear medicine physicians and radiologists in interpreting [¹⁸F] florbetapir PET brain scans and other brain imaging agents. The promising results from this initial study support future larger and prospective studies, including determining the performance of semiquantification strategies for [¹⁸F] florbetapir and other β -amyloid radiopharmaceuticals to establish ranges for negative and positive, compared against clinical and histopathologic reference standards.

ACKNOWLEDGMENTS

Data used in the preparation of this article were obtained from the Alzheimer's Disease Neuroimaging Initiative data base (adni.loni.ucla.edu), a \$60 million public-private partnership launched in 2003 by the National Institute on Aging, the National Institute of Biomedical Imaging and Bioengineering, the Food and Drug Administration, private pharmaceutical companies, and nonprofit organizations. The primary goal of ADNI has been to test whether serial brain imaging studies, clinical and neuropsychological assessments, and other biologic markers can be combined to measure the progression of mild cognitive impairment and early AD to aid researchers and clinicians in developing new treatments and monitoring their effectiveness. ADNI, led by Principal Investigator Michael W. Weiner, MD, VA Medical Center and University of California, San Francisco, is the result of efforts of many coinvestigators from a broad range of academic institutions and private corporations, and subjects have been recruited from >50 sites across the United States and Canada. For up-to-date information and descriptions of PET imaging acquisition parameters, see www.adni-info.org.

Disclosures: Armea P. Nayate—*RELATED: Grant:* This study was partially funded by Siemens.* Jacob G. Dubroff—*RELATED: Grant:* Siemens provided the software (syngo Scenium) to calculate the SUVr and partial funding*; *Payment for Lectures (including service on Speakers Bureaus):* Webinar for Applied Radiology. *Comments:* Twenty-one months ago (August 2012), a \$1000 one-time honorarium was paid to me for giving a Webinar for Applied Radiology; my institution and department were/are aware of the relationship. James E. Schmitt—*UNRELATED: Grants/Grants Pending:* National Institutes of Health, Radiological Society of North America. *Comments:* T32 Training Grant from the National Institutes of Health (EB004311, to Mitch Schnall), Fellow Grant from the Radiological Society of North America (Imaging Genomic Analysis of the 22q11DS Syndrome). Rekha Kishore—*RELATED: Grant:* This study was partially funded by Siemens*; *UNRELATED: Stock/Stock Options:* Merck. *Comments:* I own a small amount of stock in Merck. David Mankoff—*RELATED: Grant:* Siemens (partial support)*; *UNRELATED: Consultancy:* GE Healthcare, Philips Healthcare, Siemens; *Grants/Grants Pending:* Siemens,* Philips Healthcare.* Daniel A. Pryma—*RELATED: Grant:* This work was partially funded by a grant from Siemens*; *Payment for Lectures (including service on Speakers Bureaus):* IBA Molecular. *Money paid to the institution.

REFERENCES

1. Alzheimer's Association. 2013 Alzheimer's disease facts and figures. *Alzheimers Dement* 2013;9:208–45

2. Holtzman DM, Morris JC, Goate AM. **Alzheimer's disease: the challenge of the second century.** *Sci Transl Med* 2011;3:77sr1
3. Hiltunen M, van Groen T, Jolkkonen J. **Functional roles of amyloid-beta protein precursor and amyloid-beta peptides: evidence from experimental studies.** *J Alzheimers Dis* 2009;18:401–12
4. Löppönen M, Raiha I, Isoaho R, et al. **Diagnosing cognitive impairment and dementia in primary health care: a more active approach is needed.** *Age Ageing* 2003;32:606–12
5. Clark CM, Schneider JA, Bedell BJ, et al. **Use of florbetapir-PET for imaging beta-amyloid pathology.** *JAMA* 2011;305:275–83
6. Wong DF, Rosenberg PB, Zhou Y, et al. **In vivo imaging of amyloid deposition in Alzheimer disease using the radioligand 18F-AV-45 (florbetapir [corrected] F 18).** *J Nucl Med* 2010;51:913–20
7. Clark CM, Pontecorvo MJ, Beach TG, et al. **Cerebral PET with florbetapir compared with neuropathology at autopsy for detection of neuritic amyloid-beta plaques: a prospective cohort study.** *Lancet Neurol* 2012;11:669–78
8. FDA advisory committee briefing document: Peripheral and Central Nervous Systems Drugs Advisory Committee—draft clinical review. December 20, 2010. <http://www.fda.gov/downloads/AdvisoryCommittees/CommitteesMeetingMaterials/Drugs/PeripheralandCentralNervousSystemDrugsAdvisoryCommittee/UCM240265.pdf>. Accessed September 12, 2013
9. FDA approves imaging drug Amyvid. <http://www.fda.gov/NewsEvents/Newsroom/PressAnnouncements/ucm299678.htm>. Accessed September 14, 2013
10. **FDA approves 18F-florbetapir PET agent.** *J Nucl Med* 2012;53:15N
11. Braak H, Braak E. **Neuropathological staging of Alzheimer-related changes.** *Acta Neuropathol* 1991;82:239–59
12. Fleisher AS, Chen K, Liu X, et al. **Using positron emission tomography and florbetapir F18 to image cortical amyloid in patients with mild cognitive impairment or dementia due to Alzheimer disease.** *Arch Neurol* 2011;68:1404–11
13. Johnson KA, Sperling RA, Gidicsin CM, et al. **Florbetapir (F18-AV-45) PET to assess amyloid burden in Alzheimer's disease dementia, mild cognitive impairment, and normal aging.** *Alzheimers Dement* 2013;9:S72–83
14. Avid Radiopharmaceuticals. Amyvid Reader Training. 2012. <http://amyvidtraining.com/>. Accessed June 14, 2013
15. Petersen R, Weiner M. ADNI 2 Procedures Manual. 2008. <http://adni.loni.usc.edu/wp-content/uploads/2008/07/adni2-procedures-manual.pdf>. Accessed June 14, 2013
16. Ghosh P, Sorger P, Buelau A, et al. **White paper: quantitative software evaluation of amyloid brain PET imaging in dementia.** 2012. http://www.healthcare.siemens.com/siemens_hwem-hwem_sxxa_websites-context-root/wcm/idc/groups/public/@global/@imaging/@molecular/documents/download/mdaw/mji1/~edisp/whitepaper15_amyloiddementia-00274875.pdf. Accessed October 15, 2013
17. Camus V, Payoux P, Barre L, et al. **Using PET with 18F-AV-45 (florbetapir) to quantify brain amyloid load in a clinical environment.** *Eur J Nucl Med Mol Imaging* 2012;39:621–31
18. Peyrat J, Joshi AD, Mintun MA, et al. **An automatic method for the quantification of uptake with florbetapir imaging.** *J Nucl Med* 2012; 53(suppl 1):210
19. Joshi AD, Pontecorvo MJ, Clark CM, et al. **Performance characteristics of amyloid PET with florbetapir F 18 in patients with Alzheimer's disease and cognitively normal subjects.** *J Nucl Med* 2012;53:378–84
20. R Development Core Team. *R: A Language and Environment for Statistical Computing.* Vienna: R Foundation for Statistical Computing; 2011
21. Gamer M, Lemon J, Fellows I, et al. The irr package, Ver. 0.83: various coefficients of interrater reliability and agreement. 2010. <http://cran.r-project.org/web/packages/irr/index.html>. Accessed April 1, 2013
22. Vanbelle S, Albert A. **A bootstrap method for comparing correlated kappa coefficients.** *Journal of Statistical Computing and Simulation* 2008;78:1009–15
23. Landis JR, Koch GG. **The measurement of observer agreement for categorical data.** *Biometrics* 1977;33:159–74
24. Ranginwala NA, Hynan LS, Weiner MF, et al. **Clinical criteria for the diagnosis of Alzheimer disease: still good after all these years.** *Am J Geriatr Psychiatry* 2008;16:384–88
25. Johnson KA, Minoshima S, Bohnen NI, et al. **Appropriate use criteria for amyloid PET: a report of the Amyloid Imaging Task Force, the Society of Nuclear Medicine and Molecular Imaging, and the Alzheimer's Association.** *J Nucl Med* 2013;54:476–90
26. Ng S, Villemagne VL, Berlangieri S, et al. **Visual assessment versus quantitative assessment of 11C-PIB PET and 18F-FDG PET for detection of Alzheimer's disease.** *J Nucl Med* 2007;48:547–52
27. Jeon KN, Goo JM, Lee CH, et al. **Computer-aided nodule detection and volumetry to reduce variability between radiologists in the interpretation of lung nodules at low-dose screening computed tomography.** *Invest Radiol* 2012;47:457–61
28. Gierada DS, Pilgram TK, Ford M, et al. **Lung cancer: interobserver agreement on interpretation of pulmonary findings at low-dose CT screening.** *Radiology* 2008;246:265–72
29. Wojcinski S, Gyapong S, Farrokh A, et al. **Diagnostic performance and inter-observer concordance in lesion detection with the automated breast volume scanner (ABVS).** *BMC Med Imaging* 2013; 13:36
30. Rosario BL, Weissfeld LA, Laymon CM, et al. **Inter-rater reliability of manual and automated region-of-interest delineation for PiB PET.** *Neuroimage* 2011;55:933–41
31. Luo P, Qian W, Romilly P. **CAD-aided mammogram training.** *Acad Radiol* 2005;12:1039–48
32. Beach TG, Monsell SE, Phillips LE, et al. **Accuracy of the clinical diagnosis of Alzheimer disease at National Institute on Aging Alzheimer Disease Centers, 2005–2010.** *J Neuropathol Exp Neurol* 2012;71:266–73
33. Lim A, Tsuang D, Kukull W, et al. **Clinico-neuropathological correlation of Alzheimer's disease in a community-based case series.** *J Am Geriatr Soc* 1999;47:564–69
34. Bennett DA, Schneider JA, Bienias JL, et al. **Mild cognitive impairment is related to Alzheimer disease pathology and cerebral infarctions.** *Neurology* 2005;64:834–41
35. Gearing M, Schneider JA, Rebeck GW, et al. **Alzheimer's disease with and without coexisting Parkinson's disease changes: apolipoprotein E genotype and neuropathologic correlates.** *Neurology* 1995;45: 1985–90
36. Morishima-Kawashima M, Oshima N, Ogata H, et al. **Effect of apolipoprotein E allele epsilon4 on the initial phase of amyloid beta-protein accumulation in the human brain.** *Am J Pathol* 2000; 157:2093–99
37. Doraiswamy PM, Sperling RA, Coleman RE, et al. **Amyloid-beta assessed by florbetapir F 18 PET and 18-month cognitive decline: a multicenter study.** *Neurology* 2012;79:1636–44
38. Doraiswamy PM, Sperling RA, Johnson K, et al. **Florbetapir F 18 amyloid PET and 36-month cognitive decline: a prospective multicenter study.** *Mol Psychiatry* 2014;19:1044–51
39. Kitazono MT, Lau CT, Parada AN, et al. **Differentiation of pleural effusions from parenchymal opacities: accuracy of bedside chest radiography.** *AJR Am J Roentgenol* 2010;194:407–12
40. Muyoyeta M, Maduskar P, Moyo M, et al. **The sensitivity and specificity of using a computer aided diagnosis program for automatically scoring chest X-rays of presumptive TB patients compared with Xpert MTB/RIF in Lusaka Zambia.** *PLoS One* 2014;9:e93757
41. Owringi AM, Entwistle B, Lu A, et al. **Semi-automated scoring of pulmonary emphysema from X-ray CT: trainee reproducibility and accuracy.** *Eur J Radiol* 2013;82:e734–41
42. Pinto LM, Dheda K, Theron G, et al. **Development of a simple reliable radiographic scoring system to aid the diagnosis of pulmonary tuberculosis.** *PLoS One* 2013;8:e54235
43. Xie X, Zhao Y, Snijder RA, et al. **Sensitivity and accuracy of volumetry of pulmonary nodules on low-dose 16- and 64-row multi-detec-**

- tor CT: an anthropomorphic phantom study.** *Eur Radiol* 2013;23:139–47
44. Carton AK, Gavenonis SC, Currivan JA, et al. **Dual-energy contrast-enhanced digital breast tomosynthesis: a feasibility study.** *Br J Radiol* 2010;83:344–50
45. Tagliafico A, Tagliafico G, Tosto S, et al. **Mammographic density estimation: comparison among BI-RADS categories, a semi-automated software and a fully automated one.** *Breast* 2009;18:35–40
46. Takeda K, Kanao S, Okada T, et al. **Assessment of CAD-generated tumor volumes measured using MRI in breast cancers before and after neoadjuvant chemotherapy.** *Eur J Radiol* 2012;81:2627–31
47. Barthel H, Luthardt J, Becker G, et al. **Individualized quantification of brain beta-amyloid burden: results of a proof of mechanism phase 0 florbetaben PET trial in patients with Alzheimer's disease and healthy controls.** *Eur J Nucl Med Mol Imaging* 2011;38:1702–14

Establishing Amyloid PET Imaging Biomarkers: Ongoing Efforts

The concept of imaging biomarkers was conceived in the late 1990s. The process of deduction from “complex” imaging data to a few simpler indices is often required for biomarkers to be quantitative and reproducible. Widespread examples in the field of PET imaging include the standard uptake value (SUV) to represent tumor FDG uptake¹ and quantitative statistical mapping methods by using the *z* scores applied to brain FDG PET scans.² Such methods have been used for the diagnosis and therapeutic evaluation of various medical conditions. Now, clinically available amyloid PET tracers permit the development of such approaches for amyloid PET interpretation.

The study by Nayate et al³ used 60 cases of amyloid PET scans (30 scans as test cases) obtained from the Alzheimer Disease Neuroimaging Initiative (<http://www.adni-info.org>). They calculated the standard uptake value ratio (SUVR) (cortical regions to whole cerebellar uptake) by using software available on a workstation and presented SUVR values to readers who were interpreting amyloid PET scans. They found that interreader agreement increased significantly when the scans were presented with SUVR information. This study illustrates nicely that quantitative biomarker information might improve scan interpretation across different readers with different degrees of experience in amyloid PET interpretation.

The group from Pittsburgh conducted the seminal work on the quantitative assessment of imaging biomarkers for amyloid PET. Lopresti et al⁴ compared more rigorous quantitative makers, such as distribution volume, that were obtained by using dynamic PET imaging and Logan graphical analysis. They found that simpler indices, such as SUVR, produced accuracy comparable with more elaborate methods in distinguishing scans of Alzheimer disease versus control conditions.⁴ One major advantage of SUVR is that it can be estimated on a single static PET scan without requiring dynamic imaging or complex tracer analysis. This simplicity is well-suited in clinical applications. Although the term “SUVR” has been used frequently in the field of amyloid PET, SUVR merely represents a ratio of radiotracer uptake of a target region (ie, cortical regions) divided by a reference region (ie, the cerebellum). Pixel counts on the reconstructed amyloid PET images do not

need to be converted to SUV values before the calculation of SUVR. It is equivalent to a “target-to-background” ratio—the index that has been used in nuclear medicine for many years.

While imaging biomarkers such as SUVR for amyloid PET can provide information complementary to qualitative scan interpretation, it is important to know that SUVR values can be affected by various factors. For example, different amyloid tracers (3 tracers are currently approved by the US FDA) can produce different SUVR values.⁵ Scan timing, size of ROIs, and image reconstruction methods can produce different SUVR values from the same patient, similar to SUV values used for FDG PET in cancer work-up. Different reference regions can produce substantially different SUV values (such as whole cerebellum versus cerebellar gray matter versus cerebral white matter). Various investigators have explored the best reference region for amyloid PET analysis. Because of the method- and tracer-dependent nature of the SUVR, the same SUVR threshold for distinguishing scans with positive-versus-negative findings cannot be applied to scans obtained with different tracers, different imaging methods, and different ROIs. There has been an ongoing effort to standardize quantitative biomarkers for amyloid PET through the Quantitative Imaging Biomarkers Alliance of the Radiological Society of North America (<http://www.rsna.org/QIBA>). A method to unify amyloid PET analysis for different radiotracers has also been proposed.⁶

One critical question that was not addressed in the current study by Nayate et al³ is the accuracy of scan interpretation by using SUVR information. Presentation of the SUVR values at the time of scan interpretation improved interreader agreement. Was the diagnostic accuracy also improved with the SUVR, or did readers consistently make wrong diagnoses on certain cases because of the SUVR values? Without a gold standard (which typically requires postmortem data), the current study by Nayate et al cannot assess such critical questions related to the accuracy of scan interpretation. When reading amyloid PET scans in the clinic, we occasionally encounter cases that have discrepant impressions from qualitative visual interpretation and quantitative SUVR assessment. In such cases,

which one should be trusted? This problem requires more robust prospective validation and standardization of amyloid PET biomarkers. Such effort is currently underway in molecular brain imaging communities.

REFERENCES

1. Wahl RL, Zasadny K, Helvie M, et al. **Metabolic monitoring of breast cancer chemohormonotherapy using positron emission tomography: initial evaluation.** *J Clin Oncol* 1993;11:2101–11
2. Minoshima S, Frey KA, Koeppe RA, et al. **A diagnostic approach in Alzheimer's disease using three-dimensional stereotactic surface projections of fluorine-18-FDG PET.** *J Nucl Med* 1995;36:1238–48
3. Nayate AP, Dubroff JG, Schmitt JE, et al; Alzheimer's Disease Neuroimaging Initiative. **Use of standardized uptake value ratios decreases interreader variability of [18F] florbetapir PET brain scan interpretation.** *AJNR Am J Neuroradiol* 2015;36:1237–44
4. Lopresti BJ, Klunk WE, Mathis CA, et al. **Simplified quantification of Pittsburgh Compound B amyloid imaging PET studies: a comparative analysis.** *J Nucl Med* 2005;46:1959–72
5. Landau SM, Thomas BA, Thurfjell L, et al; Alzheimer's Disease Neuroimaging Initiative. **Amyloid PET imaging in Alzheimer's disease: a comparison of three radiotracers.** *Eur J Nucl Med Mol Imaging* 2014;41:1398–407
6. Klunk WE, Koeppe RA, Price JC, et al. **The Centiloid project: standardizing quantitative amyloid plaque estimation by PET.** *Alzheimers Dement* 2015;11:1–15.e1–4

S. Minoshima

Department of Radiology
University of Utah
Salt Lake City, Utah

<http://dx.doi.org/10.3174/ajnr.A4433>

Prognostic Value of Dynamic Susceptibility Contrast-Enhanced and Diffusion-Weighted MR Imaging in Patients with Glioblastomas

G. Çoban, S. Mohan, F. Kural, S. Wang, D.M. O'Rourke, and H. Poptani



ABSTRACT

BACKGROUND AND PURPOSE: Prediction of survival in patients with glioblastomas is important for individualized treatment planning. This study aimed to assess the prognostic utility of presurgical dynamic susceptibility contrast and diffusion-weighted imaging for overall survival in patients with glioblastoma.

MATERIALS AND METHODS: MR imaging data from pathologically proved glioblastomas between June 2006 to December 2013 in 58 patients (mean age, 62.7 years; age range, 22–89 years) were included in this retrospective study. Patients were divided into long survival (≥ 15 months) and short survival (< 15 months) groups, depending on overall survival time. Patients underwent dynamic susceptibility contrast perfusion and DWI before surgery and were treated with chemotherapy and radiation therapy. The maximum relative cerebral blood volume and minimum mean diffusivity values were measured from the enhancing part of the tumor.

RESULTS: Maximum relative cerebral blood volume values in patients with short survival were significantly higher compared with those who demonstrated long survival ($P < .05$). No significant difference was observed in the minimum mean diffusivity between short and long survivors. Receiver operator curve analysis demonstrated that a maximum relative cerebral blood volume cutoff value of 5.79 differentiated patients with low and high survival with an area under the curve of 0.93, sensitivity of 0.89, and specificity of 0.90 ($P < .001$), while a minimum mean diffusivity cutoff value of $8.35 \times 10^{-4} \text{ mm}^2/\text{s}$ had an area under the curve of 0.55, sensitivity of 0.71, and specificity of 0.47 ($P > .05$) in separating the 2 groups.

CONCLUSIONS: Maximum relative cerebral blood volume may be used as a prognostic marker of overall survival in patients with glioblastomas.

ABBREVIATIONS: EGFR = epidermal growth factor receptor; GBM = glioblastoma; MD = mean diffusivity; MD_{min} = minimum mean diffusivity; rCBV = relative cerebral blood volume; rCBV_{max} = maximum relative cerebral blood volume

Glioblastomas (GBMs) are the most common malignant tumors of the central nervous system in adults, representing 50% of all gliomas and 20% of all intracranial solid lesions.¹ The prognosis of GBM is poor, and median overall survival is < 1 year.² Even in optimal conditions (young patients treated by radical surgery, radiation therapy, and chemotherapy), death usually occurs within 2 years.^{3,4} Several factors, both clinical (age, performance status) and therapeutic (extent of surgery, radiation ther-

apy, chemotherapy), as well as specific tumor characteristics such as location and nature (de novo or secondary from a low-grade glioma)^{5,6} have been studied as potential prognostic markers of overall survival with variable degrees of sensitivity and specificity. Recently, tumor genetics is also being investigated as a prognostic index.^{7,8}

Conventional MR imaging is widely used as the technique of choice for GBM diagnosis and also has an important role in monitoring disease progression and response to therapy for patients with GBM. Additional advanced imaging techniques, such as relative cerebral blood volume (rCBV) obtained from dynamic susceptibility contrast perfusion imaging, have been used to predict glioma grade⁹⁻¹¹ and assess treatment response.¹² A recent report¹⁰ indicated that maximum relative cerebral blood volume (rCBV_{max}) can be used as a predictive marker of progression-free survival in patients with gliomas, regardless of the tumor grade.

Similar to perfusion imaging, diffusion-weighted imaging has also been used for diagnosis of tumors. Tumors with high cellu-

Received August 29, 2014; accepted after revision December 14.

From the Department of Radiology (G.Ç., F.K.), Baskent University School of Medicine, Ankara, Turkey; and Departments of Radiology (G.Ç., S.M., F.K., S.W., H.P.) and Neurosurgery (D.M.O.), University of Pennsylvania, Philadelphia, Pennsylvania.

G. Çoban and S. Mohan contributed equally to this work.

Please address correspondence to Harish Poptani, PhD, Department of Cellular and Molecular Physiology, University of Liverpool, 2/012 Nuffield Building, Crown St, Liverpool L69 3BX, UK; e-mail: Harish.Poptani@liverpool.ac.uk

Indicates article with supplemental on-line tables.

<http://dx.doi.org/10.3174/ajnr.A4284>

larity demonstrate restricted diffusion and thus low mean diffusivity (MD) or apparent diffusion coefficient, which inversely correlates with tumor cellularity.^{13,14} Areas with minimum mean diffusivity (MD_{min}) reflect the sites of highest cellularity, and tumors with a low MD tend to have a poor prognosis.¹⁵⁻¹⁸

Radiation therapy and chemotherapy with temozolomide have become the standard of care in the treatment of GBM and have demonstrated increased survival benefits in patients with newly diagnosed GBM.¹⁹ However, several clinical trials, including blocking the tyrosine kinase activity of epidermal growth factor receptor (EGFR),^{20,21} using competitive and noncompetitive kinase inhibitors in combination with radiation and temozolomide,^{20,21} and using monoclonal antibodies,²⁰ are also investigating the treatment of GBMs. The exact value of each of these therapeutic strategies remains investigative though. The overall survival of patients with glioblastomas varies significantly,^{17,18} and it is imperative to know which patients will do better or worse, preferably before initiation of treatment, by using a noninvasive imaging method, so as to tailor fit the therapy for the best management and hopefully increased survival. We have evaluated the role of DSC-MR imaging and DWI as potential prognostic imaging markers in patients with GBM with an eventual goal of using these parameters in the selection of the optimal treatment option for these patients.

MATERIALS AND METHODS

MR Imaging

This retrospective study was approved by the institutional review board and was compliant with the Health Insurance Portability and Accountability Act. A total of 564 treatment-naïve patients diagnosed with GBM at the University of Pennsylvania from June 2006 to December 2013 were retrospectively reviewed. Because we were interested in evaluating the role of perfusion-weighted imaging and diffusion-weighted imaging, we excluded the cases in which the PWI or DWI scans were not available. In addition, we analyzed the pretreatment MR imaging scans of only those patients who had gross total resection of their tumors so that the extent of surgery was not a confounder in the analysis. Furthermore, we also excluded all GBMs with oligodendroglial features. Of the 564 cases reviewed, 58 patients (32 men and 26 women; mean age, 62.71 ± 13.2 years; age range, 22–89 years) with a pathologically proved GBM met our inclusion criteria and were included in the study. After surgery, all the patients were treated with chemotherapy and radiation therapy.

We used a 15-month overall survival as the cutoff to evaluate rCBV_{max} and MD_{min} as predictive markers because several previous studies have reported a median overall survival time of 12–15 months for patients with GBM.^{2,18,19} Thus, the 58 patients in our study were divided into 2 groups: patients having long survival ($n = 30$, patients who had an overall survival of ≥15 months) and short survival ($n = 28$, patients who had an overall survival of <15 months). The survival time was calculated as the time (in months) from the initial date of diagnosis until the date of death. The clinical symptoms, survival duration, Karnofsky score, and lesion diameter of the patients demonstrating short and long survival are reported in On-line Tables 1 and 2. The MR images acquired before surgery (<1 week) were evaluated in this study.

All MR images were obtained on a 3T clinical MR imaging system (Tim Trio; Siemens, Erlangen, Germany), equipped with a 12-channel phased array head coil. The imaging protocol included a 3-plane scout localizer, axial 3D T1-weighted magnetization-prepared rapid acquisition of gradient-echo images by using the following parameters: TR, 1760 ms; TE, 3.1 ms; TI, 950 ms; matrix size, 192 × 256; FOV, 25 × 25 cm²; and 1-mm section thickness; and FLAIR images with TR, 9420 ms; TE, 141 ms; TI, 2500 ms; matrix size, 192 × 256; and 3-mm thick contiguous sections with no gap. DWI data were acquired by using a single-shot spin-echo echo-planar imaging sequence with parallel imaging by using a generalized autocalibrating partially parallel acquisition and an acceleration factor of 2. Other sequence parameters were as follows: FOV = 22 × 22 cm²; $b=0$, 1000 s/mm²; section thickness, 3 mm; number of sections, 40; acquisition time, 8 minutes.

For dynamic susceptibility contrast imaging, a bolus of gadobenate dimeglumine (MultiHance; Bracco Diagnostics, Princeton, New Jersey) was injected as the preloading dose of 0.07 mmol/kg. The preloading dose was administered to reduce the effect of contrast agent leakage on CBV measurements. A DSC T2*-weighted gradient-echo, echo-planar sequence was obtained during the second 0.07-mmol/kg bolus of intravenous contrast agent. The injection rate was 5 mL/s for all patients and was immediately followed by a bolus injection of saline (total of 20 mL at the same rate). DSC sequence parameters included the following: TR/TE, 2000/45 ms; FOV, 22 × 22 cm²; in-plane resolution, 1.72 × 1.72 × 3 mm³; slab of 20 sections covering the tumor region; and acquisition time of 1 minute 38 seconds. A long TR and a low flip angle were used to reduce the effect of changes in T1 relaxation from contrast agent leakage.²² Post-contrast-enhanced T1-weighted MPRAGE images were acquired after completion of the DSC sequence.

Image Processing

The rCBV was calculated from PWI data by using the intravascular indicator dilution algorithms described previously.²³⁻²⁵ Data processing was performed by using PWI Task Card (Massachusetts General Hospital, Boston, Massachusetts) on a Leonardo workstation (Siemens). MD maps were automatically generated by using the software tools available on the scanner by using a monoexponential fit to the multiple b-value images. Measurements were obtained by 2 radiologists (G.Ç. and F.K., with >4 years of experience reading brain MR imaging). We meticulously chose multiple ROIs from the enhancing part of the tumor, avoiding areas of cerebral blood vessels, calcifications, hemorrhage, and CSF-filled sulci to measure a reliable CBV value as proposed earlier.²⁶⁻²⁷ The ROIs were drawn and chosen in agreement by the 2 readers, thereby reducing any interobserver variability. The commonly used rCBV_{max} parameter²⁸ was computed by calculating the mean CBV values from 3 circular ROIs measuring 30–50 mm² from areas of visually high CBV as reported previously.²⁶⁻²⁷ For normalization, 3 circular ROIs of the same size were drawn in the contralateral normal-appearing white matter. A similar analysis method was used to investigate the minimum mean diffusivity. Three circular ROIs measuring 30–50 mm² from the visually low-

est MD values were used to compute MD_{min}, representing high cellularity as reported previously.^{13,17}

Statistical Analysis

The long and short survival patient groups were compared by using a Student *t* test. A *P* value < .05 was considered significant. A receiver operating characteristic analysis was performed to evaluate the predictive power of rCBV_{max} and MD_{min} for overall survival. Areas under the curve were computed. A cutoff value for each parameter was determined by maximizing the sum of sensitivity and specificity. Kaplan-Meier survival curves were used to characterize and compare the groups with high-versus-low rCBV_{max} and high-versus-low MD_{min} in terms of overall survival. All statistical analyses were conducted by using PASW Statistics, Version 18 (IBM, Armonk, New York).

RESULTS

Representative images of patients with GBM with long and short survival are shown in Fig 1. The contrast-enhanced T1-weighted images and FLAIR images from these patients look similar, showing heterogeneous peripheral enhancement and extensive surrounding FLAIR signal abnormality. All tumors showed prominent enhancement after IV contrast administra-

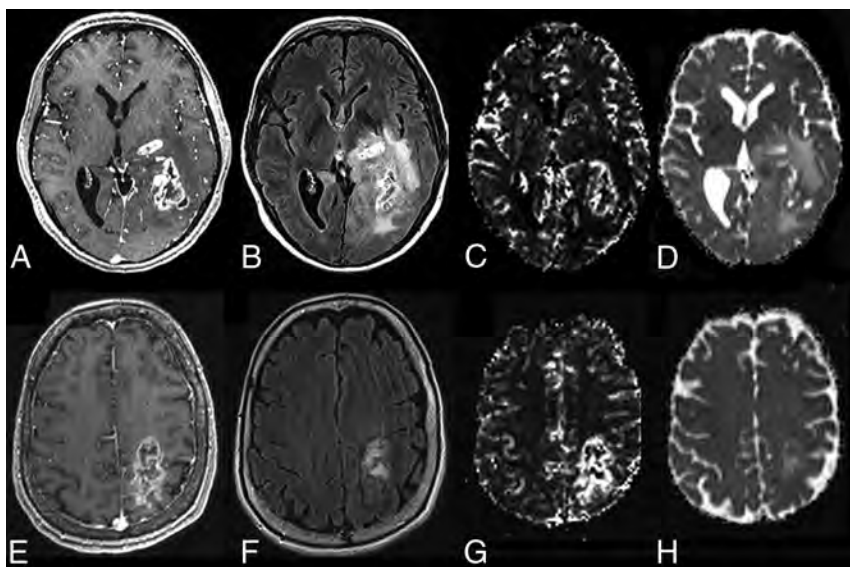


FIG 1. Representative MR images and parametric maps from patients with GBM. The top row (A–D) shows images from a 66-year-old woman with GBM who survived for >58 months after gross total resection of her GBM in the left temporo-occipital lobe. Representative MR images from a 75-year-old man with a GBM in the left parietal lobe with only a 5-month survival are shown (E–H). Images of both patients demonstrate heterogeneous peripheral enhancement (A and E) and extensive surrounding FLAIR signal abnormality (B and F) on axial contrast-enhanced T1-weighted and FLAIR images, respectively. The patient with short survival has a higher CBV (G) (rCBV_{max} = 12.22) in comparison with the patient with long survival (C) (rCBV_{max} = 3.57). The MD maps from these patients (D and H) do not show any difference ($6.50 \times 10^{-4} \text{ mm}^2/\text{s}$ versus $6.80 \times 10^{-4} \text{ mm}^2/\text{s}$).

Average \pm SD, sensitivity, specificity, PPV, and NPV of pretreatment rCBV_{max} and MD_{min} in patients with GBM demonstrating long (≥ 15 mo) survival and short (<15 mo) survival

	Long Survival (n = 30)	Short Survival (n = 28)	Cutoff	AUC	Sensitivity	Specificity	PPV	NPV
	Mean \pm SD	Mean \pm SD						
rCBV _{max}	4.78 \pm 1.30	9.90 \pm 4.01 ^a	5.79	0.93	0.89	0.90	0.89	0.90
MD _{min} ($10^{-3} \text{ mm}^2/\text{s}$)	0.80 \pm 0.17	0.75 \pm 0.15	0.83	0.55	0.71	0.47	0.56	0.64

Note.—NPV indicates negative predictive value; PPV, positive predictive value; AUC, area under the curve.

^a *P* < .01.

tion. The patient with short survival demonstrated higher rCBV_{max} compared with the patient who exhibited long survival.

The rCBV_{max} values of patients with short survival (9.90 ± 4.01) were significantly higher compared with those of long survival (4.78 ± 1.30 , *P* < .05). There was no significant difference in the MD_{min} values between the 2 groups: 0.80 ± 0.17 versus $0.75 \pm 0.15 \times 10^{-3} \text{ mm}^2/\text{s}$ (Table).

Receiver operating characteristic analysis indicated that a rCBV_{max} cutoff value of 5.79 was the best parameter for predicting overall survival with an area under the curve of 0.93, sensitivity of 0.89, specificity of 0.90, positive predictive value of 0.89, and negative predictive value of 0.90 (Fig 2 and Table). The MD_{min} cutoff value of $8.35 \times 10^{-4} \text{ mm}^2/\text{s}$, on the other hand, showed only a modest area under the curve of 0.55, sensitivity of 0.71, specificity of 0.47, positive predictive value of 0.56, and negative predictive value of 0.64 (Fig 2 and Table). A combination of rCBV_{max} and MD_{min} did not improve the prediction capability and had an area under the curve (0.93) similar to that of rCBV_{max}. Kaplan-Meier survival curves demonstrated that GBMs with low rCBV_{max} (<5.79) had a median survival time of 23 ± 3.4 months, whereas GBMs with high rCBV_{max} (≥ 5.79) had a median survival time of 5 ± 1.9 months (Fig 3). There was a significant difference

in patients with high rCBV_{max} and low rCBV_{max} (*P* < .001). For the DWI measurements, GBMs with low MD_{min} (< $8.35 \times 10^{-4} \text{ mm}^2/\text{s}$) had a median survival time of 14 ± 2.0 months, whereas GBMs with high MD_{min} ($>8.35 \times 10^{-4} \text{ mm}^2/\text{s}$) had a median survival time of 18 ± 1.4 months, and there was no significant difference between the 2 groups (*P* > .05) (Fig 4).

DISCUSSION

Our study suggests that pretreatment rCBV_{max} can be used as a prognostic marker for overall survival in patients with GBM. In particular, patients with high pretreatment rCBV_{max} demonstrated lower survival in comparison with patients with low pretreatment rCBV_{max}, who exhibited longer survival of >15 months. These results could have a potential clinical benefit and in the future may aid in individualized treatment planning because patients with high pretreatment rCBV_{max} can be offered upfront alternative treatment

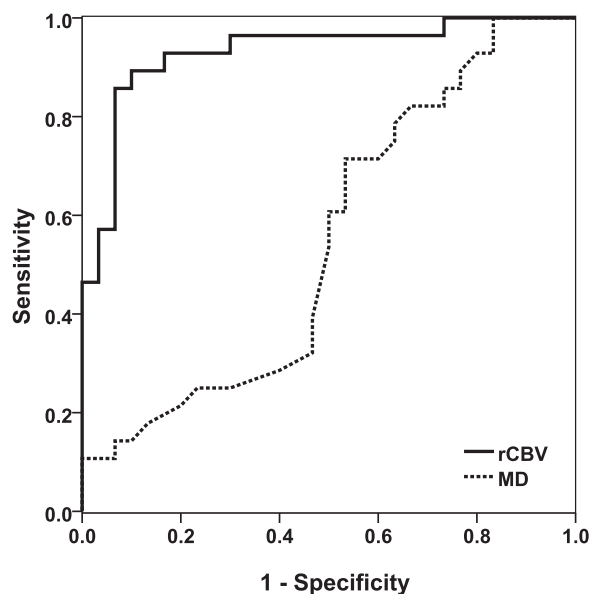


FIG 2. Receiver operating characteristic curves of $rCBV_{max}$ (solid line) by using a $rCBV_{max}$ cutoff value of 5.79. The area under the curve was 0.93. The receiver operating curve of MD_{min} (dotted line) by using a cutoff value of $8.35 \times 10^{-4} \text{ mm}^2/\text{s}$ demonstrated only a modest area under the curve of 0.55.

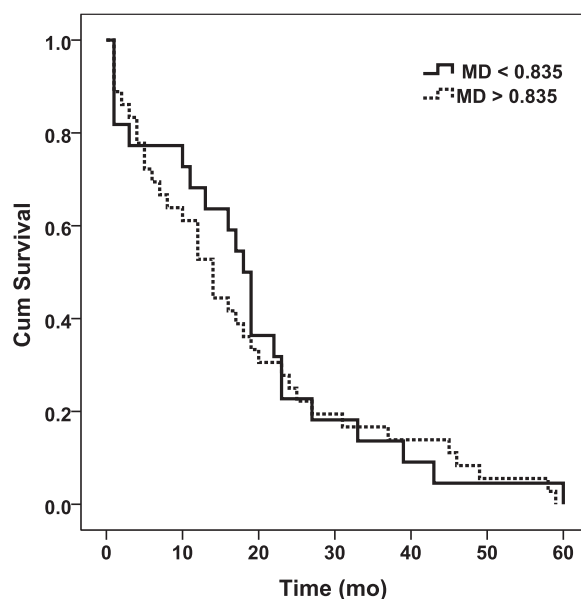


FIG 4. Kaplan-Meier curves for patients with GBM with low ($<0.835 \times 10^{-3} \text{ mm}^2/\text{s}$, solid line) and high ($\geq 0.835 \times 10^{-3} \text{ mm}^2/\text{s}$, dotted line) MD_{min} . GBMs with a low MD_{min} have a median survival time of 14 ± 2.0 months, whereas GBMs with a high MD_{min} have a median survival time of 18 ± 1.4 months. There is no significant difference between the 2 groups ($P > .05$). Cum indicates cumulative.

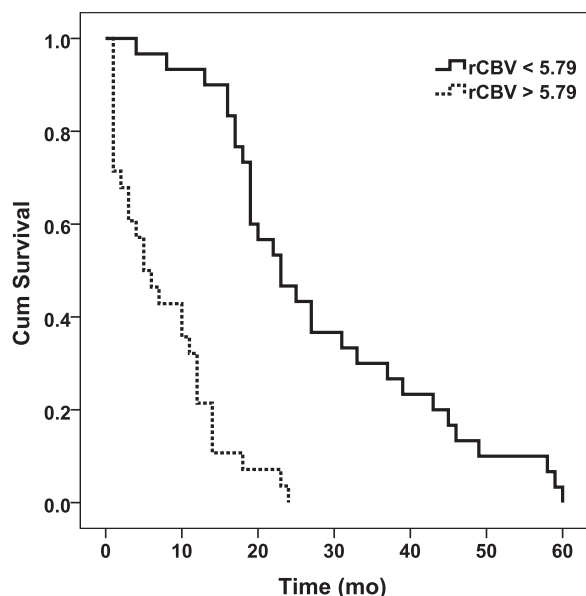


FIG 3. Kaplan-Meier curves for patients with low (<5.79 , solid line) and high (≥ 5.79 , dotted line) $rCBV_{max}$. GBMs with low $rCBV_{max}$ had a median survival time of 23 ± 3.4 months, whereas GBMs with high $rCBV_{max}$ had a median survival time of 5 ± 1.9 months ($P < .001$). Cum indicates cumulative.

strategies, including bevacizumab, immunotherapy, or other therapies targeted toward increased survival.

Conventional imaging characteristics of GBM, including location, size, and degree of enhancement; necrosis; and extent of edema, have been studied for prediction of survival.^{9-11,29-36} Although contrast enhancement is generally used to estimate the extent of the tumor, it is clear from the literature that conventional radiologic findings, such as the absence of contrast enhancement, are not only poor predictors of tumor grade but may

or may not be prognostic factors for either survival or progression-free survival.^{12,37} PWI is increasingly being used to assess microvascular changes associated with the tumor grade, and it is widely used to assess tumor angiogenesis and microvasculature.^{34,35,38} Law et al³⁰ suggested that $rCBV$ measurements in low-grade gliomas correlated more accurately with time to progression than the initial histopathologic grading of the tumor. Although Oh et al¹⁸ suggested that $rCBV$ had no predictive value with respect to the prognosis in GBM, they evaluated GBM tumors after surgical resection; thus, it is unclear whether the extent of surgery played a role in determining the prognostic value in their study.¹⁸ Bisdas et al¹¹ reported that there was no correlation among CBV , World Health Organization grade, and progression-free survival in a mixed population of gliomas. Similar to ours, findings of Mangla et al³² were that $rCBV$ was useful for predicting progression-free survival in anaplastic astrocytomas, but not for grade III tumors with oligodendroglial components.

We observed that an $rCBV_{max}$ threshold value of 5.79 was the best predictor for overall survival with a very high sensitivity and specificity. In other words, this threshold was evaluated as a prognostic index of survival in GBM and not for predicting tumor grade, for which a much lower $rCBV$ threshold was reported by Bisdas et al¹¹ (4.2), Lev et al²⁹ (1.5), Law et al³¹ (1.75), and Mangla et al³² (2.55).

High-grade brain tumors are usually associated with high cellularity and therefore exhibit low MD values.¹⁵⁻¹⁷ Previous studies^{15,16,39} reported that MD_{min} was a sensitive marker for prognosis and survival. The cutoff MD values used in these studies were $0.74 \times 10^{-3} \text{ mm}^2/\text{s}$, $0.90 \times 10^{-3} \text{ mm}^2/\text{s}$, $0.93 \times 10^{-3} \text{ mm}^2/\text{s}$, and $1.00 \times 10^{-3} \text{ mm}^2/\text{s}$, respectively.¹⁵⁻¹⁸ Higano et al¹⁶ studied 37 malignant astrocytic tumors, including 22 GBMs, and reported a significant negative correlation between MD_{min} and

Ki-67, which may explain the poor prognosis of patients with lower MD_{min}. The authors of that study also reported that the MD_{min} ($0.834 \times 10^{-3} \text{mm}^2/\text{s}$) of GBM was significantly lower than the MD_{min} ($1.06 \times 10^{-3} \text{mm}^2/\text{s}$) of anaplastic astrocytomas. In another study, Murakami et al¹⁵ studied 79 malignant supratentorial astrocytic tumors, including 50 patients with GBMs, and observed that patients with an MD_{min} of $>1.00 \times 10^{-3} \text{mm}^2/\text{s}$ had better outcomes than patients with an MD_{min} of $\leq 1.00 \times 10^{-3} \text{mm}^2/\text{s}$. Yamasaki et al³⁹ reported that MD_{min} also predicted overall survival in patients with GBMs who did not have a complete- or near-total resection of their tumors. We did not observe an MD_{min} cutoff value that could differentiate patients having short or long survival (Fig 4). However, in comparison with these previous studies, we studied a homogeneous population of patients with GBMs who had undergone gross total resection of their tumors, which may partially explain the difference in our results.

Because GBM is composed of prominent necrosis, nuclear atypia, cellular proliferation, and microvascular hyperplasia, the extent of necrosis and the amount of edema have been shown to negatively correlate with survival.^{5,40} Immunohistochemical staining for p53, Ki-67, and EGFR is generally used for differential diagnosis and grading of these tumors.⁴¹ Previous studies have shown that abnormal microvasculature may be associated with increased endothelial cellularity, proliferation, and tumor grade.^{42,43} Tumors with increased EGFR, Ki-67, and p53 staining are more invasive and exhibit a more malignant phenotype. A tumor-specific mutant of the EGFR, EGFRvIII, causes constitutive upregulation of the tyrosine kinase activity of the receptor and is frequently expressed in primary GBMs. EGFR signaling has, therefore, been the target for GBM therapy. It is also possible that rCBV measurements are revealing changes in microvascular attenuation that precede malignant transformation⁴⁴ and may be indicative of poor prognosis as demonstrated in our study.

Previous survival analysis studies for patients with brain tumors have evaluated several factors: tumor grade, extent of resection, radiation dose, age, and Karnofsky score.^{5,6} Based on the results of some prospective clinical trials that evaluated patients with gliomas, the important prognostic factors for predicting outcome in gliomas are the extent of surgical resection, histologic results, and size of the lesion.^{12,45,46} Tumors not involving eloquent regions of the brain undergo gross total resection because it has been shown that maximal resection improves survival in patients with gliomas.^{12,45,46} Preoperative knowledge of the rCBV_{max} of a tumor may help to determine whether to biopsy or to resect, the aggressiveness of resection, the use of pre-/postoperative adjuvant radiation therapy and chemotherapy, and the frequency of follow-up examinations.

Although our study indicates the role of pretreatment rCBV_{max} as a potential imaging biomarker for predicting survival in GBM, the results should be interpreted in light of the limitations of the study. One was the use of hand-drawn ROIs for data analysis, which, though being simple and straightforward, tend to be subjective. Future studies involving semiautomated segmentation routines^{47,48} may be needed to analyze the data more objectively without any user bias. In addition, we did not evaluate other perfusion variables from the DSC data, such as cerebral blood

flow and mean transit time values. Increasing the TR is only one of the methods to reduce the effects of T1, but it comes with a penalty of increased acquisition time. In addition to the simplistic measurements of MD_{min}, other parameters from diffusion imaging can be computed, such as fractional anisotropy and radial and axial diffusivity. It would be desirable to perform a multivariate analysis by using these varied imaging parameters to evaluate whether these additional parameters further increase the sensitivity and specificity in the overall prognosis of patients with GBM. The study was performed retrospectively, and the sample size for the Kaplan-Meier analysis was relatively small. The survival of patients with GBM can also be affected by other factors such as the location, tumor size, and Karnofsky score. A larger sample size would be necessary to perform a Kaplan-Meier analysis of the rCBV_{max} accounting for these confounding factors. We have limited the number of confounders, including selection of pure GBM (excluding patients with oligodendroglial features) and selection of patients with near-total resection of the mass, and restricted the analysis to tumors with a similar initial size in the 2 groups. A prospective study on a larger cohort of patients with GBM needs to be performed to further establish rCBV as a marker for overall survival in GBM.

CONCLUSIONS

Our results indicate that pretreatment rCBV_{max} may be used as a sensitive prognostic marker for overall survival in patients with glioblastomas.

Disclosures: Donald M. O'Rourke—UNRELATED: Medicolegal opinions, clinical neurosurgery only; Grants/Grants Pending: National Institutes of Health,* Comments: 1) RO1 and R21 applications on glioblastoma pathobiology and imaging; 2) Celldex Therapeutics sponsored imaging research, EGFRvIII and glioblastoma: Patents (planned, pending or issued): issued US patent,* Comments: EGFR/radiation treatment, issued December 1, 2009, US patent No. 7,625,558. Harish Poptani—UNRELATED: Consultancy: American College of Radiology, Image Metrix; Grants/Grants Pending: National Institutes of Health.* *Money paid to the institution.

REFERENCES

- Ohgaki H, Kleihues P. **Epidemiology and etiology of gliomas.** *Acta Neuropathol* 2005;109:93–108
- Behin A, Hoang-Xuan K, Carpentier AF, et al. **Primary brain tumours in adults.** *Lancet* 2003;361:323–31
- Stark AM, Nabavi A, Mehdorn HM, et al. **Glioblastoma multiforme: report of 267 cases treated at a single institution.** *Surg Neurol* 2005;63:162–69
- Kleihues P, Ohgaki H. **Primary and secondary glioblastomas: from concept to clinical diagnosis.** *Neuro Oncol* 1999;1:44–51
- Lacroix M, Abi-Said D, Fourney DR, et al. **A multivariate analysis of 416 patients with glioblastoma multiforme: prognosis, extent of resection and survival.** *J Neurosurg* 2001;95:190–98
- Mangiola A, Maira G, De Bonis P, et al. **Glioblastoma multiforme in the elderly: a therapeutic challenge.** *J Neurooncol* 2006;76:159–63
- Galanis E, Buckner J, Kimmel D, et al. **Gene amplification as a prognostic factor in primary and secondary high-grade malignant gliomas.** *Int J Oncol* 1998;13:717–24
- Shinojima N, Tada K, Shiraishi S, et al. **Prognostic value of epidermal growth factor receptor in patients with glioblastoma multiforme.** *Cancer Res* 2003;63:6962–70
- Law M, Young RJ, Babb JS, et al. **Gliomas: predicting time to progression or survival with cerebral blood volume measurements at dynamic susceptibility-weighted contrast-enhanced perfusion MR imaging.** *Radiology* 2008;247:490–98
- Spampinato MV, Schiavelli C, Cianfoni A, et al. **Correlation between**

- cerebral blood volume measurements by perfusion-weighted magnetic resonance imaging and two-year progression-free survival in gliomas. *Neuroradiol J* 2013;26:385–95
11. Bisdas S, Kirkpatrick M, Giglio P, et al. Cerebral blood volume measurements by perfusion-weighted MR imaging in gliomas: ready for prime time in predicting short-term outcome and recurrent disease? *AJNR Am J Neuroradiol* 2009;30:681–88
 12. Bampoe J, Bernstein M. The role of surgery in low grade gliomas. *J Neurooncol* 1999;42:259–69
 13. Murakami R, Hirai T, Sugahara T, et al. Grading astrocytic tumors by using apparent diffusion coefficient parameters: superiority of a one versus two-parameter pilot method. *Radiology* 2009;251:838–45
 14. Bode MK, Ruohonen J, Nieminen MT, et al. Potential of diffusion imaging in brain tumors: a review. *Acta Radiol* 2006;47:585–94
 15. Murakami R, Sugahara T, Nakamura H, et al. Malignant supratentorial astrocytoma treated with postoperative radiation therapy: prognostic value of pretreatment quantitative diffusion-weighted MR imaging. *Radiology* 2007;243:493–99
 16. Higano S, Yun X, Kumabe T, et al. Malignant astrocytic tumors: clinical importance of apparent diffusion coefficient in prediction of grade and prognosis. *Radiology* 2006;241:839–46
 17. Nakamura H, Murakami R, Hirai T, et al. Can MRI-derived factors predict the survival in glioblastoma patients treated with postoperative chemoradiation therapy? *Acta Radiol* 2013;54:214–20
 18. Oh J, Henry RG, Pirzkall A, et al. Survival analysis in patients with glioblastoma multiforme: predictive value of choline-to-N-acetylaspartate index, apparent diffusion coefficient, and relative cerebral blood volume. *J Magn Reson Imaging* 2004;19:546–54
 19. Stupp R, Mason WP, van den Bent MJ, et al. Radiotherapy plus concomitant and adjuvant temozolomide for glioblastoma. *N Engl J Med* 2005;352:987–96
 20. Paul I, Bhattacharya S, Chatterjee A, et al. Current understanding on EGFR and Wnt/ β -catenin signaling in glioma and their possible crosstalk. *Genes Cancer* 2013;4:427–46
 21. Yiin JJ, Hu B, Schornack PA, et al. ZD6474, a multitargeted inhibitor for receptor tyrosine kinases, suppresses growth of gliomas expressing an epidermal growth factor receptor mutant, EGFRvIII, in the brain. *Mol Cancer Ther* 2010;9:929–41
 22. Johnson G, Wetzel SG, Cha S, et al. Measuring blood volume and vascular transfer constant from dynamic, T(2)*-weighted contrast-enhanced MRI. *Magn Reson Med* 2004;51:961–68
 23. Knopp EA, Cha S, Johnson G, et al. Glial neoplasms: dynamic contrast-enhanced T2*-weighted MR imaging. *Radiology* 1999;211:791–98
 24. Rosen BR, Belliveau JW, Buchbinder BR, et al. Contrast agents and cerebral hemodynamics. *Magn Reson Med* 1991;19:285–92
 25. Rosen BR, Belliveau JW, Vevea JM, et al. Perfusion imaging with NMR contrast agents. *Magn Reson Med* 1990;14:249–65
 26. Spampinato MV, Wooten C, Dorlon M, et al. Comparison of first-pass and second-bolus dynamic susceptibility perfusion MRI in brain tumors. *Neuroradiology* 2006;48:867–74
 27. Wetzel SG, Cha S, Johnson G, et al. Relative cerebral blood volume measurements in intracranial mass lesions: interobserver and intraobserver reproducibility study. *Radiology* 2002;224:797–803
 28. Wang S, Kim S, Chawla S, et al. Differentiation between glioblastomas, solitary brain metastases, and primary cerebral lymphomas using diffusion tensor and dynamic susceptibility contrast-enhanced MR imaging. *AJNR Am J Neuroradiol* 2011;32:507–14
 29. Lev MH, Ozsunar Y, Henson JW, et al. Glial tumor grading and outcome prediction using dynamic spin-echo MR susceptibility mapping compared with conventional contrast-enhanced MR: confounding effect of elevated rCBV of oligodendrogliomas. *AJNR Am J Neuroradiol* 2004;25:214–21
 30. Law M, Oh S, Babb JS, et al. Low-grade gliomas: dynamic susceptibility weighted contrast-enhanced perfusion MR imaging-prediction of patient clinical response. *Radiology* 2006;238:658–67
 31. Law M, Yang S, Babb JS, et al. Comparison of cerebral blood volume and vascular permeability from dynamic susceptibility contrast-enhanced perfusion MR imaging with glioma grade. *AJNR Am J Neuroradiol* 2004;25:746–55
 32. Mangla R, Ginat DT, Kamalian S, et al. Correlation between progression free survival and dynamic susceptibility contrast MRI perfusion in WHO grade III glioma subtypes. *J Neurooncol* 2014;116:325–31
 33. Hirai T, Murakami R, Nakamura H, et al. Prognostic value of perfusion MR imaging of high-grade astrocytomas: long-term follow-up study. *AJNR Am J Neuroradiol* 2008;29:1505–10
 34. Cha S, Tihan T, Crawford F, et al. Differentiation of low grade oligodendrogliomas from low-grade astrocytomas by using quantitative blood-volume measurements derived from dynamic susceptibility contrast-enhanced MR imaging. *AJNR Am J Neuroradiol* 2005;26:266–73
 35. Essock-Burns E, Philips JJ, Molinaro AM, et al. Comparison of DSC-MRI post-processing techniques in predicting microvascular histopathology in patients newly diagnosed with GBM. *J Magn Reson Imaging* 2013;38:388–400
 36. Morita N, Wang S, Chawla S, et al. Dynamic susceptibility contrast perfusion weighted imaging in grading of non-enhancing astrocytomas. *J Magn Reson Imaging* 2010;32:803–08
 37. Wu WC, Chen CY, Chung HW, et al. Discrepant MR spectroscopic and perfusion imaging results in a case of malignant transformation of cerebral glioma. *AJNR Am J Neuroradiol* 2002;23:1775–78
 38. Nelson SJ. Assessment of therapeutic response and treatment planning for brain tumors using metabolic and physiological MRI. *NMR Biomed* 2011;24:734–49
 39. Yamasaki F, Sugiyama K, Ohtaki M, et al. Glioblastoma treated with postoperative radiochemotherapy: prognostic value of apparent diffusion coefficient at MR imaging. *Eur J Radiol* 2010;73:532–37
 40. Pierallini A, Bonamini M, Pantano P, et al. Radiological assessment of necrosis in glioblastoma: variability and prognostic value. *Neuroradiology* 1998;40:150–53
 41. Ru P, Williams TM, Chakravarti A, et al. Tumor metabolism of malignant gliomas. *Cancers* 2013;5:1469–84
 42. Miyagami M, Katayama Y. Angiogenesis of glioma: evaluation of ultrastructural characteristics of microvessels and tubular bodies (Weibel-Palade) in endothelial cells and immunohistochemical findings with VEGF and p53 protein. *Med Mol Morphol* 2005;38:36–42
 43. Kapoor GS, Gocke TA, Chawla S, et al. Magnetic resonance perfusion weighted imaging defines angiogenic subtypes of oligodendroglioma according to 1p19q and EGFR status. *J Neurooncol* 2009;92:373–86
 44. Abdulrauf SI, Edvardsen K, Ho KL, et al. Vascular endothelial growth factor expression and vascular density as prognostic markers of survival in patients with low-grade astrocytoma. *J Neurosurg* 1998;88:513–20
 45. Shaw EG, Tatter SB, Lesser GJ, et al. Current controversies in the radiotherapeutic management of adult low-grade glioma. *Semin Oncol* 2004;31:653–58
 46. Stupp R, Baumert BG. Promises and controversies in the management of low-grade glioma. *Ann Oncol* 2003;14:1695–96
 47. Xie K, Yang J, Zhang ZG, et al. Semi-automated brain tumor and edema segmentation using MRI. *Eur J Radiol* 2005;56:12–19
 48. Kaus MR, Warfield SK, Nabavi A, et al. Automated segmentation of MR images of brain tumors. *Radiology* 2001;218:586–91

Chordoid Meningioma: Differentiating a Rare World Health Organization Grade II Tumor from Other Meningioma Histologic Subtypes Using MRI

J.B. Pond, T.G. Morgan, K.J. Hatanpaa, Z.F. Yetkin, B.E. Mickey, and D.B. Mendelsohn



ABSTRACT

BACKGROUND AND PURPOSE: Meningiomas are very commonly diagnosed intracranial primary neoplasms, of which the chordoid subtype is seldom encountered. Our aim was to retrospectively review preoperative MR imaging of intracranial chordoid meningiomas, a rare WHO grade II variant, in an effort to determine if there exist distinguishing MR imaging characteristics that can aid in differentiating this atypical variety from other meningioma subtypes.

MATERIALS AND METHODS: Ten cases of WHO grade II chordoid meningioma were diagnosed at our institution over an 11-year span, 8 of which had preoperative MR imaging available for review and were included in our analysis. Chordoid meningioma MR imaging characteristics, including ADC values and normalized ADC ratios, were compared with those of 80 consecutive cases of WHO grade I meningioma, 21 consecutive cases of nonchordoid WHO grade II meningioma, and 1 case of WHO grade III meningioma.

RESULTS: Preoperative MR imaging revealed no significant differences in size, location, signal characteristics, or contrast enhancement between chordoid meningiomas and other meningiomas. There were, however, clear differences in the ADC values and normalized ADC ratios, with a mean absolute ADC value of $1.62 \pm 0.33 \times 10^{-3} \text{ mm}^2/\text{s}$ and a mean normalized ADC ratio of $2.22 \pm 0.47 \times 10^{-3} \text{ mm}^2/\text{s}$ in chordoid meningiomas compared with mean ADC and normalized ADC values, respectively, of $0.88 \pm 0.13 \times 10^{-3} \text{ mm}^2/\text{s}$ and $1.17 \pm 0.16 \times 10^{-3} \text{ mm}^2/\text{s}$ in benign WHO grade I meningiomas, $0.84 \pm 0.11 \times 10^{-3} \text{ mm}^2/\text{s}$ and $1.11 \pm 0.15 \times 10^{-3} \text{ mm}^2/\text{s}$ in nonchordoid WHO grade II meningiomas, and $0.57 \times 10^{-3} \text{ mm}^2/\text{s}$ and $0.75 \times 10^{-3} \text{ mm}^2/\text{s}$ in the 1 WHO grade III meningioma.

CONCLUSIONS: Chordoid meningiomas have statistically significant elevations of ADC and normalized ADC values when compared with all other WHO grade I, II, and III subtypes, which enables reliable preoperative prediction of this atypical histopathologic diagnosis.

ABBREVIATIONS: NADC = normalized ADC; WHO = World Health Organization

Meningiomas are the second most common primary intracranial neoplasm, constituting approximately 13%–25% of such tumors.¹ There are 15 variants of meningioma according to the 2007 World Health Organization (WHO) classification of tumors of the central nervous system.² Although 80%–90% of meningiomas are classified as benign WHO grade I tumors, WHO grade II and III varieties demonstrate a more aggressive clinical course and

have a greater propensity for recurrence, and the grade and extent of original resection accounts for these differences.³ Ideally, preoperative imaging to identify the potentially more aggressive grade II and III varieties would be helpful for presurgical planning and subsequent imaging follow-up. One such rare variant is the WHO grade II chordoid meningioma. A little more than 100 cases of chordoid meningioma have been described in the English-language literature, the majority of which are in the pathology and neurosurgery literature.^{4–9}

Attempts to distinguish benign from atypical and malignant meningiomas have been undertaken with variable results, and DWI and ADC values have provided the most reliable means of differentiation,^{10,11} though no data analysis specifically examining the chordoid morphologic variant has been performed. To the best of our knowledge, only 3 case reports in which the MR imaging characteristics of chordoid meningiomas were described have been published in the radiology literature.^{12–14}

Received October 18, 2014; accepted after revision November 22.

From the Departments of Neuroradiology (J.B.P., T.G.M., Z.F.Y., D.B.M.), Neuropathology (K.J.H.), and Neurosurgery (B.E.M.), University of Texas Southwestern Medical Center, Dallas, Texas.

Please address correspondence to Jason Pond, MD, Department of Radiology, University of Texas Southwestern Medical Center, 5323 Harry Hines Blvd, Dallas, TX 75390-8896; e-mail: jasonbpond@gmail.com

Indicates article with supplemental on-line tables.

<http://dx.doi.org/10.3174/ajnr.A4309>

We compared 8 cases of intracranial chordoid meningioma to 80 consecutive cases of WHO grade I meningioma, 21 consecutive cases of nonchordoid WHO grade II meningioma, and 1 WHO grade III meningioma in an effort to determine if there exist distinguishing MR imaging characteristics that can aid in differentiating this particular subtype.

MATERIALS AND METHODS

This was a retrospective institutional review board–approved study.

Case Selection

Ten cases of histologically proven WHO grade II chordoid meningioma were diagnosed at our institution from August 2002 through December 2012. We performed a retrospective review of the preoperative MR imaging of 8 patients. Two patients were excluded from our analysis, 1 because of intraspinal tumor location and 1 because of a lack of available preoperative imaging. All the patients maintained routine neurosurgical clinic and imaging follow-ups at our institution.

Using an institutional neuropathologic database, we compared these chordoid meningiomas to 80 consecutive cases of WHO grade I meningioma, 21 consecutive cases of WHO grade II (nonchordoid) meningioma, and a single case of WHO grade III meningioma for which preoperative MR imaging was performed at our institution with the appropriate imaging sequences available for comparison. Subtypes of WHO grade I meningioma included 38 meningothelial, 15 transitional, 12 fibroblastic, 5 microcystic, 4 angiomatous, 3 secretory, 2 metaplastic, and 1 lymphoplasmacyte-rich meningioma. Nonchordoid WHO grade II meningioma subtypes included 20 atypical and 1 clear-cell meningioma. The single case of WHO grade III meningioma was of the anaplastic subtype.

MR Imaging Protocol

Five MR examinations were performed at our institution, and 3 patients received preoperative imaging at outside institutions. MR imaging at our institution was performed by using our institutional standard tumor protocol with conventional acquisition of fast spin-echo T1-weighted imaging, fast spin-echo T2-weighted imaging, T2-weighted FLAIR imaging, contrast-enhanced T1-weighted imaging after administration of an intravenous Gd-DTPA contrast agent (0.1 mmol/kg), and DWI. DWI scans at our institution were acquired before contrast by using single-shot multisection spin-echo echo-planar imaging with fat saturation, b values of 0 and 1000 s/mm², 4- to 5-mm-thick sections with 0.5- to 1.0-mm gaps, a field of view of 220–230 mm, a minimum matrix size of 128 × 128, and minimal TE. Processing of the ADC maps was performed automatically on the MR scanners by using the diffusion-weighted ($b=0$ and $b=1000$) images. Outside studies were uploaded to our PACS for review and consisted of at least fast spin-echo T1-weighted, T2-weighted, T2-weighted FLAIR, and post-contrast-enhanced T1-weighted images. DWI was obtained from 1 of the 3 outside studies.

Data Analysis

The patient age at diagnosis, sex, and clinical follow-up data were obtained via the institution's electronic medical record. Three investigators (J.B.P., T.G.M., and D.B.M.) evaluated the MR im-

aging by consensus reading. Images were analyzed for tumor location, size (maximal axial dimension), T1 and T2/FLAIR signal characteristics, peritumoral edema, enhancement characteristics, cystic necrosis, bone changes, restricted diffusion, ADC values, and normalized ADC (NADC) ratios. Signal characteristics were classified as hypointense, isointense, or hyperintense compared with normal gray matter. Enhancement characteristics were classified as homogeneous or inhomogeneous. Tumoral ADC values were measured by 2 investigators (J.B.P. and T.G.M.) directly from the PACS workstation in units of $\times 10^{-3}$ mm²/s by using manual freehand regions of interest to include the entirety of the tumor in the axial section demonstrating the greatest tumor diameter, with exclusion of any calcification or cystic necrosis. NADC ratios were calculated by using the formula $NADC = \text{tumor ADC}/\text{control ADC}$. Control ADC values were obtained from contralateral normal white matter. ADC maps were available for 4 of the 8 chordoid meningiomas and for all of the included WHO I, II, and III tumors. Intraclass correlation coefficients were calculated to determine interrater reliability of the measured ADC values of the chordoid meningiomas. Generalized linear model and Tukey-Kramer method analyses were used to compare ADC values and NADC ratios across all the histologic subtypes. Follow-up MR imaging was performed on all 8 patients at various intervals as deemed appropriate by the neurosurgical providers and retrospectively reviewed for evidence of tumor recurrence by the 3 principal investigators.

RESULTS

The 8 patients with chordoid meningioma consisted of 6 women and 2 men. Age at diagnosis ranged from 34 to 66 years (mean age, 47 years). The presenting symptoms were variable and included headache, visual disturbance, seizure, altered mental status, and gait instability. A frontal/parietal convexity location was most prevalent, occurring in 4 patients. The remaining tumors were located along the sphenoid wing, tentorium cerebelli, parasagittal region, and at the foramen magnum. In 3 cases, preoperative MR imaging revealed the presence of multiple meningiomas. Of these cases, none proved on subsequent histopathologic analysis to be multifocal chordoid meningioma but rather a single chordoid meningioma in the presence of other WHO grade I meningiomas.

The preoperative MR imaging characteristics of chordoid meningiomas, WHO grade I meningiomas, nonchordoid WHO grade II meningiomas, and WHO grade III meningiomas are summarized in On-line Tables 1, 2, 3, and 4, respectively.

Evaluation of the signal characteristics of chordoid meningioma revealed mild hyperintensity to gray matter on T2 FLAIR imaging in all cases, 7 of the 8 tumors demonstrated T1 isointensity to gray matter, and 6 of the 8 tumors demonstrated avid homogeneous contrast enhancement (Fig 1). The 2 tumors that showed avid inhomogeneous enhancement did so as a result of cystic necrosis. Two patients had marked peritumoral edema on T2 FLAIR imaging, 1 patient had trace peritumoral edema, and the remaining patients had no appreciable edema. Involvement of the adjacent calvaria with extension into the orbit was seen in 1 patient.

Evaluations of DWI revealed variable signal intensities. No restricted diffusion was identified in any chordoid meningioma;

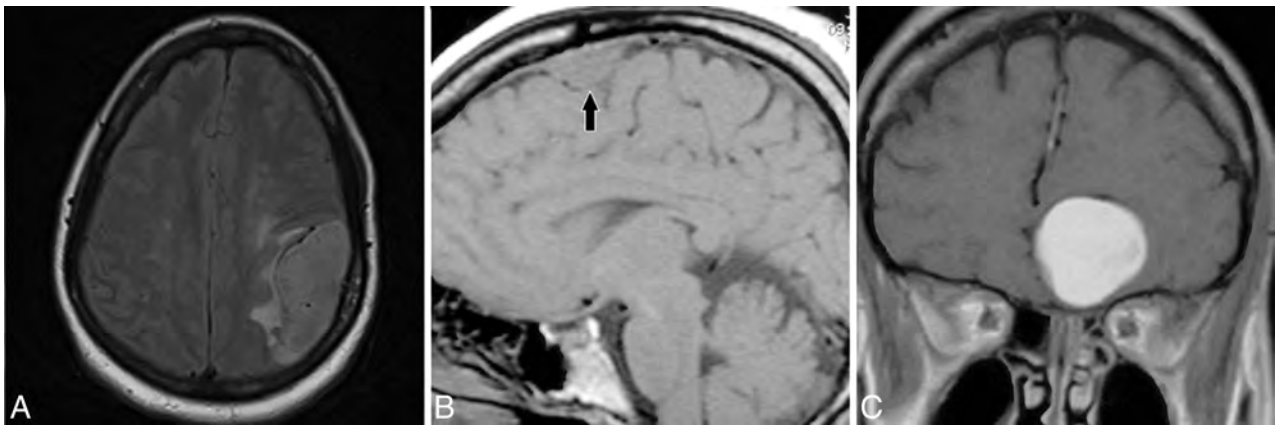


FIG 1. Three different cases of chordoid meningioma show the characteristic T1, T2 FLAIR, and postcontrast T1 appearances, which are similar to those of other meningioma subtypes. A, T2-weighted FLAIR image shows slight hyperintensity to gray matter with mild surrounding edema. B, T1-weighted image shows isointensity of the chordoid meningioma (arrow) to gray matter. C, Contrast-enhanced T1-weighted image shows avid homogeneous enhancement of the meningioma.

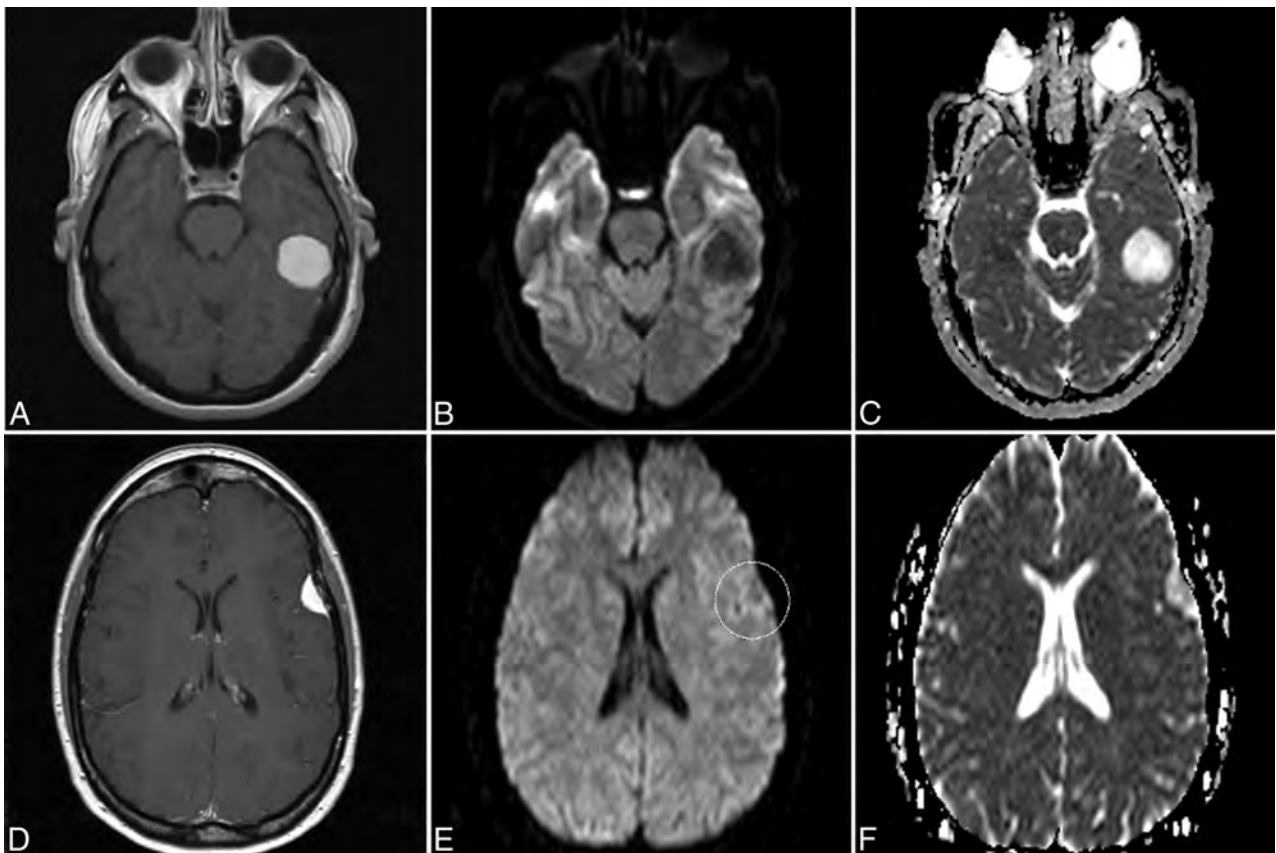


FIG 2. Chordoid meningioma shows facilitated diffusion. A, Postcontrast T1-weighted image showing avid homogeneous enhancement of a left temporal chordoid meningioma. B, DWI shows hypointensity of this chordoid meningioma. C, ADC map corresponding to the tumor shown in B depicting hyperintensity of the meningioma with an ADC value of 2.11 and an NADC ratio of 2.93, which represent increased diffusion. D, Postcontrast T1-weighted image of a different patient shows avid homogeneous enhancement of a left frontal convexity chordoid meningioma. E, DWI of this tumor shows isointensity to slight hypointensity of the tumor. F, ADC map corresponding to tumor shown in E shows increased signal of the meningioma with an ADC value of 1.47 and an NADC ratio of 1.99, which are consistent with facilitated diffusion.

rather, increased signal was present on the ADC map in each case, which is consistent with facilitated diffusion (Fig 2). The outside study from which absolute ADC values could not be obtained revealed relative hyperintensity within the tumor compared with the contralateral unaffected white matter, in keeping with facilitated diffusion.

Each patient underwent surgery in which total meningioma resection was achieved. Follow-up scans were performed in each case. One patient experienced recurrent disease at the site of surgical resection 3 years after resection; however, subsequent surgery and histopathologic evaluation of this lesion revealed a WHO grade I meningotheial meningioma. To date,

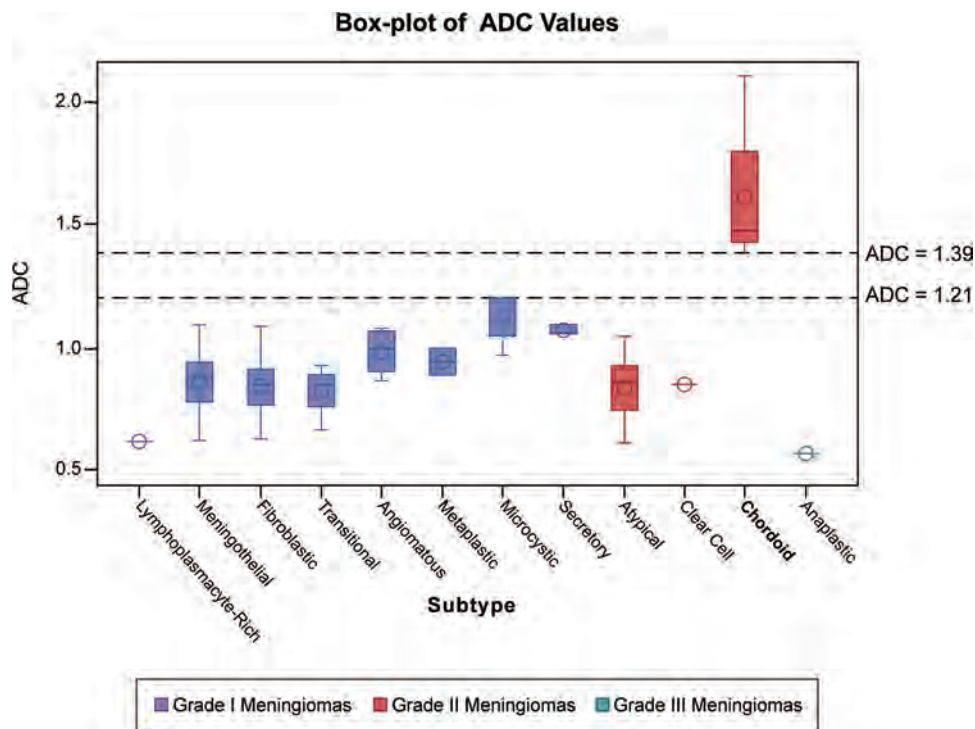


FIG 3. Boxplot of the ADC values of all WHO grade I, II, and III meningiomas shows that chordoid meningiomas have significantly higher ADC values than all other subtypes, and there is a clear gap between the lowest chordoid meningioma ADC and the highest ADC from all other subtypes.

no recurrent chordoid meningiomas have occurred in our patient cohort.

The MR imaging characteristics of chordoid meningioma compared with those of WHO grade I, II, and III meningiomas revealed no significant differences in size, location, signal characteristics, or contrast enhancement. In addition, the presence and degree of peritumoral edema and the involvement of the adjacent calvaria were variable, which did not allow for reliable differentiation between histologic subtypes. There were, however, clear differences in the ADC values (Fig 3) and NADC ratios (Fig 4), with a mean absolute ADC value of $1.62 \pm 0.33 \times 10^{-3} \text{ mm}^2/\text{s}$ and a mean NADC ratio of $2.22 \pm 0.47 \times 10^{-3} \text{ mm}^2/\text{s}$ in chordoid meningiomas compared with mean ADC and NADC values, respectively, of $0.88 \pm 0.13 \times 10^{-3} \text{ mm}^2/\text{s}$ and $1.17 \pm 0.16 \times 10^{-3} \text{ mm}^2/\text{s}$ in benign WHO grade I meningiomas, $0.84 \pm 0.11 \times 10^{-3} \text{ mm}^2/\text{s}$ and $1.11 \pm 0.15 \times 10^{-3} \text{ mm}^2/\text{s}$ in nonchordoid WHO grade II meningiomas, and 0.57×10^{-3} and $0.75 \times 10^{-3} \text{ mm}^2/\text{s}$ in the 1 case of WHO grade III meningioma. The intraclass correlation coefficient of measured ADC values between the raters was 0.996 (95% confidence interval, 0.938–0.999). Statistical analyses of the absolute ADC values and NADC ratios by using the generalized linear model and the Tukey-Kramer method revealed a statistically significant difference between chordoid meningiomas and all other WHO grade I, II, and III subtypes (all pair-wise *P* values, <.01). ADC and NADC cutoff values of 1.39 and 1.93, respectively, enable the distinction of the chordoid variant.

DISCUSSION

Our analysis demonstrates an MR imaging characteristic of the chordoid meningioma subtype that clearly differentiates it from

all other subtypes, with statistically significant increases in the ADC value and NADC ratio of the chordoid meningioma. Greater diffusivity, as demonstrated by elevated ADC values, was seen consistently in all the chordoid meningiomas in our review, and there was a clear gap between the lowest chordoid meningioma value and the highest values of all other subtypes. No other MR imaging characteristic reliably enabled distinction among the subtypes.

The hypothesized basis for these results is the unique tumoral architecture and cytologic features of the chordoid subtype. Differences in extracellular matrix, cell density, and the nucleus-to-cytoplasm ratio have been shown to contribute to the diffusivity of water as detected on diffusion-weighted imaging.¹⁵⁻¹⁷ Microscopic evaluation of the chordoid meningioma subtype reveals epithelioid cells with some degree of cytoplasmic vacuolization, which form cords in a pale basophilic mucoid matrix rich in hyaluronic acid and chondroitin sulfate.⁸ This mucoid extracellular matrix is unique to the chordoid subtype among the histopathologic meningioma variants. The presence of the mucoid stroma results in relatively free extracellular water motion, which is in keeping with multiple studies in which elevated ADC values were found in other tumors that are composed of myxoid stroma, such as chordomas, chondrosarcomas, and myxoid soft-tissue tumors.^{18,19} In addition, a component of cell vacuolization resulting in a decreased nucleus-to-cytoplasm ratio likely contributes further to an increase in the diffusivity of water in these tumors.

Our findings differ from previously published data which reveal that atypical WHO grade II/III meningiomas show decreased ADC values consistent with a greater degree of restricted diffusion

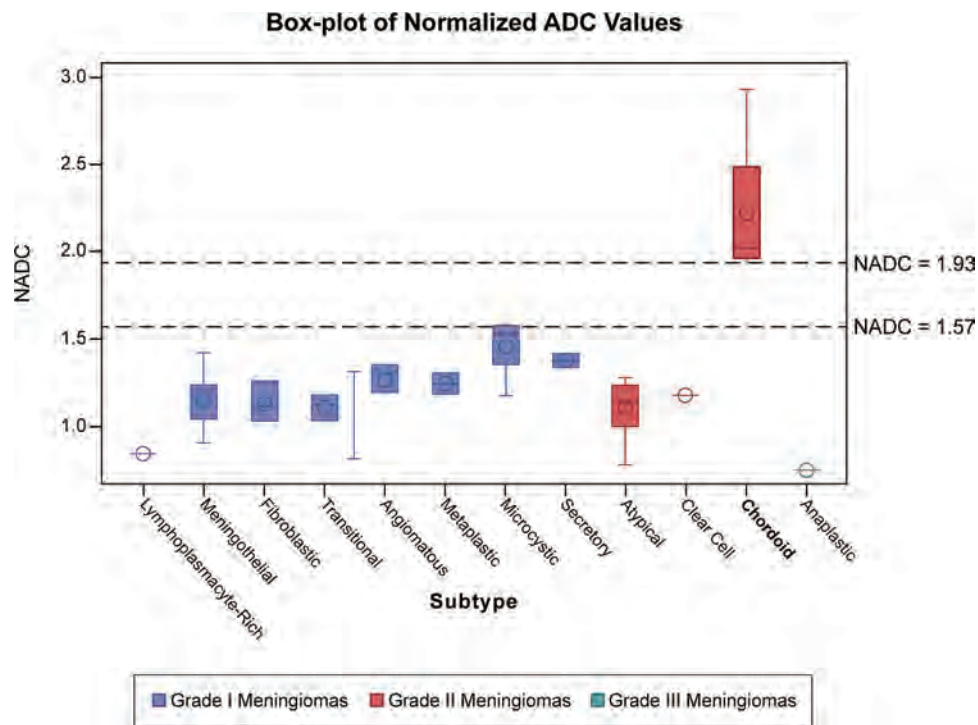


FIG 4. Boxplot of the NADC ratios of all WHO grade I, II, and III meningiomas shows that chordoid meningioma tumors have significantly higher NADC ratios than all other subtypes, and there is a clear gap between the lowest chordoid meningioma NADC ratio and the highest NADC ratio from all other types.

compared with that of typical WHO grade I meningioma subtypes.^{10,11,20} It should be noted that these previous studies included fewer cases and that none included the chordoid variant. To our knowledge, ours is the largest case study to date and included 12 of the 15 meningioma variants, with the only subtype in our analysis demonstrating statistically significant differences in ADC values being the chordoid meningioma; these ADC values were elevated, not decreased, compared with those of typical WHO grade I meningiomas and all other subtypes. Potential explanations for these apparently contradictory results include the exclusion of the chordoid variant among these other studies and the lack of significant numbers of WHO grade III subtypes in our study. Our single WHO grade III anaplastic tumor demonstrated restriction with a markedly reduced ADC value, and it might be hypothesized that if a greater number of WHO grade III tumors had been included, statistically significantly decreased ADC values among these tumors could have been identified.

The primary limitation of this study is the small sample size of chordoid meningiomas. Given its rarity, only 10 cases of chordoid meningioma were diagnosed at our institution over an 11-year span, and only 4 had ADC maps available for review. However, to our knowledge, our case series includes the largest cohort of patients with chordoid meningioma in the radiology literature and demonstrates a statistically significant difference between ADC values and NADC ratios of the chordoid meningiomas and those of all other variants. An additional potential limitation is the inherent difficulty of measuring ADC values with small tumors and those near air-bone interfaces; however, this does not seem to be a limiting factor in our analysis, because we demonstrated very high interobserver reliability.

The clinical implications of our findings are significant in that surgical planning may be altered if the chordoid meningioma subtype can be reliably identified on preoperative MR imaging. The extent of resection is largely predictive of recurrence rates, especially with atypical meningiomas. This seems to hold especially true in the case of the chordoid variant. In the Couce et al⁸ study of 42 chordoid meningiomas, all 13 meningiomas that underwent subtotal resection recurred, whereas only 1 of the 29 meningiomas that underwent total resection recurred. In our review, all 8 chordoid meningiomas were totally resected with no evidence of recurrence, further demonstrating the importance of total resection of this variant. If the extent of disease precludes total resection, knowledge of this subtype's propensity to recur should initiate a more rigorous imaging and clinical follow-up regimen.

CONCLUSIONS

Preoperative identification of atypical meningioma variants, such as chordoid meningioma, would be beneficial for treatment planning and follow-up surveillance. Our review revealed statistically significant elevations in ADC and NADC values of chordoid meningiomas when compared with those of all other WHO grade I, II, and III subtypes, with threshold values of 1.39 and 1.93, respectively, which enables reliable presurgical prediction of this atypical histopathologic diagnosis.

ACKNOWLEDGMENTS

The authors acknowledge Yin Xi for his contribution to statistical analysis.

Disclosures: B.E. Mickey—UNRELATED: Expert Testimony: Rare cases reviewed as defense witness, none in past year; all money collected by UT Southwestern.*
*Money paid to the institution.

REFERENCES

1. Park BJ, Kim HK, Sade B, et al. **Epidemiology.** In: Lee JH. *Meningiomas: Diagnosis, Treatment, and Outcome.* London: Springer-Verlag; 2009:11
2. Perry A, Louis DN, Scheithauer BW, et al. **Meningiomas.** In: Louis DN, Ohgaki H, Wiestler OD, et al, eds. *WHO Classification of Tumours of the Central Nervous System.* 4th ed. Geneva: World Health Organization; 2007:164–72
3. Perry A, Stafford SL, Scheithauer BW, et al. **Meningioma grading: an analysis of histologic parameters.** *Am J Surg Pathol* 1997;21:1455–65
4. Kozler P, Benes V, Netuka D, et al. **Chordoid meningioma: presentation of two case reports, review of the literature, and plea for data standardisation.** *J Neurooncol* 2008;88:115–20
5. Kepes JJ, Chen WY, Connors MH, et al. **“Chordoid” meningeal tumors in young individuals with peritumoral lymphoplasmacellular infiltrates causing systemic manifestations of the Castleman syndrome. A report of seven cases.** *Cancer* 1988;62:391–406
6. Lin JW, Ho JT, Lin YJ, et al. **Chordoid meningioma: a clinicopathologic study of 11 cases at a single institution.** *J Neurooncol* 2010; 100:465–73
7. Epari S, Sharma MC, Sarkar C, et al. **Chordoid meningioma, an uncommon variant of meningioma: a clinicopathologic study of 12 cases.** *J Neurooncol* 2006;78:263–69
8. Couce ME, Aker FV, Scheithauer BW. **Chordoid meningioma: a clinicopathologic study of 42 cases.** *Am J Surg Pathol* 2000;24: 899–905
9. Zhu HD, Chen H, Xie Q, et al. **Chordoid meningioma: a retrospective study of 17 cases at a single institution.** *Chin Med J* 2013; 126:789–91
10. Nagar VA, Ye JR, Ng WH, et al. **Diffusion-weighted MR imaging: diagnosing atypical or malignant meningiomas and detecting tumor dedifferentiation.** *AJNR Am J Neuroradiol* 2008;29:1147–52
11. Filippi CG, Edgar MA, Ulug AZ, et al. **Appearance of meningiomas on diffusion-weighted images: correlating diffusion constants with histopathologic findings.** *AJNR Am J Neuroradiol* 2001;22:65–72
12. Glasier CM, Husain MM, Chaddock W, et al. **Meningiomas in children: MR and histopathologic findings.** *AJNR Am J Neuroradiol* 1993;14:237–41
13. Tokgoz N, Oner YA, Kaymaz M, et al. **Primary intraosseous meningioma: CT and MRI appearance.** *AJNR Am J Neuroradiol* 2005;26:2053–56
14. Soo MY, Ng T, Gomes L, et al. **Skull base chordoid meningioma: imaging features and pathology.** *Australas Radiol* 2004;48:233–36
15. Sugahara T, Korogi Y, Kochi M, et al. **Usefulness of diffusion-weighted MRI with echo-planar technique in evaluation of cellularity in gliomas.** *J Magn Reson Imaging* 1999;9:53–60
16. Rumboldt Z, Camacho DL, Lake D, et al. **Apparent diffusion coefficients for differentiation of cerebellar tumors in children.** *AJNR Am J Neuroradiol* 2006;27:1362–69
17. Ginat DT, Mangla R, Yeane G, et al. **Diffusion-weighted imaging for differentiating benign from malignant skull lesions and correlation with cell density.** *Am J Roentgenol* 2012;198:W597–601
18. Yeom KW, Lober RM, Mobley BC, et al. **Diffusion-weighted MRI: distinction of skull base chordoma from chondrosarcoma.** *AJNR Am J Neuroradiol* 2013;34:1056–61
19. Nagata S, Nishimura H, Uchida M, et al. **Diffusion-weighted imaging of soft tissue tumors: usefulness of the apparent diffusion coefficient for differential diagnosis.** *Radiat Med* 2008;26:287–95
20. Toh CH, Castillo M, Wong AMC, et al. **Differentiation between classic and atypical meningiomas with use of diffusion tensor imaging.** *AJNR Am J Neuroradiol* 2008;29:1630–35

Diffusion Tensor Imaging Mapping of Brain White Matter Pathology in Mitochondrial Optic Neuropathies

D.N. Manners, G. Rizzo, C. La Morgia, C. Tonon, C. Testa, P. Barboni, E. Malucelli, M.L. Valentino, L. Caporali, D. Strobbe, V. Carelli, and R. Lodi



ABSTRACT

BACKGROUND AND PURPOSE: Brain white matter is frequently affected in mitochondrial diseases; *optic atrophy gene 1*-autosomal dominant optic atrophy and Leber hereditary optic neuropathy are the most frequent mitochondrial monosymptomatic optic neuropathies. In this observational study, brain white matter microstructure was characterized by DTI in patients with *optic atrophy gene 1*-autosomal dominant optic atrophy and Leber hereditary optic neuropathy, in relation to clinical and genetic features.

MATERIALS AND METHODS: Nineteen patients with *optic atrophy gene 1*-autosomal dominant optic atrophy and 17 with Leber hereditary optic neuropathy older than 18 years of age, all genetically diagnosed, and 19 healthy volunteers underwent DTI by using a 1.5T MR imaging scanner and neurologic and ophthalmologic assessments. Brain white matter DTI metrics were calculated for all participants, and, in patients, their correlations with genetics and clinical findings were calculated.

RESULTS: Compared with controls, patients with *optic atrophy gene 1*-autosomal dominant optic atrophy had an increased mean diffusivity in 29.2% of voxels analyzed within major white matter tracts distributed throughout the brain, while fractional anisotropy was reduced in 30.3% of voxels. For patients with Leber hereditary optic neuropathy, the proportion of altered voxels was only 0.5% and 5.5%, respectively, of which half was found within the optic radiation and 3.5%, in the smaller acoustic radiation. In almost all regions, fractional anisotropy diminished with age in patients with *optic atrophy gene 1*-autosomal dominant optic atrophy and correlated with average retinal nerve fiber layer thickness in several areas. Mean diffusivity increased in those with a missense mutation. Patients with Leber hereditary optic neuropathy taking idebenone had slightly milder changes.

CONCLUSIONS: Patients with Leber hereditary optic neuropathy had preferential involvement of the optic and acoustic radiations, consistent with trans-synaptic degeneration, whereas patients with *optic atrophy gene 1*-autosomal dominant optic atrophy presented with widespread involvement suggestive of a multisystemic, possibly a congenital/developmental, disorder. White matter changes in Leber hereditary optic neuropathy and *optic atrophy gene 1*-autosomal dominant optic atrophy may be exploitable as biomarkers.

ABBREVIATIONS: DOA = autosomal dominant optic atrophy; FA = fractional anisotropy; LHON = Leber hereditary optic neuropathy; MD = mean diffusivity; OPA1 = *optic atrophy gene 1*; OR = optic radiation; RNFL = retinal nerve fiber layer; TBSS = tract-based spatial statistics

Mutations in *optic atrophy gene 1* are the main cause of autosomal dominant optic atrophy (DOA) (Online Mendelian Inheritance in Man 605290).^{1,2} DOA is characterized clinically by insidiously progressive visual loss in childhood, centrocecal sco-

toma, dyschromatopsia, and temporal or diffuse pallor of the optic discs, due to selective loss of retinal ganglion cells leading to atrophy of the optic nerve.^{1,2} Similarly, Leber hereditary optic neuropathy (LHON) (Online Mendelian Inheritance in Man 535000) is characterized by subacute loss of central vision, dyschromatopsia, and optic atrophy due to maternally inherited

Received October 2, 2014; accepted after revision December 5.

From the Functional MR Unit (D.N.M., G.R., C.Tonon, C.Testa, R.L.) and Neurology Unit (G.R., C.L.M., M.L.V., L.C., D.S., V.C.), Department of Biomedical and NeuroMotor Sciences, and Department of Pharmacy and Biotechnology (E.M.), University of Bologna, Bologna, Italy; "Istituto di Ricovero e Cura a Carattere Scientifico Istituto delle Scienze Neurologiche di Bologna" (C.L.M., M.L.V., L.C., D.S., V.C.), Bologna, Italy; and Studio Oculistico d'Azeglio (P.B.), Bologna, Italy.

D.N. Manners and G. Rizzo contributed equally to this work.

The work was financially supported, in part, by Telethon-Italy grants GGP06233 and GPPI0005 and the E-RARE project ERMION: OIGMI006. The funding organizations played no part in the design or conduct of the study; collection, management, analysis, or interpretation of the data; or in the preparation, review, or approval of the article.

Please address correspondence to Raffaele Lodi, MD, Functional MR Unit, Department of Biomedical and NeuroMotor Sciences, Via Massarenti 9, 40138 Bologna, Italy; e-mail: raffaele.lodi@unibo.it; Valerio Carelli, MD, PhD, IRCCS Istituto delle Scienze Neurologiche di Bologna, Ospedale Bellaria, Via Altura 3, 40139 Bologna, Italy; e-mail: valerio.carelli@unibo.it

Indicates open access to non-subscribers at www.ajnr.org

Indicates article with supplemental on-line tables.

Indicates article with supplemental on-line photo.

<http://dx.doi.org/10.3174/ajnr.A4272>

point mutations in mitochondrial DNA that affect respiratory complex I.^{1,2}

DOA and LHON represent the so-called nonsyndromic mitochondrial optic neuropathies, characterized by optic nerve atrophy as the only or at least prevalent pathologic feature with an early and preferential involvement of the small fibers in the papillomacular bundle.^{3,4} Recent MR imaging studies by using voxel-based morphometry,⁵ DWI,⁶ and DTI⁷ have also indicated abnormalities of the optic radiation in patients with LHON, confirmed by postmortem investigation,⁶ suggesting a trans-synaptic degeneration. A similar secondary involvement of the retrogeniculate visual pathway could also be hypothesized in patients with DOA. Furthermore, given that the *optic atrophy gene 1 (OPA1)* is highly expressed in the retina but also in the brain^{1,2,8} and that a subgroup of patients with specific *OPA1* mutations have a multisystem neurologic disorder,⁹ it is reasonable to also hypothesize a subclinical extravascular brain involvement in patients with *OPA1*-DOA.

The aim of the present study was to investigate the brain white matter of patients with *OPA1*-DOA compared with those with LHON and healthy controls, by using a voxelwise analysis of DTI, which can disclose abnormal water diffusivity in brain areas where atrophy and/or gliosis occur,¹⁰ to look for subtle structural alterations.

MATERIALS AND METHODS

Subjects

Between October 2008 and May 2012, 19 adult patients with a definite diagnosis of *OPA1*-DOA and 17 adult patients with LHON were recruited for DTI evaluation. Inclusion criteria were 18 years of age and older, absence of white matter abnormalities as reported by previous conventional MR imaging, and availability of a genetic diagnosis. In addition, 19 control subjects with similar demographic characteristics were recruited within the same period. The characteristics of these cohorts are reported in and On-line Tables 1 and 2. All subjects gave written informed consent, and the local institutional review board approved the study.

MR Imaging Acquisition

Each subject underwent MR imaging examination by using a 1.5T Signa HDx scanner (GE Healthcare, Milwaukee, Wisconsin), with a protocol that included the following sequences: T2-weighted FLAIR (TR/TE/TI, 8000/85/2000 ms; axial FOV, 24 cm; 256 × 256 in-plane resolution; 3-mm sections); T2-weighted FSE (TR, 5.6–6.5 seconds; TE, 107 ms; coronal FOV, 24 cm; 256 × 256 in-plane resolution; 4-mm sections); T1-weighted volumetric imaging (fast-spoiled gradient recalled imaging; TR/TE, 12.3/5.2 ms; 1-mm isotropic resolution); DTI (TR/TE, 10,000/82 ms; 7 + 64 acquisitions with noncollinear field gradients; b-value = 0 or 900 s mm⁻²; axial oblique FOV, 32 cm; 128 × 128 in-plane resolution; 3-mm sections). Conventional images were evaluated to confirm the absence of white matter lesions. None of the subjects studied showed evidence of such abnormalities.

DTI Data Processing

Following affine registration of all volumes to the first (by using eddy_correct; fMRI of the Brain Software Library[FSL]; [\[www.fmrib.ox.ac.uk/fsl\]\(http://www.fmrib.ox.ac.uk/fsl\)\) to account for eddy current effects and subject motion, DTI data were processed to provide voxelwise estimates of tensor parameters, including mean diffusivity \(MD\) and fractional anisotropy \(FA\). FA and MD volumes from each subject were rigidly aligned to a standard template by using the fMRI of the Brain Linear Image Registration Tool \(FLIRT; <http://www.fmrib.ox.ac.uk>\) with 6 *df*. FA and MD volumes were jointly registered by nonlinear deformation \(Diffeomorphic Anatomical Registration Through Exponentiated Lie Algebra Toolbox, SPM8; <http://www.fil.ion.ucl.ac.uk/spm/software/spm8>\) to a study-specific template generated by using data from all study participants. Major white matter tracts were identified by using the tract-based spatial statistics \(TBSS\) procedure \(in FSL\), by using high-diffusion anisotropy as a marker of uniform fiber orientation, with an FA threshold of 0.2.](http://</p></div><div data-bbox=)

DTI Statistical Analysis

The focus of the statistical analysis was to identify areas showing altered white matter compared with the control group and relate such alterations to relevant clinical and genetic factors. Nonparametric statistical inference was performed on the basis of a generalized linear model framework (by using Randomize; <http://fsl.fmrib.ox.ac.uk/fsl/fslwiki/randomize>, with cluster-free enhancement),¹¹ yielding voxelwise probability estimates, adjusted by controlling the family-wise error rate. After intermediate processing, described above, DTI data were analyzed in 2 stages. In the first stage, group differences between each patient group and controls were assessed (for voxels within the TBSS mask) by using a single-sided *t* test. We assumed that MD should increase and FA, decrease in patients compared with controls on the basis of previous observations of degenerative brain disease.¹² Voxels showing a difference at *P* < .05 after family-wise error correction were deemed significantly altered. To reduce the possible confounding effect of demographic factors, we embedded the *t* test in an ANCOVA-type analysis, first with age and sex as covariates, and repeated it with a history of idebenone therapy as a potential additional confounder. Because 3 patients with *OPA1*-DOA (patients 4, 6, and 7; On-line Table 1) presented with an arguably distinct pathology, we reran the analysis, placing these participants in a separate group, to exclude the possibility that they alone were driving any possible group differences between *OPA1*-DOA and healthy control groups.

To summarize findings, we classified voxels within the TBSS white matter skeleton as belonging to the optic radiation (OR) or to other white matter bundles, by using standard FSL brain atlases,¹³⁻¹⁵ and checked them by back-projecting the resulting labels onto the original individual FA images, to guard against possible tract misidentification.¹⁶ The number of significantly abnormal OR voxels is also reported as a fraction of all abnormal voxels.

We assumed that given the relatively low sensitivity of (appropriately corrected) voxel-based statistical analysis, correlations between altered tissue microstructure and underlying causative variables might be apparent in the patient groups, even in regions not showing significant differences from healthy controls. Hence, in parallel, exploratory regression analysis was performed for FA and MD for all voxels within the previously identified major white matter tracts, against clinical and genetic factors with a known or

putative importance in determining the phenotype of the pathology under consideration. Results were not corrected for multiple comparisons beyond voxelwise family-wise error correction.

For both patient groups, subject age, estimated age at onset of symptoms, and disease duration were considered. In addition, a regression on control subject age was performed as a baseline check. Indicators of visual system involvement in disease progression, visual acuity, and retinal nerve fiber layer (RNFL) thickness assessed by optical coherence tomography¹⁷—specifically the average and temporal quadrant RNFL thickness—were used to perform a linear regression.

Categoric factors potentially modifying disease natural history were identified and analyzed by using a *t* test. These were the mitochondrial DNA haplogroup and a history of idebenone therapy.

OPA1 mutations were grouped as either missense or haploinsufficiency on the basis of their pathogenic mechanism and under the hypothesis that the haploinsufficiency mutations would result in a less severe disease phenotype.⁹ For patients with LHON only, the history of visual recovery was considered as an additional factor for a subgroup *t* test.

RESULTS

Most patients with LHON had the 11778 ND4 mutation (13 of 17), whereas 17 different *OPA1* mutations were found among the patients with *OPA1*-DOA (On-line Table 1). Data regarding the mitochondrial DNA haplogroup, a potential modifying factor in either disorder, were also available for patients and showed the expected variation in a population of European descent, with preponderant occurrence of the most common haplogroup H (On-line Table 1). Three patients with *OPA1*-DOA had extravisual symptoms (patients 4, 6, and 7; On-line Table 1) and were classified as “plus.” Eleven patients with LHON and 9 patients with *OPA1*-DOA were administered idebenone (270–675 mg/day) (On-line Table 1). Data on visual acuity and RNFL thickness were available for almost all patients, though with variable timing with respect to the scan, and are presented in On-line Table 2.

In total, the white matter skeleton generated by TBSS covered 132,617 voxels, of which 12% were estimated as belonging to the OR; 1.9%, to the acoustic radiation; and the remainder, to other white matter bundles.

Group Comparisons

Patients with *OPA1*-DOA and LHON showed significant increases in white matter MD and decreases in FA compared with controls (Table 1). For both patient groups, FA was the more severely affected in almost all areas. The number of voxels with a significant difference in terms of diffusivity parameters was considerably higher in patients with *OPA1*-DOA than in those with LHON. Furthermore, in the patients with LHON, half of these voxels were within the OR and the other half were within other white matter areas, in which the acoustic radiation was the most consistent, affected bilaterally (3.5% of all affected voxels, for FA), while the remainder included the superior corona radiata, superior longitudinal fasciculus, and medial corpus callosum only in the right side (Figs 1 and 2A, -C). The results were different in patients with *OPA1*-DOA, given that only one-fifth of the voxels affected belonged

Table 1: Significant results of a *t* test for comparison of DTI parameters between patients and controls

Quantity	Contrast	Whole White Matter Skeleton ^a		
		Voxels	%	Threshold <i>t</i>
FA	Controls > LHON	7310	5.5	1.54
	Controls > <i>OPA1</i> -DOA ^b	40,197	30.3	1.02
	Controls > pure <i>OPA1</i> -DOA ^c	19,006	14.3	1.18
MD	LHON > controls	652	0.5	0.95
	<i>OPA1</i> -DOA > controls ^b	38,789	29.2	2.33
	Pure <i>OPA1</i> -DOA > controls ^c	19,170	14.5	1.13

^a Results are expressed as the number of voxels within the TBSS skeleton showing significant differences, along with the percentage so affected.

^b All patients included.

^c Three cases with *OPA1* plus are excluded.

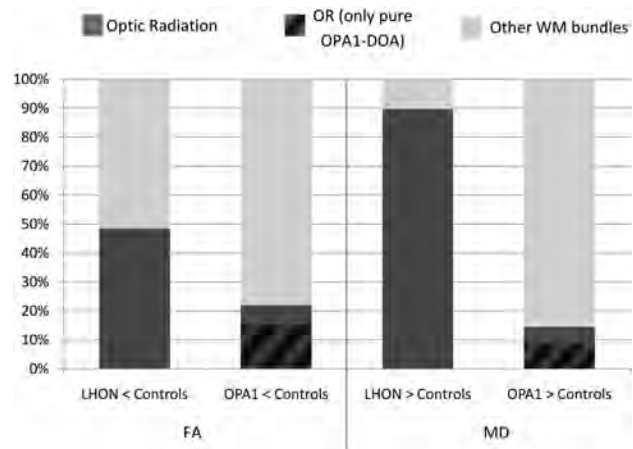


FIG 1. The number of significantly abnormal OR voxels as a proportion of all abnormal voxels in patients with LHON and *OPA1*-dominant optic atrophy.

to the OR, while most were distributed evenly throughout the whole white matter, including several areas not involved in patients with LHON and involving almost all bundles within the supratentorial and infratentorial compartments (Figs 1 and 2B, -D). On-line Figs 1–6 show the complete set of results for both groups.

For the comparison of patients with LHON and controls, the inclusion of treatment with idebenone as a covariate increased the number of affected voxels (by 45% for FA and 175% for MD, dispersed both within and beyond the OR), while for those with *OPA1*-DOA compared with controls, there was essentially no change (–1.7% and 0.9%, respectively).

If we excluded the patients with *OPA1* “plus” (with nonvisual symptoms) from the analysis, the decrease in FA and increase in MD remained in about half the voxels that were altered for the whole group of patients with *OPA1*-DOA compared with controls (Table 1). The proportion of altered voxels outside the OR remained similar (Fig 1). FA values were lower for “plus” compared with nonsyndromic patients at the level of the right internal and external capsules, left OR, and splenium of corpus callosum bilaterally.

Regression Analysis

Exploratory regression analyses are summarized in Table 2 and revealed a highly significant reduction in FA with age in patients with *OPA1*-DOA in almost all of the areas considered. The regression of FA on subject age for the control group was negative,

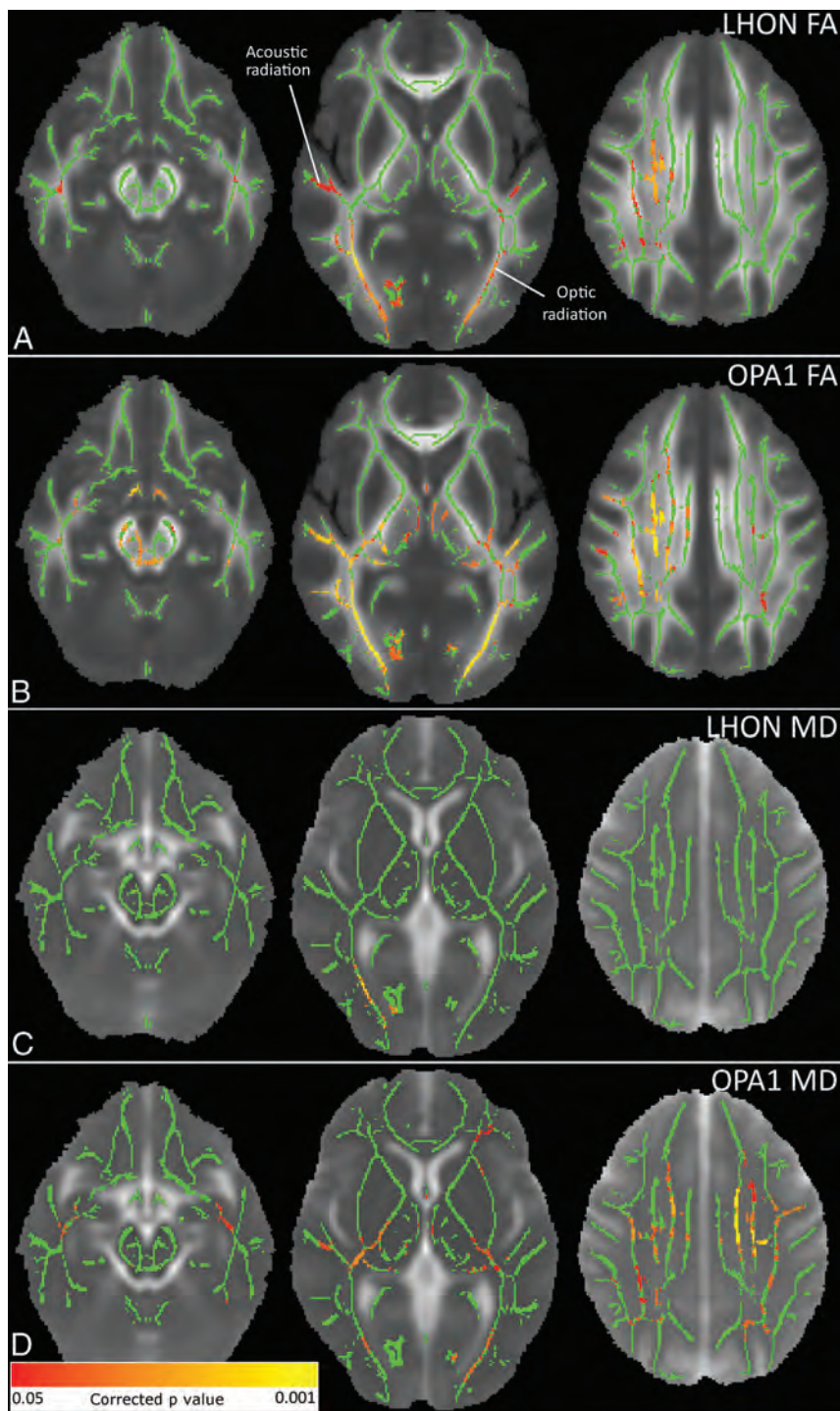


FIG 2. Representative axial sections are shown on the white matter tract skeleton (in green) projected onto the mean FA and MD maps. Voxels showing significant differences between patients and controls (corrected $P < .05$) are shown in a red-yellow scale. **A,** LHON FA $<$ control FA: bilateral optic and acoustic radiation and right superior corona radiata, superior longitudinal fasciculus, and middle corpus callosum were significant. **B,** OPA1-DOA FA $<$ control FA: widespread reduction of FA involving almost all white matter bundles was present. **C and D,** Patient MD $>$ control MD: increased MD was found in the same areas where FA was reduced, though to a lesser extent, in both groups of patients. Complete results in both groups of patients are shown in On-line Figs 1–6.

strengthening the likelihood that the positive finding for patients with OPA1-DOA was group-specific. MD was higher in patients with OPA1-DOA with a missense mutation compared with those with haploinsufficiency mutations (mean WM skele-

ton value, 0.815 ± 0.229 versus $0.741 \pm 0.170 \times 10^{-3} \text{mm}^2 \text{s}^{-1}$), and again this finding was true of the OR and almost all other WM areas. In addition, FA values directly correlated with average RNFL thickness in several areas, mostly within the OR, optic tract, internal and external capsules, and corona radiata bilaterally. A trend toward higher MD values ($P = .05$, corrected) was evident in patients with OPA1-DOA with worse visual acuity, at the level of the anterior cingulum, genu of corpus callosum, and prefrontal WM of the left side. Other trends ($.05 < P < .07$, corrected) were disclosed in patients with OPA1-DOA. Specifically, disease duration was diffusely and inversely correlated with FA values (prevalent in the right hemisphere); finally, FA values in the genu of corpus callosum were higher in patients taking idebenone compared with untreated patients (mean corpus callosum WM skeleton value, 0.745 ± 0.087 versus 0.618 ± 0.136).

Considering patients with LHON, the only significant regression analysis was for idebenone therapy, showing that patients taking idebenone had lower MD values within the anterior cingulum (0.750 ± 0.035 versus 0.773 ± 0.039), genu of corpus callosum (0.784 ± 0.071 versus 0.814 ± 0.058), olfactory tracts bilaterally (0.750 ± 0.120 versus 0.769 ± 0.095), and in the left prefrontal WM (0.728 ± 0.053 versus 0.740 ± 0.045) compared with untreated patients. No other regression analysis yielded positive results.

DISCUSSION

In this study, we evaluated the integrity of brain WM in patients with mitochondrial optic neuropathies, by using a voxelwise analysis of DTI, demonstrating that in both LHON and OPA1-DOA, there are pathologic changes, but with a different distribution. Patients with LHON showed abnormal diffusion mainly in the bilateral OR, with some involvement of the acoustic radiation and a few other areas. In contrast, patients with OPA1-DOA showed changes not only in the OR but also throughout

much of the white matter, indicating a widespread pathology affecting the central nervous system.

The involvement of the OR in patients with LHON confirms and extends the results of recent imaging studies,^{5–7} suggesting

Table 2: Significant results of analyses of DTI parameters for patient groups

	Quantity	Explanatory Variable	Test	Threshold <i>P</i> Value	% Suprathreshold Voxels ^a	Threshold <i>r</i> ^b
OPA1-DOA	FA	Age	Regression	.05	14.5%	−0.299
		Mean RNFL	Regression	.05	8.0%	+0.318
		Disease duration	Regression	.07 ^c	7.1%	+0.224
		Idebenone	t test	.07 ^c	0.6%	NA
	MD	Mutation	t test	.05	60.8%	NA
		Visual acuity	Regression	.07 ^c	31.0%	+0.224
LHON	MD	Idebenone	t test	.05	4.2%	NA

^a Results are expressed as the percentage of voxels within the TBSS skeleton showing *P* value indicated.

^b *R* indicates the Pearson product moment correlation coefficient.

^c Trend finding.

the probable trans-synaptic nature of this impairment. This interpretation was supported by a postmortem investigation in 1 case of LHON, detecting atrophy (40%–45% decrease of neuron soma size) and, to a lesser extent, degeneration (approximately a 28% decrease of neuron attenuation) in the lateral geniculate nucleus, in contrast to the extremely severe axonal loss (99%) in the optic nerve.⁶ In one of these imaging studies, the reduced attenuation of the OR detected by voxel-based morphometry analysis correlated with the average and temporal RNFL thickness.⁵ This correlation was not apparent in the previous DTI study on the same patients⁷ or in our study, though missing ophthalmologic data for a few patients and the variable timing with respect to the scan could have affected our regression analysis.

Our results also demonstrate the bilateral involvement of the acoustic radiation in patients with LHON, a finding not apparent in previous studies in which whole-brain analysis was performed. The presence of auditory dysfunction in LHON had been studied in the past, with conflicting results. An early study found auditory brain stem–evoked potential abnormalities in 7 of 11 patients,¹⁸ and subsequently 2 cases of LHON with auditory neuropathy were reported.¹⁹ A further study on a sample of 10 patients found no evidence of auditory neural abnormalities,²⁰ while a more recent study on 48 subjects carrying a LHON mutation disclosed that >25% of both symptomatic and asymptomatic participants showed electrophysiologic evidence of auditory neuropathy with either absent or severely delayed auditory brain stem potentials.²¹ Our current results of white matter changes in the auditory radiation may represent the auditory counterpart of the trans-synaptic degeneration attributable to the OR.

Furthermore, we have found some other brain diffusion changes in LHON at the level of the right superior corona radiata, superior longitudinal fasciculus, and medial corpus callosum. These results are more difficult to interpret but may indicate a microscopic and diffuse, though variable, white matter pathology associated with the primary mitochondrial impairment. This was previously suggested by older studies using phosphorus MR spectroscopy to show bioenergetic dysfunction in the occipital lobes²² and mild abnormalities of the whole normal-appearing white matter using histogram analysis of magnetization transfer imaging and DWI.²³ These findings may also relate to the occasional co-occurrence of a multiple sclerosis–like illness in patients with LHON,²⁴ in which an autoimmune process could be triggered by the release of immunogenic material due to myelin damage caused by mitochondrial dysfunction in the presence of a specific predisposition.²⁵

Most interesting, in patients with LHON treated with ide-

benone, the MD values within the anterior cingulum, genu of corpus callosum, olfactory tracts bilaterally, and left prefrontal WM were lower compared with untreated patients. Conversely, patient-control differences were more readily apparent when idebenone treatment was included as a confounding factor. Although this result should be considered with caution, it is compatible with previous clinical evidence of the partial efficacy of idebenone treatment in LHON.^{26,27}

However, the most interesting findings of the current study concern our results in OPA1-DOA, to our knowledge the first for this patient group based on DTI. We found widespread WM diffusivity changes without a clear prevalence in a specific pathway. This finding implies that besides trans-synaptic degeneration, there is also a primary WM pathology involving multiple brain systems, a finding in close agreement with the mounting clinical evidence that subjects carrying OPA1 mutations may have a multisystem neurologic disease (DOA “plus”), including sensorineural deafness, ataxia, sensory-motor polyneuropathy, chronic progressive external ophthalmoplegia, and mitochondrial myopathy,^{9,28,29} in addition to optic atrophy. Other reported clinical presentations may include spastic paraparesis mimicking hereditary spastic paraplegia,⁹ multiple sclerosis–like illness,^{9,30} cervical dystonia,³¹ and even a multisystemic disorder in the absence of optic atrophy.³² Furthermore, patients with “pure” optic atrophy may have evidence of subclinical corticospinal tract involvement as shown by electrophysiologic evaluation.³³ All these observations fit well with our finding of subclinical impairment of several white matter pathways, which correlates with optic atrophy, as quantified by the average RNFL thickness. These observations are consistent with white matter sensitivity to mitochondrial dysfunction.^{1,25} In particular, complex I deficiency, as obviously occurring in LHON and also demonstrated in OPA1-DOA with haploinsufficiency,³⁴ is frequently associated with leukoencephalopathy or other white matter pathology.³⁵ Most interesting, recent studies propose that myelin itself has an autonomous respiratory activity, thus linking white matter integrity to defective oxidative phosphorylation.³⁶

An interesting and strong correlation was found between diffusivity parameters and age for patients with OPA1-DOA, but not for those with LHON or healthy controls, suggesting a disease-specific association. The absence of a correlation with “apparent” disease duration ($.05 < P < .07$ in the same areas) and the difficulty of accurately defining the onset of this insidious disease in clinical practice suggest that OPA1-DOA may be a congenital disease. Indeed, it has been shown that patients have a significantly smaller optic nerve head compared with controls, leading to the

hypothesis of a developmental disorder.³⁷ In addition, the role of the *OPA1* protein in controlling apoptosis is well-documented,^{38,39} and it may be postulated that *OPA1* mutations alter the pattern of developmental apoptosis during embryonic stages leading to a congenital “weakness” of the optic nerve and other brain structures.

Almost all WM areas in patients with *OPA1*-DOA had higher MD values in the presence of a missense mutation compared with those predicted to lead to haploinsufficiency. This finding is not surprising because the occurrence of clinical multisystem neurologic disease, though associated with all mutational subtypes, has been reported to be increased 3-fold with missense mutations.⁹ The 3 patients with DOA “plus” tended to have greater pathologic changes compared with nonsyndromic patients, both within and beyond the OR. The findings regarding the effect of idebenone treatment are inconclusive but give limited support to previous preliminary clinical results showing a slight improvement of visual function in patients with DOA after idebenone therapy.⁴⁰

CONCLUSIONS

Voxelwise analysis of DTI was used to evaluate brain WM integrity in patients with LHON and, for the first time, in patients with *OPA1*-DOA, with clear-cut differences between the 2 disorders. Patients with LHON presented with a preferential involvement of the optic and acoustic radiations, possibly due to trans-synaptic degeneration. Patients with *OPA1*-DOA presented with a widespread WM involvement, supporting the view of *OPA1*-associated disorders as a multisystemic disease, not merely limited to the optic nerve. The strong and specific correlation between diffusivity abnormalities and the age of these patients also supports the hypothesis of a congenital and developmental disorder, an issue that will require further investigation. Finally, our study shows that DTI can evaluate white matter integrity in mitochondrial optic neuropathies and may yield useful surrogate biomarkers of disease severity and progression, to evaluate therapeutic efficacy in these mitochondrial optic neuropathies.

Disclosures: David N. Manners—OTHER RELATIONSHIPS: The study was financially supported in part by Telethon-Italy grants GGP06233 and GPPI0005 and by E-RARE project ERMION (European Research project on Mendelian Inherited Optic Neuropathies); OIGM1006. The funding organizations played no part in the design or conduct of the study; collection, management, analysis, or interpretation of the data; or in the preparation, review, or approval of the manuscript. Valerio Carelli—RELATED: Grant: Telethon Italy grants GGP06233 and GPPI0005,* and E-RARE project ERMION: OIGM1006.* Comments: grants to Valerio Carelli for research on inherited optic neuropathies; UNRELATED: Grants/Grants Pending: Program ER-MITO from the Italian region Emilia Romagna, Comments: This is a Program Project for epidemiology on mitochondrial diseases in the Italian region Emilia Romagna; OTHER RELATIONSHIPS: currently involved in clinical trials with EPI-743 (α -tocotrienol quinone) in Leber hereditary optic neuropathy (Edison Pharmaceuticals, Mountain View, California) and with l-acetyl carnitine in Leber hereditary optic neuropathy (Sigma-Tau, Italy). *Money paid to the institution.

REFERENCES

1. Carelli V, Ross-Cisneros FN, Sadun AA. **Mitochondrial dysfunction as a cause of optic neuropathies.** *Prog Retin Eye Res* 2004;23:53–89
2. Yu-Wai-Man P, Griffiths PG, Chinnery PF. **Mitochondrial optic neuropathies: disease mechanisms and therapeutic strategies.** *Prog Retin Eye Res* 2011;30:81–114
3. Sadun AA, Win PH, Ross-Cisneros FN, et al. **Leber’s hereditary optic neuropathy differentially affects smaller axons in the optic nerve.** *Trans Am Ophthalmol Soc* 2000;98:223–32
4. Pan BX, Ross-Cisneros FN, Carelli V, et al. **Mathematically modeling the involvement of axons in Leber’s hereditary optic neuropathy.** *Invest Ophthalmol Vis Sci* 2012;53:7608–17
5. Barcella V, Rocca MA, Bianchi-Marzoli S, et al. **Evidence for retrochiasmatic tissue loss in Leber’s hereditary optic neuropathy.** *Hum Brain Mapp* 2010;31:1900–06
6. Rizzo G, Tozer KR, Tonon C, et al. **Secondary post-geniculate involvement in Leber’s hereditary optic neuropathy.** *PLoS One* 2012;7:e50230
7. Milesi J, Rocca MA, Bianchi-Marzoli S, et al. **Patterns of white matter diffusivity abnormalities in Leber’s hereditary optic neuropathy: a tract-based spatial statistics study.** *J Neurol* 2012;259:1801–07
8. Bette S, Schlasz H, Wissinger B, et al. ***OPA1*, associated with autosomal dominant optic atrophy, is widely expressed in the human brain.** *Acta Neuropathol* 2005;109:393–99
9. Yu-Wai-Man P, Griffiths PG, Gorman GS, et al. **Multi-system neurological disease is common in patients with *OPA1* mutations.** *Brain* 2010;133:771–86
10. Pierpaoli C, Jezzard P, Basser PJ, et al. **Diffusion tensor MR imaging of the human brain.** *Radiology* 1996;201:637–48
11. Winkler A, Ridgway G, Webster M, et al. **Permutation inference for the general linear model.** *Neuroimage* 2014;92:381–97
12. Nucifora PG, Verma R, Lee SK, et al. **Diffusion-tensor MR imaging and tractography: exploring brain microstructure and connectivity.** *Radiology* 2007;245:367–84
13. Mori S, Wakana S, van Zijl PC, et al. *MRI Atlas of Human White Matter.* Amsterdam: Elsevier; 2005
14. Hua K, Zhang J, Wakana S, et al. **Tract probability maps in stereotaxic spaces: analyses of white matter anatomy and tract-specific quantification.** *Neuroimage* 2008;39:336–47
15. Eickhoff SB, Stephan KE, Mohlberg H, et al. **A new SPM toolbox for combining probabilistic cytoarchitectonic maps and functional imaging data.** *Neuroimage* 2005;25:1325–35
16. Bach M, Laun FB, Leemans A, et al. **Methodological considerations on tract-based spatial statistics (TBSS).** *Neuroimage* 2014;100:358–69
17. Barboni P, Savini G, Parisi V, et al. **Retinal nerve fiber layer thickness in dominant optic atrophy measurements by optical coherence tomography and correlation with age.** *Ophthalmology* 2011;118:2076–80
18. Mondelli M, Rossi A, Scarpini C, et al. **BAEP changes in Leber’s hereditary optic neuropathy—further confirmation of multisystem involvement.** *Acta Neurol Scand* 1990;81:349–53
19. Ceranić B, Luxon LM. **Progressive auditory neuropathy in patients with Leber’s hereditary optic neuropathy.** *J Neurol Neurosurg Psychiatry* 2004;75:626–30
20. Yu-Wai-Man P, Elliot C, Griffiths PG, et al. **Investigation of auditory dysfunction in Leber hereditary optic neuropathy.** *Acta Ophthalmol* 2008;86:630–33
21. Rance G, Kearns LS, Tan J, et al. **Auditory function in individuals within Leber’s hereditary optic neuropathy pedigrees.** *J Neurol* 2012;259:542–50
22. Cortelli P, Montagna P, Avoni P, et al. **Leber’s hereditary optic neuropathy: genetic, biochemical, and phosphorus magnetic resonance spectroscopy study in an Italian family.** *Neurology* 1991;41:1211–15
23. Inglese M, Rovaris M, Bianchi S, et al. **Magnetic resonance imaging, magnetisation transfer imaging, and diffusion weighted imaging correlates of optic nerve, brain, and cervical cord damage in Leber’s hereditary optic neuropathy.** *J Neurol Neurosurg Psychiatry* 2001;70:444–49
24. Harding AE, Sweeney MG, Miller DH, et al. **Occurrence of a multiple sclerosis-like illness in women who have a Leber’s hereditary optic neuropathy mitochondrial DNA mutation.** *Brain* 1992;115:979–89
25. Carelli V, Bellan M. **Myelin, mitochondria, and autoimmunity: what’s the connection?** *Neurology* 2008;70:1075–76
26. Klopstock T, Yu-Wai-Man P, Dimitriadis K, et al. **A randomized placebo-controlled trial of idebenone in Leber’s hereditary optic neuropathy.** *Brain* 2011;134:2677–86

27. Carelli V, La Morgia C, Valentino ML, et al. **Idebenone treatment in Leber's hereditary optic neuropathy.** *Brain* 2011;134:e188
28. Hudson G, Amati-Bonneau P, Blakely EL, et al. **Mutation of OPA1 causes dominant optic atrophy with external ophthalmoplegia, ataxia, deafness and multiple mitochondrial DNA deletions: a novel disorder of mtDNA maintenance.** *Brain* 2008;131:329–37
29. Amati-Bonneau P, Valentino ML, Reynier P, et al. **OPA1 mutations induce mitochondrial DNA instability and optic atrophy 'plus' phenotypes.** *Brain* 2008;131:338–51
30. Verny C, Loiseau D, Scherer C, et al. **Multiple sclerosis-like disorder in OPA1-related autosomal dominant optic atrophy.** *Neurology* 2008;70:1152–53
31. Liskova P, Ulmanova O, Tesina P, et al. **Novel OPA1 missense mutation in a family with optic atrophy and severe widespread neurological disorder.** *Acta Ophthalmol* 2013;91:e225–31
32. Milone M, Younge BR, Wang J, et al. **Mitochondrial disorder with OPA1 mutation lacking optic atrophy.** *Mitochondrion* 2009;9:279–81
33. Baker MR, Fisher KM, Whittaker RG, et al. **Subclinical multisystem neurologic disease in "pure" OPA1 autosomal dominant optic atrophy.** *Neurology* 2011;77:1309–12
34. Zanna C, Ghelli A, Porcelli AM, et al. **OPA1 mutations associated with dominant optic atrophy impair oxidative phosphorylation and mitochondrial fusion.** *Brain* 2008;131:352–67
35. Koene S, Rodenburg RJ, van der Knaap MS, et al. **Natural disease course and genotype-phenotype correlations in complex I deficiency caused by nuclear gene defects: what we learned from 130 cases.** *J Inherit Metab Dis* 2012;35:737–47
36. Morelli A, Ravera S, Panfoli I. **Hypothesis of an energetic function for myelin.** *Cell Biochem Biophys* 2011;61:179–87
37. Barboni P, Carbonelli M, Savini G, et al. **OPA1 mutations associated with dominant optic atrophy influence optic nerve head size.** *Ophthalmology* 2010;117:1547–53
38. Frezza C, Cipolat S, Martins de Brito O, et al. **OPA1 controls apoptotic cristae remodeling independently from mitochondrial fusion.** *Cell* 2006;126:177–89
39. Cipolat S, Rudka T, Hartmann D, et al. **Mitochondrial rhomboid PARL regulates cytochrome c release during apoptosis via OPA1-dependent cristae remodeling.** *Cell* 2006;126:163–75
40. Barboni P, Valentino ML, La Morgia C, et al. **Idebenone treatment in patients with OPA1-mutant dominant optic atrophy.** *Brain* 2013;136:e231

Negative Susceptibility Vessel Sign and Underlying Intracranial Atherosclerotic Stenosis in Acute Middle Cerebral Artery Occlusion

S.K. Kim, W. Yoon, T.W. Heo, M.S. Park, and H.K. Kang

ABSTRACT

BACKGROUND AND PURPOSE: The role of MR imaging in predicting underlying intracranial atherosclerotic stenosis before endovascular stroke therapy has not been studied. Our aim was to determine the diagnostic value of the negative susceptibility vessel sign on T2*-weighted gradient-echo MR imaging for predicting underlying intracranial atherosclerotic stenosis in patients with acute MCA occlusion.

MATERIALS AND METHODS: Ninety-one consecutive patients with acute stroke because of MCA occlusion underwent gradient-echo MR imaging and MRA before endovascular therapy. The negative susceptibility vessel sign was defined as an absence of a hypointense signal change within the occluded MCA on gradient-echo imaging. Underlying intracranial atherosclerotic stenosis was determined by conventional angiography. The sensitivity, specificity, predictive values, and accuracy of the negative susceptibility vessel sign for predicting the presence of underlying intracranial atherosclerotic stenosis were assessed.

RESULTS: The negative susceptibility vessel sign was identified in 42 (46.1%) of 91 patients, and 18 (19.8%) patients had an underlying intracranial atherosclerotic stenosis responsible for acute ischemic symptoms. The negative susceptibility vessel sign was more frequently observed in patients with intracranial atherosclerotic stenosis than in those without it (100% versus 32.9%, $P < .001$). In the prediction of an underlying intracranial atherosclerotic stenosis, the negative susceptibility vessel sign had 100% sensitivity, 67.1% specificity, 42.9% positive predictive value, 100% negative predictive value, and an accuracy of 73.6%.

CONCLUSIONS: The negative susceptibility vessel sign on gradient-echo MR imaging is a sensitive marker with a high negative predictive value for the presence of an underlying intracranial atherosclerotic stenosis in patients with acute ischemic stroke because of MCA occlusions. The susceptibility vessel sign can be used in decision-making when performing subsequent endovascular revascularization therapy in patients with acute MCA occlusions.

ABBREVIATIONS: GRE = gradient-echo; ICAS = intracranial atherosclerotic stenosis; SBT = stent-based thrombectomy; SVS = susceptibility vessel sign

Intracranial atherosclerotic stenosis (ICAS) is one of the most common causes of ischemic stroke worldwide and is particularly prevalent in Asian, black, Hispanic, and Indian populations.^{1,2} Underlying ICAS can be a hidden cause of refractory occlusions following modern mechanical thrombectomy procedures, such as stent-based thrombectomy (SBT) or manual aspiration thrombectomy in patients with acute ischemic stroke.³ Thus, preprocedural identification of underlying ICAS in patients

with intracranial large-vessel occlusions is of particular importance when performing endovascular stroke therapy.

On MR imaging, hypointense signal changes in the occluded MCA on gradient-echo (GRE) sequences have been described as a susceptibility vessel sign (SVS).^{4,5} The pathophysiologic basis for this sign in patients with an acute MCA occlusion is a T2-shortening effect of the intracellular deoxyhemoglobin component in erythrocytes within the clot.⁴ Several researchers showed that the SVS was more commonly seen in red blood cell–dominant and mixed clots than in fibrin-dominant clots and could therefore reflect the composition of the clots.⁶ In addition, GRE SVS was observed more frequently in patients with cardiogenic embolic stroke than in those with other stroke subtypes.⁵ In contrast, the absence of the GRE SVS might be associated with a smaller clot burden or a fibrin-dominant clot that forms as a result of rupture of the underlying atherosclerotic plaque. Thus, we hypothesized

Received November 9, 2014; accepted after revision January 14, 2015.

From the Departments of Radiology (S.K.K., W.Y., T.W.H., H.K.K.) and Neurology (M.S.P.), Chonnam National University Medical School, Chonnam National University Hospital, Gwangju, Republic of Korea.

Please address correspondence to Woong Yoon, MD, Department of Radiology, Chonnam National University Hospital, 42 Jebong-Ro, Dong-Gu, Gwangju, 501-757, Republic of Korea; e-mail: radyoon@jnu.ac.kr

<http://dx.doi.org/10.3174/ajnr.A4280>

that the absence of the GRE SVS despite the presence of intracranial large-vessel occlusions could indicate an underlying ICAS in patients with acute ischemic stroke within 6 hours of stroke onset, and we termed this finding the “negative SVS.” Despite the widespread use of MR imaging for the diagnosis of acute ischemic stroke, the role of MR imaging in predicting underlying ICAS before endovascular therapy has not been studied, to our knowledge. In this study, we evaluated the diagnostic value of the negative SVS on GRE imaging for the prediction of underlying ICAS in patients with acute MCA occlusion.

MATERIALS AND METHODS

Patients

From January 2011 to February 2013, 101 consecutive patients presenting with acute ischemic stroke from MCA occlusion within 6 hours of symptom onset were treated with multimodal endovascular revascularization therapy at a tertiary university hospital. Of these patients, those who did not undergo the GRE sequence ($n = 8$) or had GRE images of insufficient quality for reliable evaluation because of motion artifacts ($n = 2$) were excluded, leaving 91 patients in this study. This retrospective study analyzed the radiologic and clinical data collected prospectively from these 91 patients. The institutional ethics committee approved this retrospective analysis and waived the requirements for informed consent on the basis of the study design.

MR Imaging Analysis

MR imaging examinations were performed by using a 1.5T unit (Signa HDxt; GE Healthcare, Milwaukee, Wisconsin). Before the endovascular procedure, patients underwent MR imaging, including DWI, GRE, FLAIR, 3D TOF MRA, and perfusion imaging. GRE sequence parameters included a TR of 750–800 ms, TE of 14 ms, flip angle of 20°, section thickness of 4 mm, intersection gap of 0 mm, and FOV of 230 × 230 mm. 3D TOF MRA parameters included a TR of 24 ms, TE of 6.9 ms, flip angle of 20°, and FOV of 240 × 240 mm.

All MR images were retrospectively reviewed by 2 neuroradiologists (with 1 and 3 years of experience, respectively) who were blinded to the findings from conventional angiography. Conclusions were reached by consensus regarding the presence or absence of the negative SVS on GRE imaging. A negative SVS was defined as the absence of the GRE SVS in the occluded MCA. GRE SVS was defined as a hypointense signal change on GRE imaging within the occluded MCA, in which the diameter of the hypointense signal exceeds that of the contralateral MCA.^{4,5}

Catheter Angiography and Endovascular Therapy

On admission, a stroke neurologist performed an assessment based on the NIHSS. The inclusion criteria for endovascular therapy were as follows: presentation within 6 hours of stroke onset for an anterior circulation stroke; baseline NIHSS score of ≥ 4 ; no intracranial hemorrhage detected on the cranial CT or MR imaging; no flow-related enhancement in the M1 or M2 segment of MCA on the MRA; a target mismatch pattern on multimodal MR imaging based on visual estimation (time-to-peak map of perfusion imaging showing a lesion volume $\geq 30\%$ larger than that

detected with DWI); infarct volume on DWI less than one-third of the MCA territory; and a premorbid mRS score of ≤ 3 .

Underlying ICAS was determined by conventional angiography when the severe stenosis ($\geq 70\%$) of the MCA, measured by the Warfarin–Aspirin Symptomatic Intracranial Disease criteria,⁷ was seen on the initial diagnostic angiography or on the follow-up angiography after the first-line SBT. For underlying ICAS that was seen after the first-line SBT, ICAS was determined if the stenotic lesion remained unchanged on the follow-up angiography performed >5 minutes after intra-arterial injection of a vasodilator (50 μg of nitroglycerin) through the guide catheter. Angiographic images were retrospectively reviewed by a neuroradiologist (with 8 years of experience) who was blinded to the findings from MR imaging.

All conventional angiography and endovascular therapy were performed by a single interventional neuroradiologist with 12 years of experience in neurovascular intervention. For each patient, written informed consent for angiography and endovascular therapy was obtained from a family member. Cerebral angiography and endovascular therapy were performed with the patient under conscious sedation. In cases of agitation, an intravenous bolus of midazolam was given and repeated if necessary. When the initial diagnostic angiography showed arterial occlusion, SBT with a Solitaire stent (Covidien, Irvine, California) was performed as the first-line endovascular treatment. When SBT was unsuccessful, additional mechanical approaches were performed, including manual aspiration thrombectomy with a Penumbra System perfusion catheter (Penumbra, Alameda, California) and intra-arterial urokinase infusion with or without clot disruption with a microguidewire. The details of the techniques used for SBT, manual aspiration thrombectomy, and clot disruption with a microwire were described previously.^{8,9}

All patients with underlying ICAS were treated with intracranial angioplasty with or without stent placement. Intracranial angioplasty was performed with a Gateway PTA balloon catheter (Stryker, Kalamazoo, Michigan). The diameter of the balloon was undersized to 80% of the normal vessel diameter just distal to the stenosis, and the shortest length was used to cover the lesion. The balloon was inflated slowly 1 or 2 times by using a screw-type pressure inflation device at 4–6 atm for 30–60 seconds. Whenever possible, intracranial stent placement with the Wingspan stent system (manufactured by Stryker, Kalamazoo, Michigan, for Boston Scientific, Natick, Massachusetts) was performed after intracranial angioplasty. The stent diameter was sized to exceed the diameter of the normal vessel by 0.5 mm. The stent length was selected to cover the entire stenotic segment. Patients who underwent intracranial angioplasty with or without stent placement received aspirin and clopidogrel bisulfate (Plavix) orally via a nasogastric tube immediately after the procedure, and dual antiplatelet therapy was continued for at least 3 months after the procedure. Revascularization status was assessed on the final angiogram and was classified according to the modified TICI scale,¹⁰ and successful revascularization was defined as a modified TICI grade 2b or 3. Clinical outcome was assessed by a stroke neurologist by using the mRS during an outpatient visit 3 months after treatment. If patients were unable to attend the outpatient clinic, outcomes were obtained via telephone interview. A good

clinical outcome was defined as an mRS score of ≤ 2 . Stroke subtypes were determined by a stroke neurologist according to the classification of the Trial of Org 10172 in Acute Stroke Treatment.¹¹

Statistical Analysis

First, we compared differences between the patients with a negative SVS (negative SVS group) and those with a GRE SVS (positive SVS group) and then differences between the ICAS group (patients with underlying ICAS) and the non-ICAS group (patients without underlying ICAS) separately. Differences in baseline characteristics and clinical outcomes between the 2 groups were compared by using bivariate analysis. The Pearson χ^2 or Fisher exact test was used for categorical variables, and the Mann-Whitney *U* test, for continuous variables. Next, diagnostic performance parameters, including sensitivity, specificity, positive predictive value, negative predictive value, and the diagnostic accuracy of the negative SVS for the prediction of underlying ICAS, were calculated. Finally, independent associations of clinical outcomes with other clinical and radiologic factors were determined with a multivariate logistic regression analysis. The variables tested in the logistic regression models were those with $P < .2$ in the univariate analysis. All statistical analyses were performed with SPSS software (Version 20.0; IBM, Armonk, New York). $P < .05$ was a statistically significant difference.

RESULTS

Of the 91 patients (52 men and 39 women; age range, 40–92 years) with acute MCA occlusions treated with multimodal endovascular therapy, a negative SVS on GRE imaging was identified in 42 (46.1%) patients. On conventional angiography, 18 (19.8%) of 91 patients had an underlying ICAS in the MCA, which was responsible for their acute ischemic symptoms. Of 18 patients with underlying ICAS, 8 exhibited a severe ($\geq 70\%$) stenosis of the target artery on the initial diagnostic conventional angiography despite the 3D TOF MRA demonstrating an absence of flow-related enhancement in the M1 and M2 segments of the MCA. The remaining 10 patients had an occlusion visible on the initial conventional angiography and had a severe stenosis at the previous occlusion site after SBT. Of these 10 patients, only 3 had visible thrombi that were captured with a Solitaire stent. The remaining 7 patients had no captured thrombi despite several passages of the Solitaire stent. Thus, overall, 15 of 18 patients (83%) with underlying ICAS had no apparent clot burden in our study. The occlusion sites were in the M1 segment in all patients with underlying ICAS, while those in the non-ICAS group were in the M1 ($n = 66$) and M2 ($n = 7$) segments.

Negative SVS versus Positive SVS

The results of comparisons between the patients with a negative SVS and those with a positive SVS are shown in Table 1. Diabetes and dyslipidemia were more frequent in patients in the negative SVS group ($P = .046$ and $P = .011$), whereas atrial fibrillation was more frequent in the positive SVS group ($P = .011$). The mean baseline NIHSS score was significantly lower in the negative SVS group compared with the positive SVS group (9.5 versus 13, $P = .003$). For stroke subtypes, the negative SVS was significantly as-

Table 1: Comparison between the negative SVS group and positive SVS group

	Negative SVS Group (n = 42)	Positive SVS Group (n = 49)	P Value
Age (yr)	69.1 ± 11.60	68.4 ± 11.40	NS
Male sex	21 (50%)	31 (63.3%)	NS
Risk factors			
Hypertension	26 (61.9%)	27 (55.1%)	NS
Diabetes mellitus	10 (23.8%)	4 (8.2%)	.046
Coronary artery disease	3 (7.1%)	2 (4.1%)	NS
Dyslipidemia	19 (45.2%)	10 (20.4%)	.011
Smoking	8 (19.0%)	17 (34.7%)	NS
Atrial fibrillation	12 (28.6%)	27 (55.1%)	.011
Congestive heart failure	1 (2.4%)	1 (2.0%)	NS
History of stroke or TIA	7 (16.7%)	5 (10.2%)	NS
Occlusion sites			
M1 segment	38 (90.5%)	46 (93.9%)	NS
M2 segment	4 (9.5%)	3 (6.1%)	NS
IV thrombolysis	20 (47.6%)	34 (69.4%)	NS
Time to procedure (min)	240 ± 115.9	250 ± 74.3	NS
Procedure time (min)	31.5 ± 9.3	30 ± 18.0	NS
Time to revascularization (min)	280 ± 117.8	276 ± 78.3	NS
Baseline NIHSS score	9.5 ± 3.7	13 ± 3.7	.003
Stroke subtypes			
Cardioembolic	11 (26.2%)	29 (59.2%)	.002
Large artery atherosclerosis	24 (57.1%)	9 (18.4%)	<.001
Others	0%	0%	NS
Undetermined	7 (16.7%)	11 (22.4%)	NS
m-TICI 2b or 3	38 (90.5%)	39 (79.6%)	NS
mRS 0–2	28 (66.7%)	21 (42.9%)	.023
Mortality	5 (11.9%)	4 (8.2%)	NS

Note:—m-TICI indicates modified TICI; NS, non-significant.

sociated with large-artery atherosclerosis. Of the 33 patients with large-artery atherosclerosis, 24 (72.7%) had a negative SVS (Fig 1), whereas 9 (27.3%) had a positive SVS ($P < .001$). In contrast, a positive SVS was significantly associated with cardioembolic stroke: Twenty-nine (72.5%) of 40 patients with cardioembolic stroke had a positive SVS (Fig 2) and 11 (27.5%) had a negative SVS ($P = .002$). Good outcomes occurred significantly more frequently in the negative SVS group than in the positive SVS group (66.7% versus 42.9%, $P = .023$).

ICAS versus Non-ICAS

The results of comparison between the ICAS group and the non-ICAS group are shown in Table 2. Patients in the ICAS group were younger than those in the non-ICAS group ($P = .026$). Diabetes and dyslipidemia were more frequent in patients with ICAS ($P = .002$ and $P < .001$, respectively), whereas atrial fibrillation was more frequent in the non-ICAS group ($P < .001$). The mean baseline NIHSS score was significantly lower in the ICAS group compared with the non-ICAS group (9.8 versus 12.7, $P = .003$). There were no significant differences between the 2 groups in other risk factors, arterial occlusion sites, use of IV thrombolysis, procedure time, and time to revascularization.

All patients with ICAS had a negative SVS, whereas only 24 patients in the non-ICAS group had a negative SVS (100% versus 32.9%, $P < .001$). The incidence of negative SVS according to occlusion site is summarized in Table 3. In the prediction of an underlying ICAS, a negative SVS had 100% (95% CI, 90%–100%) sensitivity, 67.1% (95% CI, 55%–77%) specificity, 42.9% (95% CI, 28%–59%) positive predictive value, 100% (95% CI, 90%–100%) negative predictive value, and 73.6% accuracy.

All 18 patients with underlying ICAS received intracranial an-

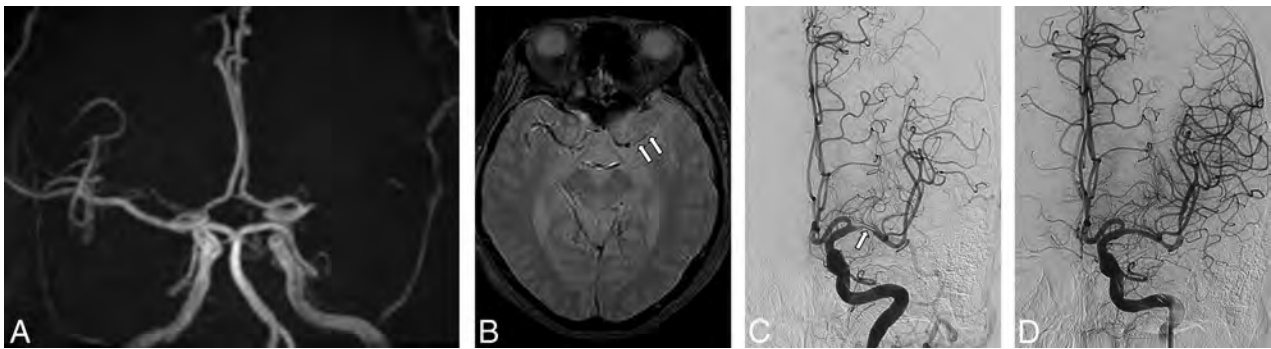


FIG 1. Brain images from a 74-year-old man with acute ischemic stroke and atherosclerotic stenosis in the MCA. *A*, 3D TOF MR angiography shows the occlusion in the proximal M1 segment of the left MCA. *B*, Axial gradient-echo image reveals a negative susceptibility vessel sign (arrows) in the M1 segment of the left MCA. *C*, Angiography after 1 passage of the Solitaire stent identifies a severe stenosis (arrow) in the proximal M1 segment of the left MCA. No thrombi were retrieved with the Solitaire stent. *D*, Angiography after intracranial angioplasty with stent placement shows complete revascularization in the left MCA territory.

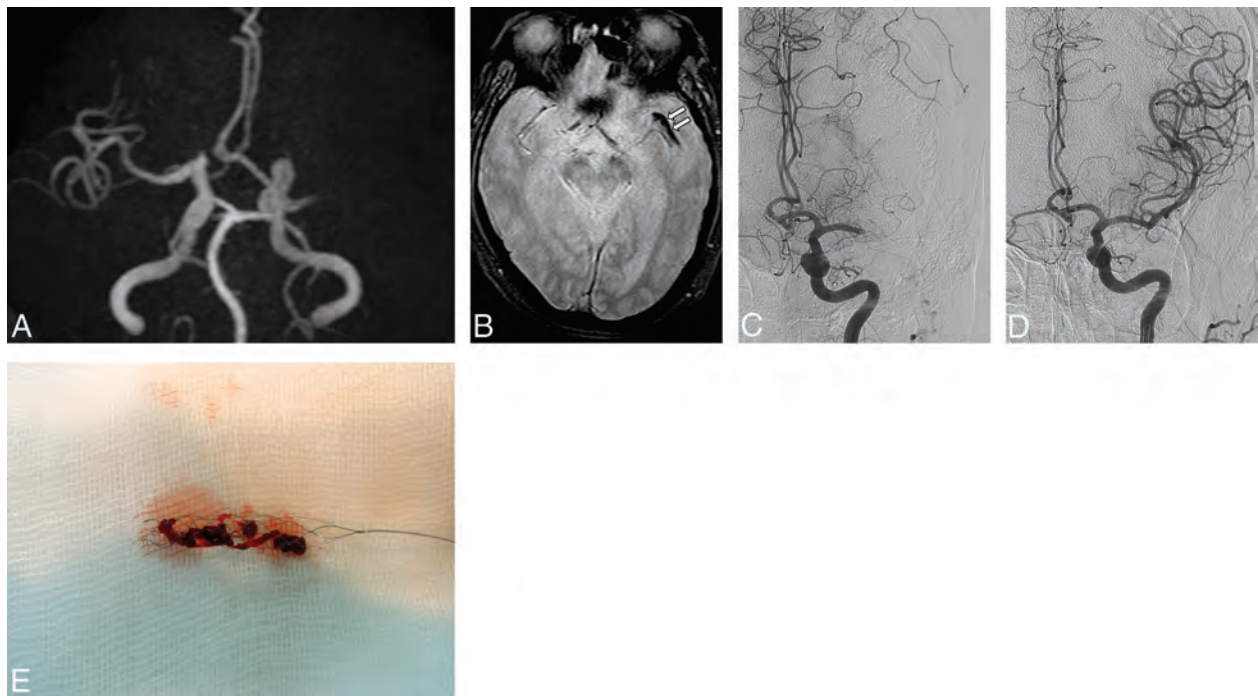


FIG 2. Brain images from a 74-year-old man with acute ischemic stroke and atrial fibrillation. *A*, 3D TOF MR angiography shows the occlusion in the M1 segment of the left MCA. *B*, Axial gradient-echo image reveals a positive susceptibility vessel sign (arrows) in the distal M1 segment of the left MCA. *C*, Conventional angiography shows the occlusion in the M1 segment of the left MCA. *D*, Angiography after 1 passage of the Solitaire stent shows complete revascularization in the left MCA territory. *E*, Photograph demonstrates red clots retrieved with a Solitaire stent.

gioplasty with or without stent placement. Overall, successful revascularization (modified TICI $\geq 2b$) was achieved in 84.6% (77/91) of patients. Successful revascularization was achieved more frequently in the ICAS group than in the non-ICAS group (100% versus 80.8%, $P = .043$). Good outcomes occurred significantly more frequently in the ICAS group than in the non-ICAS group (77.8% versus 47.9%, $P = .034$). There was no newly developed arterial occlusion distal to the angioplasty site on postangioplasty angiograms in all patients who underwent intracranial angioplasty with or without stent placement.

Predictors of Clinical Outcome

Multivariate analysis showed that age (OR, 1.067; 95% CI, 1.013–1.124; $P = .014$) and revascularization (OR, 9.180; 95% CI, 1.545–

54.526; $P = .015$) were independent predictors of good clinical outcome when adjusting for age, sex, dyslipidemia, atrial fibrillation, coronary artery disease, IV thrombolysis, baseline NIHSS score, revascularization (modified TICI $\geq 2b$), posttreatment intracranial hemorrhage, ICAS, and SVS.

DISCUSSION

In the present study, a negative SVS on GRE imaging was a highly sensitive marker with a high negative predictive value for the presence of an underlying ICAS in the setting of acute stroke because of an acute MCA occlusion. A negative SVS on GRE imaging was significantly associated with an underlying ICAS in the occluded MCA (100% in the ICAS group versus 32.9% in the non-ICAS

Table 2: Comparison between the ICAS group and non-ICAS group

	ICAS Group (n = 18)	Non-ICAS Group (n = 73)	P Value
Age (yr)	63.8 ± 10.4	69.9 ± 11.4	.026
Male sex	11 (61.1%)	41 (56.2%)	NS
Risk factors			
Hypertension	12 (66.7%)	41 (56.2%)	NS
Diabetes mellitus	7 (38.9%)	7 (9.6%)	.002
Coronary artery disease	0 (0%)	5 (6.8%)	NS
Dyslipidemia	12 (66.7%)	17 (23.2%)	<.001
Smoking	3 (16.7%)	22 (30.1%)	NS
Atrial fibrillation	1 (5.6%)	38 (52.1%)	<.001
Congestive heart failure	0 (0%)	2 (2.7%)	NS
History of stroke or TIA	1 (5.6%)	11 (15.1%)	NS
Occlusion sites			
M1 segment	18 (100%)	66 (90.4%)	NS
M2 segment	0 (0%)	7 (9.6%)	NS
IV thrombolysis	7 (38.9%)	47 (64.4%)	NS
Time to procedure (min)	253.8 ± 115.9	250.5 ± 74.2	NS
Procedure time (min)	31.9 ± 9.3	33.6 ± 18.0	NS
Time to revascularization (min)	285.8 ± 117.8	284.3 ± 78.2	NS
Baseline NIHSS score	9.8 ± 3.6	12.7 ± 3.7	.003
m-TICI 2b or 3	18 (100%)	59 (80.8%)	.043
mRS 0–2	14 (77.8%)	35 (47.9%)	.034
Mortality	1 (5.6%)	8 (10.9%)	NS
N-SVS	18 (100%)	24 (32.9%)	<.001

Note:—N-SVS indicates negative susceptibility vessel sign; m-TICI, modified TICI; NS, non-significant.

Table 3: Summary of GRE MRI findings according to occlusion sites

Location	ICAS Group (n = 18)		Non-ICAS Group (n = 73)	
	SVS Absent	SVS Present	SVS Absent	SVS Present
M1	18	0	20	46
M2	0	0	4	3
Total (n = 91)	18	0	24	49

group, $P < .001$) with a high sensitivity (100%) and a high negative predictive value (100%). For stroke subtypes, 72.7% (24/33) of patients with large-artery atherosclerosis had a negative SVS and 72.5% (29/40) of patients with cardioembolic stroke had a positive SVS in our study. In comparison, Cho et al⁵ reported that 83.7% of those with large-artery atherosclerosis had a negative SVS and 77.5% of those with cardioembolic stroke had a positive SVS.

Several studies reported that GRE MR imaging can be used to depict blood clots within occluded intracranial arteries and to evaluate the clot composition in the setting of acute ischemic stroke.^{4,6,12} Paramagnetic intracellular deoxyhemoglobin is present at high concentrations in acute clots, leading to a nonuniform magnetic field that causes marked signal loss on the GRE sequence because of dephasing of spins.¹³ Recently, several investigators reported the results of histologic studies analyzing the composition of the clots retrieved by mechanical thrombectomy in patients with acute ischemic stroke.^{6,14–16} These studies demonstrated that the presence of an SVS on GRE imaging was notably associated with a higher red blood cell content in the clots, whereas an absence of SVS was associated with fibrin-rich clots. Fibrin-dominant clots are usually formed because of injury to the

endothelium overlying the complicated atheromatous plaque. Clots formed at the site of underlying ICAS mainly consist of a fibrin network superimposed on the underlying platelet aggregates^{5,17} and would not appear as a hypointense vessel on GRE imaging because of the lack of deoxyhemoglobin. The results from our study support this hypothesis; all patients with underlying ICAS in the occluded MCA had a negative SVS on GRE imaging.

Another plausible explanation for the high incidence of negative SVSs in patients with underlying ICAS would be that such patients had a smaller clot burden compared with those having other stroke subtypes. In our study, 8 of 18 patients with underlying ICAS had a severe stenosis on the initial conventional angiography. Of the 10 patients who underwent SBT with the Solitaire stent because of an occlusion seen on the initial conventional angiography, only 3 patients had visible thrombi that were captured with a stent. The remaining 7 patients had no captured thrombi despite several passages of the stent and had a severe stenosis at the previous occlusion site without angiographic evidence of distal migration of thrombi on follow-up angiography. Thus, overall, 15 of 18 patients (83%) with underlying ICAS had no apparent clot burden in our study.

In our study, the negative SVS showed low specificity and low positive predictive values for predicting ICAS because of a high incidence of false-positive findings (24 cases) in the non-ICAS group. The false-positive cases showing a negative SVS despite the absence of ICAS in the non-ICAS group might be attributed to the size or aging of the clots and their components. Red blood cell-dominant clots that are smaller than the section thickness of the GRE sequence may not demonstrate GRE SVS. In addition, fresh clots cannot demonstrate hypointense signal changes on GRE MR imaging because the main component of hyperacute clots would be oxyhemoglobin.¹⁸

ICAS also can be detected and evaluated with high-resolution vessel wall MR imaging. Recent advances in MR imaging have made it possible to reliably image intracranial vessel wall pathologies, including ICAS.¹⁹ Vessel wall MR imaging can reveal the presence of atherosclerotic plaques or focal thickening and enhancement of the intracranial vessel wall in patients with ICAS. In addition, recent studies showed that vessel wall MR imaging might be used for the characterization of intracranial atherosclerotic plaques to assess the vulnerability of these plaques.²⁰ A high-resolution vessel wall MR imaging sequence may be included in the clinical scan protocol for ischemic stroke in the future. However, it is generally not possible to obtain vessel wall images of sufficient quality for interpretation from patients with stroke in the hyperacute period because of long scan times.

Although the optimal treatment for underlying ICAS in patients presenting with hyperacute stroke remains unknown,²¹ the identification of underlying ICAS before endovascular therapy could help interventionists make appropriate therapeutic decisions.^{5,18,22} Recently, Kang et al²² reported that patients with underlying ICAS who presented with acute stroke had an increased tendency for instant reocclusion of the treated arteries after the initial mechanical thrombectomy. They suggested that the infusion of intra-arterial antiplatelet agents in combination with a thrombolytic agent might reduce the rate of reocclusion in pa-

tients with acute stroke with underlying ICAS. In our study, we performed intracranial angioplasty, with or without stent placement, in all patients with underlying ICAS, which resulted in high rates of revascularization (100%) and good outcome (77.8%) and low mortality rates (5.6%). Although a randomized controlled trial (Stenting and Aggressive Medical Management for Preventing Recurrent stroke in Intracranial Stenosis) failed to show a benefit for intracranial stent placement over intensive medical management in preventing stroke recurrence in high-risk patients with symptomatic ICAS,²³ our study suggests that intracranial angioplasty, with or without stent placement, remains a promising method in the setting of hyperacute stroke secondary to underlying ICAS.

This single-center retrospective study has limitations inherent to this type of case series, including the lack of a prospective study design. In our study, the section thickness of the GRE sequence was 4 mm. Red blood cell–dominant clots smaller than 4 mm may not be seen on GRE images; this possibility might have affected the results of the study. In addition, it might be difficult to differentiate underlying stenosis from residual emboli after mechanical thrombectomy on angiograms. However, there was no newly developed arterial occlusion distal to the angioplasty site when comparing pre- and postangioplasty angiograms in all patients, which could confirm stenotic lesions not being caused by residual emboli. Finally, this study was conducted in an Asian country in which ICAS is more prevalent than in Europe and the United States. Thus, a high incidence (19.8%) of patients with ICAS received endovascular therapy in the setting of hyperacute stroke. However, the global burden of ICAS is increasing, and it is generally accepted that ICAS is now a major worldwide stroke problem that cannot be ignored.²¹

CONCLUSIONS

This study suggests that a negative SVS on GRE MR imaging is a sensitive marker with a high negative predictive value for the presence of an underlying ICAS in patients with acute ischemic stroke because of MCA occlusion. A predictor such as this would be helpful for interventionists when performing subsequent endovascular stroke therapy.

REFERENCES

- Holmstedt CA, Turan TN, Chimowitz MI. **Atherosclerotic intracranial arterial stenosis: risk factors, diagnosis, and treatment.** *Lancet Neurol* 2013;12:1106–14
- Qureshi AI, Caplan LR. **Intracranial atherosclerosis.** *Lancet* 2014;383:984–98
- Shi ZS, Liebeskind DS, Loh Y, et al. **Predictors of subarachnoid hemorrhage in acute ischemic stroke with endovascular therapy.** *Stroke* 2010;41:2775–81
- Rovira A, Orellana P, Alvarez-Sabin J, et al. **Hyperacute ischemic stroke: middle cerebral artery susceptibility sign at echo-planar gradient-echo MR imaging.** *Radiology* 2004;232:466–73
- Cho KH, Kim JS, Kwon SU, et al. **Significance of susceptibility vessel**

- sign on T2*-weighted gradient echo imaging for identification of stroke subtypes.** *Stroke* 2005;36:2379–83
- Liebeskind DS, Sanossian N, Yong WH, et al. **CT and MRI early vessel signs reflect clot composition in acute stroke.** *Stroke* 2011;42:1237–43
- Samuels OB, Joseph GJ, Lynn MJ, et al. **A standardized method for measuring intracranial arterial stenosis.** *AJNR Am J Neuroradiol* 2000;21:643–46
- Yoon W, Jung MY, Jung SH, et al. **Subarachnoid hemorrhage in a multimodal approach heavily weighted toward mechanical thrombectomy with Solitaire stent in acute stroke.** *Stroke* 2013;44:414–19
- Kim SK, Yoon W, Moon SM, et al. **Outcomes of manual aspiration thrombectomy for acute ischemic stroke refractory to stent-based thrombectomy.** *J Neurointerv Surg* 2015;7:473–77
- Zaidat OO, Yoo AJ, Khatri P, et al. **Recommendations on angiographic revascularization grading standards for acute ischemic stroke: a consensus statement.** *Stroke* 2013;44:2650–63
- Adams HP Jr, Bendixen BH, Kappelle LJ, et al. **Classification of subtype of acute ischemic stroke: definitions for use in a multicenter clinical trial—TOAST. Trial of Org 10172 in Acute Stroke Treatment.** *Stroke* 1993;24:35–41
- Naggara O, Raymond J, Domingo Ayllon M, et al. **T2* “susceptibility vessel sign” demonstrates clot location and length in acute ischemic stroke.** *PLoS One* 2013;8:e76727
- Patel MR, Edelman RR, Warach S. **Detection of hyperacute primary intraparenchymal hemorrhage by magnetic resonance imaging.** *Stroke* 1996;27:2321–24
- Marder VJ, Chute DJ, Starkman S, et al. **Analysis of thrombi retrieved from cerebral arteries of patients with acute ischemic stroke.** *Stroke* 2006;37:2086–93
- Yuki I, Kan I, Vinters HV, et al. **The impact of thromboemboli histology on the performance of a mechanical thrombectomy device.** *AJNR Am J Neuroradiol* 2012;33:643–48
- Nielsen JM, van der Schaaf IC, van Dam L, et al. **Histopathologic composition of cerebral thrombi of acute stroke patients is correlated with stroke subtype and thrombus attenuation.** *PLoS One* 2014;9:e88882
- Brogan GX Jr. **Bench to bedside: pathophysiology of acute coronary syndromes and implications for therapy.** *Acad Emerg Med* 2002;9:1029–44
- Kimura K, Iguchi Y, Shibasaki K, et al. **M1 susceptibility vessel sign on T2* as a strong predictor for no early recanalization after IV-t-PA in acute ischemic stroke.** *Stroke* 2009;40:3130–32
- Dieleman N, van der Kolk AG, Zwanenburg JJ, et al. **Imaging intracranial vessel wall pathology with magnetic resonance imaging: current prospects and future directions.** *Circulation* 2014;130:192–201
- van der Kolk AG, Zwanenburg JJ, Denswil NP, et al. **Imaging the intracranial atherosclerotic vessel wall using 7T MRI: initial comparison with histopathology.** *AJNR Am J Neuroradiol* 2015;36:694–701
- Gorelick PB, Wong KS, Bae HJ, et al. **Large artery intracranial occlusive disease: a large worldwide burden but a relatively neglected frontier.** *Stroke* 2008;39:2396–99
- Kang DH, Kim YW, Hwang YH, et al. **Instant reocclusion following mechanical thrombectomy of in situ thromboocclusion and the role of low-dose intra-arterial tirofiban.** *Cerebrovasc Dis* 2014;37:350–55
- Derdeyn CP, Chimowitz MI, Lynn MJ, et al. **Aggressive medical treatment with or without stenting in high-risk patients with intracranial artery stenosis (SAMMPRIS): the final results of a randomised trial.** *Lancet* 2014;383:333–41

Degree of Collaterals and Not Time Is the Determining Factor of Core Infarct Volume within 6 Hours of Stroke Onset

E. Cheng-Ching, J.A. Frontera, S. Man, J. Aoki, Y. Tateishi, F.K. Hui, D. Wisco, P. Ruggieri, M.S. Hussain, and K. Uchino



ABSTRACT

BACKGROUND AND PURPOSE: Growth of the core infarct during the first hours of ischemia onset is not well-understood. We hypothesized that factors other than time from onset of ischemia contribute to core infarct volume as measured by MR imaging.

MATERIALS AND METHODS: Prospectively collected clinical and imaging data of consecutive patients with stroke presenting between March 2008 and April 2013 with anterior circulation large-vessel occlusion and MR imaging performed within 6 hours from the time of onset were reviewed. The association of time from onset, clinical, and radiographic features with DWI volume was assessed by using χ^2 and Mann-Whitney *U* tests.

RESULTS: Of 91 patients, 21 (23%) underwent MR imaging within 0–3 hours from onset, and 70 (76%), within 3–6 hours. Median MR imaging infarct volume was similar in both timeframes, (24.7 versus 29.4 mL, $P = .906$), and there was no difference in the proportion of patients with large infarct volumes (≥ 70 mL, 23.8% versus 22.8%, $P = .928$). Using receiver operating characteristic analysis, we detected no association between the time from onset and MR imaging infarct volume (area under the curve = 0.509). In multivariate analysis, CTA collaterals ($>50\%$ of the territory) (adjusted OR, 0.192; 95% CI, 0.04–0.9; $P = .046$), CTA ASPECTS (adjusted OR, 0.464; 95% CI, 0.3–0.8; $P = .003$), and a history of hyperlipidemia (adjusted OR, 11.0; 95% CI, 1.4–88.0; $P = .023$) (but not time from stroke onset to imaging) were independent predictors of MR imaging infarct volume.

CONCLUSIONS: Collateral status but not time from stroke onset to imaging was a predictor of the size of core infarct in patients with anterior circulation large-vessel occlusion presenting within 6 hours from onset.

ABBREVIATIONS: IQR = interquartile range; LSW = last seen well

Intravenous tPA administered within 4.5 hours from symptom onset improves clinical outcomes in patients with acute ischemic stroke.^{1,2} The importance of time from stroke onset to thrombolysis has been extensively demonstrated as a predictor of improved outcomes. The National Institute of Neurologic Disorders and Stroke tPA trial and pooled analysis from major randomized stroke IV tPA trials showed that late tPA administration is associated with lower likelihood of good clinical outcomes.³ In a cohort of patients treated with intravenous/intra-arterial therapy,

Khatri et al⁴ demonstrated that the probability of good clinical outcome following angiographic reperfusion is time-dependent, with a reduced probability of good outcome as the time to recanalization increases. Despite the importance of time from clinical stroke onset to treatment, other parameters play a major role in influencing clinical outcome, including age and baseline NIHSS score. Infarct volume at baseline has also been demonstrated to be a strong predictor of clinical outcome.^{5–8} The association between time from stroke onset to presentation and core infarct volume is unclear, and factors other than time may have a major influence in the first hours from ischemia onset. A recently published study analyzed a group of patients with anterior circulation large-vessel-occlusion strokes who underwent MR imaging with DWI within 30 hours from stroke onset and found no correlation between the time of onset and stroke volume. The authors suggested that other factors more powerful than time (such as collateral circulation) determine infarct size in these first 30 hours.⁹ It is important to determine what relationship exists between time and infarct volume, especially in the early hours from stroke onset because this

Received October 12, 2014; accepted after revision January 6, 2015.

From the Cerebrovascular Center (E.C.-C., J.A.F., S.M., F.K.H., D.W., M.S.H., K.U.) and Department of Neuroradiology (P.R.), Imaging Institute, Cleveland Clinic, Cleveland, Ohio; Department of Neurology and Cerebrovascular Disease (J.A.), Nippon Medical School, Tokyo, Japan; and Cerebrovascular Center (Y.T.), Department of Neurology and Stroke, Nagasaki University Hospital, Nagasaki, Japan.

Please address correspondence to Ken Uchino, MD, Cerebrovascular Center, Neurological Institute, Cleveland Clinic, 9500 Euclid Ave, S-80, Cleveland, OH 44195; e-mail: uchinok@ccf.org

Indicates article with supplemental on-line table.

<http://dx.doi.org/10.3174/ajnr.A4274>

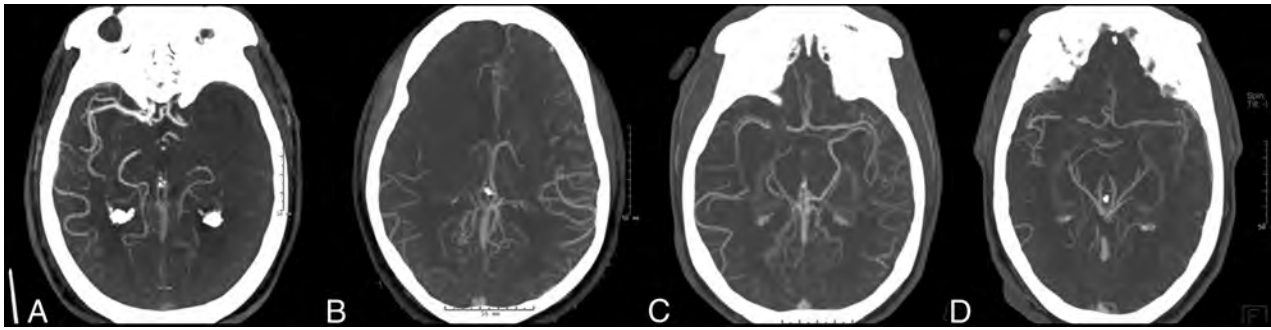


FIG 1. CTA collateral status in the region of the occluded vessel. A, Absent collaterals. B, Minimal (<50%) collaterals. C, Partial (>50%) collaterals. D, Full presence of collaterals.

may have implications in the decisions for imaging selection and treatment. The goal of this study was to explore the relationship of DWI lesion volume to time from stroke onset to imaging within the first 6 hours and to describe imaging characteristics in anterior circulation large-vessel-occlusion strokes at 0–6 hours from the time the patients were last seen well (LSW). We further assessed potential variables that may influence core infarct volume other than time and sought to evaluate predictors of small and large infarct volumes independent of the time factor.

MATERIALS AND METHODS

Study Population

Using a prospectively collected acute stroke data base, we retrospectively identified consecutive patients with acute ischemic stroke admitted to our institution between March 2008 and April 2013. We included only patients with anterior circulation strokes and large-artery occlusion on CTA (involving the intracranial ICA and the M1 or M2 segment of the MCA) in whom MR imaging of the brain was performed within 6 hours from the time LSW and before any endovascular reperfusion therapy was initiated. A reported witnessed time of LSW was required for inclusion, and this time point was used as a surrogate for the time of stroke onset. Baseline clinical characteristics were systematically collected, including demographic data, stroke risk factors, and admission NIHSS scores.

Acute Imaging

At our institution, in every patient who presents with an acute ischemic stroke within 8 hours from symptom onset in whom the NIHSS score is ≥ 8 , we perform a noncontrast CT and CTA if no contraindications exist. If a large-vessel occlusion (ICA, the M1 and/or M2 segment of the MCA, basilar occlusion) is detected and there are no contraindications, a “hyperacute” MR imaging of the brain is performed immediately to assess infarct volume and to evaluate the region of ischemic penumbra.

Noncontrast CT is performed with a multisection CT scanner (Somatom Sensation 64/16; Siemens, Erlangen, Germany) with 1.2-mm collimation, 4.5-mm sections (Sensation 64); and 1.5-mm collimation, 4.8-mm sections (Sensation 16). CTA is performed with a helical scan technique, with acquisitions obtained after a single intravenous bolus injection of 80 mL of nonionic contrast (iopromide, Ultravist 370; Bayer Healthcare LLC, Whippany, New Jersey) into an antecubital vein at a rate of 4 mL/s. The CTA acquisition includes the region of the aortic arch to the centrum semiovale or the vertex with spiral 0.6-mm collimation,

0.6-mm section thickness, 0.6-mm interval (Sensation 64); and spiral 0.75-mm collimation, 0.75-mm section thickness, and 0.75-mm interval (Sensation 16). MR imaging studies were performed by using a commercially available echo-planar instrument on a 1.5T Magnetom Aera system with software version, syngo MR D11 (Siemens). The neuroimaging protocol for acute stroke in our hospital includes a diffusion-weighted imaging sequence (TR/TE, 3500/114 ms; b-values, 0 and 1400 s/mm²; FOV, 230 mm; section thickness, 5.0 mm; base resolution, 128; bandwidth, 1260 Hz); a FLAIR sequence (TR/TE, 8360/94 ms; TI, 2200 ms; flip angle, 180°; FOV, 210 mm; section thickness, 4.0 mm; base resolution, 256; bandwidth, 208 Hz); and a dynamic susceptibility contrast PWI sequence (TR/TE, 2000/45 ms; flip angle, 90°; FOV, 230 mm; section thickness, 5.0 mm; base resolution, 128; bandwidth, 1260 Hz).

Imaging Assessment

An experienced neuroradiologist (F.K.H.) led and oversaw the imaging analysis. Admission pretreatment noncontrast CT and CTA were reviewed, and an Alberta Stroke Program Early CT Score was calculated. Noncontrast CT images were not available for ASPECTS evaluation in 10 patients (1 from 0 to <3 hours, and 9 from 3 to <6 hours). Pretreatment CTA collateral status was analyzed and classified into absent, minimal (<50%), partial (>50%), and full presence of collateral branches opacifying the major intracranial vascular territory that normally supplies the region of the acute infarct (Fig 1).¹⁰ CTA was not available for collateral vessel evaluation in 15 patients (2 from 0 to <3 hours, and 13 from 3 to <6 hours). Under the direct supervision of a neuroradiologist (F.K.H.), 4 vascular neurologists (J.A., Y.T., E.C.-C., and S.M.), blinded to the clinical information, reviewed and analyzed the MR images by using commercial software (syngoMMWP VE36A, syngoVE32D, WinNT 5.2, Service Pack 2; Siemens) on a dedicated workstation. Infarct volumes were obtained from DWI. The area of the infarct on each section was obtained by the software after manually outlining the perimeter of the lesion. The infarct volume was calculated by adding the infarct areas on each section and multiplying by the section thickness.

Statistical Analysis

The cohort of patients was divided into groups according to time intervals from LSW to MR imaging (0–3 hours versus 3–6 hours). We used a cutoff of 70 mL of DWI infarct volume to group pa-

Imaging characteristics by time from last seen well to MRI

	0 to <3 Hours (n = 21)	3–6 Hours (n = 70)	0–6 Hours (Entire Cohort) (n = 91)	P Value (Difference, 0–3 vs 3–6)
Age (yr) (median) (IQR)	58 (54–77)	73 (63.25–83)	70 (59–82)	.034
NIHSS (median) (IQR)	13 (11–19)	17 (13–22.75)	17 (12–21.5)	.050
CT ASPECTS (median) (IQR)	9 (7–10)	8 (6–9)	8 (6–9)	.202
CT ASPECTS ≥ 7 (No.) (%)	17/20 (85%)	42/61 (69%)	59/81 (72%)	.159
CTA collaterals >50% (No.) (%)	14/19 (74%)	37/57 (65%)	51/76 (67%)	.481
DWI volume (mL) (median) (IQR)	24.7 (13.9–63.8)	29.4 (12.1–68.5)	29.2 (12.3–68.5)	.906
MRI DWI volume ≥ 70 mL of DWI volume (No.) (%)	5 (23.8%)	16 (22.8%)	21 (22.8%)	.928
MRI DWI volume ≥ 100 mL of DWI volume (No.) (%)	4 (19%)	13 (18.6%)	17 (18.7%)	.961
Terminal ICA occlusion (No.) (%)	5 (23.8%)	18 (25.7%)	23 (25.3%)	.961
Proximal M1 occlusion (No.) (%)	5 (23.8%)	21 (30%)	26 (28.6%)	.706
Distal M1 occlusion (No.) (%)	11 (52.4%)	31 (44.3%)	42 (46.1%)	.393

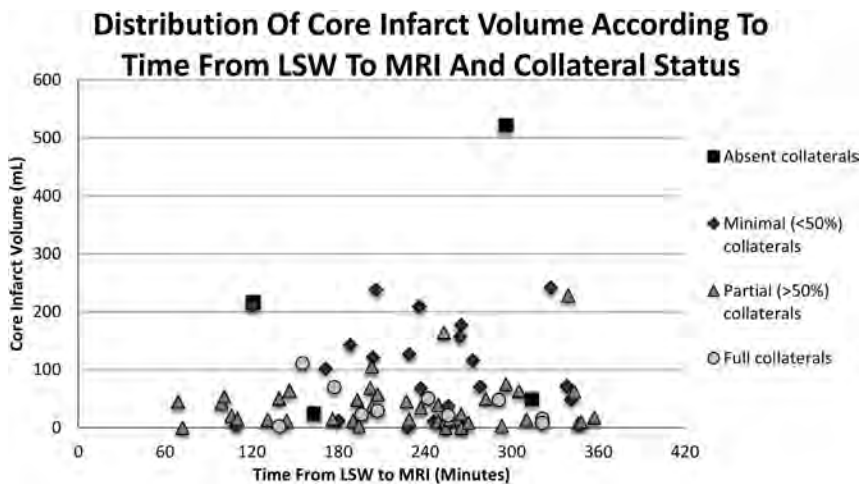


FIG 2. Distribution of DWI infarct volume of each patient according to the time from last seen well to MR imaging and collateral status.

tients into large infarcts (≥ 70 mL) and small infarcts (< 70 mL), and these groups were compared.⁸

Demographics, medical history, and clinical and radiographic features were compared between patients who underwent early MR imaging (0–3 hours from LSW) versus late MR imaging (3–6 hours from LSW) and between patients with large (≥ 70 mL) versus small (< 70 mL) infarcts by using the Pearson χ^2 and Mann-Whitney *U* tests. A receiver operating characteristic curve was constructed to assess the sensitivity and specificity of predicting DWI volume on the basis of time from LSW to MR imaging (0–3 versus 3–6 hours). Backward stepwise multivariable logistic regression analysis was performed to identify independent predictors of DWI volume (≥ 70 mL).

RESULTS

Ninety-one patients met the inclusion criteria and were included in our study analysis. The median age of the overall group was 70 years (interquartile range [IQR], 59–82 years), the median NIHSS score was 17 (IQR, 12–21.5), and the median CT ASPECTS was 8 (IQR, 6–9). The median time from LSW to MR imaging was 239 minutes (range, 69–357 minutes; IQR, 189–280 minutes). The mean DWI infarct volume for the entire group of patients was 57.9 ± 77.9 mL, with a median of 29.2 mL (IQR, 12.3–68.5 mL). The Table shows clinical, demographic, and radiographic characteristics of patients according to the time inter-

val from LSW to MR imaging. When we compared patients presenting early who underwent MR imaging within 0–3 hours from LSW and those patients who presented later who underwent MR imaging within 3–6 hours from LSW, the earlier group tended to be younger (median age, 58 years; IQR, 54–77 years versus 73 years; IQR, 63.25–83 years; $P = .034$) and had lower NIHSS scores (median, 13; IQR, 11–19 versus 17; IQR, 13–22.75; $P = .050$). However, the median infarct volume was similar between early and late imaging groups (24.7 mL; IQR, 13.9–63.8 mL; and 29.4 mL; IQR, 12.1–68.5 mL; $P = .906$). A large infarct (≥ 70 mL) was seen in 23.8% of patients with imaging within 3 hours from LSW compared with 22.8% of patients who presented 3–6 hours from LSW ($P = .928$). Similarly, there was no difference in rates of large infarcts by using a cut-point of 100 mL between those who underwent MR imaging within 0–3 versus 3–6 hours (Table).

Eight patients presented very early, in whom an MR imaging was obtained < 2 hours from LSW. In this very early group, the median DWI infarct volume was 18 mL (IQR, 5.6–43 mL), and none was larger than 70 mL. From 2 to < 3 hours from LSW, the median DWI infarct volume was 50.3 mL (IQR, 14.8–102.5 mL), and 38.4% had large infarcts (≥ 70 mL). Figure 2 shows the DWI volume by time intervals from LSW to MR imaging and the degree of collaterals for each patient. A receiver operating characteristic curve assessing the time from LSW to MR imaging (0–3 versus 3–6 hours) and DWI volume was obtained with an area under the curve of 0.509, demonstrating no association between time from LSW to MR imaging and DWI infarct volume (Fig 3).

The On-line Table shows demographic, clinical, and radiographic patient characteristics according to DWI infarct volume. Those with larger infarcts were more likely to have a history of hyperlipidemia (81% versus 40%, $P = .049$), coronary artery disease (57% versus 11%, $P = .027$), and lower noncontrast CT ASPECTS (5.5 versus 9, $P < .001$) and CTA ASPECTS (5 versus 9, $P < .001$). Patients with smaller infarcts (≤ 70 mL) were more likely to have at least partial ($> 50\%$ of the territory) or better collaterals on CTA compared with those with large infarcts (64%

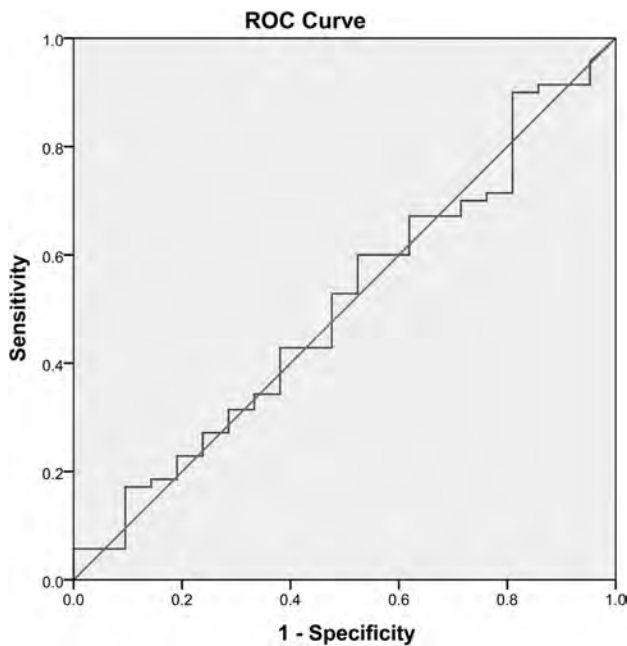


FIG 3. Receiver operating characteristic curve demonstrating no association between the time from LSW to MR imaging (0–3 hours versus 3–6 hours) and DWI infarct volume.

versus 29%, $P = .001$). The group with large DWI infarct volumes was more likely to have occlusion of the cervical ICA (29% versus 6%, $P = .018$), proximal M1 MCA segment occlusion (52% versus 23%, $P = .001$), or either terminal ICA or proximal M1 occlusion (57% versus 31%, $P = .003$). The use of IV tPA before MR imaging and stroke mechanism were not associated with infarct volume.

In multivariate analysis, the time from stroke onset was not a predictor of infarct volume. CTA collaterals of $>50\%$ of the territory involved (adjusted OR, 0.192; 95% CI, 0.04–0.9; $P = .046$) and the CTA ASPECTS (adjusted OR, 0.464; 95% CI, 0.3–0.8; $P = .003$) were negative independent predictors of large infarct volume (≥ 70 mL). History of hyperlipidemia (adjusted OR, 11.0; 95% CI, 1.4–88.0; $P = .023$) was an independent predictor of large infarcts. There was neither a significant interaction between a history of hyperlipidemia and CTA collaterals nor an association of baseline statin use with infarct volume.

DISCUSSION

In a cohort of patients with anterior circulation large-vessel occlusion imaged with DWI within 6 hours from stroke onset, we demonstrate that time to imaging is not a determinant of core infarct as measured by DWI. Hakimelahi et al⁹ found no correlation between infarct volume and time after stroke onset within 30 hours from presentation. We confirmed this finding in a group of patients imaged at an earlier timeframe from stroke onset that is more clinically relevant for decision-making in regard to endovascular intervention. We found that large infarct volumes can be seen in patients presenting equally early and late within the time studied, and we were able to verify that collateral status does indeed have a significant impact on infarct volume. The clinical implications of our study include the possibilities of both safer patient selection for endovascular reperfusion within conventional time windows and extension of these treatment windows.

The definition of large stroke was based on a DWI lesion volume of at least 70 mL. We were also unable to detect a difference in DWI volume by using a larger threshold of 100 mL between those who underwent MR imaging between 0–3 versus 3–6 hours. These 2 values have been demonstrated to be significant thresholds impacting clinical outcome in patients with stroke with anterior circulation large-vessel occlusions.^{8,11,12} A study by using MR imaging–based selection of patients with anterior circulation large-vessel-occlusion ischemic stroke demonstrated that the best clinical outcomes and least infarct growth occur in those with DWI infarct volume of <70 mL who underwent early recanalization and that an infarct of 70 mL is the threshold above which patients do poorly despite treatment.⁸ The Diffusion and Perfusion Imaging Evaluation for Understanding Stroke Evolution trial demonstrated that MR imaging selection can identify patients who may benefit from reperfusion therapy (such as those with target mismatch and likely smaller DWI infarct volumes), and at the same time, it showed that patients with a large DWI lesion (malignant profile with DWI lesion volume >100 mL and/or PWI of >100 mL with time-to-maximum delay of >8 seconds) had a high risk of symptomatic intracerebral hemorrhage with recanalization, suggesting that patients with large strokes should not receive reperfusion therapy.^{11,12} Identification of large DWI infarcts in a similar proportion of patients presenting at early and late timeframes suggests the potential importance of imaging selection for reperfusion therapy among patients presenting within 6 hours from stroke onset. The impact of DWI infarct volume on clinical outcomes with and without reperfusion therapy has been previously described.^{5–8,11} Wisco et al¹³ demonstrated that MR imaging patient selection may reduce the number of futile and harmful interventions; this reduction may translate to better clinical outcomes for patients without revascularization. In our study, nearly 25% of patients who underwent MR imaging within 3 hours of stroke onset had large acute strokes with volumes of >70 mL. These data imply that early reperfusion therapy in all patients without imaging selection may yield a substantial proportion of patients who will not do well, and this implication should be taken into account in clinical practice and in the design of future clinical trials.

The findings of this study should not undermine the importance of time to treatment as a major factor influencing clinical outcomes and the importance of shorter time to treatment, which has been extensively demonstrated.^{1,2,4,14} We observed that those presenting ultra-early, within 2 hours from onset, had core infarct volumes of <70 mL. It can be argued that this ultra-early patient population with small infarct volumes can potentially benefit the most from reperfusion therapies, suggesting that very early reperfusion therapy may have the greatest impact on outcomes in anterior circulation large-vessel-occlusion ischemic strokes. In this very early group, we did not find large infarcts, but the number of patients was small.

When we compared large and small strokes, the proportion of patients presenting within 0–3 hours from onset was not significantly different between the 2 groups, while the degree of collateral circulation and a history of hyperlipidemia were found to be independent predictors of large infarct volumes. In a retrospective study, Menon et al¹⁵ showed that better CTA collateral status was associated with higher follow-up CT ASPECTS and lower 3-month modified Rankin Scale scores. In a study with a small

number of patients presenting with anterior circulation large-vessel-occlusion ischemic strokes who underwent CTA evaluation and intra-arterial therapy, Angermaier et al¹⁶ demonstrated that reperfusion and the extent of CTA collaterals (but not time to treatment) were independent predictors of final infarct volume on follow-up noncontrast CT. In the setting of an arterial occlusion, collateral circulation may provide alternative routes of blood supply to the parenchyma in the distribution of the occluded vessel and potentially limit the size of the infarcted core and penumbra, at least temporarily. During the first minutes to hours after an acute arterial occlusion, collateral circulation may be the only source of perfusion; therefore, the presence of poor collateral status on admission may be associated with large strokes independent of the time elapsed from the onset of the occlusion. In a study of patients with anterior circulation large-artery-occlusion ischemic strokes presenting within 9 hours from onset of symptoms, Souza et al¹⁷ showed that a malignant CTA collateral profile (absent collaterals) strongly correlated and was highly specific for large DWI lesions on admission MR imaging.

We found the large-infarct group to be associated with a history of hyperlipidemia. This finding may be a type 1 error from multiple comparisons because it cannot be explained and has not been reported previously, to our knowledge. Menon et al¹⁸ reported an association between metabolic syndrome and poor leptomeningeal collateral status in a group of patients presenting with acute ischemic stroke and large anterior circulation vessel occlusion in South Korea; however, no causative explanation was studied, and further investigation was recommended. It is possible that hyperlipidemia may be a maker of vasculopathy and dysfunctional autoregulation with a reduced capacity of collateral recruitment; however, this possibility cannot be assessed in this retrospective study and requires further investigation.

This study has several limitations. It has the inherent limitations of a retrospective observational study. The sample size was small, especially when breaking down the cohort into groups by time intervals, in which we see a smaller number of patients presenting in the early times. An exact time of symptom onset was not available in all patients; therefore, the time from LSW was used as the most accurate surrogate for time of stroke-symptom onset. Even though using the time of LSW may overestimate the actual time interval between onset and imaging, an overestimation is preferred rather than an underestimation, given the focus of our study in detecting large strokes at early time points. Using the time of LSW to MR imaging from 0 to 6 hours, we are certain that stroke onset occurred within this timeframe; therefore, our cohort consists of patients with a well-established time of stroke onset to MR imaging within the time window criteria for this study. This patient group correlates with real-world clinical care in which the exact time of onset is frequently unknown, but the time of LSW is used more often when deciding treatment for these patients.

CONCLUSIONS

In this cohort, time from stroke onset to imaging was not a determinant of core infarct size in patients with stroke with anterior circulation large-vessel occlusion within the first 6 hours. Collateral status and the CTA ASPECTS are independent predictors of infarct volume within this period.

Disclosures: Esteban Cheng-Ching—UNRELATED: Royalties: Lippincott Williams & Wilkins, Comments: royalties for authorship of the book *Comprehensive Review in Clinical Neurology*.

REFERENCES

1. The National Institute of Neurological Disorders and Stroke rt-PA Stroke Study Group. **Tissue plasminogen activator for acute ischemic stroke.** *N Engl J Med* 1995;333:1581–87
2. Hacke W, Kaste M, Bluhmki E, et al. **Thrombolysis with alteplase 3 to 4.5 hours after acute ischemic stroke.** *N Engl J Med* 2008; 359:1317–29
3. Lees KR, Bluhmki E, von Kummer R, et al. **Time to treatment with intravenous alteplase and outcome in stroke: an updated pooled analysis of ECASS, ATLANTIS, NINDS, and EPITHET trials.** *Lancet* 2010;375:1695–703
4. Khatri P, Abruzzo T, Yeatts SD, et al. **Good clinical outcome after ischemic stroke with successful revascularization is time-dependent.** *Neurology* 2009;73:1066–72
5. Sanák D, Nosál' V, Horák D, et al. **Impact of diffusion-weighted MRI-measured initial cerebral infarction volume on clinical outcome in acute stroke patients with middle cerebral artery occlusion treated by thrombolysis.** *Neuroradiology* 2006;48:632–39
6. Thijs VN, Lansberg MG, Beaulieu C, et al. **Is early ischemic lesion volume on diffusion-weighted imaging an independent predictor of stroke outcome? A multivariable analysis.** *Stroke* 2000;31:2597–602
7. Vogt G, Laage R, Shuaib A, et al. **Initial lesion volume is an independent predictor of clinical stroke outcome at day 90: an analysis of the Virtual International Stroke Trials Archive (VISTA) database.** *Stroke* 2012;43:1266–72
8. Yoo AJ, Verduzco LA, Schaefer PW, et al. **MRI-based selection for intra-arterial stroke therapy: value of pretreatment diffusion-weighted imaging lesion volume in selecting patients with acute stroke who will benefit from early recanalization.** *Stroke* 2009; 40:2046–54
9. Hakimelahi R, Vachha BA, Copen WA, et al. **Time and diffusion lesion size in major anterior circulation ischemic strokes.** *Stroke* 2014;45:2936–41
10. Tan JC, Dillon WP, Liu S, et al. **Systematic comparison of perfusion-CT and CT-angiography in acute stroke patients.** *Ann Neurol* 2007;61:533–43
11. Albers GW, Thijs VN, Wechsler L, et al. **Magnetic resonance imaging profiles predict clinical response to early reperfusion: the Diffusion and Perfusion Imaging Evaluation for Understanding Stroke Evolution (DEFUSE) study.** *Ann Neurol* 2006;60:508–17
12. Lansberg MG, Straka M, Kemp S, et al. **MRI profile and response to endovascular reperfusion after stroke (DEFUSE 2): a prospective cohort study.** *Lancet Neurol* 2012;11:860–67
13. Wisco D, Uchino K, Saqqur M, et al. **Addition of hyperacute MRI AIDs in patient selection, decreasing the use of endovascular stroke therapy.** *Stroke* 2014;45:467–72
14. Hacke W, Donnan G, Fieschi C, et al. **Association of outcome with early stroke treatment: pooled analysis of ATLANTIS, ECASS, and NINDS rt-PA stroke trials.** *Lancet* 2004;363:768–74
15. Menon BK, Smith EE, Modi J, et al. **Regional leptomeningeal score on CT angiography predicts clinical and imaging outcomes in patients with acute anterior circulation occlusions.** *AJNR Am J Neuroradiol* 2011;32:1640–45
16. Angermaier A, Langner S, Kirsch M, et al. **CT-angiographic collateralization predicts final infarct volume after intra-arterial thrombolysis for acute anterior circulation ischemic stroke.** *Cerebrovasc Dis* 2011;31:177–84
17. Souza LC, Yoo AJ, Chaudhry ZA, et al. **Malignant CTA collateral profile is highly specific for large admission DWI infarct core and poor outcome in acute stroke.** *AJNR Am J Neuroradiol* 2012;33:1331–36
18. Menon BK, Smith EE, Coutts SB, et al. **Leptomeningeal collaterals are associated with modifiable metabolic risk factors.** *Ann Neurol* 2013;74:241–48

Whole-Brain Susceptibility-Weighted Thrombus Imaging in Stroke: Fragmented Thrombi Predict Worse Outcome

P.P. Gratz, G. Schroth, J. Gralla, H.P. Mattle, U. Fischer, S. Jung, P. Mordasini, K. Hsieh, R.K. Verma, C. Weisstanner, and M. El-Koussy



ABSTRACT

BACKGROUND AND PURPOSE: The prevalence and clinical importance of primarily fragmented thrombi in patients with acute ischemic stroke remains elusive. Whole-brain SWI was used to detect multiple thrombus fragments, and their clinical significance was analyzed.

MATERIALS AND METHODS: Pretreatment SWI was analyzed for the presence of a single intracranial thrombus or multiple intracranial thrombi. Associations with baseline clinical characteristics, complications, and clinical outcome were studied.

RESULTS: Single intracranial thrombi were detected in 300 (92.6%), and multiple thrombi, in 24 of 324 patients (7.4%). In 23 patients with multiple thrombi, all thrombus fragments were located in the vascular territory distal to the primary occluding thrombus; in 1 patient, thrombi were found both in the anterior and posterior circulation. Only a minority of thrombus fragments were detected on TOF-MRA, first-pass gadolinium-enhanced MRA, or DSA. Patients with multiple intracranial thrombi presented with more severe symptoms (median NIHSS scores, 15 versus 11; $P = .014$) and larger ischemic areas (median DWI ASPECTS, 5 versus 7; $P = .006$); good collaterals, rated on DSA, were fewer than those in patients with a single thrombus (21.1% versus 44.2%, $P = .051$). The presence of multiple thrombi was a predictor of unfavorable outcome at 3 months ($P = .040$; OR, 0.251; 95% CI, 0.067–0.939).

CONCLUSIONS: Patients with multiple intracranial thrombus fragments constitute a small subgroup of patients with stroke with a worse outcome than patients with single thrombi.

ABBREVIATION: SVS = susceptibility vessel sign

Little is known about the proportion of acute ischemic strokes caused by multiple intracranial thrombi. Rarely, distal thrombus fragments that are separate from the primary occluding thrombus can be detected on DSA. Incomplete vessel occlusion by the primary thrombus with distal passage of contrast is required for this observation. Therefore, the true prevalence of multiple intracranial thrombi in the stroke population and the implications for clinical outcome remain unknown.

Advanced gradient-echo-based MR imaging sequences, such as SWI, are highly sensitive in distinguishing structures that have different susceptibility values than their surroundings (eg, deox-

xygenated blood, hemosiderin, ferritin, or calcium).¹ SWI offers the possibility to directly visualize thrombotic material, commonly referred to as the susceptibility vessel sign (SVS), independent of the presence of blood flow or contrast media.^{2–4} Recent studies confirmed that 1.5T and 3T SWI is a fast, robust, and highly sensitive imaging technique in acute stroke without relevant image interference following gadolinium application.^{5,6} We performed SWI, covering the whole brain in patients with acute ischemic stroke of the anterior or posterior circulation to determine the prevalence of multiple intracranial thrombi before thrombolytic treatment and to study the associations between the presence of fragmented thrombi and baseline clinical and imaging characteristics, stroke etiology, and clinical outcome.

MATERIALS AND METHODS

Patients and Clinical Data

Five hundred fifty-seven patients with acute ischemic stroke treated at our stroke unit from January 2010 to August 2013 underwent MR imaging after admission. Of these, 442 patients had MR imaging including SWI before initiation of thrombolytic therapy. Patients with anterior or posterior circulation stroke due to tandem occlusions (ICA and MCA), carotid-T occlusions, iso-

Received October 24, 2014; accepted after revision December 11.

From the Departments of Diagnostic and Interventional Neuroradiology (P.P.G., G.S., J.G., S.J., P.M., K.H., R.K.V., C.W., M.E.-K.) and Neurology (H.P.M., U.F., S.J.), Inselspital, Bern University Hospital and University of Bern, Bern, Switzerland.

Paper previously presented in part at: XXIII European Stroke Conference, May 12–15, 2014; Nice, France.

Please address correspondence to Gerhard Schroth, MD, Department of Diagnostic and Interventional Neuroradiology, University of Bern, Inselspital, Freiburgstr 10, 3010 Bern, Switzerland; e-mail: gerhard.schroth@insel.ch

Indicates open access to non-subscribers at www.ajnr.org

<http://dx.doi.org/10.3174/ajnr.A4275>

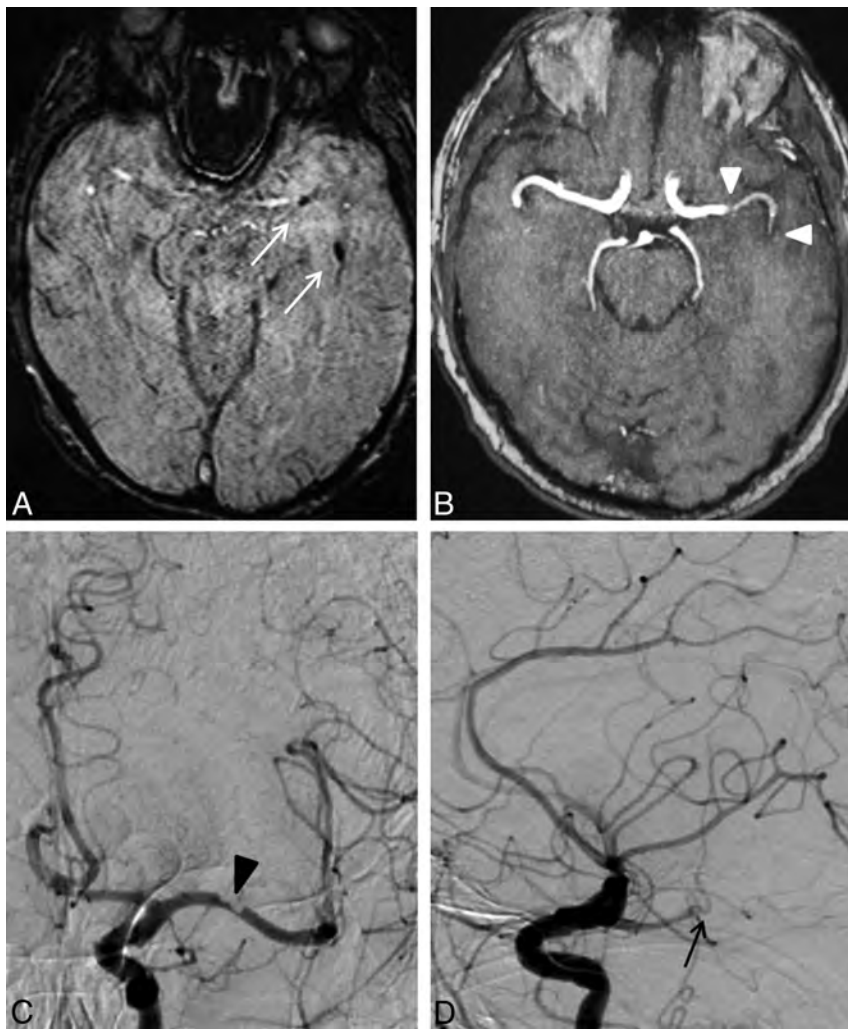


FIG 1. An 85-year-old man with right-sided hemiparesis and aphasia (NIHSS 13). Pretreatment SWI shows susceptibility vessel signs in the left M1 and M2 segments (A, white arrows). On TOF-MRA (MIP), diminished flow signal is seen distal to the thrombus fragment in the M1 segment with complete loss of flow signal at the site of the distal thrombus fragment (B, white arrowheads). DSA demonstrates incomplete occlusion of the vessel lumen by a thrombus in the M1 segment (C, anteroposterior projection, black arrowhead). On the lateral projection, occlusion of the temporo-occipital M2 branch by a more distal thrombus fragment is visible (D, black arrow). Although both TOF-MRA and DSA can show the distal vessel occlusion, only SWI allows estimation of the length of the distal fragment and exclusion of additional distal thrombi.

lated occlusions of the MCA (M1, M2, or M3/4 segments), occlusions of the anterior cerebral artery, occlusions of the basilar artery either isolated or in combination with the vertebral artery, and occlusions of the posterior cerebral artery were considered for the final analysis. Three hundred forty-seven patients fulfilled all inclusion criteria. Following the imaging, all patients underwent recanalization therapy with IV rtPA, endovascular techniques, or a combination of both.

Clinical data were continuously recorded in the data base of our stroke center. The Trial of Org 10172 in Acute Stroke Treatment criteria were used for the categorization of stroke etiology.⁷ The occurrence of symptomatic and asymptomatic intracranial hemorrhage, within 72 hours from stroke onset, was recorded according to the Prolyse in Acute Cerebral Thromboembolism II criteria.⁸ Clinical outcome was assessed 3 months after stroke by

using the modified Rankin Scale. The study was approved by our institutional review board.

Imaging

Standard stroke MR imaging protocol was performed, which included diffusion-weighted imaging, T2-weighted imaging, TOF-MRA, SWI, first-pass gadolinium-enhanced MRA of the cervical and intracranial arteries, and perfusion imaging. The scans were acquired on 1.5T and 3T MR imaging systems (Magnetom Avanto and Magnetom Verio; Siemens, Erlangen, Germany).

For the 1.5T scanner, the SWI parameters were the following: TR, 49 ms; TE, 40 ms; number of averages, 1; FOV read, 230 mm; FOV phase, 75.0%; voxel size, $0.9 \times 0.7 \times 1.8$ mm; flip angle, 15°; acquisition time, 2 minutes 59 seconds. For the 3T scanner, the parameters were as follows: TR, 28 ms; TE, 20 ms; number of averages, 1; FOV read, 230 mm; FOV phase, 75.0%; voxel size, $0.9 \times 0.9 \times 2.0$ mm; flip angle, 15°; acquisition time, 2 minutes 59 seconds. The SWI and minimum-intensity-projection images were generated automatically by the scanner software.

DSA was performed via a transfemoral approach by using a biplane, high-resolution angiographic system (Axiom Artis zee; Siemens).

Image Analysis

MR images were interpreted in consensus by a neuroradiologist and a radiologist in training. SWI was analyzed for the presence of the SVS in the supraclinoid segment of the ICA, the MCA, the anterior cerebral artery, the intradural segment of the vertebral artery, the basilar artery, and the posterior cerebral artery. The SVS was defined as an area of signal drop within the course of an artery that either exceeded the diameter of the contralateral nonoccluded vessel or that of the adjacent vessel segment on both the SWI and minimum-intensity-projection series.³ The length of the main thrombus and distal thrombus fragments, if applicable, was measured on SWI. In case of carotid-T, tandem, and combined basilar artery and vertebral artery occlusions, total clot length could not be determined because of either susceptibility artifacts in the proximity of the skull base or thrombi located partially outside the FOV.

A distal thrombus fragment was defined as an SVS being separated from the more proximal SVS by >2 mm—that is, the largest dimension of a voxel in SWI (Figs 1 and 2). The distance between the primary occluding thrombus and distal thrombus

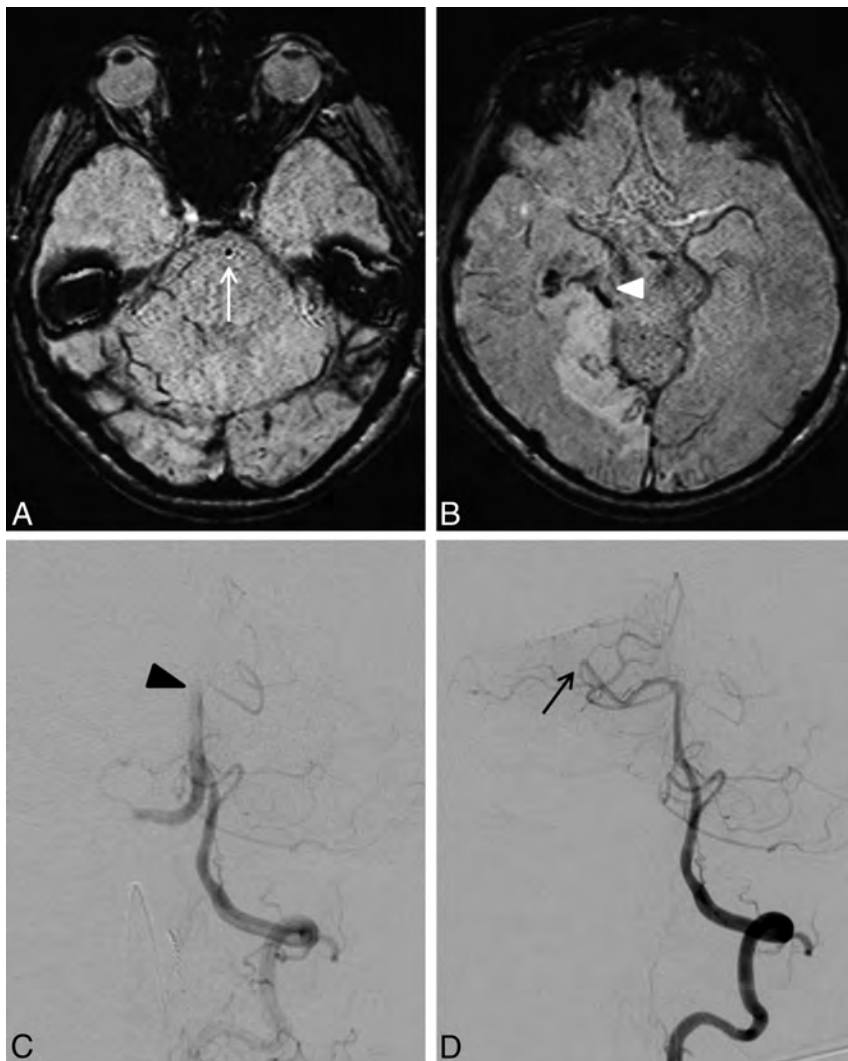


FIG 2. A 69-year-old male patient with a sudden decrease in consciousness. SWI shows susceptibility artifacts from thrombotic material in the basilar artery (A, white arrow) and the right posterior cerebral artery (B, white arrowhead). Hemorrhagic transformation of a subacute infarction in the vascular territory of the right posterior cerebral artery is seen. DSA confirms occlusion of the basilar artery (C, anteroposterior projection, black arrowhead). Following successful endovascular recanalization of the basilar artery, the occlusion in the perimesencephalic segment of the right posterior cerebral artery, already known from pretreatment SWI, becomes visible in DSA as well (D, anteroposterior projection, black arrow).

fragments was measured on a reconstructed plane, including both the distal part of the primary occluding thrombus and the proximal part of the thrombus fragment.

In patients with anterior circulation stroke, with the exception of the 4 patients with isolated anterior cerebral artery occlusion, the extent of ischemic lesions was assessed on pretreatment DWI by using the Alberta Stroke Program Early CT Score.⁹

Leptomeningeal collaterals were assessed on DSA as described previously.¹⁰

Statistical Analysis

Categorical variables were compared with the χ^2 test and the Fisher exact test as appropriate, and continuous variables, with the Mann-Whitney *U* test. To determine the predictors of clinical outcome, we performed a forward stepwise logistic regression, including all variables with a *P* < .2 in univariate analysis. These

variables were age, sex, baseline NIHSS score, occlusion site, degree of collaterals, DWI ASPECTS, atrial fibrillation, diabetes mellitus, arterial hypertension, hypercholesterolemia, coronary artery disease, current smoking, and the presence of multiple intracranial thrombi on pretreatment imaging. Clinical outcome was dichotomized into favorable (mRS 0–2) and poor outcome (mRS 3–6). Collateral status was dichotomized into good and moderate/poor collaterals. A *P* value < .05 was considered significant. Statistics were performed with SPSS, Version 21 (IBM, Armonk, New York).

RESULTS

The SVS was detected in 324 of 347 patients (93.4%) on pretreatment SWI. Multiple intracranial thrombi were found in 24 patients (7.4% of all patients with visible SVSs). Fragmented thrombi occurred with a similar frequency in anterior and posterior circulation strokes (3/36 [8.3%] versus 21/288 [7.3%], *P* = .739). Nineteen patients had 1 distal fragment, 3 had 2 fragments, and 2 had 3 fragments. One of 31 fragments was located in the M1 segment of the MCA; 15, in the M2 segment; 11, in the M3 or M4 segment; 2, in the P2 segment of the posterior cerebral artery, and 2, in the P3 segment. Thirty thrombus fragments were found in the vascular territory distal to the primary occluding thrombus. One patient with a carotid-T occlusion was found to have a thrombus fragment in the P3 segment of the ipsilateral posterior cerebral artery, most likely by distal migration through a fetal variant of the posterior cerebral artery.

The mean distance of thrombus fragments from the primary occluding thrombus was 19.6 ± 15.6 mm. The mean length of thrombus fragments was 7.1 ± 4.0 mm.

TOF-MRA and first-pass gadolinium-enhanced MRA detected distal thrombus fragments in 8 and 11 of 24 patients (25.0% and 33.3%, respectively), with multiple intracranial thrombi on SWI. Nineteen of the 24 patients with multiple intracranial thrombi on SWI underwent DSA. In this group, thrombus fragments were confirmed in 8 patients (42.1%) on DSA.

Baseline clinical characteristics of patients with fragmented and single thrombi are shown in Table 1. Patients with multiple intracranial thrombi presented with a significantly higher median NIHSS score on admission (15 versus 11, *P* = .014). No significant difference in vascular risk factors or stroke etiology was found between the 2 groups. The prestroke use of antiplatelet

Table 1: Baseline clinical characteristics

	Fragmented Thrombus (n = 24) (7.4%)	Single Thrombus (n = 300) (92.6%)	P
Age (yr) (mean) (SD)	73.1 (11.3)	68.6 (14.0)	.109
Women (No.) (%)	9 (37.5)	139 (46.3)	.403
Baseline NIHSS score (median) (range)	15 (6–36)	11 (1–36)	.014
Vascular risk factors			
Hypertension (No.) (%)	15 (62.5)	192 (64.0)	.883
Diabetes mellitus (No.) (%)	5 (20.8)	45/298 (15.1)	.395
Atrial fibrillation (No.) (%)	13/23 (56.5)	123/263 (46.8)	.392
Current smoking (No.) (%)	2/22 (9.1)	57/286 (19.9)	.271
Hypercholesterolemia (No.) (%)	14/23 (60.9)	161/296 (54.4)	.548
Coronary artery disease (No.) (%)	5 (20.8)	58/298 (19.5)	.794
Previous stroke (No.) (%)	2 (8.3)	31/298 (10.4)	1.00
Stroke etiology			
Large artery disease (No.) (%)	3 (12.5)	31 (10.3)	.558
Cardioembolic stroke (No.) (%)	14 (58.3)	135 (45.0)	
Other determined etiology (No.) (%)	2 (8.3)	38 (12.7)	
Unknown etiology (No.) (%)	5 (20.8)	96 (32.0)	

Table 2: Imaging characteristics and treatment

	Fragmented Thrombus (n = 24) (7.4%)	Single Thrombus (n = 300) (92.6%)	P
Affected vascular territory			.739
Anterior circulation (No.) (%)	21 (87.5)	267 (89.0)	
Posterior circulation (No.) (%)	3 (12.5)	33 (11.0)	
Occlusion site			.372
Tandem occlusion (No.) (%)	3 (12.5)	29 (9.7)	
Carotid-T (No.) (%)	3 (12.5)	14 (4.7)	
MCA M1 (No.) (%)	8 (33.3)	123 (41.0)	
MCA M2 (No.) (%)	6 (25.0)	74 (24.7)	
MCA M3/4 (No.) (%)	1 (4.2)	23 (7.7)	
Anterior cerebral artery (No.) (%)	0 (0.0)	4 (1.3)	
Basilar artery (No.) (%)	3 (12.5)	16 (5.3)	
Posterior cerebral artery (No.) (%)	0 (0.0)	17 (5.7)	
Primary thrombus length on SWI (mm) (mean) (SD)	10.3 (6.4) (n = 18)	10.3 (5.6) (n = 248)	.699
Total clot length (mm) (mean) (SD)	20.1 (10.7) (n = 18)	10.3 (5.6) (n = 248)	<.001
DWI ASPECTS (media) (range)	5 (0–8) (n = 21)	7 (0–10) (n = 263)	.006
Leptomeningeal collaterals	n = 19	n = 199	.051
Good (No.) (%)	4 (21.1)	88 (44.2)	
Moderate/poor (No.) (%)	15 (78.9)	111 (55.8)	
Treatment			.625
Intravenous thrombolysis only (No.) (%)	6 (25.0)	102 (34.0)	
Bridging thrombolysis (No.) (%)	7 (29.2)	69 (23.0)	
Endovascular intervention only (No.) (%)	11 (45.8)	129 (43.0)	

Table 3: Intracranial bleeding complications and clinical outcome

	Fragmented Thrombus (n = 24) (7.4%)	Single Thrombus (n = 300) (92.6%)	P
Symptomatic intracranial hemorrhage (No.) (%)	3 (12.5)	17 (5.7)	.176
Asymptomatic intracranial hemorrhage (No.) (%)	6 (25.0)	34 (11.3)	.097
Favorable outcome (mRS 0–2) at 3 months (No.) (%)	6/23 (26.1)	171/286 (59.8)	.002
Death at 3 months (No.) (%)	7/23 (30.4)	43/292 (14.7)	.069

drugs or anticoagulants did not differ between the groups. Imaging characteristics and treatment are compared in Table 2. In patients with isolated MCA, anterior cerebral artery, basilar artery, and posterior cerebral artery occlusions, total clot length was determined. Clot length in patients with fragmented thrombi was significantly higher than that in patients with a solitary thrombus (20.1 ± 10.7 versus 10.3 ± 5.6 mm, $P < .001$).

proximal occluding thrombus and were therefore a priori invisible with normal angiographic techniques. We found significant associations between the presence of multiple intracranial thrombi and a higher NIHSS score on admission as well as larger ischemic areas on pretreatment DWI. The presence of fragmented thrombi was a predictor of unfavorable clinical outcome at 3 months.

Patients with fragmented thrombi had significantly lower median DWI ASPECTS, meaning larger ischemic areas on DWI, than patients with a solitary thrombus (5 versus 7, $P = .006$). Good collaterals as assessed on DSA were found in fewer patients with fragmented thrombi than in those without, but the difference was not significant (4/19 [21.1%] versus 88/199 [44.2%], $P = .051$). One hundred eight patients (33.3%) were treated with IV rtPA alone, 140 (43.2%) underwent endovascular treatment, and 76 (23.5%) had a combination of both. Treatment was similar in both groups. Clinical outcome at 3 months was worse in patients with fragmented thrombi (mRS 0–2: 6/23 [26.1%] versus 171/286 [59.8%]; $P = .002$; Table 3).

The following variables showed $P < .2$ in univariate analysis and were included in the binary logistic regression analysis: NIHSS, age, DWI ASPECTS, multiple intracranial thrombi on pretreatment imaging, occlusion site, atrial fibrillation, diabetes mellitus, arterial hypertension, coronary artery disease, and current smoking. In our stepwise regression model, NIHSS was included as the first variable, followed by age, DWI ASPECTS, and finally the presence of multiple thrombi. The absence of multiple thrombus fragments ($P = .040$; OR, 0.251; 95% CI, 0.067–0.939), higher DWI ASPECTS ($P = .004$; OR, 1.328; 95% CI, 1.093–1.614), younger age ($P < .001$; OR, 0.919; 95% CI, 0.889–0.950), and lower NIHSS score ($P < .001$; OR, 0.832; 95% CI, 0.773–0.894) predicted good outcome.

DISCUSSION

Using whole-brain SWI, we found multiple intracranial thrombi in 24 of 324 patients with acute stroke with the SVS (7.4%) before initiation of any thrombolytic therapy. Most distal thrombus fragments (95.8%) affected the same vascular territory distal to the

A study that analyzed the histologic structure of clots extracted by endovascular means by using the Merci retriever (Concentric Medical, Mountain View, California) reported that in 64% of cases, thrombi were retrieved in multiple fragments.¹¹ It is likely that the prevalence of fragmented thrombi had been lower before mechanical disruption of the clot during deployment and retraction of the thrombectomy device. This supposition is supported by our *in vivo* studies demonstrating thrombus fragmentation and distal embolization during retrieval of the initially single thrombus with distal thrombectomy devices.¹²

Although our results are based purely on thrombus fragmentation before thrombolytic treatment, it could be speculated that iatrogenic thrombus fragmentation might have a similarly negative impact on outcome. This may, among other contributing factors, explain the disappointing clinical outcome in studies that used thrombus fragmentation techniques exclusively (Multi Mechanical Embolus Removal in Cerebral Ischemia, Penumbra Pivotal Stroke Trial, Mechanical Retrieval and REcanalization of Stroke Clots Using Embolectomy trials)¹³⁻¹⁵ or in part (Interventional Management of Stroke III, SYNTHESIS Expansion [A randomized controlled trial between loco-regional intra-arterial and systemic intravenous thrombolysis with Alteplase in acute ischemic stroke]).^{16,17} The SYNTHESIS Expansion study reported that thrombus fragmentation with a microguidewire was performed in approximately two-thirds of patients.¹⁷ In contrast, the goal of current mechanical thrombectomy in acute stroke is removal of the thrombus *en bloc* with the lowest possible rate of thrombus fragmentation, as applied and improved in experienced stroke centers.^{10,18,19}

In our series, good collaterals as assessed on DSA were found in fewer patients with multiple intracranial thrombi, though the difference was not significant. No additional differences in other well-known predictors of outcome were found between patients with and without multiple thrombi. There is evidence from multiple studies that good leptomeningeal collaterals reduce and slow penumbral tissue loss, resulting in better clinical outcome.^{20,21} When one considers the differences in collateral status between patients with and without multiple fragments, the probable role of autolysis should be discussed. Zanette et al²² reported that spontaneous lysis occurs in a high percentage of patients with distal MCA occlusions, similar to the sites where most of the distal thrombus fragments were found in our cohort. Because good collaterals were seen less often in patients with multiple thrombus fragments than in those with a single thrombus, one could hypothesize that fewer endogenous thrombolytic factors may have reached the distal thrombus fragments in patients with poor collateralization, resulting in the persistence of these fragments.

Thrombus burden must be taken into account when looking for factors that could explain the differences in outcome. Total clot length, defined as the combined length of the primary occluding thrombus and the distal thrombus fragments, was significantly higher in patients with fragmented thrombi compared with those with a solitary thrombus. It remains unclear whether longer thrombi are more likely to fragment or distal fragments lead to secondary clot formation due to stagnation of blood flow, thus increasing total clot length. A recent study assessed clot burden in patients with anterior circulation stroke on T2*-weighted imag-

ing by using a scoring system based on the vessel segments that were affected by thrombotic material. Patients with fewer and more distal vessel segments involved had a higher revascularization rate and were more likely to have favorable clinical outcome.²³ Because absolute thrombus length was not part of the scoring system, the comparability with our results is limited. One has to consider that assessment of thrombus burden by measuring the total length of thrombus fragments could result in overestimation in patients with multiple thrombi. Migration of distal thrombus fragments to smaller-sized vessels may result in reorientation and elongation of distal thrombi, resulting in a total clot length disproportionate to total clot volume.

TOF-MRA, first-pass gadolinium-enhanced MRA, and DSA detected only a minority of distal thrombus fragments seen on SWI. The lower yield of these imaging techniques in the detection of distal thrombus fragments most likely results from their dependence on the presence of blood flow or contrast media, both of which are usually reduced or absent distal to the primary vessel occlusion. Besides DWI and imaging of the whole angioarchitecture from the aortic arch up to distal branches of the cerebral arteries, imaging of the thrombus and its fragments with SWI has become a standard sequence of our stroke protocol due to its high therapeutic relevance.⁵

Our study has some limitations. Image analysis was only performed in consensus. In our experience, the SVS and distal thrombus fragments are easily detectable and we did not deem it necessary to additionally assess interobserver variability. Furthermore, each MR imaging study was routinely evaluated by a neuroradiologist and radiologist in training, and the findings were documented in our PACS. In 16 of the 24 patients (66.7%) with multiple thrombi on SWI, a distal vessel occlusion or thrombus fragment or both separate from the primary occlusion had already been described in the radiology report. Most interesting, in the 8 patients in whom distal thrombus fragments were not described initially, the fragments were located in closer proximity to the primary thrombus than in those in whom the distal occlusion was mentioned (7.0 ± 4.0 versus 24.2 ± 15.9 mm). One could speculate that these fragments were either harder to detect or had not been considered important enough to be described in the radiology report. In this single-center study, data from imaging were partly analyzed retrospectively. The small size of the patient group with fragmented thrombi limits the generalizability of the results. Evaluation of ICA and basilar artery thrombi on SWI was greatly limited by the extensive susceptibility artifacts in the proximity of the skull base.

CONCLUSIONS

Multiple intracranial thrombi were detected on pretreatment SWI in 7.4% of patients with acute ischemic stroke of the anterior or posterior circulation. The presence of fragmented thrombi was a predictor of worse outcome. Patients with multiple thrombus fragments presented with more severe symptoms on admission, had more extensive ischemic areas on pretreatment DWI, and demonstrated worse collaterals as seen on biplane angiography. To know that multiple thrombi are present not only helps in planning the endovascular treatment, especially mechanical thrombectomy because distal fragments render the intervention more

difficult, but may also be of use in prognostication of functional outcome.

ACKNOWLEDGMENTS

We thank Pietro Ballinari for statistical advice.

Disclosures: Jan Gralla—UNRELATED: Consultancy: Covidien,* Comments: Global Principal Investigator of the Solitaire FR Thrombectomy for Acute Revascularization Study and consultant for Covidien. Heinrich P. Mattle—UNRELATED: Consultancy: Bayer, Biogen, Boehringer Ingelheim, Daiichi-Sankyo, Genzyme, Merck, Neuravi, Novartis, Pfizer, Teva; Grants/Grants Pending: Swiss Heart Foundation,* Swiss National Science Foundation*; Payment for Lectures (including service on Speakers Bureaus): Bayer, Biogen, Boehringer Ingelheim, Covidien, Daiichi Sankyo, Genzyme, Neuravi, Novartis, Pfizer; Royalties: for textbooks on neurology I have written. *Money paid to the institution.

REFERENCES

1. Haacke EM, Mittal S, Wu Z, et al. **Susceptibility-weighted imaging: technical aspects and clinical applications, part 1.** *AJNR Am J Neuroradiol* 2009;30:19–30
2. Flacke S, Urbach H, Keller E, et al. **Middle cerebral artery (MCA) susceptibility sign at susceptibility-based perfusion MR imaging: clinical importance and comparison with hyperdense MCA sign at CT.** *Radiology* 2000;215:476–82
3. Rovira A, Orellana P, Alvarez-Sabín J, et al. **Hyperacute ischemic stroke: middle cerebral artery susceptibility sign at echo-planar gradient-echo MR imaging.** *Radiology* 2004;232:466–73
4. Cho KH, Kim JS, Kwon SU, et al. **Significance of susceptibility vessel sign on T2*-weighted gradient echo imaging for identification of stroke subtypes.** *Stroke* 2005;36:2379–83
5. Weisstanner C, Gratz PP, Schroth G, et al. **Thrombus imaging in acute stroke: correlation of thrombus length on susceptibility-weighted imaging with endovascular reperfusion success.** *Eur Radiol* 2014;24:1735–41
6. El-Koussy M, Schenk P, Kiefer C, et al. **Susceptibility-weighted imaging of the brain: does gadolinium administration matter?** *Eur J Radiol* 2012;81:272–76
7. Adams HP Jr, Bendixen BH, Kappelle LJ, et al. **Classification of subtype of acute ischemic stroke: definitions for use in a multicenter clinical trial: TOAST—Trial of Org 10172 in Acute Stroke Treatment.** *Stroke* 1993;24:35–41
8. Furlan A, Higashida R, Wechsler L, et al. **Intra-arterial prourokinase for acute ischemic stroke: the PROACT II study—a randomized controlled trial. Prolyse in Acute Cerebral Thromboembolism.** *JAMA* 1999;282:2003–11
9. Pexman JH, Barber PA, Hill MD, et al. **Use of the Alberta Stroke Program Early CT Score (ASPECTS) for assessing CT scans in patients with acute stroke.** *AJNR Am J Neuroradiol* 2001;22:1534–42
10. Gratz PP, Jung S, Schroth G, et al. **Outcome of standard and high-risk patients with acute anterior circulation stroke after stent retriever thrombectomy.** *Stroke* 2014;45:152–58
11. Marder VJ, Chute DJ, Starkman S, et al. **Analysis of thrombi retrieved from cerebral arteries of patients with acute ischemic stroke.** *Stroke* 2006;37:2086–93
12. Brekenfeld C, Schroth G, El-Koussy M, et al. **Mechanical thromboembolectomy for acute ischemic stroke: comparison of the Catch thrombectomy device and the Merci retriever in vivo.** *Stroke* 2008;39:1213–19
13. Smith WS, Sung G, Saver J, et al. **Mechanical thrombectomy for acute ischemic stroke: final results of the Multi MERCI trial.** *Stroke* 2008;39:1205–12
14. Penumbra Pivotal Stroke Trial Investigators. **The Penumbra pivotal stroke trial: safety and effectiveness of a new generation of mechanical devices for clot removal in intracranial large vessel occlusive disease.** *Stroke* 2009;40:2761–68
15. Kidwell CS, Jahan R, Gornbein J. **A trial of imaging selection and endovascular treatment for ischemic stroke.** *N Engl J Med* 2013;368:914–23
16. Broderick JP, Palesch YY, Demchuk AM, et al. **Endovascular therapy after intravenous t-PA versus t-PA alone for stroke.** *N Engl J Med* 2013;368:893–903
17. Ciccone A, Valvassori L, Nichelatti M, et al. **Endovascular treatment for acute ischemic stroke.** *N Engl J Med* 2013;368:904–13
18. Pereira VM, Gralla J, Davalos A, et al. **Prospective, multicenter, single-arm study of mechanical thrombectomy using Solitaire Flow Restoration in acute ischemic stroke.** *Stroke* 2013;44:2802–7
19. Dávalos A, Pereira VM, Chapot R, et al. **Retrospective multicenter study of Solitaire FR for revascularization in the treatment of acute ischemic stroke.** *Stroke* 2012;43:2699–705
20. Jung S, Gilgen M, Slotboom J, et al. **Factors that determine penumbral tissue loss in acute ischaemic stroke.** *Brain* 2013;136:3554–60
21. Lima FO, Furie KL, Silva GS, et al. **The pattern of leptomeningeal collaterals on CT angiography is a strong predictor of long-term functional outcome in stroke patients with large vessel intracranial occlusion.** *Stroke* 2010;41:2316–22
22. Zanette EM, Roberti C, Mancini G, et al. **Spontaneous middle cerebral artery reperfusion in ischemic stroke: a follow-up study with transcranial Doppler.** *Stroke* 1995;26:430–33
23. Legrand L, Naggara O, Turc G, et al. **Clot burden score on admission T2*-MRI predicts recanalization in acute stroke.** *Stroke* 2013;44:1878–84

Early MRI Characteristics after MRI-Guided Laser-Assisted Cingulotomy for Intractable Pain Control

S.H. Sundararajan, P. Belani, S. Danish, and I. Keller

ABSTRACT

BACKGROUND AND PURPOSE: Cingulotomy is a well-accepted stereotactic procedure in the treatment of debilitating pain syndromes. At our institution, we used a 980-nm diode laser to perform MR imaging–guided laser-assisted cingulotomy. We report the early MR imaging changes associated with this technique.

MATERIALS AND METHODS: In this retrospective analysis, MR imaging–guided laser-assisted cingulotomy was performed in 4 patients with intractable pain secondary to metastatic disease. Patients were imaged at various time points postprocedure, with visual analysis of MR imaging changes in the cingulate gyri during that timeframe.

RESULTS: Twenty-four hours postablation, 4 distinct zones of concentric rings reminiscent of an “owl eye” shape were noted in the cingulate gyri. Extrapolating from the imaging characteristics of the rings, we defined each zone as follows: The central zone (zone 1) represents a laser probe void with fluid, zones 2 and 3 have signal characteristics that represent hemorrhage and leaked protein, and zone 4 has a peripheral ring of acute infarction, enhancement, and surrounding edema. One patient with 1-year follow-up showed persistent concentric rings with resolution of enhancement and edema.

CONCLUSIONS: Post-MR imaging–guided laser-assisted cingulotomy rings appear to represent a continuum of injury created by the laser probe and thermal injury. The imaging changes are similar to those described for laser ablation of tumor-infiltrated brain with a 1064-nm laser. This is the first study to characterize early MR imaging changes after MR imaging–guided laser-assisted cingulotomy by using a 980-nm laser. It is important for neuroradiologists and neurosurgeons to understand expected imaging findings as laser ablation cingulotomy re-emerges to treat intractable pain.

ABBREVIATION: MRgLAC = MR imaging–guided laser-assisted cingulotomy

The cingulate gyrus is an important part of the limbic system and is involved in the emotional response to pain.¹ Anterior cingulotomy has been a well-accepted stereotactic procedure in the treatment of both refractory obsessive-compulsive disorder and debilitating pain syndromes.^{2,3} The objective of cingulotomy is the severing of the supracallosal fibers of the cingulum bundle, which pass through the anterior cingulate gyrus.⁴

For several decades, the cingulate gyrus has been a surgical target to treat a variety of disorders.⁵ In 1948, open cingulotomy

were first described for the treatment of schizophrenia.⁶ In 1962, pneumoencephalographic guidance for performing closed-cingulotomy was introduced by Foltz and White⁷ for pain. In 1973, Balasubramaniam et al⁸ described the technique of stereotactic cingulotomy in the management of patients with alcohol addiction. This frame-based stereotactic approach combined pneumoencephalographic and angiographic guidance for well-defined resection of the cingulate gyri.

During the 1990s, early guidance techniques with the patient under general anesthesia were replaced by MR imaging guidance with the patient under local anesthesia. Since then, the procedure has been performed by using a radiofrequency probe with or without MR imaging stereotaxis.⁹ Hassenbusch et al¹⁰ created a spheric radiofrequency lesion in 4 patients by applying 75°C for 60 seconds by using this technique, for which he reported significant improvement of intractable pain. At our institution, we have recently introduced the use of a 980-nm diode laser to perform MR imaging–guided laser-assisted cingulotomy (MRgLAC).

Received November 2, 2014; accepted after revision January 15, 2015.

From the Department of Radiology (S.H.S., P.B.), Rutgers-Robert Wood Johnson Medical School, New Brunswick, New Jersey; Departments of Neurosurgery (S.D.) and Radiology (I.K.), Rutgers-Robert Wood Johnson Medical School and University Hospital, New Brunswick, New Jersey; and University Radiology Group (I.K.), East Brunswick, New Jersey.

Please address correspondence to Sri Hari Sundararajan, MD, Robert Wood Johnson Medical School, Department of Radiology, MEB 404, One Robert Wood Johnson Pl, New Brunswick, NJ 08903-0019; e-mail: ssundararajan@univrad.com; @radiolosi

<http://dx.doi.org/10.3174/ajnr.A4289>

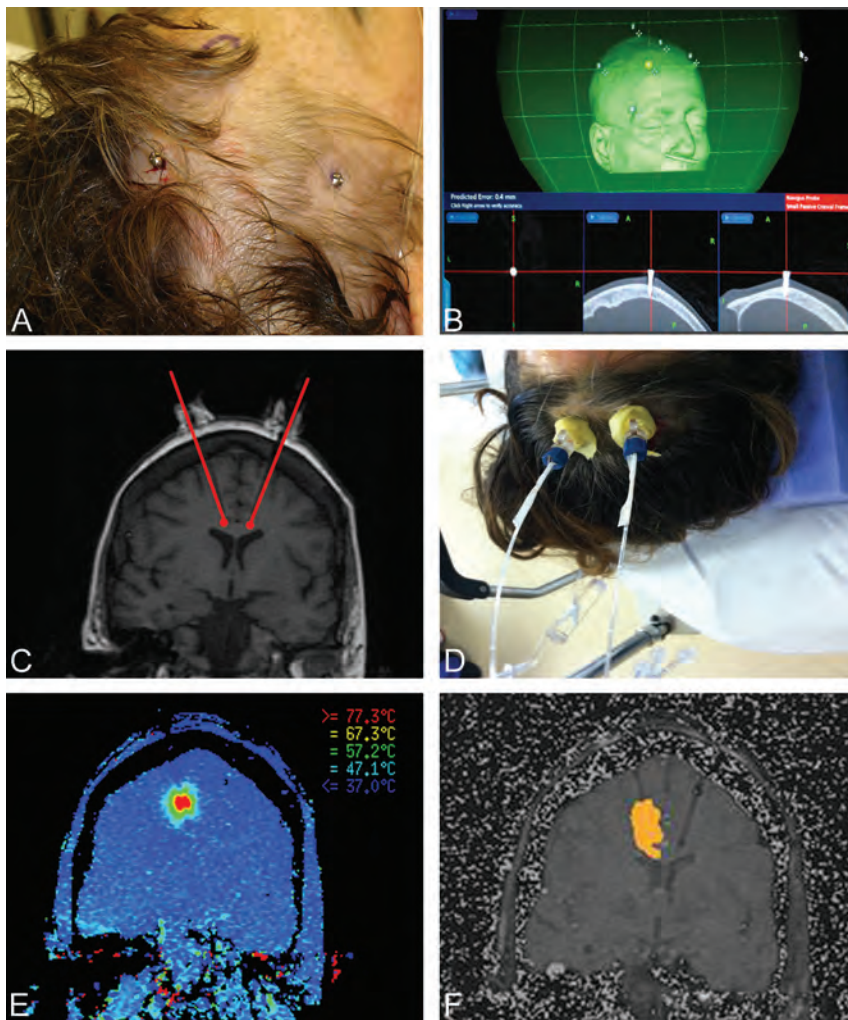


FIG 1. Fiducial markers are placed (A) with follow-up registration imaging performed for confirmed localization (B). Alignment of the navigation probe within a precision aiming device is ensured before it is locked into position (C and D). Thermal localization is performed to estimate approximate temperatures to be reached during MRgLAC to ensure that the temperature does not exceed 90°C. This is demonstrated by color gradients representing measured temperature gradients (E). Sequential real-time images obtained during MRgLAC of the right cingulum are then acquired. Note placement and location of the probes in both gyri and a steadily increasing region of thermal ablation in the right cingulate (F).

Patient demographics

Patient No.	Age (yr)	Sex	Metastatic Neoplasm	Post-MRgLAC Follow-Up
1	47	Female	Liposarcoma	24 hours
2	38	Female	Breast	24 hours
3	51	Female	Colon	24 hours
4	82	Female	Colon	1 year

MR imaging findings in patients after laser ablative cingulotomy have been previously described.⁹⁻¹² However, these studies reported only T1- and T2-weighted imaging features and lacked discussion of potential etiologies and evolution of reported signal changes. The multisequential MR imaging characteristics of laser-guided cingulotomy for patients with intractable pain have not been previously characterized, to our knowledge. The purpose of this study was to report the early MR imaging changes associated with cingulotomy by using a 980-nm diode laser. Our descriptions are based on the original work by Spangler et al,¹¹

who, in 1996, described the postoperative MR imaging characteristics of cingulotomies for the treatment of psychiatric disorders.

MATERIALS AND METHODS

Between 2012 and 2013, 4 patients were selected for laser ablation cingulotomy. These patients had systemic metastatic cancer, with a life expectancy of fewer than 6 months and intractable pain that was not relieved by conventional pain management. After review by a multidisciplinary tumor board, MRgLAC was offered as a palliative procedure for intractable pain management. All patients were enrolled in an institutional review board–approved protocol.

One-millimeter CT images (Light-Speed Pro 16; GE Healthcare, Milwaukee, Wisconsin) and postgadolinium axial T1 echo-spoiled gradient-echo and axial FLAIR MR images (Optima MR450w 1.5T with a GEM Suite; GE Healthcare) were obtained for preprocedural planning on a StealthStation S7 (Medtronic Navigation, Minneapolis, Minnesota). The FLAIR is a 2D sequence fused with the echo-spoiled gradient echo. This sequence is not necessary, but we have found it useful in certain cases in which the cingulate sulcus is not clearly visualized on the coronal reconstructions of the echo-spoiled gradient-echo sequence.

The targeting method was derived from that used by Richter et al.¹³ Two ablations within each cingulate gyrus were planned. A target point was placed approximately 20 mm posterior to the

tip of the frontal horn (y-coordinate), parallel with the roof of the lateral ventricle within the cingulate gyrus. The planning trajectory was made perpendicular to the long axis of the corpus callosum on the sagittal image.¹⁴

The patient was first placed under general anesthesia. After confirmation of the position and trajectory, an incision is made with a No. 15 scalpel. A twist drill craniotomy was created and used to pass the plastic bone anchor into the skull along the proper trajectory. Once in place, the laser-cooling catheter was passed to the appropriate depth and secured. The process was repeated on the contralateral side.¹⁴

The patient was transported with lasers in place to diagnostic MR imaging, where the laser catheters were connected to the Thermal Therapy System (Visualase, Houston, Texas). A T1 echo-spoiled gradient-echo coronal image was acquired as a reference image. We used an oblique coronal reference so that both ablations could be performed with the same reference image.

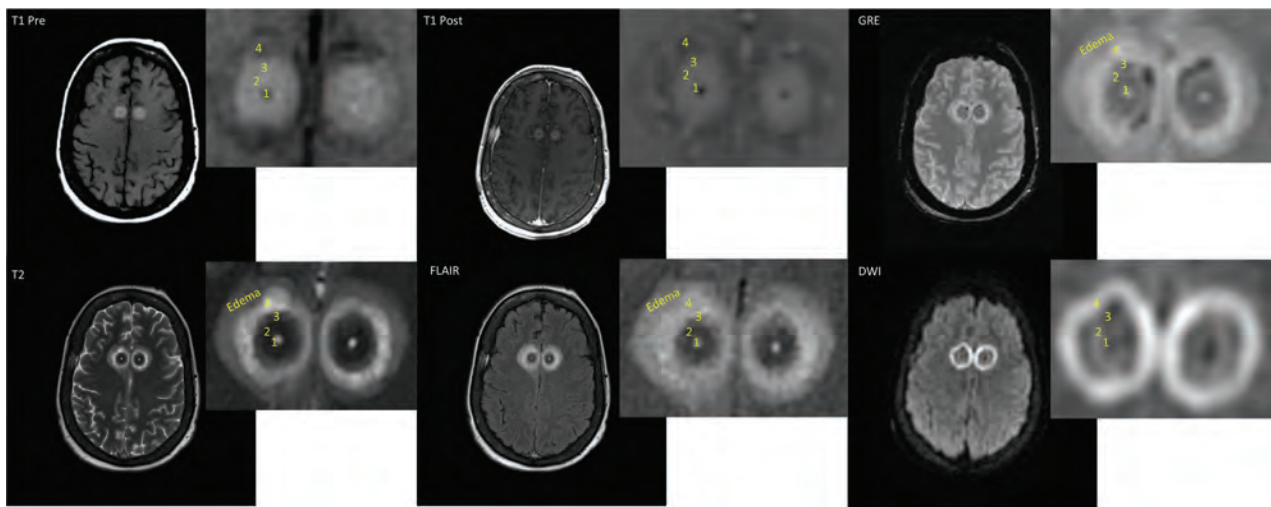


FIG 2. The above owl eye–appearing lesions are recorded 24 hours post-laser ablation of the cingulate gyri in patient 1. Four discrete zones are noted, labeled 1–4 from central to peripheral. All patients who underwent MRgLAC demonstrated this zonal distribution of signal abnormality.

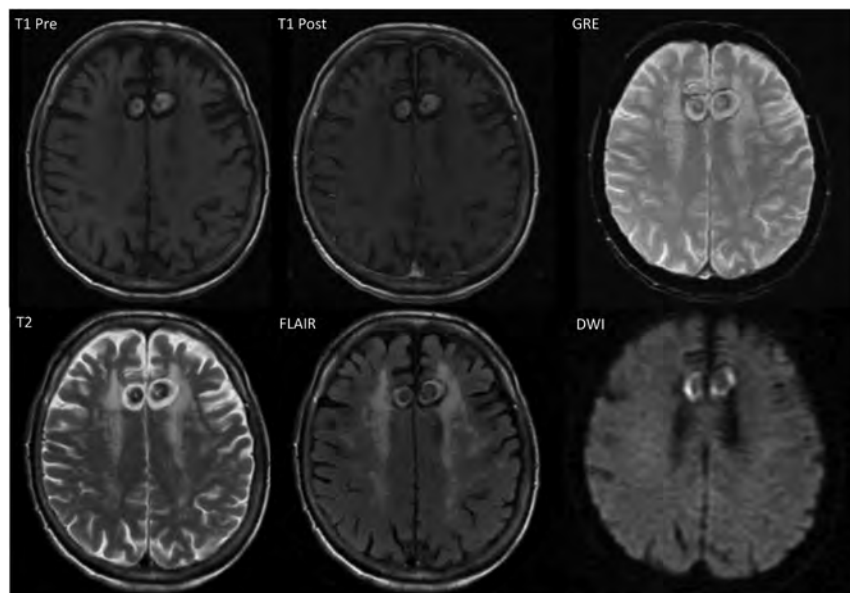


FIG 3. Imaging performed in patient 4 one year following MRgLAC demonstrates the persistent appearance of bilateral concentric zones of thermal ablation with a preserved owl eyes configuration. Note the lack of enhancement on postcontrast imaging, resolution of postprocedural edema, and T2-shinethrough on diffusion-weighted imaging.

High-temperature limits (90°C) were set near the tip of the applicators to avoid production of steam. Low temperature limits (50°C) were set at the borders of the target areas to avoid unintended thermal damage to nearby critical structures, such as the corpus callosum. Real-time thermal damage was estimated by an MR imaging pixel shift of the target tissue in response to thermal damage (Fig 1).^{14,15}

Two ablations were performed in each cingulum. The initial ablation was made within the anterior cingulate gyrus. The inferior ablation boundary was the corpus callosum. Medially, the ablation was bounded by the pia mater of the gyrus. Laterally, the ablation was bounded by the limits of the thermal energy distribution. The second ablation was performed to incorporate the medial prefrontal cortex and medial white matter. The superior

limit of the second ablation was kept below the subcortical U-fibers of the superior and middle frontal gyri. The total ablation volume within each cingulum was approximately 1.5 mL. Baseline immediate postablation imaging was performed at the conclusion of the procedure.

All patients were imaged immediately after and 24 hours after the procedure, with patient demographics as listed in the Table. Patient 4 unexpectedly survived, allowing 1-year follow-up imaging to be obtained in this patient also. Imaging sequences included T1, T1 postcontrast, T2, FLAIR postcontrast, gradient recalled-echo, DWI, and ADC mapping. Signal changes were graded as isointense, hypointense, or hyperintense relative to gray matter in the specific imaging sequence.

RESULTS

Postprocedural assessment of the 4 different patients after MRgLAC at 24 hours demonstrated a broad circular region of thermal-induced injury with 4 concentric rings in the bilateral cingulate gyri. These regions of varying signal intensity extended from the center to the periphery and were arbitrarily labeled zones 1–4 (Fig 2). These concentric rings persisted 1 year following thermal ablation in 1 patient (Fig 3).

Signal changes in the described zones were graded as hypointense, isointense, or hyperintense relative to the gray matter intensity of the sequence. Zone 1 demonstrated central T1 hypointensity with thin peripheral enhancement on postcontrast imaging. There was corresponding hyperintensity on T2 with correspondingly less intensity on FLAIR imaging. Gradient recalled-

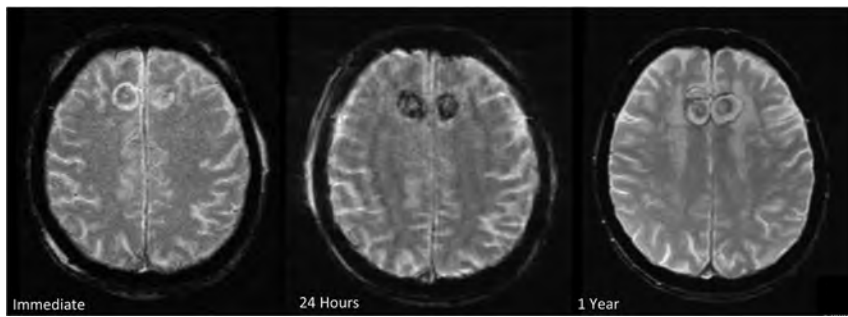


FIG 4. The following gradient recalled-echo images from patient 4 demonstrate evolution of postprocedural gradient-echo imaging changes related to MRgLAC. There is an interval increase in the magnetic susceptibility signal in zone 3 between the immediate and post-24 hour images. Note is made of residual peripheral magnetic susceptibility 1 year following the procedure.

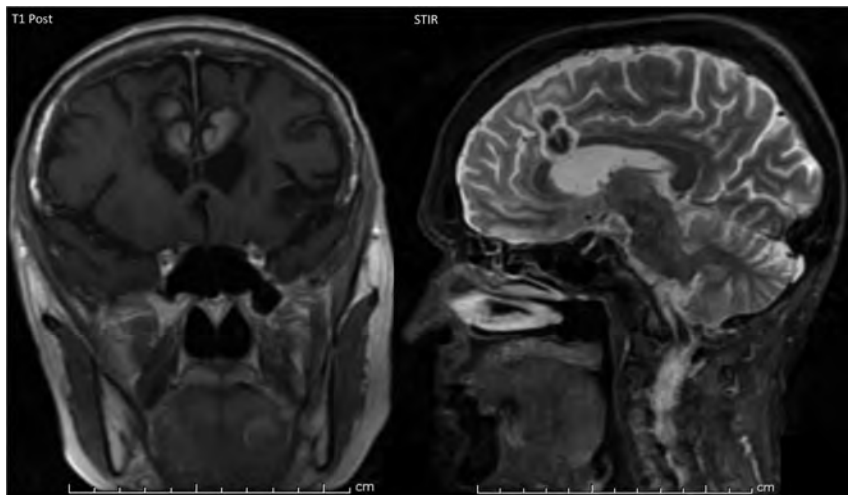


FIG 5. Coronal T1 postcontrast and sagittal STIR imaging performed on patient 4 one year following MRgLAC demonstrates 2 pairs of concentric rings in each cingulate. These correspond to the 2 adjacent areas of thermal ablation produced in each cingulum.

echo imaging showed no magnetic susceptibility in this location, and diffusion-weighted imaging showed no evidence of restricted diffusion in this location (Fig 2).

Zones 2 and 3 shared similar imaging characteristics. They were iso- to hyperintense on T1-weighted imaging and did not demonstrate enhancement on postcontrast imaging. A clearer distinction between zones 2 and 3 was noted on T2-weighted and FLAIR imaging, with a hypointense zone 2 and mixed hypo-/isointense zone 3 noted. Varying degrees of magnetic susceptibility were noted along the periphery of zone 3. No restricted diffusion was noted in either zone 2 or 3 (Figs 2 and 4).

Zone 4 was broader than the previously mentioned zones. The parenchyma within this zone demonstrated mixed iso-/hypointensity on T1-weighted imaging and was without enhancement on contrast-enhanced T1WI. Its characteristic signal properties included its true restricted diffusion with corresponding T2 and FLAIR hyperintensity. Variable magnetic susceptibility was seen, which could persist even up to 1 year. An ill-defined circumferential region of T2 and FLAIR hyperintensity corresponding to thermal-induced edema surrounded this zone. The 1-year follow-up MR imaging of patient 4 showed resolu-

tion of postprocedural edema, lack of enhancement on postcontrast imaging, and T2-shinethrough on diffusion-weighted imaging (Figs 2, 4, and 5).

DISCUSSION

Thermal ablation involves the deposition and absorption of light energy to generate controlled regions of volumetric heat distribution within a target tissue. Fiber optics are MR imaging-compatible and are used to target light energy deposition during thermal image-guided applications. The degree of volumetric heating induced within a given target tissue is determined by the wavelength of emitted light and the absorption peak of light of the target tissue at a given wavelength. The MR imaging concentric ring characteristics of thermal ablative therapy of the brain with radiofrequency ablation and 1048-nm lasers have been described previously. Those reports were based on imaging paradigms limited to T1 and T2 sequences obtained without gadolinium.⁹⁻¹²

Several notable factors distinguish our case series from previously reported thermal-ablative changes. Our retrospective study was performed on 4 patients who underwent MR imaging-guided laser ablation cingulotomy by using a state-of-the-art 980-nm laser. Radiofrequency ablation intracranial 1048-nm lasers are produced by a neodymium-doped yttrium aluminum garnet source. While they are effective in producing controlled zones of thermal ablation, some factors limiting their widespread utility include the high current consumption of the source, a power requirement of up to 220 V, and the need for active water cooling. In contrast, diode-based lasers producing lasers at a wavelength of 980 nm are capable of producing fast, precise, and tighter zones of ablation. Diode-based sources use semiconductors that lower both the laser's power requirement to 110 V and cooling requirement to air cooling. Furthermore, the absorption coefficient for water with a 980-nm laser being 3 times higher than that with a 1048-nm laser (0.482 versus 0.144 cm^{-1}) allows a greater rate of heating per unit of time.¹⁶

Our imaging sequences were also more extensive than the ones previously applied and included both pre- and postgadolinium sequences. This change allowed improved characterization of the lesions. T1, T2, postcontrast T1, FLAIR, gradient recalled-echo, and DWI pulse sequences were used in this study. The zones of thermal injury were evaluated within 24 hours of surgery in all our patients. Long-term follow-up imaging in these patients was not performed because our patient life expectancy for this pilot study was fewer than 6 months. However, patient 4 survived beyond the

Our imaging sequences were also more extensive than the ones previously applied and included both pre- and postgadolinium sequences. This change allowed improved characterization of the lesions. T1, T2, postcontrast T1, FLAIR, gradient recalled-echo, and DWI pulse sequences were used in this study. The zones of thermal injury were evaluated within 24 hours of surgery in all our patients. Long-term follow-up imaging in these patients was not performed because our patient life expectancy for this pilot study was fewer than 6 months. However, patient 4 survived beyond the

estimated life expectancy and was able to undergo follow-up imaging.

Four concentric zones of injury were identified on axial plane imaging. The 2 regions of thermal ablation produced in each cingulum are best appreciated on sagittal and coronal planes (Fig 3).

Zone 1 (the central zone) demonstrated hypointense signal on noncontrast T1WI and FLAIR sequences with corresponding rim enhancement on the postgadolinium FLAIR sequence. These findings represent a CSF-filled cleft produced by the void of the probe that is removed after ablation. Zones 2 and 3 demonstrated heterogeneous T1 signal without significant enhancement. Acute blood products may contribute to T1 shortening as denoted by the evolution of magnetic susceptibility in these zones. However, we believe the increased T1 signal in these zones is more related to leakage of intracellular proteins, given the relative discordance with corresponding magnetic susceptibility on gradient-echo imaging in some patients (Figs 2 and 4).

Zone 4 demonstrates restricted diffusion with associated hypointensity on ADC and patchy enhancement. Gross specimens from tissues treated with a 980-nm laser show hyperemic rings along the outermost margin of an ablated site that histologically represents thermal necrosis.¹⁶ As such, the noted signal changes in zone 4 are more suggestive of true infarction of the outermost layer, with patchy enhancement in this location likely related to a combination of postprocedural enhancement and enhancement from subacute infarction.

Unexpected imaging of patient 4 performed 1 year after MRgLAC confirmed this maintained zonal distribution. This follow-up imaging also showed resolution of postprocedural edema and maturation of zone 4 infarction, as noted by the lack of enhancement on postcontrast imaging and the lack of true restricted diffusion (Fig 3).

CONCLUSIONS

MRgLAC is a newly introduced technique to perform bilateral anterior cingulotomy for intractable pain control. The perioperative imaging changes seem similar to those described for laser ablation of tumor-infiltrated tissue with a 1064-nm laser. This is the first study to characterize early MR imaging changes after MRgLAC by using a 980-nm laser. We plan to expand this description by adding time points to the follow-up imaging and characterization of additional patients with future planned studies.

Disclosures: Shabbar Danish—UNRELATED: Payment for Lectures (including service on Speakers Bureaus); Medtronic, Comments: received honoraria as a faculty member for training courses.

REFERENCES

1. Vogt BA. Pain and emotion interactions in the subregions of the cingulate gyrus. *Nat Rev Neurosci* 2005;6:533–44
2. Harsh V, Viswanathan A. Surgical/radiological interventions for cancer pain. *Curr Pain Headache Rep* 2013;17:331
3. Christman D, Morrison C, Eljamel M, et al. Neurosurgery for mental disorders. *Adv Psychiatr Treat* 2004;10:189–99
4. Yen CP, Kuan CY, Sheehan J, et al. Impact of bilateral anterior cingulotomy on neurocognitive function in patients with intractable pain. *J Clin Neurosci* 2009;16:214–19
5. Brotis AG, Kapsalaki EZ, Paterakis K, et al. Historic evolutions of open cingulectomy and stereotactic cingulotomy in the management of medically intractable psychiatric disorders, pain and drug addiction. *Stereotact Funct Neurosurg* 2009;87:271–91
6. Ward AA Jr. The anterior cingulate gyrus and personality. *Res Publ Assoc Res Nerv Ment Dis* 1948;27:438–45
7. Foltz EL, White LE Jr. Pain 'relief' by frontal cingulotomy. *J Neurosurg* 1962;19:89–100
8. Balasubramaniam V, Kanaka TS, Ramanujam PB. Stereotaxic cingulotomy for drug addiction. *Neurol India* 1973;21:63–66
9. De Salles AA, Brekhus SD, De Souza EC, et al. Early postoperative appearance of radiofrequency lesions on magnetic resonance imaging. *Neurosurgery* 1995;36:932–36; discussion 936–37
10. Hassenbusch SJ, Pillay PK, Barnett GH. Radiofrequency cingulotomy for intractable cancer pain using stereotaxis guided by magnetic resonance imaging. *Neurosurgery* 1990;27:220–23
11. Spangler WJ, Cosgrove GR, Ballantine HT Jr, et al. Magnetic resonance image-guided stereotactic cingulotomy for intractable psychiatric disease. *Neurosurgery* 1996;38:1071–76; discussion 1076–78
12. Schwabe B, Kahn T, Harth T, et al. Laser-induced thermal lesions in the human brain: short- and long-term appearance on MRI. *J Comput Assist Tomogr* 1997;21:818–25
13. Richter EO, Davis KD, Hutchison WD, et al. Cingulotomy for psychiatric disease: microelectrode guidance, a callosal reference system for documenting lesion location, and clinical results. *Neurosurgery* 2004;54:622–28; discussion 628–30
14. Jethwa PR, Barrese JC, Gowda A, et al. Magnetic resonance thermometry-guided laser-induced thermal therapy for intracranial neoplasms: initial experience. *Neurosurgery* 2012;71(1 suppl operative):133–44; 144–45
15. Rieke V, Pauly KB. MR thermometry. *J Magn Reson Imaging* 2008;27:376–90
16. Ahrar K, Gowda A, Javadi S, et al. Preclinical assessment of a 980-nm diode laser ablation system in a large animal tumor model. *J Vasc Interv Radiol* 2010;21:555–61

Intravenous Infusion of Nitroglycerine Leads to Increased Permeability on Dynamic Contrast-Enhanced MR Imaging in Pig Brains

J. Carl, D.A. Tideman, S. Ravn, K. Lund, S.O. Magnisdottir, and B. Kjærgaard

ABSTRACT

BACKGROUND AND PURPOSE: It has been suggested that off-label use of transdermal nitroglycerine patches to prevent frostbite may lead to severe acute mountain sickness and ataxia. The aim of this study was to investigate the effect of nitroglycerine on brain vascular permeability by using dynamic contrast-enhanced MR imaging in a swine model.

MATERIALS AND METHODS: Eight Danish Landrace-Yorkshire-Danish Landrace pigs of approximately 20–25 kg were scanned with a dynamic contrast-enhanced MR perfusion protocol with and without nitroglycerine intravenous infusion. Compartmental analysis was performed on the basis of the Tofts model, and voxel-based quantitative values of the volume transfer constants from the vascular to the extracellular space were determined.

RESULTS: The scan with nitroglycerine infusion resulted in significantly higher volume transfer constant values than values derived from the first scan without nitroglycerine infusion. Increased volume transfer constant values were observed in 6 of 8 animals.

CONCLUSIONS: Infusion of nitroglycerine increases the vascular permeability of the swine brain on the basis of the transfer constant estimated from dynamic contrast-enhanced MR imaging.

ABBREVIATIONS: DCE-MR = dynamic contrast-enhanced MR imaging; ISP = IntelliSpace Portal; K^{trans} = volume transfer constant from the vascular to the extracellular space; MANOVA = multivariate analysis of variance; NTG = nitroglycerine

Nitroglycerine (NTG) or nitrates are old drugs that were introduced into medical treatment >100 years ago for angina pectoris. The typical hemodynamic, anti-ischemic effects in humans were described in the 1950s and 1960s and are mediated through the release of nitric oxide in the walls of blood vessels, leading to relaxation of vascular smooth-muscle tone.^{1,2}

Acute mountain sickness may affect mountaineers in high altitudes and has been ascribed to intracranial hypertension caused by extracellular vasogenic edematous brain swelling after mechanical disruption of the blood-brain barrier due to hypoxia.³ Off-label use of transdermal NTG patches to prevent frostbite may lead to severe acute mountain sickness and ataxia.³ Nitrate-induced cerebral vasodilation and high-altitude cerebral edema are theoretically possible on a pathophysiologic basis. Others have suggested that acute mountain sickness may be associated with

altered redox homeostasis and disordered cerebral autoregulation independent of barrier disruption.^{4,5} The cerebral hemodynamic effects of vasodilators are of clinical interest because a decrease in mean arterial pressure might alter global cerebral blood flow and brain perfusion. Increased permeability of the blood-brain barrier has been observed in NTG-treated animals (common carp, *Cyprinus carpio* L) on the basis of Evans blue capillary leakage into the brain tissue.⁶

New imaging techniques to study brain perfusion and vascular permeability have emerged in the past few decades. One such technique is dynamic contrast-enhanced T1-weighted MR imaging (DCE-MR) by using diffusible agents such as gadopentetate dimeglumine.⁷ DCE-MR has the potential of characterizing abnormal capillary leakage. The use of pharmacokinetic compartment models to analyze DCE-MR data and obtain standardized quantitative parameters has been refined in recent years.⁸ These refinements have included the definition of the volume transfer constant (K^{trans}) (minute^{-1}) in the Tofts model, which represents the permeability surface area product per unit volume of tissue under permeability-limited or high-flow conditions.⁷ DCE-MR has been used in an MR imaging-integrated real-time swine intracerebral hemorrhage model to study acute hematoma growth and contrast extravasation.⁹ The purpose of the present study was

Received September 25, 2014; accepted after revision January 2, 2015.

From the Department of Medical Physics, Oncology (J.C., D.A.T., S.R., K.L.), and Biomedical Research Laboratory (S.O.M., B.K.), Aalborg University Hospital, Aalborg, Denmark.

Please address correspondence to Jesper Carl, PhD, Department of Medical Physics, Oncology, Aalborg University Hospital, Hobrovej 18–22, 9000 Aalborg, Denmark; e-mail: jhc@rn.dk

<http://dx.doi.org/10.3174/ajnr.A4279>

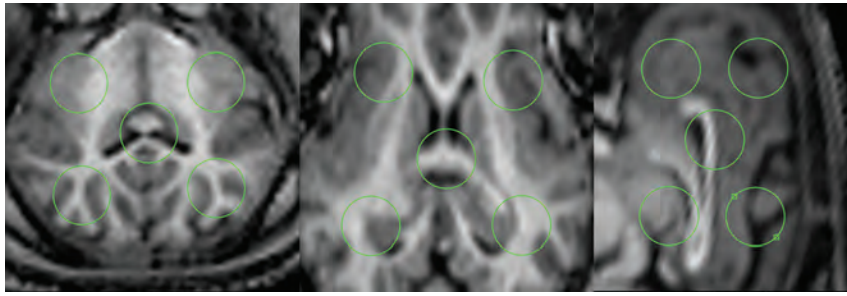


FIG 1. Example of the 5 ROIs (green circles) for reading mean K^{trans} in each of the 3 different T1 turbo field echo scan planes of a pig brain. Panels from left to right are the axial, coronal, and sagittal planes.

to investigate the effect on brain permeability of administration of NTG by using DCE-MR in a swine model. The study was approved by the Danish Animal Experiments Inspectorate, reference number 2104-15-0201-00029.

MATERIALS AND METHODS

Eight Danish Landrace-Yorkshire-Danish Landrace pigs of approximately 20–25 kg were used in the present study. The animals were anesthetized by using tiletamine-zolazepam (Zoletil), a mixture of 2 dissociative anesthetics (ketamine, 6.25 mg/mL, and tiletamine, 6.25 mg/mL), a benzodiazepine (Zolazepam 6.25 mg/mL), a synthetic opioid (butorphanol, 1.25 mg/mL), and xylazine (6.5 mg/mL); the mixture contains sedative, hypnotic, analgesic, and muscle-relaxing properties. This mixture was administered as an intramuscular injection at 1 mL/10 kg/h for a total of 2–2.5 mL every hour. After sedation was initiated, the animals were subsequently transferred to the scanner room. The animals were placed in a vacuum cushion on a table in a 3T MR imaging scanner (Ingenia 3T; Philips Healthcare, Best, the Netherlands) with the head and brain positioned within the standard head coil (15-channel dStream HeadSpine coil; Philips). The animals were first scanned with a 3D T1 axial turbo field echo anatomy protocol with TR = 8.1 ms, TE = 3.7 ms, and voxel size = $0.9 \times 0.9 \times 1 \text{ mm}^3$. This scanning was used to obtain a high-resolution image of the anatomy in the pig's brain. Subsequently, the animals were scanned with a DCE-MR perfusion protocol. The DCE-MR protocol consisted of the following 3 scan sequences: a 3D T1 fast-field echo prescan sequence with flip angle = 6° , TR = 50 ms, TE = 1.7 ms, and voxel size = $2.5 \times 2.5 \times 5.0 \text{ mm}^3$. This sequence was followed by an identical prescan sequence, but with a flip angle of 16° . Finally, a dynamic 3D T1 turbo field echo sequence with a TR = 4 ms, TE = 1.7 ms; the same voxel size as in the prescans; and 12° flip angles was used during the contrast infusion. All images had a 5-mm section thickness and 2.5-mm separation. Volume images were sampled at 4-second intervals for up to 7 minutes (434 seconds). For the dynamic acquisition, the MR imaging gadolinium contrast agent (gadoterate dimeglumine, Dotarem, 0.5 nm/mL; Guerbet, Aulnay-sous-Bois, France) was administered intravenously into an ear vein. With an automated injector, we administered a total of 2.5 mL of Dotarem at 3 mL/s followed by a 20-mL saline flush.

Compartment analysis was performed by using the MR perfusion tool in IntelliSpace Portal (ISP, Version 5; Philips), which uses the Tofts model.⁷ The ISP software uses the 2 flip angle pres-

cans to estimate a true T1 relaxation map of the brain tissue. The ISP software then recalibrates the intensity in the DCE-MR dynamic series by using the T1 relaxation map, the Dotarem r1 relaxation constant of $3.9 \text{ seconds}^{-1} \times \text{mmol}^{-1}$, and a hematocrit value of 45%. After calibration, the MR signal is proportional to the concentration of the gadolinium concentration in the tissue. ISP then uses the recalibrated MR signal in a compartmental analysis based on the Tofts model.⁷ The standard arterial input function derived from a human population was used in the ISP software (population-averaged arterial input function) for the compartmental analysis with the Tofts model. The ISP analysis provided parametric volume images of the estimated tracer kinetic parameters in the Tofts model. This study particularly focused on the parametric images of K^{trans} in the brain.

The animals were scanned on 2 different days, 2 weeks apart. On the first scanning day, the animals were subjected to 2 consecutive DCE-MR images, both without NTG, to evaluate the reproducibility of the method. On the second scanning day, the animals were subjected first to a DCE-MR image without NTG and, subsequently, a scan after NTG infusion. Before scanning, we loaded the injector with a 50- $\mu\text{g/mL}$ NTG solution. The solution was injected at a rate of 0.07 mL/s for 5 minutes. Infusion started immediately before the first prescan in the DCE-MR protocol. The total injected dose of NTG was 40 $\mu\text{g/kg}$ during 5 minutes. After scanning, 15 circular ROIs were drawn on the image planes in the brain by 1 radiographer independent of the later statistical analysis. Each ROI had an area of 80 mm^2 and was placed in a standardized and evenly distributed way in all 3 image planes, as shown in Fig 1. For each ROI, the mean value of K^{trans} was calculated by using the ISP software. Statistical analysis was performed by using Statistica software (StatSoft, Tulsa, Oklahoma).

RESULTS

On the first scanning day, only 7 animals were scanned because scanning in 1 animal had to be abandoned due to respiratory distress symptoms when lying in the supine position. All 8 animals were scanned successfully on the second scanning day. Figure 2 demonstrates the effect of NTG infusion on the permeability in brain tissue. Increased permeability is observed as areas of confluent purple against the normal black background in the brain tissue when comparing the K^{trans} parametric images with and without NTG infusion. The distribution of K^{trans} values determined from the K^{trans} maps was skewed; therefore, the numbers had to be logarithmically transformed to obtain a normal distribution of K^{trans} values. Subsequently, multivariate analysis of variance (MANOVA) was applied by using K^{trans} in the 2 subsequent DCE-MR images as dependent variables and animal ear tag, position, and image plane of ROI as categorical predictors. Valid MANOVA assumptions were tested by using a P-P plot to demonstrate normal distribution of $\log(K^{trans})$ values qualitatively and the Levene test for variance homogeneity. Thus, mean K^{trans}

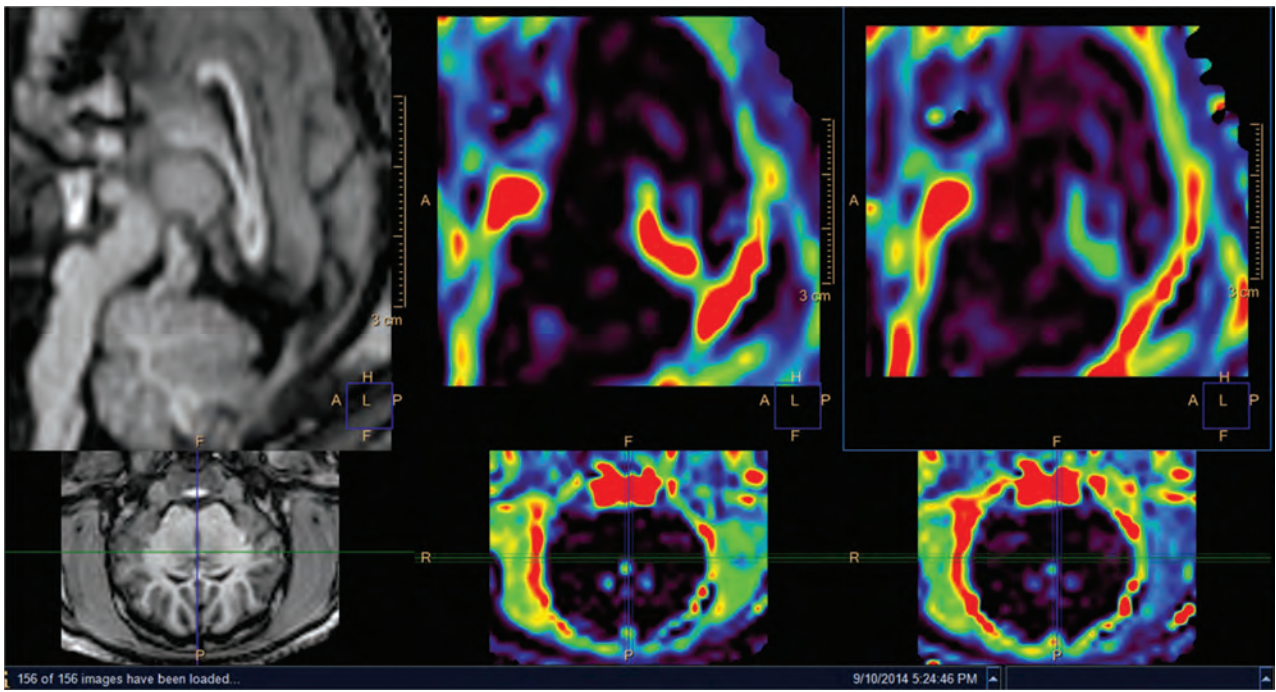


FIG 2. Left panel: axial and sagittal views of pig brain T1 turbo field echo scan. Middle panel: corresponding parametric K^{trans} maps determined from a DCE-MR image of the same pig brain. Right panel: corresponding axial and sagittal views and similar parametric K^{trans} maps determined from a DCE scan of the same pig brain after continuous infusion of nitroglycerine.

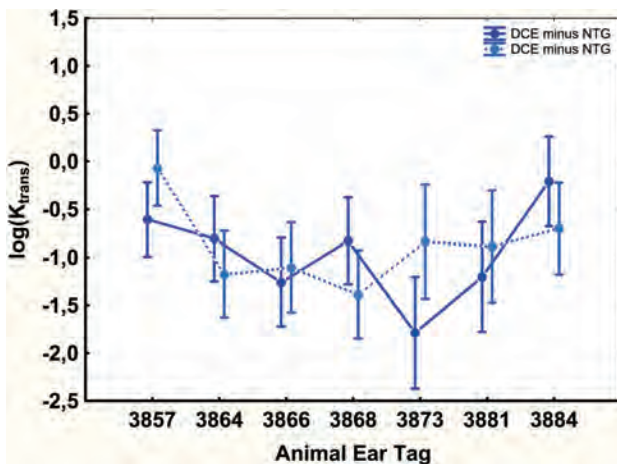


FIG 3. Plot of $\log(K^{trans})$ from 7 different pigs (ear tag). The plot represents the mean values (filled circles) and the 95% confidence interval of the mean (error bars) for each animal. Means and SDs were determined by using a MANOVA analysis on 15 evenly distributed ROIs in the K^{trans} volume map in the brain of each pig. The plot represents data from 2 different DCE-MR images obtained subsequently on the same day in each animal. K^{trans} values determined in the 2 subsequent DCE-MR images, the first scan (dark blue solid line) and the second scan (light blue dotted line).

values in subsequent DCE-MR images in each animal could be corrected to influence the ROI from the position and image plane.

On the first scanning day, both DCE-MR images were obtained without infusion of NTG. The MANOVA analysis showed no significant changes in K^{trans} values between the first and second (subsequent) DCE-MR images. Consequently, K^{trans} values were reproducible for all 7 animals within the same scanning day, as demonstrated in Fig 3. On the second scanning day, the first DCE-MR image was obtained as on the first scanning day. Before

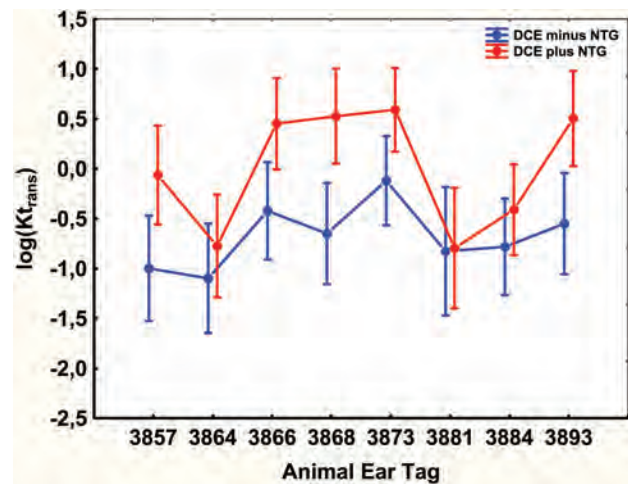


FIG 4. Plot of $\log(K^{trans})$ from 8 different pigs (ear tag). The plot represents mean values (filled circles) and the 95% confidence interval of the mean (error bars) of each animal. Means and SDs were determined by using a MANOVA analysis of 15 evenly distributed ROIs in the K^{trans} volume map in the brain of each pig. The plot represents data from 2 different DCE-MR images obtained subsequently on the same day in each animal. K^{trans} values are from the first DCE-MR image (dark blue solid line) and the second DCE-MR image after infusion of nitroglycerine (red solid line).

the second DCE-MR image on the second scanning day, NTG was infused. Using the MANOVA analysis, we observed statistically significant higher estimated K^{trans} values in 6 of the 8 animals after NTG infusion compared with values derived from the scan with no NTG infusion. The increase in K^{trans} following NTG administration is shown in Fig 4. The corresponding values from the plot in Fig 4 are tabulated in Table 1. Analogously, similar results were obtained by using a paired t test of log-transformed K^{trans} values for each animal, as shown in Table 2.

Table 1: Mean and standard error of the mean versus animal ear tag from the MANOVA analysis performed on $\log(K^{trans})$ and plotted in Fig 4^a

Animal Ear Tag	Mean (-NTG)	SE (-NTG)	Mean (+NTG)	SE (+NTG)
3857	-1.00	0.26	-0.06	0.25
3864	-1.10	0.28	-0.78	0.26
3866	-0.42	0.25	0.45	0.23
3868	-0.65	0.25	0.53	0.24
3873	-0.12	0.22	0.59	0.21
3881	-0.83	0.32	-0.80	0.30
3884	-0.78	0.24	-0.41	0.23
3893	-0.55	0.25	0.50	0.24

Note:—SE indicates standard error.

^a The error bars in Fig 4 indicate the 95% confidence interval of the mean.

Table 2: The P values in the last column show results from the paired t test analysis on $\log(K^{trans})$ in pig brains estimated from DCE-MR^a

Animal Ear Tag	K^{trans} (95% CI)		Paired t Test $\log(K^{trans})$
	-NTG (min^{-1})	+NTG (min^{-1})	
3857	0.4 (0.2–0.9)	1.0 (0.4–2.3)	$P = .0003^b$
3864	0.4 (0.2–0.9)	0.5 (0.2–1.3)	$P = .25$
3866	0.7 (0.3–1.8)	1.7 (0.9–3.1)	$P = .002^b$
3868	0.6 (0.2–1.5)	1.8 (1.1–2.8)	$P = .02^b$
3873	0.8 (0.4–1.7)	1.7 (0.9–3.0)	$P = .003^b$
3881	0.7 (0.3–1.7)	0.7 (0.2–1.7)	$P = .72$
3884	0.5 (0.2–1.1)	0.6 (0.3–1.4)	$P = .02^b$
3893	0.6 (0.3–1.3)	1.8 (1.0–3.3)	$P = .002^b$

^a The t test demonstrated significantly higher values after intravenous infusion of nitroglycerine in 6 of 8 animals. The columns -NTG and +NTG represent back-transformed values with and without nitroglycerine, respectively.

^b Significant.

DISCUSSION

This study demonstrated increased brain permeability estimated on DCE-MR after NTG was administered intravenously in a swine model. To our knowledge, this is the first time DCE-MR has been used to visualize and measure the effects of NTG in the brain. The present study demonstrated a significant increase in brain permeability during the infusion of NTG in 6 of 8 animals. Only a relatively small number of studies exist on changes in brain functionality after the use of NTG in humans. The effects on cerebral hemodynamics from NTG administration as described in the literature are not fully understood and are sometimes ambiguous. Studies using MR angiography have demonstrated that NTG in humans increases the diameters of basal cerebral arteries.^{10,11} Intravenous infusion of NTG, 0.1–0.5 $\mu\text{g}/\text{kg}$, in healthy human volunteers has been studied by using $\text{H}_2[^{15}\text{O}]\text{-PET}$, and the study has shown that nitroglycerin increased global CBF.¹² However, the use of transdermal NTG (5 mg) in patients with acute stroke was not associated with changes in CBF, cerebral perfusion pressure, or cerebral steal when studied by using xenon-enhanced CT.¹³ Accordingly, others have demonstrated that the blood oxygen level–dependent MR signal was inversely related to CBF but did not change during administration of NTG in humans. This finding could indicate that NTG only exerts an effect on the large vessels.¹⁴ However, other studies have demonstrated contrary results. For example, the use of near-infrared spectrometry measuring cerebral oxygen saturation has demonstrated that NTG supports or may increase brain oxygenation.^{15,16} Analogously, another study demonstrated increased vascular diam-

eter, blood flow, and endothelial permeability by using a different vasodilator, captopril (nitric oxide donor), in both in vitro and in vivo models.¹⁷ The results obtained in this study also indicate that the infusion of NTG has a significant effect on the vascular permeability in the brain of some but not all animals.

Large vessels in the brain may mimic increased permeability. When we placed the circular measuring areas in the 3 image planes in the brain, areas with large vessels were avoided. However, this was not entirely possible and may be why K^{trans} values in some cases were relatively high, considering that an intact BBB is virtually impermeable to standard gadolinium-based contrast agents. This risk of including large vessels was the reason for using the MANOVA analysis with both animal reading plane and circle position as independent variables. Further studies are needed to understand this effect in detail. A better understanding of the mechanisms behind the effect of NTG on brain vasculature and hemodynamics is important because it might modulate the mechanisms of other drugs crossing the blood-brain barrier.¹⁸ Thus, it may implicate a therapeutic advantage in combining NTG with drugs that need to have a higher general availability in the brain.

CONCLUSIONS

Infusion of nitroglycerine increases the vascular permeability of the swine brain on the basis of the transfer constant estimated from dynamic contrast-enhanced MR imaging. Significantly increased permeability was observed in the brains of 6 of 8 Danish Landrace-Yorkshire-Danish Landrace pigs.

REFERENCES

- Lichtlen PR. The mechanism of action of nitrates, 1988 status [in German]. *Z Kardiol* 1989;78(suppl 2):3–10; discussion 64–67
- Dewey M, Hoffmann H, Hamm B. Multislice CT coronary angiography: effect of sublingual nitroglycerine on the diameter of coronary arteries. *Rofo* 2006;178:600–04
- Mazzuero G, Mazzuero A, Pascariello A. Severe acute mountain sickness and suspect high altitude cerebral edema related to nitroglycerin use. *High Alt Med Biol* 2008;9:241–43
- Bailey DM, Bärtsch P, Knauth M, et al. Emerging concepts in acute mountain sickness and high-altitude cerebral edema: from the molecular to the morphological. *Cell Mol Life Sci* 2009;66:3583–94
- Cochand NJ, Wild M, Brugniaux JV, et al. Sea-level assessment of dynamic cerebral autoregulation predicts susceptibility to acute mountain sickness at high altitude. *Stroke* 2011;42:3628–30
- Kovacic S, Petrincic Z, Matasin Z, et al. Increased permeability of the blood-brain barrier following administration of glyceryl trinitrate in common carp (*Cyprinus carpio* L.). *Coll Antropol* 2008;32(suppl 1):99–103
- Tofts PS, Brix G, Buckley DL, et al. Estimating kinetic parameters from dynamic contrast-enhanced T(1)-weighted MRI of a diffusible tracer: standardized quantities and symbols. *J Magn Reson Imaging* 1999;10:223–32
- Tofts PS. Optimal detection of blood-brain barrier defects with Gd-DTPA MR: the influences of delayed imaging and optimised repetition time. *Magn Reson Imaging* 1996;14:373–80
- Aviv RI, Huynh T, Huang Y, et al. An in vivo, MRI-integrated real-time model of active contrast extravasation in acute intracerebral hemorrhage. *AJNR Am J Neuroradiol* 2014;35:1693–99
- Niehaus L, Gottschalk S, Weber U. Effect of drug-induced vasodilation of basal brain arteries with nitroglycerin on blood flow velocity and volume flow in the middle cerebral artery [in German]. *Ultraschall Med* 1998;19:225–29
- Siepmann M, Kirch W. Effects of nitroglycerine on cerebral blood

- flow velocity, quantitative electroencephalogram and cognitive performance. *Eur J Clin Invest* 2000;30:832–37
12. Bednarczyk EM, Wack DS, Kassab MY, et al. **Brain blood flow in the nitroglycerin (GTN) model of migraine: measurement using positron emission tomography and transcranial Doppler.** *Cephalalgia* 2002;22:749–57
 13. Willmot M, Ghadami A, Whysall B, et al. **Transdermal glyceryl trinitrate lowers blood pressure and maintains cerebral blood flow in recent stroke.** *Hypertension* 2006;47:1209–15
 14. Asghar MS, Hansen AE, Pedersen S, et al. **Pharmacological modulation of the BOLD response: a study of acetazolamide and glyceryl trinitrate in humans.** *J Magn Reson Imaging* 2011;34:921–27
 15. Kadoi Y, Saito S, Morita T, et al. **The differential effects of prostaglandin E1 and nitroglycerin on regional cerebral oxygenation in anesthetized patients.** *Anesth Analg* 1997;85:1054–59
 16. Hare GM. **Nitroglycerin and cerebral oxygen saturation.** *Can J Anaesth* 2008;55:52–53; author reply 53
 17. Jia L, Wong H. **In vitro and in vivo assessment of cellular permeability and pharmacodynamics of S-nitrosylated captopril, a nitric oxide donor.** *Br J Pharmacol* 2001;134:1697–704
 18. Abe H. **Effects of combination of vasodilator drugs and hypertonic solutions on methotrexate distribution into the rat brain.** *Jpn J Pharmacol* 1988;48:373–76

Deconstructive and Reconstructive Techniques in Treatment of Vertebrobasilar Dissecting Aneurysms: A Systematic Review and Meta-Analysis

Ö. Sönmez, W. Brinjikji, M.H. Murad, and G. Lanzino



ABSTRACT

BACKGROUND AND PURPOSE: Various endovascular techniques have been applied to the treatment of vertebrobasilar dissecting aneurysms, including parent artery preservation with coiling, stent placement or flow diverter placement, and trapping and proximal occlusion. We performed a systematic review and meta-analysis to study clinical and angiographic outcomes of patients undergoing endovascular treatment of vertebrobasilar dissecting aneurysms.

MATERIALS AND METHODS: We performed a comprehensive literature search for studies on the endovascular treatment of vertebrobasilar dissecting aneurysms. From each study we abstracted the following data: immediate occlusion, long-term occlusion, long-term good neurologic outcome, perioperative morbidity, perioperative mortality, rebleed (ruptured only), recurrence, and retreatment. We performed subgroup analyses of patients undergoing deconstructive-versus-reconstructive techniques. Meta-analysis was performed by using a random effects model.

RESULTS: Seventeen studies with 478 patients were included in this analysis. Sixteen studies had at least 6 months of clinical/angiographic follow-up. Endovascular treatment was associated with high rates of long-term occlusion (87.0%; 95% CI, 74.0%–94.0%) and low recurrence (7.0%; 95% CI, 5.0%–10.0%) and retreatment rates (3.0%; 95% CI, 2.0%–6.0%). Long-term good neurologic outcome was 84.0% (95% CI, 65.0%–94.0%). Deconstructive techniques were associated with higher rates of long-term complete occlusion compared with reconstructive techniques (88.0%; 95% CI, 35.0%–99.0% versus 81.0%; 95% CI, 64.0%–91.0%; $P < .0001$). Deconstructive and reconstructive techniques were both associated with high rates of good neurologic outcome (86.0%; 95% CI, 68.0%–95.0% versus 92.0%; 95% CI, 86.0%–95.0%; $P = .10$).

CONCLUSIONS: Endovascular treatment of vertebrobasilar dissecting aneurysms is associated with high rates of complete occlusion and good long-term neurologic outcomes. Deconstructive techniques are associated with higher occlusion rates. There was no statistical difference in neurologic outcomes between groups, possibly due to low power.

ABBREVIATION: VBDA = vertebrobasilar dissecting aneurysms

The best therapeutic choice for treatment of vertebrobasilar dissecting aneurysms (VBDA) is controversial. Ruptured VBDA are associated with a poor natural history with high rates of rebleed, stroke, and death when left untreated.¹ Unruptured VBDA have a benign clinical course when not associated with

stroke or mass effect; however, they are prone to rupture and stroke when symptomatic.^{2,3} Surgical and endovascular treatment of these lesions has proved successful. Endovascular therapies have emerged as the treatment of choice due to perceived lower rates of treatment-related morbidity as well as their efficacy. However, a number of endovascular approaches to the treatment of VBDA exist. Parent artery occlusion or trapping of the aneurysm was the initial treatment of choice. With the advent of stents and flow diverters however, parent artery preservation has emerged as an effective treatment technique.

Because most series on the treatment of VBDA are small single-center case series, the safety and efficacy of the various endovascular treatments for these lesions have not been well established. Specifically, little is known regarding whether newer, parent artery preservation techniques are associated with similar

Received November 13, 2014; accepted after revision January 9, 2015.

From the Departments of Neurosurgery (Ö.S., G.L.) and Radiology (W.B.) and Center for Science of Healthcare Delivery (M.H.M.), Mayo Clinic, Rochester, Minnesota.

Please address correspondence to Waleed Brinjikji, MD, Mayo Clinic, Department of Radiology, 200 1st St SW, Rochester, MN 55901; e-mail: brinjikji.waleed@mayo.edu; @WBrinjikji



Indicates article with supplemental on-line photo.



Evidence-Based Medicine Level 1.

<http://dx.doi.org/10.3174/ajnr.A4360>

Table 1: Summary of studies

Author, Year	No. of Patients	No. Ruptured	No. Unruptured	Reconstructive Techniques	Deconstructive Techniques	Mean Follow-Up
Jin et al, 2009 ¹⁵	42	29	13	9	33	30 Mo
Kai et al, 2011 ¹⁸	8	0	8	0	8	24 Mo
Kashiwazaki et al, 2013 ¹³	73	45	28	0	73	56 Mo
Kim et al, 2011 ⁷	119	73	46	62	57	13 Mo
Luo et al, 2005 ²²	10	0	10	0	10	15 Mo
Park et al, 2009 ¹²	27	11	16	27	0	12 Mo
Purkayastha et al, 2006 ²³	8	8	0	0	8	37 Mo
Rabinov et al, 2003 ¹⁶	26	21	5	0	26	40 Mo
Rho et al, 2013 ²⁴	5	5	0	5	0	40 Mo
Suh et al, 2009 ²⁵	11	11	0	11	0	15 Mo
Tsuura et al, 1999 ²⁶	12	12	0	0	12	6 Mo
Wakhloo et al, 2008 ⁸	8	2	6	8	0	37 Mo
Wang et al, 2013 ²⁷	11	3	8	2	9	10 Mo
Yamaura et al, 1999 ²⁸	6	6	0	0	6	12 Mo
Yoon et al, 2010 ¹¹	24	6	18	24	0	16 Mo
Yuki et al, 2005 ¹⁷	29	29	0	0	29	5.3 Days
Zhao et al, 2013 ¹⁰	57	57	0	57	0	27 Mo

rates of angiographic occlusion and improved clinical outcomes. Therefore, we performed a systematic review of the literature examining the overall efficacy of endovascular treatments for VBDA and comparing outcomes of reconstructive techniques such as stent placement, flow diversion, and stent-assisted coiling with deconstructive techniques such as parent artery occlusion and trapping.

MATERIALS AND METHODS

Literature Search

A comprehensive literature search of the data bases PubMed, Ovid MEDLINE, and Ovid EMBASE was designed and conducted by an experienced librarian with input from the authors. The key words, “endovascular,” “catheterization,” “percutaneous,” “embolization,” “coil,” “stent,” “flow diverter,” “intracranial,” “vertebrobasilar,” “posterior circulation,” “aneurysm,” “dissecting,” and “dissection,” were used in both “AND” and “OR” combinations. The search was limited to articles published from 1980 to June 2014 in the English language only. All studies reporting patients treated with endovascular therapy for VBDA were selected. Inclusion criteria were a series of >5 patients, with available data on clinical and/or angiographic outcomes. Two reviewers selected the included studies.

For each study, we extracted the following information: patient presentation (ruptured or unruptured), treatment technique (stent, stent-assisted coiling, coiling, parent artery occlusion, trapping), long-term good neurologic outcome, immediate angiographic occlusion, long-term angiographic occlusion, perioperative morbidity (resulting from procedural complications), perioperative mortality (all cause), rebleeding (for ruptured only), recurrence, and retreatment. Good neurologic outcome was defined as a modified Rankin Scale score of ≤ 2 . In cases in which a modified Rankin Scale score was not available, good neurologic outcome was determined if the study used terms such as “no morbidity” or “good recovery.”

Outcomes were obtained for the overall population of patients receiving endovascular treatment of VBDA, in addition to determining outcomes by aneurysm rupture status. Separate analyses were also performed comparing outcomes between patients re-

ceiving reconstructive techniques with preservation of the parent artery including stent placement and stent-assisted coiling and those undergoing deconstructive techniques such as trapping or parent artery occlusion.

Statistical Analysis

All included studies were noncomparative. We estimated from each cohort the cumulative incidence (event rate) and 95% confidence interval for each outcome. Event rates for each intervention were pooled in a meta-analysis across studies by using the random effects model.⁴ Anticipating heterogeneity among studies, we chose this model a priori because it incorporates within-study variance and between-study variance. Heterogeneity of the treatment effect across studies was evaluated by using the I^2 statistic and the Cochrane Q test for heterogeneity.^{5,6} We considered an I^2 statistic of >50% or a P value for the heterogeneity test of <.05 to suggest significant heterogeneity. We were unable to test for publication bias due to the noncomparative nature of the studies.

RESULTS

Literature Review

The initial literature search yielded 615 articles. On initial abstract and title review, 552 articles were excluded because they were deemed not relevant to the current study. Sixty-three studies were reviewed in additional detail. Twenty-five studies were excluded because they dealt with outcomes of treatment of vertebrobasilar dissections, not vertebrobasilar dissecting aneurysms. Twenty-one studies were excluded because they were either case reports or had too few patients. In total, 17 studies with 476 patients were included. Three hundred eighteen patients (66.8%) presented with ruptured VBDA, and 158 patients (33.2%) presented with unruptured VBDA. Two hundred five patients (43.1%) were treated with reconstructive techniques, and 271 patients (56.9%) were treated with deconstructive techniques. Mean follow-up was at least 6 months for 16 of the 17 studies. Mean follow-up was only 5.3 days for 1 study. These data are summarized in Table 1.

Table 2: Meta-analysis outcomes

Outcome	All Patients		Deconstructive		Reconstructive		P Deconstructive versus Reconstructive
	Event Rate (95% CI)	I ²	Event Rate (95% CI)	I ²	Event Rate (95% CI)	I ²	
All patients							
Immediate occlusion	75.0 (55.0–88.0)	83	88.0 (47.0–98.0)	86	53.0 (31.0–74.0)	71	<.0001
Long-term occlusion	87.0 (74.0–94.0)	82	88.0 (35.0–99.0)	91	81.0 (64.0–91.0)	62	<.0001
Perioperative morbidity	12.0 (9.0–16.0)	0	12.0 (7.0–18.0)	0	4.0 (2.0–10.0)	0	.04
Perioperative mortality	8.0 (6.0–11.0)	0	10.0 (6.0–17.0)	0	4.0 (2.0–10.0)	0	.11
Recurrence	7.0 (5.0–10.0)	0	5.0 (2.0–10.0)	0	5.0 (2.0–11.0)	0	.89
Retreatment	3.0 (2.0–6.0)	0	5.0 (2.0–10.0)	0	3.0 (1.0–8.0)	0	.25
Long-term good clinical outcome	84.0 (65.0–94.0)	89	86.0 (68.0–95.0)	68	92.0 (86.0–95.0)	0	.10
Patients with rupture							
Immediate occlusion	78.0 (55.0–91.0)	78	94.0 (84.0–98.0)	0	43.0 (18.0–73.0)	57	<.0001
Long-term occlusion	88.0 (83.0–92.0)	0	95.0 (86.0–98.0)	0	83.0 (74.0–90.0)	0	.02
Perioperative morbidity	16.0 (11.0–22.0)	10	14.0 (8.0–23.0)	0	7.0 (3.0–17.0)	0	.82
Perioperative mortality	11.0 (8.0–16.0)	0	13.0 (8.0–22.0)	0	7.0 (3.0–15.0)	0	.82
Rebleed	9.0 (6.0–13.0)	0	9.0 (4.0–20.0)	12	7.0 (3.0–14.0)	0	.75
Recurrence	8.0 (5.0–13.0)	0	6.0 (2.0–13.0)	0	7.0 (2.0–17.0)	1	1.00
Retreatment	5.0 (3.0–8.0)	0	6.0 (2.0–13.0)	0	5.0 (2.0–15.0)	0	.25
Long-term good clinical outcome	79.0 (68.0–87.0)	59	83.0 (62.0–94.0)	64	88.0 (79.0–94.0)	0	.19
Patients without rupture							
Immediate occlusion	80.0 (48.0–94.0)	74	94.0 (68.0–99.0)	28	57.0 (25.0–84.0)	65	<.0001
Long-term occlusion	86.0 (69.0–94.0)	64	97.0 (81.0–100.0)	0	68.0 (47.0–83.0)	31	<.0001
Perioperative morbidity	6.0 (3.0–12.0)	0	7.0 (2.0–19.0)	0	7.0 (2.0–19.0)	0	.58
Perioperative mortality	4.0 (2.0–9.0)	0	4.0 (1.0–18.0)	0	5.0 (1.0–15.0)	0	1.00
Recurrence	7.0 (4.0–13.0)	0	4.0 (1.0–18.0)	0	7.0 (2.0–20.0)	0	1.00
Retreatment	4.0 (2.0–9.0)	0	4.0 (1.0–18.0)	0	5.0 (1.0–15.0)	0	1.00
Long-term good clinical outcome	95.0 (89.0–98.0)	0	93.0 (76.0–98.0)	0	94.0 (84.0–98.0)	0	1.00

Overall Outcomes of Endovascular Treatment of VBDA

Considering all patients treated by either reconstructive or deconstructive techniques, immediate occlusion rates were 75.0% (95% CI, 55.0%–88.0%) and long-term occlusion rates were 87.0% (95% CI, 74.0%–94.0%). Angiographic recurrence rates were 7.0% (95% CI, 5.0%–10.0%) with a retreatment rate of 3.0% (95% CI, 2.0%–6.0%). Perioperative morbidity was 12.0% (95% CI, 9.0%–16.0%), and all-cause perioperative mortality was 8.0% (95% CI, 6.0%–11.0%). Patients with ruptured VBDA made up a majority of patients with VBDA with perioperative mortality (11.0%; 95% CI, 8.0%–16.0%). All-cause perioperative mortality for unruptured VBDA was 4.0% (95% CI, 2.0%–9.0%). The overall rebleed rate for patients with ruptured VBDA was 9.0% (95% CI, 6.0%–13.0%). These data are summarized in Table 2. Forest plots for the overall outcomes are provided in On-line Figs 1–8.

Deconstructive versus Reconstructive Techniques: All Patients with VBDA

Patients treated with deconstructive techniques had higher rates of complete occlusion on immediate posttreatment angiography than those treated with reconstructive techniques (88.0% versus 53.0%, $P < .0001$). The same was true for long-term posttreatment angiography (88.0% versus 81.0%, $P < .0001$). Perioperative morbidity was lower in the reconstructive group compared with the deconstructive group (4.0% versus 12.0%, $P = .04$). There was a trend toward decreased perioperative mortality rates in the reconstructive group (4.0% versus 10.0%, $P = .11$) and a trend toward higher rates of long-term good clinical outcome in the reconstructive group (92.0% versus 86.0%, $P = .10$). These data are summarized in Table 2.

Deconstructive versus Reconstructive Techniques: Patients with Ruptured VBDA

Patients treated with deconstructive techniques had higher rates of complete occlusion on immediate posttreatment angiography than those treated with reconstructive techniques (94.0% versus 43.0%, $P < .0001$). The same was true for long-term posttreatment angiography (95.0% versus 83.0%, $P = .02$). Perioperative morbidity rates were similar in the reconstructive group compared with the deconstructive group (7.0% versus 14.0%, $P = .82$). Perioperative mortality was 13.0% (95% CI, 8.0%–22.0%) in the deconstructive group versus 7.0% (95% CI, 3.0%–15.0%) in the reconstructive group ($P = .82$). Long-term good clinical outcome rates were similar between the reconstructive (88.0%; 95% CI, 79.0%–94.0%) and deconstructive groups (83.0%; 95% CI, 62.0%–94.0%) ($P = .19$). Rebleeding rates were similar between the deconstructive (9.0%; 95% CI, 4.0%–20.0%) and reconstructive (7.0%; 95% CI, 3.0%–14.0%) techniques ($P = .75$). These data are summarized in Table 2.

Deconstructive versus Reconstructive Techniques: Patients with Unruptured VBDA

Patients treated with deconstructive techniques had higher rates of complete occlusion on immediate posttreatment angiography than those treated with reconstructive techniques (94.0% versus 57.0%, $P < .0001$). The same was true for long-term posttreatment angiography (97.0% versus 68.0%, $P = .02$). Perioperative morbidity rates were similar in the reconstructive group compared with the deconstructive group (7.0% versus 7.0%, $P = .57$). Perioperative mortality was 4.0% (95% CI, 1.0%–18.0%) in the deconstructive group versus 5.0% (95% CI, 1.0%–15.0%) in the

reconstructive group ($P = 1.00$). Long-term good clinical outcome rates were similar between the reconstructive (94.0%; 95% CI, 84.0%–98.0%) and deconstructive groups (93.0%; 95% CI, 76.0%–98.0%) ($P = 1.00$). These data are summarized in Table 2.

Study Heterogeneity

Significant heterogeneity (I^2 value of $>50\%$ and P value for the Cochrane Q test of $<.05$) was noted in the analyses of 3 outcomes (immediate occlusion, long-term good clinical outcome, and long-term occlusion). Therefore, confidence in a pooled summary estimate for these 3 outcomes is limited. On the other hand, the results were very consistent across studies for all of the remaining outcomes.

DISCUSSION

This systematic review and meta-analysis demonstrated that both deconstructive (parent artery occlusion, aneurysm trapping) and reconstructive (stent placement/stent-assisted coiling) techniques are effective in the treatment of ruptured and unruptured VBDA. Deconstructive techniques achieved higher rates of complete angiographic occlusion compared with reconstructive techniques; however, periprocedural morbidity rates were lower for reconstructive techniques. Both techniques resulted in high rates of good long-term neurologic outcome and similar low rates of recurrence and retreatment. Overall, these findings suggest that reconstructive techniques may be as effective as and possibly safer than deconstructive techniques; especially in cases in which patients lack sufficient collateral circulation.

Comparisons of clinical and angiographic outcomes between reconstructive and deconstructive techniques in the literature are limited, largely due to the small sizes of most case series. The largest study to date comparing deconstructive and reconstructive techniques was that of Kim et al,⁷ which compared 62 VBDA treated with reconstructive techniques and 57 treated with deconstructive techniques. This study demonstrated no difference in recurrence and rebleeding rates between reconstructive and deconstructive techniques. Recurrence rates were 10.2% for patients treated with reconstructive techniques versus 17.1% for those treated with deconstructive techniques. Although our study found that deconstructive techniques result in higher angiographic occlusion rates, we found no difference in recurrence, retreatment, and rebleeding rates when comparing reconstructive and deconstructive techniques. These findings are important because they run contrary to the expectation that reconstructive techniques result in higher recanalization and rebleeding rates. With the advent of flow diverters and increased use of multiple overlapping stents in the treatment of dissecting VBDA, it is likely that angiographic outcomes of patients treated with reconstructive techniques will improve with time.^{7–9} Higher rates of long-term angiographic occlusion with multiple overlapping stents compared with single-stent treatment have been demonstrated in multiple series.^{10–12}

Our study found similar rates of good long-term neurologic outcome between patients treated with reconstructive and deconstructive techniques but higher rates of perioperative morbidity among patients treated with deconstructive techniques. Patients

treated with deconstructive techniques are at a higher risk of neurologic complications secondary to ischemia resulting from sacrifice of the parent vessel. Most ischemic complications are the result of the occlusion and ischemia of perforating arteries and the anterior spinal artery.¹³ In a series of 72 patients treated with deconstructive techniques, Kashiwazaki et al¹³ reported 2 cases of spinal cord infarction and 7 cases of partial Wallenberg syndrome secondary to occlusion of vertebrobasilar dissecting aneurysms involving the PICA. Despite these perforator complications, only 1 patient died and the remaining patients had mRS ≤ 2 . Perforator infarctions are rare with stent and flow-diverter reconstruction for treatment of vertebrobasilar aneurysms.¹⁴ Large-vessel infarcts resulting from thrombotic complications or hemodynamic alterations in the setting of deconstructive techniques are rare as well.^{15–17}

Despite their overall lower rate of perioperative morbidity, reconstructive techniques are far from a panacea in the treatment of VBDA. One major limitation of treatment of VBDA with stents is in the treatment of PICA-origin VBDA. Especially in the setting of ruptured VBDA, complete obliteration of the aneurysm should be the primary goal because recanalization is associated with a high rate of rupture. Deconstructive techniques could be considered in this setting; however, in the absence of adequate cerebellar circulation, these are associated with a high risk of stroke and associated mass effect.¹² Reconstruction of PICA-involving lesions often requires the aneurysm sac to be left partially open to ensure adequate PICA flow.¹⁸ This places the patient at a high risk of recanalization, which, in the setting of ruptured VBDA, can result in hemorrhage. Thus, for these types of lesions, bypass surgery should be considered.¹⁹ Reconstructive treatments are also associated with a host of other complications, including stent migration, in-stent thrombosis leading to stroke, and dissection. However, these complications are rare.^{7,10,12}

The most important consideration in the treatment of VBDA is weighing the risks of treatment with the risks of the natural history of these lesions. Ruptured VBDA are known to have a poor natural history with high rates of rebleeding and mortality.¹ Rabinov et al¹⁶ compared mortality rates among patients with ruptured VBDA treated with deconstructive techniques and surgical clipping with a small group of patients managed conservatively and found that mortality rates in the conservative group were 50% compared with 20% in the treatment group. Kobayashi et al³ followed 113 patients with unruptured VBDA without ischemic symptoms at presentation for a mean of 3 years and found a 3% morbidity at follow-up, with 2 patients having clinical deterioration due to mass effect and 1 patient having ischemic stroke and hemorrhage. Five patients had enlargement of the aneurysm in this series.³

Strengths and Limitations

The strengths of this study include following a priori established protocol, the comprehensive literature search that involved multiple databases, and the process of study selection by independent reviewers. The main limitation of this analysis is the noncomparative and nonrandomized nature of the studies. It is difficult to perform comparative studies on treatment of VBDA because treatment decisions for lesions are dependent on multiple factors

such as the presence of collateral circulation, involvement of branch vessels or perforators, and lesion severity. Due to the rarity, variable appearance, and severity of these lesions and the multitude of treatment options available, prospective clinical registries should be considered to determine which treatment modalities provide superior outcomes for various lesion types. Furthermore, development of a validated classification system for vertebrobasilar dissecting aneurysm severity could be considered. There are no validated tools to evaluate the methodologic quality of noncomparative series. Therefore, the risk of bias associated with inferences from studies with this design should be considered high. There are no reliable tests to evaluate publication bias in the setting of noncomparative studies. Publication bias is very likely in the setting of small observational studies because patients who had either uneventful or poor outcomes may have been excluded from published results. Furthermore, when performing single-institution retrospective review series, an investigator can easily look at the outcomes and not publish them when they are not favoring the investigator's point of view. Moreover, treatment modalities have varied during the time course of the published series; this variation makes standardization of treatment paradigms difficult.

Last, uniform assessment and reporting of complications in a standardized fashion was lacking. Using the Grading of Recommendations, Assessment, Development, and Evaluation framework,^{20,21} the quality of evidence (confidence in estimates) is very low because of the imprecision, heterogeneity, and methodologic limitations of the included studies, most important because they were noncomparative. Nevertheless, this meta-analysis provides useful data to share with patients and families when assessing the risks of treatment of VBDA and represents a benchmark against which future studies can be compared. With analysis of >470 patients, this is currently the largest study examining outcomes of the endovascular treatment of VBDA.

CONCLUSIONS

Endovascular treatment of VBDA may be associated with high rates of complete occlusion and good long-term neurologic outcomes. Deconstructive techniques may result in higher rates of complete angiographic occlusion, while reconstructive techniques may be associated with less perioperative morbidity. However, long-term neurologic outcomes and retreatment rates are statistically similar between these 2 treatment modalities, possibly due to low power to detect differences between the groups. Comparative studies are needed to further confirm these findings. Use of either of these 2 modalities seems to be safe and effective in the right clinical setting. When deciding to treat unruptured VBDA, the risks of the treatment should be weighed against the risks of the natural history of these lesions.

Disclosures: Giuseppe Lanzino—UNRELATED: Consultancy: Covidien/ev3.* *Money paid to the institution.

REFERENCES

- Mizutani T, Aruga T, Kirino T, et al. **Recurrent subarachnoid hemorrhage from untreated ruptured vertebrobasilar dissecting aneurysms.** *Neurosurgery* 1995;36:905–11; discussion 912–13
- Yoshimoto Y, Wakai S. **Unruptured intracranial vertebral artery**

- dissection: clinical course and serial radiographic imagings.** *Stroke* 1997;28:370–74
- Kobayashi N, Murayama Y, Yuki I, et al. **Natural course of dissecting vertebrobasilar artery aneurysms without stroke.** *AJNR Am J Neuroradiol* 2014;35:1371–75
- DerSimonian R, Laird N. **Meta-analysis in clinical trials.** *Control Clin Trials* 1986;7:177–88
- Higgins JP, Thompson SG, Deeks JJ, et al. **Measuring inconsistency in meta-analyses.** *BMJ* 2003;327:557–60
- Higgins JP, Thompson SG. **Quantifying heterogeneity in a meta-analysis.** *Stat Med* 2002;21:1539–58
- Kim BM, Shin YS, Kim SH, et al. **Incidence and risk factors of recurrence after endovascular treatment of intracranial vertebrobasilar dissecting aneurysms.** *Stroke* 2011;42:2425–30
- Wakhloo AK, Mandell J, Gounis MJ, et al. **Stent-assisted reconstructive endovascular repair of cranial fusiform atherosclerotic and dissecting aneurysms: long-term clinical and angiographic follow-up.** *Stroke* 2008;39:3288–96
- Zenteno MA, Murillo-Bonilla LM, Guinto G, et al. **Sole stenting bypass for the treatment of vertebral artery aneurysms: technical case report.** *Neurosurgery* 2005;57(1 suppl):E208; discussion E208
- Zhao KJ, Fang YB, Huang QH, et al. **Reconstructive treatment of ruptured intracranial spontaneous vertebral artery dissection aneurysms: long-term results and predictors of unfavorable outcomes.** *PLoS One* 2013;8:e67169
- Yoon WK, Kim YW, Kim SR, et al. **Angiographic and clinical outcomes of stent-alone treatment for spontaneous vertebrobasilar dissecting aneurysm.** *Acta Neurochir (Wein)* 2010;152:1477–86; discussion 1486
- Park SI, Kim BM, Kim DI, et al. **Clinical and angiographic follow-up of stent-only therapy for acute intracranial vertebrobasilar dissecting aneurysms.** *AJNR Am J Neuroradiol* 2009;30:1351–56
- Kashiwazaki D, Ushikoshi S, Asano T, et al. **Long-term clinical and radiological results of endovascular internal trapping in vertebral artery dissection.** *Neuroradiology* 2013;55:201–06
- Brinjikji W, Murad MH, Lanzino G, et al. **Endovascular treatment of intracranial aneurysms with flow diverters: a meta-analysis.** *Stroke* 2013;44:442–47
- Jin SC, Kwon DH, Choi CG, et al. **Endovascular strategies for vertebrobasilar dissecting aneurysms.** *AJNR Am J Neuroradiol* 2009;30:1518–23
- Rabinov JD, Hellinger FR, Morris PP, et al. **Endovascular management of vertebrobasilar dissecting aneurysms.** *AJNR Am J Neuroradiol* 2003;24:1421–28
- Yuki I, Murayama Y, Vinuela F. **Endovascular management of dissecting vertebrobasilar artery aneurysms in patients presenting with acute subarachnoid hemorrhage.** *J Neurosurg* 2005;103:649–55
- Kai Y, Nishi T, Watanabe M, et al. **Strategy for treating unruptured vertebral artery dissecting aneurysms.** *Neurosurgery* 2011;69:1085–91
- Park W, Ahn JS, Park JC, et al. **Occipital artery-posterior inferior cerebellar artery bypass for the treatment of aneurysms arising from the vertebral artery and its branches.** *World Neurosurg* 2014;82:714–21
- Balshem H, Helfand M, Schunemann HJ, et al. **GRADE guidelines. 3. Rating the quality of evidence.** *J Clin Epidemiol* 2011;64:401–06
- Guyatt GH, Oxman AD, Kunz R, et al. **GRADE guidelines. 6. Rating the quality of evidence—imprecision.** *J Clin Epidemiol* 2011;64:1283–93
- Luo CB, Chang CY, Teng MM, et al. **Endovascular treatment of ruptured vertebral dissecting aneurysms with electrodetachable coils.** *J Chin Med Assoc* 2005;68:578–84
- Purkayastha S, Gupta K, Krishnamoorthy AT, et al. **Endovascular treatment of ruptured posterior circulation dissecting aneurysms.** *J Neuroradiol* 2006;33:329–37
- Rho MH, Park HJ, Chung EC, et al. **Various techniques of stent-assisted coil embolization of wide-necked or fusiform atherosclerotic and dissecting unruptured vertebrobasilar artery aneurysms**

- for reducing recanalization: mid-term results. *Acta Neurochir (Wein)* 2013;155:2009–17
25. Suh SH, Kim BM, Park SI, et al. **Stent-assisted coil embolization followed by a stent-within-a-stent technique for ruptured dissecting aneurysms of the intracranial vertebrobasilar artery: clinical article.** *J Neurosurg* 2009;111:48–52
26. Tsuura M, Terada T, Yokote H, et al. **Endovascular treatment for vertebral dissecting aneurysm presenting with subarachnoid hemorrhage.** *Interv Neuroradiol* 1999;5(suppl 1):203–06
27. Wang J, Sun Z, Bao J, et al. **Endovascular management of vertebrobasilar artery dissecting aneurysms.** *Turk Neurosurg* 2013;23:323–28
28. Yamaura I, Tani E, Yokota M, et al. **Endovascular treatment of ruptured dissecting aneurysms aimed at occlusion of the dissected site by using Guglielmi detachable coils.** *J Neurosurg* 1999;90:853–56

Endoluminal Reconstruction for Nonsaccular Aneurysms of the Proximal Posterior Cerebral Artery with the Pipeline Embolization Device

D.W. Zumofen, M. Shapiro, T. Becske, E. Raz, M.B. Potts, H.A. Riina, and P.K. Nelson



ABSTRACT

BACKGROUND AND PURPOSE: Treatment options for nonsaccular posterior cerebral artery aneurysms include a range of surgical and endovascular reconstructive and deconstructive methods. However, no truly satisfactory treatment option is available to date for lesions arising from the P1 and P2 segments. The purpose of the present case series is to investigate both the efficacy and safety of the Pipeline Embolization Device in treating these challenging aneurysms.

MATERIALS AND METHODS: We present a series of 6 consecutive patients who underwent endoluminal reconstruction with the Pipeline Embolization Device for nonsaccular P1 or P2 segment aneurysms between January 2009 and June 2013.

RESULTS: Aneurysm location included the P1 segment in 2 patients and the P2 segment in 4 patients. Mean aneurysm diameter was 23 mm (range, 5–44 mm). Mean length of the arterial segment involved was 10 mm (range, 6–19 mm). Clinical presentation included mass effect in 4 patients and perforator stroke and subacute aneurysmal subarachnoid hemorrhage in 1 patient each. Endovascular reconstruction was performed by using 1 Pipeline Embolization Device in 5 patients and 2 overlapping Pipeline Embolization Devices in the remaining patient. Angiographic aneurysm occlusion was immediate in 1 patient, within 6 months in 4 patients, and within 1 year in the remaining patient. Index symptoms resolved in 4 patients and stabilized in the remaining 2. No new permanent neurologic sequelae and no aneurysm recurrence were recorded during the mean follow-up period of 613 days (range, 540–725 days).

CONCLUSIONS: Endovascular reconstruction with the Pipeline Embolization Device for nonsaccular aneurysms arising from the P1 and P2 segments compares favorably with historical treatment options in terms of occlusion rate, margin of safety, and neurologic outcome.

ABBREVIATIONS: aSAH = aneurysmal subarachnoid hemorrhage; CN = cranial nerve; PCA = posterior cerebral artery; PED = Pipeline Embolization Device

Nonsaccular posterior cerebral artery (PCA) aneurysms comprise a spectrum of arterial wall diseases spanning a variety of often complex, partially thrombosed lesions with holosegmental involvement as a common attribute.¹ Proposed etiologies include congenitally derived lesions, atherosclerosis, and arterial wall dissections of idiopathic, inflammatory, or traumatic origin.² Whereas the dissecting subset may have a tendency to present

early with acute hemorrhagic or ischemic stroke, the remaining aneurysms typically come to clinical attention later in the course of their development and hence at comparatively large dimensions.³ Nondissecting, nonsaccular PCA aneurysms have a predilection for P1 and P2⁴ segments and have a tendency to have a sizable thrombotic subcompartment.^{5,6}

The infrequency of these lesions has relegated the surgical and endovascular experience to a relatively thin body of literature.^{1,5,7-15} Reported treatment strategies include a range of reconstructive and deconstructive methods, often distinguished by their variability in outcome (On-line Table 1). We now report and discuss our experience with use of the Pipeline Embolization Device (PED; Covidien, Irvine, California) to treat a series of 6 consecutive cases of complex aneurysms arising from the P1 or P2 segment.

MATERIALS AND METHODS

Six consecutive patients with nonsaccular aneurysms (circumferentially involving the parent vessel) of the P1 and P2 segments

Received August 6, 2014; accepted after revision November 17.

From the Bernard and Irene Schwartz Interventional Neuroradiology Section, Department of Radiology (D.W.Z., M.S., T.B., E.R., M.B.P., H.A.R., P.K.N.), and Departments of Neurological Surgery (D.W.Z., M.B.P., H.A.R., P.K.N.) and Neurology (M.S., T.B.), New York University School of Medicine, New York, New York.

Daniel W. Zumofen has a personal scholarship from the Fund Helmut Hartweg for the promotion of young researchers in the field of medical radiology and the Schweizerische Akademie der Medizinischen Wissenschaften.

Please address correspondence to Peter Kim Nelson, MD, Bernard and Irene Schwartz Interventional Neuroradiology Section, Department of Radiology, New York University School of Medicine, 560 First Ave, 7th floor, New York, NY 10016; e-mail: peter.nelson@nyumc.org

Indicates article with supplemental on-line tables.

<http://dx.doi.org/10.3174/ajnr.A4261>

underwent endovascular reconstruction with the PED by our team between January 2009 and June 2013. Basilar apex aneurysms involving the P1 segment were excluded from the present series because in our opinion, they represent a different disease with a very different set of challenges. Patient characteristics are provided in On-line Table 2. The average aneurysm diameter was 23 mm (range, 5–44 mm). The mean length of the arterial segment involved was 10 mm (range, 6–19 mm). Five aneurysms were unruptured, and 1 came to our attention several months following low-grade aneurysmal subarachnoid hemorrhage (aSAH) related to the index P1 aneurysm—initially managed with observation at an outside institution. Index symptoms of the 5 patients with unruptured aneurysms included mass effect–related compression symptoms in 4 patients and hemiparesis following a thalamic perforator stroke in the remaining patient. Mass effect–related compression symptoms included cranial nerve (CN) III palsy in 2 patients, sensorimotor hemisindrome combined with CN III palsy in 1 patient, and dizziness in 1 patient. Four of the 6 aneurysms included in the present series showed sizable (subtotal) thrombotic subcompartment, 1 showed minimal thrombosis, and the remaining one showed no evidence of thrombosis.

All patients were pretreated with acetylsalicylic acid, 325 mg daily, and clopidogrel, 75 mg daily, for at least 5 days. A P2Y12 assay (VerifyNow; Accumetrics, San Diego, California) was obtained at the beginning of the procedure and thereafter daily until discharge to evaluate and confirm the level of platelet inhibition obtained by the dual antiplatelet regimen. Endoluminal reconstruction was performed in all except 1 case by using a single PED. In patient 4, we elected to overlap 2 devices to maintain single coverage of the normal vascular segments proximal and distal to the aneurysm, with double-coverage of the aneurysm neck. The specific dimensions of the PED were chosen after determination of the length of the aneurysmal arterial segment and parent vessel diameter at the landing zones, proximal and distal to the aneurysm.¹⁶ The Marksman (Covidien) microcatheter was used for all embolizations, with a variety of proximal support systems. In cases in which distal access with the Marksman could not be primarily established, microcatheterization was performed with an Excelsior SL-10 microcatheter (Stryker, Kalamzoo, Michigan), followed by an over-the-wire exchange for a Marksman by using a Transend Floppy 0.014 300-cm wire (Stryker). PEDs were deployed by using previously described methods of unsheathing and delivery-wire advancement.¹⁷ An immediate postprocedure non-contrast-enhanced head CT scan was routinely performed. In the absence of intracranial hemorrhage, IV heparin infusion was continued for at least 12 hours at rate of 500–700 IU/h.

Clinical follow-up was performed at 1 month, 6 months, and annually thereafter. Follow-up DSA was performed at 6 months and 1 year. Continued growth of the aneurysmal mass despite angiographic “cure” was ruled out in all cases clinically by regression of mass effect–related symptoms when present and was confirmed by serial transaxial follow-up imaging (CT or MR imaging). With the exception of 1 patient whose clopidogrel therapy was prematurely interrupted at 4 months post-PED to allow performance of urgent abdominal surgery unrelated to the aneurysm, dual antiplatelet inhibition was continued for 12 months, with acetylsalicylic acid therapy maintained indefinitely.

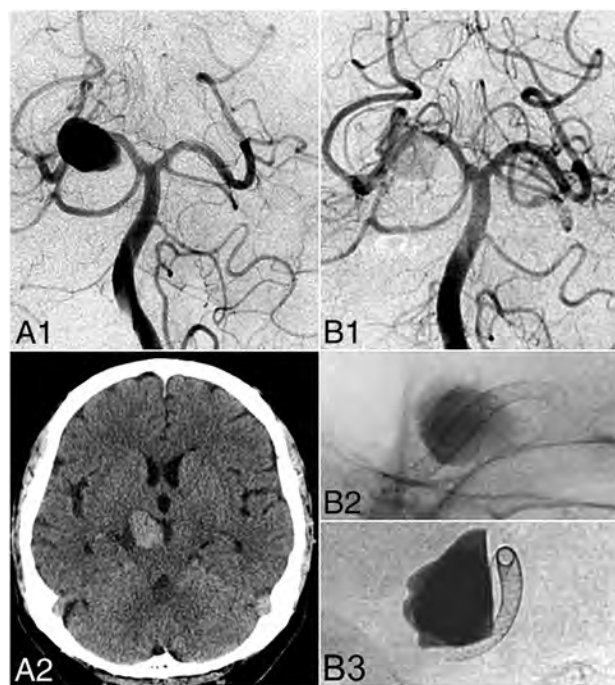


FIG 1. Illustrative case (patient 4). A 68-year-old man presented with right oculomotor nerve palsy. DSA (A1) and noncontrast head CT (A2) reveal a fusiform P2 aneurysm with a maximum diameter of 23 mm and a 7-mm length of the arterial segment involved (neck width). Endovascular reconstruction with 2 overlapping PED devices (2.5 × 20 mm, 2.75 × 10 mm) led to considerable stasis of contrast in the aneurysm body illustrated on postembolization control DSA (B1) and unsubtracted angiography (B2 and B3).

RESULTS

The results are listed in On-line Table 2. Angiographic aneurysm occlusion was immediate in 1 patient, within 6 months in 4 patients, and within 1 year in the remaining patient. In the patient requiring clopidogrel discontinuation to allow abdominal surgery, the parent artery was occluded at 6-month angiographic follow-up, without clinical or radiographic evidence of infarction. Index symptoms resolved in 4 of 6 patients and stabilized in the remaining 2. Patients presenting with subacute aSAH (patient 1) and a small mesencephalic perforator stroke (patient 2) recovered from their index symptoms. Mass effect–related index symptoms resolved in 2 of 4 patients and stabilized in the remaining 2. Third cranial nerve palsy (patients 4 and 6) completely resolved. In the 2 patients who presented with symptoms related to long-standing brain stem compression (patients 3 and 5), index symptoms stabilized, but did not resolve. There were no instances of new permanent neurologic deficits during the entire mean of 613 days (range, 540–725 days) of clinical follow-up. An illustrative case (patient 4) is shown in Figs 1 and 2.

Delivery of the PED in patient 3 required advancement of a 5F Navien (Covidien) intracranial support catheter into the distal basilar artery and was associated with perforation of the left P1, documented by slow contrast extravasation on DSA. PED deployment was completed across the aneurysm neck and perforation site, leading to immediate hemostasis. Postprocedure non-contrast-enhanced head CT demonstrated subarachnoid blood and contrast within the basal cisterns and the medial left Sylvian fissure. The patient, who initially presented with mass

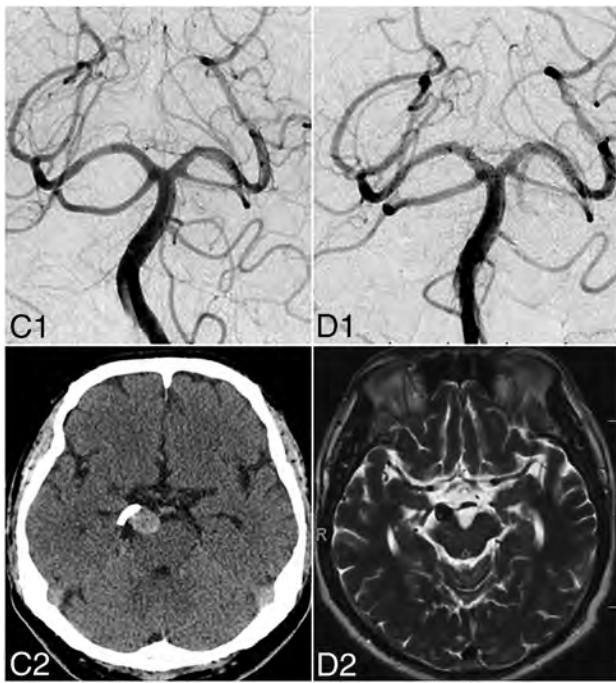


FIG 2. In the same patient, at 6 months, DSA shows complete angiographic aneurysm occlusion (C1). Regression of mass effect–related symptoms (CN III palsy) is correlated with the regression of aneurysm mass effect as illustrated on 6-month follow-up noncontrast head CT (C2). At 1 year, DSA (D1) confirms stable angiographic cure, and axial T2-weighted MR imaging (D2) shows nearly complete involution of the aneurysm sac.

effect symptoms of dizziness and right-sided sensorimotor deficits, emerged from anesthesia with a new headache and worsened right-sided sensorimotor symptoms. She recovered to her preprocedural baseline neurologic status during the next several weeks, without additional endovascular or surgical intervention.

DISCUSSION

The advent of minimally porous endoluminal devices has produced a paradigm shift in the treatment of both anterior and posterior circulation aneurysms^{17,18} and, in particular, has generated enthusiasm for their use in challenging posterior circulation lesions. Although the early experience with flow diverters in the posterior circulation has been mixed,^{9,19} the variability in outcomes likely reflects, in part, the heterogeneity of lesions involving the posterior circulation group rather than an inherent limitation of the treatment technique per se. The current small series illustrates this point, demonstrating both the efficacy and reasonable safety of the PED in treating proximal PCA aneurysms. This is further underscored by the large size and complex geometry of lesions in this series and by the single technical complication related to device deployment in a case of particularly challenging geometry.

For the most part, treatment with the PED was limited to a single device due to concern for coverage of eloquent regional perforators. This was circumvented in patient 4, in whom it was elected to overlap 2 shorter devices across the aneurysm neck in a manner that maintained single coverage of the normal vascular segments proximal and distal to the aneurysm, illustrating one

technical refinement to enable increased selective coverage of the aneurysm, while concomitantly minimizing the associated coverage risk to adjacent perforators.²⁰ Given reports of occasional late in-stent thrombosis, particularly in the posterior circulation,²¹ it may be prudent to prolong dual antiplatelet therapy (12 months or longer) and to consider indefinite single agent maintenance. We think that the single incidence of in-stent thrombosis in our series upon after required deliberate discontinuation of clopidogrel clearly supports such and antiplatelet regimen.

In line with previously reported results for endoluminal reconstruction by using the PED for large and giant aneurysms in the anterior circulation,²² 2 of 4 patients who presented with long-standing neural compression symptoms did not experience full clinical recovery despite documented aneurysm involution. In our opinion, these results are largely in line with those that would be expected after classic deconstructive treatment such as proximal parent artery clip or coil occlusion. In the present series, transaxial follow-up imaging was performed in all cases, demonstrating, in line with previous reports,^{22,23} an acute stage of thrombolysis consistently followed by aneurysm involution during several months. Two of 3 patients who had CN III palsy recovered rapidly, with the third patient (patient 5) with a giant 44-mm aneurysm displacing CN III and the adjacent brain stem. Patient 3, who also presented with long-standing brain stem dysfunction related to a particularly large aneurysm, showed stabilization, but not complete resolution of index symptoms as well. Based on our results we advocate that clinical recovery parallels to a large degree the degree and duration of neural compression, and the specific sensitivity of the involved neural structures to compression. In conclusion, therapeutic parent artery sacrifice may allow more immediate mass effect reduction, but the benefit of more rapid decompression remains, to our knowledge, unproven. Also, deconstructive methods fundamentally rely on the competence of the collateral arterial supply,¹¹ and ischemic complications following therapeutic parent vessel sacrifice include hemianopia or thalamic perforator stroke and certainly do occur as illustrated in On-line Table 1.^{1,5,10-15,24} Based on our experience, we hence propose that endoluminal reconstruction with the PED likely falls within the range of deconstructive methods in terms of relieving mass effect but offers the benefits of preserved anterograde flow in the parent PCA.

Nonsaccular proximal PCA aneurysms are formidable lesions that remain challenging to treat with any existing method. Despite the encouraging results reported in the present series, there remain limits with the currently available generation of PED. The potentially fatal incident that occurred in patient 3 illustrates how PED deployment becomes progressively more challenging in the more tortuous distal territories, in part due to the relative stiffness of the currently available PED delivery platform. This point is underscored by the extremely complex vascular geometry, the large size of the aneurysm (31 mm), and the fact that a single 35-mm PED was used in patient 3. Although in our case, full deployment of the PED covered the site of arterial injury and hence was an immediate bailout, future device development will need to address the limitations of the current generation of PED. Depending on the local vascular geometry, we also advocate, in selected cases, overlapping 2 shorter, hence more flex-

ible devices, which are less prone to torsion during deployment devices, in a manner maintaining single coverage of the normal arterial segments proximal and distal to the aneurysm while maximizing selective coverage across the aneurysm neck (eg, illustrative case, patient 4).

CONCLUSIONS

PED embolization of nonsaccular aneurysms arising from the proximal PCA compares favorably with historical treatment options in terms of occlusion rate, margin of safety, and neurologic outcome. The present series lends support to the use of the PED, under appropriate clinical circumstances, as a first-line strategy in carefully chosen lesions.

Disclosures: Daniel W. Zumofen—UNRELATED: Employment: New York University School of Medicine, Department of Radiology, Comments: fellow salary for my fellow/clinical instructor position in the Department of Radiology, New York University School of Medicine, New York, New York; Grants/Grants Pending: personal scholarship from the Fund Helmut Hartweg and the Swiss Academy of Medical Science, Comments: 1-year personal scholarship from the Fund Helmut Hartweg and the Swiss Academy of Medical Science to cofinance my fellowship at the New York University School of Medicine. Maksim Shapiro—UNRELATED: Consultancy: Covidien, Comments: I am a Pipeline device proctor and consultant with Covidien; Payment for Development of Educational Presentations: Covidien, Comments: I am a Pipeline device proctor and consultant with Covidien. Tibor Becske—UNRELATED: Consultancy: Covidien/ev3 (consultant); Payment for Lectures (including service on Speakers Bureaus): Covidien/ev3, Comments: I have given lectures for honoraria in the past; Payment for Development of Educational Presentations: Covidien/ev3, Comments: I participated in developing training programs for US physicians in the use of the Pipeline device. Peter K. Nelson—RELATED: Consulting Fee or Honorarium: Covidien; UNRELATED: Consultancy: Covidien.

REFERENCES

- Drake CG, Peerless SJ. Giant fusiform intracranial aneurysms: review of 120 patients treated surgically from 1965 to 1992. *J Neurosurg* 1997;87:141–62
- Mizutani T, Miki Y, Kojima H, et al. Proposed classification of non-atherosclerotic cerebral fusiform and dissecting aneurysms. *Neurosurgery* 1999;45:253–59; discussion 259–60
- de Sousa AA, Dantas FL, Neto AP, et al. Giant posterior cerebral artery aneurysm in a 4-year-old child: case report. *Surg Neurol* 1996;45:31–35
- Zeal AA, Rhoton AL Jr. Microsurgical anatomy of the posterior cerebral artery. *J Neurosurg* 1978;48:534–59
- Ciceri EF, Klucznik RP, Grossman RG, et al. Aneurysms of the posterior cerebral artery: classification and endovascular treatment. *AJNR Am J Neuroradiol* 2001;22:27–34
- Pia HW, Fontana H. Aneurysms of the posterior cerebral artery. Locations and clinical pictures. *Acta Neurochir (Wien)* 1977;38:13–35
- Fischer S, Perez MA, Kurre W, et al. Pipeline embolization device for the treatment of intra- and extracranial fusiform and dissecting aneurysms: initial experience and long-term follow-up. *Neurosurgery* 2014;75:364–74; discussion 374
- Pistocchi S, Blanc R, Bartolini B, et al. Flow diverters at and beyond the level of the circle of Willis for the treatment of intracranial aneurysms. *Stroke* 2012;43:1032–38
- Phillips TJ, Wenderoth JD, Phatouros CC, et al. Safety of the Pipeline embolization device in treatment of posterior circulation aneurysms. *AJNR Am J Neuroradiol* 2012;33:1225–31
- Hallacq P, Piotin M, Moret J. Endovascular occlusion of the posterior cerebral artery for the treatment of P2 segment aneurysms: retrospective review of a 10-year series. *AJNR Am J Neuroradiol* 2002;23:1128–36
- Chao KH, Riina HA, Heier L, et al. Endovascular management of dolichoectasia of the posterior cerebral artery report. *AJNR Am J Neuroradiol* 2004;25:1790–91
- van Rooij WJ, Sluzewski M, Beute GN. Endovascular treatment of posterior cerebral artery aneurysms. *AJNR Am J Neuroradiol* 2006;27:300–05
- Cotroneo E, Gigli R, Guglielmi G. Endovascular occlusion of the posterior cerebral artery in the treatment of P2 ruptured aneurysms. *Interv Neuroradiol* 2007;13:127–32
- Roh HG, Kim SS, Han H, et al. Endovascular treatment of posterior cerebral artery aneurysms using detachable coils. *Neuroradiology* 2008;50:237–42
- Kocaeli H, Chaalala C, Abruzzo TA, et al. Results of surgical management for posterior cerebral artery aneurysms: 7-year experience in the endovascular era. *Acta Neurochir (Wien)* 2009;151:1583–91
- Shapiro M, Raz E, Becske T, et al. Variable porosity of the Pipeline embolization device in straight and curved vessels: a guide for optimal deployment strategy. *AJNR Am J Neuroradiol* 2014;35:727–33
- Nelson PK, Lylyk P, Szikora I, et al. The Pipeline embolization device for the intracranial treatment of aneurysms trial. *AJNR Am J Neuroradiol* 2011;32:34–40
- Becske T, Kallmes DF, Saatci I, et al. Pipeline for uncoilable or failed aneurysms: results from a multicenter clinical trial. *Radiology* 2013;267:858–68
- Siddiqui AH, Abla AA, Kan P, et al. Panacea or problem: flow diverters in the treatment of symptomatic large or giant fusiform vertebral-basilar aneurysms. *J Neurosurg* 2012;116:1258–66
- Shapiro M, Raz E, Becske T, et al. Building multidevice Pipeline constructs of favorable metal coverage: a practical guide. *AJNR Am J Neuroradiol* 2014;35:1556–61
- Klisch J, Turk A, Turner R, et al. Very late thrombosis of flow-diverting constructs after the treatment of large fusiform posterior circulation aneurysms. *AJNR Am J Neuroradiol* 2011;32:627–32
- Szikora I, Marosfoi M, Salomvary B, et al. Resolution of mass effect and compression symptoms following endoluminal flow diversion for the treatment of intracranial aneurysms. *AJNR Am J Neuroradiol* 2013;34:935–39
- Hammoud D, Gailloud P, Olivi A, et al. Acute vasogenic edema induced by thrombosis of a giant intracranial aneurysm: a cause of pseudostroke after therapeutic occlusion of the parent vessel. *AJNR Am J Neuroradiol* 2003;24:1237–39
- Liu L, He H, Jiang C, et al. Deliberate parent artery occlusion for non-saccular posterior cerebral artery aneurysms. *Interv Neuroradiol* 2011;17:159–68
- Yonekawa Y, Roth P, Fandino J, et al. Aneurysms of the posterior cerebral artery and approach selection in their microsurgical treatment: emphasis on the approaches—SAHEA and SCTTA. *Acta Neurochir Suppl* 2011;112:85–92
- Lee JY, Kwon BJ, Kang HS, et al. Subarachnoid hemorrhage from a dissecting aneurysm of the posterior cerebral artery in a child: rebleeding after stent-assisted coiling followed by stent-within-stent technique. *J Korean Neurosurg Soc* 2011;49:134–38
- Wang H, Du R, Stary J, et al. Dissecting aneurysms of the posterior cerebral artery: current endovascular/surgical evaluation and treatment strategies. *Neurosurgery* 2012;70:1581–88; discussion 1588
- Briganti F, Napoli M, Tortora F, et al. Italian multicenter experience with flow-diverter devices for intracranial unruptured aneurysm treatment with periprocedural complications—a retrospective data analysis. *Neuroradiology* 2013;54:1145–52
- Jennett B, Bond M. Assessment of outcome after severe brain damage. *Lancet* 1975;1:480–84
- Farrell B, Godwin J, Richards S, et al. The United Kingdom transient ischaemic attack (UK-TIA) aspirin trial: final results. *J Neurol Neurosurg Psychiatry* 1991;54:1044–54

Application of a Novel Brain Arteriovenous Malformation Endovascular Grading Scale for Transarterial Embolization

D.L. Bell, T.M. Leslie-Mazwi, A.J. Yoo, J.D. Rabinov, W.E. Butler, J.E. Bell, and J.A. Hirsch

ABSTRACT

BACKGROUND AND PURPOSE: The advent of modern neuroendovascular techniques has highlighted the need for a simple, effective, and reliable brain arteriovenous malformation endovascular grading scale. A novel scale of this type has recently been described. It incorporates the number of feeding arteries, eloquence, and the presence of an arteriovenous fistula component. Our aim is to assess the validity of this grading scale.

MATERIALS AND METHODS: We retrospectively reviewed all suspected brain arteriovenous malformations at Massachusetts General Hospital from 2005 to 2013, identifying 126 patients who met the inclusion criteria. Spearman correlations between endovascular and Spetzler-Martin grading scales and long-term outcomes were performed. Median endovascular grades were compared between treatment modalities and endovascular outcomes. Binary regression analysis was performed with major endovascular complications as a dichotomized dependent variable. Intraclass correlation coefficients were calculated for interobserver reliability of the endovascular grading scale.

RESULTS: A significant Spearman correlation between the endovascular grade and the Spetzler-Martin grade was demonstrated ($\rho = 0.5$, $P < .01$). Differences in the median endovascular grades between the endovascular cure (median = 2) and endovascular complication groups (median = 4) ($P < .05$) and between the endovascular cure and successful multimodal treatment groups (median = 3) ($P < .05$) were demonstrated. The endovascular grade was the only independent predictor of complications (OR = 0.5, $P < .01$). The intraclass correlation coefficient of the endovascular grade was 0.71 ($P < .01$).

CONCLUSIONS: Validation of a brain arteriovenous malformation endovascular grading scale demonstrated that endovascular grades of \leq II were associated with endovascular cure, while endovascular grades of \leq III were associated with multimodal cure or significant lesion reduction and favorable outcome. The endovascular grade provides useful information to refine risk stratification for endovascular and multimodal treatment.

ABBREVIATIONS: ARUBA = A Randomized Trial of Unruptured Brain Arteriovenous Malformations; bAVM = brain arteriovenous malformation; SIVMS = Scottish Intracranial Vascular Malformation Study

Since the first description of ethylene-vinyl alcohol copolymer as a liquid embolic agent for brain arteriovenous malformations (bAVMs) by Taki et al¹ in 1990 and its regulatory approval in the United States in 2005, the application and proficiency of its use in the treatment of bAVMs has steadily evolved and improved. Dissolved in dimethyl-sulfoxide and known commer-

cially as Onyx (Covidien, Irvine, California), the agent has expanded from its initial role as a palliative or presurgical/preradiosurgical embolization agent to a stand-alone curative agent in selected cases. In the most recent large Onyx transarterial embolization series that included 350 patients, the rate of curative, durable Onyx embolization was 51%, with 7.1% permanent morbidity and 1.4% mortality rates.² Additionally, in complex lesions, particularly ruptured, deep, and/or lesions with arterial feeders en passage, transvenous Onyx embolization has been successful.³⁻⁵

With expanded capability, appropriate patient selection becomes paramount. This was recently highlighted in the results of the controversial A Randomized Trial of Unruptured Brain Arteriovenous Malformations (ARUBA), which demonstrated a 3-fold increased morbidity and mortality from multimodal inter-

Received October 15, 2014; accepted after revision January 2, 2015.

From the Department of Radiology, Neuroendovascular Program (D.L.B., A.J.Y., J.D.R., J.A.H.), Department of Neurology and Radiology, Neurocritical Care and Neuroendovascular Program (T.M.L.-M.), and Department of Neurosurgery, Vascular Center (W.E.B.), Massachusetts General Hospital, Boston, Massachusetts; Harvard Medical School (D.L.B., T.M.L.-M., J.D.R., W.E.B., J.A.H.), Boston, Massachusetts; and Texas Stroke Institute (A.J.Y.), Plano, Texas.

Please address correspondence to Donnie L. Bell, MD, Massachusetts General Hospital, GRB 241, Boston, MA 02115; e-mail: d.l.belljr@gmail.com

<http://dx.doi.org/10.3174/ajnr.A4286>

Table 1: Endovascular grading scale^a

Feature and Value	Points
No. of feeding arteries ^b	
<3	1
≥3, <6	2
≥6	3
Eloquence of adjacent areas	
Noneloquent	0
Eloquent	1
Presence of arteriovenous fistula component ^c	
No AVF	0
AVF	1

^a Modified from Feliciano et al.¹²

^b An arterial feeder was defined as a separate arterial pedicle or a pedicle arising ≥ 1.5 cm from another arterial pedicle. En passage arterial feeders were given a score of 3.

^c The presence of an arteriovenous fistula was determined by criteria described by Yuki et al.¹³ including an abnormally dilated feeding artery, a direct arteriovenous connection to a dilated venous component or varix, the absence of a plexiform component between the 2 structures, and a diameter of the feeding artery more than twice as large as that of the arteries supplying the comparable areas not supplying the AVM (eg, the corresponding contralateral cerebral artery) or feeding artery diameter of >2 mm.

ventional therapy as opposed to medical management (30.7% versus 10.1%, respectively). Notably, ARUBA was a pooled analysis incorporating bAVMs of varying Spetzler-Martin grades, limiting the applicability of the trial results to specific lesion types; additionally, 32% of the patients were treated with stand-alone embolization without standardized selection criteria.^{6,7} The findings of ARUBA were corroborated by the Scottish Intracranial Vascular Malformation Study (SIVMS), in which conservative management was associated with lower progression to the primary outcome, death, or sustained morbidity, with a hazard ratio of 0.6.⁸ In a similar fashion to ARUBA however, SIVMS was a pooled analysis of heterogeneous bAVMs, with 21.4% of patients treated with stand-alone embolization without standardized selection criteria.^{8,9}

Although, the Spetzler-Martin and radiosurgical grading scales are validated means of predicting the safety and efficacy of surgery and radiosurgery respectively, application to endovascular or multimodal treatment (embolization plus radiosurgery or surgery) may be suboptimal as these grading schemes may not be sensitive to the procedural risk unique to transarterial embolization.^{10,11} No simple and effective endovascular grading scale for predicting procedural morbidity and/or mortality has been widely accepted. In 2011, Feliciano et al¹² performed a literature review of the factors associated with outcomes in bAVM transarterial embolization and developed an endovascular grading scale incorporating the number of feeding arteries, eloquence, and the presence of an arteriovenous fistula component based on this review and their clinical experience. While intriguing due to its simplicity and incorporation of factors thought to predict transarterial embolization safety and efficacy, no criteria defining bAVMs amenable to endovascular treatment were defined and the grading scale was not validated. We aimed to refine this scale (Table 1) and apply it retrospectively to our bAVM database to assess its validity.

MATERIALS AND METHODS

Study Population

We performed a retrospective analysis of the clinical data and imaging from 270 patients suspected of having ruptured or un-

ruptured bAVMs presenting to the Massachusetts General Hospital from 2005 to 2013. Institutional review board approval for accessing these records for clinical research purposes was obtained from Massachusetts General Hospital. Onyx was the primary agent used during this study. Lesions were initially treated with transarterial embolization using Onyx for palliation or pre-surgical/preradiosurgical embolization; yet following the evolution of Onyx embolization techniques, we pursued the primary intention of endovascular cure in selected cases.

Patients were included in the study if they had a bAVM initially diagnosed and subsequently treated at Massachusetts General Hospital, with available clinical data and CT, MR imaging, or catheter digital subtraction cerebral angiography images in the electronic medical record. We excluded patients under the following circumstances: having incomplete clinical or imaging data; being lost to follow-up; lesions previously treated, treated at a different institution, that underwent autothrombosis, that were observed and medically managed, with only feeding or intranidal aneurysms treated, and that were deemed not bAVMs on catheter digital subtraction cerebral angiography. This left 126 patients for analysis.

Data Collection

Data collected from the electronic medical record included but was not limited to age, sex, presentation (hemorrhage, seizure, neurologic deficit, incidental finding), treatment technique (surgical, radiosurgical, endovascular, or multimodal—embolization followed by surgery or radiosurgery), modified Rankin scale (at presentation, following treatment, and at ≥ 90 days), number of arterial feeders, presence of deep arterial feeders, arteriovenous fistula component, feeding artery or intranidal aneurysms, lesion volume, Spetzler-Martin grade, radiosurgical grade, and endovascular grade. Initial digital subtraction cerebral angiography images before any treatment were used for analysis. The images were independently reviewed by 2 neuroendovascular specialists (D.L.B., T.M.L.-M.), who assigned endovascular grades blinded to eventual treatment technique and outcomes. In lesions bordering eloquent areas and when functional imaging was performed, the functional imaging was used in determining Spetzler-Martin and endovascular grades. Final scores were adjudicated by the 2 reviewers.

Endovascular Grading Scale

The published scale was modified for the study, to make the scale more granular (Table 1).¹² An arterial feeder was defined as a unique arterial pedicle if it originated ≥ 1.5 cm from another arterial pedicle. Arterial feeders were categorized into 3 groups based on the number (ie, 1–2 feeders, 3–5 feeders, and ≥ 6 feeders, scored 1, 2, and 3 points, respectively). Predominant en passage arterial feeders were given a maximal score of 3. Eloquence (absence = 0, presence = 1 point) was defined as outlined in the original description from the Spetzler-Martin grading scale.¹⁰ The presence of an arteriovenous fistula component (absence = 0, presence = 1 point) was determined by criteria described by Yuki et al,¹³ including an abnormally dilated feeding artery, a direct arteriovenous connection to a dilated venous component or varix, the absence of a plexiform

Table 2: Characteristics of the population and treatment groups

	All Patients (n = 126)	Endovascular (n = 8)	Radiotherapy ^a (n = 39)	Surgical (n = 44)	Multimodal ^a (n = 31)	Endovascular Complications (n = 4)
Age (yr) (mean) (SD)	44.9 (±16.9)	42.8 (16.9)	45.6 (17.2)	48.7 (16.3)	37.9 (14.7)	41.3 (20.5)
Female sex (%)	52	50	53	63	32	25
Endovascular grade (median) (IQR)	3 (2–4)	2 (1.75–2)	4 (2–4)	3 (2–3)	3 (2–4)	4 (3.5–4.25)
Spetzler-Martin grade (median) (IQR)	2 (1–3)	1 (1.5–2)	3 (2–3)	1 (1–2)	3 (2–4)	3.5 (3–4)
bAVM volume (mL) (mean) (SD)	9.8 (±17.2)	2.1 (±1.8)	9.7 (±13.4)	1.7 (±2.4)	17.4 (±19.2)	54.1 (±45.2)
No. of feeding arteries (score) (median) (IQR)	2 (2–3)	1 (1–1.25)	3 (2–3)	3 (1–3)	2 (2–3)	3 (2.75–3)
AVF component (%)	9%	0	10%	2%	9%	25%
Eloquent (%)	53%	63%	74%	31%	54%	75%
Final mRS score (median) (IQR)	0 (0–1)	0 (0–0)	0 (0–1)	0 (0–1)	1 (0–1)	5 (3.5–6)

Note:—IQR indicates interquartile range.

^a Cured or significantly reduced lesions without complications (in the “Multimodal” category, this includes embolization plus radiosurgery).

component between the 2 structures, and a diameter of the feeding artery more than twice as large as that of the arteries supplying the comparable areas not supplying the bAVM (for example, the corresponding contralateral cerebral artery) or a feeding artery diameter of >2 mm. As these authors report and as described by Lasjaunias et al,¹⁴ bAVMs may demonstrate a complex arterial nidus accompanied by arteriovenous fistula components that require selective microcatheter digital subtraction cerebral angiography for reliable identification. Because selective microcatheter digital subtraction cerebral angiography was not routinely performed during diagnostic digital subtraction cerebral angiography for bAVMs, our sensitivity for the detection of this component was reduced.

Treatment

Endovascular. Using Onyx-compatible microcatheters, bAVM arterial pedicles were superselected following the standard technique. Microcatheter digital subtraction cerebral angiography was then performed to elucidate the relationship of the arterial pedicle to other arterial branches, resolve the angioarchitecture of the bAVM, and define the venous egress. Patients with predominant en passage arterial feeders were not treated with transarterial embolization via those pedicles. Using intermittent blank roadmaps, we administered Onyx slowly using a thumb-tapping technique to establish a plug, followed by nidal penetration, without interruption of the Onyx injection for >2 minutes. Neither a detachable tip nor dual-lumen balloon microcatheters were available and/or used during the study period.

Surgical. The head was positioned for optimal exposure of the lesion and placed in fixation, and stereotactic craniotomy was performed. Microsurgical obliteration of bAVMs was achieved with the aid of stereotactic neuronavigation for bAVM localization. In ruptured lesions, concomitant hematoma evacuation was performed when indicated. Following surgical obliteration of the lesion, immediate postoperative digital subtraction cerebral angiography was performed to confirm resection.

Radiosurgical. Three stainless steel skull fiducials were placed for localization. The Gill-Thomas-Cosman stereotactic head frame was applied in the usual fashion. Using the skull fiducials for radiographic reference, the bAVM volume was adjusted at the isocenter and proton radiation was delivered. Each portal was

Table 3: Treatment by Spetzler-Martin grade

	Grade I/II Lesions (n = 71)	Grade III Lesions (n = 37)	Grade IV/V Lesions (n = 18)
Surgery	58%	8%	0%
Endovascular	12%	5%	12%
Radiosurgery	15%	54%	44%
Multimodal ^a	15%	32%	44%

^a Embolization followed by surgery or radiosurgery.

custom-collimated and back-edge-compensated to provide maximum conformality to the dose distribution.

Follow-Up

Standard follow-up imaging was performed per institutional protocol in all treated cases. For surgery and endovascular treatment, it was 3-month posttreatment catheter digital subtraction cerebral angiography. For radiosurgical treatment delayed noninvasive imaging, typically contrast-enhanced MR imaging was performed at 2 years from treatment and then catheter digital subtraction cerebral angiography was performed at 3 years to document bAVM status at that time. Cured lesions were considered those without residual arteriovenous shunting on catheter digital subtraction cerebral angiography. A ≥50% reduction in the lesion volume on any imaging technique was considered significant. Successful multimodal treatment was any cured or significantly reduced lesion without complications.

Statistical Analysis

Univariate Spearman correlation was performed with the endovascular grading scale, Spetzler-Martin grading scale, and 90 days mRS. A 2-tailed Mann-Whitney *U* test was performed to compare the median endovascular grades between the endovascular cure and the endovascular complication groups and between the endovascular cure and the successful multimodal treatment groups. Backward stepwise binary regression analysis was performed with major endovascular complication as the dichotomized dependent variable and the number of arterial feeders, eloquence, arteriovenous fistula component, Spetzler-Martin grade, and endovascular grade as independent variables. Interobserver reliability of the endovascular grading scale and its components were calculated with intraclass correlation coefficients using a 2-way random model of absolute agreement type. SPSS, Version 21 (IBM, Armonk, New York) was used for statistical analysis.

RESULTS

Total cohort demographics and of the 4 comparison groups are presented in Table 2. Treatment by the Spetzler-Martin grade is presented in Table 3. Notably, 58% of grade I/II lesions were treated with surgical resection; 54% and 32% of grade III lesions were treated with radiosurgery and multimodal treatment, respectively; and 88% of grade IV/V lesions were treated with an even split of radiosurgery and multimodal treatment. Stand-alone endovascular treatment was performed in 12% of grade I/II lesions, 5% of grade III lesions, and 12% of grade IV/V lesions. Of the 31 patients treated with multimodal therapy, 68% were treated with transarterial embolization followed by surgery, while 32% were treated with transarterial embolization followed by radiosurgery. In the entire cohort, 38% presented with intracranial hemorrhage secondary to the bAVM. The overall and endovascular (as a stand-alone treatment and as part of multimodal treatment) rates of complications resulting in major morbidity or death were 3.4% and 9.3%, respectively.

A statistically significant Spearman correlation between the endovascular grade and Spetzler-Martin grade was demonstrated ($\rho = 0.5, P < .01$). No correlations between the Spetzler-Martin or endovascular grade and the long-term mRS were identified.

There were significant differences in the median endovascular grades between the endovascular cure group (median = 2; interquartile range, 1.75–2) and the endovascular complication group (median = 4; interquartile range, 3.5–4.25; Mann-Whitney *U* test = 3.5, $P < .05$) and between the endovascular cure group and the successful multimodal treatment group (median = 3, interquartile range, 2–4; Mann-Whitney *U* test = 56.5, $P < .05$).

Backward stepwise binary regression analysis demonstrated the endovascular grade as the only independent predictor of complications (OR = 0.5, $P < .01$).

The interobserver reliability of the endovascular grade was good, with an intraclass correlation coefficient of 0.71 ($P < .01$). The intraclass correlation coefficients of the number of feeding arteries, eloquence, and arteriovenous fistulous component were 0.66, 0.61, and 0.53, respectively ($P < .01$).

DISCUSSION

Application of an endovascular grading scale incorporating the number of feeding arteries (1–2, 1 point; 3–5, 2 points; ≥ 6 , 3 points), eloquence (absence = 0, presence = 1 point), and the presence of an arteriovenous fistula component (absence = 0, presence = 1 point) demonstrated that endovascular grades of \leq II were associated with endovascular cure, while endovascular grades of \leq III were associated with multimodal cure or significant reduction and favorable outcomes ($P < .05$). Moreover, the endovascular grade was the only independent predictor of major endovascular complications, demonstrated good interobserver reliability with an intraclass correlation coefficient of 0.71 ($P < .01$), and correlated with the Spetzler-Martin grade. Illustrative lesions can be seen in Figs 1 and 2.

As neuroendovascular proficiency continues to advance, refinement of bAVM risk stratification for endovascular treatment is imperative in ensuring favorable outcomes. The Spetzler-Martin grade has been adapted to predict morbidity associated with stand-alone embolization with long-term rates of neurologic deficits after embolization of 0%, 5%, 7%, 10%, and 18%, respectively, for Spetzler-

Martin grades I through V.¹⁵ However, in this study, *n*-butyl cyanoacrylate and coils were the primary agents as opposed to Onyx. The Spetzler-Martin grading scale has also been shown to correlate with outcomes in patients undergoing multimodal treatment.^{16,17} Nevertheless, it was created for surgical risk assessment, and because transarterial embolization of bAVMs aims to obliterate bAVMs via endovascular arterial occlusion and inflammatory changes leading to angioneurosis while carrying the risk of premature venous occlusion before complete devascularization of the lesion, the factors influencing the safety and efficacy of transarterial embolization likely differ from those governing the success of surgery.¹⁸

To our knowledge, this is the first validation of an endovascular grading scale for bAVMs for transarterial embolization since the advent of current neuroendovascular techniques. Previously, an endovascular grading scale was reported by Willinsky et al¹⁹ in 2001 for bAVMs of < 3 cm; this scale included nidus type/size (fistula = 0; < 1 cm = 1 point; 1–3 cm = 2 points), type of feeding arteries (cortical = 0, perforator or choroidal = 1 point), number of feeding arteries (single = 0, multiple = 2 points), and the number of draining veins (single = 0, multiple = 1 point). In 80 patients, the authors demonstrated a cure rate of 86% in grade 0–2 lesions and suggested that this scale was a better predictor of endovascular cure, morbidity, and mortality than the Spetzler-Martin grade. A key differentiating factor between the grading scale presented by Willinsky et al¹⁹ and the endovascular grading scale presented here is the grading of arteriovenous fistula components. In the previous grading system, arteriovenous fistula components did not increase the endovascular grade as they do in the current grading system. Most interesting, 3 of 7 complications experienced by Willinsky et al were the result of venous penetration of the embolic agent, and whether an arteriovenous fistula component played a role in these outcomes might be questioned. An additional distinguishing factor is the incorporation of the number of draining veins that did not correlate with cure rates in their study, which is absent in the grading scale presented here.¹⁹ Finally, the prior scale was developed with the use of isobutyl cyanoacrylate and *n*-butyl cyanoacrylate as the liquid embolic agents. Isobutyl cyanoacrylate is no longer in use, and *n*-butyl cyanoacrylate is now typically an adjunctive endovascular agent or a primary agent in selected cases.

Since the report by Willinsky et al,¹⁹ Onyx has been introduced; neuroendovascular techniques have evolved; and myriad factors, including the Spetzler-Martin grade, periprocedural hemorrhage, deep venous drainage, number of embolized branches, age, absence of neurologic deficit, hemorrhagic presentation, small bAVM size, the presence of deep arterial feeders, eloquent location, the presence of arteriovenous fistula components, and venous penetration of embolic agents, have been associated with endovascular complications and unfavorable outcomes.^{15,19–23} Furthermore, adding to our understanding of the mechanisms underlying complications and their frequencies following bAVM transarterial embolization, Baharvahdat et al²⁴ noted in their series of 846 cases primarily treated with Onyx that of the 11% of patients experiencing hemorrhagic complications, those complications could be divided into 2 categories: arterial perforation (48%) and all others (52%). Arterial perforation occurred during either microcatheter navigation or retrieval. Of the hemorrhagic complications not attributable to arterial perforation, premature venous deposition was an independent predictor of com-

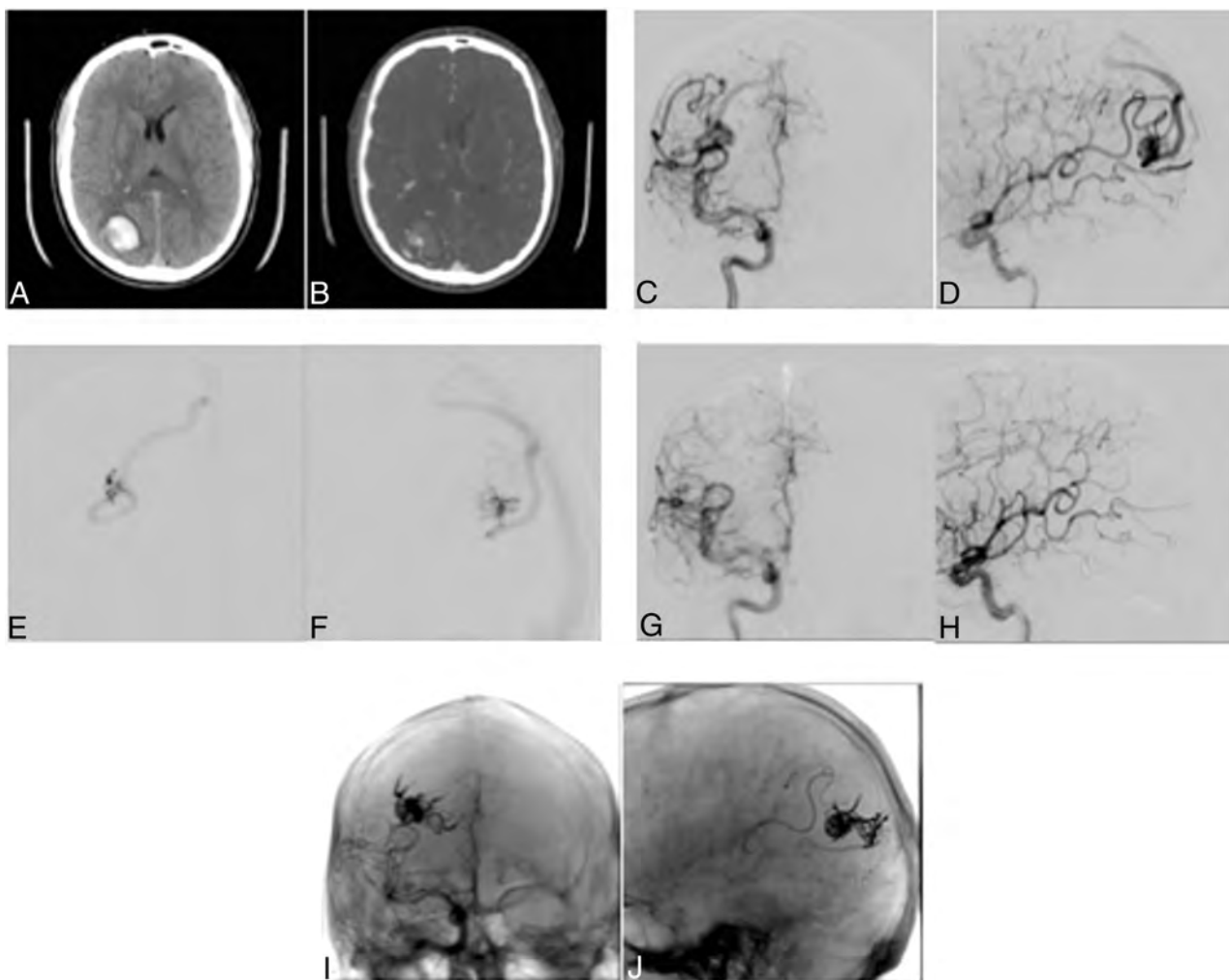


FIG 1. A 35-year-old man presenting with acute onset of dizziness and headache. *A* and *B*, noncontrast head CT and head CTA demonstrate a 3.4-cm right parietal hematoma and a 1.9-cm bAVM, respectively. *C* and *D*, Diagnostic right internal carotid artery anteroposterior and lateral angiograms demonstrate a Spetzler-Martin grade II (S1, E1, V0) and endovascular grade II (A2, E0, F0) bAVM supplied via angular branches of the right middle cerebral artery (supplementary right posterior cerebral artery supply not shown) with superficial venous drainage via mildly dilated cortical veins. *E* and *F*, Intraprocedural right middle cerebral artery angular branch microcatheter anteroposterior and lateral angiograms demonstrate a distinct plexiform nidus and no arteriovenous fistulous component. *G* and *H*, Right internal carotid artery anteroposterior and lateral angiograms following Onyx embolization via the right middle cerebral artery angular branch demonstrate resolution of arteriovenous shunting (left vertebral artery injection also documented resolution of arteriovenous shunting from a supplementary right posterior cerebral artery supply, not shown). *I* and *J*, Skull anteroposterior and lateral radiographs demonstrate the Onyx cast; note penetration of the Onyx material into a posterior component supplied by the right posterior cerebral artery on the lateral projection. Final mRS = 0. S indicates size; E, eloquence; V, vein; A, artery; F, fistula.

plications. Notably, complications did not correlate with increasing Spetzler-Martin grade.²⁴ Intuitively then, increasing numbers of arterial feeders requiring multiple microcatheterizations and/or multi-stage procedures, the presence of an arteriovenous fistula component increasing the likelihood of premature venous embolization, and eloquent regions intolerant to insult are likely to be associated with complications and poor outcomes following transarterial embolization.

With the recent results of the ARUBA and SIVMS trials, patient selection for bAVM treatment will likely come under greater scrutiny. The limitations of these trials are well recognized, including the lack of standardized interventional arm treatment algorithms, selection bias, variable participating site characteristics, short follow-up period, the relatively small number of Spetzler-Martin grade I and II lesions treated with surgery, and the small sample size that limited subset analysis.^{7,9,25} Although the literature suggests that the Spet-

zler-Martin grading scale may be applicable to endovascular and multimodal treatment in some cases, discrepant lesions with low Spetzler-Martin grades and high endovascular grades might pose a challenge regarding patient selection. In our cohort, 3 of the 4 patients with major complications had an endovascular grade of ≥ 4 with 1 lesion harboring an arteriovenous fistula component that was prematurely embolized, resulting in occlusive hyperemia and hemorrhagic venous infarction (Fig 2). Notably, in 2 of these 4 lesions, the endovascular grade was higher than the Spetzler-Martin grade, including the lesion in Fig 2. Given this finding, the endovascular grading scale may supplement Spetzler-Martin grades in lesions under consideration for endovascular and multimodal treatment, improving patient selection.

The interobserver agreement of the endovascular grading scale was good and approaching excellent, with an intraclass correlation coefficient of 0.71 ($P < .01$). Interobserver variability largely

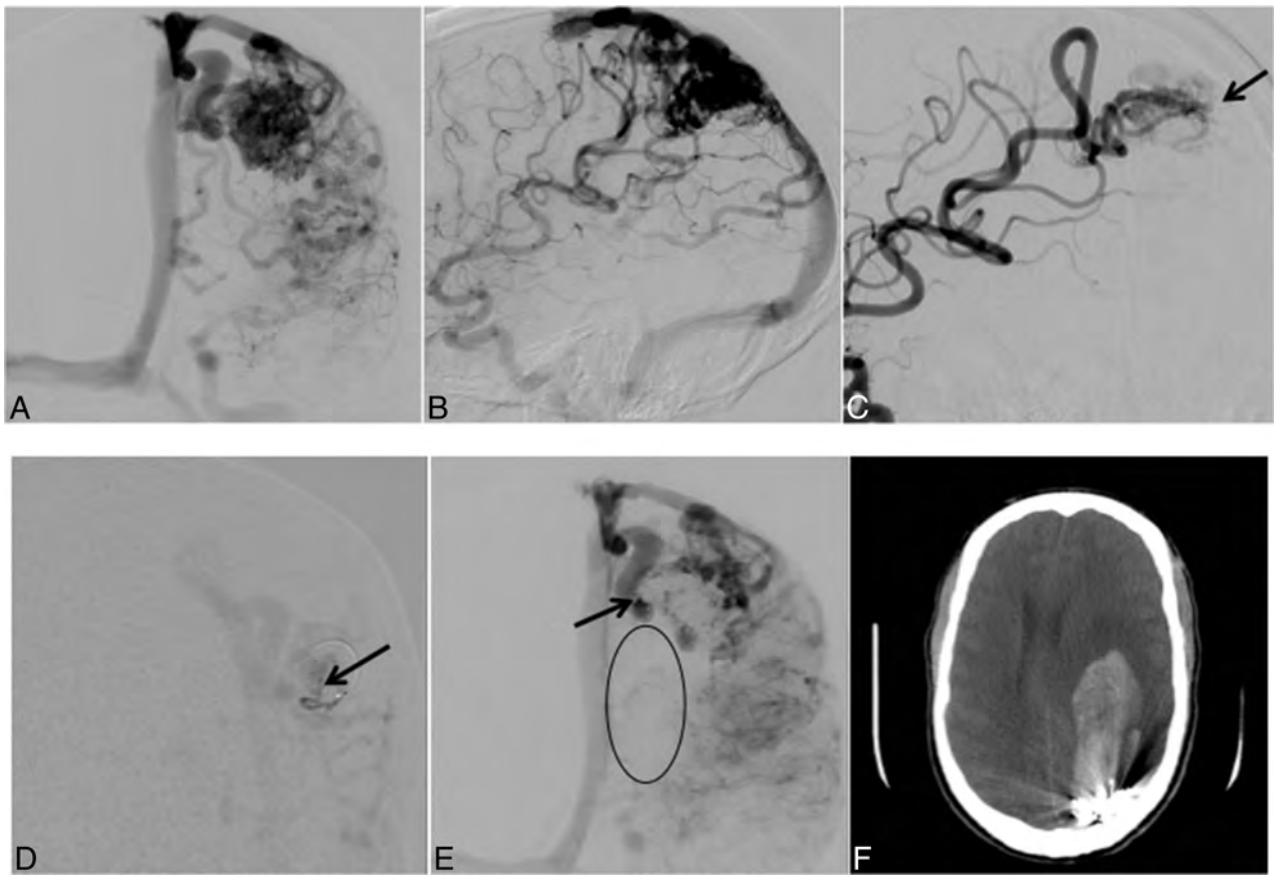


FIG 2. A 31-year-old man presenting with seizures found to have a 3.8-cm left frontoparietal bAVM, Spetzler-Martin grade III (S2, E1, V0), and endovascular grade V (A3, E1, F1). A and B, Diagnostic left internal carotid anteroposterior and lateral angiograms demonstrate predominant arterial supply to the lesion via posterior frontal and parietal branches of the left middle cerebral artery with superficial venous drainage via moderately dilated cortical veins. Supplemental supply via the left anterior and posterior cerebral arteries was also present (not shown) C, Diagnostic left middle cerebral artery lateral magnification angiogram demonstrates a dilated angular branch >2 mm with a direct venous connection consistent with an arteriovenous fistula component (*arrow*). D, Intraprocedural left middle cerebral artery angular branch superselective microcatheter injection oblique anteroposterior angiogram again demonstrates an arteriovenous fistula component (*arrow*). E, Following stage I Onyx embolization, the medial portion of the Onyx cast (Onyx subtracted, seen as absence of contrast enhancement within the previous nidus compared to image A) can be seen within a dilated medial cortical vein (*arrow*), and the previously seen dilated cortical veins coursing inferiorly in image A are no longer visualized consistent with venous occlusion (*ellipse*). F, Postprocedural day 2 emergent noncontrast head CT performed for neurologic deterioration and a dilated left pupil demonstrates a large 3.8×7.4 cm left frontal hemorrhage anterior to the Onyx cast with surrounding cerebral edema, causing moderate-to-severe rightward midline shift. The hematoma and residual bAVM underwent emergent surgical resection. Final mRS was 6 due to neurologic decline and ventilator-associated pneumonia. S indicates size; E, eloquence; V, vein; A, artery; F, fistula.

arose from discrepancies in the designation of arterial feeders en passage, determining eloquence in lesions bordering eloquent areas, and detection of arteriovenous fistula components. Variability in arterial feeders en passage and arteriovenous fistula components might be resolved by superselective catheterization in diagnostic digital subtraction cerebral angiography or at treatment in lesions preliminarily deemed amenable to transarterial embolization. A consensus agreement regarding areas bordering eloquent regions, overlapping eloquent and noneloquent lesions graded as eloquent, and/or performance of functional imaging or superselective provocative pharmacologic testing could be used in lesions in which eloquence is in question.

We did not demonstrate a correlation between Spetzler-Martin and endovascular grades with long-term outcomes. Potential explanations include patient selection (only 8% of lesions Spetzler-Martin grade III or higher were treated with surgery, and a large fraction, 72%, of patients treated with transarterial embolization were treated as part of multimodal therapy), a low overall complication rate, and a small sample size.

While we have detailed criteria for an endovascular grading scale for transarterial embolization of bAVMs and demonstrated its utility and reliability, there are several limitations of our study. The small sample size and retrospective, single-center study design limit generalization. The lack of routine arterial pedicle superselective microcatheter digital subtraction cerebral angiography during diagnostic evaluation decreased the sensitivity for the detection of arterial feeders en passage and arteriovenous fistula components. Also the applicability of the endovascular grading scale to risk stratification for transvenous bAVM embolization and newer transarterial embolization methods, including the pressure cooker and the dual-lumen balloon microcatheter techniques, which may expand the types of bAVMs amenable to safe and effective endovascular treatment, cannot be assessed. Further, the endovascular grading scale does not incorporate hemodynamic data such as wall shear stress and other flow-related parameters, which may identify bAVM components susceptible to hemorrhage or complications following transarterial embolization. Finally, despite our diligent search, there may have been occa-

sional cases that were not identified and hence not analyzed.²⁶⁻³⁰ In the case of venous egress, a dichotomized variable for the number of venous egress pathways (single = 0, multiple = 1 point) or variations thereof, in addition to or supplanting the number of arterial feeders, might extend the applicability of this grading scale to the transvenous approach. Future studies evaluating the endovascular grading scale in a prospective manner are warranted.

CONCLUSIONS

A novel endovascular grading scale for bAVM transarterial embolization incorporating the number of feeding arteries (1–2, 1 point; 3–5, 2 points; ≥ 6 , 3 points), eloquence (absence = 0, presence = 1 point), and the presence of an arteriovenous fistula component (absence = 0, presence = 1 point) demonstrated that endovascular grades of \leq II were associated with endovascular cure, while endovascular grades of \leq III were associated with a multimodal cure or significant lesion reduction and favorable outcomes. Moreover, the endovascular grade was an independent predictor of major endovascular complications and demonstrated good interobserver reliability. The endovascular grading scale may supplement Spetzler-Martin grades to refine risk stratification for endovascular and multimodal bAVM treatment. Further validation is warranted.

ACKNOWLEDGMENTS

We thank Drs Johnny Pryor, Christopher Ogilvy, and Paul Chapman as clinical investigators who provided and cared for study patients.

Disclosures: Joshua A. Hirsch—UNRELATED: Consultancy: Medtronic, Comments: interventional spine; Stock/Stock Options: Intratech, Comments: developmental-stage interventional stroke company.

REFERENCES

1. Taki W, Yonekawa Y, Iwata H, et al. **A new liquid material for embolization of arteriovenous malformations.** *AJNR Am J Neuroradiol* 1990;11:163–68
2. Saatci I, Geyik S, Yavuz K, et al. **Endovascular treatment of brain arteriovenous malformations with prolonged intranidal Onyx injection technique: long-term results in 350 consecutive patients with completed endovascular treatment course.** *J Neurosurg* 2011;115:78–88
3. Albuquerque FC, Ducruet AF, Crowley RW, et al. **Transvenous to arterial Onyx embolization.** *J Neurointerv Surg* 2014;6:281–85
4. Consoli A, Renieri L, Nappini S, et al. **Endovascular treatment of deep hemorrhagic brain arteriovenous malformations with transvenous Onyx embolization.** *AJNR Am J Neuroradiol* 2013;34:1805–11
5. Nguyen TN, Chin LS, Souza R, et al. **Transvenous embolization of a ruptured cerebral arteriovenous malformation with en-passage arterial supply: initial case report.** *J Neurointerv Surg* 2010;2:150–52
6. Mohr JP, Parides MK, Stapf C, et al. **Medical management with or without interventional therapy for unruptured brain arteriovenous malformations (ARUBA): a multicentre, non-blinded, randomised trial.** *Lancet* 2014;383:614–21
7. Bambakidis NC, Cockcroft KM, Hirsch JA, et al. **The case against a randomized trial of unruptured brain arteriovenous malformations: misinterpretation of a flawed study.** *Stroke* 2014;45:2808–10
8. Al-Shahi Salman R, White PM, Counsell CE, et al. **Outcome after conservative management or intervention for unruptured brain arteriovenous malformations.** *JAMA* 2014;311:1661–69
9. Zaidi HA, Russin JJ, Spetzler RF. **Conservative management vs intervention for unruptured brain arteriovenous malformations.** *JAMA* 2014;312:1058
10. Spetzler RF, Martin NA. **A proposed grading system for arteriovenous malformations.** *J Neurosurg* 1986;65:476–83
11. Pollock BE, Flickinger JC. **A proposed radiosurgery-based grading system for arteriovenous malformations.** *J Neurosurg* 2002;96:79–85
12. Feliciano C, de León-Berra R, Hernández-Gaitán MS, et al. **A proposal for a new arteriovenous malformation grading scale for neuroendovascular procedures and literature review.** *P R Heal Sci J* 2011;29:117–20
13. Yuki I, Kim RH, Duckwiler G, et al. **Treatment of brain arteriovenous malformations with high-flow arteriovenous fistulas: risk and complications associated with endovascular embolization in multimodality treatment: clinical article.** *J Neurosurg* 2010;113:715–22
14. Lasjaunias P, Manelfe C, Chiu M. **Angiographic architecture of intracranial vascular malformations and fistulas: pretherapeutic aspects.** *Neurosurg Rev* 1986;9:253–63
15. Kim LJ, Albuquerque FC, Spetzler RF, et al. **Postembolization neurological deficits in cerebral arteriovenous malformations: stratification by arteriovenous malformation grade.** *Neurosurgery* 2006;59:53–59; discussion 53–59
16. Deruty R, Pelissou-Guyotat I, Mottotese C, et al. **Prognostic value of the Spetzler's grading system in a series of cerebral AVMs treated by a combined management.** *Acta Neurochir (Wien)* 1994;131:169–75
17. Nataraj A, Mohamed MB, Gholkar A, et al. **Multimodality treatment of cerebral arteriovenous malformations.** *World Neurosurg* 2014;82:149–59
18. Jahan R, Murayama Y, Gobin YP, et al. **Embolization of arteriovenous malformations with Onyx: clinicopathological experience in 23 patients.** *Neurosurgery* 2001;48:984–95; discussion 995–97
19. Willinsky R, Goyal M, Terbrugge K, et al. **Embolisation of small (<3 cm) brain arteriovenous malformations: correlation of angiographic results to a proposed angioarchitecture grading system.** *Interv Neuroradiol* 2001;7:19–27
20. Ledezma CJ, Hoh BL, Carter BS, et al. **Complications of cerebral arteriovenous malformation embolization: multivariate analysis of predictive factors.** *Neurosurgery* 2006;58:602–11; discussion 602–11
21. Gobin YP, Laurent A, Merienne L, et al. **Treatment of brain arteriovenous malformations by embolization and radiosurgery.** *J Neurosurg* 1996;85:19–28
22. Hartmann A, Mast H, Mohr JP, et al. **Determinants of staged endovascular and surgical treatment outcome of brain arteriovenous malformations.** *Stroke* 2005;36:2431–35
23. Haw CS, terBrugge K, Willinsky R, et al. **Complications of embolization of arteriovenous malformations of the brain.** *J Neurosurg* 2006;104:226–32
24. Baharvahdat H, Blanc R, Termechi R, et al. **Hemorrhagic complications after endovascular treatment of cerebral arteriovenous malformations.** *AJNR Am J Neuroradiol* 2014;35:978–83
25. Amin-Hanjani S, Albuquerque FC. **Commentary: unruptured brain arteriovenous malformations—what a tangled web they weave.** *Neurosurgery* 2014;75:195–96
26. Chapot R, Stracke P, Velasco A, et al. **The pressure cooker technique for the treatment of brain AVMs.** *J Neuroradiol* 2014;41:87–91
27. Illies T, Forkert ND, Ries T, et al. **Classification of cerebral arteriovenous malformations and intranidal flow patterns by color-encoded 4D-hybrid-MRA.** *AJNR Am J Neuroradiol* 2013;34:46–53
28. Ansari SA, Schnell S, Carroll T, et al. **Intracranial 4D flow MRI: toward individualized assessment of arteriovenous malformation hemodynamics and treatment-induced changes.** *AJNR Am J Neuroradiol* 2013;34:1922–28
29. Orozco LD, Luzardo GD, Buciuic RF. **Transarterial balloon assisted Onyx embolization of pericallosal arteriovenous malformations.** *J Neurointerv Surg* 2013;5:e18
30. Jagadeesan BD, Grigoryan M, Hassan AE, et al. **Endovascular balloon-assisted embolization of intracranial and cervical arteriovenous malformations using dual-lumen coaxial balloon microcatheters and Onyx: initial experience.** *Neurosurgery* 2013;73(2 suppl operative):ons238–43; discussion ons243

Narrowing the Expertise Gap for Predicting Intracranial Aneurysm Hemodynamics: Impact of Solver Numerics versus Mesh and Time-Step Resolution

M.O. Khan, K. Valen-Sendstad, and D.A. Steinman

ABSTRACT

BACKGROUND AND PURPOSE: Recent high-resolution computational fluid dynamics studies have uncovered the presence of laminar flow instabilities and possible transitional or turbulent flow in some intracranial aneurysms. The purpose of this study was to elucidate requirements for computational fluid dynamics to detect these complex flows, and, in particular, to discriminate the impact of solver numerics versus mesh and time-step resolution.

MATERIALS AND METHODS: We focused on 3 MCA aneurysms, exemplifying highly unstable, mildly unstable, or stable flow phenotypes, respectively. For each, the number of mesh elements was varied by 320× and the number of time-steps by 25×. Computational fluid dynamics simulations were performed by using an optimized second-order, minimally dissipative solver, and a more typical first-order, stabilized solver.

RESULTS: With the optimized solver and settings, qualitative differences in flow and wall shear stress patterns were negligible for models down to ~800,000 tetrahedra and ~5000 time-steps per cardiac cycle and could be solved within clinically acceptable timeframes. At the same model resolutions, however, the stabilized solver had poorer accuracy and completely suppressed flow instabilities for the 2 unstable flow cases. These findings were verified by using the popular commercial computational fluid dynamics solver, Fluent.

CONCLUSIONS: Solver numerics must be considered at least as important as mesh and time-step resolution in determining the quality of aneurysm computational fluid dynamics simulations. Proper computational fluid dynamics verification studies, and not just superficial grid refinements, are therefore required to avoid overlooking potentially clinically and biologically relevant flow features.

ABBREVIATIONS: CFD = computational fluid dynamics; HR = high-resolution; k = thousand; M = million; MWSS = maximum wall shear stress; NR = normal-resolution; OSI = oscillatory shear index; WSS = wall shear stress

Image-based computational fluid dynamics (CFD) has become an essential tool for investigating intracranial aneurysm hemodynamics and its possible role in aneurysm initiation, growth, rupture, and treatment outcome. Notably, retrospective studies have demonstrated associations between low or high wall shear stress (WSS) and rupture status, with the goal of improving rup-

ture-risk assessment. Although attempts have been made to unify these opposing hemodynamic factors,¹ skepticism about CFD remains, owing to the wide variety of proposed hemodynamic factors and definitions,² the various modeling assumptions and uncertainties,³ and the focus on lumen versus the wall.⁴ Nevertheless, medical imaging vendors are actively seeking to deploy CFD solvers on their scanner platforms.⁵

A recent study has highlighted a largely unacknowledged source of uncertainty: the strong dependence of the simulations on the CFD solution strategy.⁶ In that study, a so-called high-

Received September 4, 2014; accepted after revision November 19.

From the Biomedical Simulation Laboratory (M.O.K., K.V.-S., D.A.S.), Department of Mechanical and Industrial Engineering, University of Toronto, Toronto, Ontario, Canada; and Center for Biomedical Computing (M.O.K., K.V.-S.), Simula Research Laboratory, Lysaker, Norway.

This work was supported by a Heart and Stroke Foundation of Canada grant (G-13-0001830) to D.A.S. Computations were performed on the General Purpose Cluster at the SciNet High Performance Computing Consortium. SciNet is funded by the Canada Foundation for Innovation under the auspices of Compute Canada; the Government of Ontario; Ontario Research Fund—Research Excellence; and the University of Toronto. D.A.S. also acknowledges the support of Mid-Career Investigator salary award from the Heart and Stroke Foundation.

Paper previously presented in part at: International Symposium on Biomechanics in Vascular Biology and Cardiovascular Disease, April 28–29, 2014, Montreal, Canada; the Interdisciplinary Cerebrovascular Symposium, June 2–4, 2014, Zurich, Switzerland; and the World Congress of Biomechanics, July 6–11, 2014, Boston, Massachusetts.

Please address correspondence to David A. Steinman, PhD, 5 King's College Rd, Toronto, ON, Canada M5S 3G8; e-mail: steinman@mie.utoronto.ca

<http://dx.doi.org/10.3174/ajnr.A4263>

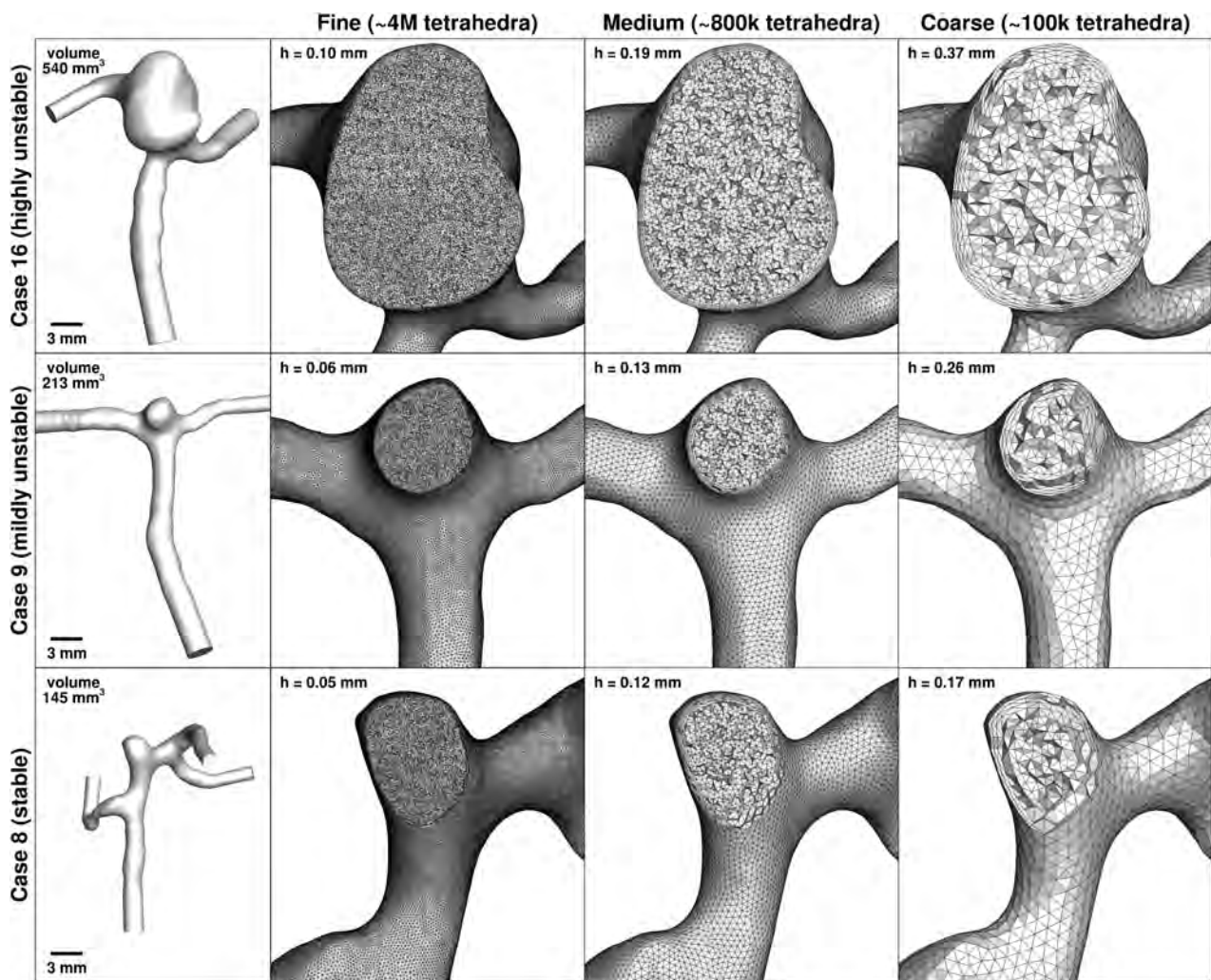


FIG 1. Fine, medium, and coarse meshes for each of the 3 MCA aneurysm cases. Nominal tetrahedral side length in the sac (h) is indicated at the top left of each mesh panel. The leftmost column shows the full lumen models, to the same scale, and with model volumes indicated. The ultrafine (32M) meshes are too attenuated to show, having effective tetrahedral side lengths of half those of the fine (4M) meshes.

resolution (HR) strategy, combining a high-fidelity CFD solver with fine mesh and time-step resolutions, uncovered high-frequency flow instabilities in 4/8 MCA bifurcation aneurysm cases. On the other hand, these instabilities were completely suppressed by a so-called normal-resolution (NR) strategy, combining a solver and resolutions more representative of the aneurysm CFD literature.

In not separating the impact of solver numerics versus model resolution, the aforementioned study may have left the impression that highly refined CFD meshes and time-steps, and thus clinically unsupported computation times, might be required to predict complex aneurysmal flow features. For the present study, we hypothesized that solver numerics (by which we mean the solver discretization scheme and settings) are at least as important as mesh and time-step resolution in determining the fidelity of aneurysm CFD solutions. To test this hypothesis and to determine whether instabilities can be detected, if not necessarily resolved, at lower CFD model resolutions (and hence more clinically supportable time scales), the present study varied, independently, the CFD solver numerics, mesh resolution, and time-stepping to

identify their relative impacts on qualitative and quantitative hemodynamics of intracranial aneurysms.

MATERIALS AND METHODS

The study focused on 3 different anatomically plausible MCA aneurysms (Fig 1), previously shown to exhibit, and specifically chosen to exemplify, highly unstable (case 16), mildly unstable (case 9), and stable (case 8) flows, respectively.^{6,7} Pulsatile simulations were performed by using an ICA flow waveform shape derived from older adults⁸ and damped by 30% to account for its transit from the cervical-to-cavernous segments.⁹ We applied a cross-sectional time-averaged velocity of 0.37 m/s,⁶ resulting in cycle-averaged flow rates of 1.11, 1.93, and 2.12 mL/s for cases 8, 9, and 16, respectively. Fully developed Womersley velocity profiles were applied at the inlet, and zero pressure was specified at the outlets. Three cardiac cycles were simulated to wash out initial transients. Blood viscosity and attenuation were assumed to be 0.035 mPa-s and 1 g/cm³, respectively.

As summarized in the Table, various permutations of spatial (mesh) resolution, temporal (time-step) resolution, and CFD

Model identifiers and CPU times for the various permutations of spatial resolution, temporal resolution, and solver

Model ID	Spatial Resolution (Mesh Elements)	Temporal Resolution (Time-Steps)	CFD Solver	CPU Hours per Cycle ^a
HR1	Ultrafine (32M)	Fine (35k)	HR	326
HR2	Fine (4M)	Fine (35k)	HR	68
HR3	Medium (800k)	Fine (35k)	HR	22
HR4	Coarse (100k)	Fine (35k)	HR	4.9
HR5	Medium (800k)	Medium (5.6k)	HR	3.5
HR6	Medium (800k)	Coarse (1.4k)	HR	0.9
HR7	Coarse (100k)	Coarse (1.4k)	HR	0.2
NR5	Medium (800k)	Medium (5.6k)	NR	28
NR6	Medium (800k)	Coarse (1.4k)	NR	7
NR7	Coarse (100k)	Coarse (1.4k)	NR	1.2

Note:—CPU indicates central processing unit; ID, identification.

^a Approximate execution time on an 8-core, 2.53-GHz Xeon E5540 CPU (Intel, Santa Clara, California).

solver were considered for each of the 3 cases. First, to isolate the effects of spatial resolution, we performed simulations by using the HR solver with fine time-stepping for 4 different meshes, generated by using the Vascular Modeling ToolKit (<http://www.vmtk.org>). The reference (ultrafine) meshes comprised ~4 million (4M) second-order tetrahedra, roughly equivalent to ~32M linear tetrahedra. The fine meshes comprised the same ~4M elements, but now by using linear tetrahedra. Medium and coarse meshes comprised ~800,000 (800k) and ~100,000 (100k) linear tetrahedra, respectively. All used 4 boundary layer elements, with the total boundary layer thickness set to the nominal tetrahedral element side length. Per Fig 1, the 320-fold difference in the number of elements corresponded to nearly an order of magnitude variation in tetrahedron side length (ie, spatial resolution).

For the above studies, a reference (fine) temporal resolution was set to 35,000 (35k) time-steps per cardiac cycle, to satisfy the well-known Courant-Friedrich-Lewy stability condition for the ultrafine meshes. Per the Table, to independently isolate the effects of temporal resolution, the number of time-steps/cycle was reduced to 5600 (5.6k) and then 1400 (1.4k). These simulations, spanning a 25-fold difference in temporal resolution, were performed by using the medium (800k) meshes, after observing that they had adequate spatial resolution. To test the limits of solution accuracy, we also performed a coarse (100k) mesh and time-step (1.4k) simulation for each case.

The above-described simulations used a second-order-accurate, minimally dissipative, and energy-preserving CFD solver¹⁰ (described previously as the HR solver,⁶ and available as an open-source code at <https://github.com/mikaem/Oasis>). To independently isolate the effect of the solver, per the Table, we performed the same simulations described for the temporal resolution subanalysis by using the NR solver,⁶ which is stabilized and first-order-accurate in space and time to mimic the default settings in commercial solvers like Fluent (ANSYS, Canonsburg, Pennsylvania) and Star-CD (CD-adapco, Melville, New York).

The impact of resolution and solver was evaluated qualitatively via volumetric maps of velocity magnitude, surface maps of cycle-averaged WSS magnitude and oscillatory shear index (OSI), and traces of velocity and WSS magnitude from selected probe points. For quantitative evaluations, we computed the

following nominal predictors of rupture status for each combination of case and model⁶: dome-averaged WSS and dome-maximum WSS (MWSS), both normalized to the parent artery WSS, and dome-averaged OSI.

RESULTS

Qualitative results are summarized in the comprehensive Fig 2. If one focuses first on spatial (mesh) resolution effects, it can be seen that from the equivalent of 32M elements down to 800k elements (HR1, HR2, and HR3), there were negligible differences in velocity, WSS, and

OSI levels and distributions for all cases. Notably, for unstable cases 16 and 9, all models appeared to capture similar flow instabilities, per the inset velocity and WSS traces. Further coarsening of the meshes to 100k elements (HR4) introduced an evident reduction in WSS levels, as well as a dampening (but not complete suppression) of velocity and WSS instabilities for cases 16 and 9. On the basis of the 320-fold difference in mesh sizes, we concluded that mesh size is relatively insensitive for the commonly reported hemodynamic variables and thus alone cannot inform whether a CFD simulation is adequate.

With the 800k meshes as a basis for the temporal (time-step) resolution investigation, negligible effects were seen in going from 35k to 5.6k steps/cycle (ie, HR3 versus HR5). Minor differences were evident with a further reduction to 1.4k steps/cycle (HR6), suggesting that a temporal resolution somewhere between these 2 values would be sufficient. This dramatic reduction in the number of time-steps had a similarly minor effect for the 100k meshes (HR4 versus HR7). Some differences were evident for the velocity traces for the 2 unstable flow cases (16 and 9), but even the coarsest models (HR7) were still able to detect, if not necessarily resolve, the flow instabilities.

On the other hand, simulations performed by using the normal-resolution solver (NR5–7 versus HR5–7) appeared to artificially suppress all flow instabilities. WSS maps were comparable with those of the corresponding HR models, but OSI was highly underestimated by the NR solver at 1.4k steps/cycle. This was improved by increasing the number of time-steps to 5.6k but still with an evident suppression of flow instabilities per the velocity and WSS traces. On the basis of the 25-fold difference in time-step size, we concluded that the number of time-steps is only moderately important, as long as the number of time-steps is >5000 per cycle.

The quantitative impact on proposed scalar metrics of rupture status is shown in Fig 3. In particular, normalized, dome-averaged (time-averaged) WSS was relatively stable with mesh and temporal resolution by using our HR solver: Errors relative to the highest resolution (HR1) models were always <10%. For MWSS, there was a more evident reduction in values with each mesh coarsening, and at the coarsest resolutions with the HR solver, the rank ordering of cases by MWSS was altered. Especially for cases 8 and 9, MWSS values were evidently less accurate for the NR-versus-HR solver. For the HR solver, dome-averaged OSI was rela-

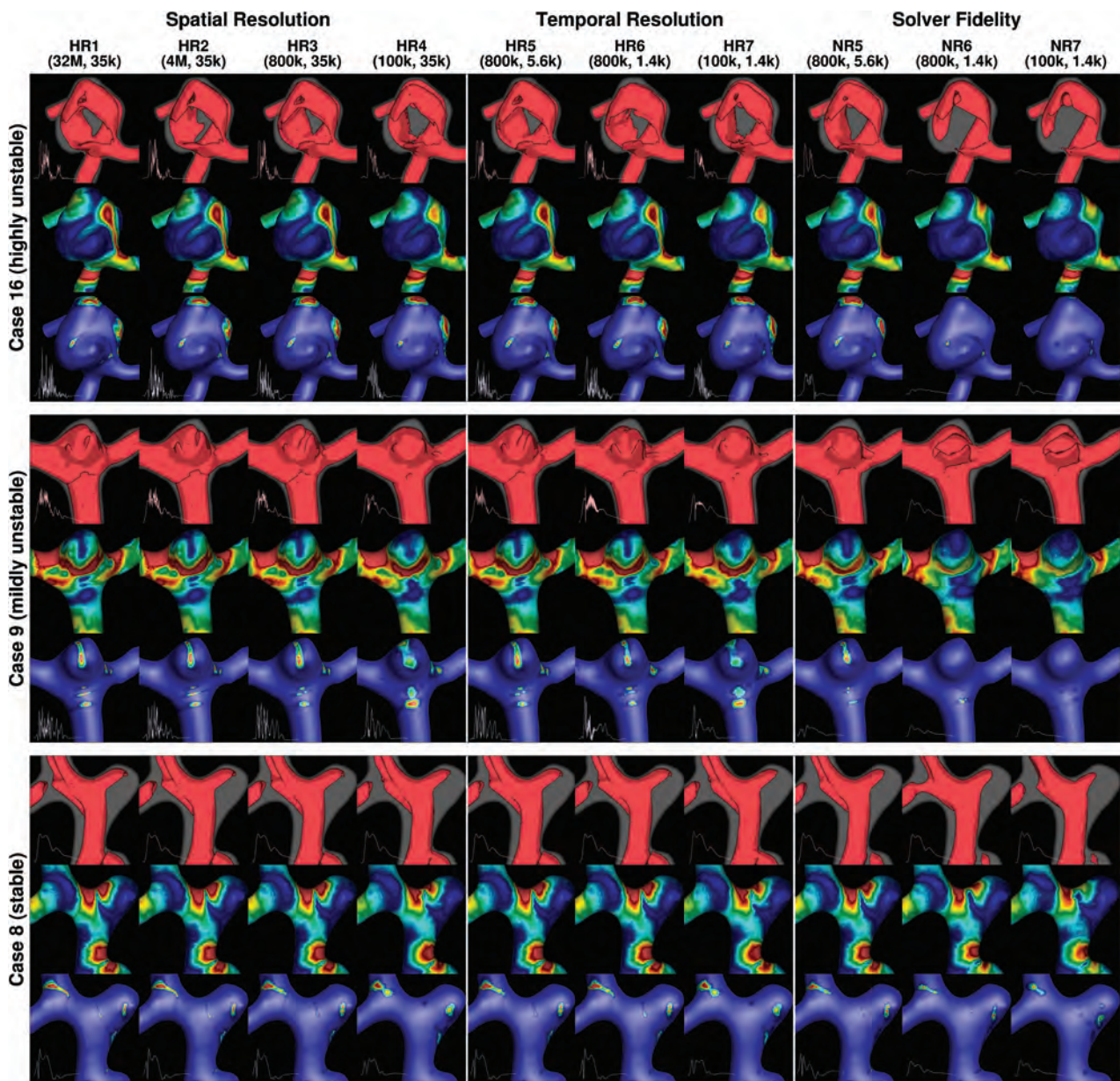


FIG 2. Qualitative impact of spatial resolution, temporal resolution, and solver fidelity on velocity and wall shear stress distributions. For each of the 3 aneurysm cases, the top row shows isosurfaces (0.3 m/s) of early diastolic velocity magnitude, the middle row shows time-averaged WSS magnitude (scale: 0–15 Pa), and the bottom row shows the oscillatory shear index (scale: 0.0–0.3). The inset into each velocity isosurface panel is a velocity-versus-time trace, from a selected point within the sac. Similarly, the inset into each OSI panel is a WSS magnitude-versus-time trace, from a point on the sac experiencing relatively high OSI.

tively unaffected down to the 800k meshes and 5.6k steps/cycle. Larger errors were evident at the coarser resolutions; however, the rank ordering by OSI was unaffected. The same could not be said for the NR solver, with almost complete suppression of OSI for the unstable cases 16 and 9, also affecting the rank ordering. Finally, even with an 8-fold increase in the number of elements (eg, NR6 versus NR7), the NR solutions were still far from the converged (HR) solutions, at least for the unstable flow cases.

DISCUSSION

We have demonstrated that CFD solver numerics had a more profound impact on commonly computed hemodynamic indices than the number of time-steps and, perhaps most surprising,

mesh resolution. As discussed below, the importance of solver numerics was expected a priori; however, we were pleasantly surprised by the coarseness and hence speed with which an HR-type solver could achieve high-quality results relative to the reference solutions. As also discussed below, these findings have implications for the utility of CFD in a clinical setting and for basic research into aneurysm mechanobiology.

Implications for Clinical Timeframes

The clearest impact of the current results is that irrespective of flow phenotype, accurate hemodynamic indices can be obtained within clinically supportable timeframes provided a HR-type CFD solver is used. Per the Table and Fig 3, accurate solutions

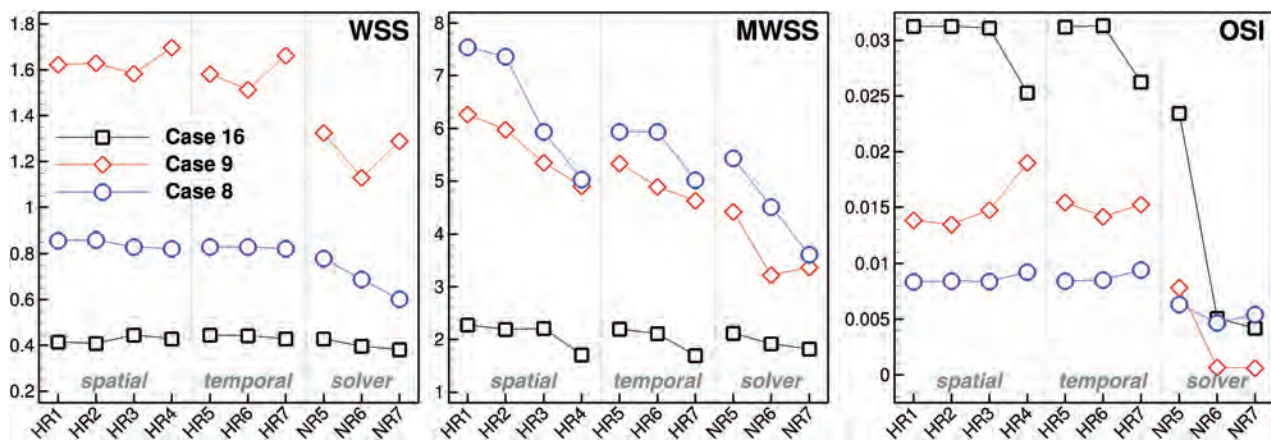


FIG 3. The quantitative impact of spatial resolution, temporal resolution, and solver fidelity on various reduced hemodynamic indices, as indicated at the top right corner of each plot.

could be achieved by the HR solver on a standard desktop computer in ~ 3 hours/cycle or ~ 10 hours for a complete simulation. Furthermore, by showing that the coarse resolution simulations could at least detect the presence of flow instabilities, we can conclude that <1 hour of simulation time would be sufficient to assess the need for further refinement, of course provided a high-fidelity solver is used.

A corollary of this is that the absence of flow instabilities in an NR-type simulation cannot be taken as *prima facie* evidence of stable aneurysm flow. As such, and as our results suggest, NR-type simulations might, ironically, require finer resolutions and hence longer run times than what is typically reported. This supposition is not to imply that detection of flow instabilities is a *sine qua non* for the investigation of aneurysm hemodynamics, but rather that their absence in the aneurysm CFD literature may be the result of numeric artifacts that are inadvertently serving to suppress plausible avenues of investigation. Nor is it intended to impugn the findings of aneurysm CFD “trials,” because we have previously shown that NR-type simulations can consistently rank cases by using reduced-order hemodynamic indices (eg, time- and dome-averaged WSS) and, hence, nominally, rupture status, albeit with a 50% underestimation of WSS magnitudes.⁶ As noted in the next section, however, results from NR solvers may well be misleading regarding the pathophysiology of aneurysm initiation and rupture.

Implications for Aneurysm Mechanobiology

Just like morphologic discriminants, reduced hemodynamic indices are only an echo of some putative mechanistic link between the hemodynamic stresses and the response of the wall. To elucidate those mechanobiologic links, one may need a thorough understanding of the spatiotemporal scales of the flow and WSS, which requires HR-type simulations. For example, by suppressing flow instabilities, NR-type simulations cannot easily explain the prevalence of aneurysm bruits,^{11,12} which are widely thought to be driven by high-frequency flow instabilities, whether laminar or turbulent. Furthermore, even though both NR5 and HR5 simulations showed comparable OSI distributions in Fig 2, the behavior behind them is different: For HR5, high OSI is due to high-frequency WSS instabilities, whereas for NR5, it is due to more

sluggish WSS oscillations. The latter is characteristic of the type of flow for which OSI was originally developed, whereas it is known that different stimuli can give rise to the same OSI value.¹³ On the basis of the turbulent-like flows from the HR simulations, it thus seems likely that any correlations between rupture status and high OSI from NR-type studies do not necessarily reflect the mechanobiologic causation.

Although it remains to be proved, it is plausible that the dynamic WSS stimuli elicited by the HR-type simulations could be of importance for understanding the mechanobiology of aneurysm growth and rupture. Focus in aneurysm research has been on spatial WSS gradients,¹⁴ whereas temporal WSS gradients, shown to be of importance to mechanotransduction and gene expression,¹⁵ have received less attention, probably because prevalent NR-type simulations are unable to detect them. For example, Davies et al¹⁶ exposed endothelial cells *in vitro* to turbulent flows (ie, WSS stimuli phenotypically similar to what we see in some of the unstable flow cases) and showed that turbulence led to a lack of endothelial cell orientation and cell depletion and loss even for low-intensity disturbances. Fry¹⁷ investigated similar effects *in vivo*, and after just an hour of exposure to turbulent flows, reported endothelial cell swelling, deformation, and disintegration downstream of the plug. In short, it seems as though temporal WSS gradients may also be of importance.

Relationship to Previous Work

As alluded to by Ventikos,¹⁸ our findings would likely have been anticipated by experienced CFD users following verification guidelines laid out by engineering journals nearly 30 years ago. In 1986, the *ASME Journal of Fluids Engineering* emphasized in their editorial policy that “a single calculation of a fixed grid is not acceptable.”¹⁹ This journal has also said, “It has been demonstrated many times that for first-order methods, the effect of numeric diffusion on the solution accuracy is devastating,”²⁰ consistent with what we have shown in the current study. However, a cursory inspection of articles published in the *American Journal of Neuroradiology* and other clinical (and indeed biomedical engineering) research journals reveals that accuracy or mesh and time-step refinement results are rarely or only superficially reported. We are aware of only 1 thorough presentation, by Hodis et

al,²¹ who carried out an extensive mesh refinement study by using the popular commercial CFD solver, Fluent. Meshes ranged from a high of nearly 7000 nodes/mm³ to a low around 100 nodes/mm³.

Our study spanned a wider range, with ultrafine meshes comprising 8000–30,000 nodes/mm³ to coarse meshes with 30–100 nodes/mm³, and allowed investigation of the isolated effects of spatial and temporal resolution errors alone, in which the most resolved model was effectively 8000 (ie, 320 × 25) times finer than the coarsest one. Hodis et al²¹ also focused on a technically detailed convergence analysis of the peak systolic velocity vector field and its error norms, which, while salient, provided little context for the qualitative differences in the overall flow and WSS fields and/or derived scalar indices of potential clinical interest. Nevertheless, we arrived at similar conclusions to those of Hodis et al, namely that refined meshes are required, particularly if point values are desired. We disagree, however, with their assertion that “each patient-specific model require[s] its own grid convergence,” because this is laborious and not practicable in a clinical setting.

Our findings could also be anticipated from the results of a recent international CFD Challenge.²² There, peak systolic flow instabilities in a giant ICA aneurysm were predicted by only a handful of the 25 participating groups. Most of the contributed solutions (most by using commercial CFD solvers, predominantly Fluent) reported laminar flows with stable peak systolic flow patterns and with aneurysm jet inflow velocities damped to varying degrees. One of the conclusions was that at least 5000 time-steps/cycle appeared to be a necessary, albeit not a sufficient, condition for detecting flow instabilities. Our present findings would seem to suggest that even 1000 time-steps/cycle—the median of that used by the various CFD Challenge participants—are insufficient to resolve the dynamics of unstable aneurysm flows, even with a minimally dissipative, second-order-accurate CFD solver.

To see whether our findings could be extrapolated to a commercial solver, we performed transient steady flow simulations (to remove the confounding effects of pulsatility) for the most unstable flow, case 16, by using Fluent (Version 14; ANSYS). Steady inflow velocity was set to 0.5 m/s, corresponding to peak systolic conditions at the MCA.⁶ Simulations were performed for the 800k mesh and 1.4k time-steps, by using first-order upwinding (Fluent’s default prior to 2012) and second-order upwinding (the current Fluent default), both with default solver settings (semi-implicit method for the pressure-linked equation method, first-order implicit time-stepping, “standard” pressure, 20 iterations/time-step, single precision, 10^{−3} convergence criterion). For second-order upwinding, the default settings were then refined (the PISO [pressure implicit with splitting of operator] method, second-order implicit time-stepping, second-order pressure, 50 iterations/time-step, double precision, 10^{−5} convergence criterion). The results, shown in Fig 4, indicate a strong sensitivity of velocity dynamics to upwind order and solver settings, independent of the solver itself. For example, the first-order upwinding of Fluent performed in a manner similar to that of our NR solver, both serving to damp any flow instabilities. The second-order upwinding of Fluent detected some flow instabilities,

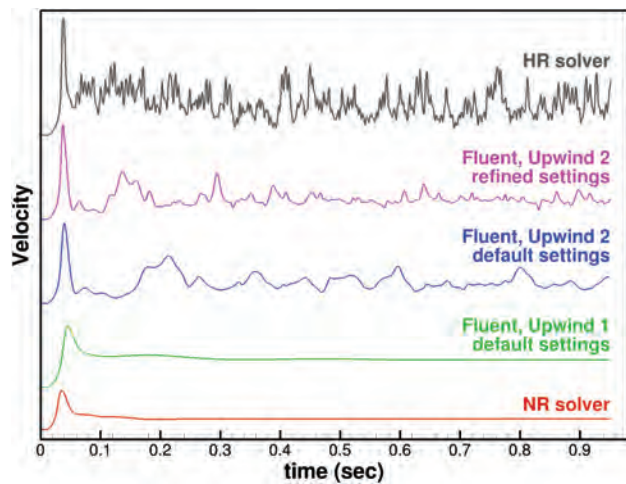


FIG 4. Impact of the progressively refined CFD solver and settings on transient simulation of steady flow for case 16, with 800k mesh and 1.4k time-steps.

the frequency of which was clearly increased by expert refining of the default solver settings. These results are, therefore, approaching a solution that is referred to as minimally dissipative and energy-preserving.²³

It is worth noting that, for these expertly refined settings, we had to adjust both the number of iterations and the convergence tolerance to reach the desired convergence level, a subtlety that might be lost on a non-expert user. Nevertheless, not being perfectly fluent in Fluent, we could not get it to match the higher frequency and amplitude fluctuations evident from our HR solver. This inability to match our results to those of Fluent is not to imply that our finite-element-based HR solver is superior to Fluent and/or the finite volume method on which it is based. Rather, it highlights the importance of understanding well the capabilities of a CFD solver and its limitations to ensure reliable results.

Potential Limitations

We assumed rigid walls, Newtonian fluid, fully developed (laminar) inflow velocities, and generalized flow rates. These are commonly accepted assumptions, and their effects are now well-documented to be of relatively minor importance, at least for NR-type simulations. Moreover, our observed impact of solver settings on hemodynamic variables was, if anything, more pronounced than the previously reported impacts of the above-noted assumptions. Relevant limitations of the current study were the following: 1) It is unclear whether blood can still be modeled as a continuum for turbulent-like unstable flows.²⁴ 2) The assumption of fully developed laminar inflow may be questioned in light of recent evidence that the carotid siphon may have flow instabilities propagating into the MCA.²⁵ 3) Our study considered only 3 cases from a particular site (MCA), albeit chosen to exemplify a range of aneurysm flow phenotypes. 4) It remains unclear what is necessary to elucidate the mechanobiology or resolve instantaneous quantities. Finally, caution must be exercised in translating too literally the numbers of elements and time-steps that were sufficient for our purposes, for 2 main reasons: First, they obviously depend on the size of the aneurysm, the extent of the do-

main, and the dynamics of the imposed flow rates. Second, as we have clearly demonstrated here, they depend critically on the choice of CFD solver and its settings. Thus, we must emphasize that the recommended mesh and time-step sizes hold only for our HR solver—each user must perform their own verification studies.

CONCLUSIONS

We have shown that a robust and minimally dissipative CFD solver can tolerate surprisingly coarse resolutions, whereas solvers using low-order and/or stabilization schemes may, ironically, require much higher resolutions to detect, let alone properly resolve, complex flow in a potentially nonnegligible number of aneurysm cases. It is therefore essential that groups perform proper verification studies, per the recommendations of technical journals and, ideally, with the help of experts in CFD theory and practice, to arrive at solver settings and mesh/time-step resolutions that can be applied uncritically to any given case. This process is much in the same way that medical physicists play a critical role in setting clinical imaging protocols. If CFD is, ultimately, to operate as a putative medical imaging tool, it must have established local protocols that too are set by expert users by using rigorous calibration (ie, verification) methodologies.

ACKNOWLEDGMENTS

The authors thank Maxwell Julian (University of Toronto), Peter Coppin (OCAD University), and Side Effects Software for their help in generating the data-driven, illustration-inspired velocity visualizations in Fig 2.

REFERENCES

- Meng H, Tutino VM, Xiang J, et al. **High WSS or low WSS? Complex interactions of hemodynamics with intracranial aneurysm initiation, growth, and rupture: toward a unifying hypothesis.** *AJNR Am J Neuroradiol* 2014;35:1254–62
- Kallmes DF. **Point: CFD-computational fluid dynamics or confounding factor dissemination.** *AJNR Am J Neuroradiol* 2012;33:395–96
- Kallmes DF. **Identifying “truth” in computational fluid dynamics research.** *AJNR Am J Neuroradiol* 2011;32:E122; author reply E123
- Krings T, Mandell DM, Kiehl TR, et al. **Intracranial aneurysms: from vessel wall pathology to therapeutic approach.** *Nat Rev Neurol* 2011;7:547–59
- Pease AF. **Killers under attack.** *Pictures of the Future: The Magazine for Research and Innovation.* Siemens AG; Fall 2010:79–81
- Valen-Sendstad K, Steinman DA. **Mind the gap: impact of computational fluid dynamics solution strategy on prediction of intracranial aneurysm hemodynamics and rupture status indicators.** *AJNR Am J Neuroradiol* 2014;35:536–43
- Valen-Sendstad K, Mardal KA, Steinman DA. **High-resolution CFD detects high-frequency velocity fluctuations in bifurcation, but not sidewall, aneurysms.** *J Biomech* 2013;46:402–07
- Hoi Y, Wasserman BA, Xie YJ, et al. **Characterization of volumetric flow rate waveforms at the carotid bifurcations of older adults.** *Physiol Meas* 2010;31:291–302
- Schubert T, Santini F, Stalder AF, et al. **Dampening of blood-flow pulsatility along the carotid siphon: does form follow function?** *AJNR Am J Neuroradiol* 2011;32:1107–12
- Mortensen M, Valen-Sendstad K. **Oasis: a high-level/high-performance open source Navier-Stokes solver.** *Comput Phys Commun* 2015;188:177–88
- Ferguson GG. **Turbulence in human intracranial saccular aneurysms.** *J Neurosurg* 1970;33:485–97
- Kurokawa Y, Abiko S, Watanabe K. **Noninvasive detection of intracranial vascular lesions by recording blood flow sounds.** *Stroke* 1994;25:397–402
- Peiffer V, Sherwin SJ, Weinberg PD. **Does low and oscillatory wall shear stress correlate spatially with early atherosclerosis? A systematic review.** *Cardiovasc Res* 2013;99:242–50
- Dolan JM, Kolega J, Meng H. **High wall shear stress and spatial gradients in vascular pathology: a review.** *Ann Biomed Eng* 2013;41:1411–27
- White CR, Stevens HY, Haidekker M, et al. **Temporal gradients in shear, but not spatial gradients, stimulate ERK1/2 activation in human endothelial cells.** *Am J Physiol Heart Circ Physiol* 2005;289:H2350–55
- Davies PF, Remuzzi A, Gordon EJ, et al. **Turbulent fluid shear stress induces vascular endothelial cell turnover in vitro.** *Proc Natl Acad Sci U S A* 1986;83:2114–17
- Fry DL. **Acute vascular endothelial changes associated with increased blood velocity gradients.** *Circ Res* 1968;22:165–97
- Ventikos Y. **Resolving the issue of resolution.** *AJNR Am J Neuroradiol* 2014;35:544–45
- Roache PJ, Ghia KN, White FM. **Editorial policy statement on the control of numerical accuracy.** *J Fluids Eng* 1986;108:2
- Journal of Fluids Engineering Editorial Policy. Statement on the Control of Numerical Accuracy. <http://journaltool.asme.org/templates/JFENumAccuracy.pdf>. Accessed September 1, 2014
- Hodis S, Uthamaraj S, Smith AL, et al. **Grid convergence errors in hemodynamic solution of patient-specific cerebral aneurysms.** *J Biomech* 2012;45:2907–13
- Steinman DA, Hoi Y, Fahy P, et al. **Variability of computational fluid dynamics solutions for pressure and flow in a giant aneurysm: the ASME 2012 Summer Bioengineering Conference CFD Challenge.** *J Biomech Eng* 2013;135:021016
- Morinishi Y, Lund TS, Vasilyev OV, et al. **Fully conservative higher order finite difference schemes for incompressible flow.** *J Comput Phys* 1998;143:90–124
- Antiga L, Steinman DA. **Rethinking turbulence in blood.** *Biorheology* 2009;46:77–81
- Valen-Sendstad K, Piccinelli M, Steinman DA. **High-resolution computational fluid dynamics detects flow instabilities in the carotid siphon: implications for aneurysm initiation and rupture?** *J Biomech* 2014;47:3210–16

Endovascular Recanalization in Acute Ischemic Stroke Using the Solitaire FR Revascularization Device with Adjunctive C-Arm CT Imaging

B.D. Mitchell, P. Chinnadurai, G. Chintalapani, H.A. Morsi, H. Shaltoni, and M.E. Mawad

ABSTRACT

SUMMARY: In this clinical report, we examined a single-center experience by using the Solitaire FR Revascularization Device in the treatment of acute ischemic stroke in which there was poor initial visualization of the occluded arterial branches by using biplanar cerebral angiography. In all cases, adjunctive C-arm CT was used during the deployment of the thrombectomy device to gain additional information regarding device placement and expansion. Outcome measures included the extent of reperfusion, posttreatment changes in NIHSS scores, posttreatment TICl scores, cerebral hemorrhage, and survival. Clot removal with successful arterial recanalization was achieved in 15/18 cases (83.3%) with TICl scores of 2b/3 in all patients who had initial recanalization. The NIHSS score improved, on average, from 19 pretreatment to 11 posttreatment, and 72% of patients survived. In cases of acute stroke in which there is little information available regarding the positioning and deployment of a retrievable stent during mechanical thrombectomy, the use of C-arm CT may provide more information about device placement across an area of thrombus.

In cases of embolic stroke in which the suspected thrombus is large and causes total occlusion of a major cerebral vessel, such as the internal carotid, middle cerebral, or basilar artery, the endovascular navigation of the intracranial vessels can be challenging, with no contrast entering the vessels ahead of the catheters or interventional devices. Recently, the use of self-expanding retrievable stents (Solitaire FR Revascularization Device; Covidien, Irvine, California; Trevo; Stryker, Kalamazoo, Michigan) has complemented the current armamentarium of endovascular treatments available for acute stroke.¹⁻⁵ Ideally, these stents are deployed within a suspected thrombus, and the stent is allowed to expand for a few minutes, at which point the stent can be retrieved, along with the thrombus.

The use of C-arm CT during endovascular interventional procedures has evolved rapidly from a technique that was relatively slow, with image quality lagging behind that of conventional CT, to one that now offers very high-resolution images that can be obtained rapidly during an interventional procedure.⁶ Recently, C-arm CT has been used for rapid acquisition of intraprocedural CT scans and ce-

rebral blood volume testing, especially during the treatment of patients with stroke,^{7,8} and can additionally provide high-quality images, even in areas of highly attenuated skull base anatomy.

Here, we report a series of 18 patients undergoing mechanical thrombectomy for acute stroke, in which initial visualization of the entire arterial anatomy was poor by using biplanar fluoroscopic methods, given the degree of occlusion (most frequently involving the entire internal carotid artery) from the suspected thrombus. In these cases, C-arm CT was used to aid overall visualization of the pertinent anatomy and to directly observe the degree of stent expansion in areas of suspected thrombus.

MATERIALS AND METHODS

Cases of 18 patients with acute stroke who underwent mechanical thrombectomy by using the Solitaire FR device at a single institution (Baylor College of Medicine) from October 2012 to January 2014 were retrospectively analyzed. Cases were selected on the basis of the following: 1) Acute stroke symptoms were present, evaluated by the neurology stroke team of the institution, with or without tPA given before angiographic evaluation. 2) Patients were angiographically evaluated within 8 hours of witnessed symptom onset. 3) There was no visualization of a major arterial branch (ICA, MCA, anterior cerebral artery, vertebral artery, or basilar artery) by using biplanar angiographic methods. 4) C-arm CT was used adjunctively for additional radiographic information during the treatment stage of the attempted thrombectomy. In each case in which the selection criteria were met, C-arm CT (syngo Dyna CT; Siemens, Erlangen, Germany) was used during

Received July 14, 2014; accepted after revision November 18.

From the Departments of Neurosurgery (B.D.M.) and Neuro-Interventional Radiology (H.A.M., H.S., M.E.M.), Baylor College of Medicine, Houston, Texas; Siemens Medical Solutions USA (P.C., G.C.), Angiography Division, Hoffman Estates, Illinois; and Neurovascular Center (H.A.M., H.S., M.E.M.), Baylor St. Luke's Hospital, Houston, Texas.

Please address correspondence to Bartley D. Mitchell, MD, PhD, Department of Neurosurgery, Baylor College of Medicine, 7200 Cambridge, Suite 9A, Houston, TX 77030; e-mail: bartley.mitchell@bcm.edu

<http://dx.doi.org/10.3174/ajnr.A4256>

Patient summary

Patient No.	Age (yr)	Sex	Thrombus Location	No. of Passes	TICI Score (Post)	NIHSS (Pre)	NIHSS (Post)	Outcome
1	66	F	Left ICA	1	2b	26	26	Died
2	74	M	Right MCA	2	0	17	17	Died
3	67	M	Left MCA	2	2b	23	9	Rehab/Home
4	76	F	Right MCA	1	3	15	15	Rehab/Home
5	65	M	Right ICA	2	2b	16	12	Rehab/Home
6	67	M	Right MCA	1	3	18	18	Died
7	58	M	Right ICA	2	3	18	2	Home
8	58	M	Left MCA	1	2b	27	11	Rehab/Home
9	71	M	Left MCA	2	2b	18	5	Rehab/Home
10	65	M	Left MCA	1	2b	16	2	Rehab/Home
11	71	M	Left MCA	2	3	19	19	Died
12	60	M	Right MCA	1	3	8	0	Home
13	67	F	Left MCA	1	3	15	1	Home
14	77	M	Left MCA	2	0	21	18	LTAC
15	27	M	Left ICA	1	3	22	5	Rehab/Home
16	79	F	Left MCA	4	0	24	24	Died
17	30	M	Right MCA	3	2b	18	7	Rehab/Home
18	60	M	Right MCA	2	2b	14	7	Rehab/Home

Note:—Pre indicates before; Post, after; Rehab, rehabilitation; LTAC, long-term acute care facility.

stent deployment at both the initial time of deployment and following a 5-minute period in which the stent was allowed to expand into the presumed clot.

Intraprocedural C-arm CT images (20-second protocol; effective dose, 2.9 mSv) were acquired in 18 patients who underwent endovascular treatment for acute ischemic stroke. C-arm CT images acquired during mechanical thrombectomy passes were coregistered together (syngo InSpace 3D Fusion; Siemens) to understand and compare the stent configuration.

Following the 5-minute waiting period to allow the stent to expand into the suspected thrombus, the stent was retracted, while using an inflatable balloon catheter and with syringe suction applied to the guide catheter to prevent any loss of the thrombus during retrieval. Additional C-arm CT images of the retrievable stents were not obtained in each case in which additional stent passes were used beyond the first pass, unless there was evidence of arterial occlusion in a separate region that was not readily visualized with fluoroscopic methods. Selective angiography was performed between each pass of the Stentriever device (Trevor) to determine the extent of recanalization from the intervention and to determine whether another pass might be of benefit in cases in which incomplete recanalization was observed.

This study was performed with human institutional review board approval: collaborative protocol #H-33379.

RESULTS

In this clinical report of 18 patients with acute stroke treated with retrievable self-expanding stents for mechanical thrombectomy, initial visualization of occluded arterial anatomy was poor, and in these cases, C-arm CT was used to obtain 3D images of the stent devices at the time of deployment, allowing improved visualization of stent position, shape, and conformation, compared with initially obtained digital subtraction angiography alone. In all cases in this series, there was an initial observable incomplete stent expansion in the presumed area of the arterial thrombus that could be seen with images obtained by using C-arm CT. In most cases (17/18 patients, 94%), the initial incomplete stent expansion resolved after the initial 5-minute waiting period, indicating that

the stent had expanded into the thrombus and was optimized for removal. In a single case, the stent did not show re-expansion, indicating the likely presence of an atherosclerotic embolus, as opposed to a softer thrombotic embolus. Overall, we were able to achieve a recanalization rate of 83.3% (15/18 patients) by using mechanical thrombectomy with retrievable stents alone. An average of 1.7 passes of the stent was used overall to achieve recanalization, with a maximum of 4 passes used in 1 case. A summary of the patient data is provided in the Table.

The NIHSS score was assessed immediately before the thrombectomy procedure and after the procedure in all cases, and overall, it was seen to improve from 19 (preprocedure) to 11 post-thrombectomy ($P = .001$, 2-tailed t test). If one considered only those patients who survived (13/18), their NIHSS score improved, on average, from 18 to 7 overall ($P < .0001$, 2-tailed t test), and all surviving patients showed improved or stable NIHSS scores following treatment with the Solitaire device. Posttreatment hemorrhage was observed in 28% of patients (5/18), though the extent of hemorrhage was limited to petechial or small basal ganglia hemorrhage in all cases observed (grades: hemorrhagic transformation 1 in 3 cases and hemorrhagic transformation 2 in 2 cases). Despite the limited extent of hemorrhage, 4 of those 5 patients actually achieved recanalization during treatment and 2 of these 5 ultimately died; these results indicate that despite recanalization, patients may have poor outcomes.

Case Illustration

A 58-year-old man with a history of atrial fibrillation, on a direct thrombin inhibitor medication, presented with a witnessed sudden-onset unilateral weakness and collapse. He was not eligible for IV tPA, given his prior history of direct thrombin inhibitor use; therefore, he was taken to the angiography suite for definitive treatment. Initial angiography showed stagnation of blood flow into the right internal carotid artery, with no intracranial flow (Fig 1A, -B), suggesting a likely T-thrombus of the internal carotid artery bifurcation, extending onto both the proximal MCA and anterior cerebral artery, though this was presumed given the lack of visual data available from biplanar angiographic imaging alone.

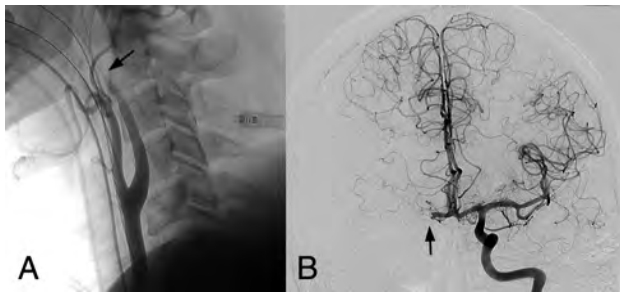


FIG 1. Preprocedural angiogram showing complete blockage of the right internal carotid artery. *A*, Oblique view of the carotid bifurcation shows complete ICA obstruction, with poor visualization of the vessels both proximal and distal to the presumed occlusion. *B*, Left ICA angiogram shows cross-filling perfusion into the right anterior cerebral artery territory, but with embolus blocking contralateral blood flow at the right anterior cerebral artery.

The right-sided anterior cerebral artery territory was cross-filled from the left carotid circulation via a patent anterior communicating artery, though the right MCA territory was completely devoid of circulation.

Further navigation of the guidewire and catheter into the right anterior circulation territory was severely limited, though the guidewire was able to be advanced into the suspected thrombus region. At this point, the Solitaire stent retrieval system was deployed within the proximal MCA, extending from the superior division of the MCA to the ICA bifurcation, though the extent of expansion of the stent was not easily viewed on conventional fluoroscopy (Fig 2*A*). C-arm CT with 3D reconstruction at this time showed that the Solitaire device was not fully expanded and was likely within the middle of the thrombus, unable to expand to the vessel inner walls (Fig 2*B*). Once retrieved, the stent was found to have removed significant amounts of fresh blood clot. The device was again deployed within the same area of the right MCA, though this time with the distal end in the inferior division of the MCA. C-arm CT during this second deployment showed significantly greater stent expansion to the margins of the vessel walls (Fig 2*C*, *-D*), though copious amounts of thrombus were again retrieved on this pass.

Following further aspiration of thrombi retained within the sheath, subsequent angiography demonstrated markedly improved blood perfusion into the right ICA/MCA/anterior cerebral artery territory, indicating a nearly complete return of blood flow to the area affected by the stroke (Fig 3). The patient recovered well, without weakness or paralysis, with no sensory loss and no speech difficulties, following successful removal of the large ICA bifurcation thrombus.

DISCUSSION

Catheter navigation and subsequent device deployment may be hindered during very large thrombus blockage of major arterial distributions during an acute stroke, especially in an ICA T-distribution thrombus, in which neither the MCA nor the anterior cerebral artery territories can be visualized. Effective treatment of this neurologically devastating condition depends largely on the rapid deployment of interventional stroke procedures, including retrievable stent devices. Although other stroke cases were treated at this institution during the time of this series, we only included patients who had large arterial segment occlusion with resulting

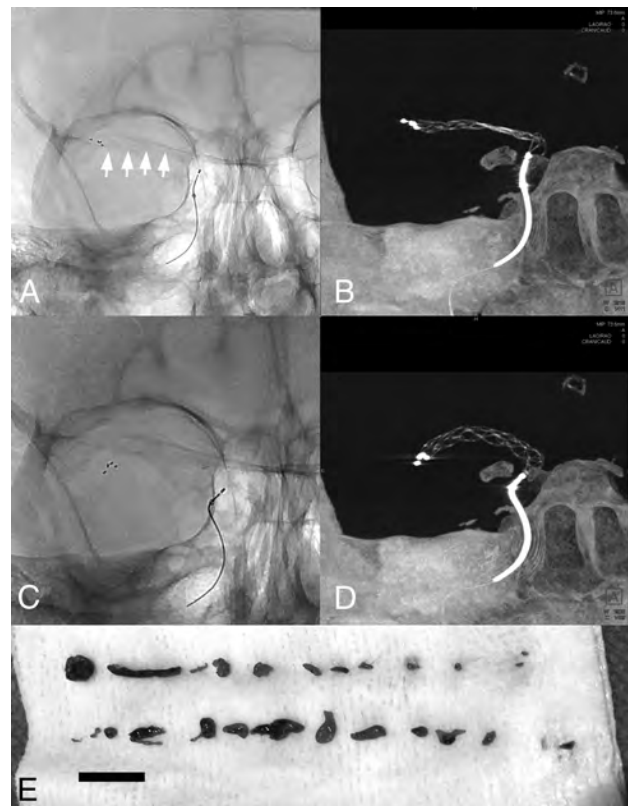


FIG 2. Comparison of images by using standard biplanar fluoroscopy versus C-arm CT. *A*, Anteroposterior fluoroscopic view of the deployed Solitaire stent device on the first pass across the thrombus. Visualization of the device is poor; *arrows* indicate approximate location of the stent. *B*, C-arm CT of the deployed stent across the thrombus. Note the narrow diameter of the stent, indicating the presence of surrounding thrombus, preventing the stent from full expansion. *C*, Anteroposterior fluoroscopic view of the second pass of the Solitaire device, again with poor visualization of the overall stent shape and conformation. *D*, C-arm CT of the second-pass of the Solitaire device. Now the stent is able to more fully expand within the artery, though there is still thrombus present. *E*, Retrieved thrombus from the first and second passes in the MCA.

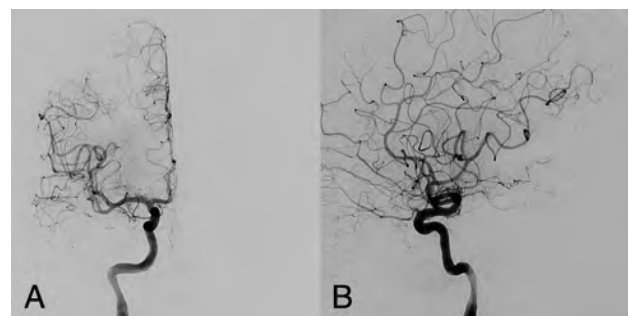


FIG 3. Postprocedural angiograms in anteroposterior (*A*) and lateral (*B*) projections show complete recanalization of right MCA and anterior cerebral artery distributions following mechanical thrombectomy with combined C-arm CT and retrievable stent deployment.

decreased visualization during imaging. In such cases in which visualization of the arterial system is poor, the concurrent use of C-arm CT during the interventional procedure provides additional information to surmise whether one has deployed the thrombectomy device within the suspected area of the thrombus by observing the diameter of the stent on deployment. In the case

of retrievable stents, the thrombus provides resistance for the stent to expand, giving it a stenotic appearance. Further comparison can also be made between the diameter of the deployed stent and the vessel diameter of the contralateral patent same-distribution arterial system. Whenever possible, however, before stent placement, we also analyze the contralateral arterial cerebral blood supply to determine whether there may be any underlying tortuous or difficult anatomy, such as congenital stenosis. We frequently use this method in our treatment center, especially in cases in which little or no information is available regarding the occluded vessel anatomy.

In this series, we showed a recanalization rate of 83%, and in all cases in which recanalization was achieved, the posttreatment TICI score was either 2b or 3 (near- or complete distal reperfusion). Our results with these cases of initial poor arterial visualization are comparable with those seen in the Solitaire With the Intention For Thrombectomy trial, with a recanalization rate of 83% in both studies (89% in the Solitaire With the Intention For Thrombectomy trial after rescue treatment).^{4,5} In all cases in this series the TICI scores were either zero or 2b/3, indicating that in our hands this type of recanalization procedure was an all or nothing procedure: either achieving near- or complete reperfusion or no reperfusion at all, with no intermediate reperfusion results. Reperfusion, however, did not necessarily translate into good patient outcomes. Of the 5 patients in this series who ultimately died, 3 of them had a postprocedural TICI score of 2b or 3. Most interesting, 4 of the 6 patients who either died or had a very poor clinical outcome (incapable of self-care, requiring long-term acute care hospital placement) also did not receive tPA before the thrombectomy procedure for various reasons. Of the remaining patients who were able to go home, only 1 patient had not received tPA before thrombectomy.

In this series, we were able to show that in cases in which an arterial system cannot be adequately visualized initially by using standard biplanar angiographic methods, C-arm CT can provide additional information that may be useful in guiding clinical decision-making. In particular, this may allow visualization of the incomplete expansion of the thrombectomy device in the presumed region of the occlusive thrombus, where the occlusion would otherwise have been difficult or impossible to visualize, compared with standard fluoroscopic views alone. Stent retriever interaction with clot material has been shown to provide key information regarding the penetration of stent struts into the thrombus,⁹ and in this report, C-arm CT also allowed evaluation of the degree of stent expansion into the thrombotic region, further allowing the operator to determine whether the region of stenosis was from thrombus or possibly from a more firm embolus or an area of pre-existing stenosis from atherosclerosis or inherent vessel stenosis. This is critical information in the setting of acute treatment for arterial blockage because in the case of atherosclerotic, embolic, or inherent vessel stenosis, multiple attempts at recanalization would be futile and would perhaps even

precipitate worse patient outcomes from stroke propagation, vessel damage, or cerebral hemorrhage.

The ability to preserve function following a stroke depends directly on the physician's ability to rapidly re-establish sufficient blood flow to the affected stroke area. Performing this task efficiently and reliably, with as much information as possible, is ideal and will likely lead to better patient outcomes, especially with large acute cerebral vessel occlusions as seen in these cases.

CONCLUSIONS

In the treatment of acute stroke when visualization of the occluded arterial branch is poor or impossible, the use of adjunctive C-arm CT can provide additional information that can aid the operator in clinical decision-making regarding the adequacy of stent placement and thrombus position.

Disclosures: Ponraj Chinnadurai—RELATED: Employment: Siemens Medical Solutions USA Inc, Comments: full-time Staff Scientist, Angiography Division. Gouthami Chintalapani—RELATED: Employment: full-time employee at Siemens Medical Solutions USA Inc. Michel E. Mawad—RELATED: Support for Travel to Meetings for the Study or Other Purposes: Covidien, Comments: I traveled to give lectures on endovascular treatment of stroke and flow diversion in aneurysm treatment. Covidien paid my airfare, and I was paid a per diem for the time spent; UNRELATED: Payment for Lectures (including service on Speakers Bureaus) & Travel/Accommodations/Meeting Expenses Unrelated to Activities Listed: I traveled to give lectures on endovascular treatment of stroke and flow diversion in aneurysm treatment. Covidien paid my airfare and I was paid a per diem for the time spent.

REFERENCES

1. Dorn F, Stehle S, Lockau H, et al. Endovascular treatment of acute intracerebral artery occlusions with the Solitaire stent: single-centre experience with 108 recanalization procedures. *Cerebrovasc Dis* 2012;34:70–77
2. Koh JS, Lee SJ, Ryu CW, et al. Safety and efficacy of mechanical thrombectomy with Solitaire stent retrieval for acute ischemic stroke: a systematic review. *Neurointervention* 2012;7:1–9
3. Mendonça N, Flores A, Pagola J, et al. Trevo versus Solitaire: a head-to-head comparison between two heavy weights of clot retrieval. *J Neuroimaging* 2014;24:167–70
4. Saver JL, Jahan R, Levy EI, et al. SOLITAIRE with the intention for thrombectomy (SWIFT) trial: design of a randomized, controlled, multicenter study comparing the SOLITAIRE flow restoration device and the MERCI retriever in acute ischaemic stroke. *Int J Stroke* 2014;9:658–68
5. Saver JL, Jahan R, Levy EI, et al. Solitaire flow restoration device versus the Merci retriever in patients with acute ischaemic stroke (SWIFT): a randomised, parallel-group, non-inferiority trial. *Lancet* 2012;380:1241–49
6. Kamran M, Nagaraja S, Byrne JV. C-arm flat detector computed tomography: the technique and its applications in interventional neuro-radiology. *Neuroradiology* 2010;52:319–27
7. Ganguly A, Fieselmann A, Boese J, et al. In vitro evaluation of the imaging accuracy of C-arm conebeam CT in cerebral perfusion imaging. *Med Phys* 2012;39:6652–59
8. Ganguly A, Fieselmann A, Marks M, et al. Cerebral CT perfusion using an interventional C-arm imaging system: cerebral blood flow measurements. *AJNR Am J Neuroradiol* 2011;32:1525–31
9. Wenger KJ, Berkefeld J, Wagner M. Flat panel detector computed tomography for the interaction between contrast-enhanced thrombi and stent retrievers in stroke therapy: a pilot study. *Clin Neuroradiol* 2014;24:251–54

Treatment of Benign Thyroid Nodules: Comparison of Surgery with Radiofrequency Ablation

Y. Che, S. Jin, C. Shi, L. Wang, X. Zhang, Y. Li, and J.H. Baek



ABSTRACT

BACKGROUND AND PURPOSE: Nodular goiter is one of the most common benign lesions in thyroid nodule. The main treatment of the disease is still the traditional surgical resection, however there are many problems such as general anesthesia, surgical scar, postoperative thyroid or parathyroid function abnormalities, and high nodules recurrence rate in residual gland. The purpose of this study was to compare the efficacy, safety, and cost-effectiveness of 2 treatment methods, surgery and radiofrequency ablation, for the treatment of benign thyroid nodules.

MATERIALS AND METHODS: From May 2012 to September 2013, 200 patients with nodular goiters who underwent surgery (group A) and 200 patients treated by radiofrequency ablation (group B) were enrolled in this study. Inclusion criteria were the following: 1) cosmetic problem, 2) nodule-related symptoms, 3) hyperfunctioning nodules related to thyrotoxicosis, and 4) refusal of surgery (for group B). An internally cooled radiofrequency ablation system and an 18-ga internally cooled electrode were used. We compared the 2 groups in terms of efficacy, safety, and cost-effectiveness during a 1-year follow-up.

RESULTS: After radiofrequency ablation, the nodule volume decreased significantly from 5.4 to 0.4 mL ($P = .002$) at the 12-month follow-up. The incidence of complications was significantly higher from surgery than from radiofrequency ablation (6.0% versus 1.0%, $P = .002$). Hypothyroidism was detected in 71.5% of patients after surgery but in none following radiofrequency ablation. The rate of residual nodules (11.9% versus 2.9%, $P = .004$) and hospitalization days was significantly greater after surgery (6.6 versus 2.1 days, $P < .001$), but the cost difference was not significant.

CONCLUSIONS: Surgical resection and radiofrequency ablation are both effective treatments of nodular goiter. Compared with surgery, the advantages of radiofrequency ablation include fewer complications, preservation of thyroid function, and fewer hospitalization days. Therefore, radiofrequency ablation should be considered a first-line treatment for benign thyroid nodules.

ABBREVIATIONS: RFA = radiofrequency ablation; US = ultrasound

The incidence of nodular goiter has been gradually increasing in recent years, but its treatment has been controversial to date.^{1,2} Current guidelines suggest that a nodule without clinical symptoms should be treated with watchful waiting; however,

some patients require treatment because of cosmetic problems or symptoms. Some investigators also believe that even if the incidence of malignancy rate is as low as 5%–15%, malignancy is still a concern. Thus, surgery has been advocated by some clinicians, but after resection of the nodules, patients often have neck scars or hypothyroidism, which seriously affects their quality of life.^{3,4} Additional issues include the risks of general anesthesia and postoperative parathyroid function abnormalities.^{1–3,5} Therefore, minimally invasive alternatives have been explored. Ethanol ablation, laser ablation, microwave ablation, and radiofrequency ablation (RFA) are safe and effective techniques for the treatment of nodular goiter.^{6–8} Ethanol ablation is useful in cystic nodules but not in solid nodules. Laser ablation, microwave ablation, and RFA are useful in different-sized nodules, respectively.⁹

Since Dupuy et al¹⁰ first pioneered the application of radiofrequency ablation to treat recurrent thyroid cancers, RFA has been widely used for the treatment of benign thyroid nodules, goiters,

Received October 26, 2014; accepted after revision December 17.

From the Departments of Ultrasound (Y.C., L.W., X.Z.), Laparoscopic Surgery (S.J.), and Pathology (C.S.), First Affiliated Hospital of Dalian Medical University, Dalian, China; Department of Radiology and Research Institute of Radiology (J.H.B.), University of Ulsan College of Medicine, Asan Medical Center, Seoul, Korea; and College of Basic Medical Sciences and Institute of Cancer Stem Cell (Y.L.), Dalian Medical University, Dalian, China.

Please address correspondence to Ying Che, MD, Department of Ultrasound, First Affiliated Hospital of Dalian Medical University, Dalian, Liaoning 116011, China; e-mail: yche1964@163.com; Jung Hwan Baek, MD, Department of Radiology and the Research Institute of Radiology, University of Ulsan College of Medicine, Asan Medical Center, 86 Asanbyeongwon-Gil, Songpa-Gu, Seoul 138–736, Korea; e-mail: radbaek@naver.com

Evidence-Based Medicine Level 2.

<http://dx.doi.org/10.3174/ajnr.A4276>

Table 1: Demographic characteristics of the experimental subjects

	Surgery (n = 200)	RFA (n = 200)	P Value
Mean age (yr) (range)	52.4 ± 13.9 (23–78)	43.8 ± 12.7 (15–84)	.76
Sex (M/F)	46:154	35:165	.89
Index nodules	403	375	
Mean diameter (cm)	4.1 ± 3.2	3.4 ± 3.7	.79
Mean volume (mL)	5.9 ± 6.4	5.4 ± 7.1	.88
No. of nodules (single/multiple)	49:151	62:138	.147

Table 2: Changes in nodule volume and percentage volume reduction before and after RFA

Period	No. of Nodules	Mean Volume (mL)	% Volume Reduction ^a	P Value ^b
Before treatment	375	5.4 ± 7.1		
1 mo	375	3.1 ± 4.4	37.5 ± 43.4	.030
3 mo	301	2.1 ± 3.0	61.3 ± 37.6	.025
6 mo	247	1.2 ± 1.9	74.6 ± 23.3	.009
12 mo	194	0.4 ± 0.7	84.8 ± 17.1	.002

^aNote that “% Volume Reduction” represents the proportion of residual volume compared with the index nodule volume.

^bP value represents a comparison of before treatment with each follow-up assessment.

and recurrent thyroid cancers.^{11–15} Recently, many studies including long-term follow-up studies,¹⁶ randomized controlled trials,^{6,17} and a meta-analysis¹⁸ have promulgated the efficacy and safety of RFA. To date, however, only 1 study has compared surgery and RFA,¹³ and it enrolled a relatively small population of 37 patients treated with RFA and 74 patients treated with surgery. The purpose of this study was to compare the efficacy, safety, and cost-effectiveness of 2 treatment methods, surgery and RFA, in a large population treated for benign thyroid nodules.

MATERIALS AND METHODS

Patients

This retrospective study was approved by the institutional review board at the First Affiliated Hospital of Dalian Medical University, and informed consent was obtained from all patients before surgery or RFA. From May 2012 to September 2013, 200 patients with nodular goiter who underwent surgery (group A) and 200 patients treated with sonography (US)-guided RFA (group B) were enrolled in this study. The surgery group was diagnosed as having a nodular goiter by surgical pathology, and the RFA group was diagnosed cytologically from 2 preoperative fine-needle aspirates.^{19,20} All the enrolled patients fulfilled the following criteria according to the RFA recommendations of the Korean Society of Thyroid Radiology²¹: 1) having a cosmetic problem, 2) having nodule-related symptoms, 3) having hyperfunctioning nodules related to thyrotoxicosis, and 4) having refused surgery. Patients without complete surgical and/or follow-up information were excluded.

Devices and Procedures

We used a HI VISION Preirus system (Hitachi Medical System, Tokyo, Japan) with a 10-MHz linear probe, internally cooled RFA system (VIVA RF generator; STARmed, Gyeonggi, Korea) with an 18-ga internally cooled electrode (VIVA; STARmed) during the US, US-guided biopsy, and RFA. Laboratory examinations included preoperative thyroid function and coagulation tests. US examination evaluated the location, size, and vascularity of the

nodules to design the treatment plan. The patients in group A underwent surgery under general anesthesia. Surgery was performed by general surgeons with >8 years’ clinical experience. The surgery methods included total thyroidectomy and lobectomy according to the guidelines of the National Comprehensive Cancer Network.²²

In group B patients, local anesthetic with 2% lidocaine was used to control pain. RFA was performed by 1 radiologist (Y.C. with 7 years’ clinical experience and 2 years’ RFA experience) by using previously described standard RFA techniques such as transisthmus approach methods and a “moving-shot” technique.^{14,21,23} The procedure was finished when an entire nodule changed to a no-enhancement zone by real-time US examination with contrast (sulphur hexafluoride microbubbles for injection, SonoVue; Bracco Suisse SA, Plan-Les-Ouates, Switzerland). The 2 groups of patients underwent a US check at 1, 6, and 12 months after treatment. In group A, an examination of thyroid function was performed to adjust the optimal dosage of levothyroxine (Euthyrox) 1 month after the thyroid resection. In group B, thyroid function was examined 1 week after RFA. If any functional anomalies were demonstrated, thyroid function was evaluated every month until normalization.

Surgical complications were monitored immediately after thyroid surgery and during the follow-up period.⁴ The complications of RFA were checked during and after treatment according to the definitions of the Society of Interventional Radiology.^{24,25} The changes in nodule volumes were evaluated before and during the follow-up periods. “Residual” was defined as a certain part of single or multiple nodules that is not completely inactivated. The residual rate was defined as the rate of the number of people who had residual goiter divided by the total number. Recurrence was defined as the regrowth of thyroid tissue after treatment according to the definition of a previous study.¹⁶ The cost was the total of hospitalization, clinical tests, and surgery costs.

Statistical Methods

SPSS (Version 11.5; IBM, Armonk, New York) statistical software was used to analyze the data. Data measurements were expressed as mean ± SD and range. Comparison of the 2 groups was done by the Wilcoxon signed rank test. The threshold for statistically significant differences was defined as $P < .05$.

RESULTS

Table 1 summarizes a comparison of demographic data of the 2 groups. No demographic data differed significantly between the 2 groups before treatment, including the mean patient age, sex, nodule size, or nodule numbers.

Efficacy

Changes in nodule volume and percentage volume reduction before and after RFA are shown in Table 2, and a representative RFA patient case is described in the Figure. The mean volume of the index nodules was 5.4 ± 7.1 mL (range, 0.3–47.1 mL). The nodule volume at 12-month follow-up had decreased significantly from

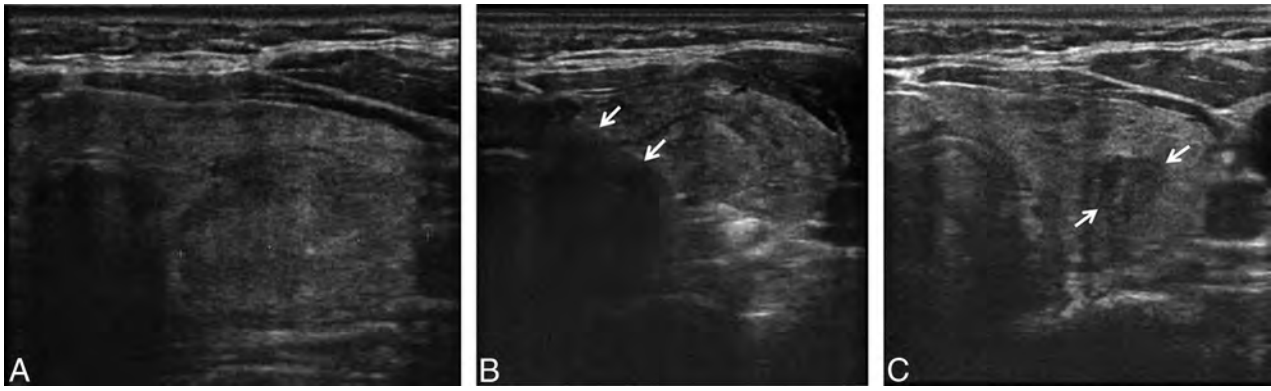


FIGURE. A 50-year-old woman with left-neck discomfort. A, Before treatment, a 3-cm solid, left thyroid nodule is evident. B, During the RF ablation, the electrode (arrows) is placed within the nodule. C, Six months after RF ablation, the treated nodule (arrows) has decreased considerably in size and measures only 8 mm.

Table 3: Overall comparison of surgery versus RFA

	Surgery (n = 200)	RFA (n = 200)	P Value
Residue ^a	11.9%	2.9%	.004
Recurrence ^b	2.5%	0.05%	.100
Complications	6%	1%	.002
Postoperative medication	71.5%	0	.002
Mean hospitalization (days)	6.6 ± 1.6	2.1 ± 0.9	.000
Cost (Chinese yuan) (US dollars)	¥15,962 ± ¥1073 (\$2556.95 ± \$171.88)	¥16,535 ± ¥2309 (\$2648.74 ± \$369.88)	.99

^a "Residue" is defined as no complicated treatment in single or multiple nodules.

^b "Recurrence" is defined as the appearance of a new goiter after treatment.

Table 4: Complications observed following surgery versus RFA^a

	Surgery (n = 200)	RFA (n = 200)
Hoarseness		
Transient	3	1
Permanent	2	0
Hypoparathyroidism transient	6	0
Hematoma	1	0
Nodule rupture	0	1
Total	12	2

^a Numbers represent the number of affected patients.

5.4 ± 7.1 mL to 0.4 ± 0.7 mL ($P = .002$), and the percentage volume reduction was 84.8 ± 17.1% (range, 61.3%–100%). Table 3 shows the results and complications of the 2 groups. The residual rate in the surgery group was significantly higher than that in the RFA group (11.9% versus 2.9%, $P = .004$).

Safety

The number of patients with complications in the 2 groups is described in Table 4. The overall complication rate in the surgery group was significantly higher than that of the RFA group (6% versus 1%, $P = .002$). Transient hoarseness was reported in 3 patients after surgery versus 1 patient after RFA, but they recovered completely during the follow-up of 1–3 months. Two patients with a permanent unilateral recurrent laryngeal nerve injury were reported only in the surgery group. Six patients with transient hypoparathyroidism were reported in the surgery group and recovered in 3–7 days after surgery. Nodule rupture was reported in 1 patient 1 week after RFA; however, he recovered without any treatment within 2 weeks.

Regarding thyroid function and medication, the surgery group showed a significantly higher postoperative medication

rate than the RFA group (71.5% versus 0%, $P = .002$). In the surgery group, 71.5% of patients showed postoperative hypothyroidism that required daily supplemental exogenous thyroid hormone (Euthyrox). Approximately 42% of those patients needed 50 µg/day of hormone, 4% needed 75 µg/day, and 25.5% needed 100 µg/day. In the RFA group, 93% of patients had normal levels of T3, T4, and thyroid-stimulating

hormone. Only 7% of patients showed a decreased thyroid-stimulating hormone without an elevation in T3 or T4 while also having no hyperthyroid symptoms. The patients recovered spontaneously from these conditions by their 1-month follow-up.

Cost Effectiveness

The mean hospitalization stay was significantly longer in the surgery group (6.6 ± 1.6 days versus 2.1 ± 0.9 days, $P = .00$). The total cost between the 2 groups was not significantly different ($P = .99$); the cost of surgery was ¥15,962 ± ¥1073 (Chinese yuan) (\$2556.95 ± \$171.88) and that of RFA was ¥16,535 ± ¥2309 (\$2648.74 ± \$369.88).

DISCUSSION

Our large-population study comparing surgery and RFA for the management of benign thyroid nodules demonstrated that RFA effectively decreases thyroid nodule volume (84.8% volume reduction at 1-year follow-up), and the recurrence rate after RFA treatment was similar to that of surgery. The complication rate was significantly lower after RFA than following surgery (6% versus 1%, $P = .002$). In addition, thyroid function after RFA treatment is well-maintained but is decreased in 71.5% of patients after surgery. The cost of RFA was found to be similar to that of surgery, and clinical recovery was faster and easier on the patient; additionally, no external scar was present.

RFA of benign thyroid nodules had a demonstrated efficacy and safety in previous studies,^{16,26,27} and the volume reduction reported is approximately 84%–90% at 1-year follow-up.^{14,16,28} We observed a similar volume reduction of 84.8% in our study. Because of the complexity of the thyroid and neck anatomy,

surgery has a high incidence of complications such as recurrent laryngeal nerve injury, hypoparathyroidism, and hypothyroidism^{3,4,29,30}; however, the complication rate reported for RFA was low in the study by Baek et al,²⁵ a 3.3% complication rate with thyroid RFA in their multicenter study. In our current study, the RFA complication rate was found to be lower than that of surgery. Recurrent laryngeal nerve injury occurred in 3.0% of our surgery group versus 0.5% for our RFA group. RFA can minimize the nerve injury rate because real-time US imaging allows the radiologist to monitor the dangerous triangle in which the recurrent laryngeal nerve is located,^{25,31} and hydrodissection has been introduced as a safe technique to prevent thermal damage to the nerve.^{32,33} The rate of hypoparathyroidism was 3.0% in our surgery group but was totally absent from our RFA group. This difference is caused by the varied position of the parathyroid gland and low resolution during the operation. During RFA, parathyroid injury has not yet been reported. Hematoma was also reported only in our surgery group. Baek et al²⁵ reported that approximately 1% of patients developed a hematoma in their large-population multicenter study. During RFA, a hemorrhage can be detected by real-time US and easily controlled by manual compression. Hypothyroidism affected 71.5% of our surgery group but none of our patients undergoing RFA. Baek et al²⁵ reported only 0.07% (1/1459) hypothyroidism after thyroid RFA. Hypothyroidism is a rare complication in thyroid RFA because RFA minimizes the chance of injury to the normal thyroid. In our RFA group, 1 patient initially experienced thyroid nodule rupture 1 week after the RFA, but this complication resolved spontaneously in 2 weeks without the need for taking antibiotics. Previous studies suggest that patients with nodule rupture should be treated conservatively rather than with an intervention.²⁵ Our results demonstrate a lower complication rate for RFA than for surgery, which is similar to the findings of Bernardi et al.¹³

In nodular goiter, most of the nodules arise in multiples. Therefore, resection of a large volume of the normal glandular tissue is the main cause of hypothyroidism. In our present study, 71.5% of patients showed a decreased level of serum thyroid hormone after surgery, which requires life-long exogenous thyroid hormone replacement therapy. By its nature, surgery removes the goiters and some surrounding normal thyroid tissue; however, RFA only ablates the goiter and spares most normal tissue. Therefore, thyroid function is better protected by an RFA approach.

Compared with the results of Bernardi et al,¹³ our current study shows the advantages of RFA in a large population. We also analyzed the detailed comparison of 2 procedures in terms of the duration of the hospital stay, residual disease, and the recurrence rate, in addition to complications and thyroid function. In our analyses, the mean hospitalization days were significantly fewer in the RFA group (6.6 ± 1.6 days versus 2.1 ± 0.9 days, $P < .001$) and residual thyroid nodules were also less frequent after RFA than surgery. RFA minimizes normal thyroid tissue injury because the radiofrequency electrode moves only within the nodule.^{9,14,21} Therefore, damage to thyroid function is rare, and few residual nodules remain after RFA. RFA showed a low recurrence rate after treatment in our patients, which is con-

sistent with published recurrence rates after RFA of 5.6% during follow-up of 4 years.¹⁶

A neck scar resulting from surgery can also be a concern to patients. Although performing thyroid surgery by laparoscope has a benefit of less neck scarring, other skin, such as the axillary and anterior chest, will still scar.³⁴ RFA is a percutaneous, minimally invasive procedure under US monitoring. Because the outer diameter of the electrode is 1.2 mm, the RFA-related wound is tiny and patients fully recover in a few weeks. Most patients can be treated on an outpatient basis and can leave the hospital 1–2 hours after RFA without any disturbance in daily activities. The costs of RFA are comparable with those of conventional surgery in China. In nearly all respects, RFA shows superior performance to surgery for the treatment of thyroid nodules.

A limitation of our study was the short follow-up and the retrospective design. However, residual nodules and recurrence are rare on the basis of previous reports. We hope our results may motivate others to perform more extensive prospective studies to assess the effectiveness of this alternative approach.

CONCLUSIONS

RFA of a benign thyroid nodule effectively treats with a low incidence of complications, no effects on thyroid or parathyroid function, low nodular recurrence rate, and shorter hospitalization periods. Hence, RFA should be considered as possibly the first-line treatment for benign thyroid nodules.

REFERENCES

- Cooper DS, Doherty GM, Haugen BR, et al. **Revised American Thyroid Association management guidelines for patients with thyroid nodules and differentiated thyroid cancer.** *Thyroid* 2009;19:1167–214
- Gharib H, Papini E, Paschke R, et al. **American Association of Clinical Endocrinologists, Associazione Medici Endocrinologi, and European Thyroid Association Medical Guidelines for Clinical Practice for the Diagnosis and Management of Thyroid Nodules.** *Endocr Pract* 2010;16(suppl 1):1–43
- Gibelin H, Sierra M, Mothes D, et al. **Risk factors for recurrent nodular goiter after thyroidectomy for benign disease: case-control study of 244 patients.** *World J Surg* 2004;28:1079–82
- Pelizzo MR, Merante Boschin I, Toniato A, et al. **Surgical therapeutic planning options in nodular goiter.** *Minerva Endocrinol* 2010;35:173–85
- Roh JL, Park JY, Park CI. **Total thyroidectomy plus neck dissection in differentiated papillary thyroid carcinoma patients: pattern of nodal metastasis, morbidity, recurrence, and postoperative levels of serum parathyroid hormone.** *Ann Surg* 2007;245:604–10
- Sung JY, Baek JH, Kim KS, et al. **Single-session treatment of benign cystic thyroid nodules with ethanol versus radiofrequency ablation: a prospective randomized study.** *Radiology* 2013;269:293–300
- Papini E, Rago T, Gambelunghe G, et al. **Long-term efficacy of ultrasound-guided laser ablation for benign solid thyroid nodules: results of a three-year multicenter prospective randomized trial.** *J Clin Endocrinol Metab* 2014;99:3653–59
- Feng B, Liang P, Cheng Z, et al. **Ultrasound-guided percutaneous microwave ablation of benign thyroid nodules: experimental and clinical studies.** *Eur J Endocrinol* 2012;166:1031–37
- Ha EJ, Baek JH. **Advances in nonsurgical treatment of benign thyroid nodules.** *Future Oncol* 2014;10:1399–405
- Dupuy DE, Monchik JM, Decrea C, et al. **Radiofrequency ablation of regional recurrence from well-differentiated thyroid malignancy.** *Surgery* 2001;130:971–77

11. Baek JH, Kim YS, Sung JY, et al. **Locoregional control of metastatic well-differentiated thyroid cancer by ultrasound-guided radiofrequency ablation.** *AJR Am J Roentgenol* 2011;197:W331–36
12. Baek JH, Moon WJ, Kim YS, et al. **Radiofrequency ablation for the treatment of autonomously functioning thyroid nodules.** *World J Surg* 2009;33:1971–77
13. Bernardi S, Dobrinja C, Fabris B, et al. **Radiofrequency ablation compared to surgery for the treatment of benign thyroid nodules.** *Int J Endocrinol* 2014;2014:934595
14. Jeong WK, Baek JH, Rhim H, et al. **Radiofrequency ablation of benign thyroid nodules: safety and imaging follow-up in 236 patients.** *Eur Radiol* 2008;18:1244–50
15. Shin JH, Baek JH, Oh YM, et al. **Combination therapy of temporary tracheal stenting and radiofrequency ablation for multinodular thyroid goiter with airway compression.** *Korean J Radiol* 2013;14:805–09
16. Lim HK, Lee JH, Ha EJ, et al. **Radiofrequency ablation of benign non-functioning thyroid nodules: 4-year follow-up results for 111 patients.** *Eur Radiol* 2013;23:1044–49
17. Faggiano A, Ramundo V, Assanti AP, et al. **Thyroid nodules treated with percutaneous radiofrequency thermal ablation: a comparative study.** *J Clin Endocrinol Metab* 2012;97:4439–45
18. Fuller CW, Nguyen SA, Lohia S, et al. **Radiofrequency ablation for treatment of benign thyroid nodules: systematic review.** *Laryngoscope* 2014;124:346–53
19. Kwak JY, Jung I, Baek JH, et al; Korean Society of Thyroid Radiology (KSThR); Korean Society of Radiology. **Image reporting and characterization system for ultrasound features of thyroid nodules: multicentric Korean retrospective study.** *Korean J Radiol* 2013;14:110–17
20. Moon WJ, Baek JH, Jung SL, et al; Korean Society of Thyroid Radiology (KSThR); Korean Society of Radiology. **Ultrasonography and the ultrasound-based management of thyroid nodules: consensus statement and recommendations.** *Korean J Radiol* 2011;12:1–14
21. Na DG, Lee JH, Jung SL, et al; Korean Society of Thyroid Radiology (KSThR); Korean Society of Radiology. **Radiofrequency ablation of benign thyroid nodules and recurrent thyroid cancers: consensus statement and recommendations.** *Korean J Radiol* 2012;13:117–25
22. Urken ML, Milas M, Randolph GW, et al. **Management of recurrent and persistent metastatic lymph nodes in well-differentiated thyroid cancer: a multifactorial decision-making guide for the thyroid cancer care collaborative.** *Head Neck* 2015;37:605–14
23. Ha EJ, Baek JH, Lee JH. **Moving-shot versus fixed electrode techniques used for radiofrequency ablation: an experimental comparison in an ex-vivo bovine liver tissue model.** *Korean J Radiol* 2014;15:836–43
24. Burke DR, Lewis CA, Cardella JF, et al. **Quality improvement guidelines for percutaneous transhepatic cholangiography and biliary drainage.** *J Vasc Interv Radiol* 2003;14:S243–46
25. Baek JH, Lee JH, Sung JY, et al. **Complications encountered in the treatment of benign thyroid nodules with US-guided radiofrequency ablation: a multicenter study.** *Radiology* 2012;262:335–42
26. Gharib H, Hegedus L, Pacella CM, et al. **Clinical review: nonsurgical, image-guided, minimally invasive therapy for thyroid nodules.** *J Clin Endocrinol Metab* 2013;98:3949–57
27. Papini E, Pacella CM, Hegedus L. **Diagnosis of endocrine disease: thyroid ultrasound (US) and US-assisted procedures: from the shadows into an array of applications.** *Eur J Endocrinol* 2014;170:R133–46
28. Spiezia S, Garberoglio R, Milone F, et al. **Thyroid nodules and related symptoms are stably controlled two years after radiofrequency thermal ablation.** *Thyroid* 2009;19:219–25
29. Hayward NJ, Grodski S, Yeung M, et al. **Recurrent laryngeal nerve injury in thyroid surgery: a review.** *ANZ J Surg* 2013;83:15–21
30. Sun GH, Peress L, Pynnonen MA. **Systematic review and meta-analysis of robotic vs conventional thyroidectomy approaches for thyroid disease.** *Otolaryngol Head Neck Surg* 2014;150:520–32
31. Shin JH, Baek JH, Ha EJ, et al. **Radiofrequency ablation of thyroid nodules: basic principles and clinical application.** *Int J Endocrinol* 2012;2012:919650
32. Lim HK, Baek JH, Lee JH, et al. **Efficacy and safety of radiofrequency ablation for treating locoregional recurrence from papillary thyroid cancer.** *Eur Radiol* 2015;25:163–70
33. Shin JE, Baek JH, Lee JH. **Radiofrequency and ethanol ablation for the treatment of recurrent thyroid cancers: current status and challenges.** *Curr Opin Oncol* 2013;25:14–19
34. Lee KE, Kim HY, Park WS, et al. **Postauricular and axillary approach endoscopic neck surgery: a new technique.** *World J Surg* 2009;33:767–72

Intratympanic Contrast in the Evaluation of Menière Disease: Understanding the Limits

J. Bykowski, J.P. Harris, M. Miller, J. Du, and M.F. Mafee

ABSTRACT

BACKGROUND AND PURPOSE: Studies describing endolymphatic hydrops in Menière disease after off-label intratympanic gadolinium-based contrast have been limited by long acquisition times. We aimed to demonstrate the feasibility of post-intratympanic imaging on a 3T MR imaging system within a clinically tolerable acquisition time and to address potential pitfalls in acquisition or interpretation.

MATERIALS AND METHODS: FDA Investigational New Drug 115,342 and institutional review board approval were obtained for intratympanic injection of 8-fold diluted Gd-DTPA into the more symptomatic ear of 6 adults with Menière disease. 3T MR imaging was performed using a 3-inch surface coil before and up to 28 hours after injection using FLAIR to define the nonenhancing endolymphatic space within the enhancing perilymph. Variable FLAIR TI images were used to determine the impact of fluid-suppression on interpretation. Image quality was assessed for perilymphatic and extralabyrinthine contrast enhancement, definition of endolymphatic anatomy, and other anatomic variants or pathologic findings.

RESULTS: The surface coil afforded 0.375×0.375 mm in-plane FLAIR resolution in <4 minutes 30 seconds, sufficient to perceive the nonenhancing spiral lamina, interscalar septa, and endolymphatic structures. Coronal views highlighted a potential interpretation pitfall of vestibular endolymphatic distention overestimation due to partial volume averaging. Varying FLAIR TI resulted in visible changes in the perception of the cochlear endolymphatic space. CSF enhancement was detectable at the internal auditory canal fundus on the injected side in half of the patients, which may confound interpretation.

CONCLUSIONS: Using a surface coil preserves high resolution within a clinically acceptable acquisition time. Pitfalls remain regarding the interpretation of these images and optimizing protocols across platforms in the absence of a clear internal reference for standardization.

ABBREVIATIONS: IAC = internal auditory canal; GBCA = gadolinium-based contrast agents; IT = intratympanic

Menière disease can be debilitating due to the severity and unpredictability of symptom onset.¹ Currently, routine MR imaging plays a supportive role in the evaluation of these patients, mainly by excluding alternative diagnoses. The translation of in-

tratympanic (IT) gadolinium-based contrast agents (GBCA) in animal models of endolymphatic hydrops²⁻⁶ into the evaluation of membranous labyrinthine spaces in human patients with Menière disease was pioneered by Nakashima et al.⁷⁻⁹ Following IT injection, contrast diffuses through the round window membrane and also likely through the oval window, resulting in perilymphatic space enhancement, while the endolymphatic space remains nonenhancing. The underlying premise is that increased production or impaired clearance of endolymph from the scala media results in deflection of the imaging-occult Reissner membrane into the perilymphatic space of the scala vestibuli.

Studies of IT injections at other centers have demonstrated that the endolymphatic space is conspicuously distended in patients with Menière disease and less commonly in other causes of sensorineural hearing loss.^{10,11} Most interesting, endolymphatic distention characterized by these methods has been demonstrated in 20%–65% of contralateral asymptomatic ears in patients with

Received September 15, 2014; accepted after revision December 28.

From the Departments of Radiology (J.B., M.F.M., J.D.) and Otolaryngology (J.P.H.), University of California, San Diego Health System, San Diego, California; and Department of Otolaryngology (M.M.), University of California, San Francisco Medical Center, San Francisco, California.

This work was supported by the William Hanafee Award, American Society of Head and Neck Radiology.

Paper previously presented in part at: Annual Meeting of the American Society of Head and Neck Radiology, October 3–7, 2012; Miami Beach, Florida; and American Society of Neuroradiology Annual Meeting and the Foundation of the ASNR Symposium, May 17–22, 2014; Montreal, Quebec, Canada.

Please address correspondence to Julie Bykowski, MD, UC San Diego Health System, Department of Radiology, 410 Dickinson St, MC 8749, San Diego, CA 92103; e-mail: jbykowski@ucsd.edu

<http://dx.doi.org/10.3174/ajnr.A4277>

Table 1: Participant demographics

No.	Age (yr)	Sex, Ethnicity	Side	Years since Onset	Prior Therapy	Symptoms	SRT/SDS ^a	
							Right	Left
1	62	Female	Left	6	HCTZ	~2 Vertigo episodes/year	20 dB 96% at 60 dB	90 dB 4% at 100 dB
2	45	Male	Right	3	HCTZ, oral steroids	Waxing/waning roaring tinnitus, occasional vertigo	15 dB 96% at 75 dB	5 dB 100% at 45 dB
3	55	Male	Right	1	HCTZ	Tinnitus ×1 year, episodic vertigo ×2 mo	15 dB 96% at 55 dB	20 dB 96% at 80 dB
4	63	Female	Right	>10	Bilateral IT steroid injection, oral steroid, HCTZ	8 Vertigo attacks within 2 mo	65 dB 56% at 80 dB	25 dB 96% at 50 dB
5	53	Female	Left	>10	Endolymphatic shunt, IT gentamicin ×9, IT steroids, gent/dex impregnated Gelfoam ^b sponge in round window niche	Tinnitus and pressure	10 dB 96% at 45 dB	30 dB 92% at 65 dB
6	35	Female	Right	3	HCTZ	Episodic vertigo within prior 2 weeks	65 dB 44% at 80 dB	10 dB 96% at 50 dB

Note:—HCTZ indicates hydrochlorothiazide; SRT, speech reception threshold; SDS, speech discrimination score (%) at supra-SRT level (decibel); gent/dex, gentamicin/dexamethasone.

^a Normal = Less than 25, mild = 26–40, moderate = 41–55, moderate/severe = 56–70, severe = 71–90, profound hearing loss >90.

^b Phadia, Uppsala, Sweden.

Menière disease via IT or IV-GBCA methods,^{12–14} furthering the debate regarding imaging overestimation or clinical underestimation of Menière disease.

A variety of sequences has been used to evaluate the ear following IT injection of GBCA, including 3D real inversion recovery,^{8,15} 3D-inversion recovery TSE,¹⁶ and 3D sampling perfection with application-optimized contrast using different flip angle evolutions FLAIR,¹² with versions of 3D FLAIR techniques most commonly used.^{7,17–19} While the availability of 32-channel head coils has improved resolution to 0.4 × 0.4 × 0.8 mm, these volumetric sequences come at the cost of time, requiring up to 15 minutes for an acquisition, with potential for motion degradation and decreased SNR due to parallel imaging techniques.^{20,21} A recent publication has shown reduced acquisition time to 5 minutes 26 seconds but at the cost of resolution, achieving only 0.7 × 0.7 × 0.8 mm.¹¹

The aims of our study were to optimize resolution of post-IT contrast images within a clinically reasonable acquisition time on a clinical 3T scanner and to address potential pitfalls in acquisition or interpretation that should be considered as research continues into this methodology.

MATERIALS AND METHODS

Participants

A 39-year-old healthy, asymptomatic adult volunteer man was recruited for noncontrast MR imaging as part of sequence optimization. Six adult patients with clinically diagnosed Menière disease and symptoms refractory to therapy were recruited from our neurotology clinic. Demographics, symptoms, and audiometric findings are summarized in Table 1. Exclusions to participation included contraindications to MR imaging or GBCA. Diuretics were not stopped for this study. All 6 patients had recent (<6 month prior) bilateral audiograms, and repeat audiometric evaluation of the symptomatic ear was performed within 1 week post-IT GBCA.

IT Injection

Under the auspices of FDA Investigational New Drug 115,342 and institutional review board approval, IT injection of the more symptomatic ear was performed by neurotology faculty or by

neurotology fellows under direct faculty supervision. The external auditory canal was cleaned, the tympanic membrane of the more symptomatic ear was anesthetized with phenol, and a small vent hole was made by using a 23-ga spinal needle. A 1-mL syringe of 1:7 volume/volume Gd-DTPA (Magnevist; Bayer HealthCare Pharmaceuticals, Wayne, New Jersey) contrast from single-use vials diluted in sterile saline was hand-warmed to minimize caloric side effects. A total of 0.4–0.5 mL of the solution was injected into the tympanic cavity under direct visualization, until reflux occurred. The patient remained in a lateral decubitus position with the injected ear up for 30 minutes to facilitate contrast diffusion into the perilymphatic space. During this time, the patient was instructed to spit instead of swallowing saliva, to minimize drainage of tympanic contrast into the Eustachian tube.

Imaging

MR imaging was performed on a 3T TwinSpeed MR imaging system (Signa Excite HD; GE Healthcare, Milwaukee, Wisconsin) by using an 8-channel head coil and a 3-inch surface coil centered over the temporomandibular joint. The primary sequence for optimization was FLAIR, with T1 and FIESTA sequences then prescribed for anatomic correlation. Parameters used clinically with the 8-channel head coil were adapted to the reduced FOV of the 3-inch surface coil while scanning the healthy volunteer subject with serial scans altering the matrix, number of excitations, section thickness, TR, and TI, with the goal of achieving at least 0.4-mm in-plane resolution in <5-minute acquisition time. Because contrast to noise could not be easily assessed on the non-contrast FLAIR sequence, emphasis was placed on appropriate fluid suppression in the internal auditory canals and labyrinthine structures. Scan parameters are summarized in Table 1.

The 6 enrolled participants underwent imaging of the more symptomatic temporal bone by using the 3-inch surface coil 20–28 hours after IT contrast injection, by using FLAIR, T1, and FIESTA sequences detailed in Table 1. The following variables were then introduced to assess the potential impact on scan schedule or interpretation: 1) Three participants also were

Table 2: MR imaging parameters and schedule^a

Coil	Sequence	TE (ms)	TI (ms)	TR (ms)	Matrix	FOV (cm)	In-Plane		Flip Angle	Bandwidth (Hz)	Time to Acquire (min:s)
							Resolution (mm)	Thickness (mm)			
8-Channel	Cisternography (FIESTA)	3		6	320 × 320	18	0.56 × 0.56	1	55°	163	4:27
	2D FLAIR	122	2500	9454	320 × 320	18	0.56 × 0.56	2	90°	122	4:06
	T1 spin-echo ^b	9		400	320 × 320	18	0.56 × 0.56	2	90°	163	4:19
3-Inch surface	Cisternography (FIESTA)	4		8	320 × 320	12	0.38 × 0.38	1	55°	163	4:35
	2D FLAIR (3 pt)	124	2000 ^c	10,000	320 × 320	12	0.38 × 0.38	2	90°	122	4:12
	2D FLAIR (3 pt)	123	2000	9000	320 × 320	12	0.38 × 0.38	2	90°	122	4:24
	T1 spin-echo ^b	11		500	320 × 320	12	0.38 × 0.38	2	90°	163	5:10

Note:—pt indicates patients.

^a Protocol 1 (n = 3), 1 scan session: 20–28 hours post-IT contrast, includes pre- and post-IV contrast images. Protocol 2 (n = 2), 3 scan sessions: 1) pre- and post-IV contrast images (no IT), 2) 2 hours post-IT contrast/4 hours post-IV contrast, 3) 20–28 hours post-IT contrast/30 hours post-IV contrast. Protocol 2B (n = 1; scheduling conflict precluded pre-IT injection imaging as above in protocol 2 number 1), 2 scan sessions: 1) 20 hours post-IT contrast with pre- and post-IV contrast images, 2) 25 hours post-IT contrast/4 hours post-IV contrast.

^b Parameters for T1 pre- and post-IV contrast scans did not change.

^c FLAIR TI was varied from 1800 to 2800 ms for 2 patient scans, with all other parameters fixed.

scanned with the surface coil within 2 hours post-IT injection to assess the extent of contrast diffusion into the perilymph. 2) In 2 participants, FLAIR TI was varied from 2000 to 2800 ms during the 20- to 28-hour post-IT delayed surface coil scan session to assess the impact of variable fluid suppression on the interpretation of endolymphatic distention. 3) In 1 participant, dedicated coronal imaging was performed by using the surface coil FLAIR sequence for orthogonal evaluation; this was incomplete on a second patient due to a technical issue that ended the scanning session. Additionally, all 6 participants had imaging of the bilateral temporal bones with the 8-channel head coil by using FLAIR, FIESTA, and pre- and post-IV contrast T1 sequences (Table 1) to evaluate any regional anatomic variants or other pathology. In 2 patients, this was before any IT contrast; in 1 patient, it was within 2 hours after IT contrast injection (due to scheduling complications precluding pre-IT injection scanning); and in 3 patients, it occurred 20–28 hours after IT contrast injection.

Assessment

Participants were asked to describe any discomfort associated with the IT injection, IV injection, or scanning session (comfort, noise, and so forth). Image quality was assessed by 2 neuroradiologists with expertise in head and neck imaging (J.B., M.F.M.) to assess perilymphatic contrast enhancement, the definition of endolymphatic anatomy, any extralabyrinthine contrast enhancement, and other anatomic variants or pathologic findings. Apparent endolymphatic volume on delayed post-IT (20–28 hour) FLAIR images obtained with the surface coil was determined by visual assessment on the PACS workstation and compared with proposed grading scales.^{8,13}

RESULTS

Four adult female and 2 adult male consenting adults with Menière symptoms refractory to medical therapy participated in this protocol (Table 2). All participants met the American Academy of Otolaryngology–Head and Neck Surgery 1995 criteria²² of “Definite Meniere’s Disease” with appropriate clinical imaging and audiometry. In-plane resolution of 0.375 × 0.375 mm was achieved for the FLAIR sequence by using the 3-inch surface coil, with a maximum acquisition time of 4 minutes 24 seconds. No scans were degraded by patient motion. There were no procedural

complications from intratympanic injection or complications associated with the MR image. Patients reported mild discomfort at the time of phenol anesthesia of the tympanic membrane and a sense of aural fullness post-IT injection. Initially, we accepted audiogram results within the prior 6 months as a baseline. One participant demonstrated a change from mild to moderate low-frequency hearing loss (250–500 Hz) on the post-IT injection audiogram compared with the baseline 5 months prior, with a speech reception threshold change from 15 dB, 96% speech discrimination score threshold, to 20 dB, 96% speech discrimination score. A repeat audiogram 6 weeks after IT contrast and 2 weeks after preplanned IT dexamethasone injection demonstrated a 10-dB hearing improvement at 250 Hz, 15-dB improvement at 500 Hz, and speech reception threshold change of 15 dB, 96% speech discrimination score. The participant had ongoing symptoms since the baseline audiogram; however, we could not exclude any changes possibly attributed to contrast injection. At the patient’s last audiogram approximately 11 months later, fluctuation was again noted, now with a speech reception threshold of 10 dB, and a 100% speech discrimination score. Therefore, we revised the protocol to perform audiometry immediately before IT injection. No other audiometric changes between pre- and postinjection were identified in the 3 subsequent participants.

Assessment of surface coil FLAIR imaging 20–28 hours after IT injection showed contrast in the perilymphatic spaces of the basal, middle, and apical cochlear turns; vestibule; and semicircular canals of all injected ears (Fig 1), sufficient to visibly discriminate the nonenhancing spiral lamina, interscalar septa, and endolymphatic structures. In the 3 ears that were also imaged with the surface coil within 2 hours post-IT injection, contrast enhancement was only evident in the cochlear basal turn and vestibule. Contrast did not persist within the tympanic cavity in any delayed scans, though contrast was seen within mastoid air cells on the side of injection in 2 patients. Contrast was not evident in the perilymphatic space along the endolymphatic duct, and there was no endolymphatic duct or sac distention in any patient.

The nonenhancing endolymphatic space represented 34%–50% of the enhancing vestibule area in 4 ears and >50% in 2 ears. This finding corresponds to mild and moderate vestibular hydrops, respectively, per the proposed Nagoya criteria,⁸ with only

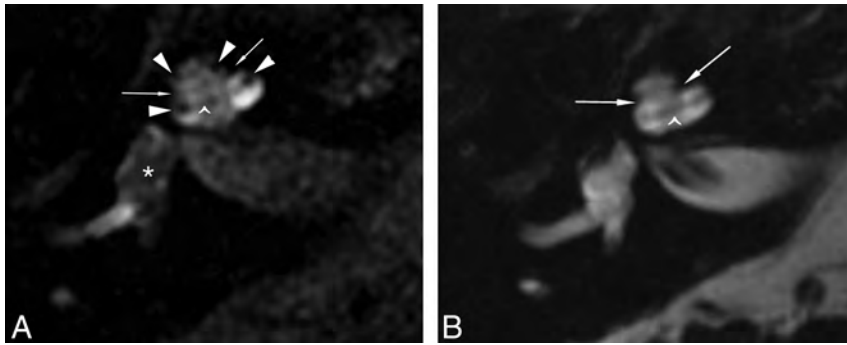


FIG 1. Differentiation of the perilymphatic-versus-endolymphatic spaces is evident when comparing FLAIR (A) and FIESTA images (B) obtained 21 hours after IT injection of 1:7 volume/volume diluted Magnevist contrast with a 3-inch surface coil. The nonenhancing fibro-osseous structures are evident on both sequences: the interscalar septa, separating the basal and middle turns and middle and apical turns (arrows), and the spiral lamina apparatus within each cochlear turn (caret). The FLAIR sequence shows central nonenhancement of the endolymphatic space of the vestibule (A, asterisk) and suggestion of distention of the scala media (A, arrowheads) into the scala vestibuli, whereas on FIESTA image (B), the endolymph and perilymph are both hyperintense and indistinguishable (patient 2).

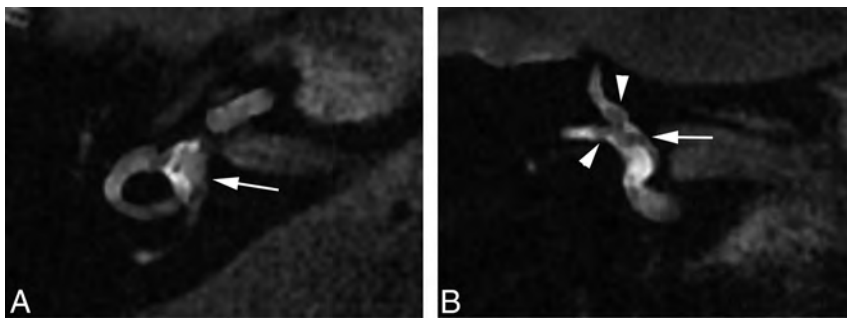


FIG 2. The nonenhancing endolymphatic space (A, arrow) occupies >33% of the area of the vestibule on axial FLAIR image (A) obtained 28 hours after IT GBCA injection, suggesting endolymphatic distention. Coronal FLAIR obtained concurrently (B) demonstrates that the extent of distention of the endolymphatic space is overestimated on the axial view, due to partial volume averaging and section prescription through the membranous utricle (B, arrow). Partial volume averaging also likely contributes to signal heterogeneity within the semicircular canals (A). Arrowheads (B) correspond to the endolymphatic ductal ampullae of the superior and lateral semicircular canals (patient 6).

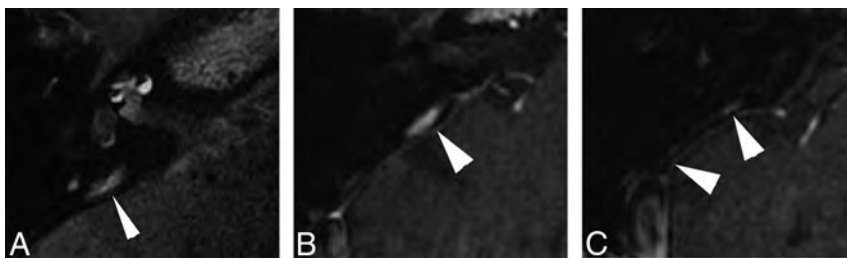


FIG 3. FLAIR imaging performed 28 hours after left IT contrast injection reveals a hyperintense structure (A, arrowhead) extending parallel to the expected course of the vestibular aqueduct (not seen). Comparison with positive-contrast T1-weighted images obtained before IT injection confirms that this structure is an enhancing dural vessel (B and C, arrowheads) coursing parallel to the posterior semicircular canal, extending from the middle cranial fossa to the sigmoid sinus. Correlation with anatomic imaging is imperative to avoid the misinterpretation of dilated endolymphatic space in the vestibular aqueduct (patient 4).

the 2 latter cases meeting grade I hydrops per Baráth et al.¹³ All surveyed ears demonstrated distention of the scala media without obliteration of the scala vestibuli, corresponding to mild cochlear hydrops⁹ and grade I hydrops,¹³ respectively. Partial volume effects were evident when comparing axial and coronal planes,

which could lead to overestimation of endolymphatic distention in the vestibule, depending on the section profile and thickness of axial images (Fig 2).

Variant vascular anatomy was noted in 3 patients, including a prominent vein paralleling the vestibular aqueduct on the symptomatic side (Fig 3), ICA hypoplasia contralateral to the symptomatic side, and a large, high-riding jugular bulb on the symptomatic side, without diverticulum.

If we kept all other parameters fixed, variation of the TI from 2000 to 2800 on surface coil FLAIR imaging 20–28 hours after IT injection resulted in a visually conspicuous difference of the nonenhancing endolymphatic space. Decreasing fluid suppression resulted in decreased conspicuity of the endolymphatic space in the cochlea at a longer TI (Fig 4).

Visual analysis of surface coil FLAIR and T1-weighted imaging 20–28 hours after IT injection revealed clear enhancement in the CSF at the internal auditory canal (IAC) fundus in 1 patient (Fig 5) and subtle enhancement in 2 additional patients. Enhancement was detectable on both FLAIR and T1 images and, therefore, was not attributed to incomplete fluid suppression; additionally, it was only evident at the fundus, not throughout the CSF of the IAC.

DISCUSSION

The diagnosis of Menière disease may be delayed for years in up to 20% of patients who ultimately receive the diagnosis.¹⁴ Since Mark et al²³ reported asymmetric labyrinthine enhancement after IV contrast in patients with sudden deafness and vertigo, continued technologic advances have improved our ability to resolve the delicate structures of the inner ear. Different methods have been used to assess the membranous labyrinth, with inherent variations among scanner vendors, protocols, coils, and contrast agents. For this project, we focused on 1 promising option by using a 3-inch surface coil 20–28 hours after IT injection of diluted Magnevist.

With an acquisition time of <4 minutes 30 seconds for the high-resolution FLAIR sequence, it could be easily added to a routine clinical IAC protocol, achieving better in-plane resolution within less time than any reported protocol to date.

Advantages of using the surface coil include the ability to re-

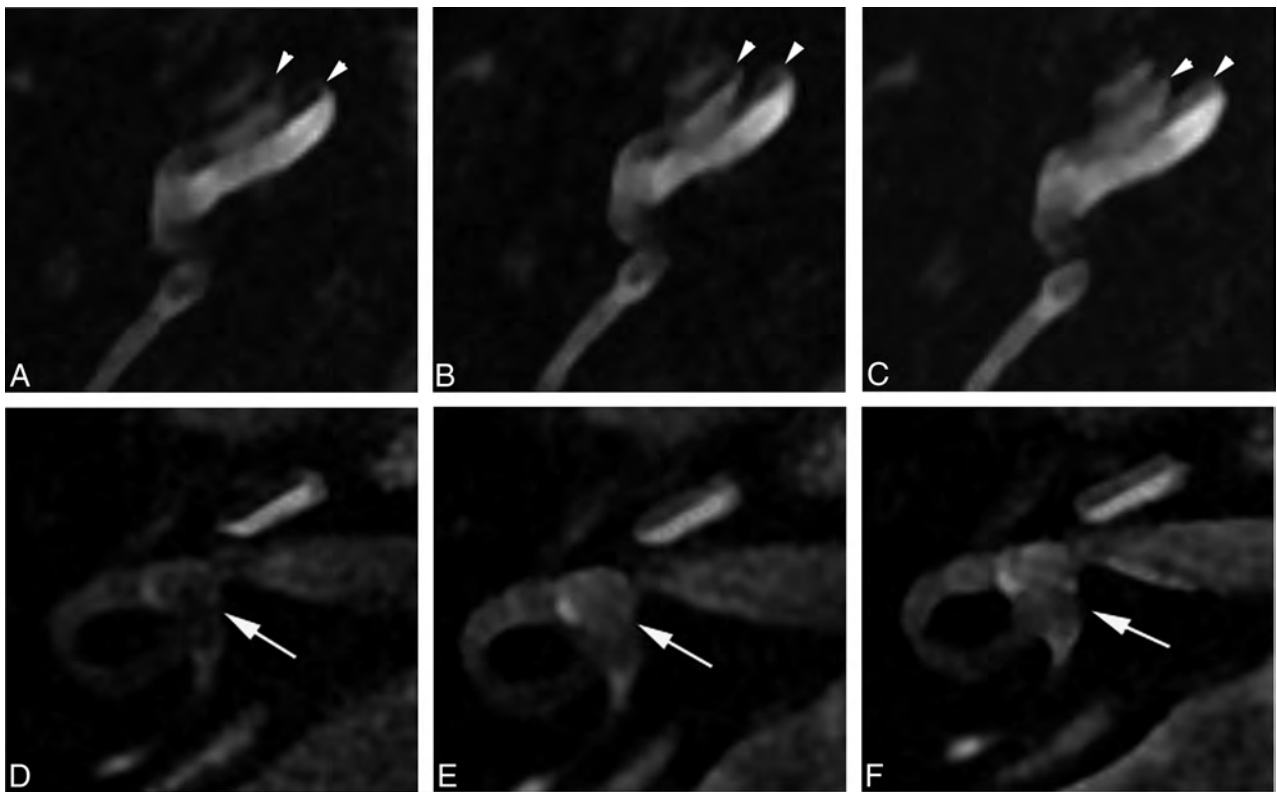


FIG 4. The impact of variable fluid suppression is visually evident with direct comparison of FLAIR sequences with TIs of 2000 ms (A and D), 2500 ms (B and E), and 2800 ms (C and F), with all other parameters remaining fixed. The nonenhancing scala media (*arrowheads*) becomes less conspicuous during this short range of TI (A–C), which may result in altered perception of endolymphatic space distention. Variation corresponding to the larger endolymphatic space in the vestibule (*arrows*, D–F) is less perceptible with changes in TI (patient 4).

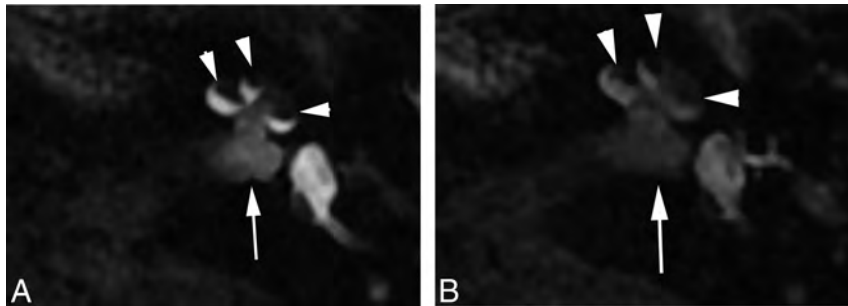


FIG 5. Enhancement is visible at the fundus of the IAC (*arrow*) on delayed imaging after IT GBCA, conspicuous on FLAIR (A) and T1-weighted imaging (B) in this patient who had profound distention of the endolymphatic space in the basal and middle cochlear turns (*arrowheads*) (patient 5).

duce the FOV with minimization of wrap artifacts due to the inherent limited penetration of the coil, reduced acquisition time compared with 3D techniques, and improved SNR relative to 3D sequences in which acceleration for parallel imaging results in signal loss.^{20,21} A limitation of the surface coil is that a 2-mm section thickness was required for optimal signal, requiring precision in the prescription for centering the cochlea and vestibule. This can be overcome with the surface coil by obtaining direct coronal and oblique acquisitions. With the shorter acquisition time per scan, there is less risk of motion degradation that may occur with longer volumetric protocols. These techniques on a GE Healthcare 3T system have not been previously reported, though multiple sites have published series performed on Siemens Verio and Trio 3T scanners (Siemens, Erlangen, Germany),^{10,12,17,18,24–26} progress-

ing from 8- to 32-channel head coils, and techniques have been reproduced on a Philips Achieva 3T system (Best, the Netherlands).²⁷ Because protocols vary across platforms and scanners, development of internal references/controls will be important for accurate characterization of findings. Our results demonstrate the visually conspicuous variation in the suppression of intrinsic endolymphatic fluid signal across a narrow range of TIs. While visual assessment can approximate the extent of fluid suppression through comparison to CSF signal

in the IAC or cerebellopontine angle cistern, some method of assessment is important as these protocols are used, to ensure normalization and reproducibility before postprocessing algorithms are applied to the data.^{19,28}

When one evaluates these protocols for the clinical setting, it is important to consider whether or how this information may change management. There remains interest in using IT GBCA as a surrogate for IT drug delivery, acknowledging differences in chemical composition and molecular weight among different GBCAs, steroids, and gentamicin.²⁹ Poor-to-absent contrast penetration into the perilymph has been reported after IT injection in up to 18% of patients,^{9,30} suggesting a means to screen for potential poor responders to IT interventions. Nevertheless, series have not found a reliable correlation between the extent of en-

dolymphatic distention and patient response to subsequent IT steroids,^{16,18} and there has been variable correlation between imaging with summing potential/action potential ratios electrocochleography and vestibular-evoked myogenic potential.^{17,25,31} These outcomes may be partially due to lack of standardization of criteria for severity based on imaging findings^{8,12,13} but also may reflect the spectrum of findings through the range associated with the natural history of Menière disease.

The delayed post-IT injection FLAIR sequence should be interpreted with multiplanar projections, to avoid interpretation errors due to partial volume averaging as illustrated in Fig 2. Additionally, any nonstandard sequences must be reviewed in the context of a full IAC protocol, including fluid-sensitive, DWI, FLAIR, and postcontrast T1 sequences of the entire auditory pathway, to exclude a schwannoma³² or other source of symptoms.

An unexpected finding in our study was the prevalence of enhancement in the CSF at the IAC fundus on 20- to 28-hour post-IT contrast FLAIR and T1 images. This was evident in half of our patients, and although our study group was small, this finding suggests that it may occur more frequently than has been noted in the literature.^{7,33,34} This observation prompts caution regarding proceeding directly to delayed postcontrast imaging in the evaluation of suspected Menière disease, to avoid potentially obscuring hemorrhage or protein that may be responsible for symptoms.^{10,35} MR imaging 4 hours after IV contrast has been promoted as an alternative, allowing simultaneous evaluation of both ears and not requiring IT injection or institutional review board approval. The 2 methods are complementary in that delayed IV methods reflect blood-labyrinthine barrier integrity, whereas IT methods reflect round window permeability; however, delayed IV methods have reduced contrast to noise. Careful attention to extralabyrinthine enhancement in both delayed IV and IT protocols is necessary for better understanding of the mechanism and significance of increased modiolar permeability and in the context of the timing of imaging for clinical interpretation. Despite the described limitations, the improved resolution and contrast achievable with IT methods should be of particular value as we continue to evaluate the reproducibility of these methods to define the normal and diseased endolymphatic systems.

CONCLUSIONS

Using a surface coil with a 3T system affords high-resolution FLAIR imaging of the inner ear after IT contrast administration in a clinically reasonable time. Because these techniques are only an indirect evaluation of endolymphatic distention, however, and not a proved surrogate for Menière symptoms or response to therapy, continued investigation is necessary before use in clinical diagnosis. Evaluation should include correlation with a full IAC protocol to exclude other sources for symptoms, with awareness that diffusion of IT contrast into the CSF in the IAC may mimic or obscure hemorrhage or enhancement. Additionally, work remains to be done to optimize protocols in the absence of a clear internal reference for standardization and to better understand the implications of modiolar permeability.

ACKNOWLEDGMENTS

The authors would like to thank Sharon Mick, NP, for her help in coordinating patient scheduling.

Disclosures: Julie Bykowski—RELATED: Grant: American Society of Head and Neck Radiology Hanafee Award*; Other: Off-label use of Magnevist contrast per FDA Investigational New Drug 115,342. Mia Miller—UNRELATED: Grants/Grants Pending: Hearing Research Inc*; Travel/Accommodations/Meeting Expenses Unrelated to Activities Listed: resident travel grant,* Mount Zion travel grant.**Money paid to the institution.

REFERENCES

1. Committee on Hearing and Equilibrium guidelines for the diagnosis and evaluation of therapy in Meniere's disease: American Academy of Otolaryngology-Head and Neck Foundation, Inc. *Otolaryngol Head Neck Surg* 1995;113:181–85
2. Counter SA, Bjelke B, Borg E, et al. Magnetic resonance imaging of the membranous labyrinth during in vivo gadolinium (Gd-DTPA-BMA) uptake in the normal and lesioned cochlea. *Neuroreport* 2000;11:3979–83
3. Duan M, Bjelke B, Fridberger A, et al. Imaging of the guinea pig cochlea following round window gadolinium application. *Neuroreport* 2004;15:1927–30
4. Zou J, Pyykko I, Bjelke B, et al. Communication between the perilymphatic scalae and spiral ligament visualized by in vivo MRI. *Audiol Neurootol* 2005;10:145–52
5. Kakigi A, Nishimura M, Takeda T, et al. Effects of gadolinium injected into the middle ear on the stria vascularis. *Acta Otolaryngol* 2008;128:841–45
6. Zou J, Poe D, Bolje B, et al. Visualization of inner ear disorders with MRI in vivo: from animal models to human applications. *Acta Otolaryngol Suppl* 2009:22–31
7. Nakashima T, Naganawa S, Suguira M, et al. Visualization of endolymphatic hydrops in patients with Meniere's disease. *Laryngoscope* 2007;117:415–20
8. Nakashima T, Naganawa S, Pyykko I, et al. Grading of endolymphatic hydrops using magnetic resonance imaging. *Acta Otolaryngol Suppl* 2009:5–8
9. Nakashima T, Naganawa S, Katayama N, et al. Clinical significance of endolymphatic imaging after intratympanic gadolinium injection. *Acta Otolaryngol Suppl* 2009:9–14
10. Sugiura M, Naganawa S, Teranishi M, et al. Three-dimensional fluid-attenuated inversion recovery magnetic resonance imaging findings in patients with sudden sensorineural hearing loss. *Laryngoscope* 2006;116:1451–54
11. Yamazaki M, Naganawa S, Tagaya M, et al. Comparison of contrast effect on the cochlear perilymph after intratympanic and intravenous gadolinium injection. *AJNR Am J Neuroradiol* 2012;33:773–78
12. Fang ZM, Chen X, Gu X, et al. A new magnetic resonance imaging scoring system for perilymphatic space appearance after intratympanic gadolinium injection, and its clinical application. *J Laryngol Otol* 2012;126:454–59
13. Baráth K, Schuknecht B, Naldi AM, et al. Detection and grading of endolymphatic hydrops in Meniere disease using MR imaging. *AJNR Am J Neuroradiol* 2014;35:1387–92
14. Pyykko I, Nakashima T, Yoshida T, et al. Meniere's disease: a reappraisal supported by a variable latency of symptoms and the MRI visualisation of endolymphatic hydrops. *BMJ Open* 2013;3:e001555
15. Naganawa S, Satake H, Kawamura M, et al. Separate visualization of endolymphatic space, perilymphatic space and bone by a single pulse sequence: 3D-inversion recovery imaging utilizing real reconstruction after intratympanic Gd-DTPA administration at 3 Tesla. *Eur Radiol* 2008;18:920–24
16. Gürkov R, Flatz W, Louza J, et al. In vivo visualization of endolymphatic hydrops in patients with Meniere's disease: correlation with audiovestibular function. *Eur Arch Otorhinolaryngol* 2011;268:1743–48
17. Seo YJ, Kim J, Choi JY, et al. Visualization of endolymphatic hy-

- drops and correlation with audio-vestibular functional testing in patients with definite Meniere's disease. *Audis Nasus Larynx* 2013; 40:167–72
18. Fiorino F, Pizzini FB, Beltramello A, et al. Reliability of magnetic resonance imaging performed after intratympanic administration of gadolinium in the identification of endolymphatic hydrops in patients with Ménière's disease. *Otol Neurotol* 2011;32:472–77
 19. Naganawa S, Yamazaki M, Kawai H, et al. Imaging of Ménière's disease by subtraction of MR cisternography from positive perilymph image. *Magn Reson Med Sci* 2012;11:303–09
 20. Glockner JF, Hu HH, Stanley DW, et al. Parallel imaging: a user's guide. *Radiographics* 2005;25:1279–97
 21. Moseley M, Liu C, Rodriguez S, et al. Advances in magnetic resonance neuroimaging. *Neurol Clin* 2009;27:1–19, xiii
 22. Monsell EM. New and revised reporting guidelines from the Committee on Hearing and Equilibrium: American Academy of Otolaryngology-Head and Neck Surgery Foundation, Inc. *Otolaryngol Head Neck Surg* 1995;113:176–78
 23. Mark AS, Seltzer S, Nelson-Drake J, et al. Labyrinthine enhancement on gadolinium-enhanced magnetic resonance imaging in sudden deafness and vertigo: correlation with audiologic and electronystagmographic studies. *Ann Otol Rhinol Laryngol* 1992;101:459–64
 24. Claes G, Van den Hauwe L, Wuyts F, et al. Does intratympanic gadolinium injection predict efficacy of gentamicin partial chemolabyrinthectomy in Ménière's disease patients? *Eur Arch Otorhinolaryngol* 2012;269:413–18
 25. Fukuoka H, Takumi Y, Tsukada K, et al. Comparison of the diagnostic value of 3 T MRI after intratympanic injection of GBCA, electrocochleography, and the glycerol test in patients with Meniere's disease. *Acta Otolaryngol* 2012;132:141–45
 26. Jerin C, Krause E, Ertl-Wagner B, et al. Longitudinal assessment of endolymphatic hydrops with contrast-enhanced magnetic resonance imaging of the labyrinth. *Otol Neurotol* 2014;35:880–83
 27. Homann G, Fahrendorf D, Niederstadt T, et al. HR 3 Tesla MRI for the diagnosis of endolymphatic hydrops and differential diagnosis of inner ear tumors: demonstrated by two cases with similar symptoms. *Rofo* 2014;186:225–29
 28. Naganawa S, Ishihara S, Iwano S, et al. Estimation of gadolinium-induced T1-shortening with measurement of simple signal intensity ratio between the cochlea and brain parenchyma on 3D-FLAIR: correlation with T1 measurement by TI scout sequence. *Magn Reson Med Sci* 2010;9:17–22
 29. Pyykko I, Zou J, Poe D, et al. Magnetic resonance imaging of the inner ear in Meniere's disease. *Otolaryngol Clin N Am* 2010;43:1059–80
 30. Yoshioka M, Naganawa S, Sone M, et al. Individual differences in the permeability of the round window: evaluating the movement of intratympanic gadolinium into the inner ear. *Otol Neurotol* 2009; 30:645–48
 31. Katayama N, Yamamoto M, Teranishi M, et al. Relationship between endolymphatic hydrops and vestibular-evoked myogenic potential. *Acta Otolaryngol* 2010;130:917–23
 32. Tieleman A, Casselman JW, Somers T, et al. Imaging of intralabyrinthine schwannomas: a retrospective study of 52 cases with emphasis on lesion growth. *AJNR Am J Neuroradiol* 2008;29:898–905
 33. Naganawa S, Satake H, Iwano S, et al. Communication between cochlear perilymph and cerebrospinal fluid through the cochlear modiolus visualized after intratympanic administration of Gd-DTPA. *Radiat Med* 2008;26:597–602
 34. Kawai H, Naganawa S, Ishihara S, et al. MR imaging of the cochlear modiolus after intratympanic administration of Gd-DTPA. *Magn Reson Med Sci* 2010;9:23–29
 35. Naganawa S, Ishihara S, Iwano S, et al. Detection of presumed hemorrhage in the ampullar endolymph of the semicircular canal: a case report. *Magn Reson Med Sci* 2009;8:187–91

Visualization of the Peripheral Branches of the Mandibular Division of the Trigeminal Nerve on 3D Double-Echo Steady-State with Water Excitation Sequence

H. Fujii, A. Fujita, A. Yang, H. Kanazawa, K. Buch, O. Sakai, and H. Sugimoto

ABSTRACT

BACKGROUND AND PURPOSE: Although visualization of the extracranial branches of the cranial nerves has improved with advances in MR imaging, only limited studies have assessed the detection of extracranial branches of the mandibular nerve (V3). We investigated the detectability of the branches of V3 on a 3D double-echo steady-state with water excitation sequence.

MATERIALS AND METHODS: We retrospectively evaluated the detectability of the 6 branches of the V3, the masseteric, buccal, auriculotemporal, lingual, inferior alveolar, and mylohyoid nerves, by using a 5-point scale (4, excellent; 3, good; 2, fair; 1, poor; and 0, none) in 86 consecutive patients who underwent MR imaging with the 3D double-echo steady-state with water excitation sequence. Weighted κ analysis was used to calculate interobserver variability among the 3 readers.

RESULTS: The detection of the lingual and inferior alveolar nerves was the most successful, with excellent average scores of 3.80 and 3.99, respectively. The detection of the masseteric, the buccal, and the auriculotemporal nerves was good, with average scores of 3.31, 2.67, and 3.11, respectively. The mylohyoid nerve was difficult to detect with poor average scores of 0.62. All nerves had excellent interobserver variability across the 3 readers (average weighted κ value, 0.95–1.00).

CONCLUSIONS: The 3D double-echo steady-state with water excitation sequence demonstrated excellent visualization of the extracranial branches of V3 in most patients. The 3D double-echo steady-state with water excitation sequence has the potential for diagnosing V3 pathologies and preoperatively identifying peripheral cranial nerves to prevent surgical complications.

ABBREVIATIONS: 3D-DESS-WE = 3D double-echo steady-state with water excitation; V3 = mandibular nerve (third division of the trigeminal nerve)

Cranial nerve deficits are not uncommon, and there are many pathologic processes that can affect the cranial nerves.^{1–10} Unfortunately, the physical examination findings are often non-specific for differentiating among these pathologic causes, and imaging plays a crucial role in diagnosing pathologic processes affecting the cranial nerves. With increasing spatial and contrast resolution of cross-sectional imaging, better visualization of the cranial nerves and their major branches has become possible, but the delineation of the entire course of the extracranial segments of the cranial nerves still remains a diagnostic challenge.^{11–17}

The trigeminal nerve has the largest distribution of innervation among all the cranial nerves in the suprahyoid neck. Even though the mandibular nerve (V3) is the largest division of the trigeminal nerve, there have been only limited studies investigating the visualization of the extracranial segments of V3 with MR imaging. Several prior studies have focused on imaging the extracranial segments of V3 by using a T1-weighted fast-spoiled gradient recalled-echo sequence with fat suppression,⁹ a T1-weighted MPRAGE sequence with water excitation fat suppression,¹⁸ or a diffusion tensor tractography sequence,¹⁹ but these studies evaluated only the inferior alveolar nerve. Another study used FIESTA and fast-spoiled gradient recalled-echo sequences to evaluate the entire V3 nerve, but the extracranial peripheral V3 branches were not well-demonstrated, with the exception of the inferior alveolar and lingual nerves.¹³

The 3D double-echo steady-state with water excitation (3D-DESS-WE) sequence is a recently introduced MR imaging technique that can delineate the peripheral cranial nerves as high-signal-intensity structures.²⁰ At our institution, this sequence has been added to our standard MR imaging protocol of the salivary

Received October 30, 2014; accepted after revision December 17.

From the Department of Radiology (H.F., A.F., H.K., H.S.), Jichi Medical University School of Medicine, Tochigi, Japan; Departments of Radiology (A.F., K.B., O.S.), Otolaryngology–Head and Neck Surgery (O.S.), and Radiation Oncology (O.S.), Boston Medical Center, and Boston University School of Medicine (A.Y.), Boston, Massachusetts.

Paper previously presented at: Annual Meeting of the American Society of Head and Neck Radiology, September 10–14, 2014; Seattle, Washington.

Please address correspondence to Akifumi Fujita, MD, Department of Radiology, Jichi Medical University School of Medicine, 3311–1, Yakushiji, Shimotsuke, Tochigi 329-0498, Japan; e-mail: akifujii@jichi.ac.jp

<http://dx.doi.org/10.3174/ajnr.A4288>

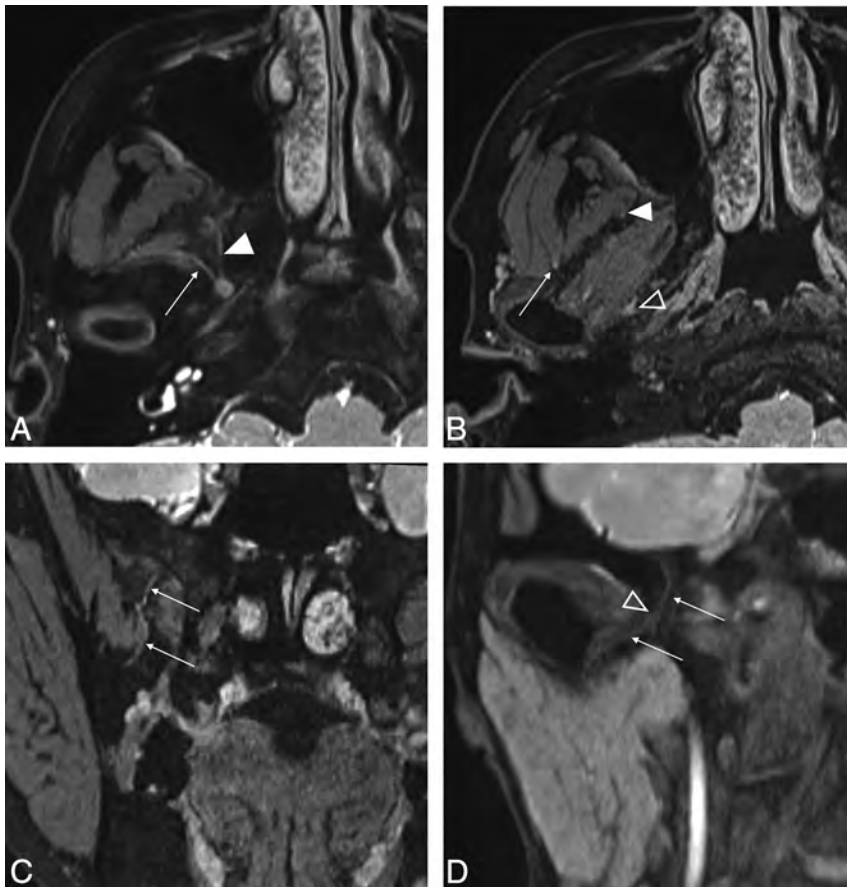


FIG 1. A and B, Axial source images of the 3D-DESS-WE sequence. C and D, Coronal reformatted images of the 3D-DESS-WE sequence. Axial image shows the masseteric nerve (A, arrow) and buccal nerve (A, solid arrowhead) arising from the V3 trunk. The intermediate point is established, where the masseteric nerve enters the deep surface of the masseter muscle (B, arrow), to divide the nerve into proximal and distal portions. The intermediate point for the buccal nerve is established as the anterolateral edge of the lateral pterygoid muscle (B, solid arrowhead). Reformatted coronal images show the course of the buccal nerve running inferiorly (C, arrows) and the auriculotemporal nerve running inferolaterally (D, arrows). The intermediate point is established where the auriculotemporal nerve enters the pterygoid venous plexus (B and D, open arrowheads).

glands and has been used routinely to evaluate the intraparotid facial nerve and salivary ducts within the salivary glands since October 2012. The purpose of this study was to investigate the detectability of the extracranial peripheral branches of V3 on the 3D-DESS-WE sequence.

MATERIALS AND METHODS

Patient Population

This retrospective study was approved by our institutional review board, and informed consent was waived. We reviewed 86 consecutive patients who underwent MR imaging for the evaluation of salivary gland lesions from October 2012 to March 2014 (40 males and 46 females; age range, 17–88 years; mean age, 58 years; median age, 63 years). Of 86 patients, the final diagnoses or suspected diagnoses were as follows: 47 benign tumors, 6 cases of Sjögren syndrome, 5 infectious diseases, 5 malignant tumors, and 5 submandibular lesions; the rest of the 18 patients were healthy or had lesions incidentally found in other locations. Patients with severe motion artifacts, metal artifacts, or large mass lesions deforming adjacent anatomic structures were excluded from evalu-

ation. Ultimately, 85 patients were included in this study, and there were certain patients whose respective nerve branches were excluded from the evaluation.

MR Imaging Procedures

All patients underwent MR imaging with a 3T unit (Magnetom Skyra; Siemens, Erlangen, Germany) by using a commercially available 20-channel head-neck coil with our routine neck protocol that included the 3D-DESS-WE sequence. The precise parameters of the 3D-DESS-WE sequence are as follows: TR/TE = 11/4.21 ms, flip angle = 30°, FOV = 200 × 200 mm, matrix = 384 × 244, effective section thickness = 0.82 mm, number of acquisitions = 1, scan time = 4 minutes 12 seconds. Slab thickness (11.2 cm) of the 3D-DESS-WE sequence is from the skull base to the mandible.

Image Evaluation

All acquired images were transferred to our clinical server and evaluated with a PACS, with a 2-megapixel high-resolution liquid-crystal display. Three readers (reader A, third-year radiology resident; reader B, first-year medical student; reader C, attending neuroradiologist with 17 years of experience) independently evaluated the 6 extracranial branches of the V3: the masseteric nerve, the buccal nerve, the auriculotemporal nerve, the lingual nerve, the inferior alveolar nerve, and the mylohyoid nerve.

The courses of the V3 branches were

determined by tracing the nerve from the foramen ovale distally, compared with anatomic diagrams from *Gray's Anatomy*.²¹ Axial source images of the 3D-DESS-WE sequence were mainly used for tracing the branches of the V3. Reconstructed sagittal and coronal thin (3-mm thick) slab MIP images of the 3D-DESS-WE sequence were also used simultaneously.

Representative images of the 6 branches of V3 are shown in Figs 1 and 2. As the V3 descends from the foramen ovale, it divides into the anterior division, which gives off the masseteric nerve and the buccal nerve (Fig 1A), and the posterior division, which gives off the auriculotemporal nerve (Fig 1D), the lingual nerve (Fig 2A), the inferior alveolar nerve (Fig 2B), and the mylohyoid nerve (Fig 2C).

We evaluated the images focusing on the continuity of each V3 branch and distinguishing the branch from the V3 trunk to avoid potential confusion of vascular structures for nerve structures. Each of the 6 branches of V3 was divided into proximal and distal portions at intermediate points to facilitate evaluation. The intermediate point for the masseteric nerve is the point at which the



FIG 2. A and B, Coronal reformatted image of the 3D-DESS-WE sequence. C, Axial source image of the 3D-DESS-WE sequence. Reformatted coronal images show the lingual nerve (A, arrows) and the inferior alveolar nerve (B, arrows). The intermediate points are established where the lingual nerve running laterally starts to change direction medially (A, arrowhead) and where the inferior alveolar nerve enters the mandibular foramen (B; arrowhead). Axial image shows that the mylohyoid nerve runs at the medial surface of the mandible (C, arrow). The intermediate point is established where the nerve enters the mylohyoid muscle (C, arrowhead).

nerve enters the deep surface of the masseter muscle (Fig 1B). The intermediate point for the buccal nerve is where the nerve enters the anterolateral edge of the lateral pterygoid muscle (Fig 1B). On the coronal image, the distal portion of the buccal nerve runs an S-shaped course (Fig 1C). The intermediate point for the auriculotemporal nerve is where the nerve enters the pterygoid venous plexus (Fig 1B, -D). The intermediate point for the lingual nerve is where the nerve running laterally starts to change direction medially (Fig 2A). The intermediate point for inferior alveolar nerve is where the nerve enters the mandibular foramen (Fig 2B). The intermediate point for the mylohyoid nerve is where the nerve enters the mylohyoid muscle (Fig 2C).

Statistical Analysis

We evaluated the capability of detecting the V3 branches with a 5-point scale with the criteria as follows: excellent (4), both the proximal and distal portions of the nerve identified; good (3), both the proximal and distal portions of the nerve identified but not continuous; fair (2), only the proximal portion of the nerve identified; poor (1), only the proximal portion of the nerve identified but not continuous; and none (0), the nerve not identified. The average scores for each reader, in addition to the average score from all 3 readers for the 6 branches of the V3, were calculated.

The weighted κ analysis used to calculate interobserver variability was defined as follows: poor, ≤ 0.2 ; fair, >0.2 to ≤ 0.4 ; moderate, >0.4 to ≤ 0.6 ; good, >0.6 to ≤ 0.8 ; and excellent, >0.8 to ≤ 1 .²²

RESULTS

The 3D-DESS-WE sequence was performed in all 86 patients, but 1 patient was excluded because of severe motion artifacts. With 85 patients, 170 nerves for each side of the V3 were reviewed. Because patients with metal artifacts and large mass lesions deforming the adjacent anatomic structures were excluded from the evaluation, 166 masseteric nerve, 166 buccal nerve, 167 auriculotemporal nerve, 159 lingual nerve, 159 inferior alveolar nerve, and 159 mylohyoid nerve segments were included in the analysis.

The average evaluation scores performed by the 3 readers and the interobserver variability are shown in Tables 1 and 2.

The detection of the lingual and the inferior alveolar nerves was excellent, with average scores of 3.80 and 3.99, respectively. The detection of the masseteric, buccal, and auriculotemporal nerves was relatively good, with average scores of 3.31, 2.67, and 3.11, respectively. The mylohyoid nerve was difficult to detect, with an average score of 0.62.

The interobserver variability was excellent among the 3 readers (average weighted κ value, 0.95–1.00).

DISCUSSION

Because the V3 is a large cranial nerve with mixed sensory and motor function that innervates a large region of the suprahyoid neck, a wide variety of physical manifestations and pathologies such as tumor, inflammatory/infectious disease, vascular disease, and trauma can be found affecting it in clinical practice.^{7,11,12} V3 contains clinically important branches often affected by head and neck cancers via direct invasion and/or perineural tumor spread. All of these pathologic etiologies have the potential to impact clinical outcomes significantly and may contribute to significant morbidity and quality of life.^{3,10,23,24} An in-depth understanding of the anatomy and normal course of the extracranial nerves is required to make the diagnosis of many of these pathologies, and more sophisticated and dedicated high-resolution MR images for peripheral cranial nerve imaging are expected to enter and influence clinical practice.

The widespread uses of volumetric CT scanners and high-field MR imaging scanners and recent advances in MR imaging technology have provided opportunities to obtain high-resolution images of the cranial nerves. Following the entire course of the cranial nerves, including the extracranial segments, however, is still a diagnostic challenge in routine clinical practice.^{1,2,11-16} Intracranial segments of the cranial nerves, particularly the cisternal segments, are readily detected by using high-resolution heavily T2-weighted imaging.^{14,15} Without the high-signal background from the CSF, however, heavily

Table 1: Average scores of the 3 readers evaluating the V3 nerves

V3 Nerves	Reader A	Reader B	Reader C	Average
Masseteric	3.34 ± 1.083	3.36 ± 1.015	3.24 ± 1.016	3.31 ± 1.038
Buccal	2.64 ± 1.308	2.75 ± 1.332	2.63 ± 1.281	2.67 ± 1.306
Auriculotemporal	3.13 ± 1.376	3.07 ± 1.220	3.13 ± 1.185	3.11 ± 1.261
Lingual	3.77 ± 0.781	3.88 ± 0.544	3.75 ± 0.682	3.80 ± 0.677
Inferior alveolar	4.00 ± 0.000	4.00 ± 0.000	3.97 ± 0.157	3.99 ± 0.091
Mylohyoid	0.46 ± 0.785	0.67 ± 0.917	0.72 ± 0.764	0.62 ± 0.831

Table 2: Interobserver variability of the 3 readers (A, B, and C) evaluating the V3 nerves

V3 Nerves	A and B	B and C	C and A	Average
Masseteric	0.960	0.970	0.961	0.96
Buccal	0.954	0.973	0.936	0.95
Auriculotemporal	0.942	0.961	0.955	0.95
Lingual	0.974	0.994	0.977	0.98
Inferior alveolar	1.000	0.998	0.998	1.00
Mylohyoid	0.983	0.967	0.959	0.97

T2-weighted imaging has not proved to be very useful in visualizing the extracranial segments of the cranial nerves. Detecting the remaining peripheral segments can be achieved with pre- and postcontrast high-resolution 3D T1-weighted images (gradient-recalled acquisition in steady state, fast-spoiled gradient recalled-echo, or MPRAGE) with and without fat suppression,^{9-13,16,18,23} but detecting the entire course of the extracranial branches of the cranial nerves is still very challenging.

The 3D-DESS-WE sequence, commonly used in musculoskeletal imaging, was recently applied for visualization of the intraparotid facial nerve and is quite successful.²⁰ In our institution, we routinely use the 3D-DESS-WE sequence when investigating parotid lesions, both for visualization of the intraparotid facial nerve to localize the parotid tumor and to detect involvement of the nerve. In this study, we assessed the detectability of the extracranial segments of V3 by using the 3D-DESS-WE sequence.

Our study demonstrates that it is possible to detect the entire course of the main branches of V3 with non-contrast-enhanced MR imaging. In a recent study performed by Cassetta et al,¹³ the detectability of the branches of the V3 (buccal, auriculotemporal, lingual, and inferior alveolar nerves) was evaluated with a combination of FIESTA and fast-spoiled gradient recalled-echo sequences performed with a 3T scanner, but the authors were not able to identify the buccal nerve or the auriculotemporal nerve in all cases. The 3D-DESS-WE sequence used in this study demonstrated superior detection of the 4 branches of the V3, including the buccal and auriculotemporal nerves. This study also builds on prior work in which we assessed the detectability of the masseteric and the mylohyoid nerves.¹³

Because the lingual and the inferior alveolar nerves are surrounded by fat and/or fatty bone marrow along their course, the detection of these nerves was excellent by using a water excitation fat-suppression technique.²⁰ The detection of the masseteric and the buccal nerves was also relatively good. The 3D-DESS-WE sequence involves the acquisition of 2 different echoes during each TR, on the basis of the steady-state free precession technique. The first echo is the free induction decay gradient echo used in the FISP sequence, and the second is the spin-echo used in the steady-state free precession sequence.²⁰ Because the steady-state free precession signal intensity has a dominant T2 contrast¹⁷ and the FISP

signal intensity provides more anatomic details with tissue contrast dominated by the T1/T2 ratio,²⁰ we speculate that the component of T2 contrast in the DESS sequence would show the nerve itself as a high-signal-intensity structure and would enable us to track the nerve easily with paging methods on the PACS viewer. In future studies, we expect that the T2 contrast of the nerve itself will enable the detection of signal abnormalities in nerves with normal morphology, such as the early stage of the perineural spread of malignancy and infection/inflammatory disease.

Although it was difficult to differentiate the auriculotemporal nerve from the pterygoid venous plexus in some patients, the detection of the auriculotemporal nerve was relatively successful in our study. Because the auriculotemporal nerve is often involved in the perineural spread of malignancy,^{3,10,24} our results suggest that the 3D-DESS-WE sequence is a promising method for evaluating perineural tumor spread. The main explanation for the poor detection of small branches is that the visualization depends on the size of the nerve. To better visualize small nerves such as the mylohyoid nerve, further refinement in the sequence design or higher magnet strength for higher SNR may be needed. Size was not the sole limitation for the detection of small nerves, however, because the masseteric, buccal, and auriculotemporal nerves were visualized well in this study. The visibility of small nerve structures may depend on the morphology and arrangement of structures adjacent to each nerve branch. Relatively lower scores of masseteric and buccal nerves compared with the auriculotemporal nerve are likely secondary to susceptibility artifacts from the sinonasal cavity air.

In this study, we evaluated the capability of depicting the segments of the V3 branches by using 3 readers of dramatically different backgrounds and levels of training: a medical student, a radiology resident, and a neuroradiology attending physician. The interobserver variabilities among the 3 readers were excellent; this outcome reflected the inherent improved diagnostic capabilities of the V3 nerves by using the 3D-DESS-WE sequence. Although the reader's experience influences the imaging interpretation and impacts the diagnostic assessment, we believe that interpreting images by tracking the nerves in this 3D-DESS-WE sequence is a promising method for detecting and evaluating the extracranial peripheral cranial nerves. The advantages of the 3D-DESS-WE sequence include its short acquisition time and using the standard head and neck coil without a surface coil, in addition to high and uniform detectability of the peripheral cranial nerves by readers at various training levels. These features make the 3D-DESS-WE sequence readily feasible in routine clinical practice.

One of the limitations of this study was the presence of susceptibility and motion artifacts, which were prominent in the 3D-DESS-WE sequence, and inhomogeneous fat suppression, which interfered with visualization of the nerves. We noticed that the

masseteric and buccal nerves are affected by the susceptibility effect from the paranasal sinus air. Applying other types of fat-suppression techniques to the 3D double-echo steady-state sequence may improve the visualization of the nerves. Another limitation is the subjective and qualitative evaluation used in this study; objective quantitative evaluation may be needed to discriminate normal and abnormal findings of the nerves in a future study. Finally, because we have no surgical or pathologic correlation with images in this study, we cannot tell whether the small-sized nerve branches are actually the small-sized nerves, but instead we relied on their having a characteristic anatomic course.

CONCLUSIONS

The 3D-DESS-WE sequence demonstrated excellent visualization of the extracranial branches of the V3, such as the masseteric nerve, buccal nerve, auriculotemporal nerve, lingual nerve, and inferior alveolar nerve, in most patients. Uniform high detectability of the normal course of peripheral branches of the V3 was obtained by readers with very different experience. The 3D-DESS-WE sequence has the potential for diagnosing V3 pathologies and for more precise preoperative identification of the peripheral nerves, which may help in preventing complications from surgical intervention with future studies.

Disclosures: Osamu Sakai—UNRELATED: Payment for Lectures (including service on Speakers Bureaus): Bracco Diagnostics, Kyorin USA, Eisai, Comments: honoraria for lectures; Royalties: McGraw-Hill.

REFERENCES

- Borges A, Casselman J. **Imaging the cranial nerves. Part I. Methodology, infectious and inflammatory, traumatic and congenital lesions.** *Eur Radiol* 2007;17:2112–25
- Borges A, Casselman J. **Imaging the cranial nerves. Part II. Primary and secondary neoplastic conditions and neurovascular conflicts.** *Eur Radiol* 2007;17:2332–44
- Chan M, Dmytriw AA, Bartlett E, et al. **Imaging of auriculotemporal nerve perineural spread.** *Ecancermedalscience* 2013;7:374
- Ginsberg LE, DeMonte F. **Imaging of perineural tumor spread from palatal carcinoma.** *AJNR Am J Neuroradiol* 1998;19:1417–22
- Ginsberg LE, Eicher SA. **Great auricular nerve: anatomy and imaging in a case of perineural tumor spread.** *AJNR Am J Neuroradiol* 2000;21:568–71
- Lian K, Bartlett E, Yu E. **Perineural tumor spread along the sixth cranial nerve: CT and MR imaging.** *AJNR Am J Neuroradiol* 2011;32:E178
- Majoie CB, Verbeeten B Jr, Dol JA, et al. **Trigeminal neuropathy: evaluation with MR imaging.** *Radiographics* 1995;15:795–811
- Sun X, Liang C, Liu C, et al. **Oculomotor paralysis: 3D-CISS MR imaging with MPR in the evaluation of neuralgic manifestation and the adjacent structures.** *Eur J Radiol* 2010;73:221–23
- Terumitsu M, Seo K, Matsuzawa H, et al. **Morphologic evaluation of the inferior alveolar nerve in patients with sensory disorders by high-resolution 3D volume rendering magnetic resonance neurography on a 3.0-T system.** *Oral Surg Oral Med Oral Pathol Oral Radiol Endod* 2011;111:95–102
- Chang PC, Fischbein NJ, McCalmont TH, et al. **Perineural spread of malignant melanoma of the head and neck: clinical and imaging features.** *AJNR Am J Neuroradiol* 2004;25:5–11
- Bathla G, Hegde AN. **The trigeminal nerve: an illustrated review of its imaging anatomy and pathology.** *Clin Radiol* 2013;68:203–13
- Borges A, Casselman J. **Imaging the trigeminal nerve.** *Eur J Radiol* 2010;74:323–40
- Cassetta M, Pranno N, Pompa V, et al. **High resolution 3-T MR imaging in the evaluation of the trigeminal nerve course.** *Eur Rev Med Pharmacol Sci* 2014;18:257–64
- Naganawa S, Koshikawa T, Fukatsu H, et al. **MR cisternography of the cerebellopontine angle: comparison of three-dimensional fast asymmetrical spin-echo and three-dimensional constructive interference in the steady-state sequences.** *AJNR Am J Neuroradiol* 2001;22:1179–85
- Sheth S, Branstetter BF, Escott EJ. **Appearance of normal cranial nerves on steady-state free precession MR images.** *Radiographics* 2009;29:1045–55
- Williams LS, Schmalfluss IM, Siström CL, et al. **MR imaging of the trigeminal ganglion, nerve, and the perineural vascular plexus: normal appearance and variants with correlation to cadaver specimens.** *AJNR Am J Neuroradiol* 2003;24:1317–23
- Zhang Z, Meng Q, Chen Y, et al. **3-T imaging of the cranial nerves using three-dimensional reversed FISP with diffusion-weighted MR sequence.** *J Magn Reson Imaging* 2008;27:454–58
- Deng W, Chen SL, Zhang ZW, et al. **High-resolution magnetic resonance imaging of the inferior alveolar nerve using 3-dimensional magnetization-prepared rapid gradient-echo sequence at 3.0T.** *J Oral Maxillofac Surg* 2008;66:2621–26
- Mori S, Kaneda T, Fujita Y, et al. **Diffusion tensor tractography for the inferior alveolar nerve (V3): initial experiment.** *Oral Surg Oral Med Oral Pathol Oral Radiol Endod* 2008;106:270–74
- Qin Y, Zhang J, Li P, et al. **3D double-echo steady-state with water excitation MR imaging of the intraparotid facial nerve at 1.5T: a pilot study.** *AJNR Am J Neuroradiol* 2011;32:1167–72
- Reynolds PA. **Face and scalp.** In: Standring S, ed. *Gray's Anatomy*. 40th ed. New York: Elsevier; 2008:541–43
- Kundel HL, Polansky M. **Measurement of observer agreement.** *Radiology* 2003;228:303–08
- Nemzek WR, Hecht S, Gandour-Edwards R, et al. **Perineural spread of head and neck tumors: how accurate is MR imaging?** *AJNR Am J Neuroradiol* 1998;19:701–06
- Schmalfluss IM, Tart RP, Mukherji S, et al. **Perineural tumor spread along the auriculotemporal nerve.** *AJNR Am J Neuroradiol* 2002;23:303–11

Predicting the Prognosis of Oral Tongue Carcinoma Using a Simple Quantitative Measurement Based on Preoperative MR Imaging: Tumor Thickness versus Tumor Volume

H. Hu, K.-L. Cheng, X.-Q. Xu, F.-Y. Wu, Y.-S. Tyan, C.-H. Tsai, and C.-Y. Shen

ABSTRACT

BACKGROUND AND PURPOSE: Several studies indicated that tumor thickness or tumor volume might be helpful predictors for the prognosis of oral tongue squamous cell carcinoma. Our aim was to compare the value of tumor thickness versus tumor volume measurement based on preoperative MR imaging in predicting the prognosis of oral tongue squamous cell carcinoma, especially focusing on lymph node metastases and local recurrence.

MATERIALS AND METHODS: Clinical, pathologic, and imaging data of patients with 46 oral tongue squamous cell carcinomas were retrospectively studied. Logistic regression analysis was used to evaluate the prognostic value of tumor thickness and tumor volume based on MR imaging. Receiver operating characteristic analysis was applied for the optimal cutoff value for the identified risk variable for prognosis.

RESULTS: A higher intraclass correlation coefficient was achieved for the measurement of tumor thickness compared with tumor volume (0.990 versus 0.972). Multivariate analysis showed that tumor thickness was a significant predictor of lymph node metastases ($P = .024$), while tumor volume was not a significant predictor of either lymph node metastases or local recurrence ($P > .05$). Receiver operating characteristic results indicated that setting a tumor thickness of 8.5 mm as a cutoff value could achieve the optimal diagnostic efficiency for predicting lymph node metastases (area under the curve, 0.753; sensitivity, 0.889; specificity, 0.536).

CONCLUSIONS: Tumor thickness based on preoperative MR imaging was useful in predicting the prognosis of oral tongue squamous cell carcinoma, especially lymph node metastases, in our patient population, while tumor volume was not.

ABBREVIATIONS: ROC = receiver operating characteristic; SCC = squamous cell carcinoma

Patients with oral tongue squamous cell carcinoma (SCC) are at risk of cervical lymph node metastases and local recurrence, with the risk increasing with the size and extent of tumor, defined by T stage, and influencing treatment strategy.¹⁻³ Previous studies indicated that tumor thickness or tumor volume might also be helpful predictors for the clinical outcomes of patients with oral tongue SCC, such as cervical lymph node metastases, local recurrence, or survival rate.²⁻¹⁰ Which one of these 2 parameters has a better prognostic value is still unclear, however, with only a few

studies focusing on this issue. Yuen et al⁴ compared the prognostic value of these 2 parameters, tumor thickness and tumor volume, together with other parameters such as tumor diameter, length, width, and area. Their measurements were based on surgical histologic specimens that were unavailable before the procedure, however, and tumor shrinkage during specimen preparation might also influence its precision in measurement.

MR imaging has been increasingly used in the preoperative evaluation of oral tongue SCCs, due to its excellent soft-tissue resolution. Preoperative MR imaging could help us to define tumor extent and volume accurately.¹¹ Therefore, our study aimed to clarify the better predictor for the short-term prognosis of oral tongue SCCs between tumor thickness and tumor volume based on preoperative MR imaging, specifically focusing on lymph node metastases and local recurrence.

MATERIALS AND METHODS

Patient Population

This study was approved by Chung Shan Medical University Hospital institutional review board. The clinical, pathologic, and preoperative MR imaging data of 223 patients with oral tongue SCC

Received September 15, 2014; accepted after revision January 3, 2015.

From the Department of Radiology (H.H., X.-Q.X., F.-Y.W.), First Affiliated Hospital of Nanjing Medical University, Nanjing, China; Departments of Medical Imaging (K.-L.C., Y.-S.T., C.-Y.S.) and Pathology (C.-H.T.), Chung Shan Medical University Hospital, Taichung, Taiwan; School of Medical Imaging and Radiological Sciences (K.-L.C., Y.-S.T., C.-Y.S.), School of Medicine (Y.-S.T., C.-H.T., C.-Y.S.), and Institute of Medicine (C.-H.T., C.-Y.S.), Chung Shan Medical University, Taichung, Taiwan; and Department of Veterinary Medicine (K.-L.C.), National Chung Hsing University, Taichung, Taiwan.

Please address correspondence to Chao-Yu Shen, MD, Department of Medical Imaging, Chung Shan Medical University Hospital, No. 110, Sec 1, Jianguo N Rd, Taichung, Taiwan (402); e-mail: shenchaoyu@gmail.com

<http://dx.doi.org/10.3174/ajnr.A4278>

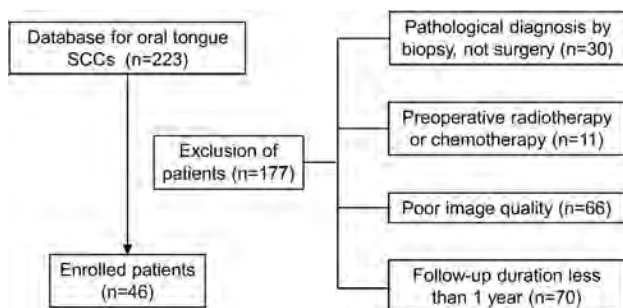


FIG 1. Study population flow chart.

during >3 years 6 months (February 2010 to October 2013) were retrospectively reviewed. One hundred seventy-seven patients were excluded for the following reasons: The pathologic diagnosis was established on the basis of the biopsy, not surgery ($n = 30$); radiation therapy or chemotherapy was performed before surgery ($n = 11$); poor image quality due to motion or dental artifacts ($n = 66$); and the duration of the follow-up was <1 year ($n = 70$). Finally, 46 patients with oral tongue SCC were enrolled in our study. The flow chart of our study population is shown in Fig 1.

The pathologic tumor stage of these 46 patients with oral tongue SCC (mean age, 51 ± 11 years; male/female ratio, 38:8) ranged from T1 to T4a. The mean follow-up duration was 21 ± 10 months. All patients underwent wide excision of the primary tumor and neck dissection. Thirty-three patients underwent supraomohyoid neck dissection, and the other 13 underwent modified radial neck dissection, with only 1 undergoing bilateral modified radial neck dissection. Seven patients received postoperative adjuvant radiation therapy, and 18 received adjuvant concurrent chemoradiotherapy. The detailed demographic features and tumor characteristics are shown in Table 1.

Imaging Technique

MR imaging was performed by using a 1.5T imaging system (Signa HDxt; GE Healthcare, Milwaukee, Wisconsin) with an 8-channel phased array neurovascular coil. Fast spin-echo sequences were used to obtain T2-weighted images (TR, 4000–7000 ms; TE, 81–90 ms; axial, coronal), T1-weighted images (TR, 450–800 ms; TE, 13–15 ms; axial), and gadolinium contrast-enhanced T1-weighted images with fat suppression (TR, 450–800 ms; TE, 12–15 ms; axial, coronal, sagittal).

Tumor Thickness and Volume Measurement

Tumor thickness and tumor volume were measured by using axial T2WI according to methods taken from previous studies.^{3,5-7} Tumor thickness was defined as the distance from the tumor surface to the deepest point of invasion. Meanwhile, after the lesion-involving area in each section was delineated by using an operator-defined ROI, the tumor volume was obtained from the sum of the areas multiplied by the section interval. The methods used for the MR imaging-based measurement of tumor thickness and tumor volume are shown in Figs 2 and 3, respectively. Imaging analysis was performed independently by 2 dedicated head and neck radiologists blinded to the pathologic results. The mean values of their measurements were calculated for further statistical analysis.

The histologic tumor thickness was also performed from the

Table 1: Patient and tumor characteristics

Characteristics	No. of Patients	%
Age (yr) (mean) (range)	51 (33–80)	
Sex		
Male	38	83
Female	8	17
Neck dissection procedure		
SOHND	33	72
MRND	13	28
Bilateral MRND	1	2
Pathologic T stage		
T1–2	33	72
T3–4	13	28
Pathologic N stage		
N0	32	70
N1–3	14	30
Pathologic differentiation		
Well	15	33
Moderate	27	59
Poor	4	9
Pathologic ECS		
Present	10	22
Absent	36	78
Postoperative treatment		
RT	7	15
CCRT	18	39

Note:—SOHND indicates supraomohyoid neck dissection; MRND, modified radial neck dissection; ECS, extracapsular spread; RT, radiotherapy; CCRT, concurrent chemoradiotherapy.

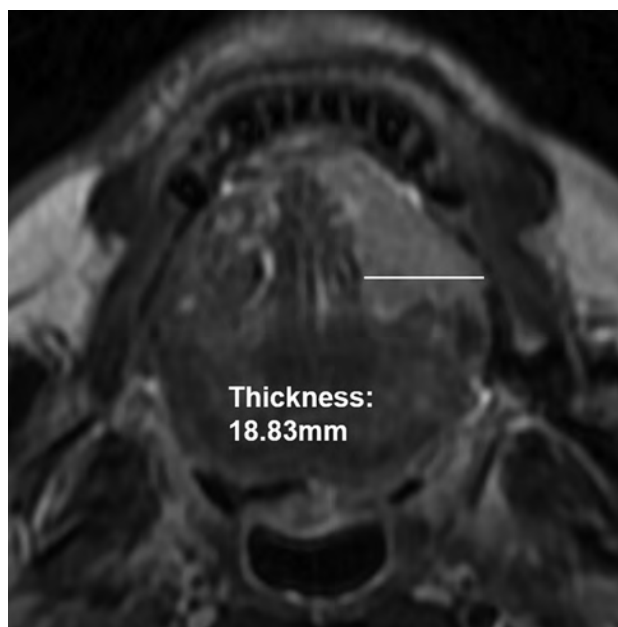


FIG 2. Tumor thickness was measured by the distance from the tumor surface to the deepest point of invasion.

tumor surface to the deepest point of invasion. Histologic tumor volume was calculated according to the previously well-documented formula^{2,12}: $V = A \times B \times C / 2$. A refers to maximum tumor diameter, B refers to minimum tumor diameter, and C refers to the depth of tumor invasion.

Prognosis

All patients were regularly followed up by MR imaging or PET/CT examination and a clinical examination. Tongue or node biopsy

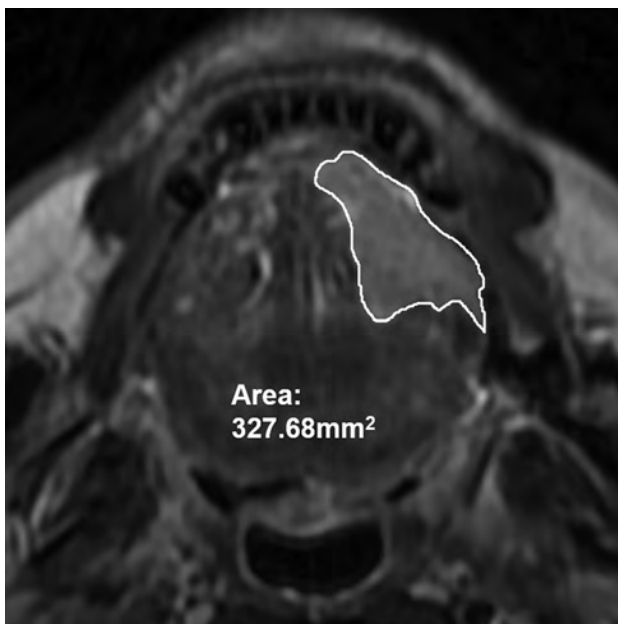


FIG 3. The lesion in each section was delineated by using an operator-defined ROI, and the volume was obtained by multiplying the entire area by the section interval.

was arranged as soon as the development of tumor local recurrence or lymph node metastasis was highly suspected after these examinations.

Lymph node metastases were defined in the following 2 situations: 1) They were confirmed pathologically from the initial surgery, and 2) no metastatic lymph node was detected during the initial surgery, and pathologically confirmed lymph node metastases occurred during the follow-up. Local recurrence was defined as a pathologically confirmed occurrence of the same malignancy at, or adjacent to, the primary tumor bed during follow-up.

Statistical Analysis

Interobserver agreement between the 2 radiologists' measurements was assessed by using the intraclass correlation coefficient. Correlations between MR imaging and histologic specimen-based measurements were assessed by using the Pearson correlation coefficient.

A univariate logistic regression analysis was initially performed to evaluate the association between each variable and lymph node metastases or local recurrence. Besides tumor thickness and tumor volume based on MR imaging, some other potential risk variables were evaluated, including sex, age, pathologic T stage (T1–2 or T3–4), pathologic N stage (N0 or N1–3), pathologic differentiation (well-moderate or poor), pathologic extracapsular spread (present or absent), and postoperative adjuvant modified radical neck dissection or concurrent chemoradiotherapy (yes or no). Then, all variables with a P value $< .10$ in the univariate logistic regression analysis were enrolled in a multivariate logistic regression analysis model by using a forced-entry process. The odds ratios and their 95% confidence intervals were calculated. Finally, receiver operating characteristic (ROC) analysis was applied to calculate the optimal cutoff value of the identified risk variables for prognosis. The numeric data were averaged and reported as means \pm SD. A P value $< .05$ indicated

statistical significance. Statistical analysis was conducted by using SPSS 17.0 (IBM, Armonk, New York).

RESULTS

Excellent interobserver agreement was achieved for both the MR imaging-based tumor thickness and tumor volume measurement, and the tumor thickness measurement had a higher intraclass correlation coefficient value than the tumor volume measurement (0.990; 95% CI, 0.965–0.997 versus 0.972; 95% CI, 0.906–0.992). The average histologic and MR imaging tumor thicknesses were 11.7 ± 9.7 mm and 13.5 ± 9.2 mm, respectively. The average histologic and MR imaging tumor volumes were 6.157 ± 10.516 cm³ and 7.559 ± 11.453 cm³, respectively. Significant correlations were found between the MR imaging-based and histologic specimen-based measurements for both tumor thickness and tumor volume ($P < .001$).

Among the 18 patients (39%) with lymph node metastases, pathologically positive nodes were found in 14 patients during the initial procedure, 8 of whom developed nodal metastases again during the follow-up. The other 4 patients initially had no positive lymph nodes but then developed nodal metastases during the follow-up. Concerning the univariate logistic regression analysis results, MR imaging-based tumor thickness ($P = .006$) and pathologic extracapsular spread ($P = .003$) had significant associations with lymph node metastases. MR imaging-based tumor volume ($P = .067$) and pathologic T stage ($P = .057$) showed close to significant associations, but pathologic differentiation ($P = .644$), sex ($P = .917$), and age ($P = .361$) showed no statistical significance. Considering that if 2 of the independent variables were highly associated with each other, collinearity might occur, causing highly unstable estimated regression coefficients, MR imaging-based tumor thickness and volume were accepted separately into different multivariate logistic regression models, due to the strongly positive correlation between them (Pearson correlation coefficient = 0.848). Multivariate logistic regression analysis results showed that MR imaging-based tumor thickness and pathologic extracapsular spread were significant predictors ($P < .05$), with MR imaging-based tumor volume and pathologic T stage not significant ($P > .05$). Multivariate logistic regression analysis results for lymph node metastases are presented in Table 2.

Fourteen patients (30%) had local recurrence during the follow-up. Four variables were found significant or close to significant in the univariate logistic regression analysis for local recurrence, including MR imaging-based tumor thickness ($P = .020$), MR imaging-based tumor volume ($P = .066$), pathologic N stage ($P = .002$), and pathologic extracapsular spread ($P = .005$). Pathologic T stage, pathologic differentiation, postoperative adjuvant modified radical neck dissection or concurrent chemoradiotherapy, sex, and age were not significant ($P > .1$). Multivariate logistic regression analysis results showed that none of the variables were a significant predictor of local recurrence ($P > .05$). Multivariate logistic regression analysis results for local recurrence are shown in Table 3.

ROC analysis indicated that the MR imaging-based tumor thickness of 8.5 mm might be the optimal threshold value for predicting lymph node metastases, with the area under the curve

Table 2: Multivariate logistic regression analysis results for lymph node metastases

Variable	β Coefficient	SE	Odds Ratio (95% CI)	P Value
Model 1				
Pathologic ECS, present	3.355	1.283	28.647 (2.319–353.900)	.009 ^a
MRI tumor thickness (mm)	0.168	0.074	1.182 (1.023–1.367)	.024 ^a
Pathologic T stage, T3–4	–2.118	1.525	0.120 (0.006–2.391)	.165
Model 2				
Pathologic ECS, present	3.330	1.207	27.116 (2.548–288.624)	.006 ^a
MRI tumor volume (cm ³)	0.066	0.056	1.068 (0.958–1.191)	.237
Pathologic T stage, T3–4	–0.679	1.379	0.507 (0.034–7.562)	.622

Note:—SE indicates standard error; ECS, extracapsular spread.

^aStatistically significant.

Table 3: Multivariate logistic regression analysis results for local recurrence

Variable	β Coefficient	SE	Odds Ratio (95% CI)	P Value
Model 1				
Pathologic ECS, present	1.110	1.038	3.035 (0.397–23.211)	.285
MRI tumor thickness (mm)	0.060	0.042	1.061 (0.978–1.152)	.153
Pathologic N-stage, N1–3	1.273	0.972	3.571 (0.531–24.019)	.191
Model 2				
Pathologic ECS, present	1.013	1.051	2.755 (0.351–21.598)	.335
MRI tumor volume (cm ³)	0.045	0.032	1.046 (0.983–1.112)	.157
Pathologic N-stage, N1–3	1.596	0.952	4.934 (0.764–31.874)	.094

Note:—SE indicates standard error; ECS, extracapsular spread.

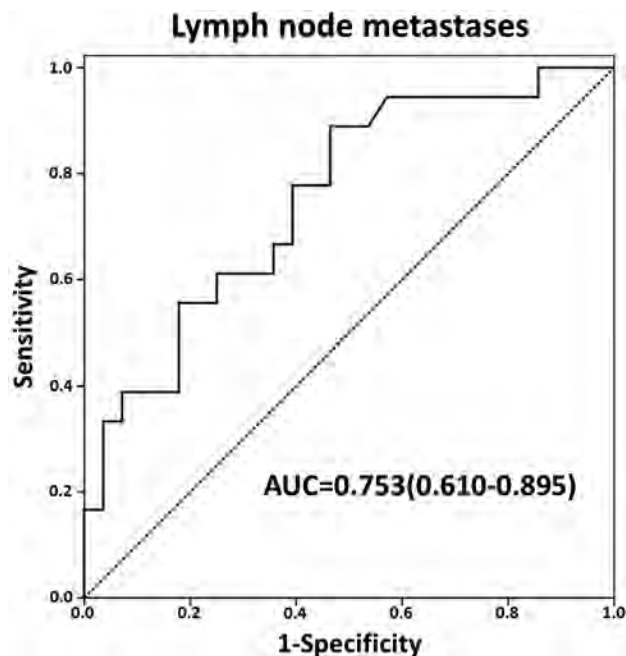


FIG 4. ROC analysis by using the measurement of tumor thickness based on MR imaging to predict lymph node metastases.

being 0.753; sensitivity, 0.889; and specificity, 0.536. The ROC curve regarding the use of MR imaging–based tumor thickness to predict lymph node metastases is shown in Fig 4.

DISCUSSION

The traditional prognostic model for oral tongue carcinoma was based on the anatomic details of tumor, as well as nodal and distant metastases. Using the single largest diameter as the distinction criterion for the T1 to T3 stages, however, did not always appropriately show the value of different T stages in relation to the oncologic outcomes.^{1,3,4} Additionally, the definition of the T4a stage, known as “invasion into deep (extrinsic) muscles of the

tongue,” seemed ambiguous. The “deep” descriptor overlooked the fact that considerable portions of extrinsic muscles lie in a very superficial plane.¹³ With growing evidence that tumor thickness or tumor volume might be a more accurate outcome predictor, our present study concentrated on and compared the predictive value of tumor thickness and tumor volume measurement based on preoperative MR imaging for short-term prognosis of oral tongue carcinoma, especially for lymph node metastases and local recurrence.

A higher intraclass correlation coefficient for the tumor thickness measurement based on MR imaging was noted than for tumor volume, indicating a relatively better reproducibility for tumor-thickness measurement. Concerning the reasons, we suggest that the delineation of the tumor border is more complicated

than the simple 2D tumor thickness measurement because of the disturbance caused by the partial volume effect, especially on the extreme tumor-imaging sections, even though the tumor was usually shown as reliably hyperintense on T2WI and not surrounded by conspicuous edema.⁵ This difficulty in delineation inevitably leads to greater disagreement between 2 different raters and further results in lower reproducibility.

The present study shows that the MR imaging–based tumor volume is not a significant predictor of either lymph node metastases or local recurrence, similar to the study by Yuen et al.⁴ They suggested that tumor thickness, not volume, is the only significant variable for the prediction of lymph node metastases, local recurrence, and survival. Nevertheless, Kuriakose et al² suggested that tumor volume significantly correlated with lymph node metastases, after analyzing the CT images of 20 tongue cancers. Joo et al³ evaluated the MR images of 47 cases of early oral tongue cancer and also found a significant positive correlation between tumor volume and lymph node metastases. This discrepancy might be due to the different imaging modalities and the different tumor stages between these studies. Therefore, further prospective and long-term studies with the same image technique and various tumor stages are recommended to confirm the definite predictive power of tumor volume on oral tongue cancer outcomes.

Our study found that the MR imaging–based tumor thickness might be a significant predictor of lymph node metastases, which is similar to findings in previous studies.^{5–7,14} However, MR imaging–based tumor thickness appears unhelpful for predicting local recurrence ($P = .153$), despite the prominently significant results from the univariate analysis ($P = .020$). Several previous studies indicated that tumor thickness might be a potentially significant predictor of local recurrence^{4,15,16}; however, all these previous measurements were based on histologic specimens. Measurements based on histologic specimens will inevitably be influenced by tissue shrinkage during fixation and embedding and thus should be cautiously adopted. However, no sufficiently strong evi-

dence has been achieved by the present study, on the basis of MR imaging, to indicate the predictive significance of tumor thickness for local recurrence. We suggest that local recurrence of the primary tumor might be more influenced by additional and multiple variables. Further larger sample studies would contribute to potentially more significant results for its prediction.

Overall, MR imaging–based tumor thickness seems to be a more powerful predictor than tumor volume, especially for lymph node metastases in oral tongue carcinoma according to our study, because, as mentioned by Piazza et al,¹ thicker tumor with deeper infiltration is more likely to precociously involve the lymphatic and blood vessels of tongue muscles. Subsequently, it will inevitably result in an increased risk of lymph node metastases. Moreover, tumor lesions do not always grow spherically and commonly share similar volumes but with distinct thicknesses. “Thin” tumors with larger surface diameters but smaller thickness might have a lower risk of lymph node metastases than “thick” ones having a smaller diameter but deeper infiltration. Thus, prognosis of patients might be profoundly different, even if they share the same tumor volume, with tumor thickness potentially predicting lymph node metastasis more accurately.

Using the ROC analysis, we found that an MR imaging–based tumor thickness of 8.5 mm might be the optimal threshold value for predicting lymph node metastases. Concerning its clinical significance, we suggest that the decision for neck dissection should be made if the tumor thickness exceeds 8.5 mm. However, considering that the precise cutoff point varied greatly among previous studies,^{5,6,17–19} more accurate results should be clarified in a prospective study by using a larger sample size.

Our study has several limitations. First, only axial MR images were used to determine tumor thickness and tumor volume without applying coronal or sagittal images. However, in most previous articles, as well as in our experience, the tumor thickness and volume of most of the oral tongue carcinomas can be measured on axial images properly. Nevertheless, further studies should focus on possible differences between axial and coronal and sagittal measurements. Second, the tumor volume measurement based on a histologic specimen was not performed by using the same method as the MR imaging–based measurement, due to the constraints of our retrospective study. However, the method used to measure the histologic tumor volume has also been widely used in previous studies,^{2,12} with the results of our study not being intrinsically affected in our opinion. Third, we only focused on the prediction of short-term prognosis, such as lymph node metastases and local recurrence. A further study with a long-term follow-up and larger sample size would be more valuable for verifying the predictive value of identified risk factors derived from MR imaging.

CONCLUSIONS

In our study, the measurement of tumor thickness based on MR imaging was more consistent and repeatable than the measurement of tumor volume. Compared with the MR imaging–based tumor volume measurements, MR imaging–based tumor thickness demonstrated a more powerful predictive value in the prognosis of oral tongue carcinoma, mainly in predicting lymph node metastases. The ROC analysis results indicate that the optimal tumor thickness cutoff value is 8.5 mm for the prediction of lymph node metastases with the best sensitivity and specificity.

Our study results still need to be verified by further studies with a larger sample size and longer follow-up time.

REFERENCES

1. Piazza C, Montalto N, Paderno A, et al. Is it time to incorporate ‘depth of infiltration’ in the T staging of oral tongue and floor of mouth cancer? *Curr Opin Otolaryngol Head Neck Surg* 2014;22:81–89
2. Kuriakose MA, Loree TR, Hicks WL, et al. Tumor volume estimated by computed tomography as a predictive factor in carcinoma of the tongue. *Br J Oral Maxillofac Surg* 2000;38:460–65
3. Joo YH, Hwang SH, Sun DI, et al. Relationships between tumor volume and lymphatic metastasis and prognosis in early oral tongue cancer. *Clin Exp Otorhinolaryngol* 2013;6:243–48
4. Yuen AP, Lam KY, Wei WI, et al. A comparison of the prognostic significance of tumor diameter, length, width, thickness, area, volume, and clinicopathological features of oral tongue carcinoma. *Am J Surg* 2000;180:139–43
5. Preda L, Chiesa F, Calabrese L, et al. Relationship between histologic thickness of tongue carcinoma and thickness estimated from preoperative MRI. *Eur Radiol* 2006;16:2242–48
6. Okura M, Iida S, Aikawa T, et al. Tumor thickness and paralingual distance of coronal MR imaging predicts cervical node metastases in oral tongue carcinoma. *AJNR Am J Neuroradiol* 2008;29:45–50
7. Iwai H, Kyomoto R, Ha-Kawa SK, et al. Magnetic resonance determination of tumor thickness as predictive factor of cervical metastasis in oral tongue carcinoma. *Laryngoscope* 2002;112:457–61
8. Chen MK, Chen CM, Lee MC, et al. Primary tumor volume is an independent predictor of outcome within pT4a-staged tongue carcinoma. *Ann Surg Oncol* 2011;18:1447–52
9. Chew MH, Khoo JB, Chong VF, et al. Significance of tumor volume measurements in tongue cancer: a novel role in staging. *ANZ J Surg* 2007;77:632–37
10. Kumar T, Patel MD. Pattern of lymphatic metastasis in relation to the depth of tumor in oral tongue cancers: a clinico pathological correlation. *Indian J Otolaryngol Head Neck Surg* 2013;65:59–63
11. Lam P, Au-Yeung KM, Cheng PW, et al. Correlating MRI and histologic tumor thickness in the assessment of oral tongue cancer. *AJR Am J Roentgenol* 2004;182:803–08
12. Williams SS, Alosco TR, Mayhew E, et al. Arrest of human lung tumor xenograft growth in severe combined immunodeficient mice using doxorubicin encapsulated in sterically stabilized liposomes. *Cancer Res* 1993;53:3964–67
13. Boland PW, Pataridis K, Eley KA, et al. Automatic upstaging of tongue squamous cell carcinoma with lateral extrinsic muscle involvement is not justified. *Int J Oral Maxillofac Surg* 2013;42:1397–402
14. Bier-Laning CM, Durazo-Arvizu R, Muzaffar K, et al. Primary tumor thickness as a risk factor for contralateral cervical metastases in T1/T2 oral tongue squamous cell carcinoma. *Laryngoscope* 2009;119:883–88
15. Sharma P, Shah SV, Taneja C, et al. A prospective study of prognostic factors for recurrence in early oral tongue cancer. *J Clin Diagn Res* 2013;7:2559–62
16. Ganly I, Goldstein D, Carlson DL, et al. Long-term regional control and survival in patients with “low-risk,” early stage oral tongue cancer managed by partial glossectomy and neck dissection without postoperative radiation: the importance of tumor thickness. *Cancer* 2013;119:1168–76
17. Huang TY, Hsu LP, Wen YH, et al. Predictors of locoregional recurrence in early stage oral cavity cancer with free surgical margins. *Oral Oncol* 2010;46:49–55
18. Jerjes W, Upile T, Petrie A, et al. Clinicopathological parameters, recurrence, locoregional and distant metastasis in 115 T1–T2 oral squamous cell carcinoma patients. *Head Neck Oncol* 2010;2:9
19. Huang SH, Hwang D, Lockwood G, et al. Predictive value of tumor thickness for cervical lymph-node involvement in squamous cell carcinoma of the oral cavity: a meta-analysis of reported studies. *Cancer* 2009;115:1489–97

Using Texture Analysis to Determine Human Papillomavirus Status of Oropharyngeal Squamous Cell Carcinomas on CT

K. Buch, A. Fujita, B. Li, Y. Kawashima, M.M. Qureshi, and O. Sakai



ABSTRACT

BACKGROUND AND PURPOSE: Human papillomavirus–associated oropharyngeal squamous cell carcinoma is increasing in prevalence and typically occurs in younger patients than human papillomavirus–negative squamous cell carcinoma. While imaging features of human papillomavirus–positive versus human papillomavirus–negative squamous cell carcinoma nodal metastases have been described, characteristics distinguishing human papillomavirus–positive from human papillomavirus–negative primary squamous cell carcinomas have not been well established. The purpose of this project was to evaluate the use of texture features to distinguish human papillomavirus–positive and human papillomavirus–negative primary oropharyngeal squamous cell carcinoma.

MATERIALS AND METHODS: Following institutional review board approval, 40 patients with primary oropharyngeal squamous cell carcinoma and known human papillomavirus status who underwent contrast-enhanced CT between December 2009 and October 2013 were included in this study. Segmentation of the primary lesion was manually performed with a semiautomated graphical-user interface. Following segmentation, an in-house-developed texture analysis program extracted 42 texture features from each segmented volume. A *t* test was used to evaluate differences in texture parameters between human papillomavirus–positive and human papillomavirus–negative squamous cell carcinomas.

RESULTS: Of the 40 included patients, 29 had human papillomavirus–positive oropharyngeal squamous cell carcinoma and 11 had human papillomavirus–negative oropharyngeal squamous cell carcinoma. Significant differences were seen in the histogram parameters median ($P = .006$) and entropy ($P = .016$) and squamous cell carcinoma entropy ($P = .043$).

CONCLUSIONS: There are statistically significant differences in some texture features between human papillomavirus–positive and human papillomavirus–negative oropharyngeal tumors. Texture analysis may be considered an adjunct to the evaluation of human papillomavirus status and characterization of squamous cell carcinoma.

ABBREVIATIONS: FDR = false discovery rate; GLCM = gray-level co-occurrence matrix; GLGM = gray-level gradient matrix; GLRL = gray-level run-length; HPV = human papillomavirus; SCC = squamous cell carcinoma

During the past few decades, oropharyngeal squamous cell carcinoma (SCC) has been one of the fastest growing disease sites for head and neck SCC.^{1–5} Human papillomavirus (HPV) infection has been demonstrated to be an independent risk factor for the development of primary oropharyngeal SCC and may be a

primary cause of the increasing incidence of oropharyngeal cancers in the United States and Europe,^{2–4} in contrast to a decreasing prevalence of smoking- and alcohol-induced oropharyngeal SCCs. HPV-positive oropharyngeal SCC has also been recognized as a distinct subtype of oropharyngeal SCC.^{1,3–6} Patients with HPV-positive oropharyngeal SCC are typically younger compared with patients with HPV-negative oropharyngeal SCC.^{1–6} In addition to different patient demographics, HPV-positive oropharyngeal SCCs have a different prognosis and behavior pattern, including fewer secondary malignancies compared with HPV-negative oropharyngeal SCCs and an overall more favorable prognosis.^{4–7}

Limited data distinguish the imaging features of primary HPV-positive oropharyngeal SCC from HPV-negative SCC.⁸ Prior data describing these differences have focused on the appearance of the margins and presence of invasion into adjacent tissues.⁸ In very small tumors, assessment of these proposed im-

Received September 26, 2014; accepted after revision December 28.

From the Departments of Radiology (K.B., A.F., B.L., Y.K., O.S.), Radiation Oncology (M.M.Q., O.S.), and Otolaryngology–Head and Neck Surgery (O.S.), Boston Medical Center, Boston University School of Medicine, Boston, Massachusetts.

Paper previously presented in part at: Annual Meeting of the American Society of Head and Neck Radiology, September 10–14, 2014; Seattle, Washington.

Please address correspondence to Osamu Sakai, MD, PhD, Department of Radiology, Boston Medical Center, Boston University School of Medicine, FGH Building, 3rd Floor, 820 Harrison Ave, Boston, MA 02118; e-mail: osamu.sakai@bmc.org

Indicates article with supplemental on-line table.

<http://dx.doi.org/10.3174/ajnr.A4285>

aging criteria can be difficult. Distinction between HPV-positive versus HPV-negative oropharyngeal SCC is important because both management and prognosis differ between these 2 groups. Prior studies have demonstrated higher response rates after induction chemotherapy and chemoradiation in addition to superior survival rates for patients with HPV-positive oropharyngeal SCCs.⁷⁻¹¹

Image texture is defined as a complex visual pattern within an image consisting of simpler subpatterns with characteristic features that may be evaluated through quantitative analysis. Texture analysis is a branch of image processing that extracts texture descriptors from the image, thereby allowing the mathematic detection of subtle CT attenuation or MR imaging signal-intensity changes among image pixels. Texture analysis has been previously applied to evaluate subtle pathologic changes in an image that are not easily quantifiable by the human eye in other areas of the body, such as the liver, brain, and cartilage.¹²⁻¹⁷

The purpose of this study was to use texture analysis to examine differences in texture features of HPV-positive and HPV-negative oropharyngeal SCC and to see whether there are significant differences in CT texture features related to HPV-positivity.

MATERIALS AND METHODS

Following institutional review board approval, 69 patients with oropharyngeal SCC and known HPV status who underwent pretreatment contrast-enhanced CT between December 2009 and October 2013 were identified, and initial contrast-enhanced CT examinations for staging were retrospectively reviewed. Examinations with significant artifacts from motion or dental hardware were excluded. Additionally, patients with very small primary tumors (<5 mm) were also excluded. Ultimately, 40 patients were included in this study.

CT Imaging Protocol

Initial contrast-enhanced CT examinations were performed independently or in combination with FDG-PET examinations and were acquired on 64- or 16-detector row CT scanners (Light-Speed VCT or Discovery STE-16 PET/CT; GE Healthcare, Milwaukee, Wisconsin). Dedicated neck CT studies were helically acquired (120-kV/auto-mAs) at 1.25-mm intervals by using a 60-second delay after intravenous contrast injection (80–160 mL iodivertol, Optiray 350; Mallinckrodt, St. Louis, Missouri; or iopamidol, Isovue 370; Bracco, Princeton, New Jersey) extending from skull base to the thoracic inlet and were reviewed in soft-tissue and bone algorithms with 2-mm thick/interval coronal and sagittal reconstructions.

Image Segmentation and Texture Analysis

The primary oropharyngeal lesion was manually contoured by a neuroradiologist with >10 years of experience in head and neck radiology and a fourth-year radiology resident, and all segmentations were validated by the neuroradiologist. Segmentation of the primary oropharyngeal lesion was performed by using a dedicated AW Workstation (GE Healthcare) with a semiautomated graphical-user interface.

Each contour was imported into in-house-developed Matlab (MathWorks, Natick, Massachusetts) texture-analysis software.

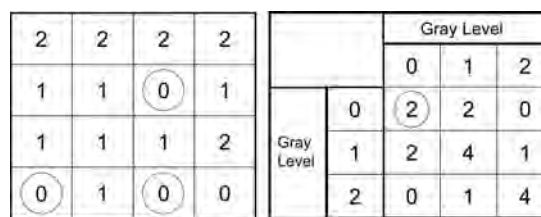


FIG 1. Representation of gray-level co-occurrence matrix features. The square on the left is a representative 2-bit image. In this schematic, the gray-level co-occurrence matrix feature will count the number of times a gray level of zero occurs 2 pixels away from another gray level of zero (black circles). In the second row, third column, a gray level of zero (circled in black) is 2 pixels away from another gray level of zero in the fourth row, third column (circled in black). That gray level of zero in the fourth row, third column, is also 2 pixels away from a second pixel of a gray level of zero in the fourth row, first column (circled in black). Therefore, for this 2-bit image, the number of times a gray level of zero is within 2 pixels of another gray level of zero is 2 (circled in black in the Table on the right). The rest of the chart on the right is completed in a similar fashion for all other gray-level combinations by using a predefined distance of 2 pixels.

In total, 42 texture features, including 13 histogram features, 5 gray-level co-occurrence matrix (GLCM) features, 11 gray-level run-length (GLRL) features, 4 gray-level gradient matrix (GLGM) features, and 9 Law's features, were computed and averaged over the images per dataset. The histogram features calculated herein consisted of the mean, median, SD, range, geometric mean, and harmonic mean of the ROIs, which are space-invariant.¹⁸

In contrast to the histogram features, the GLCM features are highly spatially dependent. The GLCM is square and symmetric with rows and columns from zero to N_g , where N_g represents the number of gray tones in the image. This notation allows the GLCM element in row i and column j to represent the number of times a given gray tone of value i is horizontally adjacent to gray tone j in the original quantized image. Herein, GLCMs were calculated by using only directly adjacent pixels for simplicity. Horizontal, 45°, vertical, and 135° directions were averaged together to eliminate any directional dependence (Fig 1). We tested the following GLCM features proposed by Haralick et al¹⁸:

- 1) Contrast = $\sum_{i,j} |i - j|^2 p(i,j)$,
- 2) Correlation = $\sum_{i,j} \frac{(i - \mu_i)(j - \mu_j)p(i,j)}{\sigma_i \sigma_j}$,
- 3) Angular Second Moment = $\sum_{i,j} p(i,j)^2$,
- 4) Homogeneity = $\sum_{i,j} \frac{p(i,j)}{1 + |i - j|}$,
- 5) Entropy = $\sum_{i,j} \ln [p(i,j)] p(i,j)$,

where $p(i,j)$ represents the (i,j) value of the GLCM.

In addition, the GLRL matrix provides additional insights into a spatial dependence.¹⁸ Similar to GLCM, the GLRL matrix is quantized to N_g gray tones to simplify texture extraction and to yield a more robust technique. The row index i of the GLRL matrix represents the gray tone of value i . In contrast, the column

2	2	2	2	Horizontal Runs	Run Length			
1	1	0	1		2	3	4	
1	1	1	2	Gray Level	0	1	0	0
0	1	0	0		1	1	1	0
					2	0	0	1

FIG 2. Representation of gray-level run-length matrix features. The square on the left is a representative 2-bit image. In this schematic, the gray-level run-length matrix will search across the image in the horizontal axis for consecutive pixels with the same gray level. In the first row of the 2-bit image, a dotted line circles the first row, which contains 4 consecutive pixels with a gray level of 2. In the chart on the right, this corresponds to a run length of 4 (circled dotted line). The second row corresponds to 2 consecutive pixels with a gray level of 1 (black circle), corresponding to a run length of 2 (circled on the right chart diagram). The third row corresponds to 3 consecutive pixels with a gray level of 1 (gray circle), which corresponds to a run length of 3 (gray circle in the chart on the right). The last column of the 2-bit image demonstrates 2 consecutive pixels with a gray level of zero (dash-dot line); therefore, the run length is 2 (circled dash dot line in the chart on the right). The calculation for gray-level run-length is also performed in the vertical axis and along a 45° axis.

index j is the run-length, which is defined as a number of adjacent and equal value pixels in a given direction. The value of each element in the GLRL matrix represents the number of pixel line segments (run) with run-length j and gray tone i (Fig 2). The same directions considered in GLCM were averaged for the GLRL matrix. The features explored included equations using short-run emphasis (SRE), long-run emphasis (LRE), gray-level nonuniformity (GLN), run-length nonuniformity (RLN), run percentage (RP), low gray-level run emphasis (LGRE), high gray-level run emphasis (HGRE), short-run low gray-level emphasis (SRLGE), short-run high gray-level emphasis (SRHGE), long-run low gray-level emphasis (LRLGE), and long-run high gray-level emphasis (LRHGE), defined as follows:

$$6) \quad SRE = \frac{1}{n_r} \sum_{i,j} \frac{p(i,j)}{j^2},$$

$$7) \quad LRE = \frac{1}{n_r} \sum_{i,j} p(i,j) j^2,$$

$$8) \quad GLN = \frac{1}{n_r} \sum_i \left(\sum_j p(i,j) \right)^2,$$

$$9) \quad RLN = \frac{1}{n_r} \sum_j \left(\sum_i p(i,j) \right)^2,$$

$$10) \quad RP = \frac{n_r}{n_p},$$

$$11) \quad LGRE = \frac{1}{n_r} \sum_{i,j} \frac{p(i,j)}{i^2},$$

$$12) \quad HGRE = \frac{1}{n_r} \sum_{i,j} p(i,j) i^2,$$

$$13) \quad SRLGE = \frac{1}{n_r} \sum_{i,j} \frac{p(i,j)}{i^2 j^2},$$

$$14) \quad SRHGE = \frac{1}{n_r} \sum_{i,j} \frac{p(i,j) i^2}{j^2},$$

$$15) \quad LRLGE = \frac{1}{n_r} \sum_{i,j} \frac{p(i,j) j^2}{i^2},$$

$$16) \quad LRHGE = \sum_{i,j} p(i,j) i^2 j^2,$$

where $p(i,j)$ represents the (i,j) value of the GLRL matrix, n_r is the total number of runs, and n_p is the total number of pixels.

Finally, the GLGM was used to provide the histogram of the absolute gradient values in the ROI. As a preprocessing step, the gradient of each pixel within the ROI was computed by using a 3×3 neighborhood. The GLGM features mathematically summarize the gradient values of the pixels in the ROI and include mean, variance, skewness, and kurtosis.

Statistical Analysis

Textures features were compared between HPV-positive and HPV-negative oropharyngeal SCCs by using a Student t test for independent samples. To adjust for multiple comparisons, we performed a false discovery rate (FDR) correction and calculated the FDR-corrected P values (termed Q values) in addition to raw P values by using the method of Glickman et al¹⁹ described in the literature. Statistical computations were performed by using SAS 9.1.3 software (SAS Institute, Cary, North Carolina). The PROC MULTTEST function in SAS was used to calculate the Q values. A 2-tailed P value $<.05$ was used to evaluate statistical significance.

RESULTS

Patient Characteristics

Twenty-nine of the 69 patients were excluded from the texture analysis. Of these 29 patients, 12 patients were excluded for artifacts generated from dental hardware and/or patient motion, 13 patients were excluded for the small size of the lesion (defined in this study as only being seen on ≤ 2 sections), and 4 patients were excluded because they came to our institution with only contrast-enhanced CT studies performed at another institution, which did not use our institutional imaging protocol. Ultimately, 40 patients with oropharyngeal SCC were included in this study. Patient ages ranged from 44 to 79 years of age (mean age, 62.6 ± 8.5 years) and included 33 men and 7 women.

Of the 40 patients with oropharyngeal SCC, 11 were HPV-negative (7 patients with primary sites involving the tonsil and 4 patients with primary sites involving the base of the tongue) and 29 patients were HPV-positive with primary sites involving the tonsil in 21 patients, base of the tongue in 7 patients, and soft palate in 1 patient (Fig 3). One patient of 11 with HPV-negative oropharyngeal SCC was imaged on a 64-detector row CT scanner, whereas the remaining 10 patients were imaged on a 16-detector row CT scanner. Similarly, 4 patients of 29 with HPV-positive oropharyngeal SCC were imaged on a 64-detector row CT scanner, whereas the remainder were imaged with 16-detector row CT.

Texture Analysis

The results of the texture analysis using 42 texture parameter features are given in the On-line Table. The histogram feature median demonstrated statistically significant differences between HPV-positive and HPV-negative tumors ($P = .006$). After using

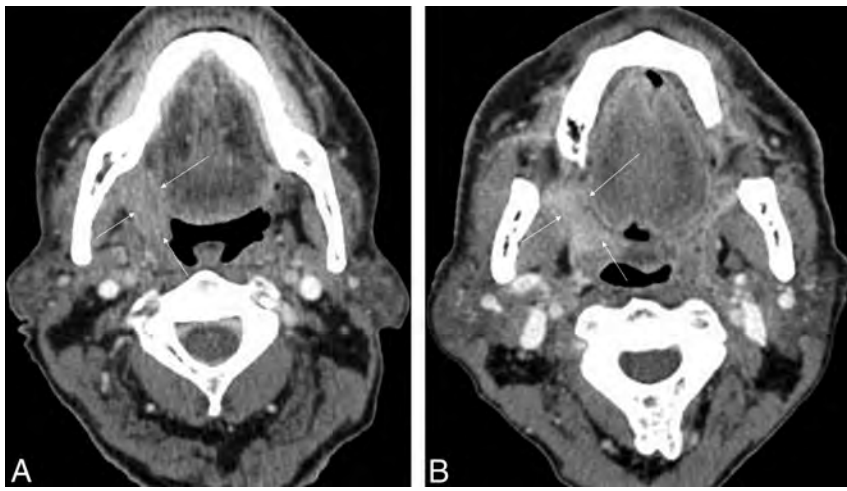


FIG 3. Representative examples of patients with HPV-positive and HPV-negative SCC. A, HPV-negative right tonsillar squamous cell carcinoma (arrows) in a 65-year-old man. B, HPV-positive right tonsillar squamous cell carcinoma (arrows) in a 65-year-old man.

the FDR correction, this difference remained statistically significant ($Q = 0.036$). The histogram feature entropy also demonstrated statistically significant differences between the 2 tumor types ($P = .016$). After we used the FDR correction, this difference remained statistically significant ($Q = 0.048$). The GLCM texture feature entropy demonstrated a statistically significant difference between HPV-positive and HPV-negative tumors ($P = .043$); however, after application of the FDR correction, this parameter was no longer statically significant ($Q = 0.21$). The remainder of the GLCM texture features and histogram features, as well as all of the GLRL features, GLGM features, and Law's features, demonstrated no statistically significant differences between HPV-positive and HPV-negative tumors.

DISCUSSION

This study demonstrated few statistically significant differences between the texture features of HPV-positive and HPV-negative primary oropharyngeal SCC. Of the 42 texture analysis features extracted from this analysis, only the histogram feature median demonstrated statistically significant differences between HPV-positive and HPV-negative oropharyngeal SCC. To date, few studies have focused on differentiating the HPV-positive and HPV-negative status of oropharyngeal SCC on CT. Cantrell et al⁸ performed a blinded analysis examining CT differences of HPV-positive and HPV-negative oropharyngeal SCC and found that HPV-negative primary tumors demonstrated ill-defined borders and an increased prevalence of invasion into adjacent muscle tissue, whereas HPV-positive primary tumors tended to have well-defined borders.⁸

This paucity of studies focused on the primary site is in contradistinction to abundant literature differentiating HPV-positive from HPV-negative nodal metastasis.^{20,21} For example, Goldenberg et al²⁰ performed a retrospective review of the pretreatment CT examinations of oropharyngeal SCC and found an increased association of cystic nodal metastases with HPV-positive base of tongue and tonsillar cancers compared with HPV-negative oropharyngeal SCCs. Well-described features of these cystic nodal metastases include a homogeneous fluid content without internal complex, irregular or solid areas, and an enhancing capsule <2

mm in thickness, whereas necrotic nodal metastases were defined as having thicker or more irregular walls with complex central low attenuation.¹³ Using these imaging criteria of nodal metastasis to predict HPV status of the primary tumors revealed an 87% sensitivity when intranodal cystic changes were used as a radiologic parameter to predict HPV positivity.⁶

The distinction of HPV status of oropharyngeal SCC is clinically important because treatment and prognosis are different. Based on histopathologic studies, HPV-positive oropharyngeal SCCs are a distinctly different histologic entity compared with HPV-negative oropharyngeal SCC.^{20,21} HPV-positive tumors have been described as exhibiting a basaloid, lymphoepithelial, and

poorly differentiated histology compared with a keratinizing histopathology seen in HPV-negative SCCs.^{7,9,22} Prior studies have described unique histologic features in nonkeratinizing HPV-positive SCCs, such as nest formation with trabeculae, pushing borders, and lack of a stromal response.^{7,9,22} Furthermore, frequent mitotic features, comedonecrosis, and the presence of spindle-shaped hyperchromatic nuclei without prominent nucleoli have been described in these HPV-positive tumors.^{7,9} In contrast, HPV-negative SCCs demonstrate keratinizing histopathologic features with polygonal cells with mature cytoplasm, distinct cell borders, and intercellular bridges.^{7,9} The growth pattern of HPV-negative SCCs exhibits an infiltrative pattern with a pronounced stromal desmoplastic reaction not appreciated in the HPV-positive tumors.^{7,9,22}

Texture analysis is a branch of image processing that seeks to reduce image information by extracting texture descriptors from the image that may allow the mathematic detection of subtle signal changes among image pixels. These techniques ultimately provide a quantitative means of extracting image features that is useful for comparative analyses. Texture analysis has been previously used to evaluate subtle pathologic changes that are not easily quantifiable by the human eye and can be particularly important in relatively normal-appearing tissues where there is subtle microscopic disruption due to early disease. Beyond the head and neck, texture analysis techniques similar to those used in this study have also been applied to myriad other organs, including the central nervous system, bone, and cartilage, among others.^{12,17,23-25}

Each texture feature evaluates alternating pixel intensities according to a mathematic algorithm. The gray-level run-length features are spatially dependent texture features, and the matrices used to compute the GLRL features are based on the length and quantity of runs (adjacent pixels with similar intensity values, as explained in the "Image Segmentation and Texture Analysis" section). The short-run emphasis feature identifies whether the image has a majority of short runs, while the long-run emphasis feature identifies a majority of long runs. The gray-level nonuniformity returns a higher value if there are more gray tones with

many runs, while run-length nonuniformity returns a higher value if there are more runs with many gray tones. Run percentage is simply the normalized quantity of runs of an image, while low gray-level run emphasis and high gray-level run emphasis assess the quantity of runs from low gray-tone levels and high gray-tone levels, respectively. The short-run low gray-level emphasis, short-run high gray-level emphasis, long-run low gray-level emphasis, and long-run high gray-level emphasis are derived by combining short-run emphasis, long-run emphasis, low gray-level run emphasis, and high gray-level run emphasis. None of these features were found to have statistically significant differences between HPV-positive and HPV-negative tumors. The lack of a significant difference in these texture features between HPV-positive and HPV-negative tumors suggests a certain degree of uniformity within the tumors along both long and short matrix runs and suggests that the attenuation of both dark and bright line-like structures within the CT images is invariant of HPV tumor status.

The spatially dependent GLCM features capture the frequency of co-occurring gray tones.¹⁸ Contrast and homogeneity are both GLCM features that represent the amount of local variation in an image; for example, high contrast and low homogeneity correspond to a finer texture with the correlation features observing streaks of similar gray-tone levels. Angular fourth moment is the fourth power of the energy of GLCM, which emphasizes a larger number of similar pixel pairs in the image. The lack of a statistically significant difference in these texture features between the 2 tumor types suggests that the level of detail of the CT images is not capable of distinguishing the 2 tumor types. The GLCM feature entropy demonstrated statistically significant differences between the 2 tumor types; however, this texture feature did not remain statistically significant after the FDR analysis. This parameter identifies the randomness and complexity of an image with higher entropy, signifying that the frequency with which 2 gray-tone values touch each other is low.¹⁸ We believe that the significant difference in the entropy of HPV-positive and HPV-negative tumors suggests that the internal consistence of these 2 tumor types is different, despite the lack of significance on the FDR analysis.

This study has several limitations. First, there is no direct comparison between the underlying tumor histopathology and correlation to the mathematic significance of the features of a texture analysis. Ultimately, while we have postulated as to the underlying meaning in terms of the tissue architecture on the basis of the mathematic parameters of the texture analysis in cases of HPV-tumor status, it is unknown what this translates to on a histopathologic level because we have no histopathologic correlation with the results of our texture analysis. Prior studies in the literature have explored the use of a texture analysis with underlying pathology such as hepatic fibrosis in liver models, with high correlations between texture features and the degree of hepatic fibrosis; however, no direct comparison between specific texture features and histopathologic features has been performed. Second, the sample size is relatively small, totaling 40 patients. We examined only primary oropharyngeal SCCs and did not expand our cohort to include additional primary sites within the head and neck. We chose to start with primary oropharyngeal SCC because HPV-positivity is a known prognostic factor for oropharyngeal

SCC.^{7,8,14} Despite our small sample size, many patients had to be eliminated from the study before we performed the texture analysis, predominately due to a combination of dental artifacts, patient motion, and small lesion size. The effects of the metallic streak artifacts and patient motion on the texture analysis are not fully known or described; therefore, for this initial pilot study, we tried to collect subjects with SCCs without metallic streak artifacts, to limit this as a potential confounder.

We set a rough threshold for the lesion size, in that it would need to be seen on at least 3 CT sections to perform a good manual contour. Last, we contoured areas of obvious necrotic and cystic changes as well as ulceration of the final contours that were imported into the texture analysis program. Both HPV-positive and HPV-negative tumors demonstrated these areas of necrosis and ulceration. We eliminated these areas because including foci of air would not accurately reflect the underlying texture features within the solid portion of the tumors. Additionally, for the purposes of this initial study, we wanted to focus on whether the texture analysis could differentiate HPV status on the basis of the solid portion of the tumors.

CONCLUSIONS

The results of this pilot study demonstrate that some texture analysis features, particularly the histogram feature median, demonstrated statistically significant differences between HPV-positive and HPV-negative oropharyngeal SCCs. This study adds to the limited previously published data and suggests a potentially novel image-based assessment of HPV status of oropharyngeal SCCs on CT. The results of this study demonstrate that the quantitative, noninvasive, postprocessing assessment of a texture analysis has the potential to be used as an adjunct for the evaluation of initial oropharyngeal SCCs on CT, but further investigation into this methodology is warranted.

Disclosures: Osamu Sakai—UNRELATED: Payment for Lectures (including service on Speakers Bureaus): Bracco, Kyorin USA, Eisai, Comments: honoraria for lecture; Royalties: McGraw-Hill.

REFERENCES

1. Chaturvedi AK. **Epidemiology and clinical aspects of HPV in head and neck cancers.** *Head Neck Pathol* 2012;(6 suppl 1):S16–24
2. Näsman A, Attner P, Hammarstedt L, et al. **Incidence of human papillomavirus (HPV) positive tonsillar carcinoma in Stockholm, Sweden: an epidemic of viral-induced carcinoma?** *Int J Cancer* 2009;125:362–66
3. Panwar A, Batra R, Lydiatt WM, et al. **Human papilloma virus positive oropharyngeal squamous cell carcinoma: a growing epidemic.** *Cancer Treat Rev* 2014;40:215–19
4. Pytynia KB, Dahlstrom KR, Sturgis EM. **Epidemiology of HPV-associated oropharyngeal cancer.** *Oral Oncol* 2014;50:380–86
5. Westra WH. **The changing face of head and neck cancer in the 21st century: the impact of HPV on the epidemiology and pathology of oral cancer.** *Head Neck Pathol* 2009;3:78–81
6. D'Souza G, Kreimer AR, Viscidi R, et al. **Case-control study of human papillomavirus and oropharyngeal cancer.** *N Engl J Med* 2007;356:1944–56
7. Ang KK, Harris J, Wheeler R, et al. **Human papillomavirus and survival of patients with oropharyngeal cancer.** *N Engl J Med* 2010;363:24–35
8. Cantrell SC, Peck BW, Li G, et al. **Differences in imaging characteristics of HPV-positive and HPV-negative oropharyngeal cancers: a blinded matched-pair analysis.** *AJNR Am J Neuroradiol* 2013;34:2005–09

9. Fakhry C, Westra WH, Li S, et al. **Improved survival of patients with human papillomavirus-positive head and neck squamous cell carcinoma in a prospective clinical trial.** *J Natl Cancer Inst* 2008;100:261–69
10. Kumar B, Cordell KG, Lee JS, et al. **Response to therapy and outcomes in oropharyngeal cancer are associated with biomarkers including human papillomavirus, epidermal growth factor receptor, gender, and smoking.** *Int J Radiat Oncol Biol Phys* 2007;69:S109–11
11. Weinberger PM, Yu Z, Haffty BG, et al. **Molecular classification identifies a subset of human papillomavirus-associated oropharyngeal cancers with favorable prognosis.** *J Clin Oncol* 2006;24:736–47
12. de Carvalho Alegro M, Valotta Silva A, Yumi Bando S, et al. **Texture analysis of high resolution MRI allows discrimination between febrile and afebrile initial precipitating injury in mesial temporal sclerosis.** *Magn Reson Med* 2012;68:1647–53
13. Mayerhoefer ME, Stelzeneder D, Bachbauer W, et al. **Quantitative analysis of lumbar intervertebral disc abnormalities at 3.0 Tesla: value of T(2) texture features and geometric parameters.** *NMR Biomed* 2012;25:866–72
14. Risse F, Pesic J, Young S, et al. **A texture analysis approach to quantify ventilation changes in hyperpolarised ³He MRI of the rat lung in an asthma model.** *NMR Biomed* 2012;25:131–41
15. Fujimoto K, Tonan T, Azuma S, et al. **Evaluation of the mean and entropy of apparent diffusion coefficient values in chronic hepatitis C: correlation with pathologic fibrosis stage and inflammatory activity grade.** *Radiology* 2011;258:739–48
16. Jiráček D, Dezortová M, Taimr P, et al. **Texture analysis of human liver.** *J Magn Reson Imaging* 2002;15:68–74
17. Anderson SW, Jara H, Ozonoff A, et al. **Effect of disease progression on liver apparent diffusion coefficient and T2 values in a murine model of hepatic fibrosis at 11.7 Tesla MRI.** *J Magn Reson Imaging* 2012;35:140–46
18. Haralick R, Shanmugam K, Dinstein I. **Textural features for image classification.** *IEEE Transactions on Systems, Man and Cybernetics* 1973;SMC-3:610–21
19. Glickman ME, Rao SR, Schultz M. **False discovery rate control is a recommended alternative to Bonferroni-type adjustments in health studies.** *J Clin Epidemiol* 2014;67:850–57
20. Goldenberg D, Begum S, Westra WH, et al. **Cystic lymph node metastasis in patients with head and neck cancer: an HPV-associated phenomenon.** *Head Neck* 2008;30:898–903
21. Marur S, D'Souza G, Westra WH, et al. **HPV-associated head and neck cancer: a virus-related cancer epidemic.** *Lancet Oncol* 2010;11:781–89
22. El-Mofty SK, Zhang MQ, Davila RM. **Histologic identification of human papillomavirus (HPV)-related squamous cell carcinoma in cervical lymph nodes: a reliable predictor of the site of an occult head and neck primary carcinoma.** *Head Neck Pathol* 2008;2:163–68
23. de Oliveira MS, D'Abreu A, França MC Jr, et al. **MRI-texture analysis of corpus callosum, thalamus, putamen, and caudate in Machado-Joseph disease.** *J Neuroimaging* 2012;22:46–52
24. Tozer DJ, Marongiu G, Swanton JK, et al. **Texture analysis of magnetization transfer maps from patients with clinically isolated syndrome and multiple sclerosis.** *J Magn Reson Imaging* 2009;30:506–13
25. Joseph GB, Baum T, Carballido-Gamio J, et al. **Texture analysis of cartilage T2 maps: individuals with risk factors for OA have higher and more heterogeneous knee cartilage MR T2 compared to normal controls—data from the osteoarthritis initiative.** *Arthritis Res Ther* 2011;13:R153

Direct Cranial Nerve Involvement by Gliomas: Case Series and Review of the Literature

M.C. Mabray, C.M. Glastonbury, M.D. Mamlouk, G.E. Punch, D.A. Solomon, and S. Cha



ABSTRACT

SUMMARY: Malignant gliomas are characterized by infiltrative growth of tumor cells, including along white matter tracts. This may result in clinical cranial neuropathy due to direct involvement of a cranial nerve rather than by leptomeningeal spread along cranial nerves. Gliomas directly involving cranial nerves III–XII are rare, with only 11 cases reported in the literature before 2014, including 8 with imaging. We present 8 additional cases demonstrating direct infiltration of a cranial nerve by a glioma. Asymmetric cisternal nerve expansion compared with the contralateral nerve was noted with a mean length of involvement of 9.4 mm. Based on our case series, the key imaging feature for recognizing direct cranial nerve involvement by a glioma is the detection of an intra-axial mass in the pons or midbrain that is directly associated with expansion, signal abnormality, and/or enhancement of the adjacent cranial nerves.

ABBREVIATIONS: WHO = World Health Organization; CN = cranial nerve

Gliomas are the most common intra-axial primary brain tumors, with World Health Organization (WHO) grade IV glioblastoma multiforme representing the most common subtype.^{1–4} Malignant gliomas are characterized by infiltrative growth of tumor cells, including along white matter tracts.^{3,5–8} The cranial nerve nuclei are within the brain parenchyma and have glial cells extending into the root entry zone and proximal cisternal segments with gradual replacement by Schwann cells of >1–9 mm.^{9–11} Therefore, infiltrating growth patterns as seen along white matter tracts intra-axially may potentially occur with known or suspected gliomas. This imaging appearance may simulate nerve sheath tumors, intracranial perineural spread of head and neck tumors, or leptomeningeal spread of disease, all of which are well-described and relatively more common disease processes.^{12–15}

If we exclude cranial nerve involvement in the setting of diffuse leptomeningeal spread of tumor, 11 unique cases of gliomas

directly infiltrating cranial nerves have been reported in the literature before 2014, 8 with imaging.^{9,16–25} Through our MR imaging glioma data base, we have identified 8 additional cases of pathologically confirmed gliomas with imaging findings indicating direct involvement of the cranial nerves. One of our cases (case 1) has since recently been separately reported in the neurosurgery literature.¹⁰ The purpose of our study was to characterize the clinical and imaging features of cranial nerve involvement by gliomas and to improve recognition and understanding of this entity.

CASE SERIES

This study was performed under institutional review board approval and was compliant with the Health Insurance Portability and Accountability Act. Individual cases of gliomas directly involving a cranial nerve were retrospectively identified through a search of our teaching file data base and radiology reporting system. Cases of cranial nerve involvement in the setting of diffuse leptomeningeal spread, as determined by the presence of other areas where the brain surface was coated with tumor, were excluded. Additionally, direct involvement of the olfactory (cranial nerve [CN] I) or optic (CN II) nerves was specifically excluded because anatomically and histologically, these nerves are white matter tract extensions of the brain and, as such, are not true cranial nerves.

Eight individual cases of pathologically proved infiltrating glioma involving the cisternal segment of ≥ 1 cranial nerve were identified (Table) from 2000 to 2013. The mean patient age was 41 years (range, 9–67 years). There were 4 male and 4 female patients. Five of the 8 (63%) cases involved the trigeminal nerve (CN V); 1, the oculomotor nerve (CN III); 1, the ipsilateral trigeminal

Received October 22, 2014; accepted after revision December 17.

From the Departments of Radiology and Biomedical Imaging (M.C.M., C.M.G., M.D.M., G.E.P., S.C.), Pathology (D.A.S.), Otolaryngology (C.M.G.), and Neurosurgery (S.C.), University of California, San Francisco, San Francisco, California.

Marc C. Mabray was supported by a National Institutes of Health T32 training grant (5T32EB001631-10) while working on this research project.

Paper previously presented as a Scientific Exhibit at: Annual Meeting of the American Society of Neuroradiology and the Foundation of the ASNR Symposium, May 17–22, 2014; Montreal, Quebec, Canada.

Please address correspondence to Marc C. Mabray, MD, Department of Radiology and Biomedical Imaging, Box 0628, 505 Parnassus Ave, San Francisco, CA 94143-0628; e-mail: marc.mabray@ucsf.edu

Indicates open access to non-subscribers at www.ajnr.org

<http://dx.doi.org/10.3174/ajnr.A4287>

Case series of patients with gliomas involving cranial nerves

Case	Age (yr)	Sex	Location	Grade (WHO)	Neuropathy	Maximal Thickness, Involved CN (mm)	Maximal Thickness, Contralateral CN (mm)	Maximal Length (mm)
1	67	M	R pons to trigeminal nerve	IV	Yes	6	2	8
2	53	F	R pons to trigeminal and vestibulocochlear nerves; separate R frontal tumor	IV	No	3	1	4
3	67	F	L pons to trigeminal nerve	II	Yes	4	1	13
4	49	F	R midbrain to R oculomotor nerve; separate R frontal tumor	IV	Yes	14	1	16
5	22	M	R pons to trigeminal nerve; separate R frontal and thalamus tumor	IV	No	4	2	7
6	9	M	R pons to trigeminal nerve; separate R thalamus and midbrain tumor	IV	No	4	2	4
7	34	M	R pons to trigeminal nerve; separate R parietal tumor	II	No	4	2	8
8	24	F	R pons to trigeminal and facial nerves	IV	Yes	8	1	15
Mean (SD)	41 (20.3)					5.9 (3.6)	1.5 (0.5)	9.4 (4.7)

Note:—R indicates right; L, left.

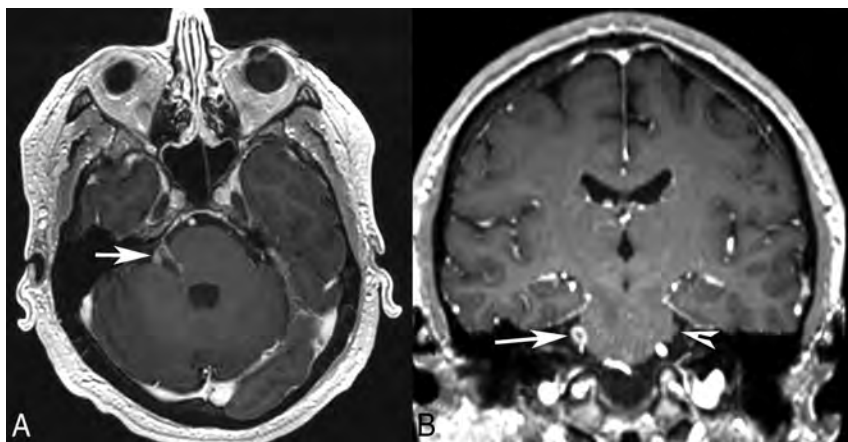


FIG 1. Patient 1. Axial (A) and coronal (B) postgadolinium T1-weighted MR images demonstrate an irregular enhancing mass involving the right pons, the expected location of trigeminal nuclei, the root entry zone, and the cisternal segment of the right trigeminal nerve (arrow). The normal left trigeminal nerve is marked on the coronal image (arrowhead). This patient presented with right facial numbness.

and facial nerves (CN VII); and 1, the ipsilateral trigeminal and vestibulocochlear nerves (CN VIII). Three cases were direct involvement from unifocal gliomas, and 5 cases were in the setting of multifocal advanced glioma. In 2 of the patients with unifocal tumors (cases 1 and 8) and in 1 of the patients with advanced multifocal tumors (case 4), cranial neuropathy was a feature of the patients' tumor presentations. The third patient with a unifocal tumor (case 3) had evidence of cranial neuropathy that became more apparent with time. Six of the cases were found at biopsy to be glioblastomas (WHO grade IV). One case had previously been determined to be WHO grade III (case 3); and 1 case, WHO grade II (case 7), which had likely dedifferentiated into a higher grade glioma as evidenced by contrast-enhancing tumor on follow-up imaging. The mean maximal thickness of the involved cisternal cranial nerve (5.9 mm) was statistically significantly thicker ($P < .01$, 2-tailed t test) than the mean thickness of the contralateral uninvolved nerve (1.5 mm), with a mean length of involvement of 9.4 mm. Involvement of the adjacent midbrain or pons deep to the root entry zone of the cranial nerves by a lesion contiguous with and matching the cranial nerve involvement in signal characteristics and enhancement pattern

was present in all cases and was a key imaging feature in identifying the intra-axial origin of disease.

Case 1

A 67-year-old man presented with an 8-week history of right facial numbness, which began in the midface and progressed to complete right facial numbness during 6 weeks. MR imaging (Figs 1 and 2) demonstrated an irregular, peripherally enhancing, T2 FLAIR hyperintense mass centered in the right pons and extending into the trigeminal root entry zone and the cisternal segment of the right trigeminal nerve. Dynamic susceptibility-weighted contrast-enhanced perfusion imaging demonstrated increased relative cerebral blood volume

within the brain stem component compared with the contralateral pons. Multivoxel MR spectroscopy demonstrated an elevated choline signal relative to the NAA signal within the brain stem component. Surgical biopsy of the lesion was performed at the root entry zone/proximal cisternal segment of the trigeminal nerve with decompression of an intraneural cyst (Fig 2). Histopathology revealed WHO grade IV glioblastoma arising in the root entry zone of the trigeminal nerve. The patient was treated with external beam radiation therapy and chemotherapy and remains alive with residual disease at 48 weeks since diagnosis.

Case 2

A 53-year-old woman with surgical biopsy 9 months prior and I-125 brachytherapy seed placement 6 months prior for residual right frontal WHO grade IV glioblastoma presented for follow-up MR imaging. The patient developed progressive disease with infiltrative T2 FLAIR hyperintensity extending into the brain stem and an irregularly enhancing mass lesion centered in the right pons. The abnormal expansion, T2 FLAIR signal abnormality, and enhancement extended into the root entry zone of the trigem-

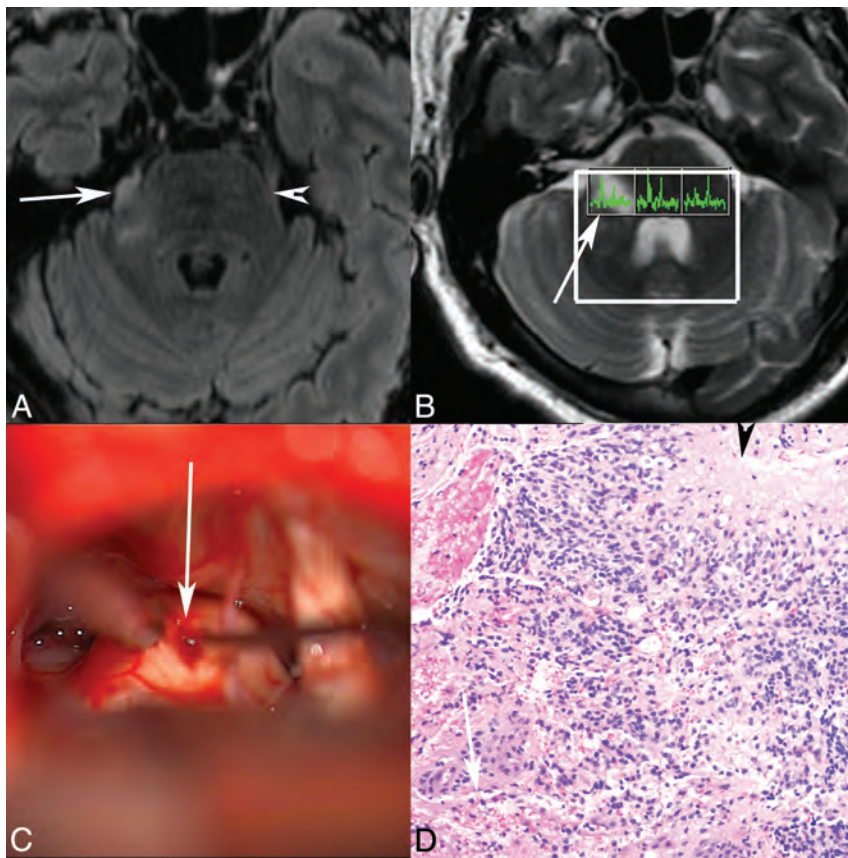


FIG 2. Patient 1. Axial T2 FLAIR (A) MR image demonstrates abnormal T2 FLAIR signal in the right lateral pons extending into the right trigeminal nerve (arrow marks the site of biopsy, arrowhead marks the normal left trigeminal nerve). B, Multivoxel MR spectroscopy demonstrates increased choline relative to NAA in the right-sided voxel corresponding to the tumor (arrow). C, Operative photograph shows a right retrosigmoid approach to the expanded right trigeminal nerve (arrow), with biopsy being obtained (courtesy of Jonathan D. Breshears, MD). D, Hematoxylin-eosin stained histology slide (original magnification $\times 20$) demonstrates an infiltrative astrocytic neoplasm with nuclear pleomorphism, brisk mitotic activity, microvascular proliferation (arrow), and pseudopalisading necrosis (arrowhead). Pathologic diagnosis was a glioblastoma, WHO grade IV. No peripheral nerve was identified in the specimen despite the biopsy location, likely reflecting the origin from glial cells in the trigeminal root entry zone.

inal nerve and proximal cisternal segment. More subtle signal abnormality and enhancement extended into the right vestibulocochlear nerve complex. No definitive symptoms of cranial neuropathy were reported. The patient had a partial response to chemotherapy and additional radiation therapy but ultimately developed progressive infiltrating glioma.

Case 3

A 67-year-old woman with known neurofibromatosis type 1 presented with headaches, dizziness, and syncope. MR imaging (Fig 3) demonstrated an expansile T2 FLAIR hyperintense, peripherally enhancing mass lesion centered in the left pons with extension into and expansion of the root entry zone of the trigeminal nerve. Surgical biopsy of the contiguous lesion in the pons yielded diffuse astrocytoma, WHO grade II (Fig 3). At presentation, the patient had symptoms referable to the brain stem and cranial nerve nuclei, including abnormal acoustic reflexes and dizziness. With time, the patient developed worsening trigeminal neuropathy as evidenced by abnormal tingling of the left lower face. The patient received radiation therapy and steroids,

with an initial response followed eventually by progressive disease.

Case 4

A 49-year-old pregnant woman presented with diplopia and was found to have right oculomotor nerve palsy (CN III). MR imaging (Fig 4) demonstrated an irregular peripherally enhancing mass lesion extending from the midbrain into the cisternal segment of the right oculomotor nerve. The mass also demonstrated T2 FLAIR hyperintensity and reduced ADC values. The patient had a separate mass in the right frontal lobe with similar imaging characteristics. Surgical biopsy of the right frontal mass was performed, which showed WHO grade IV glioblastoma. The patient underwent external beam radiation therapy with concurrent temozolomide chemotherapy and, at the time of clinical recurrence, was started on bevacizumab (Avastin), but the tumor disseminated widely within the CSF, including to the spinal canal.

Case 5

A 22-year-old man with a history of a right frontal lobe WHO grade IV glioblastoma, partially resected 18 and 11 months prior, was noted on follow-up imaging to have new right thalamic and right pontine masses. The T2 FLAIR hyperintense mass centered in the right pons demonstrated expansion of the root entry zone of the trigeminal nerve and extension into its cisternal segment.

No definitive symptoms of trigeminal neuropathy were noted, though the patient had altered mental status. The patient developed progressive disease despite additional therapy.

Case 6

A 9-year-old boy with a history of a right thalamic WHO grade IV glioblastoma, partially resected 3 months prior, was found to have increasing T2 FLAIR hyperintense signal with associated irregular enhancement extending inferiorly into the right pons with involvement at the root entry zone and proximal cisternal segment of the right trigeminal nerve. The patient did not have any symptoms definitively referable to trigeminal neuropathy; his dysarthria and left-sided facial weakness were presumed to be related to the thalamic tumor. The patient received additional chemotherapy and ultimately developed progressive disease.

Case 7

A 34-year-old man with resection of a right temporal lobe oligodendroglioma 8 years ago and re-resection 32 months prior for recurrent disease re-presented for follow-up MR imaging. Enlarg-

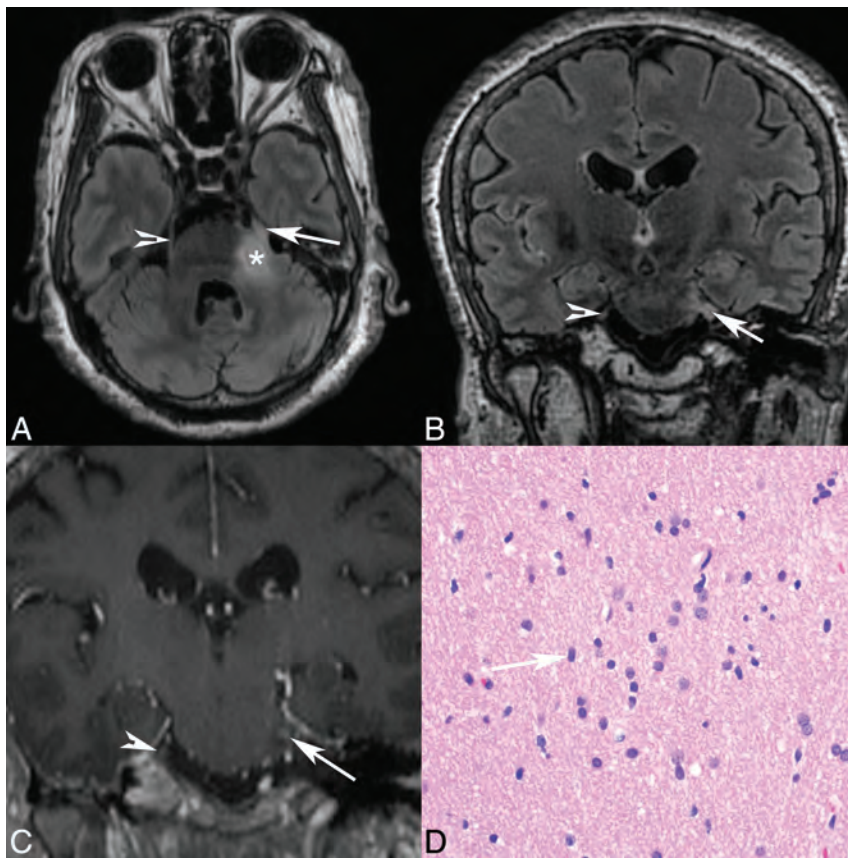


FIG 3. Patient 3. Axial T2 FLAIR (A), coronal T2 FLAIR (B), and coronal postgadolinium T1 (C) MR images demonstrate abnormal T2 FLAIR signal in the left lateral pons extending into the expanded left trigeminal nerve (arrow), with enhancement shown at the root entry zone (C). The arrowhead marks the normal right trigeminal nerve, and the asterisk marks the approximate site of biopsy in the pons. D, Hematoxylin-eosin stained histology slide (original magnification $\times 40$) demonstrates an infiltrating population of neoplastic astrocytes with irregular ovoid nuclei (arrow) and coarse chromatin and scant eosinophilic cytoplasm. No mitotic activity, microvascular proliferation, or foci of necrosis are present. The pathologic diagnosis was a diffuse astrocytoma, WHO grade II.



FIG 4. Patient 4. Axial postgadolinium T1-weighted MR image (A) and ADC map (B) show an irregularly enhancing, mass with restricted diffusion (arrow) involving the root exit zone and the cisternal course of the right oculomotor nerve in the interpeduncular cistern. This patient presented with right oculomotor palsy.

ing T2 FLAIR hyperintense signal with associated irregular nodular enhancement was demonstrated in the right pons with new contiguous involvement of the root entry zone and proximal cisternal segment of the right trigeminal nerve. Biopsy of the more

accessible right parietal component demonstrated a recurrent WHO grade II oligodendroglioma, though the enhancing portion was not biopsied and the possibility of an undersampled higher grade component could not be excluded. No definitive symptoms of trigeminal neuropathy were present. The patient received additional chemotherapy and ultimately developed progressive disease.

Case 8

A 24-year-old woman presented with ipsilateral trigeminal and facial neuropathies manifesting as right facial numbness and weakness, respectively. MR imaging (Fig 5) demonstrated a T2 FLAIR hyperintense mass with irregular peripheral enhancement involving the right pons, with extension into the right cerebellopontine angle and internal auditory canal along the facial and vestibulocochlear nerve complex and extension into the right trigeminal nerve root entry zone and cisternal segment. Dynamic susceptibility-weighted contrast-enhanced perfusion imaging was performed, which demonstrated increased relative cerebral blood volume within the lesion compared with the contralateral pons. Clinically, there were no features of vestibular or cochlear nerve involvement. Histopathology of the contiguous pontine lesion showed WHO grade IV glioblastoma (Fig 5). This patient received radiation and chemotherapy and ultimately developed progressive disease with right-sided hearing loss later in the course of her disease.

DISCUSSION

We have presented a series of 8 cases of direct invasion of a cranial nerve by a glioma. This is a rare phenomenon, with only 11 unique cases reported in the literature before 2014.^{9,16-25} All 8 cases demonstrated abnormal T2 FLAIR hyperintensity, contrast enhancement, and expansion of a cisternal cranial nerve and its root entry zone contiguous with a brain stem parenchymal lesion.

The literature from 1904 to 2011 describes 11 unique cases of a glial neoplasm involving a cranial nerve.^{9,16-25}

Only 8 of the cases describe imaging findings because 3 of the cases predate modern imaging. In 8 of the reported patients, patient age was available and revealed a mean age of 36 years with a range of 8–70 years. Eight cases were reported to involve the vestibulocochlear nerve (CN VIII); 1 case,

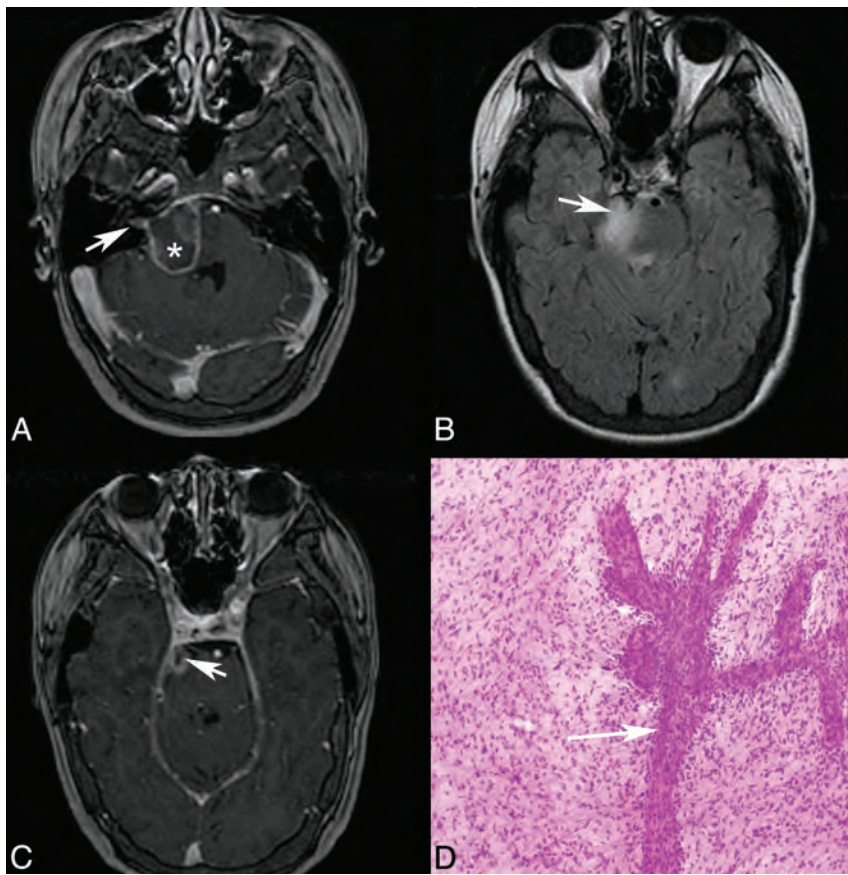


FIG 5. Patient 8. Axial postgadolinium T1 (A and C) and axial T2 FLAIR (B) MR images demonstrate an irregularly enhancing, T2 FLAIR hyperintense mass involving the right lateral pons and expected origins and intracranial course of both the right facial (A) and the trigeminal (B and C, *arrow*) nerves. Enhancement also extends into the right internal auditory canal along its anterior and superior aspect where the extra-axial facial nerve courses (A, *arrow*). Asterisk (A) marks the approximate site of biopsy. D, Hematoxylin-eosin-stained intraoperative smear preparation (original magnification $\times 10$) demonstrates a population of neoplastic astrocytes with nuclear pleomorphism and numerous mitotic figures. A vessel with extensive budding and endothelial proliferation is present (*arrow*). Pathologic diagnosis was a glioblastoma, WHO grade IV. This patient presented with right facial numbness and weakness, but no clinical evidence of vestibulocochlear nerve involvement until later in the disease course.

to involve the oculomotor nerve (CN III); 1 case, to involve the trigeminal nerve (CN V); and 1 case, to involve the vestibulocochlear, facial, and trigeminal nerves (CNs V, VII, and VIII). The reported histopathology in 9 of the cases was low-grade glioma (WHO grades I–II), and in 2 cases, it was glioblastoma (WHO grade IV).

While the ages of patients in our case series and the literature are similar, our series differs from the prior reported cases in tumor grade and the specific cranial nerve involved. The tumors in our case series are of a higher grade than those identified in the literature, with 6 of 8 (75%) being grade III–IV tumors in our series compared with 2 of 11 (18%) in the prior literature. The most common cranial nerve involved in our series was the trigeminal nerve, which was involved in 7 of 8 cases (88%) compared with 2 of the prior 11 (18%); the most common cranial nerve previously reported in the literature was the vestibulocochlear nerve, which was involved in 9 of 11 cases (82%) in the prior literature compared with being involved in 1 of 8 (13%) in our series. A number of confounding factors may potentially result in these differences. The prior literature has shown an emphasis on

gliomas found at surgery for what had been presumed to be a vestibular schwannoma. Our institution is a referral center that uses frequent imaging in patients with known aggressive gliomas. Additionally, modern high-resolution MR imaging techniques make cranial nerve involvement more readily apparent, and this phenomenon might have been under-recognized and under-reported in the past.

Three of the 8 (38%) patients in our series presented with new cranial neuropathy corresponding to the involved nerve, including 1 patient with involvement of 2 cranial nerves. A fourth patient had more subtle evidence of trigeminal neuropathy, which increased with time. Most interesting, 4 of the 8 (50%) patients did not have reported clinical symptomatology referable to cranial nerve involvement. These 4 cases were all in the setting of advanced multifocal glioma with cranial nerve involvement manifesting later in the disease course. Recognizing clinical cranial neuropathy in patients presenting initially with cranial nerve involvement rather than in those developing it later in their disease course may be more likely. Our finding of clinical cranial neuropathy being an inconsistent feature is similar to that seen with perineural spread of head and neck cancer, in which up to 40% of patients are reported to be asymptomatic.^{14,26} The inconsistency of clinical cranial neuropathy in both situations may be related to the heterogeneous nature of cranial nerve involvement histologically and mechanically.^{14,27}

The tumors in our case series demonstrated evidence of intra-axial origin and have the typical imaging characteristics of gliomas elsewhere in the central nervous system. The adjacent pons or midbrain was abnormally expanded, with tumor involvement in all cases that was contiguous with the proximal cisternal cranial nerve involvement; this feature was key to recognizing the intra-axial origin of the tumors and helped to differentiate them from other lesions considered at these locations, including nerve sheath tumors, meningiomas, perineural spread of head and neck malignancies, and diffuse neoplastic, infectious, or inflammatory leptomeningeal disease, all of which would be expected to have different imaging findings from those in our cases.

Gliomas directly involving the cranial nerves are rare, with only 11 cases reported in the literature; we have presented an additional 8 cases. These are intra-axial, intraparenchymal tumors, which, despite their unusual locations, demonstrate the imaging features typical of gliomas with the additional feature of extension into and expansion

of the cranial nerve. These tumors can cause clinically evident cranial neuropathy, though this was not a consistent feature in our series. Recognition of the intra-axial, intraparenchymal origin of cranial nerve involvement by gliomas is a key imaging feature for the accurate diagnosis and correct management of these patients.

Disclosures: Christine M. Glastonbury—UNRELATED: Royalties: Amirsys, Comments: from book and participation in StatDx; Stock/Stock Options: Amirsys.

REFERENCES

- Dolecek TA, Propp JM, Stroup NE, et al. **CBTRUS statistical report: primary brain and central nervous system tumors diagnosed in the United States in 2005–2009.** *Neuro Oncol* 2012;14(suppl 5):v1–49
- Louis DN, Ohgaki H, Wiestler OD, et al. **The 2007 WHO classification of tumours of the central nervous system.** *Acta Neuropathol* 2007;114:97–109
- Cha S. **Update on brain tumor imaging: from anatomy to physiology.** *AJNR Am J Neuroradiol* 2006;27:475–87
- Omuro A, DeAngelis LM. **Glioblastoma and other malignant gliomas: a clinical review.** *JAMA* 2013;310:1842–50
- Barajas RF Jr, Hess CP, Phillips JJ, et al. **Super-resolution track density imaging of glioblastoma: histopathologic correlation.** *AJNR Am J Neuroradiol* 2013;34:1319–25
- Barajas R Jr, Phillips JJ, Parvataneni R, et al. **Regional variation in histopathologic features of tumor specimens from treatment-naïve glioblastoma correlates with anatomic and physiologic MR imaging.** *Neuro Oncol* 2012;14:942–54
- Giese A, Westphal M. **Glioma invasion in the central nervous system.** *Neurosurgery* 1996;39:235–50; discussion 250–52
- Giese A, Kluwe L, Laube B, et al. **Migration of human glioma cells on myelin.** *Neurosurgery* 1996;38:755–64
- Arnautovic KI, Husain MM, Linskey ME. **Cranial nerve root entry zone primary cerebellopontine angle gliomas: a rare and poorly recognized subset of extraparenchymal tumors.** *J Neurooncol* 2000;49:205–12
- Breshears JD, Ivan ME, Cotter JA, et al. **Primary glioblastoma of the trigeminal nerve root entry zone: case report.** *J Neurosurg* 2015;122:78–81
- Bridger MW, Farkashidy J. **The distribution of neuroglia and Schwann cells in the 8th nerve of man.** *J Laryngol Otol* 1980;94:1353–62
- Borges A, Casselman J. **Imaging the cranial nerves. Part I. Methodology, infectious and inflammatory, traumatic and congenital lesions.** *Eur Radiol* 2007;17:2112–25
- Borges A, Casselman J. **Imaging the cranial nerves. Part II. Primary and secondary neoplastic conditions and neurovascular conflicts.** *Eur Radiol* 2007;17:2332–44
- Paes FM, Singer AD, Checkver AN, et al. **Perineural spread in head and neck malignancies: clinical significance and evaluation with 18F-FDG PET/CT.** *Radiographics* 2013;33:1717–36
- Muzzafar S, Ketonen L, Weinberg JS, et al. **Imaging and clinical features of an intra-axial brain stem schwannoma.** *AJNR Am J Neuroradiol* 2010;31:567–69
- Cushing H. *Tumors of the Nervus Acusticus and the Syndrome of the Cerebellopontine Angle.* Philadelphia: WB Saunders; 1917
- Panse R. **Ein Gliom des Akustikus.** *Arch Ohr Heilk* 1904;61:251–55
- Wu B, Liu W, Zhu H, et al. **Primary glioblastoma of the cerebellopontine angle in adults.** *J Neurosurg* 2011;114:1288–93
- Mirone G, Schiabello L, Chibbaro S, et al. **Pediatric primary pilocytic astrocytoma of the cerebellopontine angle: a case report.** *Childs Nerv Syst* 2009;25:247–51
- Ree A, Jain R, Rock J, et al. **Direct infiltration of brainstem glioma along the cranial nerves.** *J Neuroimaging* 2005;15:197–99
- Takada Y, Ohno K, Tamaki M, et al. **Cerebellopontine angle pilocytic astrocytoma mimicking acoustic schwannoma.** *Neuroradiology* 1999;41:949–50
- Reifenberger G, Bostrom J, Bettag M, et al. **Primary glioblastoma multiforme of the oculomotor nerve: case report.** *J Neurosurg* 1996;84:1062–66
- Beutler AS, Hsiang JK, Moorhouse DF, et al. **Pilocytic astrocytoma presenting as an extra-axial tumor in the cerebellopontine angle: case report.** *Neurosurgery* 1995;37:125–28
- Forton G, Verlooy J, Cras P, et al. **Problems with flute playing: an otological problem? Case report of a peculiar cerebellar astrocytoma [in Dutch].** *Acta Otorhinolaryngol Belg* 1992;46:405–10
- Kasantikul V, Palmer JO, Netsky MG, et al. **Glioma of the acoustic nerve.** *Arch Otolaryngol* 1980;106:456–59
- Gandhi D, Gujar S, Mukherji SK. **Magnetic resonance imaging of perineural spread of head and neck malignancies.** *Top Magn Reson Imaging* 2004;15:79–85
- Binmadi NO, Basile JR. **Perineural invasion in oral squamous cell carcinoma: a discussion of significance and review of the literature.** *Oral Oncol* 2011;47:1005–10

Parry Romberg Syndrome: 7 Cases and Literature Review

M. Wong, C.D. Phillips, M. Hagiwara, and D.R. Shatzkes

ABSTRACT

SUMMARY: Parry Romberg syndrome is a rare progressive hemiatrophy of the face that typically occurs in children and young adults and has a peculiar progression that ceases without apparent cause after a highly variable period. Only a subset of patients with Parry Romberg syndrome will develop secondary neurologic or ophthalmologic symptoms, and prognosis is highly variable. Inconsistency in the pattern of atrophy and the development of associated symptoms in patients with Parry Romberg syndrome has made it challenging to diagnose, prognosticate, and treat. The precise etiology of this disease remains unknown, but some authors have implicated sympathetic cervical ganglion dysfunction, abnormal embryogenesis, autoimmune and inflammatory mechanisms, or vasculopathy as potential causes. We present 7 cases of Parry Romberg syndrome and their associated clinical and imaging findings with specific attention to the radiographic characteristics of this disease.

ABBREVIATION: PRS = Parry Romberg syndrome

Initially described by Drs Caleb Hillier Parry and Moritz Heinrich Romberg in 1825 and 1846, respectively,²⁴ Parry Romberg syndrome (PRS), also known as progressive facial hemiatrophy, is a rare, insidious, and self-limiting hemiatrophy of the face. It characteristically involves the skin and subcutaneous connective tissues and may later progress to affect the underlying musculature, cartilage, and osseous structures with or without development of neurologic symptoms.^{1-20,23,26} PRS typically presents initially in children and young adults and slowly progresses over a highly variable course ranging from 2 to 20 years, eventually reaching a “burned-out phase” and stabilizing for no apparent reason.^{2-6,8-10,14-17} This peculiar disease course, along with highly variable signs and symptoms, impedes consistent understanding of the underlying pathophysiology of PRS. Many theories about PRS have emerged throughout the years, attributing this syndrome to widely varying etiologies such as infection, trauma, sympathetic nervous system dysfunction, vascular abnormalities, inflammatory conditions, and autoimmune disorders, but at this time, a specific etiology remains uncertain.^{1-9,13-17,20,25}

Received July 25, 2014; accepted after revision January 11, 2015.

From the Department of Radiology (M.W., D.R.S.), Lenox Hill Hospital, North Shore Long Island Jewish Health System, New York, New York; Department of Radiology (C.D.P.), Division of Neuroradiology, Weill Medical College of Cornell University, New York Presbyterian Hospital, New York, New York; and Department of Radiology (M.H.), New York University Langone Medical Center, New York, New York.

Please address correspondence to Deborah R. Shatzkes, MD, Lenox Hill Hospital, North Shore Long Island Jewish Health System, Radiology Department, 100 E 77th St, New York, NY 10075; e-mail: dshatzkes@nshs.edu

<http://dx.doi.org/10.3174/ajnr.A4297>

Changes of cutaneous PRS may be subtle on imaging studies, but 20% of these patients will have intracranial manifestations that may not correspond to the severity of soft-tissue involvement or neurologic symptoms.^{13,18,20} Radiologic examinations may identify clinically occult intracranial involvement, facilitate the exclusion of other differential diagnostic considerations,¹⁵ and aid in monitoring disease progression.⁷ We present 7 cases of PRS to illustrate its wide variety of extracranial and intracranial imaging findings, along with a discussion of the clinical course, differential diagnoses, and treatment options. The role of the radiologist in diagnosis and management is emphasized.

Case Series

Case 1. A 44-year-old woman with known right-sided PRS underwent CT for the evaluation of disease extent and cosmetic surgical planning. CT demonstrated thinning of the skin and subcutaneous fat of the right side of the face extending inferiorly to the suprahyoid neck. There was atrophy of the right platysma and muscles of mastication, with substantial asymmetry in the size of the parotid gland (Fig 1A). Osseous asymmetry was most pronounced in the maxilla and zygoma, though the right hemimandible was smaller than the left one (Fig 1B). Considerable right enophthalmos was present (Fig 1C). No brain imaging was performed.

Case 2. A 14-year-old boy presented with progressive atrophy of the left side of the face. CT and MR imaging examinations revealed hemiatrophy most prominently involving left-sided skin and subcutaneous fat, with lesser involvement of the mus-

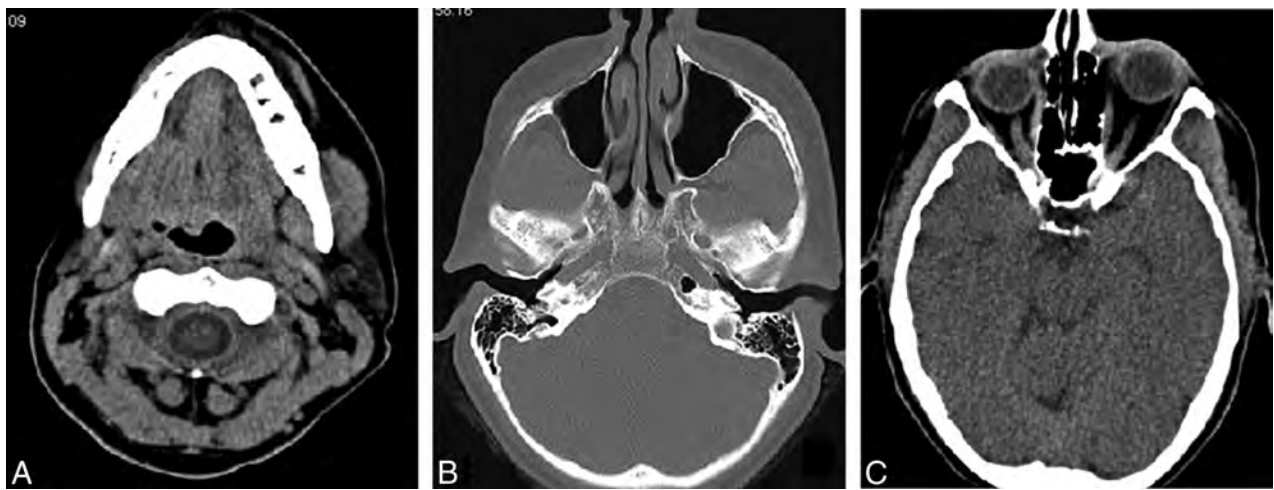


FIG 1. Axial CT images of a 44-year-old woman with PRS obtained for cosmetic surgical planning. *A*, There is prominent hemiatrophy of the skin, subcutaneous fat, and masseter muscle. *B*, The right maxillary sinus is considerably smaller than the left. *C*, Marked right enophthalmos is present.

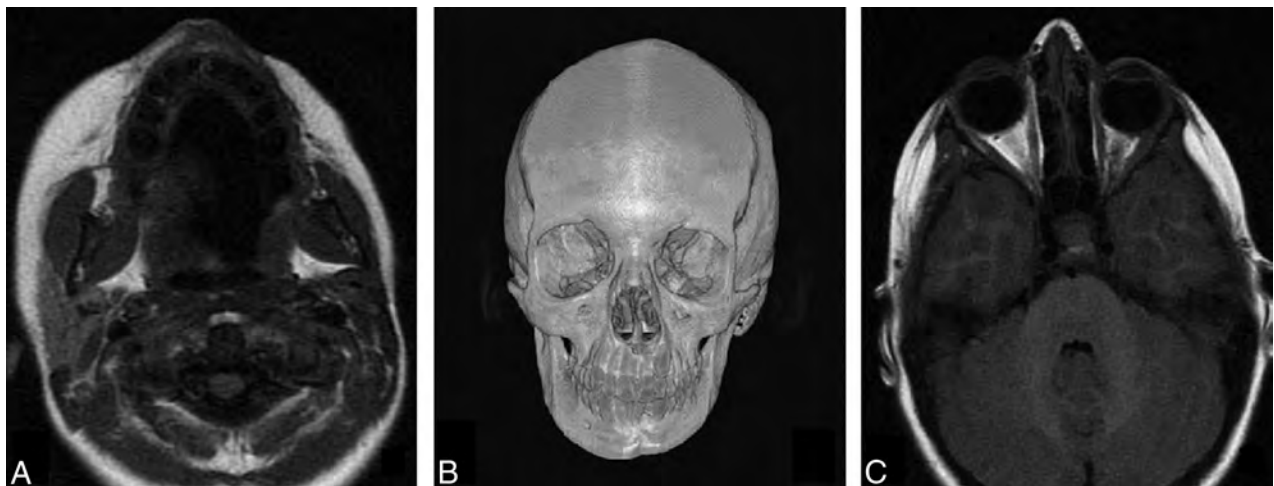


FIG 2. A 14-year-old boy who presented with progressive atrophy of the left face. *A*, T1-weighted image shows striking paucity of fat in the left face. *B*, 3D reconstruction of a CT series demonstrates left facial hemiatrophy, particularly involving the mandible. *C*, T1-weighted image at the level of the orbits reveals left enophthalmos.

cles of mastication (Fig 2A). Skeletal findings were most pronounced in the mandible (Fig 2B). Enophthalmos of the left globe was present with relative paucity of retrobulbar fat (Fig 2C). No intracranial imaging findings were observed at the time of presentation.

Case 3. A 24-year-old man with progressive hemiatrophy of the left lower face and left facial nerve dysfunction during the past 3 years presented for imaging evaluation of symptoms. MR imaging demonstrated near-absence of subcutaneous fat involving the inframaxillary face extending inferiorly to the visualized portions of the suprahyoid neck (Fig 3A). Only minimal asymmetry was noted involving the muscles and skeletal structures (Fig 3B). Involved tissues demonstrated normal T1 and T2 signal without pathologic contrast enhancement (Fig 3C). Limited evaluation of intracranial content revealed no abnormality. Diagnosis of PRS was made, given imaging findings and compatible clinical history and examination.

Case 4. An 11-year-old girl with a known diagnosis of PRS of unknown duration was experiencing increasing dermal sensi-

tivity and tightness of the left hemiface and occasional pain along the left temple for the past year. CT revealed soft-tissue atrophy and osseous asymmetry most prominently in the left maxilla (Fig 4A), with extension to the left frontal scalp superiorly and left mandible inferiorly. There was deviation of the nose toward the side of atrophy (Fig 4B). The maxillary sinus, ethmoidal air cells, mandible, and osseous orbit were relatively smaller on the left (Fig 4C). No dedicated intracranial imaging was performed.

Case 5. A 30-year-old woman with known PRS presented with weakness and recurrent headaches and underwent MR imaging of the brain. Subtle thinning of the subcutaneous skin and fat was seen along the right scalp (Fig 5A). On FLAIR and T2-weighted images, increased signal was present in the ipsilateral subinsular, temporal, and occipital lobe white matter and in the cerebral peduncle (Fig 5B, -C). Susceptibility-weighted imaging demonstrated innumerable punctate foci throughout the right temporal, frontal, and occipital lobes and in the cerebellum (Fig 5D). The left hemisphere was normal.

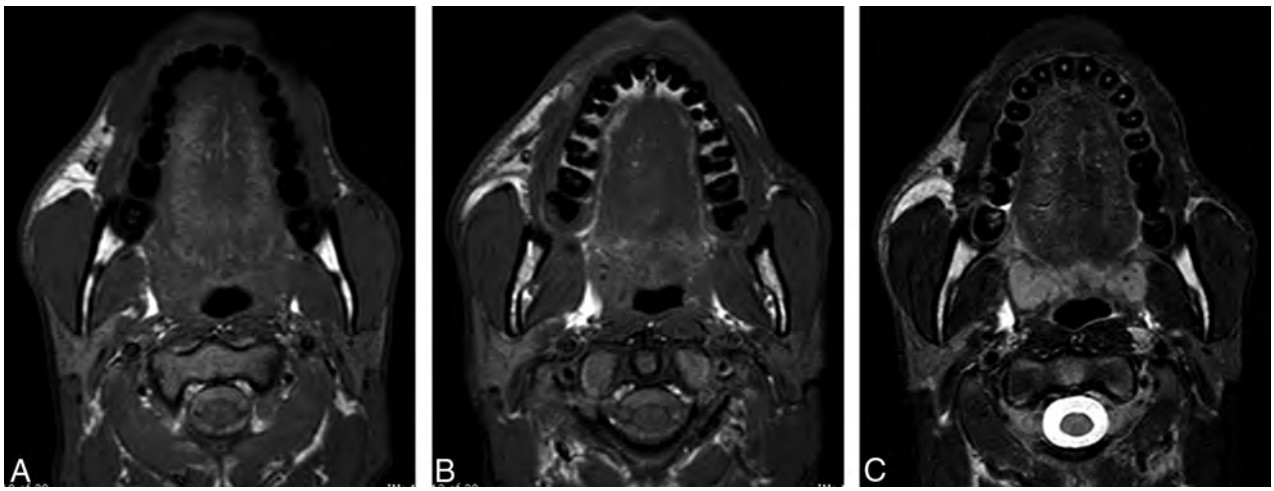


FIG 3. A 24-year-old man with progressive atrophy of the left face. *A* and *B*, Axial T1-weighted MR images demonstrate left hemifacial atrophy primarily involving the skin and subcutaneous fat; only subtle asymmetry of the masseter is noted. *C*, T2-weighted image at the same level demonstrates normal T2 signal in the affected structures.

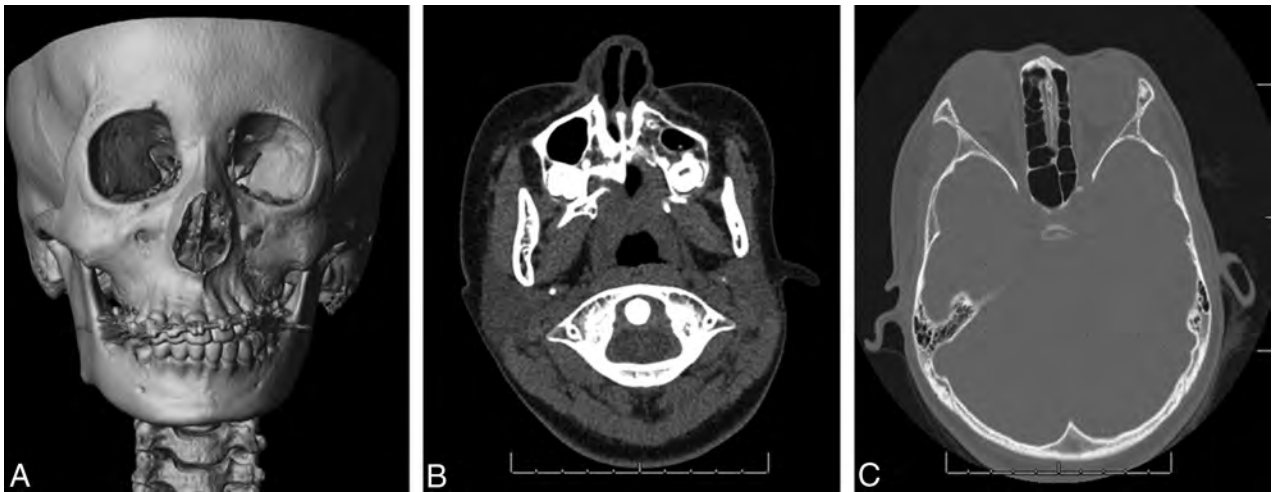


FIG 4. An 11-year-old girl with left-face sensitivity and left-temple pain. *A*, 3D reconstructions of a CT series show osseous asymmetry, most prominently in the left maxilla. *B*, Axial CT image at soft-tissue windows demonstrates deviation of the nose toward the affected side. *C*, Axial bone window demonstrates marked asymmetry in the volume of ethmoidal air cells.

Case 6. A 35-year-old woman with known left PRS presented with headache and weakness. MR imaging demonstrated increased T2 signal in the left hemispheric white matter. Involvement was geographic, with regional areas of confluent periventricular, deep, and subcortical white matter hyperintensity (Fig 6). The right hemisphere demonstrated only nonspecific punctate foci of white matter hyperintensity.

Case 7. A 68-year-old man with known PRS presented with clinical acute right middle cerebral artery occlusion. Noncontrast head CT demonstrated marked thinning of the left frontal scalp similar to an en coup de sabre deformity (Fig 7A). MR imaging demonstrated findings consistent with right MCA acute infarction (not shown). The left hemisphere was markedly abnormal with extensive white matter signal abnormality (Fig 7B). Asymmetric left ventriculomegaly and a relatively small ipsilateral sulcal size (Fig 7C) were present and suggested hydrocephalus, but their etiology remained unexplained.

DISCUSSION

Parry Romberg syndrome is a sporadic and rare condition that has been reported to be more common in females,^{2-6,10,15-17,20} without apparent geographic or ethnic predilection.¹⁵ Onset typically occurs during the first and second decades of life, resulting in an initially insidious but progressive hemiatrophy of the face during a span of 2–20 years, with a slight propensity for the left side.^{3-6,8-10,13-17,20,25} Seemingly without cause, the progression abruptly arrests and stabilizes, reaching a “burned-out” phase.^{2,3,8-10,14-17,25} Diagnosis of PRS mainly relies on the clinical history and examination and exclusion of other possibilities, supported by histopathologic and imaging studies.¹⁶

Patients characteristically experience atrophy of the skin and subcutaneous tissues and may develop atrophy of the underlying muscular, cartilaginous, osseous, and glandular structures as the disease progresses.^{1-9,13-17,20} The affected area typically begins in the maxillary or periorbital region and may expand to involve the forehead, perioral region, teeth, jaw, and neck to varying de-

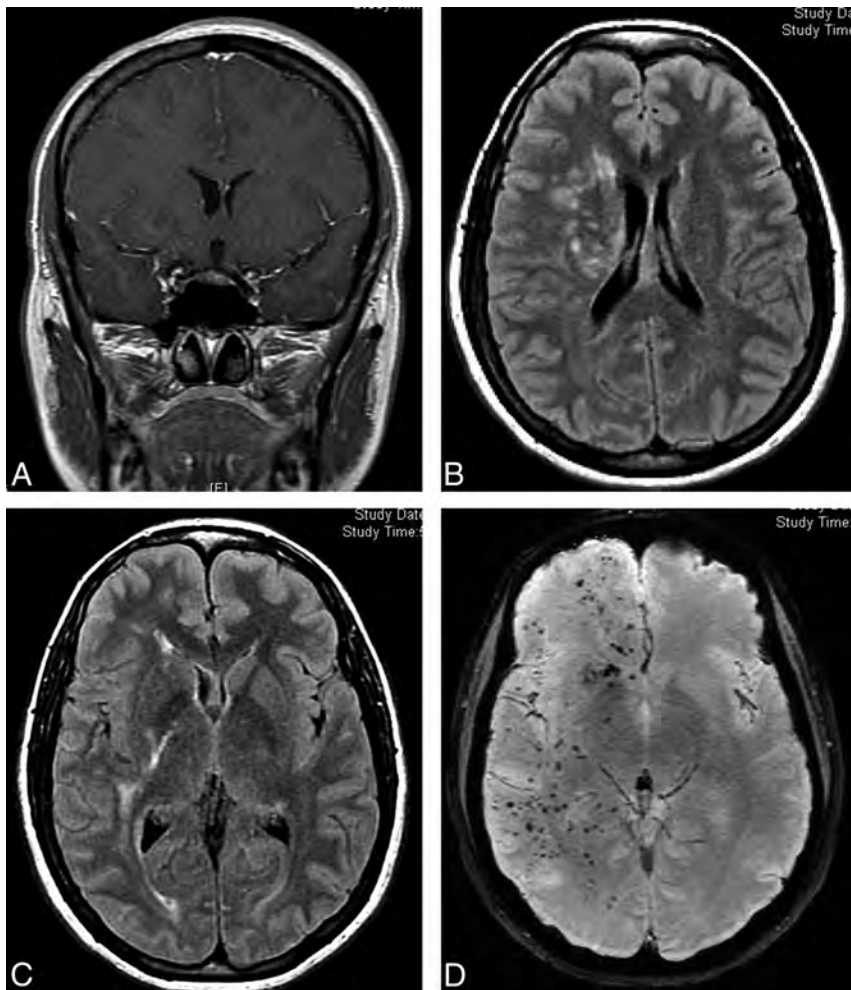


FIG 5. A 30-year-old woman with a history of PRS who presented for MR imaging evaluation for weakness and recurrent headaches. *A*, Coronal enhanced T1-weighted MR image demonstrates mild asymmetry of scalp thickness with relative paucity of subcutaneous fat on the right. *B* and *C*, Axial FLAIR images demonstrate abnormal hyperintensity of the white matter in the right corona radiata, internal capsule, and temporal region. *D*, Axial susceptibility-weighted image demonstrates innumerable punctate foci of susceptibility throughout the right cerebral hemisphere.

grees.^{5-7,12,14-17} Involvement of the teeth may help in determining the age of onset in unclear cases,¹⁷ because the presence of relatively smaller teeth with short roots has been reported in PRS.²¹ Earlier onset and longer duration of PRS have been reported to relate to increased severity of the disease.^{3,17} Superficial changes such as skin discoloration and cicatricial alopecia may occur as well.^{5,7,15-17} PRS is typically limited to 1 side of the head and neck, but bilateral disease has been reported. Similar manifestations involving the trunk and extremities are even rarer.¹⁴⁻¹⁷

Neurologic symptoms occur in 15%–20% of patients, with the most common being ipsilateral headaches, facial pain, and seizures, which may be refractory to treatment.^{5,6,8,9,12-16} Other reported neurologic symptoms include trigeminal neuritis, facial paresthesia, cranial nerve dysfunction, fixed focal neurologic defects, hemiparesis, and cognitive impairment.^{1-3,5,8,9,11-16} Ophthalmologic symptoms occur in 10%–35% of patients and usually involve the ipsilateral orbit. Enophthalmos is common due to atrophy of the retrobulbar fat^{2,6,15-17}; other potential orbital abnormalities include uveitis and retinal or optic nerve alterations.^{1,2,12,15-17}

Many theories have developed during the years in an attempt to explain this peculiar disease. However, no single theory has been satisfactory in fully characterizing and predicting PRS, and our understanding of the underlying

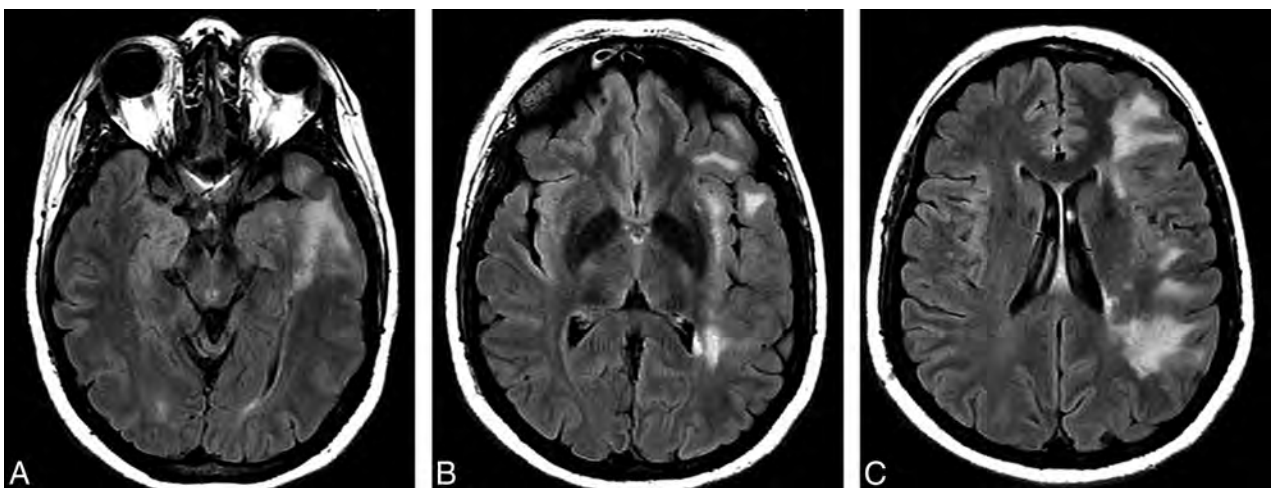


FIG 6. A 35-year-old woman with a history of PRS presented for MR imaging evaluation for headaches and weakness. Axial FLAIR images demonstrate hyperintensity in the left cerebral periventricular to subcortical white matter. The pattern of signal abnormality is geographic, with subtotal involvement of frontal, parietal, and temporal lobes.

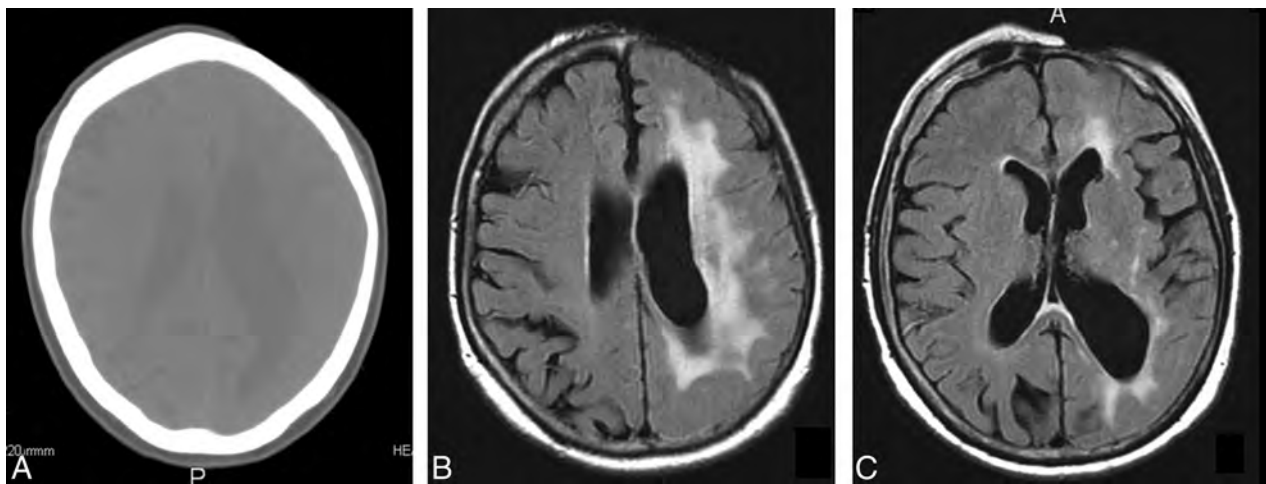


FIG 7. A 68-year-old man with PRS who presented with acute right MCA infarct. *A*, Axial CT image demonstrates striking focal loss of scalp thickness in the left frontal region. *B*, Axial FLAIR images demonstrate confluent signal abnormality in the high left frontal and parietal white matter. *C*, Etiology of left ventriculomegaly and sulcal asymmetry was uncertain.

pathophysiology remains limited.³ Proposed etiologies have included trauma, genetic predisposition, infection, radiation exposure, embryonic developmental dysfunction, sympathetic cervical ganglion dysfunction, and metabolic and endocrinologic disturbances.^{1-3,5-8,13-17} Currently, the strongest laboratory and histologic evidence supports an inflammatory autoimmune disorder with or without associated vasculopathy.^{1-6,12,14,15,17} Clinical improvement with immunosuppressive therapy during active disease further supports an underlying immunologic-mediated process.^{8,25}

On radiologic assessment, common facial imaging findings include varying degrees of hemiatrophy accompanied by obliteration of fat planes, ipsilateral deviation of the aerodigestive tract, and enophthalmos due to loss of retrobulbar fat.^{15,17} No abnormal CT attenuation or MR signal has been reported within the affected facial structures.¹⁵ Intracranially, the most common findings are the following: 1) ipsilateral linear or discrete subcortical calcifications in the frontal lobe, 2) white matter hypoattenuation on CT corresponding to hyperintense T2 signal on MR imaging,^{1-3,7-10,13-18} and 3) ipsilateral focal or hemispheric brain atrophy.¹⁶⁻¹⁸ These findings typically occur ipsilateral to the affected side of the face¹⁵ and may worsen with disease progression.¹ Less frequently described imaging findings include the loss of cortical gyration, cortical thickening, ventricular dilation, focal corpus callosum infarcts, leptomeningeal thickening and contrast enhancement, attenuated mineral deposits, hamartomas, and MR signal abnormality involving the thalamus or gray matter.^{2,3,7,13,15-17} Vascular abnormalities such as microhemorrhages, malformations, stenoses, and aneurysms have also been reported in association with PRS.^{3,13,15-17,25}

In our case series, we demonstrated a variety of imaging findings in 7 patients with PRS. All patients had varying degrees of facial atrophy, and the affected extracranial structures retained normal signal patterns on MR imaging. Our first 4 patients underwent scanning for evaluation of facial findings. In 1 of the 4 patients, additional brain imaging was performed but revealed no abnormality. The remaining 3 patients with known diagnoses of PRS underwent dedicated brain imaging to evaluate neurologic

symptoms; all had substantial intracranial manifestations with white matter signal abnormality ipsilateral to the side of facial atrophy being a consistent finding. One patient demonstrated a striking pattern of innumerable foci of susceptibility in the ipsilateral brain—these may represent microhemorrhages or foci of mineralization. In another patient, unexplained ventriculomegaly and associated small sulci could represent underlying hydrocephalus or may reflect an as-yet-undocumented intracranial manifestation of PRS.

PRS shares many clinical features, such as age of onset, associated neurologic symptoms, and cutaneous presentations with en coup de sabre, a rare variant of linear scleroderma that occurs along the anterior aspect of the scalp.^{10,25,26} These 2 entities are commonly discussed in conjunction due to their overlapping presentations and lack of distinguishing clinical features.^{3,5,8,10,17,25} To make differentiation even more complicated, conversion of en coup de sabre to PRS has been reported,^{7,17,21} and 30%–40% of patients with PRS have changes typical of scleroderma localized outside the face.^{5,8,12} This has led many authors to consider these 2 entities variants that share a common underlying pathogenesis related to linear scleroderma.^{17-19,21,22,25} Other authors, however, argue against this claim^{10,26} because deeper head and neck structures, such as the oral or pharyngeal musculature, are not commonly involved in en coup de sabre, and there are typically elevated titers of autoantibodies in en coup de sabre but not in PRS.^{21,22} On the other hand, PRS demonstrates little-to-no sclerosis of the cutaneous and subcutaneous structures, variable perivascular chronic inflammation, and preservation of dermal elastic tissue on histopathologic examinations, differentiating it from the spectrum of scleroderma diseases.^{3,16,17,25,26}

PRS also shares features with Rasmussen encephalitis, an autoimmune/inflammatory disorder affecting 1 side of the brain, resulting in refractory epilepsy and progressive hemiplegia and typically affecting children in the first decade of life.^{14,27,28} On imaging, Rasmussen encephalitis is characterized by predominately unilateral hemispheric areas of hyperintense T2 signal with eventual development of unilateral ce-

rebral atrophy,^{27,28} findings that may be indistinguishable from intracranial imaging features of PRS. There have been reported cases of coexisting Rasmussen encephalitis and PRS in pediatric patients,^{4,8,14,15,17} supporting a possible pathophysiological correlation between these 2 entities. In younger patients, differentiating these 2 entities may be difficult, but clinical signs and symptoms, such as the presence of epilepsy partialis continua, a hallmark symptom of Rasmussen encephalitis, and involvement of cutaneous structures should guide the clinician and radiologist to the correct diagnosis.^{1,4,7,8,27,28}

Other diseases in which facial asymmetry is a prominent clinical feature include hemifacial microsomia (first and second brachial arch syndrome) and Goldenhar syndrome, but unlike PRS, these conditions are typically congenital and non-progressive.^{19,21,22} Hemifacial hyperplasia causes asymmetry of the face as well, but rather than atrophy, this entity is characterized by overgrowth and hyperplasia.^{21,29} Partial lipodystrophy (Barraque-Simons syndrome) may have manifestations similar to those of PRS, but typically these are bilateral.^{19,22} Silent sinus syndrome may also be considered, but these patients present later in life with characteristic imaging findings of opacification and atelectasis of the maxillary sinus and evidence of ipsilateral ostiomeatal unit obstruction.³⁰

No standard treatment algorithm currently exists for PRS,^{12,17} especially given that response to treatment is difficult to assess.¹⁵ In general, treatment goals are to obtain seizure control if seizures are present, provide symptomatic relief, and halt disease progression.^{17,18} PRS-related seizures are usually treated with anticonvulsive therapy despite their commonly refractory nature.^{1,4,14} At times, lobectomy may be warranted for seizure control.^{4,8} Additionally, similar to treatments for scleroderma, immunosuppressive therapies, ranging from topical corticosteroids to systemic corticosteroids, immunomodulators, and plasmapheresis, have been used with varying degrees of success. Antimalarials, antibiotics, vitamin D₃ analogues, and penicillamine are also treatment options that have demonstrated variable responses.^{5,8,10,14-18} Once the disease stabilizes, cosmetic therapies, including pulse dye lasers, dermal fat grafts, autologous fat grafts, muscle flap grafts, free silicone injections, and bone augmentations, are available for aesthetic management.^{10,23,24} Recently, autologous fat grafting with adipose-derived stem cells has been shown to provide the most favorable cosmetic results.^{23,24} In these incidences, objective serial volumetric analysis of both hemifaces is important to monitor fat reabsorption, an indicator of successful grafting. Volumetric calculations can be easily achieved with 3D reconstructions of CT data acquired periprocedurally and on serial follow-up examinations, but alternative methods are being investigated as well due to concerns for cost and patient radiation exposure.^{23,24}

In summary, PRS is a rare, self-limiting, and slowly progressive hemiatrophy of the face that typically affects the skin and subcutaneous tissues and may affect deeper tissues such as the musculature, cartilage, and osseous structures. Neurologic and ophthalmologic symptoms are common, but underlying pathophysiology remains uncertain. Intracranial involvement is best evaluated with MR imaging and can range widely, with the most common findings being parenchymal calcifications,

white matter abnormalities, and brain atrophy. In addition to evaluating the extent of disease, radiologic assessments may also facilitate the exclusion of other differential considerations, help monitor disease progression, and evaluate posttreatment responses.

REFERENCES

1. Yano T, Sawaishi Y, Toyono M, et al. **Progressive facial hemiatrophy after epileptic seizures.** *Pediatr Neurol* 2000;23:164–66
2. Aynaci FM, Sen Y, Erdol H, et al. **Parry-Romberg syndrome associated with Adie's pupil and radiologic findings.** *Pediatr Neurol* 2001;25:416–18
3. Pichiecchio A, Uggetti C, Egitto MG, et al. **Parry-Romberg syndrome with migraine and intracranial aneurysm.** *Neurology* 2002;59:606–08
4. Shah JR, Juhasz C, Kupsky WJ, et al. **Rasmussen encephalitis associated with Parry-Romberg syndrome.** *Neurology* 2003;61:395–97
5. Stone J. **Parry-Romberg syndrome: a global survey of 205 patients using the internet.** *Neurology* 2003;61:674–76
6. Moko SB, Mistry Y, Blandin de Chalaïn TM. **Parry-Romberg syndrome: intracranial MRI appearances.** *J Craniomaxillofac Surg* 2003;31:321–24
7. Sommer A, Gambichler T, Bacharach-Buhles M, et al. **Clinical and serological characteristics of progressive facial hemiatrophy: a case series of 12 patients.** *J Am Acad of Dermatol* 2006;54:227–33
8. Paprocka J, Jamroz E, Adamek D, et al. **Difficulties in differentiation of Parry-Romberg syndrome, unilateral facial scleroderma, and Rasmussen syndrome.** *Childs Nerv Syst* 2006;22:409–15
9. Okumura A, Ikuta T, Tsuchi T, et al. **Parry-Romberg syndrome with a clinically silent white matter lesion.** *AJNR Am J Neuroradiol* 2006;27:1729–31
10. Tollefson MM, Witman PM. **En coup de sabre morphea and Parry-Romberg syndrome: a retrospective review of 54 patients.** *J Am Acad of Dermatol* 2007;56:257–63
11. Restivo DA, Milone P. **Teaching neuroimages: progressive facial hemiatrophy (Parry-Romberg syndrome) with ipsilateral cerebral hemiatrophy.** *Neurology* 2010;74:e11
12. Lazaridou E, Giannopoulou C, Apalla Zoi, et al. **Parry-Romberg syndrome.** *J Dermatol Case Rep* 2010;4:30–32
13. Blistein MK, Vecchione MJ, Tung GA. **Parry-Romberg syndrome.** *Applied Radiol* 2011;40:34–36
14. Longo D, Paonessa A, Specchio N, et al. **Parry-Romberg syndrome and Rasmussen encephalitis: possible association: clinical and neuroimaging features.** *J Neuroimaging* 2011;21:188–93
15. Sharma M, Bharatha A, Antonyshyn OM, et al. **Case 178: Parry-Romberg syndrome.** *Radiology* 2012;262:721–25
16. Madasamy R, Jayanandan M, Adhavan UR, et al. **Parry Romberg syndrome: a case report and discussion.** *J Oral Maxillofac Pathol* 2012;16:406–10
17. El-Kehdy J, Abbas O, Rubeiz N. **A review of Parry-Romberg syndrome.** *J Am Acad of Dermatol* 2012;67:769–84
18. Chiu YE, Vora S, Kwon EK, et al. **A significant proportion of children with morphea en coup de sabre and Parry-Romberg syndrome have neuroimaging findings.** *Pediatr Dermatol* 2012;29:738–48
19. Vykuntaraju KN, Sahana, Shivananda. **Parry-Romberg syndrome.** *Indian Pediatr* 2013;50:255
20. Dalla Costa G, Colombo B, Libera DD, et al. **Parry Romberg syndrome associated with chronic facial pain.** *J Clin Neurosci* 2013;20:1320–22
21. Khan M, Khan M, Negi R, et al. **PRS with localized scleroderma: a case report.** *J Clin Exp Dent* 2014;6:e313–16
22. Trisal D, Kumar N, Dembla G, et al. **Parry-Romberg syndrome: uncommon but interesting.** *BMJ Case Rep* 2014;pii:bcr2013201969
23. Koh KS, Oh TS, Kim H, et al. **Clinical application of human adipose tissue-derived mesenchymal stem cells in progressive hemifacial atrophy (Parry-Romberg disease) with microfat grafting techniques using 3-dimensional computed tomography and 3-dimensional camera.** *Ann Plast Surg* 2012;69:331–37

24. Chang Q, Li J, Dong Z, et al. **Quantitative volumetric analysis of progressive hemifacial atrophy corrected using stromal vascular fraction-supplemented autologous fat grafts.** *Dermatol Surg* 2013; 39:1465–73
25. Kister I, Inglese M, Laxer RM, et al. **Neurologic manifestations of localized scleroderma: a case report and literature review.** *Neurology* 2008;71:1538–45
26. Miller K, Lehrhoff S, Fischer M, et al. **Linear morphea of the forehead (en coup de sabre).** *Dermatol Online J* 2012;18:22
27. Geller E, Faerber EN, Legido A, et al. **Rasmussen encephalitis: complementary role of multitechnique neuroimaging.** *AJNR Am J Neuroradiol* 1998;19:445–49
28. Faria AV, Reis F, Dabus GC, et al. **MRI findings in the diagnosis and monitoring of Rasmussen's encephalitis.** *Arg Neuropsiquiatr* 2009; 67:792–97
29. Bou-Haidar P, Taub P, Som P. **Hemifacial lipomatosis, a possible subtype of partial hemifacial hyperplasia: CT and MR imaging findings.** *AJNR Am J Neuroradiol* 2010;31:891–93
30. Hourany R, Aygun N, Della Santina CC, et al. **Silent sinus syndrome: an acquired condition.** *AJNR Am J Neuroradiol* 2005;26:2390–92

Disrupted Global and Regional Structural Networks and Subnetworks in Children with Localization-Related Epilepsy

E. Widjaja, M. Zamyadi, C. Raybaud, O.C. Snead, S.M. Doesburg, and M.L. Smith



ABSTRACT

BACKGROUND AND PURPOSE: Structural connectivity has been thought to be a less sensitive measure of network changes relative to functional connectivity in children with localization-related epilepsy. The aims of this study were to investigate the structural networks in children with localization-related epilepsy and to assess the relation among structural connectivity, intelligence quotient, and clinical parameters.

MATERIALS AND METHODS: Forty-five children with nonlesional localization-related epilepsy and 28 healthy controls underwent DTI. Global network (network strength, clustering coefficient, characteristic path length, global efficiency, and small-world parameters), regional network (nodal efficiency), and the network-based statistic were compared between patients and controls and correlated with intelligence quotient and clinical parameters.

RESULTS: Patients showed disrupted global network connectivity relative to controls, including reduced network strength, increased characteristic path length and reduced global efficiency, and reduced nodal efficiency in the frontal, temporal, and occipital lobes. Connectivity in multiple subnetworks was reduced in patients, including the frontal-temporal, insula-temporal, temporal-temporal, frontal-occipital, and temporal-occipital lobes. The frontal lobe epilepsy subgroup demonstrated more areas with reduced nodal efficiency and more impaired subnetworks than the temporal lobe epilepsy subgroup. Network parameters were not significantly associated with intelligence quotient, age at seizure onset, or duration of epilepsy.

CONCLUSIONS: We found disruption in global and regional networks and subnetworks in children with localization-related epilepsy. Regional efficiency and subnetworks were more impaired in frontal lobe epilepsy than in temporal lobe epilepsy. Future studies are needed to evaluate the implications of disrupted networks for surgical resection and outcomes for specific epileptogenic zones and the relation of disrupted networks to more complex cognitive function.

ABBREVIATIONS: AAL = automated anatomic labeling; FLE = frontal lobe epilepsy; IQ = intelligence quotient; NBS = network-based statistic; TLE = temporal lobe epilepsy

Epilepsy has been considered a disorder of neural networks, in which activity in one part of the network is influenced by activity elsewhere in the network.¹ The epileptogenic network could

be responsible for the development and spread of seizures or could develop secondary to reorganization of the normal neural networks from recurrent seizures. Children with localization-related epilepsy, including those with frontal lobe epilepsy (FLE), have demonstrated abnormal resting-state functional connectivity in the default mode network and in other resting-state networks, such as attention, frontal, visual, auditory, and somatosensory networks.^{2,3} Graph theoretical measures of functional connectivity have also been shown to be abnormal in children with FLE, particularly in those who were cognitively impaired, with increased path length, an increased weighted cluster coefficient, and higher modularity, implying that the networks are less integrated and more segregated.⁴

Less is known about structural connectivity in children with localization-related epilepsy other than FLE. DTI measures of WM microstructural organization such as fractional anisotropy

Received September 21, 2014; accepted after revision January 2, 2015.

From the Department of Diagnostic Imaging (E.W., M.Z., C.R., S.M.D.), Division of Neurology (E.W., O.C.S.), and Neuroscience and Mental Health at Research Institute (S.M.D.), Hospital for Sick Children, Toronto, Ontario, Canada; and Department of Psychology (M.L.S.), University of Toronto, Toronto, Ontario, Canada.

This work was supported by SickKids Foundation/Canadian Institutes of Health Research, Institute of Human Development, Child and Youth Health, and the Derek Harwood Nash Chair fund.

Please address correspondence to E. Widjaja, MD, 555 University Ave, Toronto, ON M5G 1X8, Canada; e-mail: Elysa.Widjaja@sickkids.ca

Indicates open access to non-subscribers at www.ajnr.org

Indicates article with supplemental on-line appendix and tables.

Evidence-Based Medicine Level 2.

<http://dx.doi.org/10.3174/ajnr.A4265>

and mean diffusivity have been shown to be impaired in children with localization-related epilepsy, also known as partial or focal epilepsy, including FLE and temporal lobe epilepsy (TLE).⁵⁻⁹ These changes were identified not only in the WM ipsilateral to seizure focus but also contralateral to the seizure focus. Given that there was bilateral structural abnormality in children with localization-related epilepsy, we postulated that there would be extensive impairment in structural connectivity despite the apparent focality of the seizure disorders. A recent study in children with FLE¹⁰ found that structural path length and clustering coefficient assessed by using DTI were normal but the functional connectivity measures assessed by using resting-state fMRI were abnormal; these findings suggest that structural connectivity may be less sensitive than functional connectivity assessment of the networks. It is not known whether the previously reported lack of changes in structural connectivity is specific to FLE and whether there are differences in structural connectivity across different types of localization-related epilepsy, because FLE involves different epileptogenic networks compared with TLE.

The aims of this study were to investigate the structural whole-brain networks by using graph theoretical measures in children with localization-related epilepsy relative to healthy controls and to assess whether there was a relation between graph measures of structural connectivity, intelligence quotient (IQ), and clinical parameters. The secondary aims of this study were to determine whether there were structural network differences between subgroups with FLE and TLE and the relations of graph measures of structural connectivity with IQ and clinical parameters.

MATERIALS AND METHODS

Subjects

This study had the approval of the research ethics board of the Hospital for Sick Children. Informed consent was obtained from parents, and assent, from children for both patients and healthy controls. Children with localization-related epilepsy who were worked up for epilepsy surgery were recruited into the study. All patients had normal 3T MR imaging findings. Location of the epileptogenic zone was determined by ictal and interictal video electroencephalography, magnetoencephalography, and FDG-PET scans. The control group consisted of healthy children with no neurologic or psychiatric disorders and normal MR imaging findings. Both patients and controls underwent the Wechsler Abbreviated Scale of Intelligence to assess IQ.

MR Imaging and DTI

MR imaging was performed on a 3T scanner (Achieva; Philips Healthcare, Best, the Netherlands) by using an 8-channel phased array head coil in all subjects. The imaging in patients consisted of axial and coronal FLAIR, proton-attenuation and T2, and volumetric T1 (TR/TE = 4.9/2.3 ms, section thickness = 1 mm, FOV = 22 cm, matrix = 220 × 220, scan time = 6 minutes 13 seconds), and DTI (TR/TE = 10,000/60 ms, section thickness = 2 mm, FOV = 22 cm, matrix = 112 × 112, NEX = 1, sensitivity encoding = 2, $b=1000$ s/mm², 31 noncollinear directions, number of sections = 70, isotropic voxel = 2 mm, scan time = 6 minutes 41 seconds). The imaging in controls included volumetric T1 and DTI, by using the same parameters as those for patients.

There were no significant differences in relative displacement between consecutive gradient images ($P = .080$) and translational ($P = .0704$) and rotational ($P = .2339$) motion between patients and controls.

Data Preprocessing

The DTI data were preprocessed by using fMRI of the Brain Software Library tools (Version 5.0, <http://www.fmrib.ox.ac.uk/fsl>). The raw diffusion tensor images were corrected for head motion and eddy current distortion.¹¹ To achieve this, we aligned all 31 diffusion-weighted images to the first B0 scan by using affine registration. The set of gradient vectors of each subject was then adjusted according to the affine transformation of the individual images.

Tractography

Tractography was initiated from seeds on the boundary of the gray-white matter interface.^{4,12} The FMRIB Automated Segmentation Tool (<http://fsl.fmrib.ox.ac.uk/fsl/fslwiki/fast>)¹³ was used to segment the individual skull-stripped structural T1 images into gray and white matter. The deep gray matter was manually removed from the whole-brain boundary mask. The seed voxels in the gray-white matter boundary were then transformed into each subject's native DTI space by using nonlinear coregistration.

The Camino toolbox¹⁴ (www.camino.org.uk) was then used to perform probabilistic tractography in the native DTI space. A Bayesian approach¹⁵ was used to initiate the fiber tracking from the gray-white matter boundary of the whole brain. This approach models the uncertainty in WM tractography by computing the likelihood of the fiber orientation by drawing a principal direction from a posterior distribution once per iteration for each seed voxel. The number of iterations at each seed voxel was set to 1000.

Network Construction

The automated anatomic labeling (AAL) template was used to define 82 cortical regions¹⁶ in each subject.¹⁷ The AAL ROIs were transformed to the native DTI space of each subject by using the following steps: First, both unweighted B0 and structural T1 images were skull-stripped, and nonlinear co-registration was performed between the T1 and B0 image by using the 3DSlicer (<http://www.slicer.org/>).¹⁸ Next, the Montreal Neurological Institute 152 brain template was nonlinearly registered to each individual's structural T1 image by using the Advanced Normalization Tools software package (<http://stnava.github.io/ANTs/>). The transformations from these 2 steps were then concatenated and used to resample the AAL atlas in the Montreal Neurological Institute space into each subject's native DTI space. Subsequently, the DTI of each subject was parcellated into 82 cortical ROIs. Each AAL ROI represented a node in the graph representation of the structural network. To construct the structural network, we extracted fiber bundles connecting each pair of AAL ROIs from the entire set of whole-brain tracts. A connectivity probability P_{ij} from a seed region i with n number of voxels to another region j was calculated by dividing the number of fibers passing through region j by $1000 \times n$.^{17,19} Next, a weighted undirected 82×82 connectivity matrix was constructed for each subject.

Table 1: Characteristics of patients with epilepsy, including those with frontal lobe epilepsy and temporal lobe epilepsy and controls

	Controls (n = 28)	All Epilepsy (n = 45)	FLE (n = 25)	TLE (n = 16)
Age (yr)	13.8 (3.1)	13.6 (3.0)	13.1 (3.3)	14.4 (2.7)
Age at seizure onset (yr)	NA	8.4 (3.9)	8.0 (4.0)	9.2 (3.5)
Duration of epilepsy (yr)	NA	5.1 (3.2)	5.1 (2.9)	4.9 (3.7)
No. of antiepileptic medications	NA	2.0 (0.7)	2.0 (0.7)	2.0 (0.7)
IQ	112.8 (10.8)	97.0 (11.9)	97.6 (10.9)	97.6 (11.9)

Note:—NA indicates not applicable.

Graph Theoretical Analysis

The Matlab-based Brain Connectivity Toolbox (<http://www.brain-connectivity-toolbox.net/>)²⁰ was used to perform graph theoretical network analysis to investigate potential differences in brain structural network parameters between patients with epilepsy and healthy controls. The metrics assessed included network strength, clustering coefficient, characteristic path length, global efficiency, small-world parameter, and nodal efficiency (On-line Appendix). The network strength is defined as the average of the strengths over all nodes in the graph. The clustering coefficient reflects functional segregation of brain networks, which is a measure of the propensity of the brain to execute specialized processes within interconnected groups of brain regions or clusters.²⁰ A high clustering coefficient indicates that the neighbors of a node are directly connected to each other.²¹ The characteristic path length is the most commonly used measure of functional integration and quantifies the ability of the network to propagate information in parallel.²⁰ Global efficiency reflects how efficiently information can be exchanged over the whole network, with larger global efficiency indicating a more efficient network. Small-world networks are defined as networks that have a characteristic path length similar to that of random networks but are significantly more clustered than random networks.²¹ Scalar measure of small-world property (σ) > 1 indicates that the network has a small-world property. The nodal efficiency quantifies the importance of the nodes for communication within the network. The nodes with high nodal efficiencies can be categorized as hubs in a network.²²

Network-Based Statistic

A network-based statistic (NBS)²³ was used to identify clusters of nodes and edges (subnetworks) in a connectivity matrix, which were differentially connected between patients and controls. First, significant nonzero connections within each group that were common across all subjects were detected, and then NBS (<http://www.nitrc.org/projects/nbs/>) was applied to those connections. A set of superthreshold links (ie, edges) was defined by applying a primary threshold ($P = .01$) to the test statistics (2-sample, 1-tailed t test) computed for each link. Any connected components and their number of links (ie, component size) were then selected among the superthreshold links. Finally, a nonparametric permutation test (10,000 permutations) and a secondary threshold of $P = .05$ were used to choose the significant components.²⁴⁻²⁶ This method effectively controls for false-positives due to multiple comparisons.

Statistical Analysis

Comparison of Network Characteristics. Differences in network characteristics (network strength, clustering coefficient, characteristic path length, global efficiency, small-world parameters, and nodal efficiency) between patients with epilepsy and controls were assessed by using 2-sample t tests. Subsequently, subgroup analyses comparing network

characteristics of FLE, TLE, and controls were performed by using 2-sample t tests.

Correlation of Clinical Parameters with Network Characteristics. Partial correlation analyses were performed to assess the relation among network characteristics, IQ, and clinical parameters (age at seizure onset and duration of epilepsy), controlling for age and sex, in all patients with epilepsy and the subgroups with FLE and TLE.

RESULTS

Subjects

Forty-five children with nonlesional localization-related epilepsy and 28 healthy controls were recruited. The mean age of patients (13.6 ± 3.0 years; range, 7.0–19.1) was not significantly different from the mean age of controls (13.8 ± 3.1 years; range, 7.0–18.8 years) ($P = .856$) (Table 1). The mean age of seizure onset was 8.4 ± 3.9 years, the mean duration of epilepsy was 5.1 ± 3.2 years, and the mean number of antiepileptic medications was 2.0 ± 0.7 . The mean IQ of patients (97.0 ± 11.9) was significantly lower than that of controls (112.8 ± 10.8) ($P < .001$). Twenty-five patients had FLE, 17 with left FLE and 8 with right FLE. Sixteen patients had TLE, 12 with left TLE and 4 with right TLE. Two patients had right hemisphere, 1 had right parietal, and another had right parieto-occipital seizure onset. There were no significant differences in age, age at seizure onset, duration of epilepsy, number of antiepileptic medications, and IQ of patients with FLE versus TLE (all, $P > .05$).

Alterations in Global Properties of Structural Networks

All Epilepsy versus Controls. The network parameters are shown in Table 2. The network strength was significantly decreased in patients ($P = .0002$), but there was no significant change in the clustering coefficient ($P = .8034$) of patients relative to controls. The characteristic path length was significantly increased ($P < .0001$), and the global efficiency was significantly decreased ($P = .0003$) in patients relative to controls. Patients and controls demonstrated small-world organization of the WM networks ($\sigma > 1$). The small-world property (σ) was greater ($P = .0353$) in patients than in controls.

FLE versus Controls. The network strength was significantly decreased in patients with FLE ($P = .0001$), but there was no significant difference in the clustering coefficient ($P = .8034$) of patients with FLE relative to controls. The characteristic path length was significantly increased ($P < .0001$), and the global efficiency was significantly decreased ($P < .0001$) in patients with FLE. Pa-

Table 2: Global properties of structural networks of controls and all patients with epilepsy, frontal lobe epilepsy, and temporal lobe epilepsy relative to controls

	Controls	All Epilepsy	FLE	TLE
Network strength \pm SD	0.7183 \pm 0.0249	0.6960 \pm 0.0226 ($P = .0002$) ^a	0.6900 \pm 0.0244 ($P = .00012$) ^a	0.7049 \pm 0.0189 ($P = .0641$)
Clustering coefficient \pm SD	0.0041 \pm 0.0004	0.0041 \pm 0.0005 ($P = .8034$)	0.0040 \pm 0.0005 ($P = .3091$)	0.0041 \pm 0.0004 ($P = .6662$)
Characteristic path length \pm SD	32.0769 \pm 1.1222	33.3724 \pm 1.3593 ($P < .0001$) ^a	33.6940 \pm 1.4205 ($P < .0001$) ^a	33.0110 \pm 1.2915 ($P = .0142$) ^a
Global efficiency \pm SD	0.0419 \pm 0.0013	0.0407 \pm 0.0014 ($P = .0003$) ^a	0.0403 \pm 0.0015 ($P < .0001$) ^a	0.0412 \pm 0.0013 ($P = .0613$)
Small-world property \pm SD	2.0018 \pm 0.1435	2.0772 \pm 0.1483 ($P = .0353$) ^a	2.0646 \pm 0.1562 ($P = .1335$)	2.0750 \pm 0.1374 ($P = .0992$)

^a $P < .05$.

tients with FLE demonstrated small-world organization of the WM networks ($\sigma > 1$). There was no significant difference in small-world property ($P = .1335$) in patients with FLE relative to controls.

TLE versus Controls. There was a trend toward reduced network strength ($P = .0641$) and no significant difference in clustering coefficient ($P = .6662$) of patients with TLE relative to controls. The characteristic path length was significantly increased ($P = .0142$), and there was a trend toward reduced global efficiency ($P = .0613$) in patients with TLE relative to controls. Patients with TLE demonstrated small-world organization of the WM networks ($\sigma > 1$). There was no significant difference in small-world property ($P = .0992$) in patients with TLE relative to controls.

FLE versus TLE. The network strength was significantly decreased ($P = .0399$), and there was a trend toward reduced global efficiency ($P = .0596$) in patients with FLE relative to those with TLE. There was no significant difference in clustering coefficient ($P = .2216$), characteristic path length ($P = .1208$), and small-world property ($P = .8250$) of patients with FLE relative to those with TLE.

Alterations in Regional Properties of Structural Networks

All Epilepsy versus Controls. Thirty-three regions showed reduced nodal efficiency ($P < .05$) in patients with epilepsy compared with controls, in the frontal, temporal, and occipital lobes (Fig 1 and On-line Table 1). The right anterior cingulate, right and left amygdalae, hippocampi, parahippocampal gyri, and superior temporal gyri showed a more statistically reliable reduction ($P < .001$) in nodal efficiency.

FLE versus Controls. Fifty-one regions showed reduced nodal efficiency ($P < .05$) in patients with FLE compared with controls, in the frontal, temporal, and occipital lobes. The right and left parahippocampal gyri, amygdalae, fusiform and superior temporal gyri, and right middle temporal gyrus showed a more statistically reliable reduction ($P < .001$) in nodal efficiency.

TLE versus Controls. Fourteen regions showed reduced nodal efficiency ($P < .05$) in patients with TLE compared with controls, in the frontal, temporal, and occipital lobes. The right and left amygdalae and right superior temporal gyrus showed a more statistically reliable reduction ($P < .001$) in nodal efficiency.

FLE versus TLE. Sixteen regions showed reduced nodal efficiency ($P < .05$) in patients with FLE relative to those with TLE, in the frontal, temporal, and occipital lobes. None of these regions showed a more statistically reliable reduction ($P < .001$) in nodal efficiency.

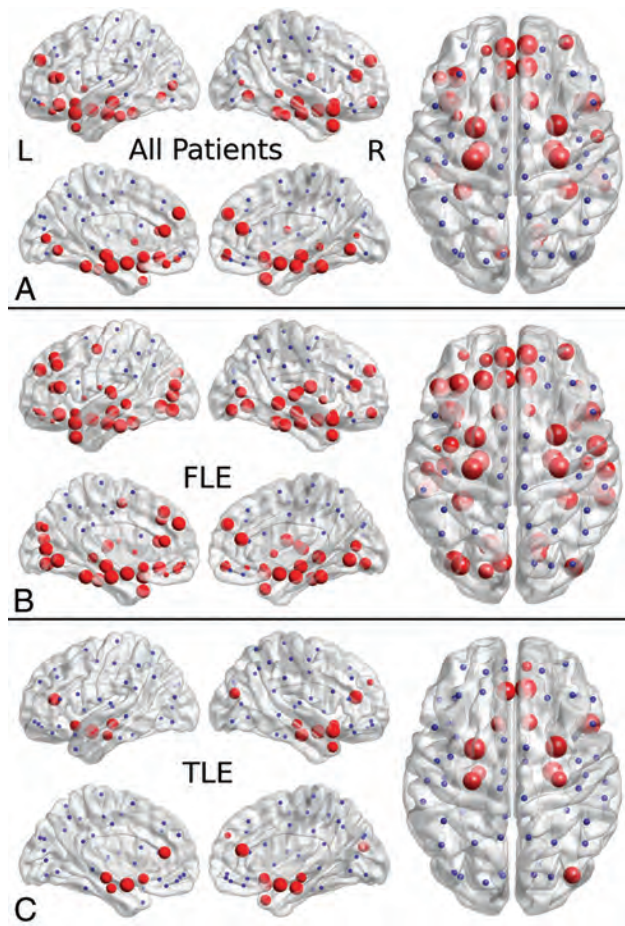


FIG 1. Reduced nodal efficiency in localization-related epilepsy (A), frontal lobe epilepsy (B), and temporal lobe epilepsy (C) in patients relative to controls. The disrupted nodes with reduced nodal efficiency are shown in red, and the unaffected nodes are shown in blue. The size of the nodes is related to the significance of between-group differences in nodal efficiency, with larger nodes representing more significant (lower P value) reduced nodal efficiency in patients relative to controls.

Network-Based Statistic

All Epilepsy versus Controls. Sixty-one connections demonstrated reduced connectivity ($P < .05$, corrected) in patients relative to controls, involving the frontal-temporal, insula-temporal, temporal-temporal, frontal-occipital, and temporal-occipital lobes (Fig 2 and On-line Table 2). None of the connections showed increased connectivity in patients relative to controls.

FLE versus Controls. Twenty connections demonstrated reduced connectivity ($P < .05$, corrected) in patients with FLE relative to controls, involving the frontal-temporal, insula-temporal, temporal-temporal, temporal-occipital, and occipital-occipital lobes.

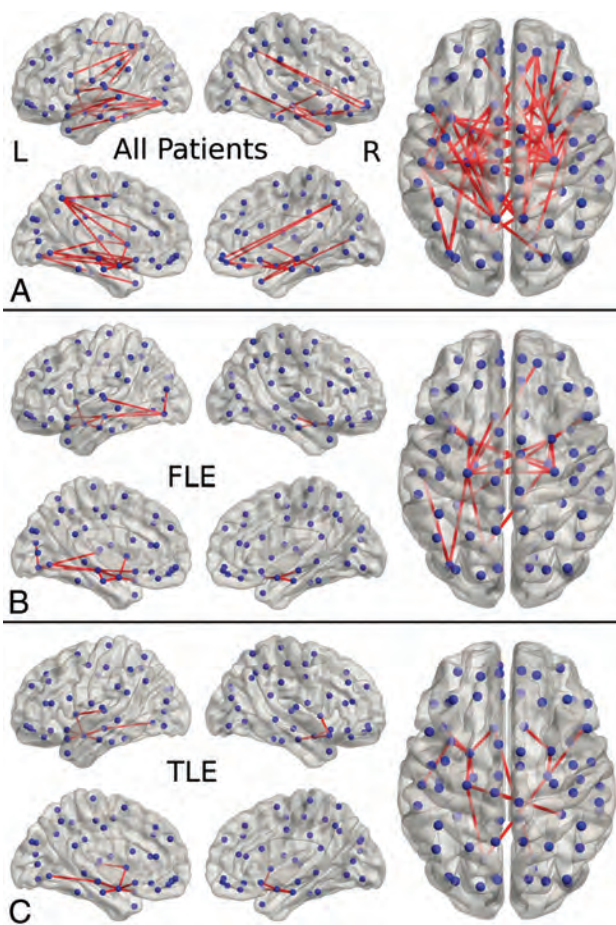


FIG 2. Results of the network-based statistical analysis of the following: A, Patients with localization-related epilepsy relative to controls, showing reduced connectivity involving the frontal-temporal, insula-temporal, temporal-temporal, frontal-occipital, and temporal-occipital lobes. B, Patients with frontal lobe epilepsy relative to controls, showing reduced connectivity involving the frontal-temporal, insula-temporal, temporal-temporal, temporal-occipital, and occipital-occipital lobes. C, Patients with temporal lobe epilepsy relative to controls, showing reduced connectivity involving the frontal-temporal, insula-temporal, temporal-temporal, temporal-occipital, and frontal-occipital lobes.

None of the connections showed increased connectivity in patients relative to controls.

TLE versus Controls. Fifteen connections demonstrated reduced connectivity ($P < .05$, corrected) in patients with TLE relative to controls, involving the frontal-temporal, insula-temporal, temporal-temporal, temporal-occipital, and frontal-occipital lobes. None of the connections showed increased connectivity in patients relative to controls.

FLE versus TLE. One hundred forty-two connections demonstrated reduced connectivity, and 26 connections showed increased connectivity ($P < .05$, corrected) in patients with FLE relative to those with TLE.

Correlation with IQ and Clinical Parameters

All Epilepsy. There was no significant correlation between global network properties and IQ, age at seizure onset, or duration of epilepsy (all, $P > .05$) in patients.

FLE. There was no significant correlation between global network properties and IQ, age at seizure onset, or duration of epilepsy (all, $P > .05$) in patients with FLE.

TLE. There was no significant correlation between global network properties and IQ, age at seizure onset, or duration of epilepsy (all, $P > .05$) in patients with TLE.

DISCUSSION

The findings of this study add to the literature by demonstrating impaired structural connectivity affecting global and regional networks and subnetworks in children with localization-related epilepsy, and the impairment in structural connectivity was extensive despite the apparent focality of the seizure disorders. To our knowledge, this is the first study that has compared the structural connectivity in FLE and TLE subgroups, and we found differences between the 2 subgroups, with more regions of reduced nodal efficiency and reduced subnetworks in FLE than in TLE. There was no significant correlation between network characteristics with IQ, age at seizure onset, or duration of epilepsy in patients.

Impairment in global functional integration, as indicated by elevated characteristic path length and decreased global efficiency, suggests that altered architecture of structural brain networks may negatively impact the ability of the brain to rapidly combine specialized information from distributed brain regions coupled with reduced efficiency of the WM networks in children with localization-related epilepsy. This reduction in integration was identified in both FLE and TLE subgroups, suggesting that impaired global functional integration is not specific to subtypes of epilepsy. There was no significant difference in the clustering coefficient between patients with epilepsy and controls, indicating that the extent of local interconnectivity in the network was preserved in the former group.²¹ Vaessen et al²⁷ also found increased path length and decreased clustering coefficient in adult patients with epilepsy with cognitive impairment relative to controls but not in those without cognitive impairment. In a subsequent study, the same authors¹⁰ showed that there were no significant differences in clustering coefficients, path length, and modularity of the WM connectivity in children with FLE relative to controls. Differences in findings could be related to different populations of FLE, with our patient population having a wider age range and possibly more severe epilepsy relative to the patients in the study by Vaessen et al.¹⁰ Disruption in the global structural network has also been identified in childhood absence epilepsy²⁸ and adults with TLE.^{29,30}

Patients with localization-related epilepsy showed reduced regional efficiency affecting multiple regions in the frontal, temporal, and occipital lobes. Liu et al³⁰ also found that adult patients with left mesial TLE have significantly reduced regional efficiency in multiple regions in the temporal, frontal, and parietal lobes. We have found more regions of reduced nodal efficiency in the FLE than in the TLE subgroup, which may be due to the rapid spread of seizure activity as a result of the extensive network of connections of the frontal lobe and more frequent seizures in FLE³¹⁻³³ or, alternatively, an inherently more extensive abnormal regional efficiency from an underlying etiology that predispose to FLE. The more extensive impaired regional networks may be associated

with poorer seizure-free surgical outcome in patients with FLE relative to those with TLE.³³

In this study, we found that children with localization-related epilepsy have extensive reduction in connectivity affecting the frontal-temporal, insula-temporal, temporal-temporal, frontal-occipital, and temporal-occipital lobes, indicating that multiple subnetworks are perturbed, despite the apparent focality of the seizure disorders. The WM tracts affected would include association fibers such as the cingulum, uncinate fasciculus, superior and inferior longitudinal fasciculus, and arcuate fasciculus, as well as the commissural fibers such as the corpus callosum, anterior commissure, and hippocampal commissure. There were more subnetworks expressing reduced structural connectivity in FLE than in TLE, probably related to the rapid spread of seizure activity and more frequent seizures in FLE.³¹⁻³³ In both subgroups, the reduced structural connectivity predominantly involved the mesial temporal and frontal basal structures compared with controls. The spread of seizures from the frontal to temporal lobes in FLE and from the temporal to frontal lobes in TLE may have contributed to reduce structural connectivity between the frontal and temporal lobes. There were more abnormal subnetworks involving the temporal than frontal lobes in those with FLE and also more abnormal subnetworks in the temporal lobes in those with FLE than in those with TLE. Although the reason for this finding is not entirely clear, reorganization of the subnetworks, due to either the spread of seizures or pre-existing abnormal subnetworks that facilitate the spread of seizures to the temporal lobes, compounded by more frequent seizures in FLE, may have contributed to the observation. Adult patients with TLE have also shown reduced structural connectivity between the temporal and frontal cortices, including the orbitofrontal cortex.^{29,30} The WM tracts connecting the frontal lobe to the temporal and occipital lobes have demonstrated smaller volumes in children with FLE compared with controls,³⁴ indicating impaired structural connections between the frontal and temporal and occipital lobes.

Vaessen et al⁴ found that the clustering coefficient was significantly positively correlated with IQ, and path length was negatively correlated with IQ in adults with cryptogenic localization-related epilepsy. In that study,⁴ the patients had a broader range of IQ scores including those who are nonimpaired (mean IQ of 97) and those who are impaired (mean IQ of 85). In a subsequent study,¹⁰ the same authors did not find an association between the clustering coefficient and path length measures of structural or functional connectivity with a computerized visual searching task in children with FLE. Liu et al³⁰ did not find any association among characteristic path length, global efficiency, and local efficiency with neurocognitive function including IQ, auditory verbal learning, and visual memory, as well as with age at seizure onset and duration of epilepsy in adults with left mesial TLE. We did not find any associations between graph network measures and IQ scores. It is possible that with the narrower range of IQs in our study population, we were not able to identify a correlation between graph measures and IQ. Alternatively, the disrupted global structural network may be associated with more complex cognitive processing beyond IQ or a computerized visual searching task.

There are several limitations in this study. We have used an

AAL template to define the ROIs, which was developed from a single adult brain. Therefore, it is possible that the ROI positioning may be less precise in children due to differences in head size. The AAL template has been used in children with absence epilepsy,²⁸ and similar finding of a disrupted global structural network was found. We have categorized the patients to the 2 main subgroups of FLE or TLE. Some heterogeneity in the epileptogenic zone was present within each subgroup, with the TLE subgroup comprising mesial and lateral TLE and the FLE subgroup comprising the epileptogenic zone in the motor or supplementary motor cortex, focal within a specific gyrus or more diffuse involvement within the frontal lobe. Due to the small sample size within each specific epileptogenic zone, we have opted to combine the patients into 2 main subgroups. Despite the heterogeneity in the subgroups, we have found differences in regional efficiency and subnetworks between FLE and TLE. Future study evaluating networks of individual patients may help clarify the differences between epileptogenic zones.

CONCLUSIONS

We found disruption in global structural networks, reduced regional efficiency in multiple lobes, and extensive reduction in subnetwork connectivity in children with localization-related epilepsy, indicating widespread disruption in structural connectivity despite the apparent focality of the seizure disorders. This disruption in structural connectivity may have been responsible for the development and propagation of seizures or may be a secondary phenomenon due to recurrent seizures reorganizing the networks or alternatively due to an underlying etiology that perturbs the neural networks and also causes seizures. Those with FLE demonstrated more areas with reduced regional efficiency and more subnetworks expressing reduced structural connectivity than did those with TLE. Future study evaluating networks of individual patients may help clarify the nuances of regional networks and subnetworks for specific epileptogenic zones and the implications of these networks on surgical resection and outcomes. We did not find any associations between global network properties and IQ. Further studies of patients with a wider range of IQs and assessing more complex cognitive function are needed to evaluate the relation between measures of global network properties and cognitive function.

Disclosures: Elysa Widjaja—RELATED: Grant: SickKids Foundation/Canadian Institutes of Health Research, Institute of Human Development, Child and Youth Health*; Derek Harwood Nash Chair fund*; UNRELATED: Grants/Grants Pending: Canadian Institute of Health Research,* Ontario Brain Institute.* *Money paid to the institution.

REFERENCES

1. Spencer SS. **Neural networks in human epilepsy: evidence of and implications for treatment.** *Epilepsia* 2002;43:219–27
2. Widjaja E, Zamyadi M, Raybaud C, et al. **Impaired default mode network on resting-state fMRI in children with medically refractory epilepsy.** *AJNR Am J Neuroradiol* 2013;34:552–57
3. Widjaja E, Zamyadi M, Raybaud C, et al. **Abnormal functional network connectivity among resting-state networks in children with frontal lobe epilepsy.** *AJNR Am J Neuroradiol* 2013;34:2386–92
4. Vaessen MJ, Jansen JF, Vlooswijk MC, et al. **White matter network abnormalities are associated with cognitive decline in chronic epilepsy.** *Cereb Cortex* 2012;22:2139–47

5. Widjaja E, Skocic J, Go C, et al. **Abnormal white matter correlates with neuropsychological impairment in children with localization-related epilepsy.** *Epilepsia* 2013;54:1065–73
6. Widjaja E, Kis A, Go C, et al. **Bilateral white matter abnormality in children with frontal lobe epilepsy.** *Epilepsy Res* 2014;108:289–94
7. Nilsson D, Go C, Rutka JT, et al. **Bilateral diffusion tensor abnormalities of temporal lobe and cingulate gyrus white matter in children with temporal lobe epilepsy.** *Epilepsy Res* 2008;81:128–35
8. Kim H, Harrison A, Kankirawatana P, et al. **Major white matter fiber changes in medically intractable neocortical epilepsy in children: a diffusion tensor imaging study.** *Epilepsy Res* 2013;103:211–20
9. Holt RL, Provenzale JM, Veerapandiyani A, et al. **Structural connectivity of the frontal lobe in children with drug-resistant partial epilepsy.** *Epilepsy Behav* 2011;21:65–70
10. Vaessen MJ, Jansen JF, Braakman HM, et al. **Functional and structural network impairment in childhood frontal lobe epilepsy.** *PLoS One* 2014;9:e90068
11. Jenkinson M, Smith S. **A global optimisation method for robust affine registration of brain images.** *Med Image Anal* 2001;5:143–56
12. Vaessen MJ, Hofman PA, Tijssen HN, et al. **The effect and reproducibility of different clinical DTI gradient sets on small world brain connectivity measures.** *Neuroimage* 2010;51:1106–16
13. Zhang Y, Brady M, Smith S. **Segmentation of brain MR images through a hidden Markov random field model and the expectation-maximization algorithm.** *IEEE Trans Med Imaging* 2001;20:45–57
14. Cook PA, Bai Y, Nedjati-Gilani S, et al. **Camino: open-source diffusion-MRI reconstruction and processing.** In: *Proceedings of the 14th Scientific Meeting of the International Society for Magnetic Resonance in Medicine*, Seattle, Washington. May 6–12, 2006:2759
15. Friman O, Farneback G, Westin CF. **A Bayesian approach for stochastic white matter tractography.** *IEEE Trans Med Imaging* 2006;25:965–78
16. Tzourio-Mazoyer N, Landeau B, Papathanassiou D, et al. **Automated anatomical labeling of activations in SPM using a macroscopic anatomical parcellation of the MNI MRI single-subject brain.** *Neuroimage* 2002;15:273–89
17. Gong G, Rosa-Neto P, Carbonell F, et al. **Age- and gender-related differences in the cortical anatomical network.** *J Neurosci* 2009;29:15684–93
18. Fedorov A, Beichel R, Kalpathy-Cramer J, et al. **3D Slicer as an image computing platform for the Quantitative Imaging Network.** *Magn Reson Imaging* 2012;30:1323–41
19. Cao Q, Shu N, An L, et al. **Probabilistic diffusion tractography and graph theory analysis reveal abnormal white matter structural connectivity networks in drug-naive boys with attention deficit/hyperactivity disorder.** *J Neurosci* 2013;33:10676–87
20. Rubinov M, Sporns O. **Complex network measures of brain connectivity: uses and interpretations.** *Neuroimage* 2010;52:1059–69
21. Watts DJ, Strogatz SH. **Collective dynamics of ‘small-world’ networks.** *Nature* 1998;393:440–42
22. Achard S, Bullmore E. **Efficiency and cost of economical brain functional networks.** *PLoS Comput Biol* 2007;3:e17
23. Zalesky A, Fornito A, Bullmore ET. **Network-based statistic: identifying differences in brain networks.** *Neuroimage* 2010;53:1197–207
24. Zhang J, Wang J, Wu Q, et al. **Disrupted brain connectivity networks in drug-naive, first-episode major depressive disorder.** *Biol Psychiatry* 2011;70:334–42
25. Bai F, Shu N, Yuan Y, et al. **Topologically convergent and divergent structural connectivity patterns between patients with remitted geriatric depression and amnesic mild cognitive impairment.** *J Neurosci* 2012;32:4307–18
26. Zalesky A, Fornito A, Seal ML, et al. **Disrupted axonal fiber connectivity in schizophrenia.** *Biol Psychiatry* 2011;69:80–89
27. Vaessen MJ, Braakman HM, Heerink JS, et al. **Abnormal modular organization of functional networks in cognitively impaired children with frontal lobe epilepsy.** *Cereb Cortex* 2013;23:1997–2006
28. Xue K, Luo C, Zhang D, et al. **Diffusion tensor tractography reveals disrupted structural connectivity in childhood absence epilepsy.** *Epilepsy Res* 2014;108:125–38
29. DeSalvo MN, Douw L, Tanaka N, et al. **Altered structural connectome in temporal lobe epilepsy.** *Radiology* 2014;270:842–48
30. Liu M, Chen Z, Beaulieu C, et al. **Disrupted anatomic white matter network in left mesial temporal lobe epilepsy.** *Epilepsia* 2014;55:674–82
31. Talairach J, Tournoux P, Musolino A, et al. **Stereotaxic exploration in frontal epilepsy.** *Adv Neurol* 1992;57:651–88
32. Harvey AS, Hopkins IJ, Bowe JM, et al. **Frontal lobe epilepsy: clinical seizure characteristics and localization with ictal 99mTc-HMPAO SPECT.** *Neurology* 1993;43:1966–80
33. Lawson JA, Cook MJ, Vogrin S, et al. **Clinical, EEG, and quantitative MRI differences in pediatric frontal and temporal lobe epilepsy.** *Neurology* 2002;58:723–29
34. Braakman HM, Vaessen MJ, Jansen JF, et al. **Pediatric frontal lobe epilepsy: white matter abnormalities and cognitive impairment.** *Acta Neurol Scand* 2014;129:252–62

Assessment of MRI-Based Automated Fetal Cerebral Cortical Folding Measures in Prediction of Gestational Age in the Third Trimester

J. Wu, S.P. Awate, D.J. Licht, C. Clouchoux, A.J. du Plessis, B.B. Avants, A. Vossough, J.C. Gee, and C. Limperopoulos



ABSTRACT

BACKGROUND AND PURPOSE: Traditional methods of dating a pregnancy based on history or sonographic assessment have a large variation in the third trimester. We aimed to assess the ability of various quantitative measures of brain cortical folding on MR imaging in determining fetal gestational age in the third trimester.

MATERIALS AND METHODS: We evaluated 8 different quantitative cortical folding measures to predict gestational age in 33 healthy fetuses by using T2-weighted fetal MR imaging. We compared the accuracy of the prediction of gestational age by these cortical folding measures with the accuracy of prediction by brain volume measurement and by a previously reported semiquantitative visual scale of brain maturity. Regression models were constructed, and measurement biases and variances were determined via a cross-validation procedure.

RESULTS: The cortical folding measures are accurate in the estimation and prediction of gestational age (mean of the absolute error, 0.43 ± 0.45 weeks) and perform better than ($P = .024$) brain volume (mean of the absolute error, 0.72 ± 0.61 weeks) or sonography measures (SDs approximately 1.5 weeks, as reported in literature). Prediction accuracy is comparable with that of the semiquantitative visual assessment score (mean, 0.57 ± 0.41 weeks).

CONCLUSIONS: Quantitative cortical folding measures such as global average curvedness can be an accurate and reliable estimator of gestational age and brain maturity for healthy fetuses in the third trimester and have the potential to be an indicator of brain-growth delays for at-risk fetuses and preterm neonates.

ABBREVIATIONS: AC = average curvedness; FTMS = fetal total maturation score; GA = gestational age

Gestational age (GA) estimation for unborn babies is crucial to any assessment of pregnancy, fetal development, and neonatal care. Obstetricians routinely use the last menstrual period to estimate the beginning date of gestation and calculate the esti-

mated date of delivery. However, it has been reported that 20%–40% of women could not determine their last menstrual period with certainty due to various reasons such as bleeding in the first trimester and pregnancy following the use of oral contraceptives.¹ Fetal growth measurements from sonography biometry are used to estimate the gestation length, if one assumes a normative growth trajectory at the time of the examination.² The most widely used fetal biometrics assessed in the first 2 trimesters³ have been shown to be more accurate than last menstrual period-based estimates.^{4,5} Consequently, sonographic measurements are recommended in place of the last menstrual period if there is a large discrepancy between the last menstrual period and sonography-based estimates before 20 weeks of gestation.⁶

Sonography-based GA estimation in the third trimester (26 weeks to birth) should be interpreted with great caution due to remarkably increased variability in organ size in the later stages of pregnancy.^{3,7} For example, biparietal diameter varies by approximately 7 days, 14 days, and 21–28 days when measured at 14–20 weeks, 21–30 weeks, and after 30 weeks GA, respectively.⁷ Consequently, it has been recommended that menstrual dates be used to

Received August 18, 2014; accepted after revision December 20.

From the Department of Radiology (J.W., B.B.A., A.V., J.C.G.), Perelman School of Medicine, University of Pennsylvania, Philadelphia, Pennsylvania; Department of Computer Science and Engineering (S.P.A.), Indian Institute of Technology Bombay, Mumbai, India; Neurovascular Imaging Lab (D.J.L.), Children's Hospital of Philadelphia, Philadelphia, Pennsylvania; Advanced Pediatric Brain Imaging Research Laboratory (C.C., C.L.), Children's National Medical Center, Washington, DC; and Departments of Neurology, Radiology, and Pediatrics (C.C., A.J.d.P., C.L.), George Washington University School of Medicine and Health Sciences, Washington, DC.

This work was supported by the National Institutes of Health (NS065347, DA022807 and DA014129), the Canadian Institutes of Health Research (MOP-81116), and the SickKids Foundation (XG 06-069).

J.C. Gee and C. Limperopoulos are co-senior authors and contributed equally to this article.

Please address correspondence to Jue Wu, PhD, University of Pennsylvania, 3600 Market St, Suite 370, Philadelphia, PA 19104; e-mail: woojohn911@gmail.com

 Indicates open access to non-subscribers at www.ajnr.org

 Indicates article with supplemental on-line photo.

<http://dx.doi.org/10.3174/ajnr.A4357>

establish GA if it is within the error range of these biometric markers during the third trimester.³

This limitation in sonographic assessment stems mostly from the inherent variability of organ size and the intrinsic signal properties of ultrasonography. In this article, we attempt to address this important problem from a different perspective—brain cortical folding. During the second half of gestation, the cortical folding of the neocortex initiates at around 20 weeks and drastically changes the brain shape throughout the third trimester, from a largely smooth surface to a complex convoluted one.⁸ The process appears to be genetically controlled and largely consistent across the healthy population.^{9,10} Primary, secondary, and tertiary gyri sulci emerge in order, and newly evolved sulci related to higher functions, such as auditory, visual, and linguistic functions, appear later than phylogenetically more primitive allocortical folding, such as the hippocampus and olfactory sulcus.⁸ Several MR imaging studies on healthy fetuses have found a linear relation between folding measures and GA.^{11,12} There was evidence that female and male preterm neonates did not differ in folding while differing in size.¹³ Data also showed that the sulcal depth of a folding measure was approximately 5% of the mean of the measure in healthy preterm neonates at around 32 weeks' GA.¹⁴ In comparison, the sonography-based measure, biparietal diameter, has a sulcal depth (1.5 mm) equal to 16% of the average biparietal diameter (9 mm) at 30–36 weeks' GA.³ The lower variance of folding when controlled for GA potentially leads to a better estimator of GA than sonography in late gestation.

MATERIALS AND METHODS

Subjects and Data Acquisition

The study cohort included healthy pregnant women who were recruited in a previously published study with local institutional review board approval.¹⁵ Exclusion criteria included GA of >36 completed weeks, multiple gestations, congenital infection, gestational diabetes, or any maternal contraindication to MR imaging. We also excluded fetuses with sonographic findings of dysmorphic features, dysgenic brain lesions, or anomalies of other organ systems.¹⁵ Written informed consent from mothers was obtained according to a protocol approved by Boston Children's Hospital Committee for Clinical Investigation, and the study was compliant with the Health Insurance Portability and Accountability Act. A cohort of 33 healthy fetuses with high-resolution reconstructed MRI was included in this study, of which 10 subjects were female and 23 were male. The cohort has been previously reported in studies of normative brain development¹⁶ but has not been used to estimate gestational age.

The mean GA at the time of MR imaging was 29.1 ± 2.8 weeks (range, 25.2–35.4 weeks). Estimated gestational age was based on maternal dates and first-trimester sonography measurements, if available, by the pregnant mother's referring obstetrician. The working gestational age as determined by the referring obstetrician at the time of MR imaging was used. All fetal MR imaging studies were performed on a 1.5T scanner (Achieva; Philips Healthcare, Best, the Netherlands) and a 5-channel phased array cardiac coil. Multiplanar single-shot turbo spin-echo imaging was performed (TE = 120 ms, TR = 12,500 ms, 0.625 signal averages, FOV = 330 mm, section thickness = 2-mm, no intersection gap,

acquisition matrix = 256×204 , acquisition time = 25–55 seconds). All fetal and postnatal MR imaging findings were normal. The Vineland Adaptive Behavior Scale¹⁷ used to assess functional performance in communication, daily living, socialization, and motor skills was age-appropriate in the subjects between 18 and 24 months of age.

Motion Correction and Manual Brain Segmentation

Spontaneous fetal motion during scanning poses a challenge for the computation of 3D measures. The imaging data used in this study were reconstructed to isotropic volumes (1 mm³) on the basis of a superresolution method.¹⁸ Other methods for correcting motion in fetal MR imaging exist,^{19,20} but we did not compare the differences among them in this article.

We created a manual mask of the intracranial region for each subject. The mask excluded all the maternal tissue and nonbrain tissue of the fetus. In addition, we also defined a cerebral mask for each subject, which was constructed manually by tracing the interface between developing white matter and cortical gray matter. The mask region excluded the cerebellum and brain stem. The boundary of the mask was used as a representation of the cortex. This mask was also used to calculate the brain/cerebral volume of the subject. Masks for the cortical lobes (frontal, temporal, parietal, occipital, and insular) and left and right hemispheres were generated by registering subject images with a manually labeled template. This template was based on a publicly available atlas, brain-development.org (www.brain-development.org),²¹ which was an average of preterm infants at a postmenstrual age of 29 weeks. Manual tracings of lobes and hemispheres were performed and visually inspected in the free software ITK-SNAP (www.itksnap.org).²²

Cortical Folding Measures

We implemented and evaluated 8 different quantitative measures of cortical folding that have been used in the literature.^{23–26} These were average curvedness (AC), Gaussian curvature (L^2) norm, mean curvature L^2 norm, intrinsic curvature index, extrinsic curvature index, convexity ratio, isoperimetric index, and average sulcal depth. The convexity ratio and isoperimetric index are globally defined, while the other measures are an average over each point on the cortex. Gaussian curvature L^2 norm, intrinsic curvature index, mean curvature L^2 norm, convexity ratio, isoperimetric index, and AC are all invariant to translation, rotation, and scaling of the cortical surface.^{25,27} The extrinsic curvature index is invariant to translation and scaling, but rotation may cause it to change sign. The convexity ratio is also shown to be area-independent (ie, invariant to the change of surface area in question).²⁶

The implementation of the folding measure computations was based on a previously established processing pipeline designed for pediatric data.^{27,28} The pipeline took in the cerebral mask and upsampled it to a higher resolution (eg, 0.45^3mm^3). Our numeric scheme for computing the quantitative folding measures depended on reliably estimating the cortical surface and sampling it fairly uniformly. The adopted numeric scheme did so by obtaining an implicit surface parameterization of the cortical surface, as a level set of a distance transform on a Cartesian grid. We used the

Regression correlation between brain measures and GA^a

Measure	AC	EC	GC	IC	MC	CR	IP	SD	BVol
Linear r	0.98	-0.96	0.97	0.98	0.98	0.95	0.95	0.97	0.95
Poly. r	0.98	-0.97	0.98	0.98	0.98	0.96	0.96	0.97	0.96
R to fTMS	0.98	-0.97	0.98	0.98	0.98	0.95	0.96	0.98	0.94

Note:—EC indicates extrinsic curvature index; GC, Gaussian curvature L² norm; IC, intrinsic curvature index; MC, mean curvature L² norm; CR, convexity ratio; IP, isoperimetric index; SD, sulcal depth; BVol, brain volume; r (R), regression; Poly., polynomial.

^a The first and second rows are correlation coefficients between each measure and GA in linear and polynomial regressions. The third row is the linear correlation coefficients between folding measures and total maturation score.

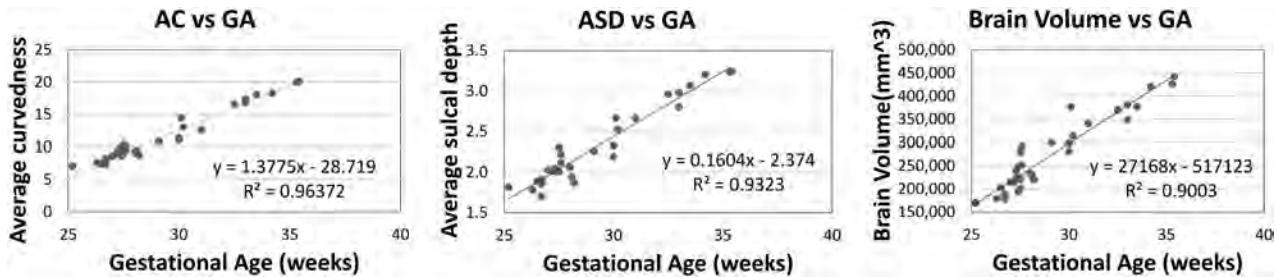


FIG 1. Bivariate plots of 2 folding measures and brain volume against GA. Squared correlation coefficients r^2 , linear regression lines, and their equations are shown on the plots.

sparse field level set representation, which was numerically efficient, on a grid of isotropic voxels with submillimeter dimension. A previous article²⁸ validated such a scheme for adult brains as well, which exhibited more complex and more folded cortical surfaces than fetal brains, thus indicating the suitability of the scheme for fetal brains. The flowchart of the processing pipeline is shown in On-line Fig 1.

Statistical Analysis

To examine whether the various cortical folding measures provided more information about GA than brain volume, we constructed a linear model with brain volume and each folding measure as 2 predictors of GA and compared the model with the reduced model with only brain volume as the predictor of GA. More specifically, we tested the null hypothesis by using analysis of variance that the following 2 linear regressions are equal:

- 1) $GA = a_0 + a_1 \times (\text{Brain Volume}) + a_2 \times (\text{Folding Measure}),$
- 2) $GA = a_0 + a_1 \times (\text{Brain Volume}).$

To assess the validity to estimate GA across various samples, we adopted a leave-k-out analysis, where k out of n subjects were chosen as a test set and the regression was performed on the remaining n-k subjects as the training set. Note that when k = 1, this cross-validation degenerates to the commonly used leave-one-out analysis scheme. A prediction error was calculated by averaging the absolute difference between the predicted GA and the known GA in the test set. For a fixed k > 1, a random test set was generated k × n times. The differences in the mean and variance of the absolute error of predicted GA were assessed by t test, F-test, and the Levene test.²⁹

To further examine the biases and variances related to the curvedness and volume-based predictions, we performed statistical tests on signed prediction errors in addition to absolute prediction errors. Bias was defined as the mean of the signed errors

for a prediction. Variance referred to the variance of the predicted GA. The difference in biases was assessed by t test, and the difference in variances was assessed by the F-test and Levene test.

RESULTS

Relations between Folding and GA

A progressive increment of cortical folding complexity can be observed with increasing GA (On-line Fig 2). The Pearson correlation coefficient (r) between each individual quantitative cortical folding measure and GA, which is shown in the Table, indicates that these measures have a very strong linear relation with GA ($P < 10^{-10}$ for all measures). For example, average curvedness and average sulcal depth accounted for 96% and 93% of the variance of GA as calculated by r^2 in the data. Three scatterplots with regression lines are shown in Fig 1. Polynomial fitting suggested that there was some slight degree of nonlinear correlation between the folding measures and age, but linear regression appeared to fit the current data well. We also examined the folding complexity in the left and right hemispheres separately and did not find significant asymmetries in terms of hemispheric folding (see left subfigure in On-line Fig 3). When the cerebrum was divided into 5 lobes, we found that the frontal lobe had the largest rate of folding, while the insular region demonstrated the lowest rate of folding (see right subfigure in On-line Fig 3).

The null hypothesis that $a_2 = 0$ in the linear model (equation 1) was rejected by the F-test ($F > 18.10, P < .0002$), and the first regression was significantly better than the second regression for any folding measure. This finding indicates that the quantitative cortical folding measures add additional and complementary information to brain volume in the prediction equation for GA. In contrast, when we swapped folding measures with brain volume in the equations, the null hypothesis was not rejected ($F < 2.34, P > .13$) for AC, Gaussian curvature L² norm, mean curvature L² norm, intrinsic curvature index, or sulcal depth. The phenomena implied that some of these folding measures could completely replace brain volume measurements when it

came to predicting GA because brain volume provided no extra information about GA compared with AC, Gaussian curvature L^2 norm, mean curvature L^2 norm, intrinsic curvature index, or sulcal depth.

An independent assessment of brain maturity in the same dataset was performed by a pediatric neurologist and a pediatric neuroradiologist (D.J.L. and A.V.), each with 8 years of fetal MR imaging experience. A single fetal total maturation score (fTMS) was calculated by summing up 6 semiquantitative subscores characterizing various visual sulcation observations, the extent and location of myelination, and evolution of the germinal matrix.¹⁶ We found that the folding measures obtained by the proposed framework were in high agreement with the average visual fTMS (Fig 2).

Prediction of GA

The resultant predictions by quantitative folding measures, brain volume, and the visual fTMS assessment in a leave-one-out scheme are shown in Fig 3. The AC-based prediction appears closer to true GA than brain volume or the fTMS-based prediction. The final errors (averaged across the $k \times n$ test sets) based on different sizes of the training set are shown in On-line Fig 4. It can be observed that using the cortical folding measure to predict GA always resulted in higher prediction accuracy (ie, smaller errors) than using brain volume. Leave-one-out cross-validation showed that the mean of absolute errors is 0.43 ± 0.45 weeks (range, 0.01–1.24 weeks) for AC and 0.72 ± 0.61 weeks (range, 0.02–2.63 weeks) for brain volume. The difference between the 2 prediction

errors was statistically significant ($P = .024$). The difference between the 2 variances of the 2 predictions was also significant based on an F -test ($P = .002$), borderline on a Levene test ($P = .06$) for training size equal to 32, and significant on a Levene test ($P < 10^{-4}$) for any other training size larger than 20. The curvedness predictor also had a slightly lower absolute error than the fTMS predictor (mean, 0.57 ± 0.41 weeks), but the difference was not significant.

The difference between the biases from curvedness and volume-based predictions was insignificant on the basis of a 2-sample t test when the training set size was reasonably large (>20). Regarding variance, the curvedness predictor had consistently smaller variance than the volume predictor (about half) when the training set size was large (>20). The 2-sample F -test showed that the variance difference between curvedness and volume predictors was significant ($P = .0041$, for the largest training size 32; for smaller training sizes, the significance was higher with a smaller P value). The Levene test also showed that the variance difference was significant ($L = 4.380$, $P = .040$, for training size 32; for smaller training sizes, the significance was higher). In summary, the biases of the 2 predictors are comparable, and the cortical folding predictor has a smaller variance than the volume predictor, which means the former is more reliable than the latter in the prediction of GA. The quantitative cortical folding predictor and visual fTMS predictor are close in both bias and variance.

DISCUSSION

To our knowledge, this article is among the first works in the literature to use various MR imaging–based computational cortical folding measures as a means to estimate GA in healthy human fetuses. All the previous studies on fetal MR imaging^{11,12,25,30-32} have regarded clinically acquired GA as an independent variable or a known reference point as opposed to a dependent variable to be predicted or estimated. The current work is also unique in the wide GA range of the cohort, which includes the period close to full term (33–36 weeks), when it is more difficult to date pregnancy.

Many studies have characterized cortical folding in preterm neonates.^{13,26,33-35} Although premature neonates are often studied as a surrogate of prenatal development of full-term infants, preterm neonates are exposed to extrauterine stressors and risk

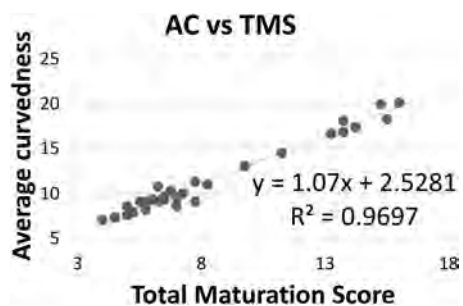


FIG 2. The plot of automatically computed average curvedness against the average total maturation score obtained by 1 pediatric neurologist and 1 pediatric neuroradiologist for the 33 healthy fetuses.

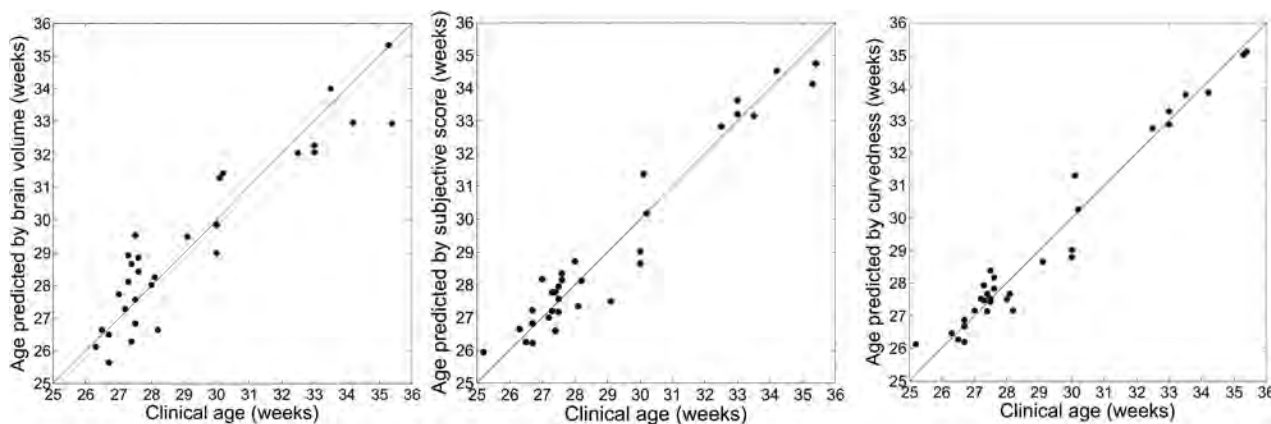


FIG 3. The left panel is a plot of GA predicted by brain volume (fTMS, AC) versus clinically estimated GA. The line in the plot represents a perfect match between the 2 variables. All the predictions were performed in a leave-one-out scheme.

factors, which often make their neurodevelopment dissimilar to normal intrauterine development.¹⁴

On the basis of the data and results, it became clear that linearity was sufficient to account for the relation between GA and folding. More than 90% of variance in gestational age can be explained by the variance in a cortical folding measure. The calculation of folding measures does not use the information of gestational age at all, so it is unlikely that the linearity manifested in the results comes from a bias in the processing that favors a linear model or any other model between GA and folding.

In embryology, GA is defined as postconception time, but in human obstetrics, it is often defined as the time since the first day of the mother's last menstrual period. The latter is approximately 2 weeks longer than the former. In this article, we used the definition of GA involving the last menstrual period, which is the common clinical practice. It is possible that there were errors in the estimation of true GA despite the best clinical practice. The potential inaccuracy of ground truth GA in these data, however, does not greatly diminish the value of the results because the folding process reflects an aspect of brain development that is complementary to size increase, which is the basis of clinical GA estimation. The fact that 2 independently obtained measures of GA (folding-based and size) are so consistent with each other indicates the improbability that either measure is erroneous. The chance that both measures are very imprecise but in high agreement is slim, if one assumes that the errors are random and independent.

The sample size of the current study is relatively small and may reduce the generalizability of the results. When dealing with a small sample size, it is important not to overfit a model by creating too many features/measures or by using a complex type of regression. By using a single whole-brain cortical folding measure and simple linear regression, we sought to avoid the overfitting problem, in which the agreement between the model and data is increased but the generalizability to more data is decreased. Linear regression strikes a good balance between the goodness of fit in the current data and the generalizability to unseen datasets. Although cortical folding may be nonlinear in its entire course, it can be approximated by a linear process within the gestational period of interest (25–36 weeks), as demonstrated in other independent studies.^{12,13,30} Another limitation of this study is that there could be some “healthy” fetuses who are later found not healthy because abnormalities were not obvious at short-term follow-ups.

CONCLUSIONS

This article demonstrated that automated quantitative measurement of fetal cerebral cortical folding can be used to estimate gestational age in the third trimester with high accuracy and reliability on a single-case basis by using clinical fetal MR imaging. The folding measures accurately predict the gestational age of a fetus in the third trimester (mean error, 0.43 ± 0.45 weeks), which can be a major challenge for sonography-based measures. Improved accuracy and reliability in GA estimation in late gestation can have a positive impact on prenatal care for underserved populations. It is also important to be able to estimate the fetal brain maturity because chronologic GA is no longer a suitable gauge for

fetuses with aberrant neurodevelopment later in gestation. Cortical folding measurement offers a potential way to accomplish that as well.

Disclosures: James C. Gee—RELATED: Grant: National Institutes of Health,* University of Pennsylvania*; UNRELATED: Consultancy: University of Texas Southwestern Medical Center, Comments: consultant on National Institutes of Health-funded project; Grants/Grants Pending: National Institutes of Health*; Stock/Stock Options: part of retirement planning; Travel/Accommodations/Meeting Expenses Unrelated to Activities Listed: advisory board meetings, international task force meetings, academic lectures, grant review panels. *Money paid to the institution.

REFERENCES

1. Dewhurst CJ, Beazley JM, Campbell S. **Assessment of fetal maturity and dysmaturity.** *Am J Obstet Gynecol* 1972;113:141–49
2. Drumm JE, Clinch J, MacKenzie G. **The ultrasonic measurement of fetal crown-rump length as a method of assessing gestational age.** *Br J Obstet Gynaecol* 1976;83:417–21
3. MacGregor SN, Sabbagha RE. **Assessment of gestational age by ultrasound.** *The Global Library of Women's Medicine*. 2008. http://www.glowm.com/section_view/heading/Assessment%20of%20Gestational%20Age%20by%20Ultrasound/item/206. Accessed April 12, 2013
4. Mongelli M, Wilcox M, Gardosi J. **Estimating the date of confinement: ultrasonographic biometry versus certain menstrual dates.** *Am J Obstet Gynecol* 1996;174:278–81
5. Bennett KA, Crane JMG, O'shea P, et al. **First trimester ultrasound screening is effective in reducing postterm labor induction rates: a randomized controlled trial.** *Am J Obstet Gynecol* 2004;190:1077–81
6. American College of Obstetricians and Gynecologists. **ACOG Practice Bulletin No. 101: ultrasonography in pregnancy.** *Obstet Gynecol* 2009;113(2 pt 1):451–61
7. Benson CB, Doubilet PM. **Sonographic prediction of gestational age: accuracy of second- and third-trimester fetal measurements.** *AJR Am J Roentgenol* 1991;157:1275–77
8. Glenn O. **Normal development of the fetal brain by MRI.** *Semin Perinatol* 2009;33:208–19
9. Rogers J, Kochunov P, Zilles K, et al. **On the genetic architecture of cortical folding and brain volume in primates.** *Neuroimage* 2010;53:1103–08
10. Garel C, Chantrel E, Brisse H, et al. **Fetal cerebral cortex: normal gestational landmarks identified using prenatal MR imaging.** *AJNR Am J Neuroradiol* 2001;22:184–89
11. Habas P, Scott J, Roosta A, et al. **Early folding patterns and asymmetries of the normal human brain detected from in utero MRI.** *Cereb Cortex* 2012;22:13–25
12. Hu HH, Hung CI, Wu YT, et al. **Regional quantification of developing human cortical shape with a three-dimensional surface-based magnetic resonance imaging analysis in utero.** *Eur J Neurosci* 2011;34:1310–19
13. Dubois J, Benders M, Cachia A, et al. **Mapping the early cortical folding process in the preterm newborn brain.** *Cereb Cortex* 2008;18:1444–54
14. Dubois J, Benders M, Borradori-Tolsa C, et al. **Primary cortical folding in the human newborn: an early marker of later functional development.** *Brain* 2008;131:2028–41
15. Limperopoulos C, Tworetzky W, McElhinney D, et al. **Brain volume and metabolism in fetuses with congenital heart disease: evaluation with quantitative magnetic resonance imaging and spectroscopy.** *Circulation* 2010;121:26–33
16. Vossough A, Limperopoulos C, Putt ME, et al. **Development and validation of a semiquantitative brain maturation score on fetal MRI: initial results.** *Radiology* 2013;268:200–07
17. Sparrow S, Cicchetti D, Balla D. *Vineland Adaptive Behavioral Scales (Vineland II)*. Circle Pines: AGS Publishing; 2005
18. Gholipour A, Estroff JA, Warfield SK. **Robust super-resolution vol-**

- ume reconstruction from slice acquisitions: application to fetal brain MRI. *IEEE Trans Med Imaging* 2010;29:1739–58
19. Jiang S, Xue H, Glover A, et al. MRI of moving subjects using multislice snapshot images with volume reconstruction (SVR): application to fetal, neonatal, and adult brain studies. *IEEE Trans Med Imaging* 2007;26:967–80
 20. Kim K, Habas P, Rousseau F, et al. Intersection based motion correction of multislice MRI for 3-D in utero fetal brain image formation. *IEEE Trans Med Imaging* 2010;29:146–58
 21. Kuklisova-Murgasova M, Aljabar P, Srinivasan L, et al. A dynamic 4D probabilistic atlas of the developing brain. *Neuroimage* 2011;54:2750–63
 22. Yushkevich PA, Piven J, Hazlett HC, et al. User-guided 3D active contour segmentation of anatomical structures: significantly improved efficiency and reliability. *Neuroimage* 2006;31:1116–28
 23. Koenderink JJ, van Doorn AJ. Surface shape and curvature scales. *Image and Vision Computing* 1992;10:557–65
 24. Van Essen DV, Drury H. Structural and functional analyses of human cerebral cortex using a surface-based atlas. *J Neurosci* 1997;17:7079–102
 25. Batchelor P, Castellano-Smith A, Hill D, et al. Measures of folding applied to the development of the human fetal brain. *IEEE Trans Med Imaging* 2002;21:953–65
 26. Rodriguez-Carranza C, Mukherjee P, Vigneron D, et al. A framework for in vivo quantification of regional brain folding in premature neonates. *Neuroimage* 2008;41:462–78
 27. Awate S, Win L, Yushkevich P, et al. 3D cerebral cortical morphometry in autism: increased folding in children and adolescents in frontal, parietal, and temporal lobes. *Med Image Comput Comput Assist Interv* 2008;11(pt 1):559–67
 28. Awate SP, Yushkevich PA, Song Z, et al. Cerebral cortical folding analysis with multivariate modeling and testing: studies on gender differences and neonatal development. *Neuroimage* 2010;53:450–59
 29. Levene H. Robust tests for equality of variances. In: Olkin I, Ghurye SG, Hoeffding W, et al, eds. *Contributions to Probability and Statistics: Essays in Honor of Harold Hotelling*. Stanford, CA: Stanford University Press; 1960:278–92
 30. Rajagopalan V, Scott J, Habas PA, et al. Local tissue growth patterns underlying normal fetal human brain gyrification quantified in utero. *J Neurosci* 2011;31:2878–87
 31. Hu H, Guo W, Chen H, et al. Morphological regionalization using fetal magnetic resonance images of normal developing brains. *Eur J Neurosci* 2009;29:1560–67
 32. Clouchoux C, Kudelski D, Gholipour A. Quantitative in vivo MRI measurement of cortical development in the fetus. *Brain Struct Funct* 2012;217:127–39
 33. Battin M, Maalouf E, Counsell S, et al. Magnetic resonance imaging of the brain in very preterm infants: visualization of the germinal matrix, early myelination, and cortical folding. *Pediatrics* 1998;101:957–62
 34. Deipolyi A, Mukherjee P, Gill K, et al. Comparing microstructural and macrostructural development of the cerebral cortex in premature newborns: diffusion tensor imaging versus cortical gyration. *Neuroimage* 2005;27:579–86
 35. Smyser CD, Kidokoro H, Inder TE. Magnetic resonance imaging of the brain at term equivalent age in extremely premature neonates: to scan or not to scan? *J Paediatr Child Health* 2012;48:794–800

Cranial Nerve Abnormalities in Oculo-Auriculo-Vertebral Spectrum

R. Manara, D. Brotto, S. Ghiselli, R. Mardari, I. Toldo, G. Schifano, E. Cantone, R. Bovo, and A. Martini



ABSTRACT

BACKGROUND AND PURPOSE: Cranial nerve abnormalities might be observed in hemifacial microsomia and microtia (oculo-auriculo-vertebral spectrum), but the rate, features, and relationship with functional impairment or phenotype severity have not yet been defined. This study aimed at investigating absence/asymmetry, abnormal origin, morphology and course of cranial nerves, and presence/asymmetry of the foramen ovale and inferior alveolar nerve canal in a cohort of oculo-auriculo-vertebral spectrum patients.

MATERIALS AND METHODS: Twenty-nine patients with oculo-auriculo-vertebral spectrum (mean age, 7 years; age range, 0.2–31 years; 12 females) underwent brain MR imaging, CT, and neurologic evaluation; 19 patients had a more severe phenotype (Goldenhar syndrome).

RESULTS: Cranial nerve abnormalities were detected only in patients with Goldenhar syndrome (17/19, bilaterally in 8) and were involved the second (4/19), third (1/18), fifth (11/19), sixth (8/16), seventh (11/18), and eighth (8/18) cranial nerves. Multiple cranial nerve abnormalities were common (11/17). Eleven patients showed bone foramina abnormalities. Trigeminal and facial nerve dysfunctions were common (44% and 58%, respectively), especially in patients with Goldenhar syndrome. Trigeminal abnormalities showed a good correlation with ipsilateral dysfunction ($P = .018$), which further increased when bone foramina abnormalities were included. The facial nerve showed a trend toward correlation with ipsilateral dysfunction ($P = .081$). Diplopia was found only in patients with Goldenhar syndrome and was associated with third and sixth cranial nerve abnormalities ($P = .006$).

CONCLUSIONS: Among patients with oculo-auriculo-vertebral spectrum, cranial nerve morphologic abnormalities are common, correlate with phenotype severity, and often entail a functional impairment. The spectrum of cranial nerve abnormalities appears wider than simple hypo-/aplasia and includes an anomalous cisternal course and partial/complete fusion of diverse cranial nerves.

ABBREVIATIONS: CN = cranial nerve; OAVS = oculo-auriculo-vertebral spectrum

Oculo-auriculo-vertebral spectrum (OAVS) (Online Mendelian Inheritance in Man, 164210)¹ is a rare heterogeneous congenital condition (incidence, 1:3500–5600 live births; male/female ratio, 3:2),^{2–4} in which the head structures originating from the first and second pharyngeal arches are incompletely developed on 1 (85% of cases) or both sides.^{3,5} The disease mostly

results in ear (microtia) and jaw (hemifacial microsomia) abnormalities (On-line Fig 1). Nonetheless, the abnormality spectrum might be fairly wide, from mild external and medium ear involvement or isolated facial asymmetry to anotia with complex facial deformity. The most severe cases also present with eye or spine involvement and are known as Goldenhar syndrome from the French ophthalmologist who first described the syndrome in 1952.⁶ Familial history suggestive of both autosomal recessive and dominant inheritance has been reported, and genes on chromosomes 5, 12, 14, and 22 have been implicated.^{7–10} However, most cases of OAVS are sporadic and without a known etiology. Abnormal embryonic vascular supply,¹¹ hematomas, and drug use during the early phases of gestation have been reported to cause the disruption of mesodermal migration, leading to defective formation of bone and soft-tissue structures.¹²

Most interesting, a few case reports and small series studies have shown a concomitant impairment of cranial nerves (CNs),^{13–26} highlighting the possible involvement of neural struc-

Received October 7, 2014; accepted after revision November 29.

From Neuroradiology (R.Manara), University of Salerno, Salerno Italy; Departments of Neuroscience (D.B., S.G., G.S., R.B., A.M.) and Pediatrics (I.T.), University of Padova, Padova, Italy; Neuroradiology (R.Mardari), University Hospital of Padova, Padova, Italy; and Ear Nose and Throat Section (E.C.), Department of Neurosciences, "Federico II" University, Napoli, Italy.

Renzo Manara and Davide Brotto contributed equally to the study and should be considered co-first authors.

Please address correspondence to Renzo Manara, MD, Neuroradiology, University of Salerno, Via S Allende 1, 89081, Salerno, Italy; e-mail: rmanara@unisa.it



Indicates article with supplemental on-line tables.



Indicates article with supplemental on-line photo.

<http://dx.doi.org/10.3174/ajnr.A4273>

tures in OAVS and addressing its potentially relevant clinical impact. To date, the underlying anatomic and structural CN abnormalities have been poorly investigated because the available data rely on anecdotal postmortem examination¹⁷ or neuroimaging findings.¹⁹ Additionally, the overall frequency of CN abnormalities, their association with CN dysfunction, and the relationship with the OAVS phenotype severity have not yet been defined, to our knowledge.

In the past few years, MR imaging has become a powerful tool for investigating *in vivo* the cisternal segment of the CNs. With routinely available 1.5T MR imaging scanners and dedicated high-resolution sequences, it is possible to verify the presence and characterize the morphology, diameter, and cisternal course of most CNs. CN MR imaging evaluation has, therefore, become helpful for diagnosing several conditions such as Kallmann syndrome, optic neuritis, septo-optic dysplasia, neurovascular conflicts, and so forth. Moreover, the evaluation of the intrameatal branches of CN VIII is included in the diagnostic work-up of implant planning in patients with congenital profound hearing loss. Besides, because skull base foramina and bone canal development is induced by the presence of the corresponding CN branch,²⁷ CN abnormalities might be also indirectly inferred by bone CT. Absence or hypoplasia/stenosis of the facial canal, internal acoustic canal, foramina ovalia and rotundum, hypoglossal canal, or inferior alveolar canal might indicate hypoplasia or aplasia of the relative nerves and branches.

Therefore, MR imaging and CT might help to detect or raise the suspicion of morphologic CN abnormalities providing relevant information, especially when the CN impairment is difficult to evaluate due to early age, concomitant facial bone and soft-tissue asymmetry, or poor compliance of patients with OAVS.

The present study aims at investigating, in patients with OAVS, the rate of CN abnormalities, the type (eg, agenesis, hypoplasia, abnormal origin, or cisternal course), the association with functional impairment, and the side of hemifacial microsomia as well as the relationship with the phenotype severity.

MATERIALS AND METHODS

Subjects

Twenty-nine patients (mean age, 7 years; age range, 0.2–31 years; 12 females) with hemifacial microsomia and microtia were considered (On-line Table 1). Nineteen patients (mean age, 7.7 years; age range, 0.2–31 years; 9 females) also presented with ocular or cervical vertebral abnormalities and fulfilled the diagnostic criteria for Goldenhar syndrome (abnormalities involving the face, ear, eye, and/or cervical vertebrae).

The phenotypic spectrum of patients with OAVS is presented in On-line Table 2.

Neuroimaging

All except 1 patient underwent 1.5T MR imaging; 3 patients underwent MR imaging in other centers, but the image quality was considered appropriate for the study purposes. Our hospital MR imaging study protocol (Achieva 1.5T; Philips Healthcare, Best, the Netherlands) included the following: 1) high-resolution T2-weighted imaging for the visualization of CNs (driven equilib-

rium sequence; TR, 1500 ms; TE, 250 ms; FOV, 130 mm; voxel-size, 0.6 × 0.6 × 0.6 mm) covering the whole brain stem; 2) high-resolution volumetric T1-weighted imaging (TR, 20 ms; TE, 5.8 ms; voxel-size, 0.66 × 0.66 × 1 mm) covering the whole brain. From both sequences, multiplanar reconstructions were generated along the 3 orthogonal planes. Contrast medium was never administered. The entire MR imaging examination lasted approximately 20–25 minutes. Patients younger than 5 years of age required sedation, except for some infants who underwent the examinations without sedation.

At MR imaging, the neuroradiologists assessed the presence/absence of the CNs, their side-to-side diameter asymmetry on images orthogonal to their cisternal course, any anomaly regarding the origin from the brain stem, the morphology, and the cisternal course.

In this study, the evaluation was mostly based on T1-weighted images for CNs I–II and on T2-weighted images for CNs III–XI. The ninth and twelfth CN cisternal course is inconstantly recognizable at 1.5T imaging, especially because these CNs are thin and there are several small vessels running in the same cisternal space; therefore, these nerves were not considered in the study. Regarding the inferior CNs, the ninth-through-eleventh CN origin together with several roots from the retro-olivary sulcus, the number of roots might vary from subject to subject, thus usually making it impossible to recognize which root belongs to a specific nerve (except for the most cranial root that certainly belongs to CN IX).

All patients with OAVS had petrous bone or head CT. The study protocol varied greatly because several examinations were performed in other centers or in our center with different scanners; section thickness was <1 mm (0.6 mm in 26 cases) with subsequent 3D multiplanar reconstructions. Examinations were not repeated in patients with CT performed in different centers unless required for clinical or surgery management, even though in some cases not all bone structures were evaluable. In particular, CT allowed the assessment of the foramen ovale and the inferior alveolar bone canal in 25/29 and 19/29 patients, respectively.

CT evaluation focused on the internal, middle, or external ear abnormalities and the presence and symmetry of the foramen ovale and the inferior alveolar bone canal. Neuroradiologists assessed the presence/absence and the side-to-side asymmetry of the above-mentioned bone foramina.

Clinical information about the third-through-seventh CN function was obtained by the pediatrician or the family doctor of 20/29 patients. In addition, the presence of anisocoria, diplopia, facial hypoesthesia (including corneal reflex), and masticatory muscle and upper and lower facial muscle weakness was assessed by neurologic evaluation. Visual and hearing abnormalities were obtained for all patients from clinical records.

All MRI and CT was evaluated in consensus by 2 experienced neuroradiologists (R.Manera, R.Mardari), blinded to the patients' clinical findings.

The study protocol was approved by our ethics committee, and all patients or parents of children gave written informed consent.

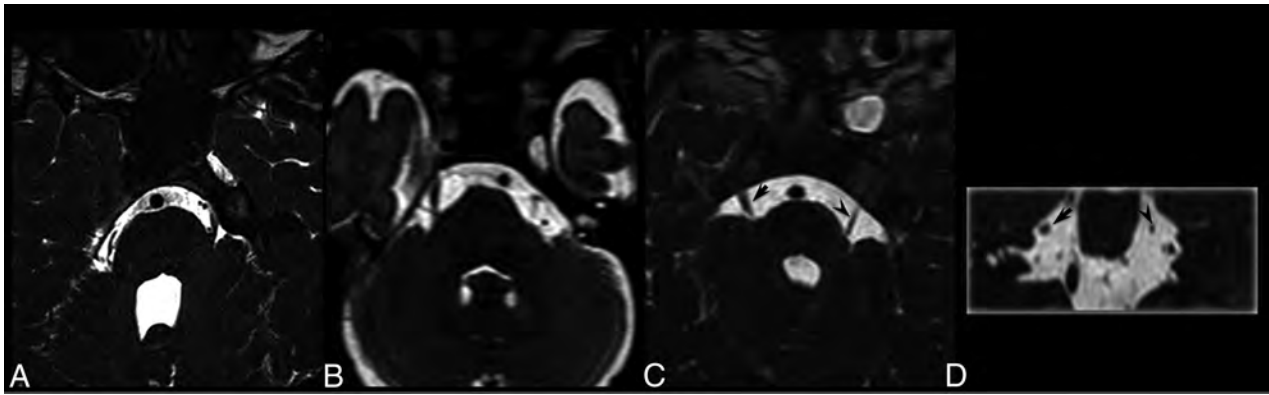


FIG 1. A–C, Axial T2-weighted images of 3 different patients with Goldenhar syndrome. A, The absence of the right trigeminal nerve. B, The absence of the left trigeminal nerve. C, The relative hypoplasia of the left trigeminal nerve (*arrowhead*). D, Coronal multiplanar reconstruction image, obtained from the same patient as in C, shows the different diameters of the trigeminal nerves (*arrow* and *arrowhead*).

Statistical Analysis

Study data were analyzed by the Fisher exact test; statistical significance was set at $P < .05$.

RESULTS

Findings on CNs and bone foramina are shown in On-line Table 3. In particular, 17/29 (59%) patients presented with intracranial CN abnormalities, and 11 patients showed abnormalities of the bone foramina of the trigeminal branches (foramen ovale, inferior alveolar nerve bone canal). Two patients presented with isolated bone foramen abnormalities without CN abnormalities at MR imaging, and 2 patients had abnormalities of the foramina without ipsilateral trigeminal nerve abnormalities. Among the 19 patients with intracranial or distal CN involvement (27 sides, 8 patients had bilateral CN involvement), the abnormalities were ipsilateral to facial microsomia in 23/27 cases; in 3/4 of the remaining patients, the CN abnormalities were bilateral, despite unilateral facial microsomia.

The trigeminal nerve (Fig 1) was the most frequently involved (11 patients, bilaterally in 5), followed by CN VII (11 subjects, bilaterally in 3) and CNs VI and VIII (8 patients, bilaterally in 3 and 2, respectively). MR imaging disclosed CN III hypoplasia in 1 patient. Five patients had micro- or anophthalmia; 4 had ipsilateral optic nerve hypoplasia; and in 1, the optic nerves were not evaluable. Among patients with globe abnormalities, only 1 had CN III and VI ipsilateral abnormalities, while in 1 patient, these CNs were not evaluable. No morphologic abnormalities of the lower CNs were found. Multiple CN abnormalities (up to 7 CNs) were found in most (11/17) patients. Among the 9 patients with foramen ovale hypo-/aplasia, 2 had normal trigeminal nerves at MR imaging; among the 8 patients with alveolar nerve bone canal hypo-/aplasia, 3 had a normal trigeminal nerve at MR imaging (On-line Fig 2). If we considered the 16 abnormal trigeminal nerves, 8 had ipsilateral bone foramina abnormalities (in all, the foramen ovale was abnormal; 5 had inferior alveolar bone canal abnormalities, while in 3, the inferior alveolar bone was not evaluable); 6 did not have ipsilateral bone foramina abnormalities; and in 2, CT did not allow foramina evaluation. Among the 9 patients with foramina ovalia abnormalities (1 patient had no foramina ovalia bilaterally),

the ipsilateral inferior alveolar bone canal was abnormal in 6 cases, normal in 1, and not evaluable in 3.

In our cohort, CN abnormalities at MR imaging were found only in patients with Goldenhar syndrome (17/19), while no patient with a mild phenotype (0/10) presented with abnormal CNs ($P = .000$). The association with the Goldenhar phenotype persisted when considering the trigeminal nerve abnormalities, either without (11/18 versus 0/10, $P = .002$) or with foramen anomalies, consistent with involvement of trigeminal branches (13/18 versus 1/10, $P = .004$). Similarly, the sixth, seventh, and eighth CN abnormalities were significantly associated with the Goldenhar phenotype compared with patients with the mild phenotype (8/16 versus 0/10, $P = .009$; 11/17 versus 0/10, $P = .001$; and 8/18 versus 0/10, $P = .025$, respectively).

Considering that some CN evaluations were not reliable because of patient age, compliance, or concomitant severe facial asymmetry among the 20 patients (11 with Goldenhar phenotype) in whom the functional evaluation was performed, facial nerve and trigeminal dysfunctions were found in 11/19 and 7/16 patients, respectively. Facial nerve and trigeminal dysfunctions were significantly more frequent in patients with Goldenhar syndrome (9/10 with Goldenhar phenotype versus 2/9 with mild phenotype, $P = .0054$; and 6/8 with Goldenhar phenotype versus 1/8 with mild phenotype, $P = .041$, respectively). Oculomotor dysfunction was found in 4 patients (2 patients were not considered due to anophthalmia, which hampered the evaluation of oculomotor function), all with Goldenhar syndrome, showing a trend of association with the phenotype (4/9 with Goldenhar phenotype versus 0/9 with mild phenotype, $P = .082$).

MR imaging of 1 patient with trigeminal dysfunction ipsilateral to hemifacial microsomia was not reliably evaluable for CN V. Among the remaining 15 patients with trigeminal function evaluation (30 trigeminal nerves), 5 had trigeminal nerve morphologic abnormalities (2 bilaterally, ie, 7 abnormal trigeminal nerves). Trigeminal dysfunction was associated with ipsilateral trigeminal nerve morphologic abnormalities (4/7 versus 2/23, $P = .016$). Of the 2 patients with no trigeminal nerve morphologic abnormalities but with trigeminal nerve dysfunction, the inferior alveolar nerve bone canal was absent in 1 patient and not evaluable in the other.

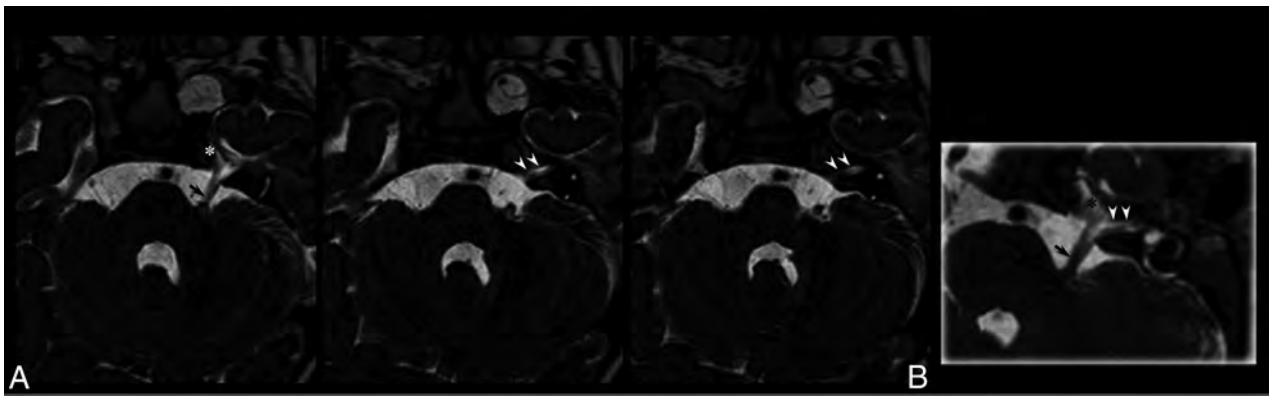


FIG 2. Brain MR imaging. *A*, Contiguous T2-weighted axial images show the common origin of the left fifth and seventh/eighth cranial nerves from the anterior profile of the middle cerebellar peduncle (*arrow*). The common trunk runs in the cisternal space and subdivides into 2 nerves entering the Meckel cave (*asterisk*) and, slightly caudally, the internal acoustic meatus (*arrowheads*). *B*, Oblique multiplanar reconstruction shows the common nerve origin and the subsequent subdivision.

Among the 18 patients (36 sides) with functional oculomotor evaluation, 4 had morphologic CN VI abnormalities (bilaterally in 2, ie, 6 abnormal abducens nerves). Oculomotor dysfunction (bilateral in 1 patient, unilateral in 3) was associated with ipsilateral CN VI morphologic abnormalities (3/6 versus 2/30, $P = .024$).

Finally, 1 patient with Goldenhar syndrome underwent multiple facial surgeries, and facial function was, therefore, not reliably evaluable. Among the remaining 19 patients (38 sides), 6 had morphologic CN VII abnormalities (bilateral in 2). Facial nerve dysfunction (bilateral in 2 patients, unilateral in 9) showed a trend toward association with ipsilateral nerve abnormalities (5/8 versus 8/30, $P = .081$).

DISCUSSION

This neuroradiologic study showed the strikingly common involvement of CNs among patients with oculo-auriculo-vertebral spectrum, especially among those presenting with the more severe phenotype (Goldenhar syndrome). In our series, at MR imaging, 17/29 patients (59%) displayed 57 abnormal CNs ranging from hypoplasia/aplasia to protean morphologic abnormalities; moreover, at CT, 4 patients showed isolated hypoplasia of the foramen ovale and/or of the inferior alveolar nerve bone canal, consistent with trigeminal branch hypo-/aplasia, thus disclosing also a possible distal CN involvement.

CN involvement in OAVS has been previously clinically and radiologically described in case reports or small series studies.¹³⁻²⁶ In 1975, a pathologic study on a child affected with Goldenhar syndrome¹⁷ showed the absence of the cisternal portion of the right trigeminal nerve along with the absence of its intra-axial nuclei, providing direct evidence of CN and central nervous system involvement in patients with OAVS. Moreover, because skull base foramina development is influenced by the existence of the corresponding CN branches,²⁷ CN abnormalities might be also be indirectly inferred by skull evaluation. The presence of hypoplastic and deformed foramina ovalia and rotundum in a paleopathologic case affected with Goldenhar syndrome²⁸ seems to confirm the possible concomitant distal involvement of the trigeminal branches (S. Panzer, MD, personal e-mail communication, January 1, 2013). Similar evaluation can be performed by CT, which

allows the precise visualization of the bone foramina. In the present study, 11/26 (42%) patients with OAVS with adequate bone CT showed foramina abnormalities, suggesting that the distal involvement of the trigeminal branches is not uncommon.

In the past few years, MR imaging has provided high-resolution images suitable for the evaluation *in vivo* of the CNs, especially at the cisternal portion, thus contributing, in some cases, to the explanation of their absent or impaired function.^{29,30} Although CNs IV and XII might be inconstantly recognizable at 1.5T and CNs IX–XI appear as an indistinguishable group of roots originating from the retro-olivary sulcus, MR imaging reliably assesses the absence or the relative hypoplasia of the remaining CNs. Thus, MR imaging has become a cornerstone in the diagnostic work-up of children with profound congenital deafness, helping in cochlear or brain stem implantation decision-making.³¹ In fact, the absence of the cisternal segment of the eighth CN or the intrameatal absence of the cochlear nerve is considered, to date, a major contraindication to cochlear implantation.

At MR imaging, besides CN aplasia (absence of the cisternal segment) or hypoplasia (significant side-to-side asymmetry of the nerve diameter), in our study population, we recognized protean morphologic changes never reported in previous publications. One patient showed a nodular thickening of the fifth CN close to its origin (On-line Fig 3). Because the distal part of the nerve was recognizable and the mass diagnosis could not be supported by histology, this patient with Goldenhar syndrome was, as a precaution, not included among those with CN abnormalities. In some patients, a single nerve was rooted from the brain stem and was divided subsequently into different CNs. In 2 patients, for example, we did not detect the cisternal portion of the facial nerve concomitant to an enlarged ipsilateral trigeminal nerve and partially preserved facial nerve function. While direct pathologic evidence was not available, these cases likely represent the abnormal fusion of the cisternal segments of the facial and trigeminal nerves. Indeed, in one of these cases, an abnormal facial bone canal/internal acoustic meatus seemed to be recognizable close to the site where the abnormal CN V reached the upper surface of the petrous bone apex (Fig 2). Similarly, in 2 patients, there was only 1 CN in the internal acoustic meatus, a condition that is consid-

ered indicative of a preserved facial nerve with CN VIII aplasia³¹; nonetheless, both patients had partially preserved auditory function. The presence of nerve fibers within a different nerve or nerve branch has been suggested in some cases in which the absence of the cochlear nerve did not correspond to a complete loss of hearing function.³² Therefore, these cases seem to increase the body of evidence against the “dogmatic” indication toward auditory brain stem implantation whenever cranial VIII or the cochlear nerves are missing at MR imaging investigation,³³ unless concomitant and coherent functional data are obtained.

In the current study, anomalies of CN II were not further considered because hypoplasia of the optic nerve was the rule when the patients presented with microphthalmia or anophthalmia. In contrast, abnormalities of the nerves that control eye movements did not correlate with abnormal eye development. Globe abnormalities were not significantly more frequent among patients with CN III or VI abnormalities (2/8 versus 3/18); this finding confirms that eye and oculomotor apparatus follow different development pathways. From a functional point of view, the association between Goldenhar syndrome and extrinsic ocular-movement impairment has been frequently noted. Duane syndrome type I has been reported in patients with Goldenhar syndrome.^{15,20-26} Among our patients with functional evaluation, 4/18 had oculomotor impairment (all Goldenhar phenotypes), while 8/28 with MR imaging evaluation presented with CN III or VI abnormalities. Considering that this study did not evaluate CN IV morphologic abnormalities and that hypoplasia of CN VI is difficult to ascertain because the nerve is very thin, our data confirm the frequent involvement of the oculomotor nerves in OAVS and explain the frequent oculomotor impairment in these patients. On the other hand, the recurrent observation of preserved oculomotor function despite CN VI aplasia seems to support the hypothesis that nerve fibers might run along alternative routes to innervate the extrinsic ocular muscles.

From a pathogenic point of view, involvement of the CNs in OAVS is likely due to the common embryologic origin of facial bones, soft tissues, and peripheral neural structures from the first and second pharyngeal arches. These structures are contiguous to the corresponding neural crests and central nervous system structures. Whatever the nature of the lesion leading to OAVS (ischemic, hemorrhagic, infectious, and so forth), CN development might be concomitantly affected: In fact, most CN abnormalities were ipsilateral to facial abnormalities. On the other hand, in our cohort, a few patients showed bilateral CN involvement despite unilateral facial involvement. This observation suggests that neural structures in OAVS might be even more vulnerable than contiguous bone and soft tissues or that the clinical evaluation of microsomnia (which is based on side-to-side comparison) might be less sensitive than the neuroradiologic or functional evaluation of the CNs.

Notably, the present study showed a strong association between Goldenhar phenotype (severe cases among the OAVS) and CN involvement. This might appear obvious because among the OAVS, Goldenhar syndrome criteria imply a more extensive involvement (facial and auricular involvement plus ocular or vertebral involvement). Nonetheless, we did not find within the Goldenhar subgroup an association between the number of fulfilled

criteria and the number of involved CNs. Patients with Goldenhar syndrome with both ocular and vertebral involvement did not show an increased number of abnormal CNs compared with patients with Goldenhar syndrome with isolated ocular or vertebral involvement. A likely explanation is that the inclusion criteria for Goldenhar syndrome do not take into account the severity of ocular or vertebral abnormalities. Besides anophthalmia and microphthalmia, coloboma, epibulbar dermoid, or even epicanthus are considered among the inclusion criteria for ocular involvement in Goldenhar syndrome, though their clinical impact and severity are clearly different.

The clinical impact of CN abnormalities in patients with OAVS has been underlined in previous studies¹³⁻²⁶; the present study on a relatively large sample shows that MR imaging and CT might provide the explanation of nerve impairment. Moreover, because neonates and infants might be difficult to evaluate and CN dysfunction might imply serious complications (eg, corneal lesions or abnormal masticatory dynamic), neuroimaging-focused evaluation might help when CN impairment is suspected in the early phases of the life of a patient with OAVS, thus helping to prevent irreversible damage. For this purpose, MR imaging is certainly the preferred tool, but in some cases, the evaluation of the foramen ovale and the inferior alveolar nerve bone canal might disclose CN abnormalities, even when the cisternal portion of the trigeminal nerve appears normal.

CONCLUSIONS

This study showed the following: 1) the frequent involvement of CNs in patients with OAVS spectrum, 2) the strong association between CN abnormalities and the Goldenhar phenotype, and 3) the association between CN abnormalities and functional impairment. Moreover, our findings widened the spectrum of CN abnormalities that is not limited to hypo-/aplasia but includes the anomalous course of the cisternal segment and the partial or complete fusion of ≥ 2 CNs. Further studies are warranted to investigate the possible role of genetics in the OAVS and the coexistence of brain, internal carotid artery, and inner ear involvement, which will probably help in understanding the likely pathogenesis of this condition.

ACKNOWLEDGMENTS

We are very grateful to Dr S. Panzer for her kindness and collaboration in providing interesting additional information about skull abnormalities of the paleopathologic case published in 2008.

Disclosures: Renzo Manara—UNRELATED: Payment for Lectures (including service on Speakers Bureaus): BioMarin, Serono, Comments: approximately €2000 (US \$2259.05).

REFERENCES

1. Online Mendelian Inheritance in Man. Goldenhar syndrome. McKusick-Nathans Institute for Genetic Medicine, Johns Hopkins University (Baltimore) and National Center for Biotechnology Information, National Library of Medicine (Baltimore). <http://www.omim.org/entry/164210?search=goldenhar%20syndrome&highlight=goldenhar%20syndrome%20syndromic>. Accessed September 12, 2009
2. Poswillo D. **Otomandibular deformity: pathogenesis as a guide to reconstruction.** *J Maxillofac Surg* 1974;2:64–72

3. Grabb WC. **The first and second branchial arch syndrome.** *Plast Reconstr Surg* 1965;36:485–508
4. Rollnick BR, Kaye CI, Nagatoshi K, et al. **Oculoauriculovertebral dysplasia and variants: phenotypic characteristics of 294 patients.** *Am J Med Genet* 1987;26:361–75
5. Mastroiacovo P, Corchia C, Botto LD, et al. **Epidemiology and genetics of microtia-anotia: a registry based study on over one million births.** *J Med Genet* 1995;32:453–57
6. Goldenhar M. **Associations malformatives de l'oeil et de l'oreille en particulaire, le syndrome dermoïde epibulbaire-appendices auriculaires-fistula auris congenital et ses relations avec le dysostose mandibulo-faciale.** *J Genet Hum* 1952;1:243–82
7. Ala-Mello S, Siggberg L, Knuutila S, et al. **Further evidence for a relationship between the 5p15 chromosome region and the oculoauriculovertebral anomaly.** *Am J Med Genet A* 2008;146A:2490–94
8. Rooryck C, Stef M, Burgelin I, et al. **Mb terminal deletion in 12p13.33 associated with oculoauriculovertebral spectrum and evaluation of WNT5B as a candidate gene.** *Eur J Med Genet* 2009;52:446–49
9. Ballesta-Martínez MJ, López-González V, Dulcet LA, et al. **Autosomal dominant oculoauriculovertebral spectrum and 14q23.1 microduplication.** *Am J Med Genet A* 2013;161A:2030–35
10. Torti EE, Braddock SR, Bernreuter K, et al. **Oculo-auriculo-vertebral spectrum, cat eye, and distal 22q11 microdeletion syndromes: a unique double rearrangement.** *Am J Med Genet A* 2013;161A:1992–98
11. Ottaviano G, Calzolari F, Martini A. **Goldenhar syndrome in association with agenesis of the internal carotid artery.** *Int J Pediatr Otorhinolaryngol* 2007;71:509–12
12. Hartsfield JK. **Review of the etiologic heterogeneity of the oculoauriculo-vertebral spectrum (hemifacial microsomia).** *Orthod Craniofac Res* 2007;10:121–28
13. Sugar HS. **The oculoauriculovertebral dysplasia syndrome of Goldenhar.** *Am J Ophthalmol* 1966;62:678–82
14. van Bijsterveld OP. **Unilateral corneal anesthesia in oculoauriculovertebral dysplasia.** *Arch Ophthalmol* 1969;82:189–90
15. Bowen DI, Collum LM, Rees DO. **Clinical aspects of oculo-auriculo-vertebral dysplasia.** *Br J Ophthalmol* 1971;55:145–54
16. Budden SS, Robinson GC. **Oculoauricular vertebral dysplasia: its association with sensorineural deafness and other abnormalities.** *Am J Dis Child* 1973;125:431–33
17. Aleksic S, Budzilovich G, Reuben R, et al. **Congenital trigeminal neuropathy in oculoauriculovertebral dysplasia-hemifacial microsomia (Goldenhar-Gorlin syndrome).** *J Neurol Neurosurg Psychiatry* 1975;38:1033–35
18. Nappi G, Alfonsi E, Bono G, et al. **Goldenhar-Gorlin syndrome: a case with congenital trigeminal neuropathy.** *Acta Neurol (Napoli)* 1983;5:368–72
19. Villanueva O, Atkinson DS, Lambert SR. **Trigeminal nerve hypoplasia and aplasia in children with Goldenhar syndrome and corneal hypoesthesia.** *J AAPOS* 2005;9:202–04
20. Miller MT. **Association of Duane retraction syndrome with craniofacial malformations.** *J Craniofac Genet Dev Biol Suppl* 1985;1:273–82
21. Dastur YK, Trivedi H, Tapaswi N, et al. **Goldenhar's syndrome with unilateral Duane retraction syndrome and "butterfly" vertebra.** *Indian J Ophthalmol* 1985;33:187–89
22. Mansour AM, Wang F, Henkind P, et al. **Ocular findings in the facioauriculovertebral sequence (Goldenhar-Gorlin syndrome).** *Am J Ophthalmol* 1985;100:555–59
23. Miller NR, Kiel SM, Green WR, et al. **Unilateral Duane retraction syndrome (type 1).** *Arch Ophthalmol* 1982;100:1468
24. Baum J, Feingold M. **Ocular aspects of Goldenhar syndrome.** *Am J Ophthalmol* 1973;75:250–57
25. Mittelman D, Herbst R, Miller M. **The many faces of Goldenhar syndrome.** In: *Proceedings of the Annual Meeting of the American Medical Association*, New York. June 1973
26. Vélez G. **Duane's retraction syndrome associated with Goldenhar's syndrome.** *Am J Ophthalmol* 1970;70:945–46
27. Yan F, Li J, Xian J, et al. **The cochlear nerve canal and internal auditory canal in children with normal cochlea but cochlear nerve deficiency.** *Acta Radiol* 2013;54:292–98
28. Panzer S, Cohen M, Esch U, et al. **Radiological evidence of Goldenhar syndrome in a paleopathological case from a South German ossuary.** *Homo* 2008;59:453–61
29. Verzijl HT, Valk J, de Vries R, et al. **Radiologic evidence for absence of the facial nerve in Möbius syndrome.** *Neurology* 2005;64:849–55
30. Joshi VM, Navlekar SK, Kishore GR, et al. **CT and MR imaging of the inner ear and brain in children with congenital sensorineural hearing loss.** *Radiographics* 2012;32:683–98
31. Vincenti V, Ormitti F, Ventura E, et al. **Cochlear implantation in children with cochlear nerve deficiency.** *Int J Pediatr Otorhinolaryngol* 2014;78:912–17
32. Warren FM 3rd, Wiggins RH 3rd, Pitt C, et al. **Apparent cochlear nerve aplasia: to implant or not to implant?** *Otol Neurotol* 2010;31:1088–94
33. Deggouj N, Gersdorff M, Garin P, et al. **Today's indications for cochlear implantation.** *B-ENT* 2007;3:9–14

Transmedullary Venous Anastomoses: Anatomy and Angiographic Visualization Using Flat Panel Catheter Angiotomography

L. Gregg and P. Gailloud



ABSTRACT

SUMMARY: Flat panel catheter angiotomography, a recently developed angiographic technique, offers a spinal equivalent to the venous phase obtained during cerebral angiography. This report of 8 clinical cases discusses the flat panel catheter angiotomography appearance of a type of spinal venous structure until now principally known through the analysis of postmortem material, transmedullary venous anastomosis. The illustrated configurations include centrodorsolateral, median anteroposterior, median anteroposterior with duplicated origin, and combined centrodorsolateral/median anteroposterior transmedullary venous anastomoses, while a pathologic example documents the potential role of transmedullary venous anastomoses as collateral venous pathways. Two of the reported configurations have not been previously documented. Transmedullary venous anastomoses are normal venous structures that need to be differentiated from spinal cord anomalies, such as intramedullary vascular malformations.

ABBREVIATIONS: AMSV = anteromedian spinal vein; FPCA = flat panel catheter angiotomography; PLSV = posterolateral spinal vein; PMSV = posteromedian spinal vein; TMVA = transmedullary venous anastomosis

The clinical evaluation of the spinal venous system is technically challenging, even with spinal DSA, the criterion standard imaging technique for spinal vasculature. This suboptimal visualization correlates with a poor understanding of spinal venous system pathology. Flat panel catheter angiotomography (FPCA), a novel angiographic technique that offers a spinal equivalent to the cerebral venous phase,¹⁻³ has shown great promise for the evaluation of the normal and abnormal spinal venous system.³⁻⁵

This retrospective review of 8 clinical cases describes the morphology and angiographic appearance of several types of transmedullary venous anastomoses (TMVAs), including some previously undocumented configurations observed during routine spinal DSA. TMVAs, rarely observed in living subjects,⁶⁻⁸ were until now essentially known through the study of postmortem material.

CASE SERIES

Acquisition Protocols

Thoracic and lumbar protocols involved 20-second nonsubtracted rotational angiograms (Artis zee; Siemens, Erlangen, Germany) obtained during the selective injection of arteries provid-

ing major radiculomedullary branches. The contrast mixture (25% contrast agent, 75% heparinized saline) was injected at a rate of 1 mL/s for 30 seconds, covering the 20-second angiography and a 10-second preacquisition delay (total volume of 30 mL, including 7.5 mL of iodinated agent). The patients were not required to breath-hold during acquisitions. The volume and rate of injection were modified for vertebral artery and costocervical trunk studies (50 mL at 2 mL/s, including 12.5 mL of iodinated agent). Areas of specific interest were reconstructed using MIP rendering by the senior author in various planes using high-resolution algorithms (voxel sizes, between 0.2 and 0.04 mm).³

Perimedullary Anastomosis

Case 1. A superficial anastomosis between the anteromedian spinal vein (AMSV) and the left posterolateral spinal vein (PLSV) was documented at T12 in a 36-year-old woman with progressive myelopathy (Fig 1).

Centrodorsolateral Anastomosis

Case 2. A centrodorsolateral TMVA connecting the AMSV to the right PLSV at the level of C3 was seen in a 51-year-old woman investigated for a C3–C4 spinal epidural arteriovenous fistula (Fig 2).

Median Anteroposterior Anastomosis

Case 3. A median anteroposterior TMVA connecting the AMSV to the posteromedian spinal vein (PMSV) at T11 was noted in a 23-year-old woman investigated for recurrent myelopathy (Fig 3).

Received November 19, 2014; accepted after revision January 13, 2015.

From the Division of Interventional Neuroradiology (L.G., P.G.), The Johns Hopkins Hospital, Baltimore, Maryland; and Department of Art as Applied to Medicine (L.G.), The Johns Hopkins University School of Medicine, Baltimore, Maryland.

Please address correspondence to Philippe Gailloud, MD, Division of Interventional Neuroradiology, The Johns Hopkins Hospital, Bloomberg 7218, 1800 Orleans St, Baltimore, MD 21287; e-mail: phg@jhmi.edu

<http://dx.doi.org/10.3174/ajnr.A4302>

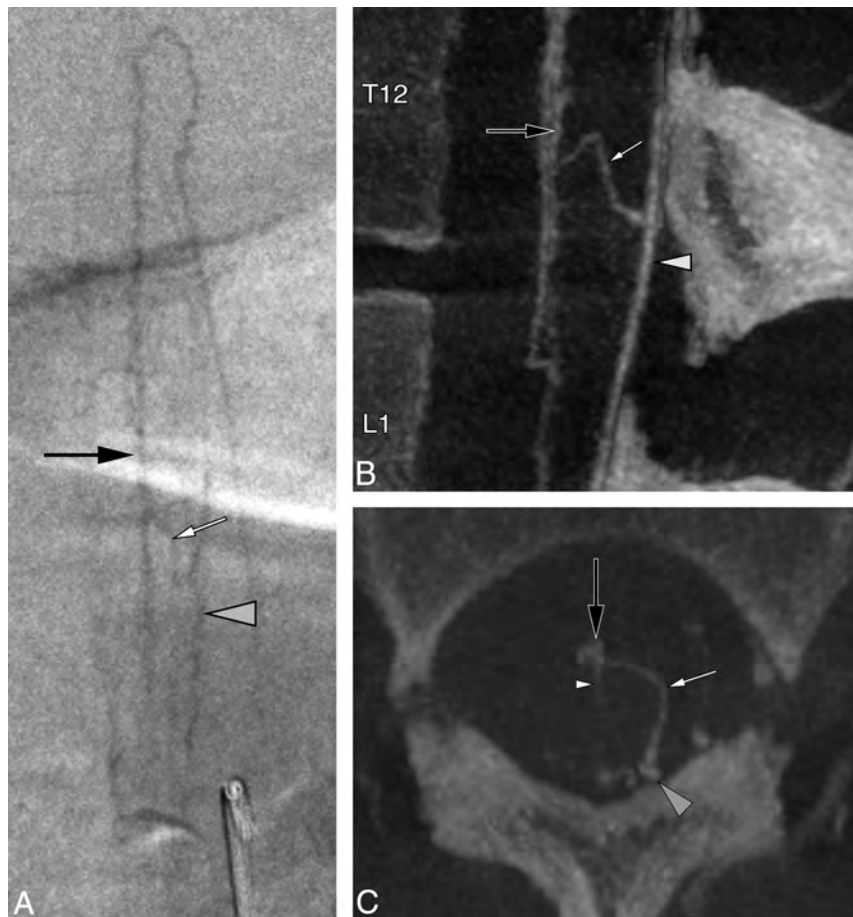


FIG 1. A 36-year-old woman with a perimedullary anastomosis. *A*, Spinal DSA, left L1 injection, posteroanterior projection, late venous phase, shows an anastomotic connection (*white arrow*) between the AMSV (*black arrow*) and the left PLSV (*gray arrowhead*). The exact location of this anastomosis (intramedullary-versus-perimedullary) cannot be clearly established in this projection. A lateral projection would not offer additional information because the ventrodorsal course of both types of anastomoses would appear similar. *B*, FPCA, left L1 injection, sagittal MIP reconstruction (thickness = 8 mm). The morphology of the anastomosis (*white arrow*) and its points of connection with the AMSV (*black arrow*) and left PLSV (*gray arrowhead*) are better appreciated. *C*, FPCA, left L1 injection, axial MIP reconstruction (thickness = 8 mm). This axial view unequivocally establishes the superficial course of the perimedullary anastomosis (*small arrow*) over the lateral aspect of the spinal cord, between the AMSV (*black arrow*) and the left PLSV (*gray arrowhead*). A central vein is documented within the anteromedian fissure (*white arrowhead*).

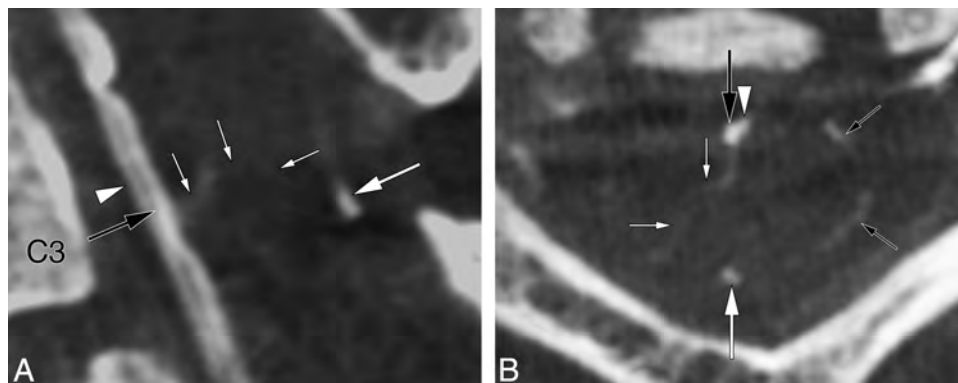


FIG 2. A 51-year-old woman with a centrodorsolateral transmedullary venous anastomosis. *A*, FPCA, left vertebral artery injection, sagittal MIP reconstruction (thickness = 5 mm) shows a centrodorsolateral TMVA (*small white arrows*) connecting the AMSV (*large black arrow*) to the right PLSV. The PMSV (*large white arrow*) and anterior spinal artery (*white arrowhead*) are also documented. *B*, FPCA, left vertebral artery injection, axial MIP reconstruction (thickness = 5 mm) shows the path taken by the centrodorsolateral TMVA (*small white arrows*) between the AMSV (*large black arrow*) and the right PLSV. The PMSV (*larger white arrow*) and segments of the coronary plexus (*small black arrows*) are seen as well.

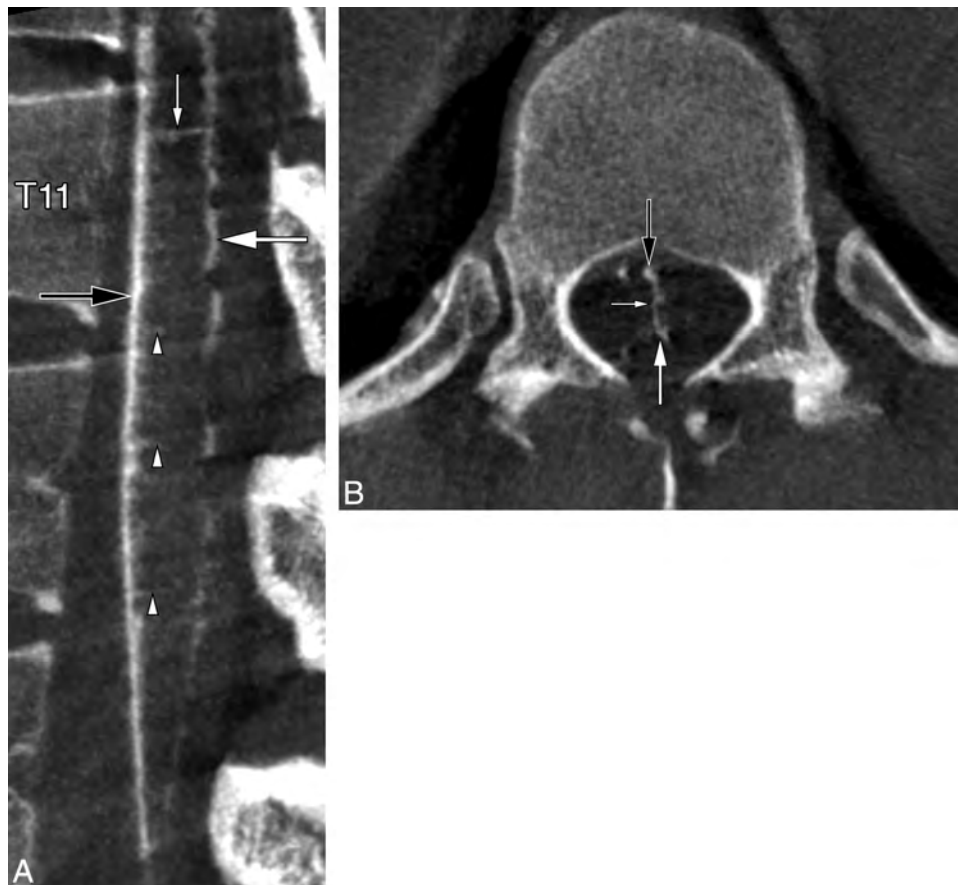


FIG 3. A 23-year-old woman with a median anteroposterior transmedullary venous anastomosis. *A*, FPCA, right T12 injection, sagittal MIP reconstruction (thickness = 3 mm). The median anteroposterior TMVA (*small white arrow*) extends between the AMSV (*black arrow*) and the PMSV (*large white arrow*) at the T11 level. Several central veins (*arrowheads*) are seen. *B*, FPCA, right T12 injection, axial MIP reconstruction (thickness = 3 mm), confirms the transmedullary course of the median anteroposterior TMVA (*small white arrow*) between the AMSV (*black arrow*) and the PMSV (*large white arrow*).

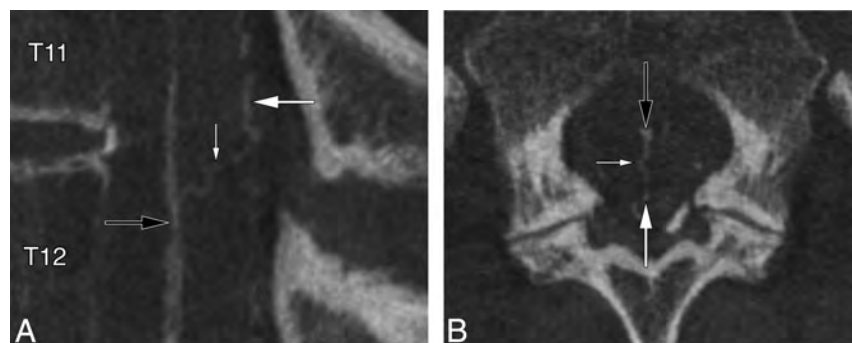


FIG 4. A 60-year-old woman with a median anteroposterior transmedullary venous anastomosis. *A*, FPCA, left L1 injection, sagittal MIP reconstruction (thickness = 3 mm), shows a median anteroposterior TMVA (*small white arrow*) coursing superiorly and posteriorly between the AMSV (*black arrow*) and the PMSV (*large white arrow*). *B*, FPCA, left L1 injection, axial MIP reconstruction (thickness = 10 mm). The median anteroposterior TMVA (*small white arrow*) extends from the AMSV (*black arrow*) to the PMSV (*large white arrow*). Note the typical lateral loop of the TMVA around the central canal at the level of the *small white arrow*.

Case 4. A median anteroposterior TMVA was documented at the T11–12 level in a 60-year-old woman investigated for progressive myelopathy (Fig 4).

Case 5. A median anteroposterior TMVA was seen at T11 in a 74-year-old man investigated for progressive myelopathy (Fig 5).

Case 6. A median anteroposterior TMVA was noted at C7 in a 40-year-old woman with progressive myelopathy (Fig 6).

Combined Anastomoses

Case 7. A 52-year-old man with progressive myelopathy was treated endovascularly for 2 spinal epidural AVFs (left T7 and T9). FPCA performed to investigate an additional cervical spinal epidural AVF showed a median anteroposterior TMVA with a duplicate origin from the AMSV at the C2 level, a combined centrodorsolateral and median anteroposterior TMVA between C2 and C3, and a

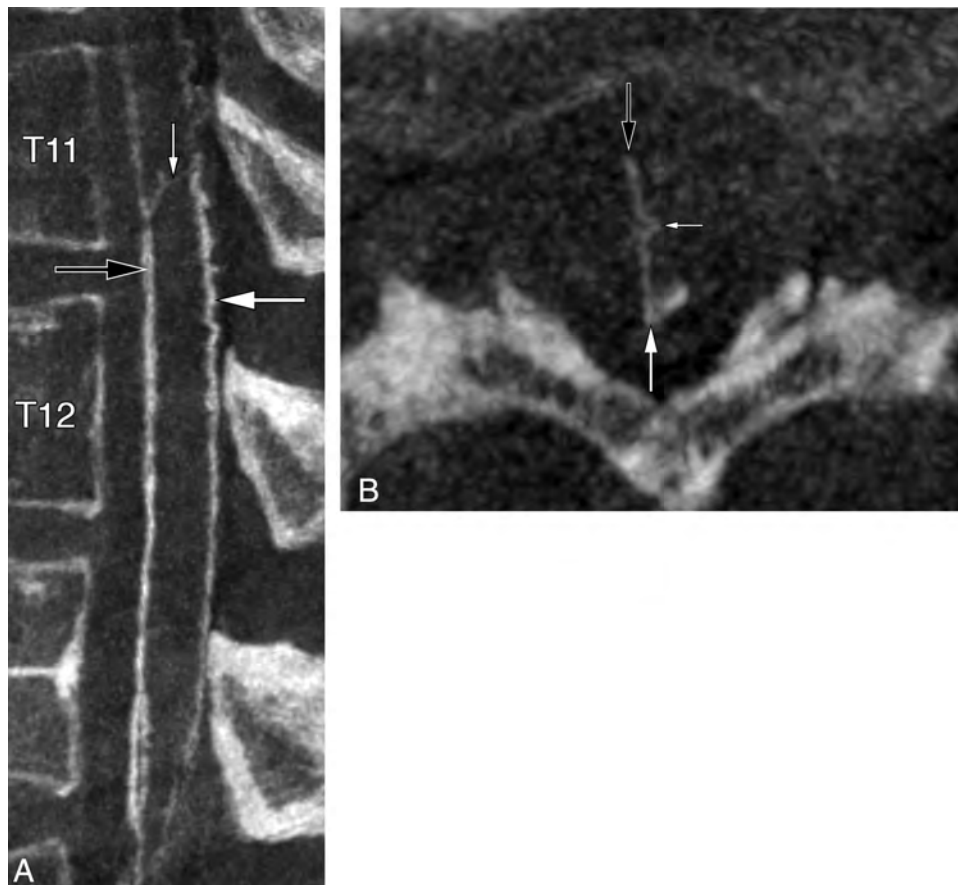


FIG 5. A 74-year-old man with a median anteroposterior transmedullary venous anastomosis. A, FPCA, left L1 injection, sagittal MIP reconstruction (thickness = 3 mm), shows a median anteroposterior TMVA (*small white arrow*) extending between the AMSV (*black arrow*) and the PMSV (*large white arrow*). B, FPCA, left L1 injection, axial MIP reconstruction (thickness = 10 mm). The median anteroposterior TMVA (*small white arrow*) courses from the AMSV (*black arrow*) to the PMSV (*large white arrow*), showing a typical deviation around the central canal.

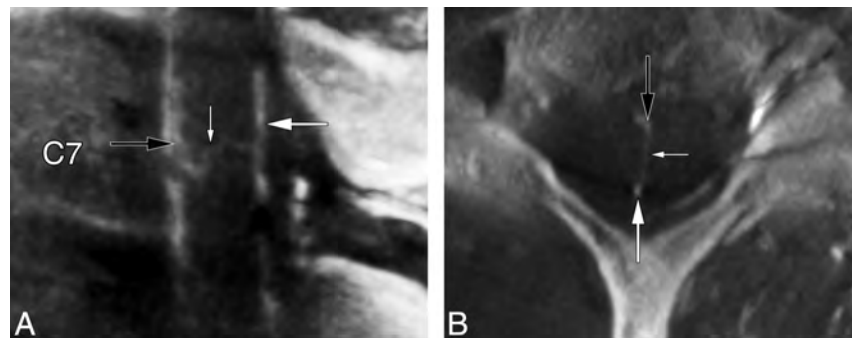


FIG 6. A 40-year-old woman with a median anteroposterior transmedullary venous anastomosis. A, FPCA, left costocervical trunk injection, sagittal MIP reconstruction (thickness = 2 mm). A median anteroposterior TMVA (*small white arrow*) connects the AMSV (*black arrow*) to the PMSV (*large white arrow*). B, FPCA, left costocervical trunk injection, axial MIP reconstruction (thickness = 4 mm), confirms the intramedullary trajectory of the median anteroposterior TMVA (*small white arrow*) between the AMSV (*black arrow*) and the PMSV (*large white arrow*).

median anteroposterior TMVA between C3 and C4, associated with a sulcal longitudinal anastomosis (Fig 7).

Pathologic Illustration

Case 8. A 57-year-old woman was investigated for a cervical stroke possibly secondary to a C3–C4 disk herniation. FPCA performed before surgery confirmed the presence of mass effect on the anterior spinal vessels by disk material, matching

the location of the ischemic lesion on MR imaging. The central veins were barely visible at the compression site yet were prominent immediately above and below it. A sulcal longitudinal anastomosis served as a collateral venous pathway in the depth of the anteromedian fissure, and several TMVAs were noted in neighboring areas, including 2 centrodorsolateral TMVAs respectively located cranially and caudally to the compression site (Fig 8).

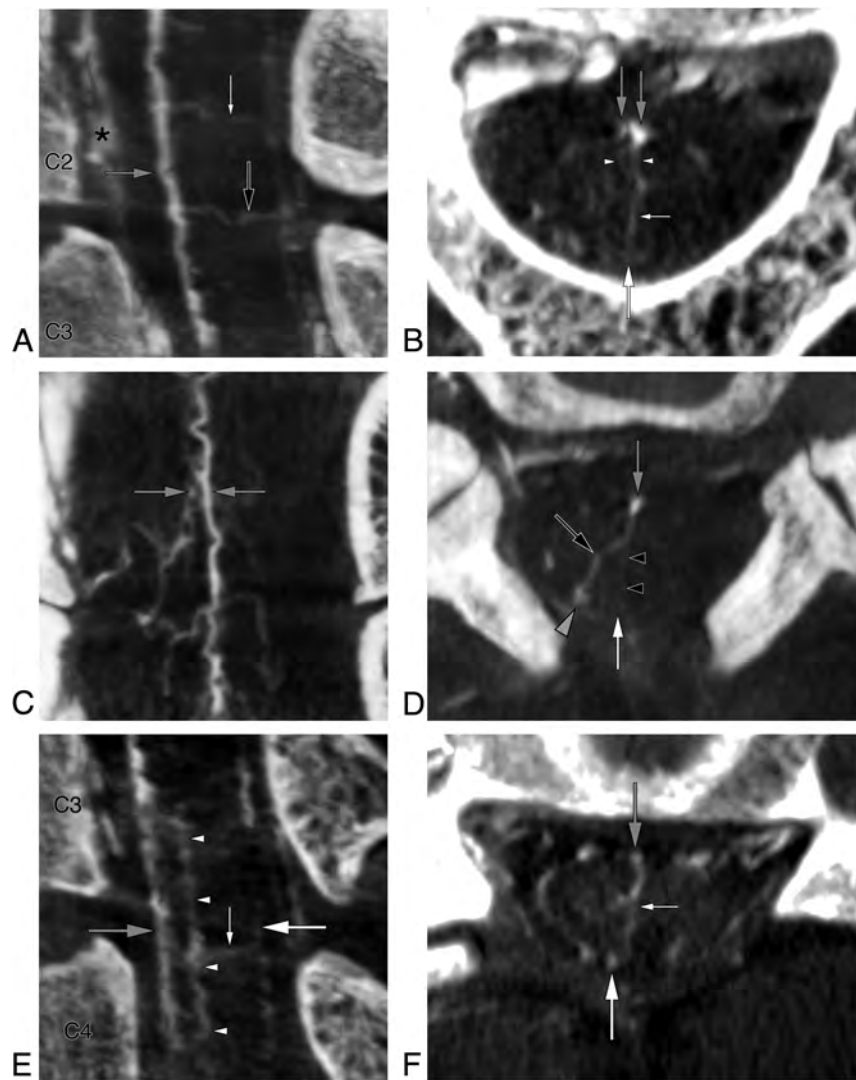


FIG 7. A 52-year-old man with 2 median anteroposterior transmedullary venous anastomoses and a combined centrodorsolateral and median anteroposterior TMVA. **A.** FPCA, right vertebral injection, sagittal MIP reconstruction (thickness = 5 mm), reveals 2 TMVAs: a median anteroposterior TMVA (*small white arrow*) with a dual origin (documented in Fig 7B) from the AMSV (*gray arrow*) at C2 and a TMVA with combined median anteroposterior and centrodorsolateral characteristics (*black arrow*) between C2 and C3. The anterior internal epidural venous plexus is well-appreciated (*asterisk*). **B.** FPCA, right vertebral injection, axial MIP reconstruction (thickness = 3 mm), shows the median anteroposterior TMVA (*small white arrow*) at the C2 level, with a dual origin (*arrowheads*) from the AMSV and the surrounding venous network (*gray arrows*). The PMSV (*large white arrow*) is seen as well. **C.** FPCA, right vertebral injection, coronal MIP reconstruction (thickness = 4 mm), documents the segment of the AMSV and surrounding venous network from which the TMVA with dual roots originates (*gray arrows*). **D.** FPCA, right vertebral injection, axial MIP reconstruction (thickness = 4 mm). The TMVA with combined median anteroposterior (*black arrowheads*) and centrodorsolateral (*black arrow*) characteristics connects the AMSV (*gray arrow*) dorsally (*white arrow*) and to the right PLSV dorsolaterally (*gray arrowhead*) between the C2 and C3 levels. **E.** FPCA, right vertebral injection, sagittal MIP reconstruction (thickness = 4 mm). A median anteroposterior TMVA (*small white arrow*) extends between the AMSV (*gray arrow*) and the PMSV (*large white arrow*). A sulcal longitudinal anastomosis (*arrowheads*) is seen within the depth of the anteromedian fissure between C3 and C4. **F.** FPCA, right vertebral injection, axial MIP reconstruction (thickness = 3 mm), shows the course of the median anteroposterior TMVA (*small white arrow*) between the AMSV (*gray arrow*) and the PMSV (*large white arrow*).

DISCUSSION

FPCA Acquisitions

All FPCA acquisitions were successful, with no intra- or post-procedural complications. FPCA is primarily performed in our practice to complement angiograms with negative findings in patients with progressive myelopathies and MR imaging findings suggesting venous hypertension, which explains the high ratio of studies with normal findings (5 of 8). 3D spinal DSA is the preferred technique for the evaluation of fast-flow lesions such as arteriovenous malformations or perimedullary arteriovenous fistulas, while FPCA is occasionally performed for

slow-flow lesions (eg, spinal epidural AVFs). Finally, the spinal venous system is not specifically studied when FPCA is performed to investigate an arterial condition (crus compression syndrome, for example).

The principal advantage of FPCA over other vascular imaging techniques such as CTA or MRA is its higher spatial resolution.³ As a drawback of its acquisition mode, FPCA will display arteries and veins simultaneously. These can, however, be differentiated on the basis of their course, branching pattern, and correlation with the corresponding 2D spinal DSA anatomy.³

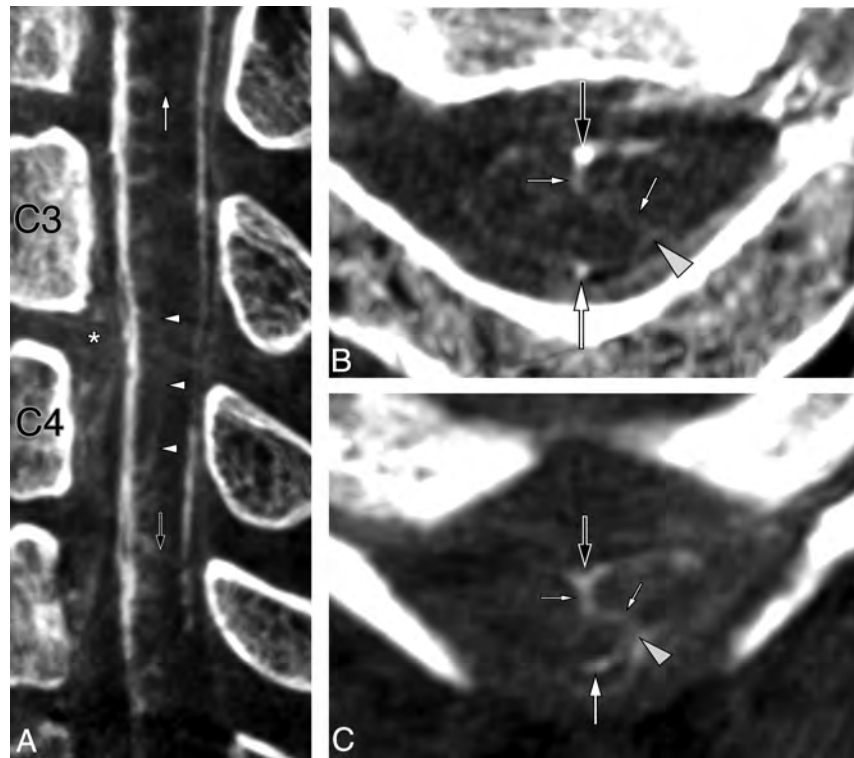


FIG 8. A 57-year-old woman with a sulcal longitudinal anastomosis and 2 centrodorsolateral transmedullary venous anastomoses. **A**, FPCA, left vertebral injection, sagittal MIP reconstruction (thickness = 5 mm), shows mass effect on the anterior aspect of the spinal cord by protruded disk material at C3–C4 (*asterisk*), with a dearth of central veins at the corresponding level. The central veins above and below the lesion are prominent. A sulcal longitudinal anastomosis (*white arrowheads*) appears to serve as a collateral venous pathway in the depth of the antero-medial fissure. Two centrodorsolateral TMVAs are noted, respectively located cranially (*white arrow*) and caudally (*black arrow*) to the compressed area. **B**, FPCA, left vertebral injection, axial MIP reconstruction (thickness = 3 mm), shows the C2–C3 centrodorsolateral TMVA (*small white arrows*) connecting the AMSV (*large black arrow*) to the left PLSV (*gray arrowhead*). The PMSV (*large white arrow*) is seen as well. **C**, FPCA, left vertebral injection, axial MIP reconstruction (thickness = 2 mm), documents a second centrodorsolateral TMVA (*small white arrows*) at C4–C5, extending between the AMSV (*large black arrow*) and left PLSV (*gray arrowhead*), which continues its course medially to connect with the PMSV (*large white arrow*).

Anatomy of the Perimedullary and Intramedullary Venous Systems

The perimedullary venous system includes the AMSV and PMSV, which are 2 anastomotic chains respectively coursing over the anteromedian and posteromedian fissures. The smaller paired PLSVs lie along the dorsal nerve rootlets (Fig 9A).^{9,10} The principal longitudinal venous axes are interconnected by the coronary plexus of the pia mater.¹¹ The coronary plexus generally includes a few larger perimedullary anastomoses that can be visualized during spinal DSA, if the venous phase is of sufficient quality. However, perimedullary anastomoses are not clearly distinguished from TMVAs without the multiplanar assistance of FPCA (Fig 1).³

The intramedullary venous network is divided into central and peripheral compartments (Fig 9A). The central veins drain the anterior and median portions of the spinal parenchyma¹² and terminate into the AMSV. Neighboring central veins can establish longitudinal anastomotic chains, both within the central gray matter (paracentral longitudinal anastomosis) and the anteromedian fissure (sulcal longitudinal anastomosis).¹² Paracentral longitudinal anastomoses can participate in aberrant intramedullary drainage patterns similar to the developmental venous anomalies seen in the brain or brainstem.⁴ When prominent, sulcal or paracentral longitudinal anastomoses can be visualized with FPCA (Fig 7E).

The peripheral veins course radially to end in the coronary plexus. Those located within the anterior and posterior radicular fasciculi are generally more developed.¹³ The septal veins drain into the PMSV. All intrinsic veins drain centrifugally into the perimedullary venous system.^{14,15}

Transmedullary Venous Anastomoses

Two types of TMVAs are classically recognized. The centrodorsolateral type was described by Kadyi¹¹ in 1889 (Fig 10):

A large anastomotic connection is established between one of the central veins and one from the posterior surface of the spinal cord. The small trunk designated by “v” does not course within the median septum, but leftward to reach the surface of the spinal cord in the vicinity of the line of emergence of the left posterior nerve rootlets.... The venous anastomosis “a” forms a loop, both legs of which run parallel to the central canal: one goes down, the other one goes up and follows a S-shaped curve before reaching the trunk of the corresponding central vein “c” (p 146, P.G. translation).

In 1939, Herren and Alexander¹⁴ further defined the centrodorsolateral anastomosis as being formed by a central vein connecting to a paracentral vein, itself continuing as a long oblique venous channel that terminates in the ipsilateral PLSV (Fig 9B).

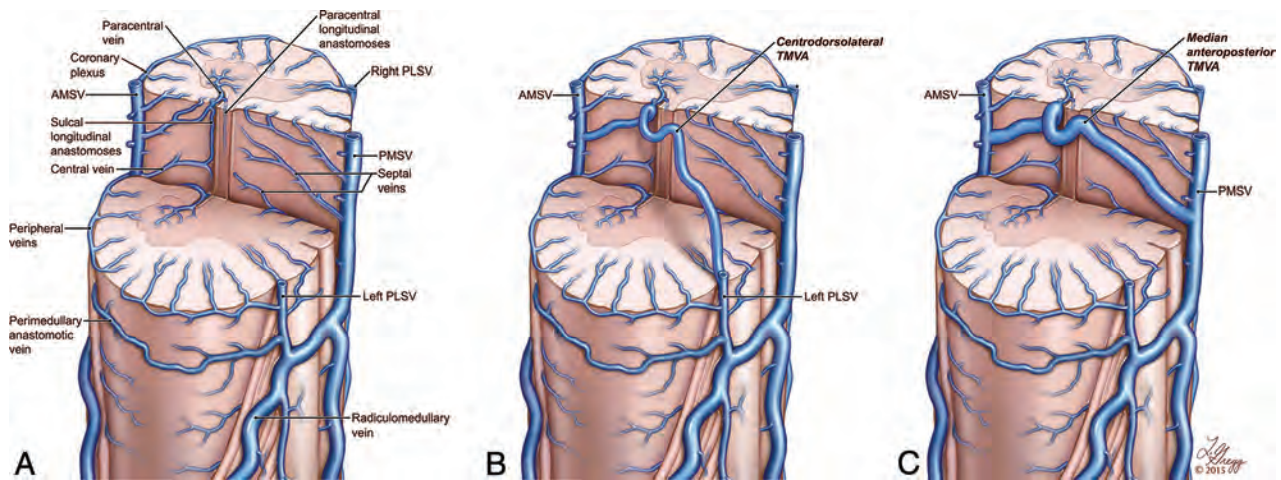


FIG 9. Artistic representation of the normal anatomy of the spinal venous system, emphasizing the 2 classic types of transmedullary venous anastomoses. A, The central veins establish longitudinal connections within the central gray matter (paracentral longitudinal anastomosis) and in the depth of the anteromedian fissure (sulcal longitudinal anastomosis). B, A centrodorsolateral TMVA is formed by a central vein connecting to a paracentral vein and continuing as a long oblique venous channel joining the ipsilateral PLSV. C, A median anteroposterior TMVA is formed by a large connection established between a central vein and a septal vein, with a typical loop around the central canal. Copyright 2015 Lydia Gregg.



FIG 10. Illustration reproduced from Kadyi H. *Über die Blutgefäße des Menschlichen Rückenmarkes*. Lemberg: Gubryonowisz & Schmidt; 1889 (Fig 9, page 146) shows the first TMVA depiction known to the authors (ie, a sagittal view of a centrodorsolateral TMVA). The vein, designated as v, courses laterally and posteriorly from the mid-sagittal plane to a PLSV. The segment a connects to a central vein c after looping around the central canal.

They specifically named this last oblique portion “centrodorsolateral anastomosis,” while Crock and Yoshizawa¹⁶ applied the term to the whole anastomotic chain, from the AMSV to the PLSV.

Crock and Yoshizawa¹⁶ described a second type of TMVA linking the AMSV to the PMSV, the median anteroposterior anastomosis (Fig 9C). This type of TMVA probably also derives from a connection established between a central vein and a paracentral

vein, which then continues dorsally as a septal vein rather than adopting a dorsolateral course.¹⁶

Case 7 revealed 2 previously unreported TMVA configurations. The first was a median anteroposterior anastomosis with a duplicated origin from the AMSV and from the surrounding venous network (Fig 7B); the second combined median anteroposterior and centrodorsolateral characteristics, draining both dorsally into the PMSV and dorsolaterally into a PLSV (Fig 7D).

While initially believed to be rare,¹² both types of TMVAs were consistently documented in a microangiographic study of post-mortem material, though with irregular sizes and topographic distributions.¹⁵ The highest prevalence was noted in the upper cervical and cervicothoracic regions (up to 2 TMVAs per centimeter). The largest channels were also found in the cervicothoracic region.¹⁵ The distance separating 2 TMVAs was increased in the lower thoracic region, while no TMVAs were noted in the lumbar region. They were occasionally documented at the level of the conus medullaris, either supplementing or replacing the anastomotic venous circle of the conus.¹⁵ Centrodorsolateral TMVAs were more frequent but generally smaller (0.1–0.2 mm) than median anteroposterior TMVAs (0.3–0.7 mm).¹⁵ Both types can be sinuous or can adopt a relatively straight intramedullary path.¹⁵ The relation between the size, number, and course of TMVAs and factors such as age and sex is currently unknown.

TMVAs receive relatively few intramedullary tributaries even though they are generally comparable in size with the principal longitudinal venous axes.^{14,15} Herren and Alexander¹⁴ proposed that rather than having a drainage function, TMVAs might help regulate pressure and flow by rapidly transferring blood from one longitudinal axis to another.¹⁴ This hypothesis was later supported by Thron and Rossberg,¹⁵ who suggested a correlation between the higher cervical and cervicothoracic prevalence of TMVAs and the greater motion range of the spine and spinal cord at these levels. TMVAs might thus protect the principal venous axes from pressure variations related to compression occurring during hyperflexion and hyperextension of the cervical spine.¹⁵

Our last example (case 8) suggests that under abnormal circumstances leading to impaired venous flow, TMVAs may indeed act as alternate drainage pathways limiting the risk of venous engorgement and ischemia (Fig 8). In this patient, a sulcal longitudinal anastomosis also appeared to play the role of a collateral pathway in the area compressed by protruding disk material.

Recognizing TMVAs as normal structures carries both diagnostic and therapeutic implications. For example, TMVAs were recently used as an access route for successful obliteration of a perimedullary arteriovenous fistula.⁸ Median anteroposterior TMVAs have been documented by contrast-enhanced MRA and by DSA,^{6,7,17} while centrodorsolateral TMVAs have, to our knowledge, not been imaged clinically until now, probably because of their smaller size.¹⁵ New imaging methods such as spinal SWI also require a sound understanding of the spinal venous system anatomy and its variants, for example, to differentiate TMVAs from small intraparenchymal hemorrhages.¹⁸

In summary, the introduction of novel imaging techniques, such as spinal FPCA or SWI, can strengthen our still deficient understanding of medullary venous pathology. This improved imaging ability creates the need for a more intricate knowledge of the anatomy of the spinal venous system. This article reports several types of TMVAs documented by FPCA. Some of these vessels were previously known, in general from postmortem investigations, while others had not yet been described. Appreciating the existence of TMVAs is clinically important because these channels may be confused with intramedullary hemorrhages or vascular malformations on noninvasive imaging.

Disclosures: Philippe Gailloud—UNRELATED: Consultancy: Codman Neurovascular; Grants/Grants Pending: Siemens Medical*; Stock/Stock Options: Artventive Medical; Other: Consultant for Penumbra. *Money paid to the institution.

REFERENCES

1. Akpek S, Brunner T, Benndorf G, et al. **Three-dimensional imaging and cone beam volume CT in C-arm angiography with flat panel detector.** *Diagn Interv Radiol* 2005;11:10–13
2. Zellerhoff M, Scholz B, Ruehrnschopf EP, et al. **Low contrast 3D**

- reconstruction from C-arm data.** *SPIE Proceedings* 2005;5745:646–55
3. Chen J, Ethiat T, Gailloud P. **Flat panel catheter angiogram of the spinal venous system: an enhanced venous phase for spinal digital subtraction angiography.** *AJNR Am J Neuroradiol* 2012;33:1875–81
4. Pearl MS, Chen JX, Gregg L, et al. **Angiographic detection and characterization of “cryptic venous anomalies” associated with spinal cord cavernous malformations using flat-panel catheter angiography.** *Neurosurgery* 2012;71:125–32
5. Aadland TD, Thielen KR, Kaufmann TJ, et al. **3D C-arm conebeam CT angiography as an adjunct in the precise anatomic characterization of spinal dural arteriovenous fistulas.** *AJNR Am J Neuroradiol* 2010;31:476–80
6. Thron AK. **Vascular anatomy of the spine and spinal cord.** In: Hurst RW, Rosenwasser RH, eds. *Neurointerventional Management: Diagnosis and Treatment.* Boca Raton, FL: CRC Press; 2012:40–58
7. Krings T. **Vascular malformations of the spine and spinal cord*: anatomy, classification, treatment.** *Clin Neuroradiol* 2010;20:5–24
8. Giese A, Winkler PA, Schichor C, et al. **A transmedullary approach to occlusion of a ventral perimedullary arteriovenous fistula of the thoracic spinal cord.** *Neurosurgery* 2010;66:611–15
9. Suh T, Alexander L. **Vascular system of the human spinal cord.** *Arch Neurol Psychiatry* 1939;41:659–77
10. Zhang ZA, Nonaka H, Hatori T. **The microvasculature of the spinal cord in the human adult.** *Neuropathology* 1997;17:32–42
11. Kadyi H. *Über die Blutgefäße des Menschlichen Rückenmarkes.* Lemberg: Gubryonowicz & Schmidt; 1889
12. Gillilan LA. **Veins of the spinal cord: anatomic details—suggested clinical applications.** *Neurology* 1970;20:860–68
13. Lazorthes G, Gouaze A, Djindjian R. *Vascularisation et circulation de la moelle épinière: anatomie, physiologie, pathologie, angiographie.* Paris: Masson & Cie; 1973
14. Herren RY, Alexander L. **Sulcal and intrinsic blood vessels of the human spinal cord.** *Arch Neurol Psychiatry* 1939;41:678–87
15. Thron AK, Rossberg C, Mironov A. *Vascular Anatomy of the Spinal Cord: Neuroradiological Investigations and Clinical Syndromes.* New York: Springer-Verlag Wien; 1988
16. Crock HV, Yoshizawa H. *The Blood Supply of the Vertebral Column and Spinal Cord in Man.* New York: Springer-Verlag; 1977
17. Thron A, Mull M. **Blood vessels of the spinal cord: anatomical and MR-imaging correlation.** *Rivista di Neuroradiologia* 2004;17:277–81
18. Ishizaka K, Kudo K, Fujima N, et al. **Detection of normal spinal veins by using susceptibility-weighted imaging.** *J Magn Reson Imaging* 2010;31:32–38

Celebrating 35 years of the AJNR

July 1980 edition

317

Images of the Optic Nerve: Anatomic-CT Correlation

Renate Unsold*,¹
Jack DeGroot†
Thomas H. Newton‡

The course of the intraorbital part of the optic nerve, as demonstrated on anatomic sections in various planes, is correlated with the appearance of the nerve in computed tomographic (CT) images. Discrepancies between the anatomic and CT appearance are analyzed and discussed. Since the optic nerve has a sinuous course to both the horizontal and vertical planes, no true axial or sagittal section can be entirely parallel to the nerve. Any section will transect the optic nerve obliquely, leading to an apparent hypodensity or "thinning" of certain segments as shown on CT. The appearance of the course of the nerve on reformatted CT images depends on the plane of the original CT section. Computed tomograms that are obtained with the eye in primary position do not allow reliable judgments regarding the course and size of the optic nerve.

Authors have indicated that detailed computed tomographic (CT) examination of the optic nerve, particularly in axial sections, is difficult [1-3]. The optic nerve cannot be visualized along its entire orbital course in thin axial sections. It usually appears irregular in caliber and density. The reason for this irregularity has been attributed to its sinuosity and rigidity within the orbit. We analyzed the appearance of the optic nerve in various axial, coronal, and sagittal anatomic sections and then correlated the anatomic and CT appearances in corresponding planes.

Materials and Methods

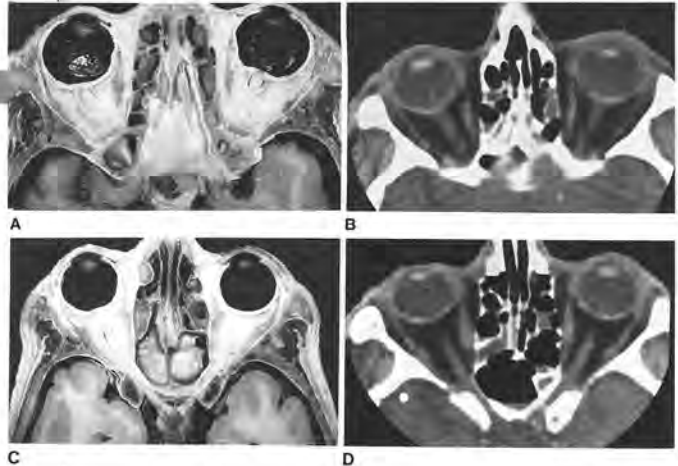
The anatomic part of the study consisted of an analysis of 2-3 mm slices of heads of embalmed human cadavers. The sections were made in various planes using a fine-tooth band saw. The axial planes chosen were those most frequently recommended for CT (Fig 1). In addition, coronal, sagittal, and oblique (through the optic nerve) sections were obtained.

The CT part of the study consisted of scanning a fresh human cadaver using the General Electric 8800 scanner, with the eyes in neutral position, looking straight on. A 1.5 mm collimator was used and sections were obtained at 1.5 mm intervals in the same axial planes described in figure 1. Reformatted views in coronal, sagittal, and oblique planes were obtained from the axial sections performed at an angle of -20° to the orbitobasilar bisectrix.

Results

Axial Planes

The appearance of the optic nerve is determined by the angulation of the axial plane of section. Sections obtained in an axial plane of -20° to the orbitobasilar bisectrix first encounter the most distal part of the optic nerve at the superior



Received December 31, 1977; accepted after revision February 11, 1980.

*R. Unsold is a Neuroanatomy Fellow, University of California, School of Medicine.

†Department of Radiology, Room M-336, University of California, School of Medicine, San Francisco, CA 94143.

‡Permanent address: Universitäts-Augenklinik, Freiburg, W. Germany.

§Department of Anatomy, University of California, School of Medicine, San Francisco, CA 94143.

This article appears in July/August 1980 AJNR and October 1980 AJR.

AJNR 1:317-320, July/August 1980
0195-9581/80/0104-317\$ 03.00
© American Roentgen Ray Society

295

Sonography of Ventricular Size and Germinal Matrix Hemorrhage in Premature Infants

D. A. London†
B. A. Carroll
D. R. Enzmann

Using the anterior fontanelle as an acoustic window, high resolution gray scale sonography brain scans with mobile apparatus were obtained in 26 premature infants. The sonographic technique provided accurate assessment of ventricular size and detected the subependymal germinal matrix and intraventricular hemorrhages. Ventricular size measurements correlated closely with computed tomographic (CT) determinations ($r = 0.83-0.97$) in 29 infants. Sonography imaged the hemorrhages as areas of increased echogenicity with mass effect located characteristically in the region of the caudate nucleus. The size of the hemorrhages could be grossly estimated, but the full extent of hemorrhages was better delineated by CT. Sonography seemed superior in detecting small hemorrhages that were isodense with surrounding brain on CT. Despite its advantages of being painless, accurate, easy of examination, and cost, our sonography technique had limitations. False-negative sonograms occurred when the hemorrhage was located only in the posterior aspects of the ventricular system. Small hemorrhages in the caudate could be missed by either CT or sonography because of sampling error. Recognition of other disease processes was limited with sonography. The sonographic brain scan is a good initial test for high risk premature infants suspected of having subependymal germinal matrix and intraventricular hemorrhages. If the sonogram is negative or not typical for subependymal germinal matrix and intraventricular hemorrhages, CT is indicated.

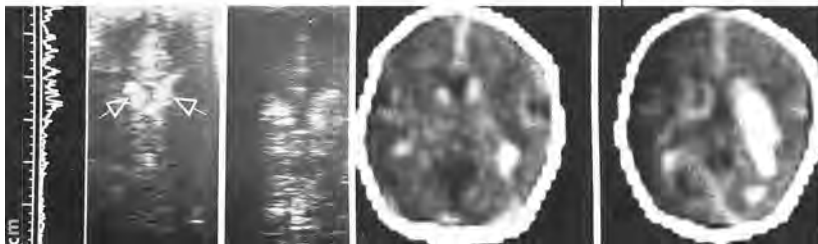
Intracranial hemorrhage is recognized as a significant factor in mortality of premature infants. Although minor advances in respiratory support and infection control have resulted in greater survival among these infants, improvements have also resulted in a significant shift in neonatal pathology. In 1972, only 25% of neonatal deaths were associated with intracranial hemorrhage; in 1978, this figure was 65% [1-3].

Computed tomographic (CT) brain scans permit accurate and noninvasive detection of subependymal germinal matrix and intraventricular hemorrhage in premature infants as well as assessment of possible sequelae such as hydrocephalus and parencephaly [4-6]. Because the accuracy of CT exceeds that of clinical examination in detecting such hemorrhages, the reported incidence of such hemorrhages has increased dramatically [5-8]. In premature infants weighing less than 1,500 g, the incidence by CT is 43%-70% [7, 8]. Unfortunately, the widespread and serial use of CT scanning for detection of hemorrhages and its sequelae is logistically limited in these fragile infants because of difficulties in transport, sedation, temperature maintenance, and respiratory support. The risk of repeated exposure to ionizing radiation must also be considered.

Sonography has been useful in determining ventricular size in both term infants and young children [9-13]. We report the use of a mobile sonography unit with a high resolution probe for measuring ventricular size and detecting subependymal germinal matrix and intraventricular hemorrhages in premature infants.

Subjects and Methods

An orbital sonography unit was adapted for use with premature infants. The linear array, high frequency (7.2 MHz) probe produces a real time, rectangular 3 x 6 cm image that can be frozen for photogramming with a standard Polaroid camera. The axial resolution is 0.2-0.3 mm. The lateral resolution is 2 mm at less than 2 cm (near field) and 4-5 mm at 9



Received November 26, 1977; accepted after revision February 12, 1980.

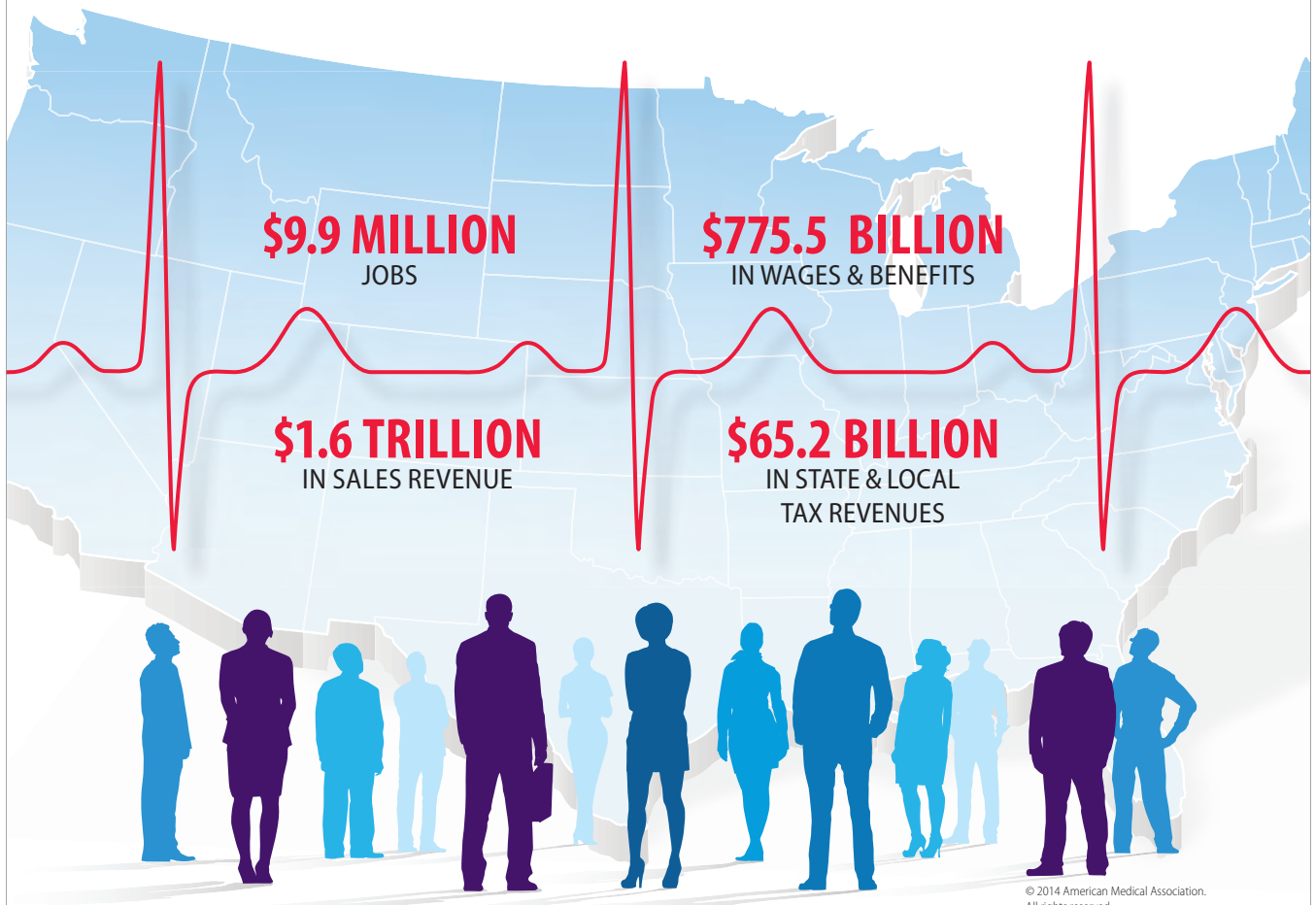
This article was supported in part by General Clinical Research Centers Program, Division of Research Services, National Institutes of Health grant 09-91.

†All authors: Department of Radiology, Diagnostic Radiology Division, Stanford University School of Medicine, Stanford, CA 94305. Address reprint requests to D. R. Enzmann.

This article appears in July/August 1980 AJNR and October 1980 AJR.

AJNR 1:295-300, July/August 1980
0195-9581/80/0104-295\$ 03.00
© American Roentgen Ray Society

PHYSICIANS BOOST THE ECONOMY.



© 2014 American Medical Association. All rights reserved.

See the effects across the nation.

The American Medical Association 2014 Economic Impact Study shows how much physicians add to the economic health of our nation.

Check the effect physicians have on the U.S. economy by viewing the entire national report from the AMA Advocacy Resource Center at ama-assn.org/go/eis.



Please activate your 2015 AMA membership by calling (800) 262-3211 or visit ama-assn.org/go/join.



Simplify

the MOC Process



Manage

your CME Credits Online

CMEgateway.org

Available to Members of Participating Societies

American Board of Radiology (ABR)
American College of Radiology (ACR)
American Roentgen Ray Society (ARRS)
American Society of Neuroradiology (ASNR)
Commission on Accreditation of Medical
Physics Educational Programs, Inc. (CAMPEP)
Radiological Society of North America (RSNA)
Society of Interventional Radiology (SIR)
SNM
The Society for Pediatric Radiology (SPR)

It's Easy and Free!

Log on to CME Gateway to:

- View or print reports of your CME credits from multiple societies from a single access point.
- Print an aggregated report or certificate from each participating organization.
- Link to SAMs and other tools to help with maintenance of certification.

American Board of Radiology (ABR) participation!

By activating ABR in your organizational profile, your MOC-fulfilling CME and SAM credits can be transferred to your own personalized database on the ABR Web site.

Sign Up Today!

go to CMEgateway.org

Target® Detachable Coil

See package insert for complete indications, contraindications, warnings and instructions for use.

INTENDED USE / INDICATIONS FOR USE

Target Detachable Coils are intended to endovascularly obstruct or occlude blood flow in vascular abnormalities of the neurovascular and peripheral vessels.

Target Detachable Coils are indicated for endovascular embolization of:

- Intracranial aneurysms
- Other neurovascular abnormalities such as arteriovenous malformations and arteriovenous fistulae
- Arterial and venous embolizations in the peripheral vasculature

CONTRAINDICATIONS

None known.

POTENTIAL ADVERSE EVENTS

Potential complications include, but are not limited to: allergic reaction, aneurysm perforation and rupture, arrhythmia, death, edema, embolus, headache, hemorrhage, infection, ischemia, neurological/intracranial sequelae, post-embolization syndrome (fever, increased white blood cell count, discomfort), TIA/stroke, vasospasm, vessel occlusion or closure, vessel perforation, dissection, trauma or damage, vessel rupture, vessel thrombosis. Other procedural complications including but not limited to: anesthetic and contrast media risks, hypotension, hypertension, access site complications.

WARNINGS

- Contents supplied STERILE using an ethylene oxide (EO) process. Do not use if sterile barrier is damaged. If damage is found, call your Stryker Neurovascular representative.
- For single use only. Do not reuse, reprocess or resterilize. Reuse, reprocessing or resterilization may compromise the structural integrity of the device and/or lead to device failure which, in turn, may result in patient injury, illness or death. Reuse, reprocessing or resterilization may also create a risk of contamination of the device and/or cause patient infection or cross-infection, including, but not limited to, the transmission of infectious disease(s) from one patient to another. Contamination of the device may lead to injury, illness or death of the patient.
- After use, dispose of product and packaging in accordance with hospital, administrative and/or local government policy.
- **This device should only be used by physicians who have received appropriate training in interventional neuroradiology or interventional radiology and preclinical training on the use of this device as established by Stryker Neurovascular.**
- Patients with hypersensitivity to 316LVM stainless steel may suffer an allergic reaction to this implant.
- MR temperature testing was not conducted in peripheral vasculature, arteriovenous malformations or fistulae models.
- The safety and performance characteristics of the Target Detachable Coil System (Target Detachable Coils, InZone Detachment Systems,

delivery systems and accessories) have not been demonstrated with other manufacturer's devices (whether coils, coil delivery devices, coil detachment systems, catheters, guidewires, and/or other accessories). Due to the potential incompatibility of non Stryker Neurovascular devices with the Target Detachable Coil System, the use of other manufacturer's device(s) with the Target Detachable Coil System is not recommended.

- To reduce risk of coil migration, the diameter of the first and second coil should never be less than the width of the ostium.
- In order to achieve optimal performance of the Target Detachable Coil System and to reduce the risk of thromboembolic complications, it is critical that a continuous infusion of appropriate flush solution be maintained between a) the femoral sheath and guiding catheter, b) the 2-tip microcatheter and guiding catheters, and c) the 2-tip microcatheter and Stryker Neurovascular guidewire and delivery wire. Continuous flush also reduces the potential for thrombus formation on, and crystallization of infusate around, the detachment zone of the Target Detachable Coil.
- Do not use the product after the "Use By" date specified on the package.
- Reuse of the flush port/dispenser coil or use with any coil other than the original coil may result in contamination of, or damage to, the coil.
- Utilization of damaged coils may affect coil delivery to, and stability inside, the vessel or aneurysm, possibly resulting in coil migration and/or stretching.
- The fluoro-saver marker is designed for use with a Rotating Hemostatic Valve (RHV). If used without an RHV, the distal end of the coil may be beyond the alignment marker when the fluoro-saver marker reaches the microcatheter hub.
- If the fluoro-saver marker is not visible, do not advance the coil without fluoroscopy.
- Do not rotate delivery wire during or after delivery of the coil. Rotating the Target Detachable Coil delivery wire may result in a stretched coil or premature detachment of the coil from the delivery wire, which could result in coil migration.
- Verify there is no coil loop protrusion into the parent vessel after coil placement and prior to coil detachment. Coil loop protrusion after coil placement may result in thromboembolic events if the coil is detached.
- Verify there is no movement of the coil after coil placement and prior to coil detachment. Movement of the coil after coil placement may indicate that the coil could migrate once it is detached.
- Failure to properly close the RHV compression fitting over the delivery wire before attaching the InZone® Detachment System could result in coil movement, aneurysm rupture or vessel perforation.
- Verify repeatedly that the distal shaft of the catheter is not under stress before detaching the Target Detachable Coil. Axial compression or tension forces could be stored in the 2-tip microcatheter causing the tip to move during coil delivery. Microcatheter tip movement could cause the aneurysm or vessel to rupture.
- Advancing the delivery wire beyond the microcatheter tip once the coil has been detached involves risk of aneurysm or vessel perforation.
- The long term effect of this product on extravascular tissues has not been established so care should be taken to retain this device in the intravascular space.

Damaged delivery wires may cause detachment failures, vessel injury or unpredictable distal tip response during coil deployment. If a delivery wire is damaged at any point during the procedure, do not attempt to straighten or otherwise repair it. Do not proceed with deployment or detachment. Remove the entire coil and replace with undamaged product.

- After use, dispose of product and packaging in accordance with hospital, administrative and/or local government policy.

CAUTIONS / PRECAUTIONS

- Federal Law (USA) restricts this device to sale by or on the order of a physician.
- Besides the number of InZone Detachment System units needed to complete the case, there must be an extra InZone Detachment System unit as back up.
- Removing the delivery wire without grasping the introducer sheath and delivery wire together may result in the detachable coil sliding out of the introducer sheath.
- Failure to remove the introducer sheath after inserting the delivery wire into the RHV of the microcatheter will interrupt normal infusion of flush solution and allow back flow of blood into the microcatheter.
- Some low level overhead light near or adjacent to the patient is required to visualize the fluoro-saver marker; monitor light alone will not allow sufficient visualization of the fluoro-saver marker.
- Advance and retract the Target Detachable Coil carefully and smoothly without excessive force. If unusual friction is noticed, slowly withdraw the Target Detachable Coil and examine for damage. If damage is present, remove and use a new Target Detachable Coil. If friction or resistance is still noted, carefully remove the Target Detachable Coil and microcatheter and examine the microcatheter for damage.
- If it is necessary to reposition the Target Detachable Coil, verify under fluoroscopy that the coil moves with a one-to-one motion. If the coil does not move with a one-to-one motion or movement is difficult, the coil may have stretched and could possibly migrate or break. Gently remove both the coil and microcatheter and replace with new devices.
- Increased detachment times may occur when:
 - Other embolic agents are present.
 - Delivery wire and microcatheter markers are not properly aligned.
 - Thrombus is present on the coil detachment zone.
- Do not use detachment systems other than the InZone Detachment System.
- Increased detachment times may occur when delivery wire and microcatheter markers are not properly aligned.
- Do not use detachment systems other than the InZone Detachment System.



Stryker Neurovascular
47900 Bayside Parkway
Fremont, CA 94538-6515

stryker.com/neurovascular

Date of Release: FEB/2014

EX_EN_US

Copyright © 2014 Stryker
NV00006677.AA

Trevo® XP ProVue Retrievers

See package insert for complete indications, complications, warnings, and instructions for use.

INDICATIONS FOR USE

The Trevo Retriever is intended to restore blood flow in the neurovasculature by removing thrombus in patients experiencing ischemic stroke within 8 hours of symptom onset. Patients who are ineligible for intravenous tissue plasminogen activator (IV t-PA) or who fail IV t-PA therapy are candidates for treatment.

COMPLICATIONS

Procedures requiring percutaneous catheter introduction should not be attempted by physicians unfamiliar with possible complications which may occur during or after the procedure. Possible complications include, but are not limited to, the following: air embolism; hematoma or hemorrhage at puncture site; infection; distal embolization; pain/headache; vessel spasm, thrombosis, dissection, or perforation; emboli; acute occlusion; ischemia; intracranial hemorrhage; false aneurysm formation; neurological deficits including stroke, and death.

COMPATIBILITY

3x20 mm retrievers are compatible with Trevo® Pro 14 Microcatheters (REF 90231) and Trevo® Pro 18 Microcatheters (REF 90238). 4x20 mm retrievers are compatible with Trevo® Pro 18 Microcatheters (REF 90238). Compatibility of the Retriever with other microcatheters has not been established. Performance of the Retriever device may be impacted if a different microcatheter is used. The Merci® Balloon Guide Catheters are recommended for use during thrombus removal procedures. Retrievers are compatible with the Abbott Vascular DOC® Guide Wire Extension (REF 22260).

WARNINGS

- Contents supplied STERILE, using an ethylene oxide (EO) process. Nonpyrogenic.
- To reduce risk of vessel damage, adhere to the following recommendations:
 - Take care to appropriately size Retriever to vessel diameter at

intended site of deployment.

- Do not perform more than six (6) retrieval attempts in same vessel using Retriever devices.
- Maintain Retriever position in vessel when removing or exchanging Microcatheter.
- To reduce risk of kinking/fracture, adhere to the following recommendations:
 - Immediately after unsheathing Retriever, position Microcatheter tip marker just proximal to shaped section. Maintain Microcatheter tip marker just proximal to shaped section of Retriever during manipulation and withdrawal.
 - Do not rotate or torque Retriever.
 - Use caution when passing Retriever through stented arteries.
- Do not resterilize and reuse. Structural integrity and/or function may be impaired by reuse or cleaning.
- The Retriever is a delicate instrument and should be handled carefully. Before use and when possible during procedure, inspect device carefully for damage. Do not use a device that shows signs of damage. Damage may prevent device from functioning and may cause complications.
- Do not advance or withdraw Retriever against resistance or significant vasospasm. Moving or torquing device against resistance or significant vasospasm may result in damage to vessel or device. Assess cause of resistance using fluoroscopy and if needed resheath the device to withdraw.
- If Retriever is difficult to withdraw from the vessel, do not torque Retriever. Advance Microcatheter distally, gently pull Retriever back into Microcatheter, and remove Retriever and Microcatheter as a unit. If undue resistance is met when withdrawing the Retriever into the Microcatheter, consider extending the Retriever using the Abbott Vascular DOC guidewire extension (REF 22260) so that the Microcatheter can be exchanged for a larger diameter catheter such as a DAC® catheter. Gently withdraw the Retriever into the larger diameter catheter.
- Administer anti-coagulation and anti-platelet medications per standard institutional guidelines.

PRECAUTIONS

- Prescription only – device restricted to use by or on order of a physician.
- Store in cool, dry, dark place.
- Do not use open or damaged packages.
- Use by "Use By" date.
- Exposure to temperatures above 54°C (130°F) may damage device and accessories. Do not autoclave.
- Do not expose Retriever to solvents.
- Use Retriever in conjunction with fluoroscopic visualization and proper anti-coagulation agents.
- To prevent thrombus formation and contrast media crystal formation, maintain a constant infusion of appropriate flush solution between guide catheter and Microcatheter and between Microcatheter and Retriever or guidewire.
- Do not attach a torque device to the shaped proximal end of DOC® Compatible Retriever. Damage may occur, preventing ability to attach DOC® Guide Wire Extension.



Concentric Medical
301 East Evelyn
Mountain View, CA 94041

EC REP

EMERGO Europe
Molenstraat 15
2513 BH, The Hague
The Netherlands

CE 0459

Stryker Neurovascular
47900 Bayside Parkway
Fremont, CA 94538-6515

stryker.com/neurovascular
stryker.com/emea/neurovascular

Date of Release: JUN/2014

EX_EN_GL

Copyright © 2014 Stryker
NV00009028.AA



Target[®] DETACHABLE COILS



Smooth and Stable

Whether you are framing, filling or finishing, Target Detachable Coils deliver consistently smooth deployment and exceptional microcatheter stability. Focused on design, Target Coils feature a host of advantages to ensure the high-powered performance you demand.

For more information, please visit www.strykerneurovascular.com/Target or contact your local Stryker Neurovascular sales representative.

stryker[®]
Neurovascular

COILING OPTIMIZED



NOW AVAILABLE

**BARRICADE COMPLEX
FINISHING COIL**

- ◆ Extremely soft profile of The Barricade Finishing coil now in a complex shape
- ◆ Excellent microcatheter stability for confident coil placement
- ◆ Available in a size range of 1mm-5mm

BARRICADE™ COIL SYSTEM



MADE IN AMERICA

The Barricade Coil System is intended for the endovascular embolization of intracranial aneurysms and other neurovascular abnormalities such as arteriovenous malformations and arteriovenous fistulae. The System is also intended for vascular occlusion of blood vessels within the neurovascular system to permanently obstruct blood flow to an aneurysm or other vascular malformation and for arterial and venous embolizations in the peripheral vasculature. Refer to the instructions for use for complete product information.

18 TECHNOLOGY DRIVE #169, IRVINE CA 92618

p: 949.788.1443 | f: 949.788.1444

WWW.BLOCKADEMEDICAL.COM

MKTG-031 Rev. A

